

# Dissertation

submitted to the

Combined Faculties for the Natural Sciences and for Mathematics  
of the Ruperto-Carola University of Heidelberg, Germany

for the degree of

Doctor of Natural Sciences

Put forward by

**Dipl.-Phys. Martin Horbanski**

born in Reutlingen, Germany

Date of oral examination: December 22<sup>nd</sup> 2015



# Emissions and Distribution of Reactive Iodine from Seaweed in Coastal Regions

Investigations using new  
mobile and in-situ DOAS techniques

Referees: Prof. Dr. Ulrich Platt  
Priv.-Doz. Dr. Christoph S. Garbe



## Abstract

Reactive iodine species impact atmospheric chemistry in several ways. They play an important role in the process of ozone destruction at mid-latitudes and possibly in polar regions. Reactive iodine compounds (besides bromine) also affect the atmospheric cleaning mechanisms by changing its oxidation capacity. Recent field studies indicate that reactive iodine may impact the local climate in coastal areas by playing a key role in the formation of new particles which could influence cloud micro physical properties. Particularly high concentrations of the reactive iodine are found at mid-latitude coastal sites, which are most likely emitted by seaweed exposed to oxidative stress during low tide. However, there is still very limited knowledge on the involved seaweed species and their contribution to local, regional and global iodine emissions and also the potential iodine mediated particle formation.

In the frame of this work a new mobile Open Path CE-DOAS instrument was developed for direct measurements of IO, one of the most important reactive iodine species. It was applied successfully in two field campaigns on the Irish west coast for measurements in the inter-tidal zone, directly above air-exposed seaweed patches. These measurements for the first time identify exposed seaweeds as IO “hot-spots” with very high IO mixing ratios often exceeding 50 ppt. This shows that local IO concentrations are sufficiently high to initiate the strong particle nucleation events previously observed at the Irish West Coast.

Furthermore, during the field campaigns on the Irish west coast, combined LP-DOAS and CE-DOAS measurements were applied, which extended previous observations of reactive iodine at Mace Head and the close by MRI to further locations. These observations now cover ten shores. This study showed that the major sources of reactive iodine at the Irish West coast are wave sheltered shores and not, as previously believed, wave exposed shores, like Mace Head. Since seaweed beds at wave sheltered shores cove larger areas and are longer exposed to air, this shows that Irish, and most likely also global, iodine emissions from coastal areas should be much higher compared to previous estimates based on wave exposed shores. From this finding a yearly emission of  $2 \cdot 10^8 \text{ g}_I \text{ a}^{-1}$  to  $3 \cdot 10^9 \text{ g}_I \text{ a}^{-1}$  is estimated for global coastal areas.

In a third field study on the east coast of the New Zealand south island, for the first time high IO mixing ratios of up to 68 ppt were observed on a southern hemispheric coast. Four, previously uninvestigated, seaweed species were identified as emitters of reactive iodine species and emission rates were estimated. The observations in New Zealand showed also distinct differences in the seaweed distribution to northern hemispheric locations which need to be considered in global estimates of coastal iodine emissions.

## Zusammenfassung

Reaktive Iodverbindungen beeinflussen die Atmosphärenchemie in vielerlei Hinsicht. Sie spielen eine wichtige Rolle bei dem Ozonabbau in mittleren Breiten sowie möglicherweise in Polargebieten. Reaktive Iodverbindungen beeinflussen auch die Selbstreinigung der Atmosphäre, indem sie die Oxidationskapazität verändern. Neue Feldstudien weisen darauf hin, dass reaktives Iod ebenfalls eine zentrale Rolle bei der Partikelbildung an Küsten spielt und somit durch Beeinflussung der mikrophysikalischen Eigenschaften von Wolken das lokale Klima beeinflussen könnte. Besonders hohe Konzentrationen vom reaktivem Iod findet man an Küstenregionen mittlerer Breiten, wo sie höchstwahrscheinlich von Makroalgen emittiert werden, wenn diese während der Ebbe unter oxidativem Stress stehen. Die bei diesen Prozessen beteiligten Makroalgen Spezies und ihr Beitrag zu den lokalen, regionalen und globalen Iod Emissionen und ihr Beitrag zur Iod basierten Partikelbildung ist bisher unzureichend Erforscht.

Im Rahmen dieser Arbeit wurde ein neues mobiles Open Path CE-DOAS Instrument für die direkte optische Messung von IO, einer der wichtigsten reaktiven Iodverbindungen, entwickelt. Dieses wurde erfolgreich in zwei Feldkampagnen an der Irischen Küste eingesetzt. Hierbei wurden Messungen in der Gezeitenzone direkt über der Umgebungsluft ausgesetzten Makroalgen durchgeführt. Diese Messungen erlauben die erstmalige Identifizierung von, der Umgebungsluft ausgesetzten, Makroalgen als IO "hot-spots" mit hohen IO Mischungsverhältnissen die oft 50 ppt übersteigen. Dies zeigt, dass die lokalen IO Konzentrationen hoch genug sind um die starke Partikelbildung zu initiieren, welche zuvor an der Irischen Westküste beobachtet wurde.

Des Weiteren wurden während der Messkampagnen an der Irischen Westküste kombinierte LP-DOAS und CE-DOAS Messungen durchgeführt, um die vorherigen Messungen in Mace Head und dem nahegelegenen MRI auf weiter Küstenabschnitte zu erweitern. Diese Studie deckt zehn Küstenabschnitte ab und zeigt, dass die Hauptquellen von reaktivem Iod brandungsgeschützte Küsten sind und nicht wie zu angenommen Küsten mit starker Brandung, wie zum Beispiel vor Mace Head, sind. An brandungsgeschützten Küsten bedecken die Makroalgen größere Flächen in der Gezeitenzone und sind länger der Luft ausgesetzt. Damit zeigt diese Studie, dass die Iod Emissionen an den Irischen und höchstwahrscheinlich auch den weltweiten Küsten deutlich größer sind als vorher angenommen aufgrund der Beobachtungen an Küsten mit starker Brandung. Basierend auf diesen neuen Erkenntnissen wurden für die weltweiten Küstenregionen jährliche Iodemissionen von  $2 \cdot 10^8 \text{ g}_I \text{ a}^{-1}$  bis  $3 \cdot 10^9 \text{ g}_I \text{ a}^{-1}$  abgeschätzt.

In einer dritten Feldstudie an der Ostküste der Neuseeländischen Südinsel konnten zum ersten Mal hohe IO Mischungsverhältnisse von bis zu 68 ppt an einer Küste auf der Südhalbkugel nachgewiesen werden. Vier zuvor noch nicht untersuchte Makroalgenpezies konnten als Emitter von reaktiven Iodverbindungen nachgewiesen werden, und deren Emissionsraten konnten abgeschätzt werden. Die Studie in Neuseeland zeigt auch charakteristische Unterschiede in der räumlichen Verteilung der Makroalgen im Vergleich zur Nordhemisphäre, die in zukünftigen globalen Abschätzungen der Iodemissionen von Küsten berücksichtigt werden müssen.

# Contents

<b>I. Introduction and Methods</b>	<b>1</b>
<b>1. Motivation</b>	<b>3</b>
1.1. Aims of This Work: . . . . .	7
1.2. Outline of the Thesis . . . . .	7
<b>2. Tropospheric Chemistry</b>	<b>9</b>
2.1. Quantification of Gas Abundances . . . . .	10
2.2. Tropospheric Radical Chemistry . . . . .	10
2.2.1. The Hydroxyl Radical OH . . . . .	11
2.2.2. Tropospheric Ozone . . . . .	14
2.2.3. The Nitrate Radical NO <sub>3</sub> . . . . .	17
2.3. Tropospheric Halogen Chemistry . . . . .	17
2.3.1. Impact of Reactive Halogen Species on Tropospheric Chemistry . .	19
2.3.2. IO in Semipolluted Environments . . . . .	24
2.3.3. Iodine Mediated Particle Formation . . . . .	26
2.3.4. Sources of Reactive Halogen Compounds . . . . .	27
<b>3. Seaweed</b>	<b>29</b>
3.1. Iodine accumulation and release by seaweeds . . . . .	30
3.1.1. Accumulation of Iodine . . . . .	31
3.1.2. Release of Molecular Iodine . . . . .	32
3.1.3. Release of Volatile Iodocarbons . . . . .	33
<b>4. Differential Optical Absorption Spectroscopy</b>	<b>37</b>
4.1. Absorption Spectroscopy . . . . .	37
4.2. The DOAS Method . . . . .	39
4.2.1. Mathematical Description of the Measurement Process . . . . .	40
4.2.2. DOAS Evaluation Procedure . . . . .	42
4.2.3. Error Analysis . . . . .	45
4.2.4. Detection Limit . . . . .	48
4.2.5. Analysis of Residual Spectra . . . . .	49
4.3. Experimental and Technical Realization of DOAS Measurements . . . . .	50
4.3.1. Multi Axis DOAS . . . . .	50
4.3.2. LP-DOAS . . . . .	50
4.3.3. Cavity Enhanced DOAS . . . . .	53

<b>II. Instrumentation</b>	<b>59</b>
<b>5. Open Path CE-DOAS Instruments</b>	<b>61</b>
5.1. Open Path CE-DOAS Mark I . . . . .	61
5.1.1. Spectrograph Linearity . . . . .	65
5.2. Open Path CE-DOAS Mark II . . . . .	67
5.2.1. Spectrograph Linearity . . . . .	67
5.3. Path Length Curve Using the Helium/air Method . . . . .	70
5.4. Wavelength Resolved CRDS . . . . .	72
5.4.1. Calibration Routine . . . . .	73
5.4.2. Comparison to the Helium/air Method . . . . .	74
5.5. Measurement Routine . . . . .	76
5.6. Spectral Evaluation . . . . .	76
5.6.1. Path length curves used in the retrieval . . . . .	77
5.6.2. Retrieval of IO, NO <sub>2</sub> and (CHO) <sub>2</sub> . . . . .	77
<b>6. The Compact Closed Path IO/NO<sub>2</sub> CE-DOAS</b>	<b>83</b>
6.1. Spectrograph Linearity . . . . .	84
6.2. Path Length Calibration . . . . .	84
6.3. Measurement Routine . . . . .	86
6.4. Spectral Retrieval . . . . .	86
<b>7. Long Path DOAS Systems</b>	<b>91</b>
7.1. Mace Head LP-DOAS . . . . .	91
7.1.1. Measurement Routine . . . . .	91
7.1.2. Spectral Evaluation . . . . .	92
7.2. Mobile LP-DOAS . . . . .	95
7.2.1. Measurement Routine . . . . .	96
7.2.2. Spectral Evaluation . . . . .	96
7.3. Amundsen LP-DOAS . . . . .	98
7.3.1. Measurement Sequence . . . . .	98
7.3.2. Data Analysis . . . . .	99
<b>8. Other Instrumentation</b>	<b>103</b>
8.1. Ireland Campaigns 2011/12 . . . . .	103
8.1.1. Meteorological Data . . . . .	103
8.1.2. Measurements of Tidal Height in Ireland . . . . .	104
8.1.3. In-situ Particle Measurements . . . . .	104
8.2. New Zealand Campaign 2013 . . . . .	105
8.2.1. Measurements of Tidal Height . . . . .	105
8.2.2. μDirac Gas Chromatograph (GC) . . . . .	105

---

<b>III. Improvement of DOAS Data Analysis</b>	<b>107</b>
<b>9. The iterative CE-DOAS (iCE-DOAS) Algorithm</b>	<b>109</b>
9.1. Simulations using the iCE-DOAS Algorithm	111
9.1.1. Evaluation with the iCE-DOAS Algorithm	113
9.1.2. Comparison iCE-DOAS vs. BBCEAS	113
<b>10. Correction of Spectrograph Nonlinearity</b>	<b>117</b>
10.1. Effect of Detector Nonlinearity	118
10.1.1. Characterization of the Detector Nonlinearity	119
10.2. Practical Examples for the Effect of Nonlinearity	122
10.2.1. CE-DOAS Analysis	122
10.2.2. Path Length Calibration by the Helium/air Method.	126
<b>11. A Corrected IO Absorption Cross Section</b>	<b>127</b>
11.1. The IO absorption cross section	127
11.1.1. Deviations Between Literature Cross Sections and CE-DOAS measurements	128
11.2. Correction of the IO Absorption Cross Section	131
11.2.1. Validation of the Correction for the IO( $2 \leftarrow 0$ ) Transition	134
11.2.2. Effect on the Data Analysis	136
<b>IV. Investigation of Iodine Emissions from Coastal Seaweed</b>	<b>139</b>
<b>12. Ireland 2011/2012</b>	<b>141</b>
12.1. Measurement Sites	141
12.1.1. Seaweed	143
12.2. Instrumentation	145
12.3. Meteorology	147
12.3.1. Meteorology 2011	147
12.3.2. Meteorology 2012	148
12.4. Results	150
12.4.1. Mace Head	154
12.4.2. Martin Ryan Institute	164
12.4.3. Lettermore Island	174
12.4.4. Cashel Bay	180
12.4.5. Ballyconneely	183
12.4.6. Mweenish Island	188
12.5. Discussion of Closed Path CE-DOAS Measurements	191
12.6. Discussion of NO <sub>x</sub> - IO Interaction	197
12.7. Discussion: Correlation of IO and Solar Irradiance	201
12.7.1. Nighttime IO	203
12.8. Discussion of the Regional IO Distribution on the Irish West Coast.	206

12.9. Discussion of IO Sources and their Spatial Distribution . . . . .	212
12.9.1. Wave Sheltered Bays . . . . .	212
12.9.2. Wave Exposed Shores . . . . .	222
12.9.3. IO over Drift Seaweed Patches . . . . .	232
12.10. Discussion: IO Emission Rates from Vertical IO Profile . . . . .	234
12.11. Conclusion on Iodine Sources . . . . .	237
12.12. Estimating the Irish and Global Iodine Emission from IO Observations . . . . .	239
<b>13. New Zealand 2013</b>	<b>241</b>
13.1. Measurement Sites and Instrumentation . . . . .	241
13.1.1. Seaweed . . . . .	244
13.2. Meteorology . . . . .	245
13.3. LP-DOAS Results . . . . .	248
13.3.1. Non-Halogen Species . . . . .	248
13.3.2. Halogen Species . . . . .	251
13.4. CE-DOAS Results . . . . .	252
13.5. Discussion of Atmospheric Measurements . . . . .	254
13.6. Discussion of Chamber Measurements . . . . .	263
13.6.1. IO Mixing Ratios for Different Seaweeds . . . . .	264
13.6.2. Estimated IO Emission Rates . . . . .	266
13.6.3. Iodocarbons as Possible IO Sources . . . . .	268
<b>V. Conclusions &amp; Outlook</b>	<b>283</b>
<b>14. Conclusions and Outlook</b>	<b>285</b>
14.1. Conclusions . . . . .	285
14.2. Outlook . . . . .	290
<b>VI. Appendix</b>	<b>291</b>
<b>A. A Corrected IO Absorption Cross Section</b>	<b>293</b>
A.1. Correction Factors for IO Bands . . . . .	293
A.2. Validation of the Correction for the IO(2 ← 0) Transition . . . . .	302
<b>B. Spectral Retrieval</b>	<b>305</b>
B.1. Used Literature Absorption Cross Sections . . . . .	305
<b>C. Ireland Campaign 2011/2012 Supplementary</b>	<b>307</b>
C.1. Open path CE-DOAS intensities and path lengths . . . . .	307
C.2. Correlation Between IO Mixing Ratios and Solar Irradiation. . . . .	310
C.3. Correlation Plots for LP-DOAS Measurements at MRI 2011 . . . . .	311

<b>D. New Zealand Campaign 2013 Supplementary</b>	<b>313</b>
D.1. GC Measurements of Halocarbons . . . . .	313
<b>Nomenclature</b>	<b>315</b>
<b>Glossary</b>	<b>319</b>
<b>Bibliography</b>	<b>321</b>
<b>Aknowledgements</b>	<b>347</b>



# **Part I.**

## **Introduction and Methods**



# 1

## Motivation

The atmosphere is a thin layer of air held around the Earth by gravitational attraction. It provides conditions essential for life on earth by absorbing the harmful UV radiation and by providing an average surface temperature above the freezing point of water through the natural greenhouse effect. While the atmosphere is mainly composed of Nitrogen (78.1 %) and Oxygen (20.95 %) it contains numerous trace constituents which play a key role for the global climate- and ecosystem. Changes in concentrations of these trace gases can have severe impacts on the global climate- and ecosystem, prominent examples are the discovery of the stratospheric ozone hole [e.g. Molina and Rowland, 1974; Farman et al., 1985], high concentrations of ground level ozone during photochemical smog events in strongly polluted urban air, which cause adverse effect on human health and vegetation [e.g. Haagen-Smit, 1952] and the increasing evidence for trace gases as drivers of global warming [Stocker et al., 2013]. The fate of atmospheric trace gases is thereby often inter-connected in complex photochemical reactions.

The presence of reactive halogen (chlorine, bromine and iodine) species (RHS) is known to have a large influence on the Earth's atmosphere. The most important consequence of halogen radicals is the destruction of ozone in catalytic cycles, in which the involved halogen compound can repeat the same reaction several thousand times. Thus, small concentrations of halogen radicals can have a substantial impact on the ozone concentration which is typically three orders of magnitude higher than that of RHS. The most prominent effect of halogen radicals in the atmosphere is the polar stratospheric ozone hole [e.g. Molina and Rowland, 1974; Farman et al., 1985]. In the last two decades, halogen species have also been identified to play an important role in the troposphere [e.g. Hausmann and Platt, 1994; Alicke et al., 1999], where ozone acts as a greenhouse gas and is the major source of hydroxyl radicals (OH). Oxidation by OH results in the removal of most naturally and anthropogenically emitted pollutants from the atmosphere. RHS further influence the atmospheric oxidizing capacity by changing the partitioning of  $\text{HO}_2/\text{OH}$  and  $\text{NO}/\text{NO}_2$  [e.g. Platt and Hönninger, 2003]. Another important consequence of the release of reactive iodine species is the formation of new particles through the polymerization of iodine oxides (see below).

This study investigates the emissions of reactive iodine species at seaweed-rich coastal mid-latitude coastal areas, where so far the highest atmospheric mixing ratios of reactive iodine species, mainly IO, have been reported. Coastal LP-DOAS studies at Mace Head Ireland

by Alicke et al. [1999] reported up to 6 ppt<sup>1</sup> IO which was confirmed by follow up studies [Hebestreit, 2001; Saiz-Lopez et al., 2006; Seitz, 2009]. Other isolated campaigns in the Northern Hemisphere also reported elevated IO levels from LP-DOAS measurements: Brittany Franc up to 7 ppt [Peters et al., 2005] and 10 ppt [Mahajan et al., 2009]; Gulf of Maine up to 4 ppt [Stutz et al., 2007]. These IO mixing ratios are clearly exceeding the reported open ocean concentrations of typically 0.5 – 2 ppt [e.g. Read et al., 2008; Großmann et al., 2013; Lampel, 2014]. Due to the correlation of coastal IO levels with daytime low tide, the most likely source is the photolysis of molecular iodine (I<sub>2</sub>) emitted by seaweed exposed to air during low tide. This is supported by several laboratory studies which found strong I<sub>2</sub> emissions from brown seaweed mainly *L. digitata* exposed to air [e.g. S. M. Ball et al., 2010; Kundel et al., 2012; Ashu-Ayem et al., 2012], and also by coastal LP-DOAS observations of elevated I<sub>2</sub> levels during nighttime (no photolysis) and low tide [e.g. Saiz-Lopez and Plane, 2004; Peters, 2005; Seitz, 2009].

Studies at Mace Head [O’Dowd et al., 2002b] observed particle nucleation events with the same correlation to solar radiation and low tide as gas phase iodine compounds. In addition, these particles were found to contain iodine. Subsequent laboratory [e.g. Hoffmann et al., 2001; Jimenez et al., 2003; Burkholder et al., 2004; Saunders et al., 2010] and modeling studies [Pechtl et al., 2006; Saiz-Lopez et al., 2006] indicated that the particle formation proceeds through the homogeneous nucleation of iodine oxides, which is initialized by the formation of OIO in the second-order IO self reaction. If those particles grew to become cloud condensation nuclei (CCN), they could change the cloud albedo and therefore influence the coastal climate [e.g. Stocker et al., 2013]. However, the current understanding of the particle formation process from reactive iodine compounds is still limited. Observation of OIO in the marine boundary layer is rare [Hebestreit, 2001; Saiz-Lopez et al., 2006; Stutz et al., 2007] and may be flawed due to instrumental problems. Furthermore a laboratory study by Burkholder et al. [2004] states that the IO mixing ratios of up to 50 to 100 ppt would be needed to explain the observed particle nucleation events with particle concentrations of 10<sup>6</sup> cm<sup>-3</sup>. This is ten times higher than the IO mixing ratios observed by LP-DOAS measurements. However, LP-DOAS measurements only give the average mixing ratio along a several km long light path, which may conceal possibly inhomogeneous distributions. Thus, Burkholder et al. [2004] suggested that IO may be distributed inhomogeneously in so called “hot-spots”.

First evidence for an inhomogeneous distribution of IO at coastal sites was given by the study of Seitz et al. [2010] on the Irish West Coast, which compared the IO column densities of two different Long Path DOAS (LP-DOAS) light paths. One light path of 500 m length (one-way) spanned exclusively over an intertidal area with seaweed exposed during low tide. A second almost parallel light path extended further, also crossing subtidal areas which were always covered by water. They found that almost all IO was concentrated along the shorter light path and therefore concluded that the sources are almost exclusively located in this area. However, due to the limited spatial resolution of 500 m they could not determine local concentrations and attribute the iodine emissions to a specific seaweed species. Further indications for an inhomogeneous IO distribution were also given by first IO point measurements at Roscoff,

---

<sup>1</sup>1 ppt = 1pmol/mol corresponds to a relative volumetric abundance (mixing ratio) of a gas of 10<sup>-12</sup>

---

France using the Laser Induced Fluorescence (LIF) technique [Furieux et al., 2010]. The LIF, setup on land at a distance of 300 m from a seaweed rich area, measured up to 30 ppt of IO which was at least twice the IO mixing ratio observed by simultaneous LP-DOAS measurements on a 6.7 km light path along the same shore. Similar observations were reported by Commane et al. [2011] for Mace Head at the Irish West Coast where a LIF observed peak IO mixing ratios of up to 29 ppt which was a factor of 6 higher compared to simultaneous LP-DOAS measurements. However, measurements by LIF could only be performed on land close to a laboratory building due to instrumental limitations (see below). Therefore LIF measurements could not determine the IO mixing ratios in potential hot spots and also not their spatial extend and distribution.

In addition to the hot-spot theory, also the global contribution of coastal sites to the reactive iodine emissions is an open question. Prior to this study, measurements were only performed at few locations in the northern hemisphere, mainly at Mace Head, Ireland. Also these studies were mainly focused on shores where the seaweed species *L. digitata* is predominant, which was expected to be the seaweed species with by far the strongest iodine emission potential [S. M. Ball et al., 2010]. At the Irish West Coast for example, other shores which feature much higher seaweed abundance, but of other species, found very little attention in previous field campaigns. First indications for significant reactive iodine emissions on these coasts were given by Seitz et al. [2010] and Huang et al. [2010a]. Furthermore, there is even less information on reactive iodine emissions at coastal sites in the southern hemisphere where different seaweed species are abundant. So far, the only observation on the southern hemisphere was made by [B. J. Allan et al., 2000] who reported up to 2.2 ppt IO at Cape Grim Tasmania. But it is not clear yet if these are marine background levels or from local emissions of coastal seaweed.

## In-situ Measurement Techniques for Reactive Iodine Species

The previous section showed the need for IO point measurements in the intertidal zone, directly above seaweeds to fully investigate the “hot-spot” theory. However, measurements in the intertidal zone are challenging since intertidal areas are exposed and covered twice daily by the tide. Therefore such instruments would need to be portable and quickly to setup. In addition they need to be very sensitive to IO due to the expected low concentrations in the ppt range. However, previously used point measurement techniques have several limitations which made them unsuitable for this kind of measurements:

**Laser Induced Fluorescence (LIF)** has been used in two recent coastal campaigns to detect IO on the shoreline [Furieux et al., 2010; Commane et al., 2011]. With typical IO detection limits of 1 – 2 ppt, this technique is sensitive to coastal levels. However, due to the relatively complicated Laser setup proper alignment is complicated and sensitive to mechanical vibrations. Additionally, these instruments typically weigh more than 100 kg. Thus, LIF is not suited for portable measurements. Furthermore, LIF needs to sample the air into a measurement cell which is generally also problematic for a highly reactive gas like IO due to potential wall losses (see sec. 12.5). However, in the case of the above described LIF instruments this is only a minor problem since very short inlets were used resulting in sufficiently short residence times in the closed cell. Finally, LIF

instrument need to be calibrated with an IO reference gas on a daily basis. This greatly complicates the operation of such instruments since, the calibration mixture needs to be produced on site due to the high reactivity of IO. Also IO calibration mixtures are hard to produce exactly, resulting in high systematic errors in the measured IO concentrations of about 20 % [Whalley et al., 2007].

**Cavity Ringdown Spectroscopy (CRDS)** was applied by Wada et al. [2007] for measurements of IO at Roscoff, France. Their instrument measures the IO concentration in an optical resonator which is open towards the atmosphere. This has the important advantage of avoiding wall losses of the highly reactivity IO. The IO concentration is measured through the decay time of the light intensity of pulsed laser light. This is alternatingly measured at two different wavelengths on and off resonance with an absorption band, which made the measurements principle selective to IO. However, this instrument also had some major disadvantages. Despite the use of on and off resonance measurements the instrument showed an interference to broadband extinction by turbulence and aerosol particles leading to a high detection limit of 12 ppt on average (but up to 20 ppt), which is hardly sufficient for measurements of atmospheric IO levels. Furthermore the relatively complicated Laser setup made the instrument large ( $1.8 \times 0.9 \times 0.9 \text{ m}^3$ ) and heavy and thus not suitable for portable operation. Also the alignment of the instrument was so sensitive that it could only be operated indoors, in front of an open window.

**A Mode Locked Cavity Enhanced Absorption Spectroscopy (ML-CEAS)** for the measurement of IO and BrO was developed by [Grilli et al., 2012b]. With a theoretical IO detection limit of 0.02 ppt this instrument is claimed to give the most sensitive IO measurements. However this instrument uses a closed measurement cell and needs several meter long sampling lines, since the instruments high sensitivity to temperature changes and mechanical vibrations requires indoors operation in a special laboratory room. [Grilli et al., 2012b] claims that the sampling system made of Teflon (PFA) has no significant IO losses, which might be appropriate under laboratory conditions [Grilli et al., 2012b; Grilli et al., 2012a]. However, this study shows very high and variable IO losses of more than 90 %, for atmospheric measurements with a very similar closed sampling system of only few cm length (see sec. 12.5). Thus the measurements by ML-CEAS from Grilli et al. [2012b] and follow up studies are problematic and most likely wrong. This also has to be suspected from their coastal measurements at Roscoff which showed no tidal pattern and one order of magnitude less IO than the previous study of [Furieux et al., 2010].

**Passive denuder sampling:** Alternatively to IO also the primary  $\text{I}_2$  emission from seaweed could be measured, which is readily photolyzed and oxidized to IO. So far the only field applicable method with sufficient sensitivity is the passive diffusion denuder sampling technique, with subsequent GC-MS quantification in a laboratory [Huang et al., 2010a, e.g.]. However, to get a sufficiently high signal they need long sampling times (typically hours) which typically allows for only one to three data points per low tide period. Also this method is very prone to interferences with other trace gas species, often leading to unpublishable data, which always leaves doubts on the validity of these measurements.

## 1.1. Aims of This Work:

This thesis investigates coastal iodine emissions of seaweeds on a local, regional and global scale. For this a mobile Open Path Cavity Enhanced (CE-) DOAS instrument was successfully developed and optimized for measurements of IO. To my knowledge it is the first such instrument. It was applied successfully in two field campaigns on the Irish West Coast, directly in intertidal areas with seaweed fields, to investigate the “hot-spot” theory. Furthermore, the field campaigns on the Irish West Coast extended the observations of reactive iodine to 8 previously uninvestigated location to get a more representative picture of the regional IO emissions in relation to previous observations at Mace Head. In a third, explorative, campaign on the east coast of the New Zealand South Island, observations of coastal iodine emissions from seaweed were extended to the southern hemisphere and iodine emissions of five previously uninvestigated seaweed species, which are specific to the Southern Hemisphere or the Pacific Ocean, were investigated in incubation chamber experiments.

## 1.2. Outline of the Thesis

This work is grouped in five parts. The first part lays out the scientific and methodological foundation of this work. Chapter 2 discusses the relevant atmospheric chemistry mechanisms with a focus on reactive halogen species (RHS) (particularly iodine) as well as the chemistry of other relevant radicals. Seaweeds are the major source of reactive iodine species at mid-latitude coastal sites. Therefore, chapter 3 describes their global distribution and discusses their iodine accumulation and release mechanisms. Chapter 4 introduces the DOAS method with an emphasis on Cavity Enhanced DOAS, the main DOAS variant applied in this work. The second part describes the Open Path CE-DOAS (chapter 5) and Closed Path CE-DOAS (chapter 6) instruments developed during this work as well as other instruments (chapter 7 and 8) used during different field campaigns. Also, along with each DOAS instrument, the measurement routine and evaluation settings are described. Part three discusses improvements of the DOAS data analysis achieved in this work. Chapter 9 introduces a new iterative algorithm for the evaluation CE-DOAS measurements. Chapter 10 analyzes the effects of spectrometer non-linearity on DOAS measurements and describes methods to characterize and correct the spectrometer non-linearity. Chapter 11 analyzes differences between the literature absorption cross section of IO and the IO absorption observed in this work and derives a corrected IO absorption cross section. Part four presents the field measurements of iodine emissions from coastal seaweed at the Irish West Coast (chapter 12) and on the east coast of the New Zealand South Island (chapter 13). Discussions of the results are included with each campaign. The final chapter concludes this thesis with a summary and an outlook.



# 2

## Tropospheric Chemistry

The study of the atmospheric composition goes back to the 18th century. In the 1950 the major components of the atmosphere  $N_2$  (78.1 %),  $O_2$  (20.95 %), the noble gases,  $CO_2$ ,  $H_2O$  and stratospheric  $O_3$  were known, but the atmosphere was regarded as chemically inert. However, today we know that natural and anthropogenic trace gases and their chemical transformations control air quality, the health of the stratospheric ozone layer and climate change [e.g. Seinfeld and Pandis, 2006].

The earth atmosphere can be subdivided into layers according to its temperature profile: the troposphere, stratosphere and upper atmosphere [e.g. Platt and Stutz, 2008]. This study focuses on the troposphere, which is the lowest layer of the atmosphere and ranges from the surface of the atmosphere to an altitude of about 8 km at the poles and to about 18 km at the equator. The majority of the atmospheric mass ( $\sim 90$  %) is contained in the troposphere as well as most of the atmospheric trace gases. The troposphere is characterized by a decrease of the mean temperature with increasing altitude which causes convective activity, leading to a well mixed layer. The troposphere can further be divided into the free troposphere and the planetary boundary layer (PBL). The PBL is the lower region of the troposphere, which is in direct contact with the earth surface and therefore also strongly influenced by surface effects. Convective air motion and surface friction tends to generate strong turbulent mixing. The PBL is typically in the range of few hundred meters to 1 – 2 km of the surface. The PBL is often separated from the free troposphere by a layer of high static stability which slows the transport of chemical species.

Most of the trace gases found in the atmosphere are emitted from natural or anthropogenic sources at the surface into the troposphere where they are subject to a complex array of chemical and physical transformations. Without efficient self cleaning processes, the levels of many trace gases could rise so high that they would drastically affect the earth's climate and ecosystem. A key process determining the atmospheric self cleaning capacity is the oxidative degradation of many trace gases, which is driven by free radicals, most importantly the hydroxyl radical OH.

The following chapter first gives a short overview on the quantification of trace gas abundances in 2.1, followed by a gives a brief description of the radical chemistry of OH,  $NO_3$  and  $O_3$  in sec. 2.2. Section 2.3 give a more detailed description on the chemistry of halogen radicals which was investigated in this work.

volume mixing ratio	relative abundance by volume	equivalent mole fraction
ppm	$10^{-6}$	$\mu\text{mol/mol}$
ppb	$10^{-9}$	$\text{nmol/mol}$
ppt	$10^{-12}$	$\text{pmol/mol}$

Table 2.1. | Typical units of mixing ratios.

## 2.1. Quantification of Gas Abundances

In this thesis two common descriptions are used to quantify the abundance of trace gases in the atmosphere. First the concentration of a trace gas  $i$  is defined by its number density:

$$\rho_i = \frac{\text{number of molecules } i}{\text{volume of air}} \left[ \frac{\text{molec}}{\text{cm}^3} = \frac{1}{\text{cm}^3} \right] \quad (2.1)$$

Secondly we define the volume mixing ratio as the ratio of the number density of a trace  $i$  to the number density of air (including the trace gas):

$$x_i = \frac{\rho_i}{\rho_{\text{air}} + \rho_i} \approx \frac{\rho_i}{\rho_{\text{air}}} \quad (2.2)$$

Typical units of volume mixing ratios are summarized in Tab. 2.1. Under ambient conditions air and trace gases can be treated in good approximation as an ideal gas. Thus, the volume mixing ratio is essentially equivalent to the mole fraction, which is the SI unit for mixing ratios.

The number density of air  $\rho_{\text{air}}$  at an arbitrary temperature  $T$  and pressure  $p$  is calculated according to the ideal gas law as:

$$pV = Nk_{\text{B}}T \quad (2.3)$$

$$\Rightarrow \rho_{\text{air}} = \frac{N}{V} = \frac{p}{k_{\text{B}}T} \quad (2.4)$$

where  $N$  is the particle number,  $V$  a volume and  $k_{\text{B}}$  the Boltzmann constant.

## 2.2. Tropospheric Radical Chemistry

Tropospheric chemistry is largely driven by the free radicals OH, NO<sub>3</sub>, O<sub>3</sub> and Halogens. Most importantly they control the atmospheres self-cleaning or oxidation capacity. This section will give a short overview of the most important reactions of OH, O<sub>3</sub>, NO<sub>x</sub> and NO<sub>3</sub> as they also play an important role in the tropospheric halogen chemistry which is discussed in sec. 2.3. For a detailed description of the complex tropospheric radical chemistry the reader is referred to B. J. Finlayson-Pitts and Pitts [2000], Monks [2005] and Seinfeld and Pandis [2006].

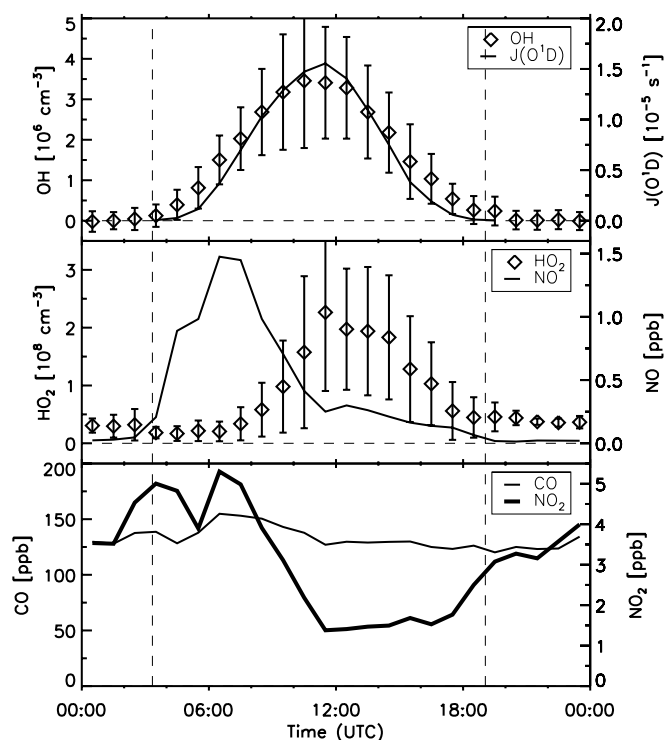
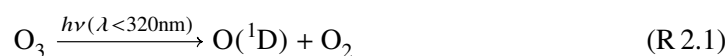


**Figure 2.1.** | Average diurnal OH, HO<sub>2</sub> and  $j(\text{O}^1\text{D})$  levels observed during a summer urban campaign. (Adopted from Holland et al. [2003], reproduced by permission of American Geophysical Union)

### 2.2.1. The Hydroxyl Radical OH

The Hydroxyl Radical OH is most important free radical in the troposphere, as it is the major scavenger of most oxidizable gases emitted in the atmosphere, especially the greenhouse gas methane, other volatile organic compounds (VOCs) and nitrogen compounds [e.g. Levy, 1971; P. Crutzen and Zimmermann, 1991; P. Crutzen et al., 1999; Atkinson, 2000]. At sufficiently high levels of nitrogen oxide levels, these reaction chains result in the photochemical production of ozone (see sec. 2.2.2.2) [e.g. Chameides and Walker, 1973]. OH is also provides one of the major oxidation pathways of dimethyl sulfide (DMS) [Yin et al., 1990], and thereby influences the aerosol and cloud particle formation [e.g. Charlson et al., 1987; Kiehl et al., 2000]. Furthermore, OH also provides the major daytime sink through the formation of HNO<sub>3</sub> (see reaction R 2.13), which is readily removed by precipitation [P. Crutzen and M. Lawrence, 2000].

The OH concentration closely follows the solar radiation with typical noontime concentrations in the order of  $10^7 \text{ cm}^{-3}$  (see Fig. 2.1). Globally, the major source of OH is the photolysis of Ozone in the presence of water vapor. The reaction starts by photolysis of O<sub>3</sub>



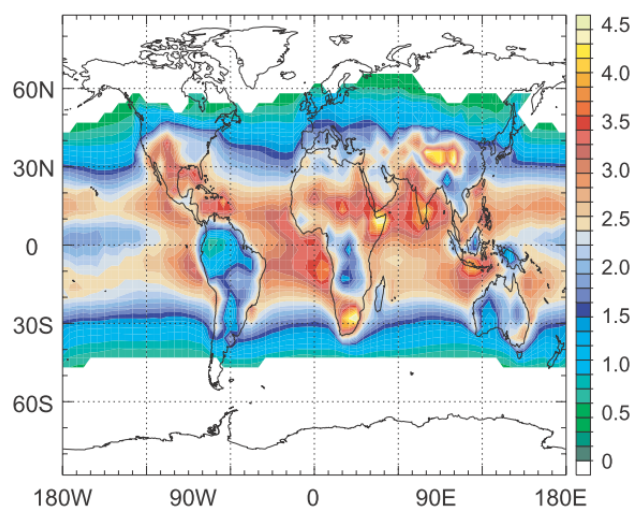


**Figure 2.2.** | Annual mean OH concentrations in the boundary layer. The units are  $10^6 \text{ cm}^{-3}$ . OH levels are highest in the tropics where the  $\text{O}_3$  photodissociation is strongest (solar zenith angle is smallest, the stratospheric ozone layer is thinnest) and humidity is highest. Adopted from Lelieveld et al. [2004].

with a photolysis frequency  $j(\text{O}^1\text{D})$  at solar zenith angle  $0^\circ$  of about  $6 \cdot 10^{-5} \text{ s}^{-1}$  [e.g. Seinfeld and Pandis, 2006]. The majority of the  $\text{O}^1\text{D}$  is quenched to the ground state by collision with  $\text{N}_2$  and  $\text{O}_2$ . This results in a null cycle since the ground rapidly recombines with  $\text{O}_2$  back to  $\text{O}_3$



with  $k_{R2.3} = 1.5 \cdot 10^{-14} \text{ cm}^3 \text{ s}^{-1}$  and for an atmospheric mixture of  $\text{N}_2$  and  $\text{O}_2$  the rate constant for quenching is  $k_{R2.2} = 2.9 \cdot 10^{-11} \text{ cm}^3 \text{ s}^{-1}$ . However, some of the  $\text{O}^1\text{D}$  atoms react with  $\text{H}_2\text{O}$  according to



with  $k_{R2.4} = 2.2 \cdot 10^{-10} \text{ cm}^3 \text{ s}^{-1}$  [Atkinson et al., 2004]. In the mid-latitude lower troposphere, the fraction of the  $\text{O}^1\text{D}$  atoms that form OH typically varies between 5% to 10% depending on the  $\text{H}_2\text{O}$  concentration. The widespread abundance of  $\text{O}_3$  and  $\text{H}_2\text{O}$ , reactions (R 2.1) and (R 2.4) are the primary source of OH in the troposphere. Therefore, OH levels are highest in the tropics where the  $\text{O}_3$  photodissociation is strongest (solar zenith angle is smallest, the stratospheric ozone layer is thinnest) and humidity is highest as shown in Fig. 2.2 [M. G. Lawrence et al., 2001; Lelieveld et al., 2002].

OH is closely connected to the concentration of the proxy radical  $\text{HO}_2$  via the reactions with CO, hydrocarbons (RH) including methane ( $\text{CH}_4$ ), NO and  $\text{O}_3$  as illustrated in Fig. 2.3.

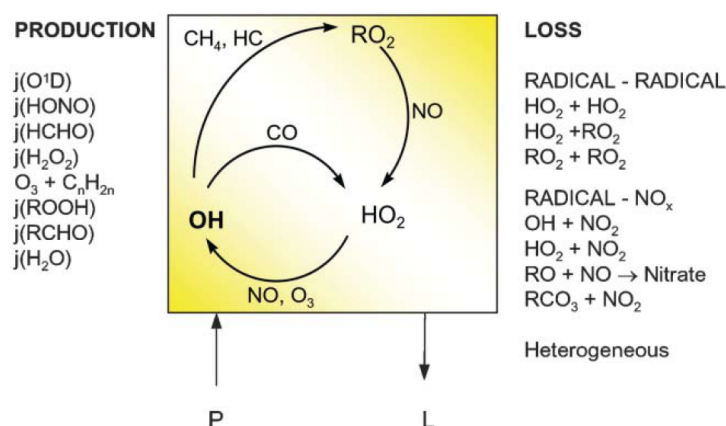


**Figure 2.3.** | Simplified sketch of the sources, interconversions and sinks for OH and HO<sub>2</sub> in the troposphere. It can be seen that OH and HO<sub>2</sub> are closely linked through the reactions with CO, hydrocarbons (HC), NO and O<sub>3</sub>. (Adopted from Monks [2005]).

Therefore, the sum of OH and HO<sub>2</sub> is commonly summarized as HO<sub>x</sub>. In section 2.2.2.2 more details are given on the reactions with CO and RH in the presence of NO, which are important for the production of tropospheric ozone. Peroxy radical concentrations are typically two orders of magnitude larger than the OH concentration (see Fig. 2.1). However, HO<sub>2</sub> is suppressed in the presence of high NO levels due to rapid recycling to OH:



with  $k_{R2.5} = 8.8 \cdot 10^{-12} \text{ cm}^3\text{s}^{-1}$ .

### 2.2.1.1. Other source of HO<sub>x</sub>

In the following other sources for HO<sub>x</sub> (OH + HO<sub>2</sub>) in the atmosphere are summarized:

- An important secondary source for HO<sub>x</sub> is the photolysis of carbonyl compounds produced in degradation of VOCs (see: 2.2.2.2 and reaction R 2.12). The simplest and most important of these is Formaldehyde HCHO, which is an oxidation product of CH<sub>4</sub> and many other hydrocarbons [Seinfeld and Pandis, 2006]:



- The photolysis of nitrous acid (HONO) is a further OH source



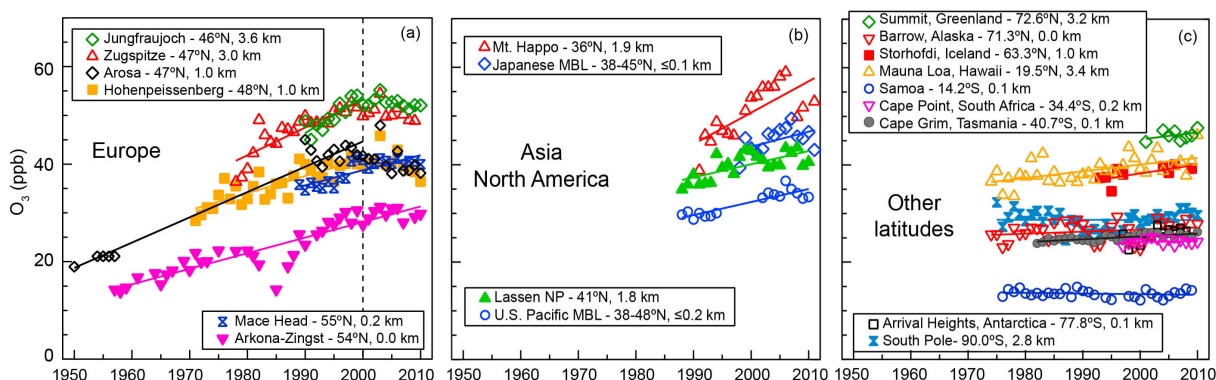


**Figure 2.4.** | Annual average surface ozone concentrations from regionally representative monitoring sites in the northern and southern Hemisphere. Increasing tropospheric ozone levels are observed mainly due to the increased  $\text{NO}_x$  emissions. Ozone levels on the southern hemisphere are generally lower compared to the northern hemisphere due to lower  $\text{NO}_x$  emissions. (Adopted from Hartmann et al. [2013]).

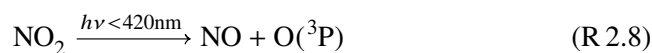
Under urban conditions HONO is formed from  $\text{NO}_x$  by heterogeneous processes [Platt and Stutz, 2008]. Another important HONO source is the soil [Su et al., 2011], where it is released particularly by ammonia-oxidizing bacteria [Oswald et al., 2013].

## 2.2.2. Tropospheric Ozone

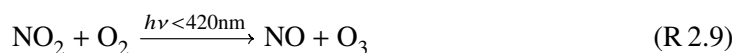
Ozone is another key compound in the tropospheric chemistry since it influences the oxidation capacity of the atmosphere. Furthermore, ozone is a component of smog and also acts as a greenhouse gas. Tropospheric ozone levels at background sites typically vary between 20 – 45 ppb but can exceed 100 ppb in urban areas due to increased  $\text{NO}_x$  and VOC levels. Increasing  $\text{NO}_x$  emissions also cause a global increase in the tropospheric ozone levels as shown in Fig. 2.4. The reactions of ozone with halogen atoms (I, Br, Cl) which can lead to catalytic ozone destruction cycles are discussed in sec. 2.3.1.1.

### 2.2.2.1. Photostationary state of ozone and $\text{NO}_x$

In the troposphere the only way for producing Ozone is the photolysis of  $\text{NO}_2$ :



since R 2.3 is very rapid this can be effectively written as



with a typical photolysis frequency at clear sky noontime of  $j(\text{NO}_2) \approx 8 \cdot 10^{-3} \text{ s}^{-1}$  [e.g. Junkermann et al., 1989]. Generally, NO is rapidly converted back to  $\text{NO}_2$  by

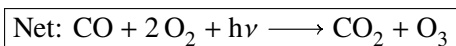
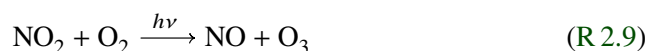
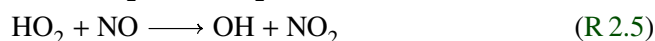


with  $k_{\text{R}2.10} = 1.8 \cdot 10^{-14} \text{ cm}^3 \text{ s}^{-1}$ . Neglecting other source and losses this leads to a photo-stationary steady state between  $\text{O}_3$ , NO and  $\text{NO}_2$  in which the respective concentrations are interconnected by the so-called *Leighton Ratio* [Leighton, 1961]:

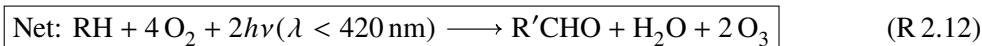
$$L = \frac{[\text{NO}_2]}{[\text{NO}]} = \frac{k_{\text{R}2.10}[\text{O}_3]}{j(\text{NO}_2)} \quad (2.5)$$

### 2.2.2.2. Ozone production

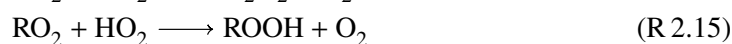
In the presence of CO the following catalytic cycle can produce Ozone [e.g. Chameides and Walker, 1973]:



As shown in Fig. 2.5 similar chain reactions, can be written for many hydrocarbons (RH) including methane ( $\text{CH}_4$ ). This chain involves the alkyl peroxy radical ( $\text{RO}_2$ ) and alkoxy radical (RO). The net reaction is:



Of course the carbonyl  $\text{R}'\text{CHO}$  can be photolyzed or undergo further oxidation by the same reaction scheme, leading to further Ozone production. A very prominent example for reaction R 2.12 is the strong  $\text{O}_3$  production in polluted urban areas, which is known as “Los Angeles smog” or photo chemical smog. Furthermore, reaction R 2.12 also plays an important role in the removal of the greenhouse gas methane. Ultimately the catalytic cycles R 2.11 and R 2.12 are terminated by reactions like:



In fact reaction R 2.13 is the major daytime sink of  $\text{NO}_x$ .

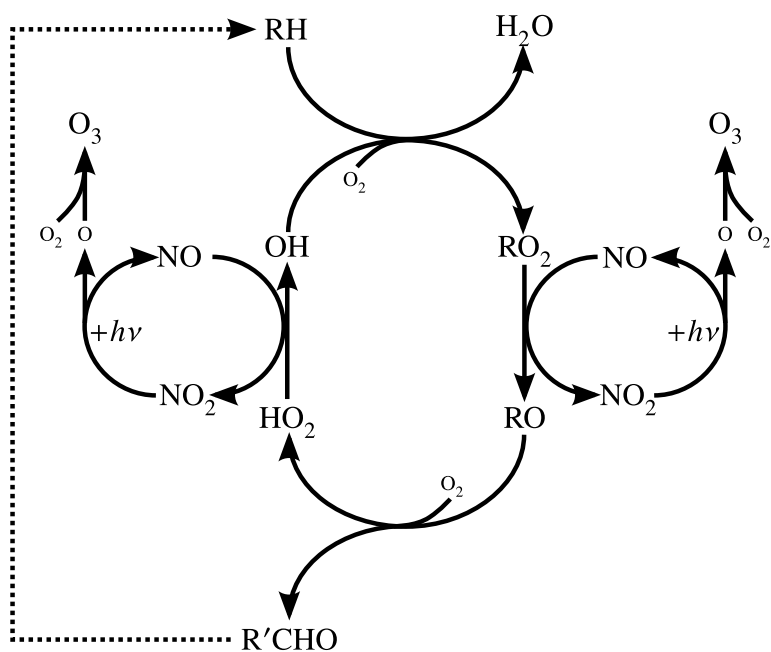


Figure 2.5. | Simplified reaction scheme for the degradation of volatile organic compounds (RH).

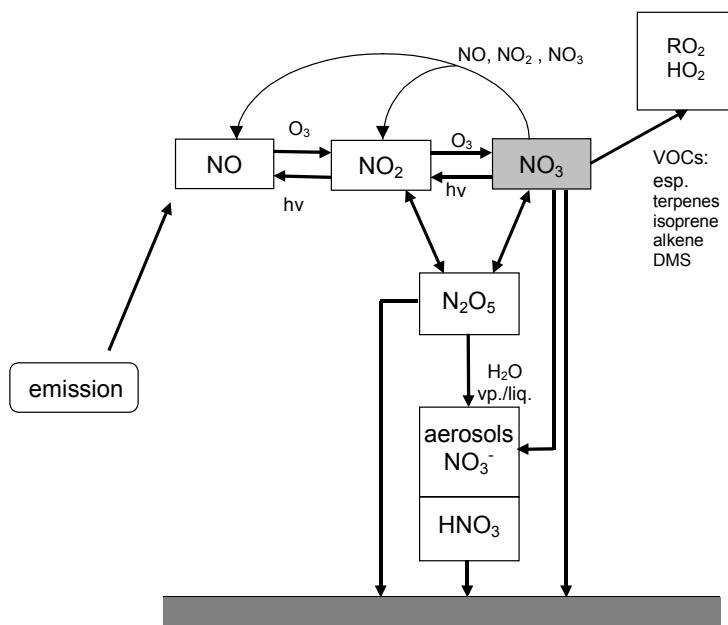


Figure 2.6. | Simplified tropospheric reaction scheme for (NO<sub>3</sub>). Reproduced from Geyer [2000]

### 2.2.3. The Nitrate Radical $\text{NO}_3$

At night time when OH concentrations are low, the main oxidant is the nitrate radical  $\text{NO}_3$ . An overview of the most important reactions of  $\text{NO}_3$  is shown in Fig. 2.6 and a recent detailed review of  $\text{NO}_3$  chemistry is given by Brown and Stutz [2012].  $\text{NO}_3$  is primarily formed by the reaction of  $\text{NO}_2$  with ozone:



with  $k_{\text{R2.16}} = 3.5 \cdot 10^{-17} \text{ cm}^3\text{s}^{-1}$  this is a relatively slow reaction (time constant  $\approx 1/2$  day at 30 ppb  $\text{O}_3$ ). During daytime, nitrate radicals are rapidly photolyzed:



with a photolytic lifetime of about 5 s for an SZA below  $70^\circ$  ( $j(\text{NO}_3) \approx 0.2 \text{ s}^{-1}$ ). The nitrate radical also reacts rapidly with NO:



with  $k_{\text{R2.18}} = 2.6 \cdot 10^{-11} \text{ cm}^3\text{s}^{-1}$ . Thus, significant  $\text{NO}_3$  is only formed at night times when there is no photolysis and NO concentrations are generally low. Since  $\text{NO}_3$  is primarily formed from  $\text{NO}_2$  nighttime  $\text{NO}_3$  concentrations show a large variation with few ground level concentration of few ppt to several ten ppt at rural sites to up to several hundred ppt in polluted areas [e.g. Brown and Stutz, 2012].

The simultaneous presence of  $\text{NO}_2$  and  $\text{NO}_3$  leads to a chemical equilibrium with  $\text{N}_2\text{O}_5$ :



Roughly equal concentrations of  $\text{NO}_3$  and  $\text{N}_2\text{O}_5$  are found at  $\text{NO}_2$  mixing ratios of about 1ppb.

$\text{NO}_3$  reacts with a variety of the VOCs. Even though the reactivity of  $\text{NO}_3$  is generally low compared to OH, this is partly compensated by the generally much higher  $\text{NO}_3$  concentrations during nighttime compared to the daytime concentrations of OH. Of particular importance are the rapid reactions with biogenic VOCs like isoprene and terpenes from plants and DMS in the marine boundary layer. For example DMS will be oxidized more rapidly by  $\text{NO}_3$  (during night), than by OH (during day), if the concentration of  $\text{NO}_2$  is more than 60% that of DMS [B. Allan et al., 1999]. However, it is important to note that  $\text{NO}_3$  can initiate but not catalyze the removal of VOC, which is a major difference to the daytime OH chemistry.

## 2.3. Tropospheric Halogen Chemistry

Halogens are the elements of the seventh main group in the periodic table and thus are characterized by a high electronegativity and a  $ns^2 np^5$  valence electron configuration, which lacks only one electron to completely fill its valence shell. These properties make halogens highly reactive, with decreasing reactivity down the group ( $\text{F} > \text{Cl} > \text{Br} > \text{I} > \text{As}$ ).

For tropospheric chemistry only iodine (I), bromine (Br) and chlorine (Cl) are of interest because astatine (As) is virtually absent on Earth and fluorine (F) very rapidly reacts with water to form the comparatively unreactive HF [e.g. B. J. Finlayson-Pitts and Pitts, 2000; Glasow and P. Crutzen, 2003]. However, several anthropogenically emitted fluorine containing species are potentially strong greenhouse gases [e.g. Harnisch, 1999]. During the last three decades, the important role of reactive halogen species (RHS = X, XO, XY, HOX and higher halogen oxides, where X,Y=I,Br,Cl) in the photochemistry of the atmosphere has found growing attention. RHS were first studied in the stratosphere where they play a key role in the formation of the ozone hole [e.g. Molina and Rowland, 1974; Yung et al., 1980; McElroy et al., 1986; Solomon, 1999]. In the last two decades, halogen species have also been identified as playing an important role in the chemistry of the troposphere [e.g. Platt and Janssen, 1995; Platt and Hönninger, 2003; Glasow and P. Crutzen, 2003; Simpson et al., 2007; Simpson et al., 2015]. In the troposphere RHS, in particular Br and I, can rapidly deplete ozone in catalytic cycles (sec. 2.3.1), affect the partitioning of HO<sub>x</sub> and NO<sub>x</sub> (sec. 2.3.1.2), oxidize DMS (sec. 2.3.1.3), and enhance the deposition of mercury (sec. 2.3.1.4), reduce the lifetime of the greenhouse gas methane and iodine oxides can cause new particle formation (sec. 2.3.3).

An impressive example is the depletion of boundary layer ozone in polar spring within days or hours in so called “bromine explosion” events (sec. 2.3.1.1). These events were observed both in the antarctic [e.g. Hausmann and Platt, 1994; Pöhler et al., 2010; Sihler, 2012] and in the arctic [e.g. Kreher et al., 1997; Frieß et al., 2004; Saiz-Lopez et al., 2007]. Satellite studies showed that BrO clouds covering area of million km<sup>2</sup> are regularly observed during polar spring [Platt and Wagner, 1998; A. Richter et al., 1998; Zeng et al., 2003; Hollwedel et al., 2004; Sihler, 2012, e.g.]. Bromine mediated Ozone destruction was also observed at the salt lakes [Stutz et al., 2002; Hönninger et al., 2004], the dead sea sea [Hebestreit et al., 1999; Holla et al., 2015] and in volcanic plumes [Bobrowski et al., 2003]. BrO was also found also found in the Marine Boundary Layer at mixing ratios off the coast of Africa by [Leser et al., 2003], in the Mauritanian upwelling [Martin et al., 2009], at Cape Verde [Read et al., 2008; Mahajan et al., 2010a; Tschirter, 2013] and in the Peruvian upwelling [Lampel, 2014]. Even though the reported levels of few ppt BrO seem little, if they were present globally, due to the large area covered by the oceans, this is expected to already significantly influence ozone destruction in the marine boundary layer (MBL) [e.g. Read et al., 2008; Mahajan et al., 2010a] and significantly enhance the oxidation of DMS [e.g. Boucher et al., 2003; Glasow et al., 2004], which could impact cloud formation. However, on a global scale observational evidence of MBL BrO is still very sparse.

The impact of iodine compounds in the boundary layer and their distribution is not well understood. The highest IO mixing ratios were reported for coastal sites where seaweeds are abundant. Coastal LP-DOAS studies at Mace Head Ireland by Alicke et al. [1999] reported up to 6 ppt IO which was confirmed by follow up studies [Hebestreit, 2001; Saiz-Lopez et al., 2006; Seitz, 2009]. Elevated IO was also reported from LP-DOAS studies at other coastal sites: Brittany France up to 7 ppt [Peters et al., 2005] and 10 ppt [Mahajan et al., 2009]; Gulf of Maine up to 4 ppt [Stutz et al., 2007]. However, these observations are limited to few locations in the northern hemisphere, and the spatial averaging by LP-DOAS over several km may conceal possibly inhomogeneous distributions. In fact model studies by Burkholder et al.

[2004] suggest local 'hot spots' with 10 times higher IO mixing ratios to explain the large aerosol production coinciding with the IO observations at Mace Head and Brittany, which is supported by first LiF in-situ IO measurements which reported up to  $(29.3 \pm 2.5)$  ppt at Mace Head [Commane et al., 2011] and up to  $(30 \pm 7)$  ppt at Roscoff, Brittany [Furieux et al., 2010]. Besides coastal regions observations of IO were also reported in the MBL with level around 1-2 ppt have been reported for the north eastern Atlantic on Cape Verde [Read et al., 2008] and Tenerife [Puentedura et al., 2012] and for the western [Großmann et al., 2013] and eastern [Mahajan et al., 2012; Lampel, 2014; Volkamer et al., 2015] Pacific Ocean. In polar regions reported IO levels showed an unexpected hemispheric difference with sub ppt to single ppt mixing ratios in the arctic [e.g. Hönninger, 2002; Pöhler et al., 2010; Mahajan et al., 2010a; Zielcke, 2015] and high IO up to more than 20 ppt in the antarctic [e.g. Frieß et al., 2001; Frieß et al., 2010; Saiz-Lopez et al., 2007; Schönhardt et al., 2008]. However, recent studies in the antarctic by Lampel [2010], Frieß et al. [2013] and Zielcke [2015] are in disagreement with the previous observations showing no or only low IO levels. In fact studies by Zielcke [2015] for the first time consistently show low IO levels in the antarctic and the arctic using multiple DOAS techniques (MAX-DOAS, LP-DOAS, Cavity Enhanced DOAS (CE-DOAS), Satellite DOAS), thus indicating that reactive iodine may only play a minor role in polar regions compared to bromine. Although it can enhance the speed of bromine chemistry even at these low concentration.

### 2.3.1. Impact of Reactive Halogen Species on Tropospheric Chemistry

This section summarizes the chemistry of reactive halogen species (RHS) in the troposphere. Figure 2.7 gives an overview of the liquid and gas phase chemistry of iodine, rate coefficients and photolysis for the iodine compounds are summarized in Tab. 2.2 and Tab. 2.3 respectively. Since the main reaction schemes for Cl, Br and I in the troposphere are similar the following description uses X and Y instead of Br, Cl and I. A more detailed description of RHS chemistry is given by e.g. by Platt and Hönninger [2003], Glasow and P. Crutzen [2003], Saiz-Lopez et al. [2012] and Simpson et al. [2015].

#### 2.3.1.1. Ozone Destruction

Halogen chemistry is usually initialized by the rapid photolysis of molecular halogens



which yields atomic halogen radicals. The most prominent reaction of halogen atoms is the fast reaction with Ozone leading to short lifetimes of the halogen atoms in the troposphere of  $\tau_{\text{Cl}} = 0.13\text{s}$ ,  $\tau_{\text{Br}} = 1.3\text{s}$  and  $\tau_{\text{I}} = 1.3\text{s}$  at a typical northern hemisphere background Ozone concentrations of 50 ppt. The formed halogen oxides are rapidly photolyzed (e.g.  $\tau_{\text{IO}} = 0.14\text{s}$

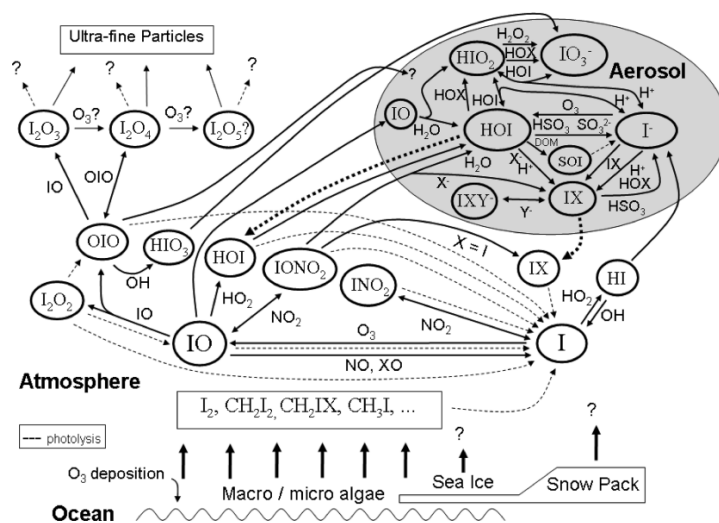


**Figure 2.7.** | Simplified diagram of gas and liquid phase iodine chemistry. Dashed lines indicate photolysis, whereas dotted lines indicate gas phase equilibration from aerosols. X and Y are halogen atoms, DOM is dissolved organic matter, and SOI is soluble organic iodine. Adopted from Saiz-Lopez et al. [2012]

Reaction	$k$ ( $\text{cm}^3\text{s}^{-1}$ )	uncertainty factor	literature ref.
$\text{I} + \text{O}_3 \rightarrow \text{IO} + \text{O}_2$	$1.2 \cdot 10^{-12}$	1.2	S. P. Sander et al. [2011]
$\text{I} + \text{NO}_2 \xrightarrow{M} \text{IONO}$	$5.2 \cdot 10^{-12}$	1.2	S. P. Sander et al. [2011]
$\text{I} + \text{NO} \xrightarrow{M} \text{INO}$	$3.9 \cdot 10^{-13}$	1.3	S. P. Sander et al. [2011]
$\text{I} + \text{NO}_3 \rightarrow \text{IO} + \text{NO}$	$(4.5 \pm 1.2) \cdot 10^{-10}$ $(1 \pm 0.3) \cdot 10^{-10}$		Chambers et al. [1992] Dillon et al. [2008]
$\text{I}_2 + \text{NO}_3 \rightarrow \text{IONO}_2 + \text{I}$	$1.5 \cdot 10^{-12}$	3.2	Chambers et al. [1992]
$\text{I} + \text{IONO}_2 \rightarrow \text{I}_2 + \text{NO}_3$	$(0.2 - 9.4) \cdot 10^{-11}$ recommended $5.5 \cdot 10^{-11}$	quantum chem. calc.	Kaltsoyannis and Plane [2008]
$\text{IO} + \text{NO}_2 \xrightarrow{M} \text{IONO}_2$	$3.7 \cdot 10^{-12}$	1.3	S. P. Sander et al. [2011]
$\text{IO} + \text{HO}_2 \rightarrow \text{HOI} + \text{O}_2$	$8.4 \cdot 10^{-11}$	1.5	S. P. Sander et al. [2011]
$\text{IO} + \text{IO} \rightarrow \text{I} + \text{OIO} \approx 40\%$ $\rightarrow \text{IOIO} \approx 50\%$ $\rightarrow \text{other products}$	$9.9 \cdot 10^{-11}$	1.3	Atkinson et al. [2007]
$\text{IO} + \text{BrO} \rightarrow \text{Br} + \text{OIO}$	$6.8 \cdot 10^{-11}$		Atkinson et al. [2007]
overall	$8.5 \cdot 10^{-11}$	1.1	Atkinson et al. [2007]
$\text{IO} + \text{ClO} \rightarrow \text{products}$	$9.9 \cdot 10^{-11}$	1.1	Atkinson et al. [2007]
$\text{BrO} + \text{BrO} \rightarrow \text{products}$	$3.2 \cdot 10^{-12}$	1.1	Atkinson et al. [2007]
$\text{IO} + \text{NO}_3 \rightarrow \text{OIO} + \text{NO}_2$	$(9 \pm 4) \cdot 10^{-12}$		Dillon et al. [2008]
$\text{I}_2 + \text{NO}_3 \rightarrow \text{I} + \text{IONO}_2$	$(1.5 \pm 0.5) \cdot 10^{-12}$		Chambers et al. [1992]
$\text{IO} + \text{DMS} \rightarrow \text{I} + \text{DMSO}$	$1.7 \cdot 10^{-14}$	1.5	S. P. Sander et al. [2011]
$(\text{OIO})_n + \text{OIO} \rightarrow (\text{OIO})_{n+1} \quad n = 1..4$	$> (1.2 \pm 0.3) \cdot 10^{-10}$		Gómez Martín et al. [2007]
$\text{OIO} + \text{IO} \rightarrow \text{I}_2\text{O}_3$	$> (5 \pm 2) \cdot 10^{-11}$		Gómez Martín et al. [2007]

**Table 2.2.** | Rate coefficients for some important reactions of iodine species. All values are given for  $p = 1013$  hPa and  $T = 293.15$  K

## 2.3. Tropospheric Halogen Chemistry

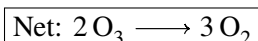
Reaction	$j$ ( $s^{-1}$ )	condition	literature ref.
$I_2 + h\nu \longrightarrow 2I$	$0.12 \pm 0.03$	$E_e \approx 1.1 \text{ kW m}^{-2}$	Saiz-Lopez et al. [2004]
$IO + h\nu \longrightarrow I + O$	0.14	SZA = 40°	Bloss et al. [2001]
$OIO + h\nu \longrightarrow IO + O$	-	$\phi < 0.007$	Ingham et al. [2000]
$OIO + h\nu \longrightarrow O_2 + I$	$< 0.028$	$\phi < 0.1$	Tucceri et al. [2006]
	0.28	$\phi = 1$	Gómez Martín et al. [2009]
$IONO_2 \xrightarrow{h\nu} \left. \begin{array}{l} I + NO_3 \approx 20 - 98 \% \\ IO + NO_2 < 2 \% \\ OIO + NO \approx 0 \% \end{array} \right\}$	$(3 \pm 2) \cdot 10^{-3}$ $4 \cdot 10^{-2}$	SZA $\approx 20^\circ - 30^\circ$	Joseph et al. [2007] Mössinger et al. [2002]
$IONO_2 \longrightarrow IO + NO_2$	$(0.07 - 1.3) \cdot 10^{-4}$	thermolysis at 290 K	Saiz-Lopez et al. [2012]

**Table 2.3.** | Photolysis frequencies  $j$  for some iodine species.

at 40° SZA )

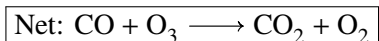


This leads to a 'null cycle' in ozone destruction. The destruction of ozone occurs via a number of catalytic cycle. In cycle one the formation of XO and YO is followed by their cross or self reaction:

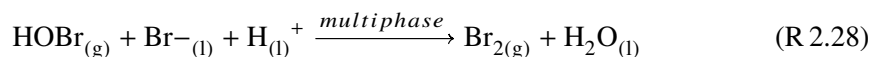


The branching ratio between R 2.24a, R 2.24b and R 2.24c and thereby also the Ozone destruction efficiency strongly depends on involved halogen species [Atkinson et al., 2007, e.g.]. The formation of OBrO and OCIO (R 2.24a) leads to a 'null cycle' since their photolysis yields a halogen monoxide and atomic oxygen which readily recombines with  $O_2$  and yield  $O_3$  reducing the efficiency of ozone destruction. Recent studies [see. Saiz-Lopez et al., 2012] indicate that the photolysis of OIO yields atomic iodine and molecular oxygen which would increase the ozone destruction efficiency of the IO self reaction. However, there is still an order of magnitude discrepancy in the reported OIO photolysis frequency between  $< 0.028 \text{ s}^{-1}$  [Tucceri et al., 2006] and  $0.28 \text{ s}^{-1}$  [Gómez Martín et al., 2009]. The rate limiting step of the ozone destruction cycle R 2.24 is the reaction of XO with YO. Generally the self reactions of halogen oxides are much slower than cross reactions especially those involving iodine. For example Mahajan et al. [2010b] showed that the presence of few ppt IO can lead to strong increase in the ozone depletion rate of BrO, present at Arctic spring-time mixing ratios of more than 10 ppt. At lower

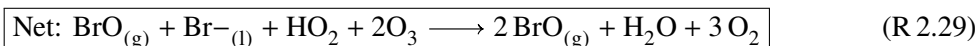
halogen concentration cycle two, which involving HO<sub>2</sub> radicals becomes important:



This cycle is dominant in remote marine environments [Read et al., 2008]. HOX can also enter the liquid phase. For the case of HOBr this leads to the activation of dissolved bromide (Br<sup>-</sup>) if the pH of the solution is sufficiently low (<6.5):



During daytime Br<sub>2</sub> is rapidly photolyzed to 2 Br and subsequently oxidized to 2 BrO. The net cycle can be summarized as



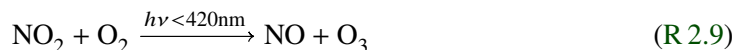
As this cycle can lead to an exponential growth in the gas phase bromine it is referred to as 'bromine explosion' [Platt and Lehrer, 1997]. This process is very effective at ozone destruction particularly during polar spring where it regularly leads to virtually complete depletion of boundary layer ozone [Simpson et al., 2007; Sihler, 2012]. A sketch of the reaction cycle is shown in Fig. 2.8

### 2.3.1.2. Changes in the HO<sub>2</sub>/HO and NO<sub>2</sub>/NO<sub>2</sub> Partitioning

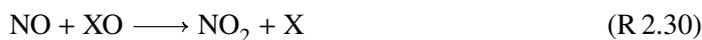
In the ozone destruction cycle 2.3.1.1, the reaction of halogen oxide XO with HO<sub>2</sub> and subsequent photolysis leads to the conversion of HO<sub>2</sub> to OH and thus reduce the HO<sub>2</sub>/HO ratio [e.g. Platt and Janssen, 1995].



As described in sec. 2.2.2 in the troposphere the NO<sub>2</sub>/NO<sub>2</sub> ratio is mainly controlled by the reactions



The reaction of XO with NO leads to conversion of NO to NO<sub>2</sub>



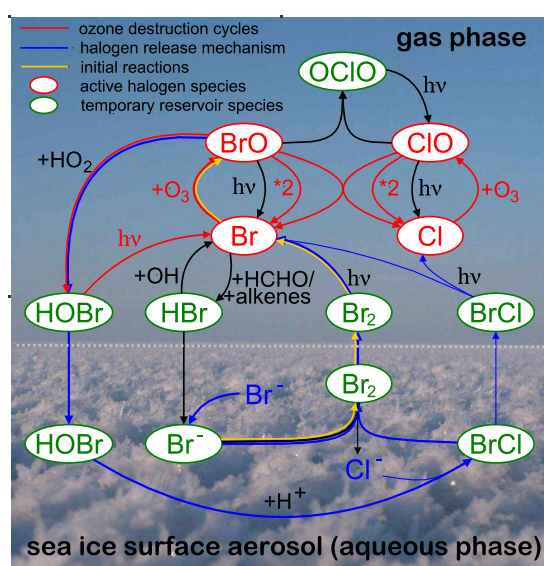


**Figure 2.8.** | Simplified diagram of the bromine explosion mechanism. The schematic also includes the inter-halogen reactions between bromine and chlorine, which can cause a significant increase in the ozone depletion rate. A detailed description is given in the text. Adopted from Pöhler et al. [2010]

and thus an increase in the Leighton ratio  $L = \frac{[\text{NO}_2]}{[\text{NO}]}$ . Even though the above effects do not directly destroy ozone they limit the NO<sub>x</sub> catalyzed ozone production (see sec. 2.2.2.2) by reducing the educts of the reaction



The overall impact of halogen oxide on the oxidation capacity of the troposphere is summarized in Fig. 2.9.

### 2.3.1.3. Oxidation of Dimethyl Sulfide

The most important gaseous precursor for sulfate aerosol over the ocean is the oxidation of DMS by OH. However, DMS can also be oxidized by BrO in a catalytic cycle [Toumi, 1994]:



which can be comparable to OH [e.g. Mahajan et al., 2010a]. This leads to reduction in the DMS to SO<sub>2</sub> conversion efficiency [Toumi, 1994; Glasow and P. J. Crutzen, 2004; Glasow et al., 2004] and thus to a reduction in the formation of cloud condensation nuclei (CCN) from sulfate aerosol. Over clean oceans with low CCN concentrations, this could have an important impact on cloud formation and cloud albedo and thus on the climate [Glasow et al., 2004]. A similar reaction with IO is was found to be negligible at ppt IO mixing ratios [Saiz-Lopez et al., 2012].

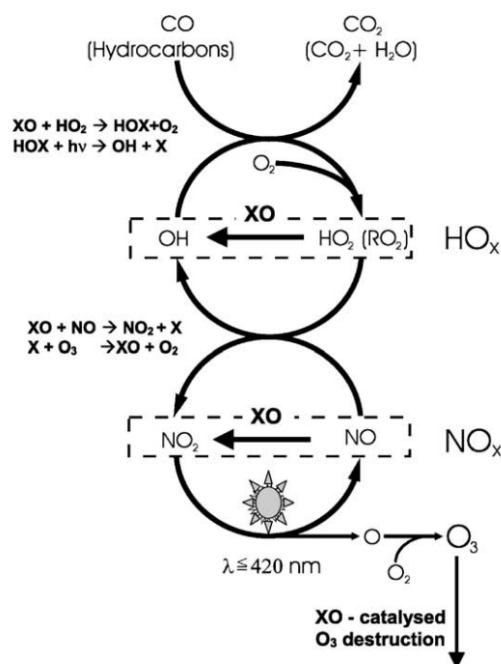


**Figure 2.9.** | The overall picture of the impact of halogen oxide radicals on the oxidation capacity of the troposphere. In addition to XO catalysed O<sub>3</sub> destruction the stationary state ratios of NO/NO<sub>2</sub> and HO<sub>2</sub>/OH are reduced. As a consequence the product [HO<sub>2</sub>] × [NO] and thus O<sub>3</sub> formation is suppressed. Adopted from Platt and Hönninger [2003]

#### 2.3.1.4. Oxidation of Elemental Mercury

Mercury is found in the atmosphere mainly in the form of gaseous elemental mercury (Hg<sup>0</sup>) with a lifetime of about a year. Oxidation by BrO converts (Hg<sup>0</sup>) into the highly toxic and bio-accumulative reactive gaseous mercury (RGM), which is compared to (Hg<sup>0</sup>) more water soluble and therefore can enter the food chain. Mercury oxidation by Halogens is particularly important in polar spring where the high levels of bromine and low temperatures enhance the formation of (RGM). Such a correlation of mercury depletion events and the 'bromine explosion' have been observed in the arctic [Barrie and Platt, 1997; Schroeder et al., 1998]. A more detailed description of the current state of knowledge can be found in [Steffen et al., 2008]

#### 2.3.2. IO in Semipolluted Environments

During the field campaigns in this on several days semi polluted conditions with more than 1 ppt NO<sub>2</sub> were encountered. In these cases the normal reaction cycles described above are disturbed:

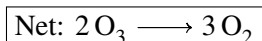
- In semi polluted environments the most important loss of iodine atoms after reaction

R 2.21 is



In polluted environment with a  $\text{NO}_2$  mixing ratios above 8 ppb R 2.32 becomes even faster than R 2.21 (assuming 30 ppb  $\text{O}_3$ ) and therefore the dominant loss for iodine atoms.

- IO is also quickly reacts with  $\text{NO}_2$  to form  $\text{IONO}_2$  ( $\tau_{\text{IO}} \approx 10$  s for 1 ppb  $\text{NO}_2$ ). In this case a third cycle for catalytic ozone destruction is possible:



However, the major photolysis pathway ( $\approx 90\%$ ) of  $\text{NO}_3$  formed in R 2.34 produces  $\text{NO}_2 + \text{O}$  leading to a 'null cycle' in ozone. Also there is order of magnitude discrepancy in the reported  $\text{IONO}_2$  photolysis frequencies (see Tab. 2.3) which translates to a range of the photolytic lifetime between 25 s and 333 s ( $\text{SZA} \approx 20^\circ - 30^\circ$ ). Furthermore, a modeling study by Kaltsoyannis and Plane [2008] suggests that  $\text{IONO}_2$  rapidly recycles back to  $\text{I}_2$  by reaction with I.



Assuming their recommended reaction rate of  $5.5 \cdot 10^{-11}$  I atoms will react with with  $\text{IONO}_2$  rather than  $\text{O}_3$  if the ratio  $[\text{IONO}_2]/[\text{O}_3]$  is  $> 0.02$  (i.e. typically  $\text{IONO}_2$  mixing ratios greater than 0.6 ppb). This reaction would limit the buildup of  $\text{IONO}_2$  and thus allow iodine chemistry even in a relatively high NOx environment.

$\text{IONO}_2$  can also be removed by the uptake on aerosol. The lifetime of  $\text{IONO}_2$  against uptake on aerosol is 12 h corresponding to a loss rate of  $\approx 2.3 \cdot 10^{-5} \text{ s}^{-1}$  at  $T = 285$  K for an accommodation coefficient of 0.05 and a typical MBL volumetric aerosol surface area of  $10^{-7} \text{ cm}^2 \text{ cm}^3$  [Saiz-Lopez et al., 2006]. However, the  $\text{IONO}_2$  uptake on aerosol could much larger, due to the dependence of the volumetric aerosol surface area and on the coastal setting and meteorology, and the large uncertainties in the accommodation coefficient.

- Saiz-Lopez et al. [2006] proposed the reaction of  $\text{I}_2$  and  $\text{NO}_3$  as a nighttime source of IO



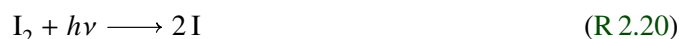
However, this reaction is still controversy discussed since night time IO was so far only observed during two coastal campaigns at Mace Head Saiz-Lopez et al. [2006] and in Brittany, France Mahajan et al. [2009] both times at a 3 ppt mixing ratio.

### 2.3.3. Iodine Mediated Particle Formation

During the PARFORCE campaign carried out 1998 at Mace Head Research station particle nucleation events with particle concentrations up to  $10^6 \text{ cm}^{-3}$  were found to correlate with solar irradiance and low tide and the particles were found to contain iodine species [Mäkelä et al., 2002; O'Dowd et al., 2002a]. Since simultaneously measured gas phase iodine compounds showed the same correlation with solar irradiance and low tide O'Dowd et al. [2002b] proposed iodine mediated particle formation. If these particles grow sufficiently to become cloud condensation nuclei (CCN), they could influence cloud properties and therefore have an impact on the coastal climate [Rosenfeld et al., 2008].

Iodine induced particle formation was subsequently investigated in several laboratory studies [e.g. Hoffmann et al., 2001; Jimenez et al., 2003; Burkholder et al., 2004; McFiggans et al., 2004; Saunders et al., 2010]. A review of the current knowledge on iodine induced particle formation is given in [Saiz-Lopez et al., 2012].

It is now established that molecular iodine ( $\text{I}_2$ ) emitted by seaweed (see sec. 3.1.2) is the most likely source of iodine oxide particles (IOP). [McFiggans et al., 2004] showed that the initially suspected short lived diiodomethane  $\text{CH}_2\text{I}_2$  and other iodocarbons are 1000 times less likely to form particles. The formation of IOPs is initialized by the photolysis of the precursor gas and subsequent reaction with  $\text{O}_3$  to form IO



Subsequently OIO is formed either by the self reaction of IO



OIO could also be formed by the cross reaction with BrO but at coastal sites with high IO concentrations the BrO concentrations are typically too low to be of importance. The major channel of the IO self reaction ( $\sim 60\%$ ) is

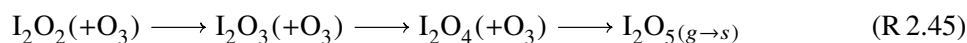


However, theoretical calculations and experimental data indicate that IOIO dissociates to  $\text{OIO} + \text{I}$  within about one second under atmospheric conditions [see Kaltsoyannis and Plane, 2008, and references therein]. Several studies suggest that OIO subsequently recombines with itself or IO [e.g. Hoffmann et al., 2001; Gómez Martín et al., 2007]

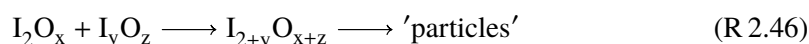


Laboratory studies by Jimenez et al. [2003] inferred that the IOPs formed in their experiments should be mainly composed of  $\text{I}_2\text{O}_4$ , while transmission electron microscope analysis by Saunders and Plane [2005] showed that IOPs generated from  $\text{I}_2$  and  $\text{O}_3$  were essentially  $\text{I}_2\text{O}_5$ .

Saunders and Plane [2005] suggest that formation of  $I_2O_5$  could occur through a sequential oxidation with  $O_3$  in the gas phase before polymerizing to form particles of pure  $I_2O_5$



However, a recent study by Saunders et al. [2010] showed that IOPs can form without  $O_3$ , which suggests that IOP formation is almost certainly initiated by the polymerization of  $I_2O_3$  and  $I_2O_4$



There are still many uncertainties regarding IOP formation, especially there is a lack of direct observation of the higher iodine oxides  $I_2O_x$  and  $I_yO_z$ . Furthermore, the polymerization rates as well as photolysis rates of higher iodine oxides are still largely unknown.

IOP formation is a higher order reaction of the initial IO thus the formation rates increase rapidly with the initial IO concentration. According to a laboratory study by [Burkholder et al., 2004], in order to reproduce the particle concentrations observed at Mace Head (and their rapid formation) high IO mixing ratios of 50 to 100 ppt are required. The IO mixing ratios of up to 7 ppt observed by LP-DOAS are however one order of magnitude lower. Since LP-DOAS gives the average mixing ratios along several km long light paths, [Burkholder et al., 2004] suggest that IO was localized 'hot spots' with above average mixing ratios. Part of this work was to study for the first time IO in-situ mixing ratios directly above seaweeds in the in tidal zone which were suspected to be the sources of IO hot spots (see chap. 12).

### 2.3.4. Sources of Reactive Halogen Compounds

There are different sources and reactions path of reactive halogen species in the troposphere: The photolytic degradation of organic halogen compounds, the emission of inorganic halogen compounds from sea salt aerosol, surface salt deposits and seawater and the molecular emission of molecular iodine from seaweed.

#### 2.3.4.1. Reactive Bromine and Chlorine Species

For reactive bromine and chlorine the major source seems to be the release of inorganic halogen species from sea salt (e.g. sea salt aerosol or sea salt), which can proceed by three main pathways:

1. The uptake of oxidizing agents as HOX and  $HNO_3$  on acidic sea salt may convert  $Br^-$  and  $Cl^-$  to gaseous  $Br_2$  or  $BrCl$ . For the case of HOBr and  $Br^-$  this can lead to the bromine explosion described in sec. 2.3.1.1 which is most prominently observed in polar regions, especially during spring, but was also observed in at salt lakes e.g. [Stutz et al., 2002; Hönninger et al., 2004; Hebestreit et al., 1999; Holla et al., 2015] and in volcanic plumes [Bobrowski et al., 2003, e.g.].

2. Strong acids can release HCl (but not HBr) from sea salt halides [Wayne et al., 1995]. Under certain conditions, the recycling of HX through heterogeneous reactions to photolabile XY is possible [e.g. McFiggans et al., 2000; R. Sander et al., 1999].
3. The nitrogen oxides  $\text{NO}_3$ ,  $\text{N}_2\text{O}_5$  and perhaps  $\text{NO}_2$  can react with NaCl or NaBr to release HBr and HCl or the photolabile species  $\text{ClNO}_2$  and  $\text{BrNO}_2$  [e.g. B. Finlayson-Pitts and Johnson, 1988; B. J. Finlayson-Pitts et al., 1989]

### 2.3.4.2. Reactive Iodine Species

The sources of reactive iodine species in the atmosphere, are less clear compared to bromine, and are a subject of current research. It is generally believed that the emission of molecular iodine and of iodocarbons and their photolysis is the major source of reactive iodine species.

The open ocean is considered the largest iodine reservoir with a total iodine content of  $\approx 0.42 - 0.44 \mu\text{mol L}^{-1}$  [Truesdale et al., 2000] and also considered the principal source of atmospheric iodine [e.g. U. Richter and Wallace, 2004]. However, most of the iodine in seawater is present in the form of iodate ( $\text{IO}_3^-$ ), which cannot be directly released. Historically the emission of  $\text{CH}_3\text{I}$ , a metabolic product of micro algae, was considered the only pathway of iodine from the ocean into the atmosphere [Cicerone, 1981]. However, due to its relatively long photolytic lifetime of about 5 days [Carpenter et al., 2014],  $\text{CH}_3\text{I}$  is not considered an efficient source of reactive iodine in the lower troposphere, and the reported total ocean emission rates of  $546 \text{ Gg}_\text{I} \text{ a}^{-1}$  [Butler et al., 2007] could not explain the observed MBL IO levels in the ppt range [e.g. Lampel, 2014; Mahajan et al., 2010a; Read et al., 2008]. Recently [Jones et al., 2010] also reported a combined global iodine emission of  $(330 \pm 190) \text{ Gg}_\text{I} \text{ a}^{-1}$  for the dihalomethanes  $\text{CH}_2\text{ICl}$ ,  $\text{CH}_2\text{IBr}$  and  $\text{CH}_2\text{I}_2$ , which have considerably shorter photolytic lifetimes of several hours [Rattigan et al., 1997], about one [Mössinger et al., 1998] and 2-10min [Mössinger et al., 1998] respectively. However, a 1D atmospheric model applied in [Jones et al., 2010] revealed that even the combined  $\text{CH}_3\text{I}$  and dihalomethanes fluxes could only account for  $\sim 10 - 20\%$  of the observed IO mixing ratios. A recent study by [Carpenter et al., 2013] suggests that the major open ocean source of reactive iodine (up to 75% over the tropical Atlantic Ocean) is the gaseous emission of  $\text{I}_2$  and HOI following the reaction of iodide with ozone.

At coastal sites ten to hundred times higher concentrations of reactive iodine species IO have been reported, compared to the open ocean. IO was mainly measured by LP-DOAS [e.g. Aliche et al., 1999; Hebestreit, 2001; Peters, 2005; Seitz, 2009; Mahajan et al., 2009] but recently also first in-situ measurements [e.g. Furneaux et al., 2010; Huang et al., 2010b; Commane et al., 2011] were reported. The observations of IO correlated the exposure of large areas of seaweed to air during low tide. Subsequent laboratory studies showed that many seaweeds are strong emitters of molecular iodine [e.g. Küpper et al., 2008; Dixneuf et al., 2009; S. M. Ball et al., 2010; Nitschke et al., 2011; Ashu-Ayem et al., 2012] and to a minor extent iodocarbons [Carpenter et al., 2000] when they are exposed to air. However, their contribution to the global iodine emissions remains unclear, with estimated emission rates ranging from  $0.01 - 0.1 \text{ Gg}_\text{I} \text{ a}^{-1}$  [O'Dowd et al., 2002b] to more than  $10 \text{ Gg}_\text{I} \text{ a}^{-1}$  [Saiz-Lopez et al., 2012]. A detailed discussion of seaweeds including their iodine accumulation and emission mechanisms is given in chapter 3.

# 3

## Seaweed

Algae, "are thallophytes (plants lacking roots, stems, and leaves) that have chlorophyll *a* as their primary photo synthetic pigment and lack a sterile covering of cells around the reproductive cells" [Lee, 2008]. Seaweeds, are marine macro algae (or macrophytes ), which are categorized based on the color of their thallus into green seaweed (class *Chlorophyta*), red seaweed (class

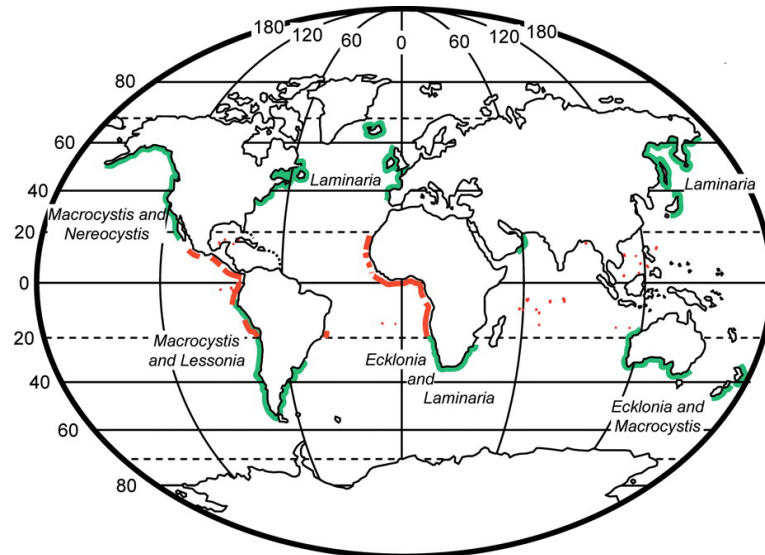


**Figure 3.1. | World distribution of kelp forests.** Geographic distribution of kelp forests in surface (green lines) and deep (red lines) waters. While *Laminaria* species are dominant in the northern Atlantic and north western Pacific, *Macrocystis* are the dominant species of the southern hemisphere and in the north eastern Pacific. Adopted from Santelices [2007], ©(2007) National Academy of Sciences, USA

*Rhodophyta*) and brown seaweed (class *Phaeophyceae*). According to AlgaeBase<sup>1</sup>, there are about 10000 seaweed species, 1000 green, 2000 brown and 7000 red species. However, the seaweed biomass is dominated by brown seaweeds of the order *Laminariales* commonly known as kelps. Kelps, which tolerate water temperatures up to 23 °C, are the dominant seaweed species in shallow, mostly subtidal habitats (<30 m) of mid-latitude to high-latitude areas [Schiel and Foster, 1986], but were recently also discovered to grow in extensive tropical deep water forests [Graham et al., 2007]. Kelps are known to form dense underwater forests and some species can grow up to 45 m length. An overview of the global kelp distribution is depicted in Fig. 3.1. It shows that there are strong regional differences. While *Laminaria* species are dominant in the northern Atlantic and north western Pacific, *Macrocystis* are the dominant species of the southern hemisphere and in the north eastern Pacific. A complete survey of the world's kelp forest is missing but estimates indicate a standing crop of ~ 7.5 Tg<sub>C</sub> up to 20 Tg<sub>C</sub> [Reed and Brzezinski, 2009], and attempts are made to get more accurate numbers using airborne and satellite remote monitoring [Casal et al., 2012; Bell et al., 2015, e.g]. In warmer sub-tropical and tropical waters, the brown seaweeds *Sargassum* are dominant [Lee, 2008], which for example form huge floating patches in the gulf of Mexico and the Sargasso sea with a total wet mass of about 2 million tonnes [Gower and King, 2011]. Depending on the geographical location and type of shore seaweeds are also abundant in the inter-tidal zone. Generally speaking, sandy beaches and exposed shores appear relatively bare of seaweed, while an increased diversity of species is found on more sheltered shores which may show an extensive seaweed cover [Little and Kitching, 1996]. For example in the mid- to high-latitude Atlantic Ocean the brown-seaweeds of the genus *Ascophyllum* and *Fucus* are dominant [Michanek, 1975] and often completely cover the intertidal zone in sheltered bays and inlets. In contrast, on the Pacific Coast of North America, turfs of red seaweed are more common while brown seaweed is much less abundant [Little and Kitching, 1996]. In the mid and high latitudes of the southern hemisphere, brown seaweeds of the genus *Durvillaea* are common in the intertidal zone of exposed shores. Similar to Kelp, *Durvillaea* is one of the larger seaweeds with blades of up to 10 m length and extends down into the in the subtidal zone [Hay, 1977]. These examples, show that the abundance, distribution and composition of the seaweeds in the intertidal zone is very site specific. More details on the seaweeds encountered at the field campaigns in Ireland and New Zealand are given in sec. 12.1.1 and sec. 13.1.1 respectively.

### 3.1. Iodine accumulation and release by seaweeds

Seaweeds also have the unique ability to strongly concentrate iodine from the seawater and release it in bursts to counter oxidation stress when exposed to air. In the following, an overview of the involved mechanisms is given.

---

<sup>1</sup>Guiry, M.D. & Guiry, G.M. AlgaeBase. World-wide electronic publication, National University of Ireland, Galway. <http://www.algaebase.org>; searched on May 5th 2015

### 3.1. Iodine accumulation and release by seaweeds

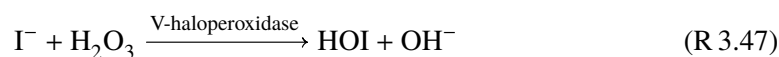
species	iodine content gI/gDw	ref
<b>brown saweed:</b>		
<i>Laminaria digitata</i>	(4 – 47) · 10 <sup>-3</sup>	Küpper et al. [1998]
	(0.8 – 5) · 10 <sup>-3</sup>	Morrissey et al. [2001]
<i>Laminaria saccharina</i>	(0.8 – 4.5) · 10 <sup>-3</sup>	Morrissey et al. [2001]
<i>Saccharina japonica</i>	5.6 · 10 <sup>-3</sup>	Saenko et al. [1978]
<i>Himantalia elongata</i>	2 · 10 <sup>-3</sup>	Morrissey et al. [2001]
<i>Ascophyllum nodosum</i>	(0.7 – 1.2) · 10 <sup>-3</sup>	Morrissey et al. [2001]
<i>Fucus Vesiculosus</i>	0.73 · 10 <sup>-3</sup>	Netten et al. [2000]
<i>Macrocystis</i>	0.24 · 10 <sup>-3</sup>	Netten et al. [2000]
<b>red saweed:</b>		
<i>Phyllophora nervosa</i>	up to 5 · 10 <sup>-3</sup>	Gazha et al. [1983]
<i>Ptilota filicina</i>	4.2 · 10 <sup>-3</sup>	Saenko et al. [1978]
<i>Palmaria palmata</i>	(0.1 – 0.5) · 10 <sup>-3</sup>	Morrissey et al. [2001]
<b>green seaweed:</b>		
<i>Ulva rigida</i>	0.24 · 10 <sup>-3</sup>	Morrissey et al. [2001]

**Table 3.1.** | **Some seaweed species with high iodine content.** The iodine content is given in gram iodine per gram dry weight.

#### 3.1.1. Accumulation of Iodine

As mentioned above, seaweeds have the unique ability to highly accumulate iodine from the seawater. In fact the element Iodine was first discovered in the ashes of burned *Laminaria* by Courtois [1813] and until the beginning of the 20th century, seaweed was the major iodine source for the chemical industry, medicine and photography. The highest accumulation was found for the kelp species *Laminaria digitata* with (in some cases) more than 1 % of their dry weight [Young and Langille, 1958]. This corresponds to a 30000 fold enrichment compared to the seawater concentration of  $\approx 0.42 - 0.44 \mu\text{mol L}^{-1}$  [Truesdale et al., 2000] where it is mainly present in the form of iodate  $\text{IO}_3^+$  and iodide  $\text{I}^-$ . As shown in Tab. 3.1, high concentrations of iodine were also found in other green, red and brown seaweeds.

So far, the iodine metabolism has only been investigated for brown seaweed species. First studies by Baily and S. Kelly [1955] on *A. nodosum* indicated that iodide and not iodate is the species that is involved in the uptake. Further studies of the iodine metabolism used the kelp species *L. digitata* due to its high iodine content. Studies by Küpper et al. [1998] and Küpper et al. [2008] indicate that the accumulation of iodine proceeds by the oxidation of  $\text{I}^-$  with hydrogen peroxide ( $\text{H}_2\text{O}_2$ ) to hypoiodous acid (HOI)



which is mediated by vanadium-dependent haloperoxidase enzymes. The iodine is subsequently stored in the reduce form of  $\text{I}^-$  in the apoplast (i.e cell walls and extracellular space) of cells in the peripheral tissue Verhaeghe et al. [2008]. The exact reduction process is still unclear. Even though this mechanism has only been studied on *L. digitata*, iodine is dominantly stored as  $\text{I}^-$  in several other seaweed species [Hou et al., 1997; Shah et al., 2005, e.g.]. In addition also vanadium-dependent haloperoxidase enzymes were found in many seaweed species [Vilter, 1984; Winter and Moore, 2009, e.g.]. Thus it is expected that the iodine accumulation

mechanism is similar for other seaweed species.

### 3.1.2. Release of Molecular Iodine

The first atmospheric observations of  $I_2$  at, at the seaweed rich coast around Mace Head, Ireland [Saiz-Lopez and Plane, 2004] correlated with tide, which hints towards intertidal seaweed as the major source. Subsequent measurements at Mace Head [Peters, 2005; Seitz, 2009] and at the coast of Brittany, France [Mahajan et al., 2009] confirmed this correlation. A study by [Küpper et al., 2008] showed for *L. digitata* that the iodide accumulation in the apoplast leads to an antioxidant reservoir that can be mobilized during oxidation stress, i.e. exposure to air or attack by micro-organisms, leading to high concentrations of iodide in the liquid film over the seaweed. Palmer et al. [2005] proposed that the formation of  $I_2$  proceeds thorough the rapid reaction of  $O_3$  with iodide, forming the steady state intermediate  $IOOO^-$ , which is hydrolyzed to give HOI. Further McFiggans et al. [2004] and Palmer et al. [2005] proposed a mechanism involving an equilibrium between  $I^-$ , HOI and  $I_2$  in aqueous solution [Truesdale et al., 1994]:



For high concentrations of  $I^-$  the equilibrium lies far towards the right-hand side even at the seawater pH-level of 8. Subsequently, since molecular iodine has a limited water solubility and is relatively volatile, it equilibrates rapidly towards the gas phase.

Incubation chamber studies by [S. M. Ball et al., 2010] found the first direct evidence for seaweed emitting  $I_2$  into the gas phase. Seaweed samples were incubated in a plastic bottle, through which a pump forced ambient air which was subsequently guided into a Cavity Enhanced DOAS (CE-DOAS) instrument where the  $I_2$  levels were measured. Tab. 3.2 gives an overview of the seaweed  $I_2$  emission rates observed by [S. M. Ball et al., 2010] and further incubation chamber studies by Kundel et al. [2012] and Ashu-Ayem et al. [2012]. The rough order of seaweed species by their emission rates is: *Fucus serratus*  $\approx$  *Fucus vesiculosus* < *Ascophyllum nodosum* < *Laminaria saccharina*  $\leq$  *Laminaria hyperborea*  $\approx$  *Laminaria digitata*. No significant  $I_2$  emission was found for the brown seaweed *Dictyopteris membranacea* [S. M. Ball et al., 2010] and the red seaweeds *Condrus crispus* and *Delessaria sanguinea* [Kundel et al., 2012]. However, the determined emission rates show large variations, for example Ashu-Ayem et al. [2012] reported average emission rates of 7 – 616 pmol/ min /gFw with a median of 55 pmol/ min /gFw for the 25 investigated specimen. This variation might be related to differences between the locations of the sampling sites, age and healthiness of the samples, the time span between collecting the samples and the measurements. A similar observation was also made by Kundel et al. [2012] for two samples of *A. nodosum*, which also very different average emission rates of 0.24 pmol/ min /gFw and 2.05 pmol/ min /gFw (average over first hour of exposure).

Kundel et al. [2012] also found distinct differences in the temporal emission profiles of different seaweed species (see Fig. 3.1.2). *L. digitata* and *L. hyperborea* showed a strong initial  $I_2$  emission peak within the first 10 min exposure to air, followed by an exponential decline of the emission rate. At the latest, after 30 min the average emission rate has dropped by one order of magnitude compared to the initial burst. *L. saccharina* and *F. serratus* showed a more

### 3.1. Iodine accumulation and release by seaweeds

species	I <sub>2</sub> emission rates pmol/ min /gFw		comment	ref.
	average	peak		
<i>Laminaria digitata</i>	3.2 ± 0.8	9.0 ± 2.3	high variability between samples	S. M. Ball et al. [2010] Kundel et al. [2012] Ashu-Ayem et al. [2012]
	2.6	~ 20		
	7 – 616	N.A.		
<i>Laminaria hyperborea</i>	0.7 ± 0.2	5.5 ± 1.4	partly decayed	S. M. Ball et al. [2010] S. M. Ball et al. [2010] Kundel et al. [2012]
	19.3 ± 4.9	35.6 ± 9.1		
	2.8	~ 40		
<i>Laminaria saccharina</i>	0.6 ± 0.2	1.01 ± 0.26		S. M. Ball et al. [2010] Kundel et al. [2012]
	2.2	~ 5.5		
<i>Ascophyllum nodosum</i>	0.06 ± 0.02	0.10 ± 0.03		S. M. Ball et al. [2010] Kundel et al. [2012]
	1.1	~ 9		
<i>Fucus Vesiculosus</i>	0.008 ± 0.007		close to det. lim.	S. M. Ball et al. [2010] Kundel et al. [2012]
	0.31	~ 1.4		
<i>Fucus serratus</i>	< 0.007		below det. lim.	S. M. Ball et al. [2010] Kundel et al. [2012]
	0.65	~ 1.2		
<i>Dictyopteris membranacea</i>	< 0.016		below det. lim.	S. M. Ball et al. [2010]

**Table 3.2.** | I<sub>2</sub> emission rates for different brown seaweed species. Averages given by Kundel et al. [2012] and Ashu-Ayem et al. [2012] are for the first hour of exposure to air respectively. The experiments by S. M. Ball et al. [2010] varied in duration and lasted for about 20 min on average.

constant emission, with the strongest emission in the first 30 min of exposure. For *A. nodosum* and *F. vesiculosus*, Kundel et al. [2012] found a very different emission behavior. Both species showed a delayed I<sub>2</sub> emission profile, with an emission rate below 0.1 pmol/ min /gFw in the first 20 min after exposure. Subsequently the release rate of *A. nodosum* rapidly increased to a maximum of about 9 pmol/ min /gFw after one hour. For *F. serratus* the emission rate increased even longer until a constant plateau of about 1.4 pmol/ min /gFw was reached 1.5h after the initial exposure to air. Thus the results by Kundel et al. [2012] showed that in the study by S. M. Ball et al. [2010] the short incubation times of 17 min, 10 min and 14 min for *A. nodosum*, *F. vesiculosus* and also *F. serratus* respectively lead to an underestimate of their emission rates and in consequence to the wrong assumption that their I<sub>2</sub> emission was insignificant. The study by Kundel et al. [2012] showed that for *A. nodosum* the integrated emission over one hour was only a factor of 2.3 lower compared to *L. digitata*, which indicated that *A. nodosum* could make a considerable contribution to atmospheric I<sub>2</sub> emission in areas where it is abundant. In fact this work shows that *A. nodosum* and *F. vesiculosus* together are the major source of atmospheric I<sub>2</sub> on the Irish west coast (see chapter 12).

#### 3.1.3. Release of Volatile Iodocarbons

Besides the release of molecular iodine, haloperoxidase enzymes can also catalyze the synthesis of halogenated halocarbons in the presence of hydrogen peroxide [Wever et al., 1991; Winter and Moore, 2009, e.g.]. The emission of volatile iodine coating compounds by seaweeds has been established by several studies [Gschwend et al., 1985; Manley and Dastoor, 1987; Nightingale et al., 1995; Carpenter et al., 2000; Kundel et al., 2012, e.g.]. It was initially

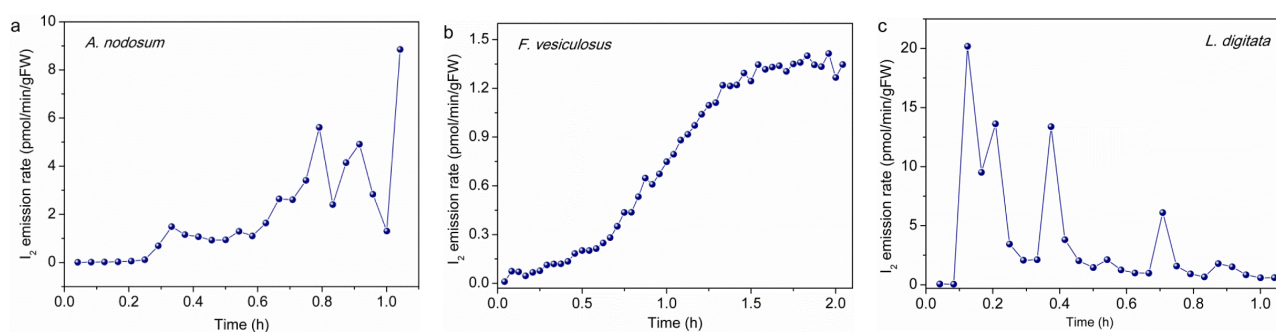


**Figure 3.2.** | Time-resolved  $I_2$  emission profiles from different seaweed species. The graphs show the  $I_2$  emission rates of Kundel et al. [2012] for a) *Ascophyllum nodosum*, b) *F. vesiculosus* and c) *Laminaria digitata* when exposed to air with 50 ppb  $O_3$  in an incubation chamber. Adapted from from Huang et al. [2013].

species	$CH_3I$	$CH_2ICl$	$CH_2IBr$	$CH_2I_2$	$\Sigma I$ -organic	$I_2$	% organic of total em. I	ref
<i>L. digitata</i>	0.019	0.04	0.04	0.13	0.24	5.2	4.4	Kundel et al. [2012]
	0.04	0.03	0.04	0.34	0.6			Carpenter et al. [1999]
<i>L. hyperborea</i>	0.08	0.02	0.03	0.08	0.23	5.6	4.1	Kundel et al. [2012]
<i>L. saccharina</i>	0.03	0.01	0.02	0.02	0.09	4.8	1.9	Kundel et al. [2012]
	0.02	0.01	0.01	0.06	0.1			Carpenter et al. [1999]
<i>A. nodosum</i>	0.005	0.004	0.006	0.006	0.02	2.2	0.9	Kundel et al. [2012]
	0.004	0.001	0.002	0.01	0.02			Carpenter et al. [1999]
<i>F. vesiculosus</i>	0.003	$5 \cdot 10^{-4}$	$8 \cdot 10^{-4}$	0.003	0.007	0.6	1.2	Kundel et al. [2012]
	0.004	0	0.001	0.005	0.01			Carpenter et al. [1999]
<i>F. serratus</i>	$4 \cdot 10^{-4}$	$2 \cdot 10^{-4}$	$5 \cdot 10^{-4}$	0.001	0.003	1.3	0.2	Kundel et al. [2012]
	$3 \cdot 10^{-4}$	$2 \cdot 10^{-4}$	$3 \cdot 10^{-4}$	0.001	0.002			Carpenter et al. [1999]

**Table 3.3.** | Total and Speciated Iodine Emission of Iodocarbons for some relevant seaweeds

speculated that photolysis of iodocarbons emitted by seaweed are the major source of reactive iodine [Carpenter et al., 1999, e.g.]. However, it is now established that iodocarbons emission rates of so far investigated seaweeds species [Carpenter et al., 2000; Kundel et al., 2012] are one to two orders of magnitude below their  $I_2$  emission. A summary of the the emission rates for relevant seaweed species is given in Tab. 3.3. Additionally, the photolytic lifetime of  $I_2$  is much lower compared to the photolytic lifetimes of iodocarbons shown in Tab. 3.4, which range from 5 min for  $CH_2I_2$  to several days for  $CH_3I$ . Therefore in order to explain same IO levels observed by LP-DOAS close to the source (short transport time), much higher iodocarbons emission rates would be needed compared to molecular  $I_2$ . Thus, at coastal sites with high seaweed abundance iodocarbons are expected to play only a very minor role as precursor for reactive iodine species.

### 3.1. Iodine accumulation and release by seaweeds

---

species	photolytic lifetime	source
CH <sub>2</sub> I <sub>2</sub>	5 minutes	Mössinger et al. [1998]
CH <sub>2</sub> IBr	60 minutes	Mössinger et al. [1998]
CH <sub>2</sub> ICl	several hours	Rattigan et al. [1997]
C <sub>2</sub> H <sub>3</sub> I	several days	Rattigan et al. [1997]
CH <sub>3</sub> I	4.3 days	Carpenter et al. [2014]
CHBr <sub>3</sub>	25 days	Carpenter et al. [2014]
CHBr <sub>2</sub> Cl	120 days	Bilde et al. [1998]
CH <sub>2</sub> Br <sub>2</sub>	no photolysis	Mössinger et al. [1998]
CH <sub>2</sub> BrCl	no photolysis	Carpenter et al. [2014]

**Table 3.4.** | **Photolytic lifetime of some halocarbons.** Photolytic lifetimes are given for the mid latitude boundary layer in summer.



# 4

## Differential Optical Absorption Spectroscopy

Differential Optical Absorption Spectroscopy (DOAS) was introduced by Perner et al. [1976], Platt et al. [1979] and Noxon [1975] and has since become an important and successful technique for the determination of atmospheric trace gas concentrations. DOAS analyzes the spectral signature of light in the ultraviolet-visible (UV-Vis) wavelength range after partial intensity attenuation along its path through a gaseous medium. Trace gases are quantitatively detected by their characteristic absorption features, which even allows the simultaneous detection of different trace gas species that absorb in the same spectral region. Thus, DOAS allows to study gas phase chemistry without influencing the system, e.g. by titration, strong radiation or reactive surfaces. This is a particular advantage for observations of highly reactive trace gases like BrO, IO, NO<sub>3</sub>, OH. Furthermore, DOAS allows remote sensing of the atmosphere from platforms on the ground, on aircraft or satellites.

DOAS applications are generally divided into active DOAS (e.g. LP-DOAS and CE-DOAS), which measures along a long light path between an artificial light sources and a receiving unit, and passive DOAS (e.g. MAX-DOAS), which uses natural light sources like direct or scattered sunlight. Generally, active DOAS has the advantage of a simple, well defined light path, which can even be folded to realize in-situ DOAS measurements, while passive DOAS is advantageous where artificial light source cannot be used to realize a long light path and for the investigation of vertical trace gas distributions.

In the following chapter the DOAS method is introduced as it was used for the spectral evaluation of the measurements central to this thesis. A detailed description of DOAS and its different applications is provided by Platt and Stutz [2008].

### 4.1. Absorption Spectroscopy

Optical absorption spectroscopy analyzes the attenuation of electromagnetic radiation from traveling through matter. In a gaseous medium attenuation is caused by the several factors. Firstly, radiation can be absorbed by molecules which are lifted into excited states. Photons in

the UV-Vis range have an energy in the order of 1 eV, which corresponds to electronic transitions (also called vibronic transitions if they involve a simultaneous change in the vibrational energy state). For bound target states, only radiation that matches the energy of the transitions is absorbed. These transitions result in a spectral signature unique to a particular atom or molecule. However, molecules exhibit broad absorption continua if the target state is above the dissociation limit or internally converted to a dissociative state. The probability of light being absorbed by a molecule is expressed by the absorption cross section  $\sigma(\lambda)$ . Secondly, radiation is attenuated by scattering on molecules or particles. Rayleigh theory approximates scattering on particles much smaller than the wavelength of the incident radiation ( e.g. for UV-Vis radiation these are molecules and aerosol particles smaller than 100 nm). Mie theory approximates scattering on particles with a diameter greater or equal to the wavelength. Although it is not an absorption process, for a narrow probing beam light scattered on its path through the measured air sample normally does not reach the detector. In this case, scattering can be treated like an absorption process with a scattering cross section. For Rayleigh scattering  $\sigma_{\text{ray}}(\lambda) \propto \lambda^{-4}$  [Rayleigh, 1899] and thus the amount of scattering strongly increases towards the UV-Vis range. Mie scattering has a much weaker wavelength dependency of  $\sigma_{\text{mie}}(\lambda) \propto \lambda^{-1.3}$  for a typical atmospheric aerosol distributions [Hulst, 1981].

The attenuation of the incoming light intensity  $I(\lambda)$  is related to the number density  $\rho_i$  of the absorbers  $i$  with absorption cross sections  $\sigma_i(\lambda)$  by the Beer–Lambert–Bouguer law, which in its differential form, is given by

$$dI(\lambda) = -I(\lambda) \sum_i \sigma_i(\lambda) \rho_i(l) dl \quad (4.1)$$

The light intensity after traveling along a light path of length  $L$  is obtained by integrating eq. (4.1)

$$I(\lambda) = I_0(\lambda) \exp\left(-\int_0^L \sum_i \sigma_i(\lambda, p(l), T(l)) \rho_i(l) dl\right) \quad (4.2)$$

with the initial intensity  $I_0(\lambda)$  and the pressure  $p(l)$  and temperature  $T(l)$ . Assuming constant pressure and temperature along the light path this can be simplified to

$$D(\lambda) = \ln\left(\frac{I_0(\lambda)}{I(\lambda)}\right) = \sum_i \sigma_i(\lambda, p, T) a_i \quad (4.3)$$

where

$$a_i = \bar{\rho}_i L = \int_0^L \rho_i(l) dl \quad (4.4)$$

is the column density and  $D(\lambda)$  is the optical density. Equation eq. (4.3) can be directly applied to retrieve trace gas number densities from spectroscopic measurements in the laboratory where  $I_0(\lambda)$  in the absence of trace gases is known. This direct application is impossible for atmospheric measurements as a measurement of the true  $I_0(\lambda)$  would require removal of all trace gases of interest from the atmosphere. Furthermore, it would also require quantification of all other effects that influence the intensity such as scattering, atmospheric turbulence and atmospheric refraction.

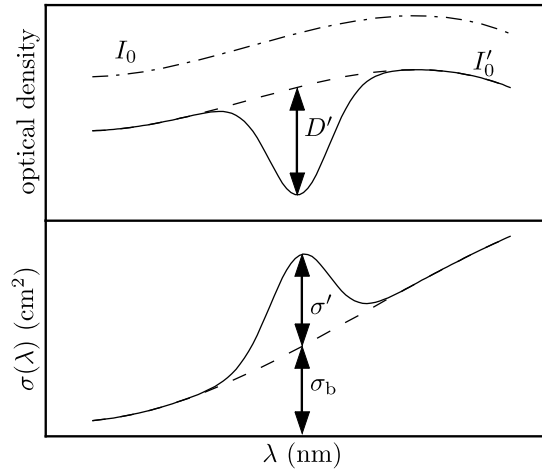


**Figure 4.1.** | **Illustration of the DOAS principle.** Narrow band absorption features  $D'$  and  $\sigma'$  are separated from the broadband part  $I'_0$  and  $\sigma_b$ . Subsequently only the narrow band part is used to determine trace gas concentrations. Adapted from Stutz [1996]

## 4.2. The DOAS Method

The underlying principle of DOAS is that trace gases with vibronic transitions have distinct narrow-band spectral structures in the UV-Vis spectral range while all unknown factors that influence the light intensity have very smooth or broadband spectral characteristic. Thus, the basic concept of DOAS is to separate broadband and narrow band spectral structures and then retrieve trace gas number densities only using the narrow-band absorption. This process is illustrated in Fig. 4.1.

The absorption cross section  $\sigma_i$  of each absorber is split into its differential part  $\sigma'_{i}$  and its broadband part  $\sigma_{b,i}$ :

$$\sigma_i = \sigma_{b,i}(\lambda) + \sigma'_i(\lambda) \quad (4.5)$$

The Beer–Lambert–Bouguer law can then be rewritten as

$$I(\lambda) = I_0(\lambda) \exp\left(-L \sum_i \sigma'_i(\lambda) \bar{\rho}_i\right) \exp\left(-L \left(\epsilon_R(\lambda) + \epsilon_M(\lambda) + \sum_i \sigma_{b,i}(\lambda) \bar{\rho}_i\right)\right) A(\lambda). \quad (4.6)$$

The first exponential contains the characteristic differential absorption. Broadband absorption and Rayleigh and Mie extinction,  $\epsilon_R(\lambda)$  and  $\epsilon_M(\lambda)$ , respectively, are described by the second exponential. The attenuation factor  $A(\lambda)$  describes all other factors that change broadband intensity, such as turbulence and atmospheric refraction and instrumental effects. All broadband contributions can now be included in a new quantity  $I'_0$  which describes the intensity in the absence of differential absorption:

$$I'_0(\lambda) = I_0(\lambda) \exp\left(-L \left(\epsilon_R(\lambda) + \epsilon_M(\lambda) + \sum_i \sigma_{b,i}(\lambda) \bar{\rho}_i\right)\right) A(\lambda) \quad (4.7)$$

This allows us to define the differential optical density analogous to eq. (4.3) as:

$$D'(\lambda) = \ln \left( \frac{I'_0(\lambda)}{I(\lambda)} \right) = L \sum_i \sigma'_i(\lambda) \bar{\rho}_i \quad (4.8)$$

The separation of broad- and narrow-band spectral structures requires the simultaneous measurement of the light intensities at several wavelengths. The number of wavelengths and the spectral range which needs to be covered for unambiguous DOAS evaluation of trace gases strongly depends upon the width and wavelength of the differential spectral absorption structures. Typical DOAS measurements sample a spectral window of 20 nm to 100 nm width at 100 to 2000 individual wavelengths.

The analysis of differential absorption features over a broad wavelength range has several advantages. The absorptions by different trace gases in eq. (4.8) can be separated based on their unique spectral signature and their number densities can be simultaneously retrieved. Furthermore, the differential optical density is unaffected by instrumental effects, such as the transmissions of the optical system, as they typically only have a broad spectral characteristic. Thus, DOAS measurements are intrinsically calibration free, which allows for a simpler instrument design and operation.

### 4.2.1. Mathematical Description of the Measurement Process

Figure 4.2 shows a simplified sketch of the DOAS measurement process. Light is sent through the atmosphere where it undergoes partial absorption by trace gases. After its pass through the atmosphere the light is focused on the entrance of a spectrograph. In the spectrograph light is dispersed by a grating and focused on a detector where it is digitized and transferred to a computer for storage and further processing. The following section gives a mathematical description of the involved processes/steps.

#### 4.2.1.1. Spectral Resolution

As shown in Fig. 4.2b), the limited resolution of optical spectrograph changes the shape of the spectrum  $I(\lambda)$ , collected by the receiving unit. Mathematically this is described by a convolution with the instrument function  $H(\lambda)$ .

$$I^*(\lambda) = (I \otimes H)(\lambda) := \int I(\lambda - \lambda') H(\lambda') d\lambda' \quad (4.9)$$

In order to determine the instrument function one can use the identity relation for a convolution with a Dirac  $\delta$  function  $H(\lambda) = (H \otimes \delta)(\lambda)$ . For spectrographs typically used in DOAS measurements, with a resolution lower than 0.1 nm, atomic emissions lines, with typical line widths in the order of 1 pm, give a very good approximation of a delta distribution.

The convolution leads to a modified non-linear Beer–Lambert–Bouguer law:

$$I^*(\lambda) = \left( \left[ I'_0 \exp \left( L \sum_i \sigma'_i \bar{\rho}_i \right) \right] \otimes H \right) (\lambda) \quad (4.10)$$

For a spectrally broad light source and weak trace gas absorption, the convolution and the exponential are (approximately) commutable operations [Wenig et al., 2005]:

$$I^*(\lambda) \approx I'_0(\lambda) \exp\left(L \sum_i (\sigma'_i \otimes H)(\lambda) \bar{\rho}_i\right) = I'_0(\lambda) \exp\left(L \sum_i S'_i(\lambda) \bar{\rho}_i\right) \quad (4.11)$$

with the low resolution absorption spectra  $S'_i(\lambda)$ . This approximation is very common for DOAS evaluations as it allows linearization of the Beer–Lambert–Bouguer law by taking the logarithm.

For the spectral analysis the low resolution absorption spectra  $S_i(\lambda)$  are typically created from literature spectra measured at high spectral resolution under laboratory conditions:

$$S'_i(\lambda) = (\sigma'_{i,\text{lit}} \otimes H)(\lambda) \quad (4.12)$$

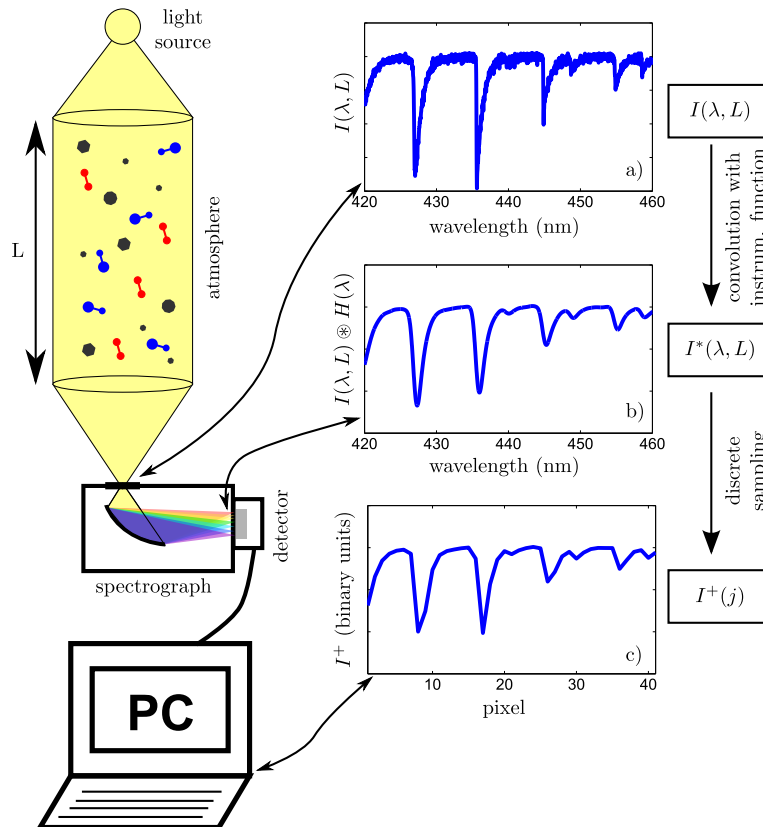


**Figure 4.2.** | Simplified sketch of the DOAS measurement process. a) On its path through the atmosphere light is partly absorbed by trace gases; here  $I_0$  is assumed to be the only absorber. b) Light is spectrally decomposed in the spectrograph. The spectrum incident on the detector is described by a convolution with the instrument function  $H(\lambda)$ . c) the spectrum is finally digitized by the detector and processed by a microcomputer. Adapted from Platt and Stutz [2008]

#### 4.2.1.2. Sampling of the Spectrum

The detector samples a spectral window of typically several 10 nm to 100 nm width a finite number of pixels, typically 100 to 2000. Each pixel  $j$  integrates the radiation intensity over a wavelength interval  $\Delta\lambda(j)$  around  $\lambda(j)$ :

$$I^+(j) = \int_{\lambda(j)-\Delta\lambda(j)/2}^{\lambda(j)+\Delta\lambda(j)/2} I^*(\lambda') d\lambda' \quad (4.13)$$

The mapping between a pixel  $j$  and its central wavelength  $\lambda(j)$  is typically approximated by a polynomial of order  $q$  with coefficients  $\gamma_k$ :

$$\lambda(j) = \sum_{k=0}^q \gamma_k i^k \quad (4.14)$$

The width of the wavelength interval  $\Delta\lambda(j)$  is given by the first derivative of the polynomial at position  $i$  and the pixel fill factor in dispersion direction (for CCDs this is typically unity).

The detector and its readout electronics also influence the measured signal. In addition to broadband structures due to wavelength dependent detector sensitivity, narrow band structures can arise due to varying quantum efficiencies of the different pixels. The narrow band structures are accounted for by the factor  $A'^+(j)$  while the broadband effects are included in  $I_0'^+(j)$  in analogy to eq. (4.7). Additional to the spectral information the measured signal also contains two additive terms.  $I_{\text{stray}}^+(j)$  describes undesired stray light reaching the detector. The term  $N^+(j)$  summarizes the CCD dark current and offset signal and the photon shot noise. The signal measured by the detector is then given by:

$$I_{\text{meas}}^+(j) = \left[ \underbrace{I_0'^+(j) \exp\left(L \sum_i S_i'^+(j) \bar{\rho}_i\right)}_{I^+(j)} + I_{\text{stray}}^+(j) \right] A'^+(j) + N^+(j) \quad (4.15)$$

### 4.2.2. DOAS Evaluation Procedure

The goal of the evaluation procedure is to retrieve the trace gas number densities  $\bar{\rho}_i$  or the respective column densities  $a_i$ . The following section describes corrections that must be applied to the recorded spectra and the retrieval process.

#### 4.2.2.1. Correction of the Measured Spectra

The term  $N^+(j)$  must be removed from eq. (4.15). While the offset and dark current signal can be characterized and subtracted from  $I_{\text{meas}}^+(j)$ , this is not possible for the photon shot noise due to its statistical nature. However, the contribution of photon shot noise can be reduced by increasing the number of collected photons  $N$  as it is proportional to  $\sqrt{N}$ . In practice this is achieved by coadding several subsequently measured spectra, in the following called scans.

Dark current and Offset are signals present even in the absence of photons striking the detector. The Dark current is caused by thermally excited electrons and grows linearly in time. Thus, it is characterized by recording a spectrum, with a shaded detector, at long exposure time (typically several 10 s). The offset is a constant signal added to each spectrum to ensure that the analog digital converter (ADC) measures a positive signal. Offset is characterized by recording dark spectra with the shortest possible exposure time, to minimize the dark current contribution, and then adding several thousand of these spectra to improve signal to noise ratio. The offset and dark current are corrected by scan weighted and exposure time weighted subtraction from  $I_{\text{meas}}^+$  respectively.

Next, the instrument characteristics  $A'^+(j)$  must be removed. However, this factor automatically cancels if  $I$  and  $I_0(j)$  are recorded with the same device, which is typically the case.

The stray light term  $I_{\text{stray}}^+(j)$  typically has two major sources. First, for active DOAS systems, solar radiation scattered into the light path adds differential spectral structures (Fraunhofer spectrum) and can further lead to a dilution of the measured absorption signal. This can be corrected by subtracting a background spectrum recorded in the presence of solar light with the light source turned off. The second contribution is spectrograph stray light, defined as light of an undesired wavelength reaching a detector pixel. This can be directional light from unwanted reflections in the spectrograph or diffuse light from scattering on a imperfect or damaged diffraction grating. Spectrograph stray light is hard to correct as it depends on the spectrum of the incident light and often originates from spectral regions that are not measured by the system. If the remaining stray light contribution is small compared to  $I$ , it is still possible to provide the desired linearized form of the Beer–Lambert–Bouguer law using the Taylor expansion  $\ln(1 + x) \approx x$  for  $|x| \ll 1$ .

$$D' = -\ln\left(\frac{I_{\text{meas}}}{I'_0}\right) = -\ln\left(\frac{I + I_{\text{stray}}}{I'_0}\right) = -\ln\left(\frac{I}{I'_0}\left(1 + \frac{I_{\text{stray}}}{I}\right)\right) \quad (4.16)$$

$$= -\ln\left(\frac{I}{I'_0}\right) - \ln\left(1 + \frac{I_{\text{stray}}}{I}\right) \quad (4.17)$$

$$= -\ln\left(\frac{I}{I'_0}\right) - \frac{I_{\text{stray}}}{I} + O\left(\frac{I_{\text{stray}}^2}{I^2}\right) \quad (I_{\text{stray}} \ll I) \quad (4.18)$$

Typically a polynomial, often referred as offset polynomial, is used to model  $I_{\text{stray}}$  in DOAS retrievals since spectrograph stray light has a smooth wavelength dependency.

Finally in order to determine the optical density the  $I_0^+(j)$  intensity needs to be determined. In active DOAS applications, typically a spectrum  $I_{0,\text{meas}}^+$  of the light source is used instead of the true  $I_0^+$ , which is usually impossible to determine. This is possible as the differences between the two spectra are only of broadband nature and thus do not change the depth of the differential absorption structures. In passive DOAS applications, an atmospheric measurement is selected as  $I_{0,\text{meas}}^+$  against which all other measurements are evaluated. Therefore, passive DOAS only measures changes in the trace gas column densities. In both cases the additional broad band structures arise that need to be eliminated. This is most commonly achieved by a polynomial fit included in the DOAS retrieval. Alternatively, a high pass filter can be applied to

the optical density prior to the DOAS retrieval. In this case it is important to also apply the same high pass filter to the absorption cross sections used in the retrieval.

#### 4.2.2.2. DOAS retrieval

In order to retrieve trace gas column densities  $a_i$ , the DOAS retrieval models the measured optical density  $D^+(j) = -I_{\text{meas}}^+(j)/I_{0,\text{meas}}^+(j)$  by a function  $F(j)$  using  $n$  literature spectra  $S_i'^+(\lambda)$ , convoluted to the resolution of the measuring spectrograph.

$$F(j, a_1, \dots, a_{n+k+l+2}) = \sum_{i=1}^n S_i'^+(j) a_i + P_k(j) + \frac{O_l(j)}{I_{\text{meas}}^+(j)} \quad (4.19)$$

The polynomial  $P_k(j)$  of order  $k$  accounts for broadband spectral structures. The order of the polynomial determines the degree of high pass filtering and has to be adjusted to the trace gases of interest. For example, a low-order polynomial should be chosen for gases with relatively few and broad absorption structures like  $\text{O}_4$  whereas a higher order can be used for gases like  $\text{NO}_2$  with numerous closely spaced narrow absorption lines. However, in some cases a reasonable polynomial order (4 or less) is not sufficient to capture the broadband structures. In these cases high pass filtering should be considered as it gives a well defined cutoff frequency between broad- and narrow-band spectral structures. If stray light needs to be considered, an additional offset polynomial  $O_l(j)$  is introduced, which is divided by the measured light intensity  $I_{\text{meas}}^+(j)$ . The parameters  $a_{n+1}$  to  $a_{n+k+l+2}$  denote the coefficients of the polynomials  $P$  and  $O$ .

In order to find the best parameter set, the least squares fitting method is used, which aims to minimize  $\chi^2$ , defined as

$$\chi^2 = \sum_j (D^+(j) - F(j, a_1, \dots, a_{n+k+l+2}))^2 \rightarrow \min \quad (4.20)$$

For a linear DOAS fit model  $F$  it is convenient to write the problem in matrix notation

$$\vec{D} = \mathbf{X} \vec{a} \quad (4.21)$$

with the optical density column vector  $\vec{D} = (D(1), D(2), \dots)$ , the parameter vector  $\vec{a} = (a(1), a(2), \dots)$  and the matrix  $\mathbf{X}$  each column containing the functional dependence of the respective fit parameter (for the first  $n$  parameters these are the literature spectra  $S_i'^+$ ). The linear least squared problem can then be solved simply by [Bevington, 1969; Albritton et al., 1976]

$$\vec{a} = [\mathbf{X}^T \mathbf{X}]^{-1} \mathbf{X}^T \vec{D} \quad (4.22)$$

However, in order to compensate for errors in the wavelength to pixel mapping, advanced DOAS analysis procedures extend the fit model to allow for a spectral shift and squeeze of the literature spectra  $S_i'^+(\lambda)$ . In this case the fit problem becomes non-linear and requires more complicated iterative minimization algorithms like the Levenberg-Marquart method [Levenberg, 1944].

The DOASIS Framework [Kraus, 2006], used for all DOAS evaluations presented in this thesis, implements a combination of a linear least squares fit and a non-linear Levenberg-Marquart fit. First, the linear problem is solved with fixed shift and squeeze parameters. Then

the linear parameters from the last step are fixed and a non-linear fit is used retrieve the shift and squeeze parameters, which are taken as input parameters for the next call of the linear fit. This alternating sequence of a linear and non-linear fit is repeated until the improvement of  $\chi^2$  is below a certain limit (typically  $10^{-3}$ ).

### 4.2.3. Error Analysis

In reality, there is always a remaining difference between the optimized fit model and the measurement. This quantity is called the residual spectrum

$$\mathcal{R}(i) = D^+(j) - F(j) \quad (4.23)$$

It is the central quantity to analyze the quality of the DOAS evaluation. The residual is influenced by errors made during the measurement and by the evaluation process. Divided into “systematic” and “random” sources, those errors need to be considered for the estimation of the Measurement error.

#### 4.2.3.1. Random errors

Typically the dominating error source in the measured optical densities is random photon shot noise. As mentioned before photon shot noise can be reduced by collecting more photons per spectrum and by coadding several measured spectra, since it only grows with the square root of the amount of measured photons. However, if the shot noise is reduced, additional random error sources need to be considered:

1. Narrow band spectral changes of the light source, for example etalon structures on light emitting diodes (LEDs) as described by Sihler et al. [2009] or unstable emission lines in Xe-arc lamps.
2. Unstable fiber coupling and bending of the fiber can influence the modes transmitted by the fiber into the spectrograph. This can result in narrow band spectral structures due to varying inhomogeneous illumination of the spectrograph between  $I$  and  $I_0$ . Artificial mode mixing as described by Stutz and Platt [1997] and Eger [2014] can be applied to ensure a homogenous illumination of the spectrograph.
3. The detector and its readout electronics are known to be sensitive to electromagnetic interference and unstable supply voltage. Both can introduce random differential structures. Usually, this can be avoided by stabilizing the supply voltage and adding proper electromagnetic shielding.

For a linear least squares fit the uncertainty of a parameter  $a_i$  due to random errors is estimated as

$$\Delta a_i = \sqrt{\Theta_{ii}} \quad (4.24)$$

$$\Theta = \sigma^2 [\mathbf{X}^T \mathbf{X}]^{-1} \quad (4.25)$$

where  $\Theta$  is the covariance matrix and  $\sigma$  is the root mean squared (RMS) of the residual spectrum  $\mathcal{R}$ . For a non-linear Levenberg-Marquard fit the errors can be estimated in a similar way [e.g. Press et al., 1992]. However, in both cases the estimated error is only correct if some assumptions are met [Albritton et al., 1976; Stutz and Platt, 1996]:

1. **Finite error variances** The error of each pixel  $D^+(j)$  must have a finite variance. For example, this assumption is valid if photonic noise, which is Poisson distributed, is the dominating factor.
2. **Uncorrelated errors** The errors of the individual pixels are assumed to be uncorrelated. Stutz and Platt [1996] describe how covariances in the pixel errors can be included into the error estimates.
3. **Zero-mean errors.** The systematic component in the error of each pixel  $D^+(j)$  is zero. Otherwise, the fitted parameters can be biased. If the systematic errors exceed the magnitude of the random errors, the error estimates for the fit parameters become meaningless.
4. **Perfect fit model** The last point also requires that the model perfectly describes the measurement. If unknown absorbers are missing or if the literature cross sections  $S^{++}$  are wrong, systematic errors would be introduced. Even though a perfect fit model does not exist it must at least good enough to make systematic errors smaller than the random errors.
5. **Distinguishable cross sections** Fitting similar cross sections should be avoided if possible as this increases the off diagonal elements of  $X^T X$  and thus the uncertainty of the fitted parameters. Furthermore, the fit becomes very vulnerable to systematic biases if non-random error sources are present. Thus, if fitting similar cross sections the optimal spectral fit interval must be found, as described in Vogel et al. [2013].

A special case occurs when there are several cross sections of the same at different temperatures. In this case orthogonalization of the cross sections improves the retrieval of the absorbers total column density.

For error sources other than photonic noise these assumptions are generally not met. Stutz and Platt [1996] used Monte-Carlo simulations to estimate a correction factor  $C(\tau, W)$  depending on  $\tau$  and  $W$ , the width of the absorption structure and the residual structure respectively (see Fig. 4.3). Typically a correction factor of two is used in this thesis. In some cases with strong residual structures a factor of three was used for a more conservative error estimate.

### 4.2.3.2. Systematic errors

Systematic errors can be introduced by stable spectral structures, missing in the fit model, or by systematic errors of other parameters used in the analysis process. These errors cannot be estimated by statistical method and therefore need to be estimated separately and added to the fit error. If they originate from stable spectral structures, analysis of the fit residual can sometimes be used to determine their origin and quantify their influence (see section 4.2.5).

One class of systematic problems are errors in the fit references causing an improper fit to the measured optical density. This makes two problems: Firstly it directly causes an error in the retrieved trace gas concentration for the species with the erroneous fit reference. Secondly, this can cause cross sensitivities for the simultaneous detection of other, especially weaker, absorbers.

The most important systematic error sources affecting the fit references are:

1. Errors in the convolution process and wavelength to pixel mapping.
2. Saturation and  $I_0$  effect. For a very structured light source and/or strongly absorbing gases the approximation  $[I'_0 \exp(L\bar{\rho}\sigma')] \otimes H \approx I'_0 \exp(L\bar{\rho}(\sigma' \otimes H))$ , introduced in sec. 4.2.1.1, does not hold anymore. Thus the convoluted reference spectra  $S = (\sigma' \otimes H)$  cannot be fitted accurately to the optical density anymore. For example a MAX-DOAS measurement of H<sub>2</sub>O band around 442 nm the saturation effect corresponds to a peak-to-peak optical density of  $3 \cdot 10^{-4}$  and the combined saturation and  $I_0$  effect add to a peak-to-peak optical density of even  $2 \cdot 10^{-3}$ , both times assuming a typical water column density of  $4 \cdot 10^{23}$  molec cm<sup>-2</sup>. However, methods have been developed to correct for these effects [see Platt and Stutz, 2008, p. 158ff] and implemented into the DOASIS software [Kraus, 2006].
3. Uncertainties in the literature absorption cross sections. The size of this error strongly depends on the trace gas and typically varies between less than 1% to several 10% can have two systematic effects. The corrections for the IO cross section determined in this thesis are an example for this problem (see chap. 11).
4. Error in the length of the absorption light path. For LP-DOAS this only causes a wrong scaling of the retrieved column to mixing ratios. However, for CE-DOAS the length of the absorption light path has a strong wavelength dependence (4.3.3). Thus for CE-DOAS a error in the path length function can introduce systematic residual structures. Also for Multi Axis DOAS (MAX-DOAS) due to radiative transport the length of the absorption path varies with wavelength and is additionally influenced by the aerosol load in the atmosphere (see. 4.3.1).

A very similar problem are unknown absorbers, which introduce differential absorption structures. In the UV-VIS spectral range the most prominent absorbers are generally known. Thus, unknown absorbers typically have optical densities on the order of  $10^{-4}$  and less. Nevertheless, they can play a very important role for the detection limit of weak absorbers like marine halogen radicals [e.g. see Lampel, 2014].

Other problems which can introduce systematic residual structures are:

1. Uncompensated stray light originating from the spectrograph or from sunlight scattered into the geometrical light path of active DOAS applications or reflected 4.2.2.1.
2. Non-linear intensity response of the spectrometers photo detector. For high grade CCD cameras the error due to detector non-linearity is typically below 1%. However, due to the simpler electronics, if compact spectrometers are applied, this error is typically in

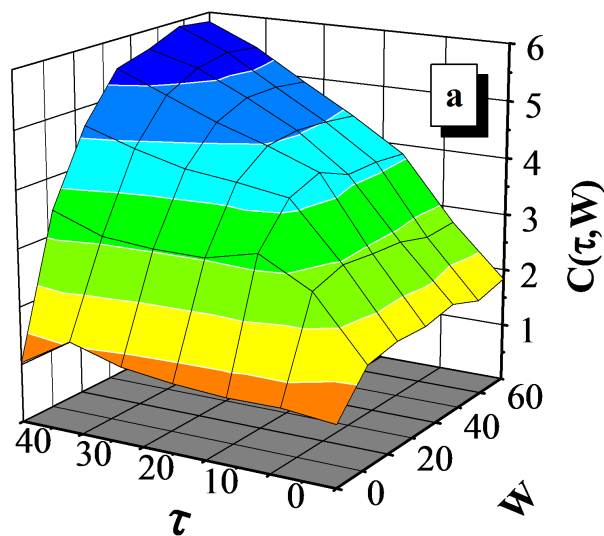


**Figure 4.3.** | Correction factor  $C(\tau, W)$  to estimate the measurement error from the least squares fit error. It depends on the the width of the absorption structure  $\tau$  and the width of the residual structures  $W$  [Stutz and Platt, 1996].

the range of several percent but can exceed 10%. These errors can be even higher if the instrument applies a light source which rapidly varies over a small spectral range (e.g. LEDs or sunlight) as these can induce additional systematic residual structures. A detailed discussion on the effects of detector non-linearity is given in sec. 10.

#### 4.2.4. Detection Limit

The detection limit defines the smallest number density for which a significant detection is possible. It is directly linked to the errors in the measurement and the DOAS analysis and therefore needs to be determined individually for each measurement. There are two methods to estimate the detection limit of a measurement:

1. **Detection limit from the measurement error:** If the measurement error is assumed to be purely statistical, it defines the  $1\sigma$  confidence interval of the measurement. Therefore if a measured value is greater than  $1\sigma$  it is considered significant since the probability for the true value to be non-zero is 95%. Since the DOAS fit generally underestimates the error it is important to include the correction factor from the last section in the calculation of the detection limit.
2. **Detection limit from the fit residual:** The detection limit of a trace gas can be estimated by comparing the strength of its absorption to the optical density of the fit residual. A

trace gas is said to be detected clearly if its absorption is stronger than the magnitude of the fit residual  $\Delta\mathcal{R}$  :

$$\bar{\rho}_i L(S'_{\max} - S'_{\min}) \geq \Delta\mathcal{R} \quad (4.26)$$

and thus

$$\bar{\rho}_{i,\min} = \frac{\Delta\mathcal{R}}{L(S'_{\max} - S'_{\min})} \quad (4.27)$$

A very conservative detection limit is obtained if the peak to peak value  $\mathcal{R}_{\max} - \mathcal{R}_{\min}$  is used as a measure for  $\Delta\mathcal{R}$ . A more realistic estimate can be obtained if  $\Delta\mathcal{R}$  is approximated by two times the RMS of  $\mathcal{R}_i$ .

In this thesis the detection limit is always obtained from the  $2\sigma$  measurement error. On the other hand, the second method is particularly useful to get a priori estimates of detection limits for newly constructed instruments, like the CE-DOAS, before any measurement is performed.

#### 4.2.5. Analysis of Residual Spectra

As discussed in sec. 4.2.3.2 systematic spectral structures which cannot be assigned to an absorber lead to systematic errors in the DOAS retrieval. In order to reduce systematic errors it is therefore important to determine their origin. Residual spectra from the DOAS-fit provide a valuable source of information for this purpose as they by definition contain all remaining spectral structures which cannot be decried by the DOAS-fit. The systematic spectral structures in the residual spectra can generally not be retrieved from a single residual spectrum and related to their sources since the fit residuum also contains random noise and is often influenced by systematic errors from several sources. However, during a measurement campaign usually several hundred or thousand spectra are measured with the same setup. Therefore the set of corresponding fit residuals can be used to determine recurring spectral structures and relate them to environmental or instrumental parameters. For this purpose several methods have been developed in the thesis of Lampel [2014] and detailed description are given therein. Therefore, in the following only a brief description is given for the multiple linear regression method, applied in this thesis.

##### 4.2.5.1. Multiple linear regression

If the parameters which are assumed to cause the residual structures are known from the DOAS-fit (concentrations of absorbers), the DOAS measurements (e.g. exposure time) or axillary measurement (e.g. temperature, solar irradiance) their corresponding spectral structures can be determined from a set of linear equations

$$Ax + \epsilon = \begin{bmatrix} a_1 & b_1 & c_1 & \cdots \\ a_2 & b_2 & c_2 & \cdots \\ \vdots & \vdots & \vdots & \ddots \\ a_b & b_n & c_n & \cdots \end{bmatrix} \cdot \begin{bmatrix} \vec{x}_a \\ \vec{x}_b \\ \vec{x}_c \\ \vdots \end{bmatrix} + \epsilon = \begin{bmatrix} \vec{R}_1 \\ \vec{R}_2 \\ \vdots \\ \vec{R}_n \end{bmatrix} \quad (4.28)$$

where  $A$  is the matrix of the parameters  $a, b, c, \dots$  for each the the  $n$  measurement,  $\vec{x}_a, \vec{x}_b, \vec{x}_c, \dots$  the set of their corresponding spectral structures and  $\epsilon$  represents the random noise in the residuals  $\vec{R}_1, \vec{R}_2, \dots, \vec{R}_n$  known from DOAS fits to  $n$  measured spectra.

The linear equation system  $Ax = R$  is usually overdetermined and can therefore be solved for the spectral structures x e.g., using a least squares method. Thus, it is possible to investigate how strong systematic structures in the fit residual depend on the different Parameters, giving valuable information on their origin and possible solutions to reduce/remove their influence on the DOAS fit. An example of such an analysis is shows in chapter 11 where it is used to analyze residual structures induced by an error in the laboratory absorption cross section of IO.

### 4.3. Experimental and Technical Realization of DOAS Measurements

There are many applications of the DOAS method with different light path arrangements and observation geometries, which are roughly divided into active and passive DOAS. Active methods light from artificial light sources like LEDs or Xe-Arc Lamps which is send to the atmosphere to a receiving unit. Passive methods use light from artificial sources, in particular direct or scattered sun light. In the following a short description of Multi Axis DOAS is given since it is the most widely used passive method, followed by a description of Long Path DOAS and Cavity Enhanced DOAS which are the two DOAS flavors used in this thesis.

#### 4.3.1. Multi Axis DOAS

In MAX-DOAS, a passive application, spectra of scattered sunlight are measured with a telescope under several different elevation angles as shown in Fig. 4.4. Measurements at different elevation angles are sensitive to different height layers in the lower troposphere but have roughly the same light path through the stratosphere. Therefore, MAX-DOAS also contain information on the vertical distributions of observed trace gases in the lower atmosphere. Typically MAX-DOAS measurements are evaluated against a reference measurement at  $90^\circ$  elevation which gives differential slant column densities (dSCDs) relative to the  $90^\circ$  measurement. However, these dSCDs cannot be simply converted into concentrations since the scattered sunlight does not have a simple well defined abortion light path, which is influenced by the the aerosol load and on the spectral range of the measurement. Light observed by a MAX-DOAS is rater a superposition of photons with different light paths. Therefore generally inverse radiative transfer modeling is required to determine trace gas concentrations and vertical profiles [e.g. Yilmaz, 2012].

#### 4.3.2. LP-DOAS

LP-DOAS is currently still the most widely used active DOAS application. Light from an artificial light source, mostly Xe-Arc Lamps or LEDs, is send through the atmosphere on a several hundred meters to kilometer long geometrical light path to a receiving unit where it is

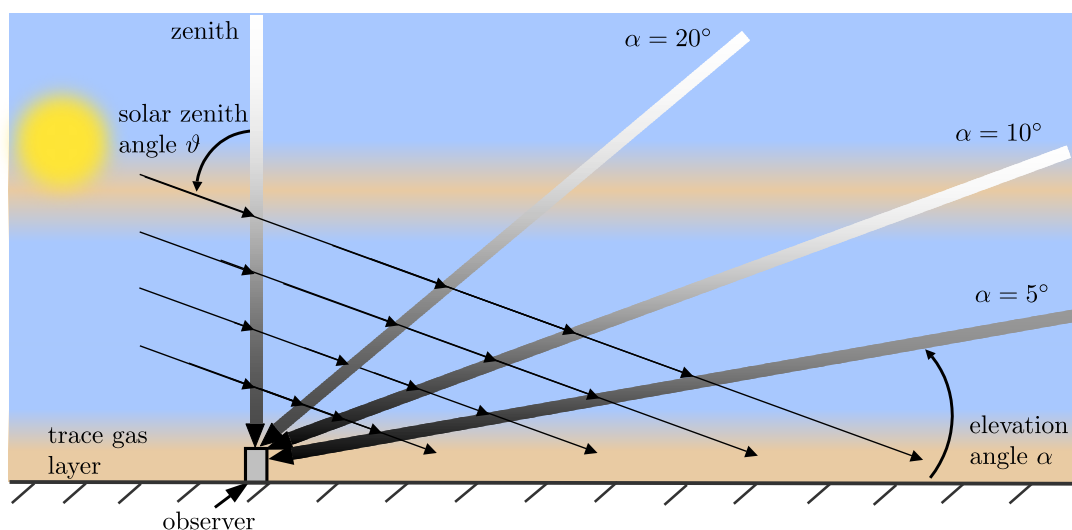


**Figure 4.4.** | Sketch of a MAX-DOAS measurement. Scattered sunlight is measured under several different elevation angles  $\alpha$ . It can be seen that measurements at different elevation angles are sensitive to different height layers and thus also get different contributions from the absorbing layers. Adapted from Hönninger [2002]

spectrally analyzed. Most LP-DOAS instruments apply a so called mono static setup which combines the sending and receiving unit in a single telescope as shown in Fig. 4.5 and use an array of retro reflectors to reflect the send light back to the telescope. In modern LP-DOAS setups, as those used in this thesis, a fiber bundle couples the light from the light source into the telescope and couples the received light out into the spectrograph, where it is analyzed [Merten, 2008]. Atmospheric measurements are typically evaluated against a spectrum of the light source which is acquired by moving a reference plate in front of the fiber bundle, sending the light directly to the spectrograph without traversing through the atmosphere. Additionally many instrument allow to quantify atmospheric background light (mostly sunlight scattered or reflected into the light path) by blocking the light source using a shutter. Correction for atmospheric background light is important to avoid stray light effects described in sec. 4.2.2.1.

LP-DOAS measurements have the advantage of a simple and well defined geometrical light path, therefore trace gas concentrations can be directly obtained from the DOAS fit. Furthermore, by using an artificial light source, LP-DOAS has the ability to measure night and day in a wide spectral including the deep UV. However, since LP-DOAS requires long geometrical light paths, it is typically limited to the measurement of spatially averaged concentrations.

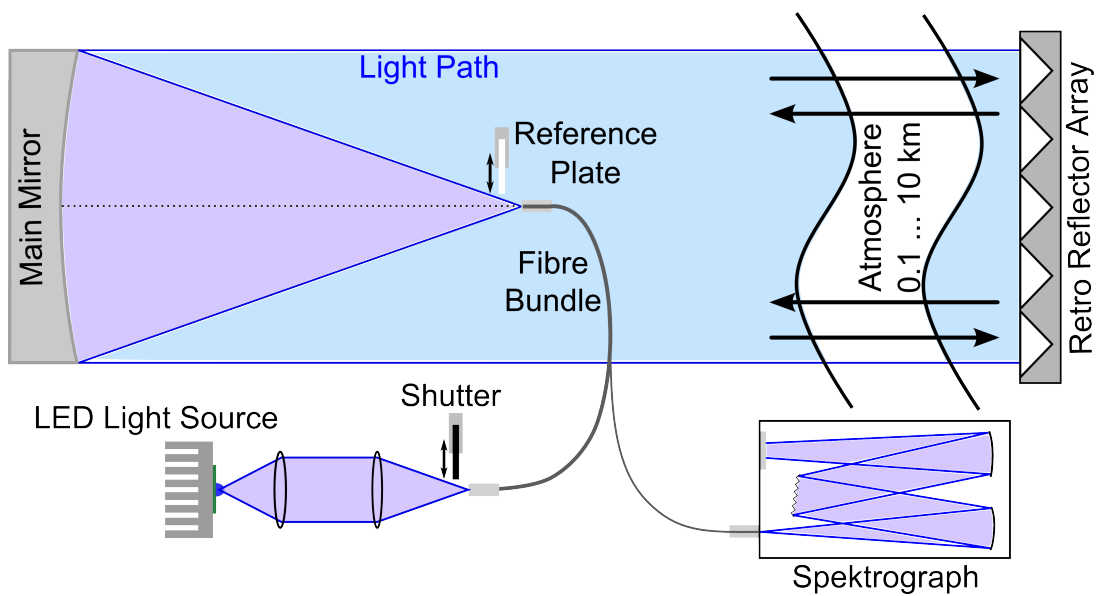


**Figure 4.5.** | Sketch of a fiber LP-DOAS instrument. Light from a light source is coupled into the telescope, via an optical fiber, and sent through the atmosphere to a retro reflector array, from where it is sent back to the telescope and coupled out through the fiber into the spectrograph where it is analyzed. (from Denis Pöhler, pers. com.)

### 4.3.3. Cavity Enhanced DOAS

Cavity Enhanced DOAS (CE-DOAS) is a relatively new active technique which allows the application of DOAS for in-situ measurements. As illustrated in Fig. 4.6 it applies an optical resonator typically built of two highly reflective mirrors, to achieve the long absorption light paths, required for sensitive trace gas measurements. Typical CE-DOAS instruments use dielectric mirrors with a reflectivity of  $R > 99.9\%$  giving more than a thousandfold light path enhancements can be achieved. Thus, CE-DOAS enables sensitive absorption spectroscopy in very compact optical setups of several 10 cm to few meters physical length. As light sources most CE-DOAS instrument use LEDs [S. Ball et al., 2004; Sihler et al., 2009], which are chosen to match the relatively narrow spectral window of few 10 nm in which the dielectric mirrors have their high reflectivity. Matching the light source to the mirrors is important as light outside its reflective range is almost completely transmitted and therefore could cause stray light problems. One important difference to most active DOAS applications is that in CE-DOAS the light path needs to be calibrated (see sec. 4.3.3.2), since it is not geometrical and very sensitively depends on the reflectivity of the mirrors, which can be strongly influenced even by very small impurities on their surface.

CE-DOAS can be realized with a open path or closed path resonator. In closed path setups the resonator is placed in measurement cell which separates it from the environment. Sample air is usually pumped through an aerosol filter into the cell. This has the advantage that the high reflective mirrors are protected from contamination with dust and aerosol. If the measurement cell is constructed of inert materials like Teflon most substances, even reactive ones, can be measured in closed-path setups. However for highly reactive substances like halogen oxides losses at surfaces and inlets can be substantial (even if Teflon is used) and an accurate quantification is difficult since losses often also depend on the environmental conditions, e.g. humidity other trace gases. Therefore, most instruments to measure highly reactive substances like IO have an open path resonator, which is open towards the environment so that no sampling is required. The major disadvantage of this configuration is that the mirrors are exposed to ambient air and

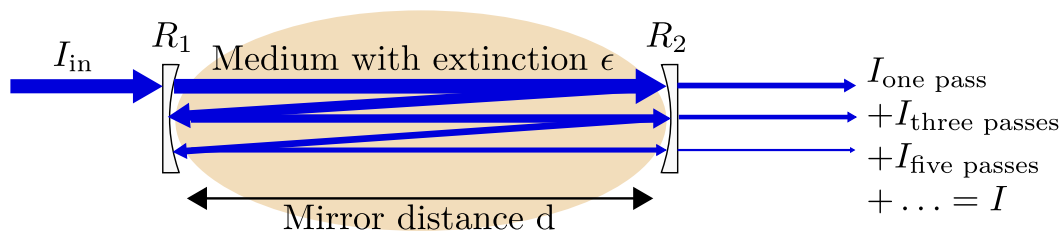


**Figure 4.6.** | Sketch of the light propagation through a CE-DOAS instrument. The optical resonator built of two highly reflecting mirrors enhances the light path through an absorbing medium. Light enters the resonator through one of the mirrors and is then on average passes several hundred to thousand times through the absorbing medium before it leaves the resonator. At each reflection a small fraction of the light leaves the cavity. The light collected on the output side, which is the sum of all transmitted parts, is then spectrally analyzed.

therefore special precautions are required to protect them from contamination (e.g. see. chap. 5).

#### 4.3.3.1. Optical density and the effective light path

As shown in Fig. 4.6 the light leaking out of the resonator is a superposition of parts which have undergone one, three, five, ... passes through the resonator. The intensity  $I$  of the light leaking out of an absorber filled resonator with an absorbing medium of extinction  $\epsilon$  is calculated as [Fiedler, 2005]:

$$\begin{aligned}
 I &= I_{\text{in}} \cdot T_{\text{mirror}}^2 \cdot e^{-d\epsilon} \\
 &+ I_{\text{in}} \cdot T_{\text{mirror}}^2 \cdot R^2 \cdot e^{-3d\epsilon} \\
 &+ \dots \\
 &+ I_{\text{in}} \cdot T_{\text{mirror}}^2 \cdot R^{2n} \cdot e^{-(2n+1)d\epsilon} \\
 &+ \dots \\
 &= I_{\text{in}} \cdot T_{\text{mirror}}^2 \sum_{n=0}^{\infty} R^{2n} \cdot e^{-(2n+1)d\epsilon}
 \end{aligned} \tag{4.29}$$

where  $I_{\text{in}}$  is the light source intensity,  $d$  is the mirror separation,  $R$  the mirror reflectivity, and  $T_{\text{mirror}}$  the the mirror transmittivity which is approximately  $T_{\text{mirror}} \approx 1 - R$ . This series converges ass  $R < 1$  and  $d\epsilon > 0$ . Note that for the sake of clarity the wavelength dependencies are not written out. In the following an approximation of eq. (4.29) for a weak absorber ( $d\epsilon \ll 1$ ) and small mirror reflectivity ( $R \rightarrow 1$ ) is used which approximates the summation over discrete  $n$  can by an Integral [Platt et al., 2009].

CE-DOAS determines the optical density  $D_{\text{CE}}$  of an absorber filled resonator relative to an “empty resonator”, by measuring the light intensity  $I_0$  leaking out an empty resonator and the light intensity  $I$  leaking out when filled with an absorber. The “empty cavity” measurements are usually made with purified zero air which has an nonzero extinction  $\epsilon_0$  mainly due to Rayleigh scattering. Thus the cavity enhanced optical density can be written as:

$$\begin{aligned}
 D_{\text{CE}} &= \ln \left( \frac{I_0}{I} \right) \\
 &= \ln \left( \frac{I_{\text{in}} \cdot T_{\text{mirror}}^2 \cdot e^{-d\epsilon_0} \int_0^{\infty} e^{-2n \cdot (d\epsilon_0 - \ln(R))} dn}{I_{\text{in}} \cdot T_{\text{mirror}}^2 \cdot e^{-d\epsilon} \int_0^{\infty} e^{-2n \cdot (d\epsilon - \ln(R))} dn} \right)
 \end{aligned} \tag{4.30}$$

Performing this integration (e.g see [Platt et al., 2009]) leads to the CE-DOAS equation

$$D_{\text{CE}}(\lambda) = \ln \left( \frac{I_0(\lambda)}{I(\lambda)} \right) = \bar{L}_{\text{eff}}(\lambda) (\epsilon(\lambda) - \epsilon_0(\lambda)) \tag{4.31}$$

which relates the extinction in the resonator to the measured intensities through the effective

### 4.3. Experimental and Technical Realization of DOAS Measurements

path length  $\bar{L}_{\text{eff}}(\lambda)$  defined as

$$\bar{L}_{\text{eff}}(\lambda) = \underbrace{\frac{d}{d \cdot \epsilon_0(\lambda) - \ln(R(\lambda))}}_{\bar{L}_0(\lambda)} \cdot \underbrace{\frac{D_{\text{CE}}(\lambda)}{e^{D_{\text{CE}}(\lambda)} - 1}}_{K(\lambda)} \quad (4.32)$$

$\bar{L}_0(\lambda)$  is the effective path length of the “empty cavity” with extinction  $\epsilon_0(\lambda)$  and  $K(\lambda)$  describes the loss of sensitivity due to additional absorption. The loss of sensitivity due to absorption is a special property of resonator based instruments which is not found in other DOAS applications. For open path CE-DOAS this is particularly a problem when trying to measure a weak absorption in the presence of high aerosol loads.

Since the correction factor  $K(\lambda)$  depends on the absorption in the resonator it is generally unknown. A common approximation is to calculate it from the measured optical density  $D_{\text{CE, meas}} = \ln(I_0/I)$ . Then eq. (4.31) becomes identical to the known BBCEAS equation [e.g. Fiedler, 2005]

$$\frac{I_0(\lambda)}{I(\lambda)} - 1 = \bar{L}_0(\lambda) (\epsilon(\lambda) - \epsilon_0(\lambda)) \quad (4.33)$$

However, this approximation of  $K(\lambda)$  comes with two problems:

1. An absolute stability of the light source intensity and the optical setup is required between the measurement of  $I_0$  and  $I$ . Changes to  $I_0$  or  $I$  which are not due to optical extinction cannot be distinguish them from an actual absorber in the resonator. Therefore they lead to an error in the correction factor  $K(\lambda)$  and thus in the retrieved trace gas concentrations. For example an absorber which causes a 10% reduction of  $I$  will also reduce the sensitivity by about 11%. Now if this change is not caused by an absorber but e.g by a fluctuation of the light source intensity, then the evaluation will overestimate all retrieved trace gas concentrations by 11%.
2.  $I$  and  $I_0$  are typically measured at a relatively low spectral resolution of about 0.5 nm. Therefore, for gases that absorb on a much narrower spectral range  $K(\lambda)$  could not be obtained correctly. For example this could be a problem in spectral ranges where water vapor strongly absorbs since it has very narrow band absorption lines of only several picometer full width at half maximum (FWHM). Lampel [2014] estimated that in the spectral range from 440 nm to 450 nm this would cause a residual with  $2 \cdot 10^{-4}$  peak-to-peak size assuming a typical marine water vapor concentration of  $\rho_{\text{H}_2\text{O}} = 5.5 \cdot 10^{17} \text{ cm}^{-3}$  a mirror reflectivity of  $R = 0.9996$  ( $\bar{L}_0(\lambda) \approx 5 \text{ km}$ ) and a mirror displacement of  $d = 200 \text{ cm}$ . However, for a mirror reflectivity of  $R = 0.9998$  ( $\bar{L}_0(\lambda) \approx 10 \text{ km}$ ) the residual would already have a peak-to-peak size of  $9 \cdot 10^{-4}$ .

For closed path systems where no aerosols are present these problems are solved by a new evaluation algorithm presented in chapter 9, which calculates  $K(\lambda)$  iteratively from the results of the DOAS retrieval.

Finally, for multiple absorbers  $i$  with number densities  $\bar{\rho}_i$  and absorption cross sections  $\sigma_i(\lambda)$  equation eq. (4.31) can be rewritten in the more common form as:

$$D_{\text{CE}}(\lambda) = \bar{L}_{\text{eff}}(\lambda) \left( \sum_i \bar{\rho}_i \sigma_i(\lambda) + \epsilon_{\text{Rayleigh}}(\lambda) + \epsilon_{\text{broadband}}(\lambda) - \epsilon_0(\lambda) \right) \quad (4.34)$$

where  $\epsilon_{\text{Rayleigh}}(\lambda)$  denotes the Rayleigh extinction of air and  $\epsilon_{\text{broadband}}(\lambda)$  summarizes all remaining broadband extinction particularly by aerosol and atmospheric turbulence. Furthermore, it should be noted that usually the extinction in the “empty cavity”  $\epsilon_0(\lambda)$  only contains the Rayleigh extinction of air and therefore cancels with  $\epsilon_{\text{Rayleigh}}(\lambda)$ .

#### 4.3.3.2. Calibration of the Optical Path Length

As described before in CE-DOAS the effective path length has a strong wavelength dependency mainly due to the reflectivity curve of the dielectric mirrors. Since the reflectivity is strongly affected even by small impurities strongly, it has to be determined experimentally at least after each cleaning procedure. Instead of measuring the mirror reflectivity curve it is more convenient to directly determine  $\bar{L}_0(\lambda)$ , the effective path length of the “empty cavity”. There are several methods to determine the effective path length  $\bar{L}_0(\lambda)$ , each with different advantages and disadvantages. In the following the methods used in this thesis are introduced.

**Different Rayleigh scatterers: Air and Helium** A common method first applied by [Washenfelder et al., 2008] uses two gases with different Rayleigh extinction. It has the advantage that Rayleigh scattering varies (relatively) slowly with wavelength ( $\propto \lambda^{-4}$ ) thus allowing to determine the path length smoothly over the entire spectral range. The precision of this method increases with the difference in Rayleigh extinction between the two gases. While one could think of using purified air at ambient pressure (or even above) and at a very low pressure, this would require a pressure-resistant measuring cell which would unnecessarily complicate the setup. It is therefore much more convenient to use two gasses at ambient pressure. Therefore we use as second gas Helium, a widely available gas with an approximately hundred times lower Rayleigh extinction with air. The calibration proceeds by subsequently pruning the resonator with purified air and Helium and measurement of the transmitted intensities  $I_{\text{air}}$  and  $I_{\text{Helium}}$ . The path length is then determined according using eq. (4.33) as

$$\bar{L}_0(\lambda) = \frac{\frac{I_{\text{air}}(\lambda)}{I_{\text{Helium}}(\lambda)} - 1}{\epsilon_{\text{Helium}}(\lambda) - \epsilon_{\text{air}}(\lambda)} \quad (4.35)$$

with the extinction coefficients for Helium  $\epsilon_{\text{Helium}}$  and air  $\epsilon_{\text{air}}$  both at ambient pressure and temperature. As described before a drawback of this method is that it critically depends on the stability of the light source intensity and the optical setup for the entire period of the calibration which typically takes several ten minutes. This makes it particularly difficult to apply this method outside of a laboratory in the field.

**Cavity Ringdown** Another method to determine the path length is the so called Cavity Ring Down Spectroscopy (CRDS) [O’Keefe and Deacon, 1988], which measures the decay of the light trapped in the resonator after switching of the light source. During each round

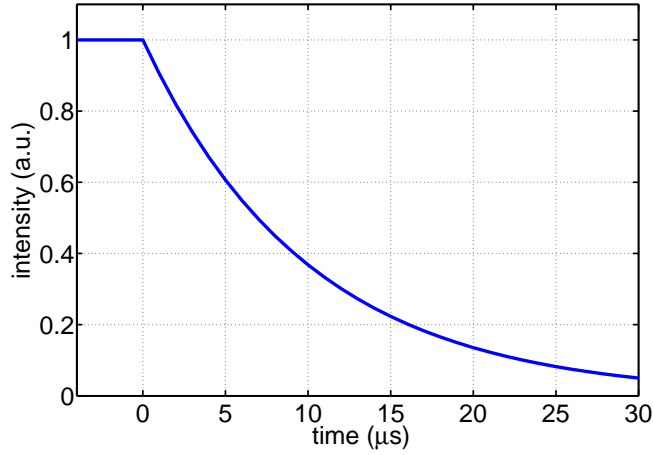


**Figure 4.7.** | **Illustration of a cavity ring down signal.** After the light source is switched off at  $t=0$ , the light which exits the resonator decays exponentially with a time constant of  $10\ \mu\text{s}$ , which corresponds to a path length of  $\bar{L}_0 = 3\ \text{km}$ .

trip the intensity of the remaining light in the resonator is reduced by a fixed factor due to optical absorption, scattering in the cell and transmission through the mirrors. This leads to an exponential decay of the light intensity leaking out of resonator as illustrated in Fig. 4.7:

$$I(t, \lambda) = I(t = 0, \lambda) \exp\left(-\frac{c_{\text{air}} t}{\bar{L}_0(\lambda)}\right) \quad (4.36)$$

where  $c_{\text{air}}$  is the speed of light in air. The path length is then simply determined by fitting the exponential model to the measured intensity data. For typical path lengths of few kilometers the ring down time is in the order of  $10\ \mu\text{s}$  which cannot be resolved with the instruments spectrograph. Therefore a fast photo detector like a photo diode or a photomultiplier tube (PMT) and an appropriate amplifier is used to measure the decay curve. The advantage of this method is that it only requires a stable light intensities on the time scale of the ring down times of several ten microseconds which is much shorter compared to the several ten minutes of stable light intensities required for the calibration with Rayleigh scatterers. Furthermore, it has the advantage that it does not requires gas cylinders which are sometimes difficult to bring along on field campaigns. However one problem is that, the photo detector by itself does not allow a spectrally resolved measurement of  $\bar{L}_0(\lambda)$ . Therefore, when using a relatively broadband light source an additional wavelength discriminating element like a band pass filter needs to be used.

Anthofer [2013] describes the calibration using a broadband bandpass filter which transmits roughly over the entire spectral window where the resonator mirrors are highly reflective. Thus, measuring the decay constants gives an average path length  $\bar{L}_{0,avg}$ . over the spectral range of the broadband bandpass filter. In lab the average path length is measured for a setup with clean mirrors  $\bar{L}_{0,avg}$ . and additionally a second spectrally resolved method, e.g. calibration with air and Helium, is used to measure  $\bar{L}_0(\lambda)$  curve. Contamination of the mirrors my dirt at a later time can be treated as a thin layer with a wavelength independent optical density  $\delta$ . Thus for a

contaminated mirror the path length is related to the clean mirror path length by

$$\bar{L}'_0(\lambda) = \frac{1}{\frac{\delta}{d} + \frac{1}{\bar{L}_0(\lambda)}}. \quad (4.37)$$

Anthofer [2013] showed that this also holds for average path length measured with the broadband CRDS setup.

$$\bar{L}'_{0,avg.} = \frac{1}{\frac{\delta}{d} + \frac{1}{\bar{L}_{0,avg.}}}. \quad (4.38)$$

Therefore, in the field the broadband CRDS measurement is sufficient to determine the optical density  $\delta$  of a mirrors contamination which can then be used to together with  $\bar{L}_0(\lambda)$  to calculate a new path length curve  $\bar{L}'_0(\lambda)$  for the contaminated mirrors. This method has been successfully applied during the Ireland 2011 campaign. However, it still has the disadvantage that at least one additional spectrally resolved calibration is necessary and therefore still relies on the availability of a lab building and consumable gases.

In order to resolve the remaining limitations of the broadband CRDS method, in the frame of this thesis and the thesis of Zielcke [2015] a new wavelength resolved CRDS calibration method was developed using a narrow dielectric band pass filter as described in sec. 5.1.

# **Part II.**

## **Instrumentation**

---

<b>field campaign</b>	<b>instrumentation</b>
Ireland 2011 (chap. 12)	Open Path CE-DOAS Mark I with BB-CRDS (sec. 5.1) Mobile Compact LP-DOAS (sec. 7.2) Meteorology (sec. 8.1)
Ireland 2012 (chap. 12)	Open Path CE-DOAS Mark I with WLR-CRDS (sec. 5.1) Compact Closed Path CE-DOAS (chap. 6) Mobile Compact LP-DOAS (sec. 7.2) stationary Mace Head LP-DOAS (sec. 7.1) Meteorology and nano-SMPS (sec. 8.1)
New Zealand 2013 (chap. 13)	Open Path CE-DOAS Mark II (sec. 5.2) Amundsen LP-DOAS (sec. 7.3) Meteorology, O <sub>3</sub> monitor and $\mu$ -Dirac GC (sec. 8.2)

**Table 4.1. | Overview of the field campaigns and applied instrumentation.**

This part describes the instrumentation applied in the three field campaigns conducted in the frame of this thesis. Tab. 4.1 gives an overview of the field campaigns and applied instrumentation.

# 5

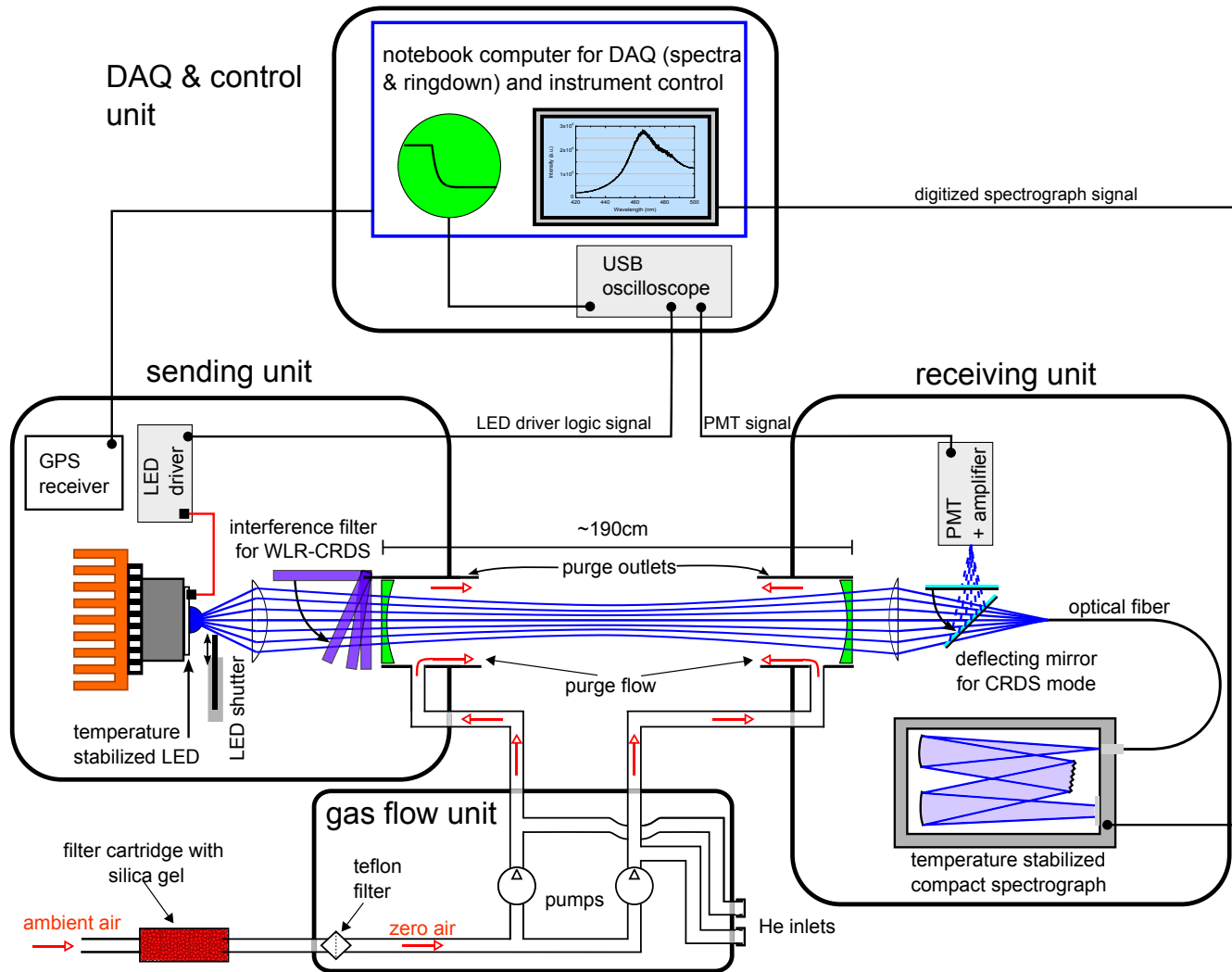
## Open Path CE-DOAS Instruments

### 5.1. Open Path CE-DOAS Mark I

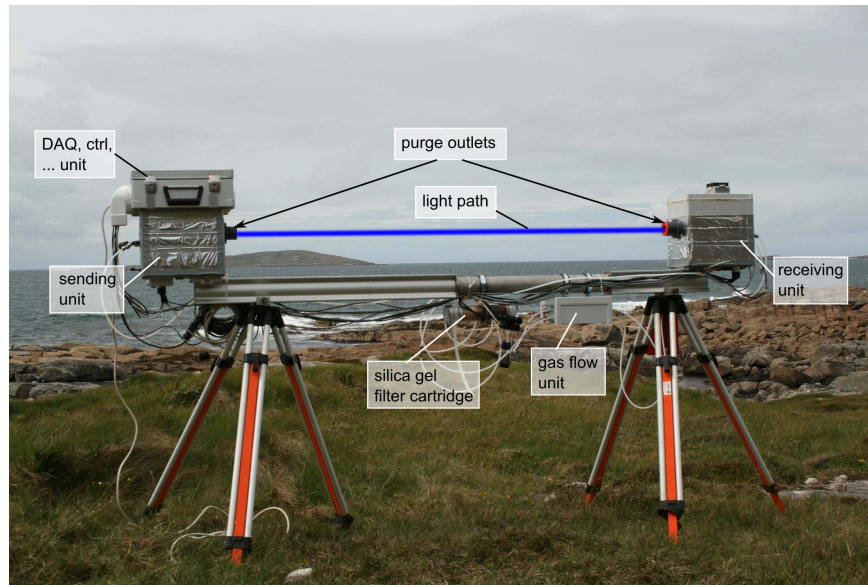
In order to investigate local sources of IO at coast sites, a mobile and light weight open path CE-DOAS instrument was desired. Previously an open path CE-DOAS instrument was developed and applied for laboratory measurements [Meinen, 2007; Thieser, 2008] and also applied in one field campaign [Anthofer, 2013]. However, the instrument was not applicable for mobile measurements since the components were distributed over seven individual, mostly non-weatherproof, boxes. Therefore, in the frame of this work the instrument was rebuilt as Open Path CE-DOAS Mark I (OP-CE-DOAS MK-I) for mobile field applications, with the objective of a compact, weather proof and light weight design. The parts that could be reused are the the weatherproof cases of the sending and receiving units with the custom made mirror mounts [Meinen, 2007] and the electronics of the CRDS path length calibration system developed by Anthofer [2013]. A list of commercially available components used in the new setup is given in Tab. 5.3.

Fig. 5.1 shows a simplified schematic of the new setup and Fig. 5.2 shows a picture of the instrument with the different components. The system weights only about 30 kg and is relatively compact with a size of about  $2.3 \text{ m} \times 0.2 \text{ m} \times 0.4 \text{ m}$ , which allows easy handling by two persons even in difficult terrain. Furthermore, this system was optimized for 12V battery operation and low power consumption of only 40 W (on average). This allows its operation also in difficult field terrain where no connection to the power grid is possible. Due to its low power consumption it can be battery operated with a typical car battery (50 A h) for more than 12 h.

The central element of the instrument is the optical resonator formed by two highly reflective dielectric mirrors with  $R=0.99975$  at  $\lambda = 445 \text{ nm}$ , where IO shows its strongest absorption bands. The mirrors have a focal length of 200 cm, and therefore a mirror distance of 190 cm was chosen to avoid the metastable confocal resonator geometry [e.g. Saleh and Teich, 1991]. With a mirror distance of of 190 cm, an effective optical path length of more than 4 km can be achieved under field conditions. Since an open resonator light path is desired, the optical setup is split into two polycarbonate boxes forming the sending and receiving unit, each containing one end of the resonator. The two boxes are mounted on a 2 m long aluminum rail with a cross section of  $(95 \times 95) \text{ mm}^2$ , which provides the mechanical stability for the resonator. For easier



**Figure 5.1.** | Simplified drawing of the OP-CE-DOAS MK-I instrument. The resonator is formed by the sending and receiving unit, which are connected by a 2 m long aluminum rail. The atmosphere between the two boxes is probed. The sending unit contains the light source and after modifications in 2012 the interference filter for wavelength resolved CRDS (WLR-CRDS) calibrations, the receiving unit contains the spectrograph and the photomultiplier tube. For the sake of clarity minor electronic components (e.g. temperature stabilization), some signal lines and power lines are not shown.



**Figure 5.2.** | Image of the OP-CE-DOAS MK-I during field work. The instrument consists of two main boxes, with the sending and receiving unit, each containing one side of the resonator. The boxes are mounted on a 2 m long aluminum rail to provide a stable optical setup. Extra boxes contain the DAQ and control unit for easier access to the computer and the gas flow unit to decouple the vibrations of the pump from the optical setup.

transport the rail was divided into three pieces two Linos X95 elements of 100 cm and 45 cm length which are connected by screws and to a custom made connecting element of 55 cm length placed in the center. The part of the resonator open towards the atmosphere has a length of 159 cm, which is accounted for in the data analysis. The custom made adjustable mirror mounts in the sensing and receiving unit are decoupled from the purge outlets outlet by a gap of about 20 mm which is sealed by Teflon foil. This is necessary to avoid misalignment the mirrors when the purge tube is inserted into the purge outlets for  $I_0$  reference measurements and path length calibration as described below. Details on the mirror mounts and the decoupling are given in Anthofer [2013].

The sending unit contains the LED light source which has a peak wavelength  $\lambda_{\text{peak}} = 445$  nm and a spectral FWHM of about 25 nm. The custom made temperature stabilization applied to the LED achieves a precision of  $\Delta T < 0.1$  K, which is necessary since open path CE-DOAS applies the classic CE-DOAS analysis described in sec. 4.3.3.1. The temperature stabilization employs a micro controller based PID controller, driving a Peltier element based on a temperature measurement at the LED. The light emitted by the LED is coupled into the resonator by a plano-convex lens with 25 mm focal length. Light leaking out on the opposite side of the resonator is focused on a multimode fiber ( $NA = 0.22$ ,  $\varnothing = 400$   $\mu\text{m}$ ,  $l = 1$  m) by another plano-convex lens with 50 mm focal length. The fiber feeds the light into the compact spectrograph, an Avantes AvaSpec ULS-2048L with a 75 mm focal length ( $f/\text{Number of } 7.1$ ), a 100  $\mu\text{m}$  entrance slit, a grating with 2400 grooves/mm, a Sony ILX554 CCD, a 16bit ADC and a spectral resolution

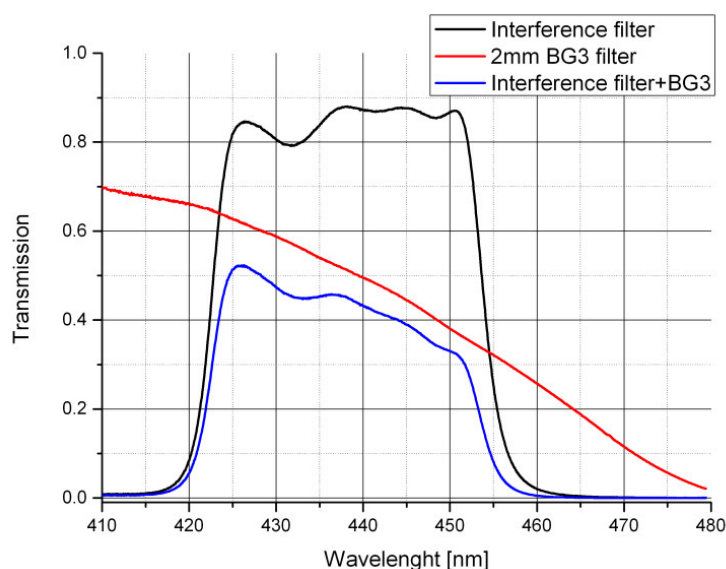


**Figure 5.3.** | Transmission of the filters used for BB-CRDS measurements during the Ireland 2011 campaign. Adopted from Anthofer [2013].

(FWHM) of 0.47 nm. The same temperature stabilization used at the LED is applied to the spectrograph with a precision of  $\Delta T < 0.1$  K, ensuring stable spectral characteristics at varying ambient temperatures. Additionally background spectra can be acquired by darkening the LED using a servo operated shutter.

A CRDS unit is also integrated in the OP-CE-DOAS MK-I for an easy calibration of the effective path length the OP-CE-DOAS MK-I. Two different CRDS methods were implemented in the OP-CE-DOAS MK-I. For the Ireland 2011 campaign the broadband CRDS (BB-CRDS) was used as described by [Anthofer, 2013], which measured the average ring down path length in the spectral window from 426.0 nm to 456.5 nm which is set using a custom made broadband interference filter (see Fig. 5.3) As shown in sec. 4.3.3.2 and [Anthofer, 2013] the broadband CRDS (BB-CRDS) measurement is used to derive a new wavelength resolved path length curve by combining it with a previously determined pair of a clean mirror path length curve (e.g. using the Helium/air method) and corresponding (broadband) ring down path length. For the Ireland 2012 campaign a wavelength resolved CRDS (WLR-CRDS) system was developed using a tunable narrow band interference filter. A detailed description of the system is given in sec. 5.4. For both CRDS variants the LED is operated in pulsed mode, which modulates the LED intensity with a square wave signal between 10 % (off) and 90 % (on) of its peak intensity with on- and off-times of 120  $\mu$ s and 60  $\mu$ s respectively, which corresponds to a pulse frequency of 5.5 kHz. In ring down mode the light leaking out of the resonator is fed into a Hamamatsu H6780-01 PMT, attached to a amplifier which is connected to a USB oscilloscope. The three stage amplifier, developed by [Anthofer, 2013], was only operated using the first two stages giving an amplification of  $10^7$ . A BG25 band pass filter is placed directly in front of the PMT to block light with wavelength above 470 nm.

The resonator mirrors are constantly flushed with a purge of purified “zero air” to avoid particles and water droplets from contaminating the mirror surfaces. For each mirror side a separate membrane pump establishes a purge flow of  $\sim 2 - 3$  L/min. Zero air is generated from ambient air using a sequence of filters, first a cartridge of silica gel followed by a PTFE aerosol filter (pore size  $2\ \mu\text{m}$ ). The gas flow unit containing the pumps and the aerosol filters is fitted into an extra box which is mounted to the optical rail using pipe clamp with extra foam rubber to allow a better decoupling of the pump vibrations from the sensitive optical setup.

The mirror purge system is also used for the regular  $I_0$  measurements where the resonator is flushed with zero air. For this the resonator is isolated from the surrounding atmosphere using a purge tube, a custom made carbon fiber telescope tube, which is inserted into the purge outlets. Sealing between the purge outlets and the purge tubes is provided by o-ring seals placed in the purge outlets. To be able to flush helium into the purge tube the purge system has a bypass behind the pumps which is routed out of the pump unit (see Fig. 5.1).

Especially when high wind and rain occur together, the purge flow is not sufficient to prevent contamination of the mirrors even though the distance between the mirrors and the purge outlets is already 17 cm. Extending the purge outlets by 5 – 10 cm using short tube pieces has proven to greatly reduce the probability of mirror contamination at least during low to moderate rain if the wind direction was roughly perpendicular to the light path. When the extensions for the tube outlets are applied this reduces the fraction of the light path open towards the atmosphere which is taken into account in the data evaluation in the geometric correction of  $\bar{L}_0(\lambda)$  described in sec 5.6.

### 5.1.1. Spectrograph Linearity

The linearity of the response of the applied spectrograph to the incident light intensity was characterized as described in sec. 10.1.1.1. Since the LED in the instrument is temperature stabilized the characterization was simply done by recording spectra at different integrations times. The exposure times were varied between 3 ms and 35 ms in 0.5 ms steps and each spectrum accumulated 1000 scans to reduce photon shot noise. This sequence was repeated for four consecutive runs to average over possible instabilities of the LED or the optical setup.

Fig. 5.4 shows the results of the characterization with the determined detector nonlinearity curve with a peak to peak value of 5 % (b), the derived nonlinearity correction function  $\alpha(I^+)$  as a function for detector counts which is well approximated by a fitted 9th order polynomial (c). After applying the polynomial correction function the deviation of the measurements from the desired linear intensity response follows a Gaussian distribution around zero with a standard deviation of 0.061 %.

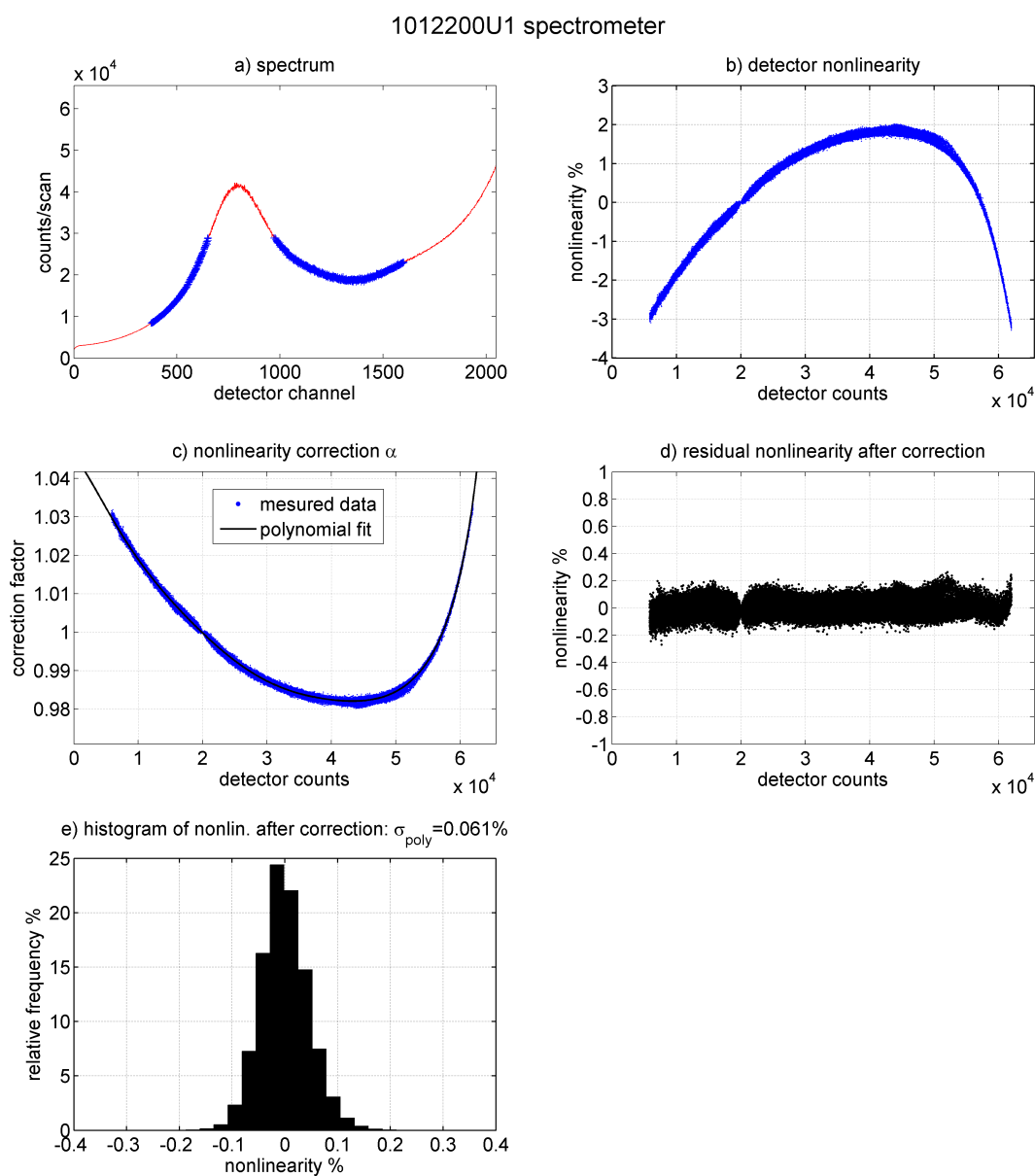


**Figure 5.4.** | Characterization of the detector nonlinearity for the spectrograph applied in the OP-CE-DOAS MK-I instrument. a) An exemplary measured spectrum: marked in blue are the spectrometer channels used for the characterization. b) The determined detector nonlinearity curve with a peak to peak value of 5%. c) The derived nonlinearity correction function  $\alpha(I^+)$  as a function for detector counts which is well approximated by a fitted 9th order polynomial. d) and e) after applying the polynomial correction function the deviation of the measurements from the desired linear intensity response follows a Gaussian distribution around zero with a standard deviation of 0.061%.

## 5.2. Open Path CE-DOAS Mark II

The Open Path CE-DOAS Mark II (OP-CE-DOAS MK-II) instrument built in the frame of this thesis and Zielcke [2015] is the successor of the OP-CE-DOAS MK-I and based on the same technical design which was modified in some minor details to be suitable for polar applications. Thus, all components including an embedded PC are integrated in two insulated boxes as shown in Fig. 5.5/5.6. Since the instrument also has the same spectral characteristics as the OP-CE-DOAS MK-I no further details on the setup are given here and the interested reader is referred to Zielcke [2015] for a detailed description. For calibration of the effective optical path length the instrument also uses the WLR-CRDS system described in sec. 5.4.

### 5.2.1. Spectrograph Linearity

The linearity of the response of the spectrograph to the incident light intensity was characterized as described in the previous section 5.1.1. The exposure times were varied between 4 ms and 500 ms in steps of 4 ms and each spectrum accumulated 400 scans to reduce photon shot noise. This sequence was repeated for ten consecutive runs to average over possible instabilities of the LED or the optical setup. The results of the characterization are shown in Fig. 5.7. Detector nonlinearity shown in sub figure b) features an odd S-shaped bend in the intensity range between  $1.3 \cdot 10^4$  and  $1.8 \cdot 10^4$  ADC counts, which corresponds to a saturation range between 20 % and 27 %. Therefore, the typically used 9th (and also tried higher) order polynomial fit does not give an accurate representation the nonlinearity correction function  $\alpha(I^+)$ . A much more accurate representation of  $\alpha(I^+)$  is achieved by averaging over intervals of 1000 counts and a subsequent spline interpolation. Sub figure d) shows the relative difference between both representations of  $\alpha(I^+)$ , which is about  $2 \cdot 10^{-3}$  peak to peak. Section 10.2.1 shows that despite the relatively small difference only the spline representation of  $\alpha(I^+)$  allows a sufficiently accurate correction of the detector nonlinearity. Therefore, for all measurements performed with the OP-CE-DOAS MK-II instrument the spline representation of  $\alpha(I^+)$  was used for nonlinearity correction.

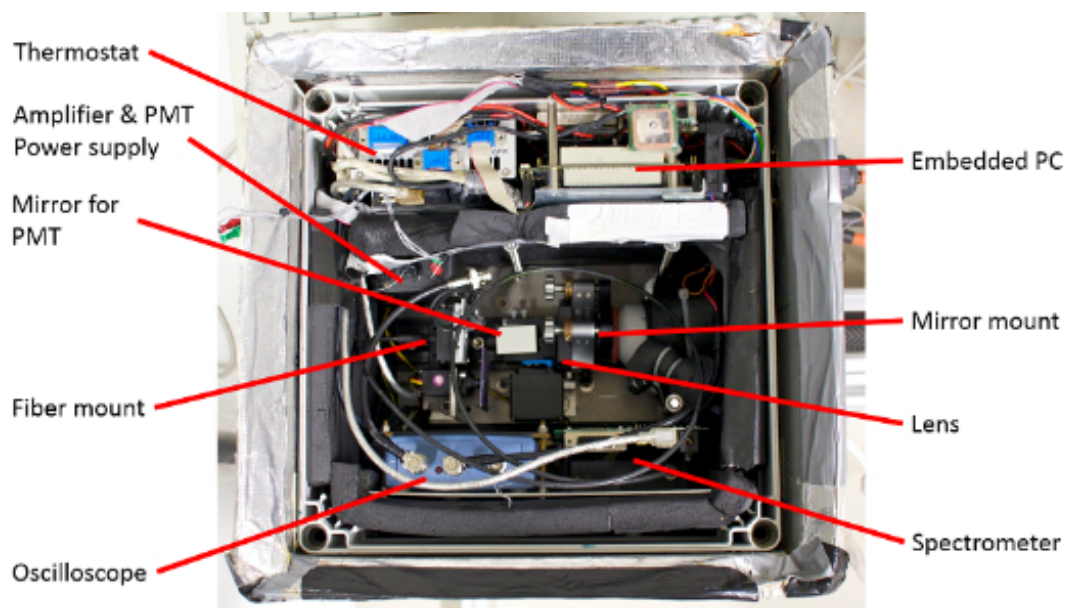


**Figure 5.5.** | View into the spectrograph box of the OP-CE-DOAS MK-II from above with the light path to the right. The module containing the PMT and amplifier is sitting above the mirror mount when mounted, here it is removed to allow a view underneath. Taken from Zielcke [2015]

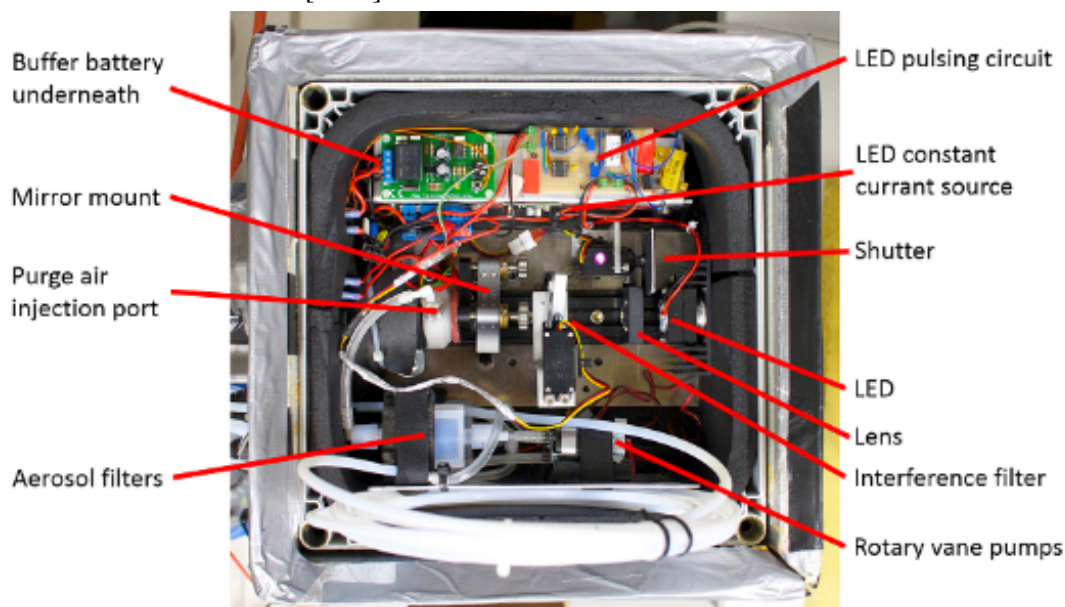


**Figure 5.6.** | View into the LED box of the OP-CE-DOAS MK-II from above with the light path to the left. At the bottom, a loop of several meters of tubing can be seen, used to warm up air before purging the mirrors. Taken from Zielcke [2015]

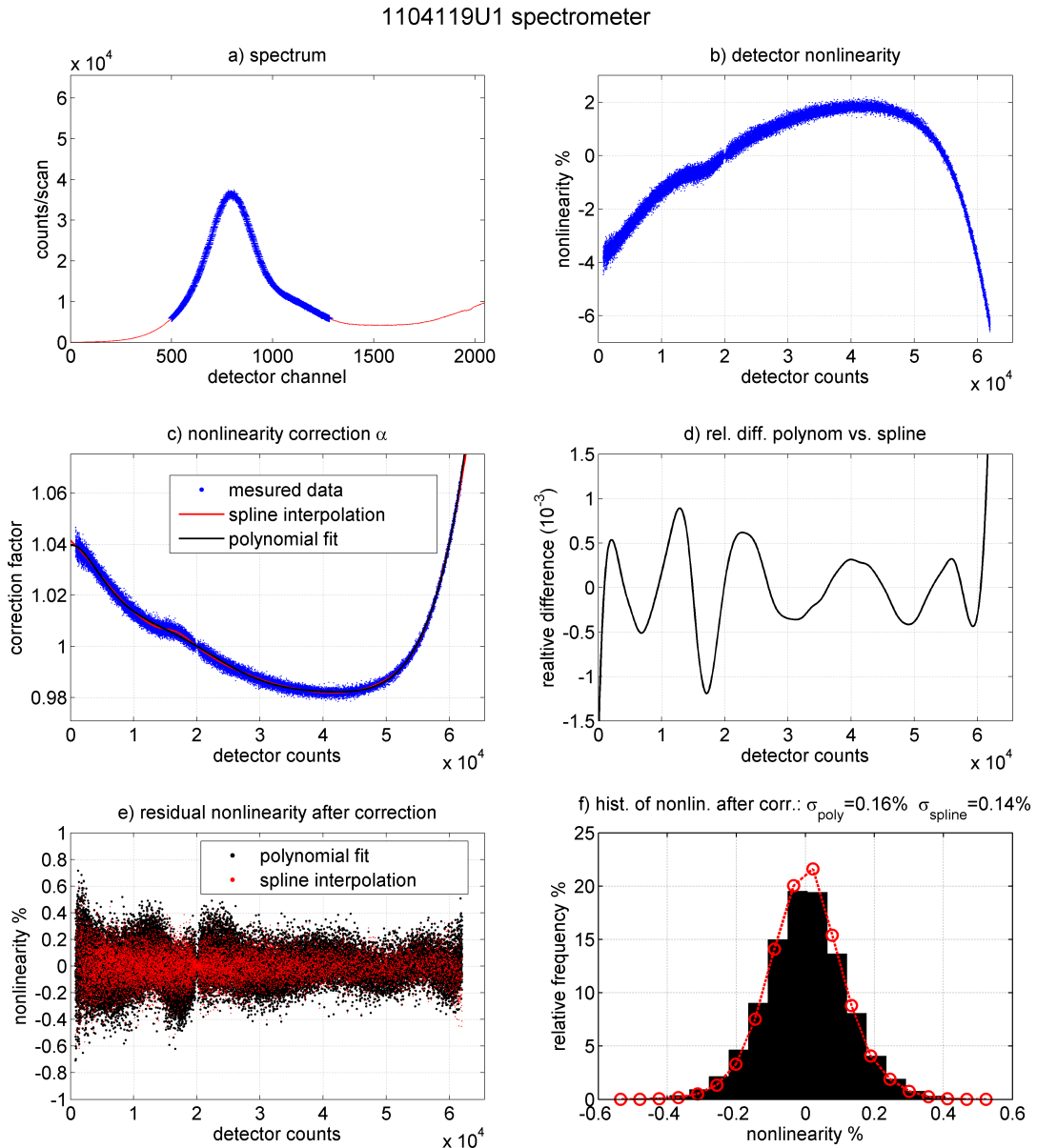


**Figure 5.7.** | **Characterization of the detector nonlinearity for the spectrograph applied in the OP-CE-DOAS MK-II instrument.** a) An exemplary measured spectrum: marked in blue are the spectrometer channels used for the characterization. b) the detector nonlinearity features an odd S-shaped bend in the saturation range between 20 % and 27 %. c) The typically used 9th (and also tried higher) order polynomial fit does not give an accurate representation the nonlinearity correction function  $\alpha(I^+)$ . A much more accurate representation of  $\alpha(I^+)$  is achieved by averaging over intervals of 1000 counts and a subsequent spline interpolation. d) The relative difference between both representations of  $\alpha(I^+)$  is about  $2 \cdot 10^{-3}$  peak to peak. e) If the polynomial is used to correct the measurements the remaining nonlinearity systematically deviates from zero, especially for detector saturations between 20 % and 27 %.

### 5.3. Path Length Curve Using the Helium/air Method

The Helium/air method, described in sec. 4.3.3.2, was applied for both the OP-CE-DOAS MK-I and the OP-CE-DOAS MK-II instrument to get a spectrally resolved measurement the  $\bar{L}_0(\lambda)$  over the entire spectral range with high mirror reflectivity. Gases applied for the calibration are zero air produced by the integrated filter system and lab grade Helium with a purity of 99.999 %. In the following the typical calibration routine is described:

1. The purge tube is inserted in the purge outlets for measurements in “zero air” as described in sec. 5.1. The air flow is reduced to  $2 \text{ L min}^{-1}$  to ensure a laminar flow in the purge tube.
2. Spectra are acquired until the intensity measured by the spectrograph is stable. A good indicator is if the relative drift of the average intensity from 435 nm to 450 nm is below  $1 \cdot 10^{-3}$ . The instrument is then considered stable enough for calibration and several more “zero air” measurements are acquired and taken as  $I_{\text{Air}, 1}(\lambda)$  for the calibration.
3. The pump is stopped, a Helium cylinder and flow regulator is connected to the inlets and Helium is purged into the resonator. The purge flow is first relatively high ( $> 3 \text{ L/ min}$ ) to ensure a quick gas exchange in the entire purge tube and thus resonator volume. For the actual measurements of light intensities with a Helium filled resonator  $I_{\text{Helium}}(\lambda)$  the flow is reduced to  $2 \text{ L/ min}$  to avoid intensity fluctuations due to turbulence.
4. After the Helium measurement the resonator is purged again with “zero air”, first at a higher flow rate ( $> 3 \text{ L/ min}$ ) until the Helium is completely replaced with air and then at  $2 \text{ L min}^{-1}$  for a second set of “zero air” measurements  $I_{\text{Air}, 2}(\lambda)$ .
5. If the relative difference between  $I_{\text{Air}, 1}(\lambda)$  and  $I_{\text{Air}, 2}(\lambda)$  is equal or lower than  $1 \cdot 10^{-3}$ , the instrument is considered stable over the time of the calibration sequence and the measurements are stopped. Otherwise the procedure is repeated, if possible, until a calibration sequence with a stable instrument characteristics is achieved.

The data analysis is performed using eq. (4.35), with the slight modification that the extinction coefficient of air  $\epsilon_{\text{air}}(\lambda)$  additionally contains some weak absorption by the oxygen collision complex  $\text{O}_4$  in this spectral range. These absorption lines are accounted for in the data analysis.

An example for a successful air/Helium/air calibration sequence and the resulting curve for  $L_0$  in “zero air” is shown in Fig. 5.8. The peak of the optical path length in “zero air” is 5.3 km, which corresponds to a mirror reflectivity of  $R_{\text{max}} = 0.9997$ . The precision of this measurement, which was recoded under optimal conditions, is of the order of 1 %. However, it usually requires laboratory like condition and more than 30 min of thermal equilibration to achieve the required instrument stability for such an accurate calibration. Therefore, such a measurement is very difficult to achieve during a typical field campaign where the temperature stability of the available space/shelter and the available time are limited.

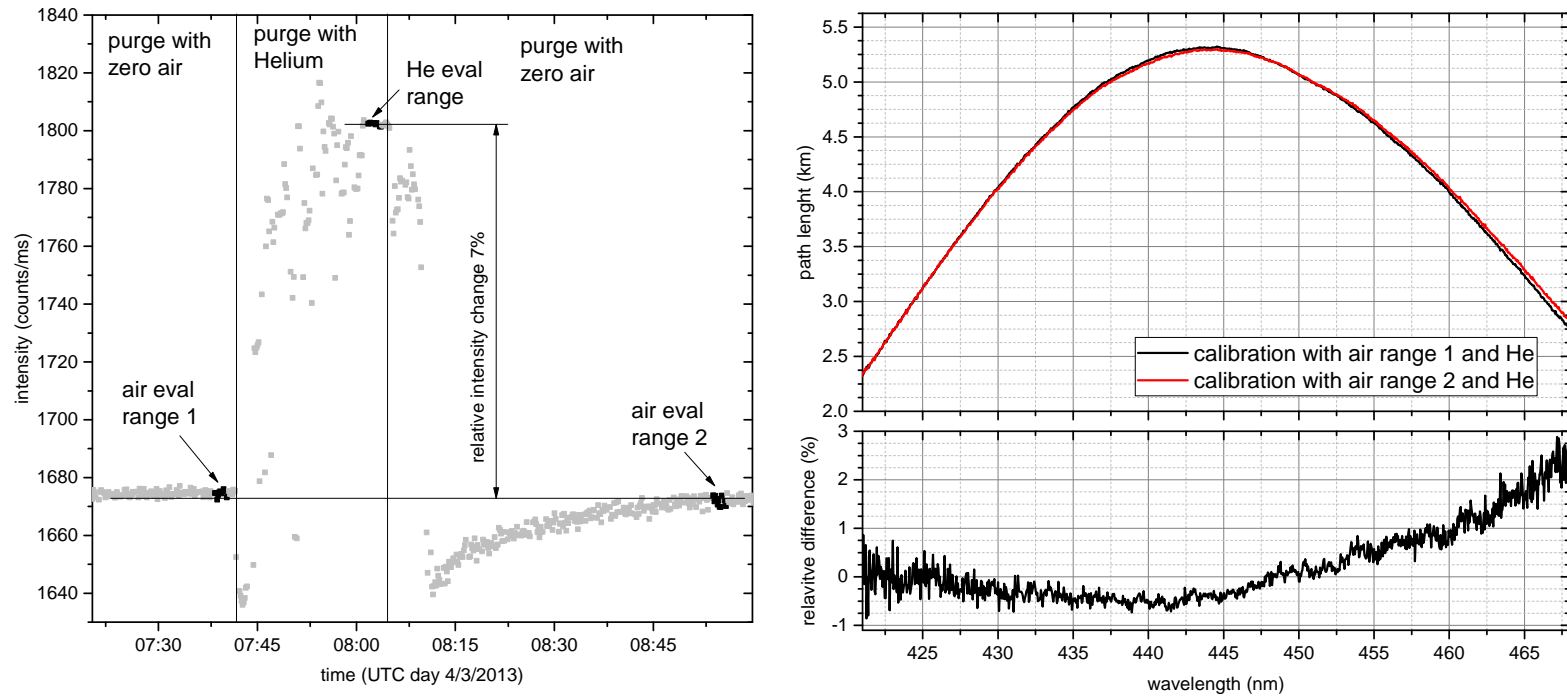


**Figure 5.8.** | Example for a path length curve calibration using the Helium/air method. Left: time series of the average light intensity (435 nm to 450 nm) during the calibration, annotated with the periods of purge with zero air and Helium. The black points mark the measurements intervals used to derive the path length curves. The difference of the light intensity between air and Helium purge is 7%. Right top: two path length curves derived using the evaluation ranges marked in the left plot. Right bottom: the two derived path length curves show an excellent agreement with a relative difference of less than one percent in the relevant spectral range from 420 nm to 460 nm. The shown measurements were performed on April 3 2013 with the OP-CE-DOAS MK-II during the New Zealand campaign.

## 5.4. Wavelength Resolved CRDS

A precise knowledge of the effective optical path length is important for CE-DOAS measurements. Therefore, especially during field measurements, where changes of the path length due to contamination of the mirrors are common, a simple method for frequent determination of the path length is desired. A new wavelength resolved CRDS (WLR-CRDS) system was co-developed and implemented in this work and in [Zielcke, 2015]. As described in sec. 4.3.3.2 this method requires an additional wavelength discriminating element. A simple tunable wavelength filter is realized by exploiting the angular dependence of the transmission curve of an interference filter [Pollack, 1966]. The applied filter is a Lot Oriel 442FS05-50 interference filter with diameter of 50 mm, a nominal spectral transmission curve width of 1.0 nm (FWHM). For perpendicular incident light it has a center wavelength of 441.6 nm and a transmission of 35 %. As shown in Fig. 5.9 the center wavelength can be tuned down to below 420 nm by tilting the incident angle. Thus, the filter covers the spectral range with strong IO absorption, which was the major criterion for the selection of the filter. For an increasing tilt the maximum of the transmission curve shifts to lower wavelengths, additionally the maximum of the curve decreases and it broadens, for example at a center wavelength of 420 nm the FWHM of the transmission increases to about 1.7 nm. However over entire tunable range the FWHM of the transmission is sufficiently narrow, as  $\bar{L}_0(\lambda)$  can be still be approximated as a linear function over these wavelengths intervals.

The interference filter was installed in the OP-CE-DOAS MK-I as shown in Fig. 5.1 and similarly in the OP-CE-DOAS MK-II. The interference filter is mounted on a servo, which

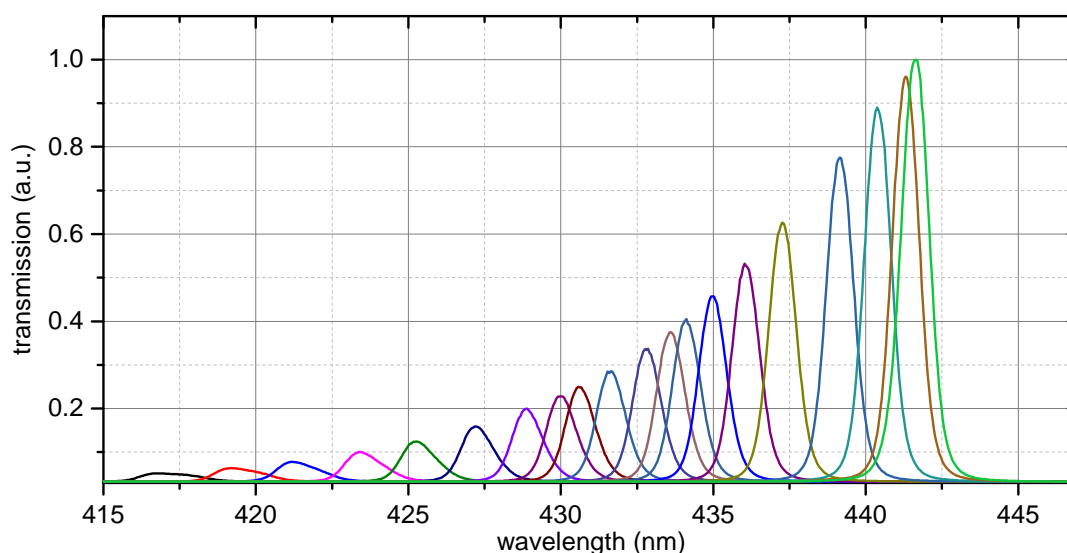


**Figure 5.9.** | Transmission curve of the interference filter for different angles of incidence. The transmissions are shown for different servo positions corresponding to angles of incidence from 0° (orthogonal) to approximately 30°.

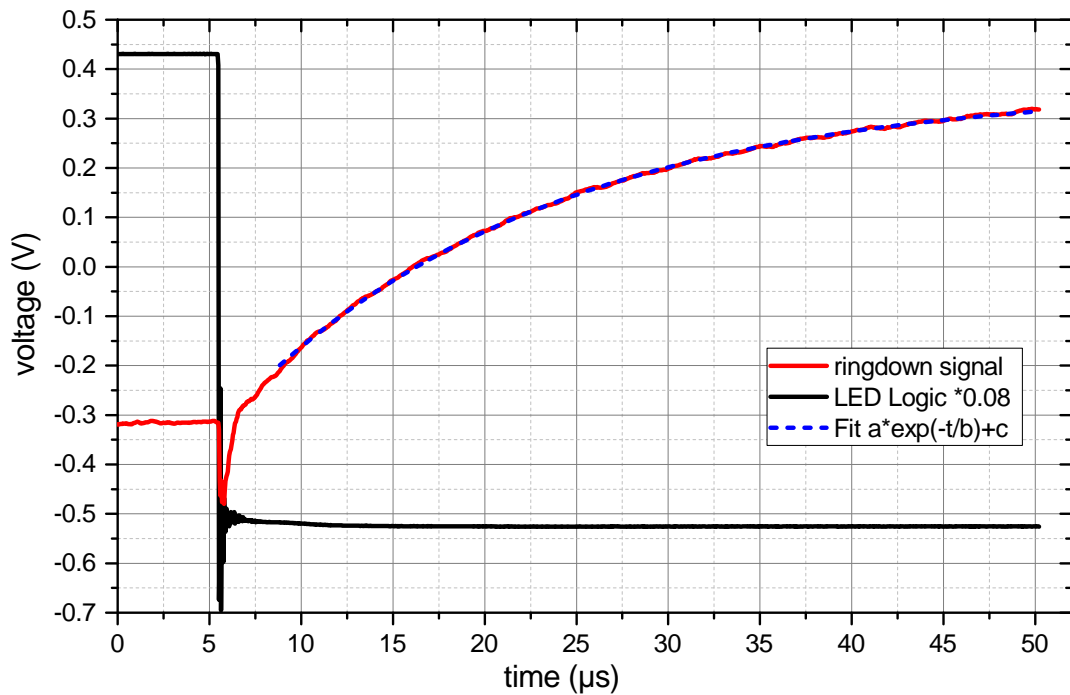


**Figure 5.10.** | Example of a recorded ringdown signal with the Open Path CE-DOAS Mark II. The blue dashed curve indicates the fitted exponential function with a decay time of  $17\ \mu\text{s}$  corresponding to a path length of 5.1 km. In black the logic signal of the LED driver is shown (high is on) and the red curve shows the output signal from the PMT amplifier.

allows to drive the interference filter into light path and adjust the incident angle of the light. The LabVIEW program from Anthofer [2013] for recording and evaluating CRDS measurements was modified to control the tilt angle of the interference filter and synchronize it with the acquisition of the ring down signals. Thus, the new LabVIEW program can now directly acquire the wavelength resolved path length curve.

### 5.4.1. Calibration Routine

Calibration of the path length curve using the WLR-CRDS is done according to the following routine.

1. The purge tube is inserted in the purge outlets for measurements in “zero air” as described in sec. 5.1.
2. For a selected number of servo positions, at which the ring down signals should be measured, the interference filter is driven into the light path and spectra of the filter

- transmission curves are acquired. Gaussian fitting to the recorded transmission curves yields a mapping of the servo positions to transmitted center wavelengths, since the spectrograph is always wavelength calibrated for the DOAS measurements.
3. The LED is switched into pulsed operation and the light leaking out of the resonator is directed onto the PMT as described in sec. 5.1.
  4. For all selected servo positions 1000 ring down signals are acquired and effective path lengths are determined by least squares fitting as described in sec. 4.3.3.2. Figure 5.10 shown a typical ring down measurement with a fitted exponential model. Usually the sequence of servo positions is repeated three to four times to determine the standard deviation of the measurements.
  5. Finally the ring down signals are combined with the calibrated servo positions to get the wavelength resolved calibration of the effective optical path length  $\bar{L}_0(\lambda)$ . Figure 5.11 shows an example of such a calibration curve.

The resulting ring-down curve is usually interpolated using a 3rd or 4th order polynomial. However, if it is desired to use the determined  $\bar{L}_0(\lambda)$  curve beyond the spectral range of the interference filter it is necessary to add additional information for example by fitting another  $\bar{L}_0(\lambda)$  curve determined in the lab using the Helium/air method.

### 5.4.2. Comparison to the Helium/air Method

A comparison of the new WLR-CRDS method with the established Helium/air method is shown in Fig. 5.11. Both method show an excellent agreement withing 2%. The error of the WLR-CRDS is based on the standard deviation of three subsequent measurement runs and the error of the Helium/air measurement is estimated from the measurements sequence shown in Fig. 5.8. Thus, this method is a very accurate alternative for the established Helium/air measurement. It should be noted that the error of the shown Helium/air measurement, which was recorded under lab conditions with several hours of thermal equilibration before the measurement, is extremely low and usually during field measurements the error would be at least one order of magnitude higher.

The WLR-CRDS method has several advantages when compared to the the Helium/air method. Firstly, no pressurized gas cylinders with calibration gases are required, which are difficult to obtain in remote areas and transport is often prohibited since they are considered hazardous goods. The method is independent of the absolute stability of the light intensity (compared to the Helium/air method) and therefore measurements are more robust and reproducible and generally also much faster since long periods of thermal equilibration prior to the measurement can be avoided. Therefore, this method was the main calibration method for open path CE-DOAS during the Ireland 2012 and New Zealand 2013 campaigns.

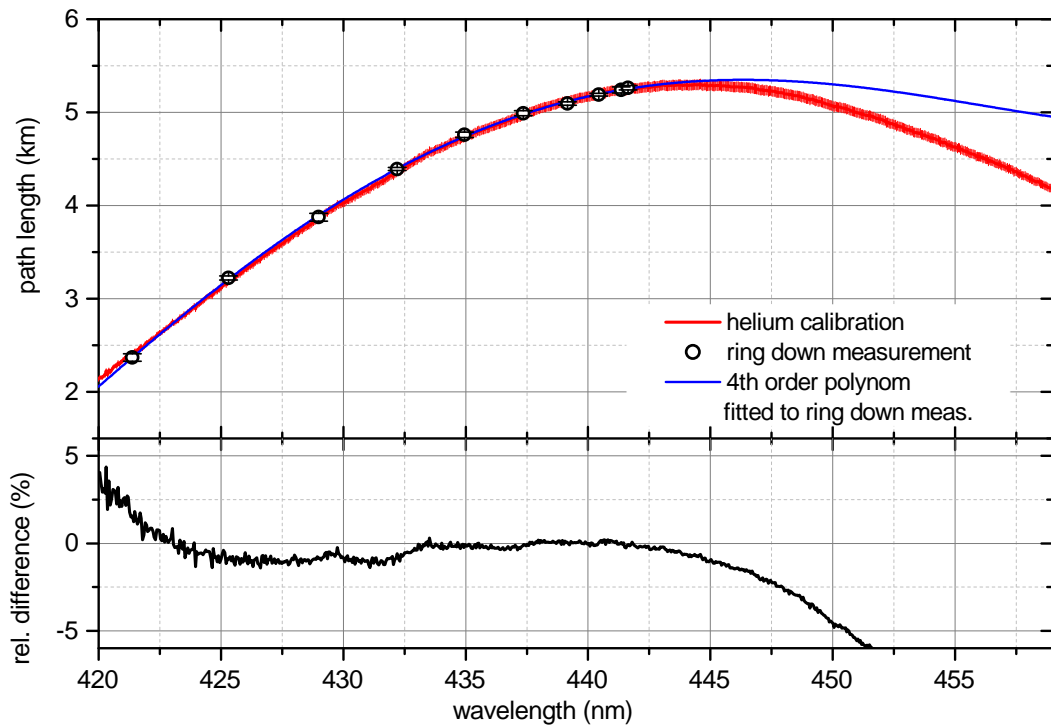


**Figure 5.11.** | Comparison between path length curves derived from the Helium/air (red) and the ring down (open circles) calibration methods. An agreement of 99% is found between a fourth order polynomial fitted to the ring down calibration agrees and Helium/air calibration, in the range of the ring down measurements. Beyond the spectral range of the ring down measurement the agreement decreases since the polynomial is not constraint.

## 5.5. Measurement Routine

All CE-DOAS field measurements were conducted following the measurement routine, instrument and campaign specific parameters that are summarized in Tab. 5.1. The instrument was setup with the purge tube mounted and several blocks of 10  $I_0$  spectra were recorded. Additionally, one background spectrum with blocked light source were recorded. The  $I_0$  spectra were checked for (spectral) intensity, which is an indicator for the quality of the optical alignment and the cleanliness of the resonator mirrors. The instrument was defined ready for field measurements if the  $I_0$  intensity was larger than 20 % compared to the last laboratory measurement, otherwise re-adjustment and/or cleaning of resonator mirrors was necessary. If ready, the effective path length was calibrated using the built in BB-CRDS or WLR-CRDS module (see Tab. 5.1). Afterwards, the purge tube was removed and the continuous atmospheric measurement loop started. In each loop cycle first a background spectrum with blocked light source was acquired followed by ten subsequent atmospheric measurements. Depending, if the CE-DOAS operation was supervised or not, the measurement loop was interrupted for acquisition of  $I_0$  spectra every 6 h to 48 h. The integration times, which are the same for  $I_0$ , atmospheric and background measurements, are given in Tab. 5.1.

During the Ireland 2011 and 2012 campaigns on days with unstable weather conditions the purge outlets were extended for better protection of the cavity mirrors. This was done by inserting tube pieces as described in sec. 5.1 and flagged in the recorded spectra for later correction in the data analysis, as it reduced the fraction of the light path open towards the atmosphere by 20 cm.

## 5.6. Spectral Evaluation

Trace gas mixing ratios were retrieved from the measurements with the software DOASIS using a script based spectral analysis developed in the frame of this thesis, which is described in the following. First the nonlinearity of the measured spectra is corrected using the determined correction function  $\alpha(I)$ . Then, the measured  $I(\lambda)$  and  $I_0(\lambda)$  spectra are corrected for the dark and background signal using the recorded background spectra. Effective optical densities are calculated using the classic CE-DOAS/BB-CEAS analysis

$$D_{\text{eff}} = \frac{I_0(\lambda)}{I(\lambda)} - 1 \quad (5.1)$$

campaign	instrument	exposure time (ms/scan)	# scans per spectrum	field path length calibration method
Ireland 2011	Mark I	30-40 see Tab. 12.1	1000	BB-CRDS
Ireland 2012	Mark I	10-20 see Tab. 12.1	1000	WLR-CRDS
New Zealand 2013	Mark II	15	5000	WLR-CRDS

**Table 5.1.** | Instrument and campaign specific parameters of the CE-DOAS measurement routine.

For the trace gases  $i$  to be retrieved, effective fit references are calculated  $\Theta_i(\lambda)$  :

$$\Theta_i(\lambda) = H(\lambda) \otimes \left( \sigma_i(\lambda) \cdot \bar{L}_0(\lambda) \frac{d_{\text{open}}}{d_0} \right) . \quad (5.2)$$

$\bar{L}_0(\lambda)$  is included to account for the wavelength dependency of the effective light path. The factor  $\frac{d_{\text{open}}}{d_0}$  is a geometrical correction for the fraction of the light path open towards the atmosphere, with the mirror displacement  $d_0$  and the open distance between the purge outlets  $d_{\text{open}}$ . Adaption to the instrument resolution is done by convolution with the instrument function  $H(\lambda)$ . Subsequently, a binomial high pass filter is applied to both,  $D_{\text{eff}}$  and the effective fit references  $\Theta_i(\lambda)$ . Finally, a DOAS fit is applied to retrieve number densities  $\rho_i$  of the trace gases which are converted into mixing ratios using the ideal gas law (see sec. 2.2).

### 5.6.1. Path length curves used in the retrieval

Path length curves  $\bar{L}_0(\lambda)$  were determined using a combination of in field CRDS measurements and laboratory calibrations using the He/air method. Two different approaches were used:

1. For the Ireland 2011 campaign BB-CRDS field measurements were used to rescale the  $\bar{L}_0(\lambda)$  curve from a laboratory calibration as described in 4.3.3.2 and Anthofer [2013].
2. During the Ireland 2012 and New Zealand 2012 campaigns, WLR-CRDS measurements directly delivered the wavelength dependency of  $\bar{L}_0(\lambda)$  in the spectral range from 420 nm to 441.6 nm. However, in order to evaluate  $(\text{CHO})_2$  the DOAS fit applied a spectral window from 421.4 nm to 458 nm, which required to extend the path length curve. A polynomial fit could not be used for this since it was not constraint beyond the wavelength range of the WLR-CRDS measurements. Therefore, a  $\bar{L}_0(\lambda)$  curve from a laboratory calibration, which extended of the entire spectral range of the instrument, was rescaled by fitting the following model to the WLR-CRDS measurements:

$$\bar{L}'_0(\lambda) = \frac{1}{\theta_1 + \frac{1}{\theta_2 \bar{L}_0(\lambda)}} . \quad (5.3)$$

where  $\theta_1$  and  $\theta_2$  are fitted parameters. The fit model eq. (5.3) was derived from the model of a contaminated resonator mirror described in sec. 4.3.3.2.

### 5.6.2. Retrieval of IO, NO<sub>2</sub> and (CHO)<sub>2</sub>

All open path CE-DOAS measurements in this work used the same retrieval settings, described in this section. Mixing ratios of IO, NO<sub>2</sub> and (CHO)<sub>2</sub> were retrieved in the spectral window from 421.4 nm to 458 nm, which was chosen to include the strongest absorption bands of IO and (CHO)<sub>2</sub>. The retrieval used a binomial high pass filter with 1000 iterations. Besides the trace gas species of interest also H<sub>2</sub>O and O<sub>4</sub> were included in the fit, since these gases also absorb in the spectral range of interest. A third order polynomial (DOAS polynomial) was included in the fit as well. The values of  $d_0$  and  $d_{\text{open}}$  used for the geometrical correction

of  $\bar{L}_0(\lambda)$  are summarized in Tab. 5.2 for the different campaigns and setups. Exemplary fits for a measurements with the Open Path CE-DOAS Mark I and II are shown in Fig. 5.12 and Fig. 5.13 respectively.

<b>campaign</b>	$d_0$ (cm)	$d_{\text{open}}$ (cm)	$d_{\text{open, reduced}}$ (cm)
Ireland 2011 before 6/2	204	174.4	163.6
Ireland 2011 after 6/2	190	149.4	-
Ireland 2012	192.5	159.2	139.4
New Zealand 2013	190	162.0	-

**Table 5.2.** | **Mirror distances and open length between the purge outlets for the different campaigns and setups.**  $d_0$  is the mirror displacement,  $d_{\text{open}}$  the normal distance between the purge outlets and  $d_{\text{open, reduced}}$  the reduced distance of the purge outlets are extended by extra tube pieces. During the Ireland 2011 campaign the mirror distance was reduced from the initial setting of 204 cm to 190 cm, since it was found that at 204 cm mirror separation the resonator was (almost) confocal, which caused stability problems.

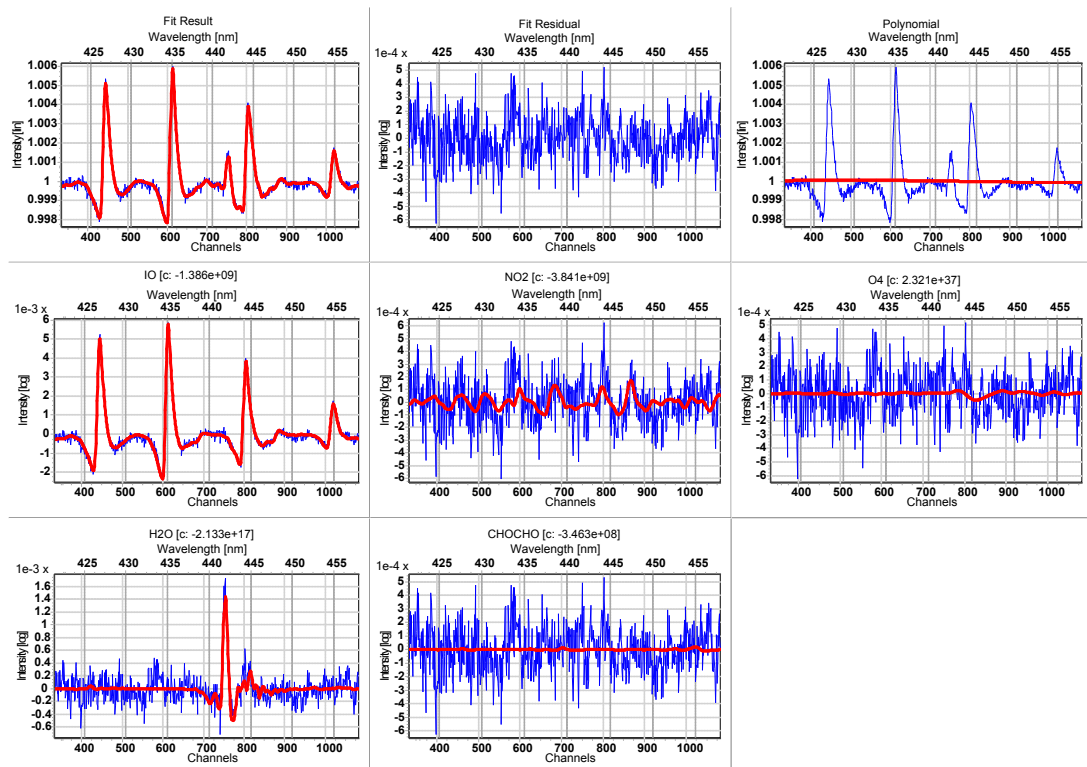


**Figure 5.12.** | Example for the spectral retrieval of IO and NO<sub>2</sub> for a measurement by the Open Path CE-DOAS Mark I. The spectrum was recorded on July 26 2012 at 15:39 UTC in at MRI in Ireland. The red lines shows the fitted references and the blue line the sum of fit result and fit residual, which has a RMS of  $1.7 \cdot 10^{-4}$ . The retrieved mixing ratios are  $(65.70 \pm 0.76)$  ppt IO,  $(0.18 \pm 0.05)$  ppb NO<sub>2</sub> and  $< 66.8$  ppt (CHO)<sub>2</sub>

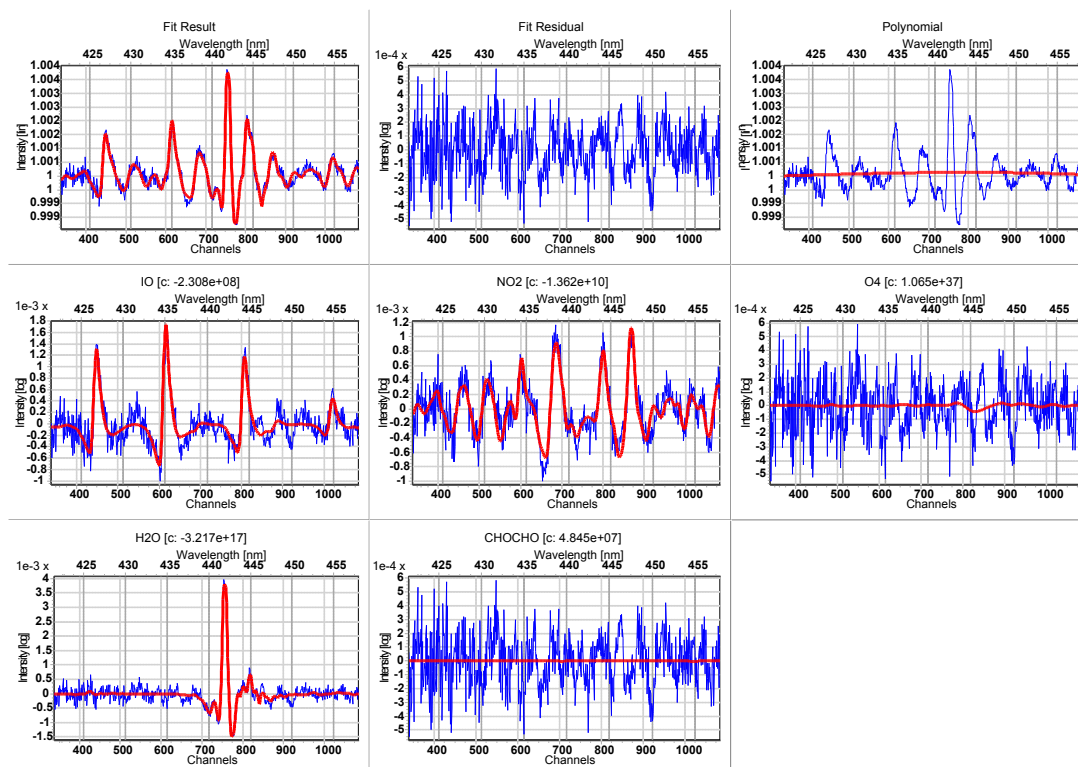


**Figure 5.13.** | Example for the spectral retrieval of IO and NO<sub>2</sub> for a measurement by the Open Path CE-DOAS Mark II. The spectrum was recorded on March 25 2013 at 02:43 UTC in New Zealand. The red lines shows the fitted references and the blue line the sum of fit result and fit residual, which has a RMS of  $1.8 \cdot 10^{-4}$ . The retrieved mixing ratios are  $(10.80 \pm 0.45)$  ppt IO,  $(0.64 \pm 0.03)$  ppb NO<sub>2</sub> and  $< 66.8$  ppt (CHO)<sub>2</sub>.

<b>Part</b>	<b>Model</b>
Spectrograph	Avantes AvaSpec ULS-2048L (S/N 1012200U1)
Resonator Mirrors	Advanced Thin Films $R > 99.975\%$ , Run V6-176, A4-A8
LED	CREE XR-E royal blue BIN D316
LED constant current source	A1W HKO-KL50-1000
Optical fiber	Lopteck quartz fiber $1\text{ m} \times \varnothing 400\ \mu\text{m}$ , 2xSMA
Photomultiplier tube (PMT)	Hamamatsu H6780-01
USB oscilloscope	PicoScope 2204
Interference filter	LOT Oriel 442FS05-50
Servo controller	Micro Maestro (6 channel)
Servos	Hitec HS-5496MH
GPS	Navilok NL-402U
Sender and receiver case	Enstio Cubo O
DAQ unit case	Zarge Alu Case K410
Outer rail	Linos X95
Inner optical mounts	Linos microbench
Diaphragm pumps	Schego W2K3

**Table 5.3.** | List of commercially available components used in the OP-CE-DOAS MK-I



# 6

## The Compact Closed Path IO/NO<sub>2</sub> CE-DOAS

The Open Path CE-DOAS systems introduced in the last chapter are light weight and robust enough to be carried into the seaweed fields for point measurements. However, they are still too heavy (30 kg plus 10 kg battery) and too large (length  $\approx$  2.3 m) to fully resolve the horizontal distribution of IO in the seaweed field, since this requires the instrument to be quickly moved in a several square kilometers large area for at least half an hour. Furthermore, due to the open light path, contamination of the cavity mirrors is a regular issue of Open Path CE-DOAS instruments, which complicating their operation in the field.

In order to overcome these limitations, the Compact Closed Path CE-DOAS (CP-CE-DOAS) instrument for measurements of IO and NO<sub>2</sub> was built in the frame of this thesis, based on the prototype developed in Horbanski [2010]. A sketch and a detailed image of the instrument are shown in Fig. 6.1. All components required for an autonomous operation are included in a small (dimensions 72 cm  $\times$  18 cm  $\times$  28 cm) and light (5 kg) box. Together with the low power consumption of 25W, which allows for several hours of field operation with a low weight Li-Po Battery, this makes the instrument very portable and suitable for in field operation by one person Fig. 6.2.

The central element of the instrument is an optical resonator with 43 cm length formed by two high reflective mirrors with 25 mm diameter and a 1 m radius of curvature. The mirrors have the same dielectric coating as those used in the Open Path CE-DOAS instrument with a maximum reflectivity of  $R=0.99975$  at  $\lambda = 445$  nm. The resonator is enclosed by a Teflon tube with gas connectors to make a closed measuring cell. As light source a CREE XP-E Royal Blue LED (BIN D316) which peaks at  $\lambda_{\text{peak}} = 445$  nm and has a FWHM of about 25 nm is used as light source. To save weight and electrical power, the light source is not thermally stabilized. This is possible since the new iterative CE-DOAS retrieval (iCE-DOAS), described in sec. 9, is used for data evaluation. The light emitted by the LED is coupled into the resonator by a plano-convex lens ( $f = 25$  mm). Light leaking out on the opposite side of the resonator is focused on a multimode fiber ( $NA = 0.22$ ,  $\varnothing = 400$   $\mu\text{m}$ ,  $l = 1$  m) by another plano-convex lens with 50 mm focal length. The fiber feeds the light into a compact spectrograph from Avantes, with the same CCD, grating and slit configuration as those applied in the Open Path CE-DOAS.

Additionally to the spectral measurements a Navilok GPS receiver provides the position of the instrument. For data acquisition an embedded PC (Toradex Robin Z530 with Daisy interface board) which runs a normal windows XP operating system is used. A scripted measurement routine, based on the DOASIS software [Kraus, 2006], is used for automated acquisition and optional on-line evaluation of the spectral data. Thus, the instrument can autonomously measure without the need of any additional, external hardware.

All parts of the gas flow system, with the exception of a few stainless steel gas connectors, are made of Teflon to avoid losses of NO<sub>2</sub> and of the even more reactive IO. To further reduce losses two pumps provide a high gas flow of 6l/min of the sample air. Thus the residence time of the air in the system is only 2.8 s. However, during the Ireland 2012 campaign it was found that the largest part of the sampled IO is lost before it can be measured. This unfortunately makes the compact CE-DOAS not useable for reliable measurements of IO. A detailed discussion and characterization of this problem is found in sec. 12.5.

The Closed Path CE-DOAS has however, proven as a very sensitive and reliable instrument for NO<sub>2</sub> measurements and has been successfully applied for measurements under clean background conditions [e.g. Herlyn, 2015] and for mobile measurements in polluted urban environments [e.g. Kanatschnig, 2014].

### 6.1. Spectrograph Linearity

The linearity of the response of the spectrograph to the incident light intensity was characterized as described in sec. 10.1.1.1. The spectrograph was characterized with a different, temperature stabilized blue LED. The characterization was then simply done by recording spectra at different integrations times. The exposure times were varied between 2 ms and 50 ms in 1 ms steps and each spectrum accumulated 500 scans to reduce photon shot noise. This sequence was repeated for four consecutive runs to average over possible instabilities of the LED or the optical setup. The results of the characterization are shown in Fig. 6.3. Without the correction the charge coupled device (CCD) detector has a nonlinearity of about 6 % or a saturation between 10 % and 70 %. The determined nonlinearity was interpolated with a 9th order polynomial, which was subsequently used to correct the measured spectra. After applying the correction polynomial measured spectra show an almost perfect linear intensity response with a standard deviation of 0.065 %.

### 6.2. Path Length Calibration

The effective path length  $\bar{L}_0(\lambda)$  in clean air was calibrated using the Helium/air method described in sec. 4.3.3.2 with the same measurement procedure used for the Open Path CE-DOAS systems in sec. 5.3 using two consecutive sequences of Helium and air measurements. The resulting  $\bar{L}_0(\lambda)$  curve with a peak value of  $(1.48 \pm 0.05)$  km at 444.6 nm is shown in Fig. 6.4.

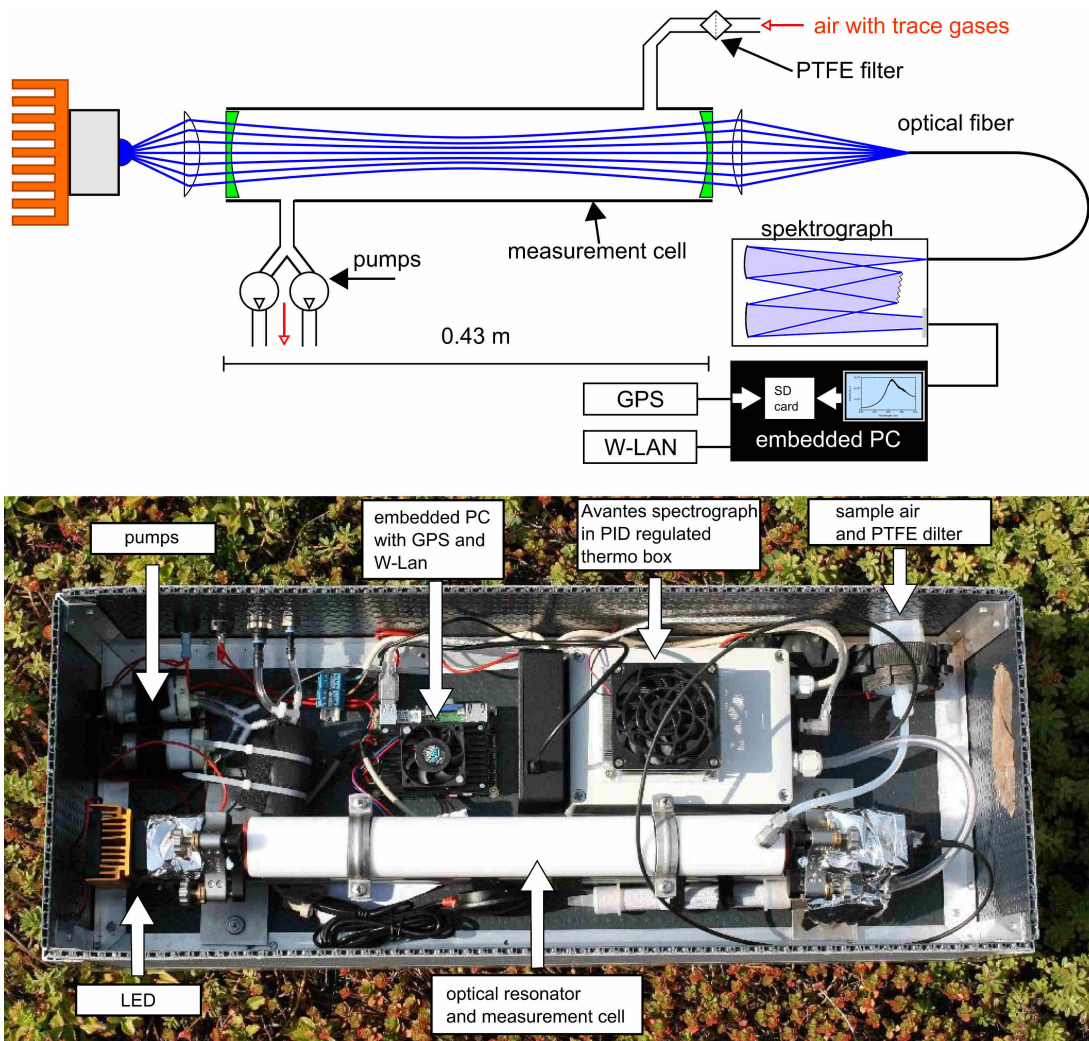


Figure 6.1. | A principle sketch (top) and picture (bottom) of the compact closed path CE-DOAS System.



**Figure 6.2.** | Closed path CE-DOAS in mobile operation during the Ireland 2012 campaign.

### 6.3. Measurement Routine

During the Ireland 2012 campaign the purge flow through the measurement cell was set to 6l/min. Spectra with 12000 accumulated scans of 6 ms exposure time were continuously acquired.  $I_0$  reference spectra were measured every one to two days with purified zero air generated using the same scrubbing system as in the Open Path CE-DOAS (sec. 5.1).

### 6.4. Spectral Retrieval

The spectral retrieval was made with the newly developed iterative CE-DOAS (iCE-DOAS) analysis described in chap. 9. Atmospheric measurements  $I$  were evaluated against the  $I_0$  reference closest in time. Measured spectra underwent the standard offset and dark current correction. Before the DOAS fit the optical density and the literature reference spectra were treated with a binomial high pass filter with 1000 iterations to remove broadband structures. NO<sub>2</sub> and IO mixing ratios were simultaneously retrieved in the spectral window from 423.1 nm to 447.6 nm. Additionally to NO<sub>2</sub> and IO the DOAS fit included O<sub>4</sub>, H<sub>2</sub>O since they also absorb in this spectral range. References for the used literature cross sections are given in the appendix in Table B.1. The DOAS polynomial was set to second order. The chosen spectral window is narrower compared to the one used for the Open Path CE-DOAS evaluation (421.4 nm to 458 nm). The reason is that the LED showed significant spectral drifts between the measurements of  $I$  and  $I_0$  as shown in Fig. 6.5, which induced spectral structures that could not be compensated by the binomial high pass filter. The spectral drift of the LED was caused by temperature changes in the instrument box with variations by more than 10 °C during a typical day. To compensate for remaining spectral structures from the drifting light source, two low pass filtered versions of the  $I_0$  spectra were included in the DOAS fit. One reference called “ $I_0\_LP\_fix$ ” had the shift fixed to zero to account for the broadband shape of  $I_0$ . The second

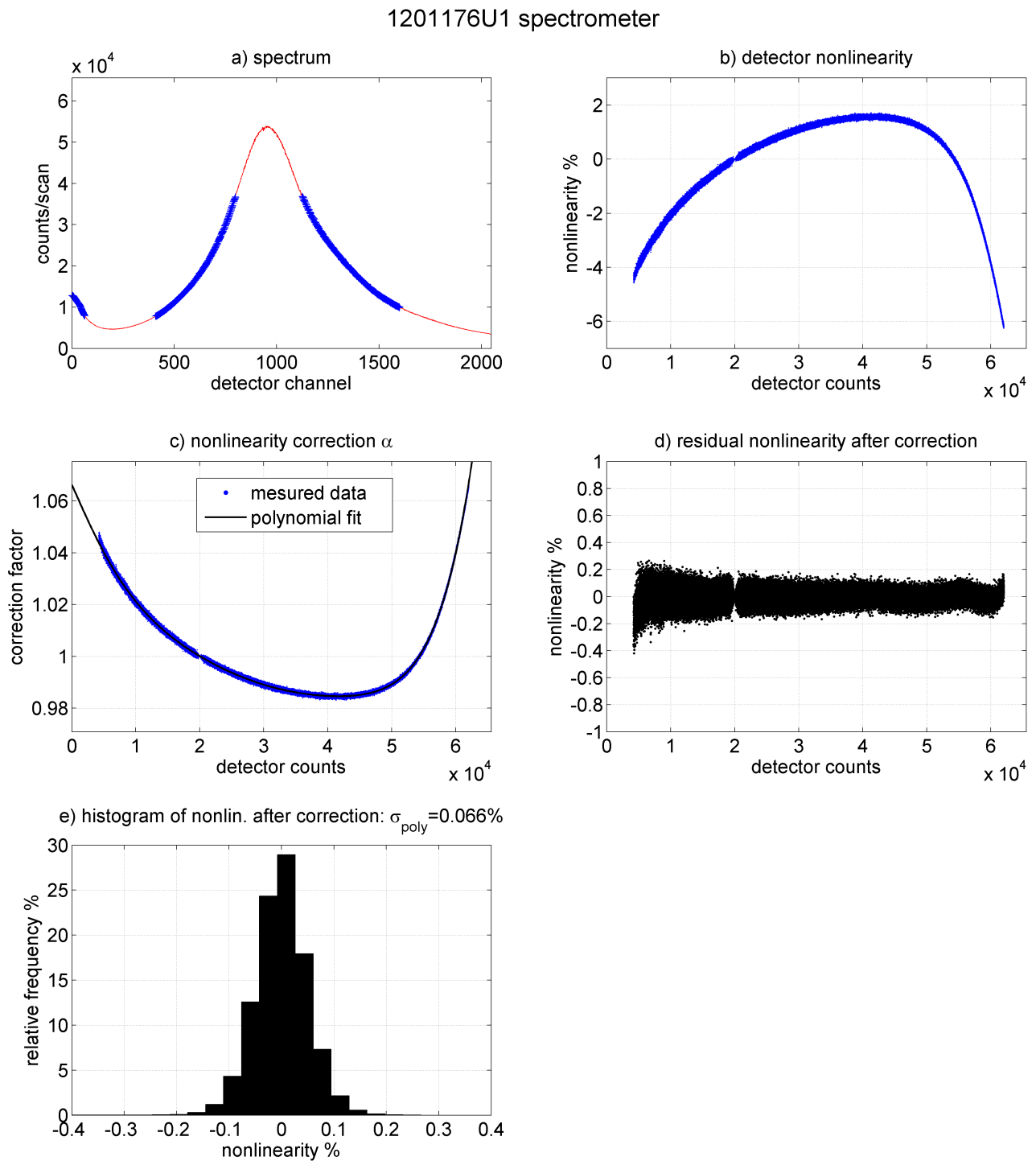


**Figure 6.3. | Characterization of the detector nonlinearity for the spectrograph applied in the CP-CE-DOAS instrument.**

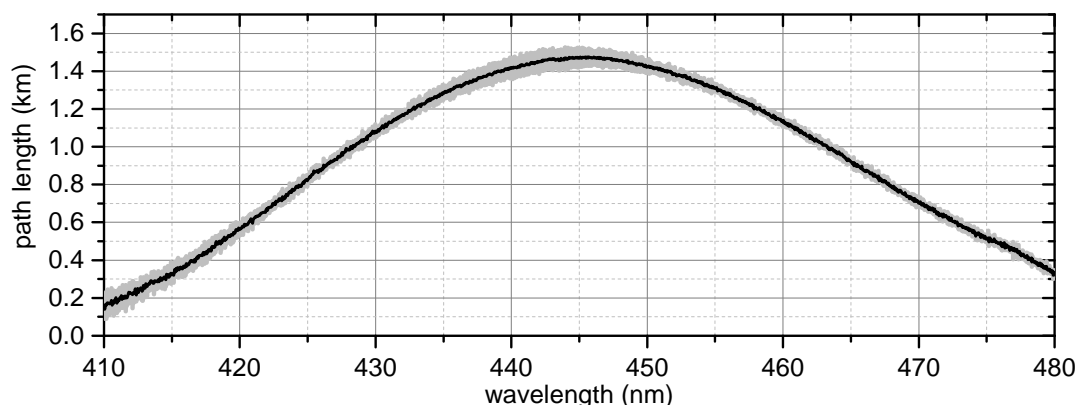


**Figure 6.4.** | Path length curve for the CP-CE-DOAS determined using the Helium/air method. The path length curve has its peak value of  $(1.48 \pm 0.05)$  km at 444.6 nm. The uncertainty of the path length curve, which varies between 20 m and 50 m, was determined from the difference between two consecutive sequences of Helium and air measurements.

one called “ $I_0$ \_LP\_free” was allowed a free shift and squeeze to compensate the shape of  $I$  which may be shifted and squeezed relative to  $I_0$ . The justification for this procedure is that the  $I_0$  signal does not contain any trace gas absorption and therefore allowing a shift and squeeze should help to compensate for the broadband spectrum of  $I$ . An example for the iCE-DOAS analysis is shown in Fig. 6.6 for a measurement with an IO mixing ratio of  $(12 \pm 1)$  ppt and no significant NO<sub>2</sub> above the detection limit of 0.12 ppt.

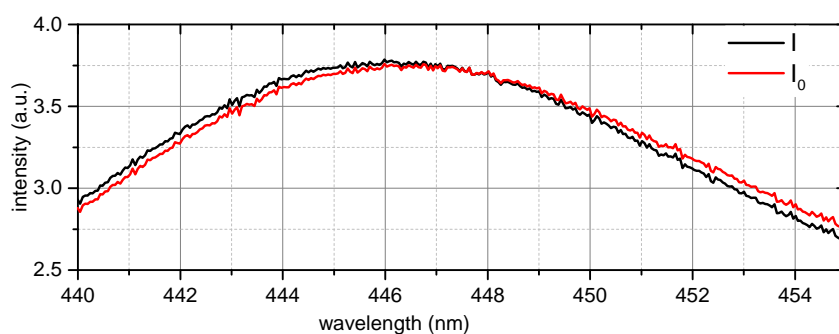


**Figure 6.5.** | Illustration of the spectral drift between a measurement of  $I(\lambda)$  and  $I_0(\lambda)$ .  $I_0(\lambda)$  is shifted by about 0.3 nm to longer wavelength compared to  $I(\lambda)$  but also shows further differences in its spectral shape. The time difference between the two spectra is 17h.

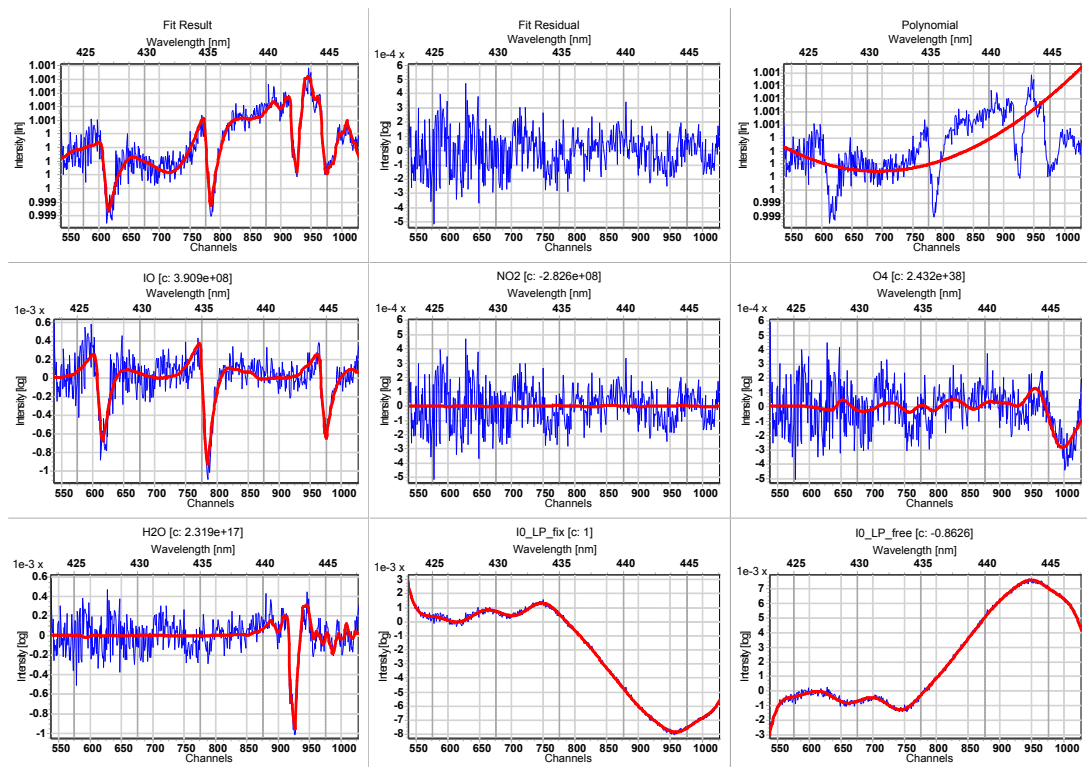


**Figure 6.6.** | Example for the spectral retrieval of IO and NO<sub>2</sub> for a measurement by the closed path CE-DOAS. The spectrum was recorded on August 8th 2012 at 12:49. The red lines shows the fitted references and the blue line the sum of fit result and fit residual, which has a RMS of  $1.4 \cdot 10^{-4}$ . The retrieved mixing ratios are  $(12 \pm 1)$  ppt IO and  $(0.08 \pm 0.06)$  ppb NO<sub>2</sub>.



# 7

## Long Path DOAS Systems

### 7.1. Mace Head LP-DOAS

The LP-DOAS system called Mace Head LP-DOAS in this work has  $f = 60$  cm telescope. It was built by Denis Pöhler and Sebasitan Landwehr in the frame of the ESCAPE campaign [Landwehr, 2010]. Its telescope is motorized allowing for an automatic adjustment of the telescope onto the retro-reflectors. In order to measure both  $I_0$  and  $I_2$ , the setup was extended to use three LED light source as shown in Fig. 7.1. A fiber bundle consisting of 7  $100\mu\text{m}$  fibers is used. The six outer fibers are used to couple light of two blue LEDs (Cree XP-E royal blue,  $\lambda_c = 450$  nm) and one green LED (Cree XP-E,  $\lambda_c = 530$  nm) into the telescope. Light from the LP-DOAS was sent to an array of 27 retro-reflectors with 7 cm diameter placed in a distance of 3.08 km. The central fiber guides the reflected light into an Ocean Optics USB 2000 spectrograph with a  $50\mu\text{m}$  entrance slit which measured the spectrum between 422 nm and 543 nm at a spectral resolution of 0.9 nm. The spectrograph was operated in temperature stabilized box at  $5^\circ\text{C}$ .

#### 7.1.1. Measurement Routine

The instrument repeatedly applied the following measurement loop to acquire spectra. First the shortcut plate is moved in front of the fiber end in the telescope to acquire shortcut spectra of the LEDs at 2000 scans. Then also the shutters at the LEDs are moved in and shortcut background spectra (basically a combination of offset and dark current) with 2000 scans are acquired. After this the shortcut and the shutters move out and the atmospheric measurements starts. First the exposure time is optimized until the CCD detector reaches a saturation of 50 % or the maximum exposure time of 150ms is reached. The number of subsequently co-added scans is adjusted to a total integration time of 15 s, with a maximum of 1000 scans per spectrum. This combination of exposure time and number of scans was used for the acquisition of the next 10 atmospheric spectra. After this the shutters at the LEDs are moved to acquire an atmospheric background spectrum at the same exposure time and number of scans. The atmospheric background spectrum characterizes the amount of scattered sunlight in each atmospheric measurement.

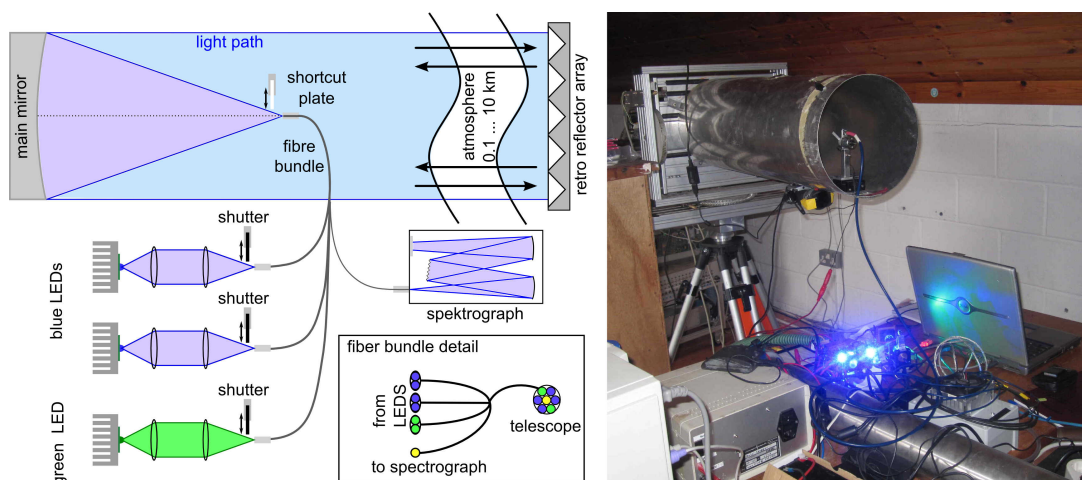


**Figure 7.1.** | **The Mace Head LP-DOAS system** The setup at Mace Head research station in 2012 is shown on the right. On the left a schematic sketch of the instrument is shown (adapted from Denis Pöhler, pers. com.).

Frequent background measurements are important since the amount of scattered sunlight in each spectrum can show strong variations on the time scale of several minutes.

### 7.1.2. Spectral Evaluation

Trace gas mixing ratios were retrieved from the measurements with the software DOASIS using a script based spectral analysis<sup>1</sup>. Optical densities are calculated from the atmospheric spectra ( $I$ ) and the LED shortcut spectra ( $I_0$ ) as described in sec. 4.2.2. In order to correct the offset and dark current the respective background spectra are subtracted. For the atmospheric measurements this also accounts for the additional scattered sunlight in each measurements. However the scattered sunlight can vary significantly on the time scale between the atmospheric measurement and the background measurement. Thus, this basic correction of background signal regularly leads to an over or underestimation of the scattered sunlight signal which would lead to an incorrect determination of the trace gas concentrations, especially IO. In order to compensate for this, the atmospheric background measurement is additionally fitted as a pseudo absorber to improve the correction of scattered sunlight. Also the lamp spectrum as seen in the  $I_0$  shortcut and the atmospheric measurement  $I$  are slightly different since there are slight differences in the optics between the atmospheric and shortcut measurement (mainly the numerical aperture of the light coupled into the spectrometer). To compensate for this difference the log shortcut spectrum  $\ln(I_0)$  is fitted as an additional pseudo absorber.

As usual, wavelength calibration of the measured spectra is done using recorded spectra of low pressure mercury and xenon lamps which have narrow emission lines (few pm) at well known wavelengths. A strong emission line, optimally close to the spectral window of the

<sup>1</sup>The LP-DOAS analysis script was developed by Denis Pöhler, pers. com.

DOAS evaluation, is also used as convolution kernel to adapt the highly resolved literature absorption cross section of the investigated gases to the instrument resolution.

Before the DOAS fit the optical density, the pseudo absorbers and the literature reference spectra are treated with a binomial high pass filter to remove broadband structures. Tab. 7.1 shows a summary of the retrieval settings for the different trace gases and Tab. B.1 gives the literature references for the used absorption cross sections. The applied spectral windows are largely predetermined by the spectra of the applied LEDs.

### 7.1.2.1. IO

The selected wavelength range from 425.4 nm to 447.3 nm includes the three strongest bands in the blue spectral range. Additionally the optical density of a night time measurement with solar zenith angle (SZA)  $> 95^\circ$  was included as a pseudo absorber, which is justified because IO is only present during daytime (see sec. 12.7.1). This is a common method to account for systematic spectral structures from unknown absorbers or differences in the optics between the  $I$  and  $I_0$  measurements. For the Mace Head LP-DOAS potential sources of unknown spectral structures are the window through which the measurements were performed and the poor optics of the Ocean Optics USB 2000, which makes it very sensitive to a slightly different illumination of the entrance slit between the atmospheric measurement and the shortcut measurement. An example for a DOAS fit with an IO mixing ratio of  $(9.30 \pm 0.96)$  ppt is shown in Fig. 7.2. The analyzed spectrum was recorded at Mace Head on August 4 2012 at 12:24 UTC.

### 7.1.2.2. NO<sub>2</sub>

NO<sub>2</sub> was evaluated in the same spectral region as IO but no night time reference can be fitted since NO<sub>2</sub> can be present at all times.

### 7.1.2.3. (CHO)<sub>2</sub>

The analysis of (CHO)<sub>2</sub> was performed between 433.1 nm and 463.6 nm where it shows its strongest differential absorption in the UV/VIS region.

### 7.1.2.4. I<sub>2</sub>

I<sub>2</sub> was evaluated between 513 nm to 533.8 nm where it shows strong almost periodic absorption bands. Care was taken to avoid strong water absorption bands around 505 nm which are known to cause severe interferences. Similar to the IO evaluation an additional daytime measurement with SZA  $< 80^\circ$  was fitted as a pseudo absorber, since I<sub>2</sub> is not present during daytime due to rapid photolysis.

trace gas	spectral window (nm)	DOAS polynomial	high pass iterations	fitted references
IO	425.4 – 447.3	3rd order	4000	IO, NO <sub>2</sub> , H <sub>2</sub> O, night ref.
NO <sub>2</sub>	425.4 – 447.3	3rd order	5000	IO, NO <sub>2</sub> , H <sub>2</sub> O
I <sub>2</sub>	513 – 533.8	3rd order	-	I <sub>2</sub> , OIO, NO <sub>2</sub> , H <sub>2</sub> O, day ref.
(CHO) <sub>2</sub>	433.1 – 463.6	5th order	5000	IO, NO <sub>2</sub> , H <sub>2</sub> O, (CHO) <sub>2</sub>

**Table 7.1.** | Overview of the analysis settings for the Mace Head LP-DOAS. Additionally, all fits include the atmospheric background spectrum and the shortcut spectrum. Literature references for the used cross sections are given in the appendix in Table B.1.

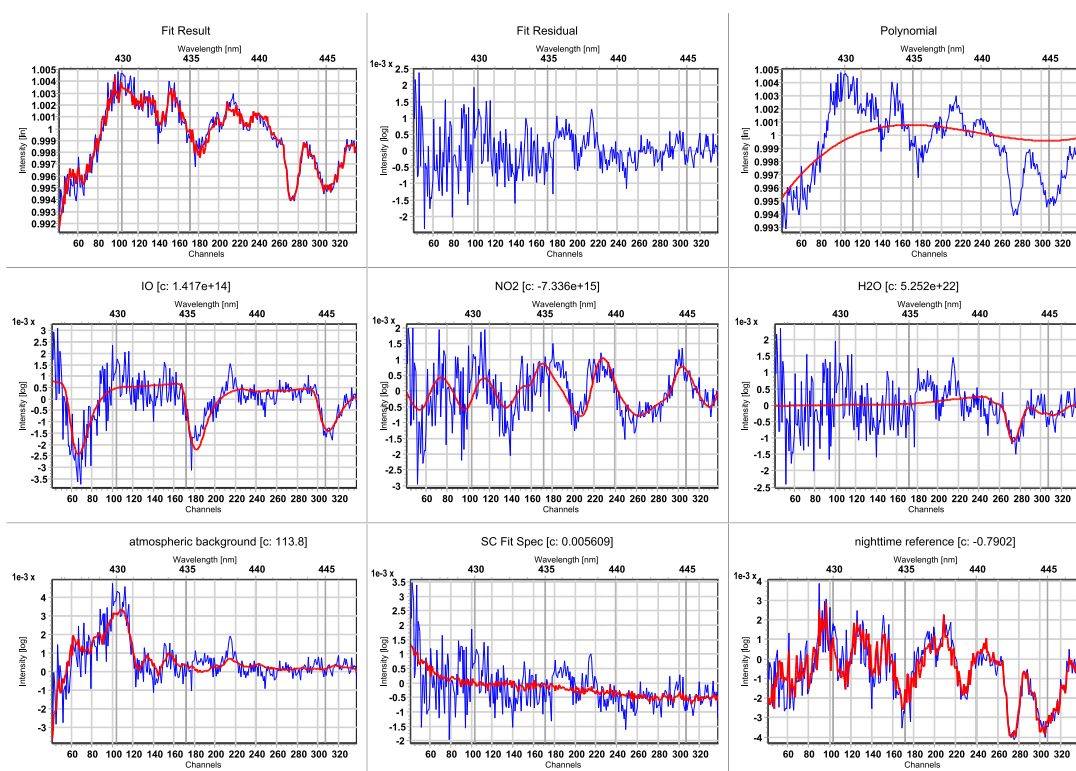


**Figure 7.2.** | Example for the spectral retrieval of IO with the Mace Head LP-DOAS. The spectrum was recorded on August 4 2012 at 12:24 UTC. The red lines shows the fitted references and the blue line the sum of fit result and fit residual. The retrieved IO mixing ratios is  $(9.30 \pm 0.96)$  ppt.

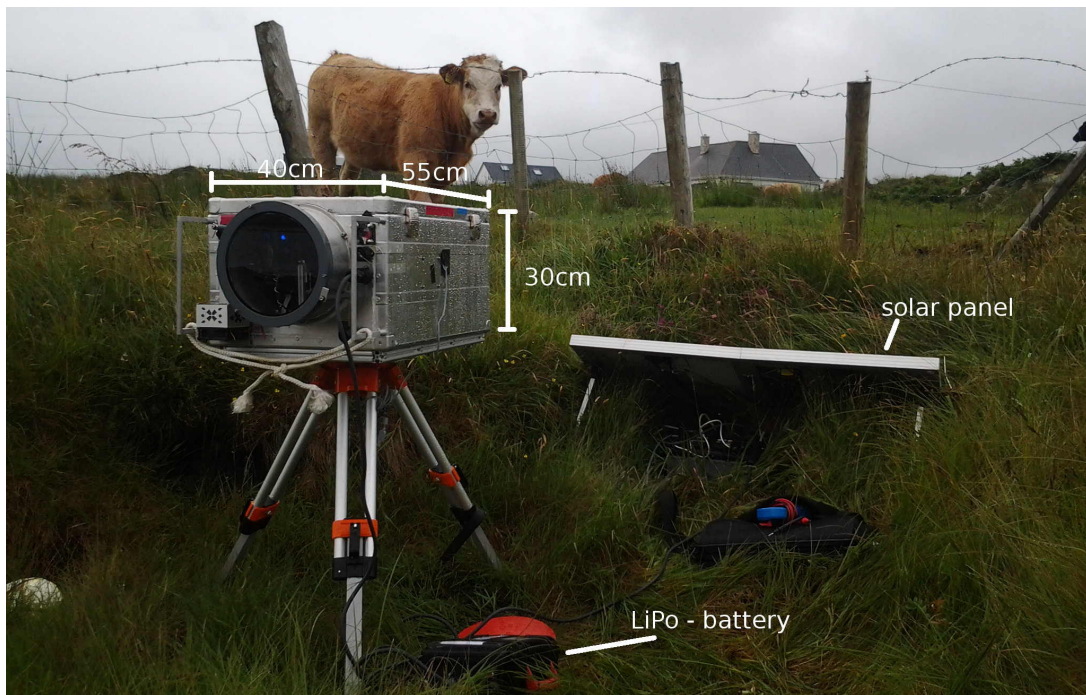


**Figure 7.3.** | The MoLP-DOAS instrument in field operation at Moyrus Bay during the Ireland 2012 campaign.

## 7.2. Mobile LP-DOAS

The Mobile Compact LP-DOAS (MoLP-DOAS) was developed in the diploma thesis of Schmitt [2011]. Compared to classical LP-DOAS instruments it is distinct by its low weight 25 kg, low power consumption of 45 W and 12V operating voltage. Furthermore, all optical and electronic components, including an embedded PC are integrated in a water tight box. Thus, it is optimized for an autonomous battery and solar panel based operation in remote areas, and therefore a key instrument for the measurement campaigns in Ireland in 2011 and 2012. The optical setup is a classical fiber LP-DOAS telescope with an  $f = 50$  cm mirror as shown in Fig. 4.5. The major difference is that the fiber in the telescope is mounted on a motorized yxz stage for an automatic adjustment of the light beam on the retro reflectors. Compared to a motorization of the entire telescope mount, as used in classic LP-DOAS setup, the motorized fiber mount is much lighter and more robust against weather since no mechanical parts are outside of the waterproof box. Furthermore, the MoLP-DOAS has an LED changing wheel which has space for seven LED light sources. Thus, a large spectral range can be covered despite the use of LEDs. However, for the measurements of IO in both Ireland only a blue LED (Cree XP-E royal blue,  $\lambda_c = 450$  nm) was necessary, except for a short period during the measurements at the MRI in 2012 where an additional green LED (Cree XP-E,  $\lambda_c = 530$  nm) was used to measure  $I_2$ . For the spectral analysis an OMT spectrograph is used, covering the spectral region from 290 nm to 440 nm at a spectral resolution of 0.8 nm. The spectrum is

recorded by a UV sensitive CCD with 2048x122 pixels in full vertical binning mode. During the measurements at the MRI, in the frame of the 2012 Ireland campaign the grating position was changed for three days between July 25 and July 27 2012. This was done to cover the spectral window from 410 nm to 551 nm, which was necessary to allow the measurement of  $I_2$ . However, this introduced systematic residual structures in the IO evaluation range, most probably due to stray light, and therefore the spectrograph was turned back for subsequent measurements.

### 7.2.1. Measurement Routine

Analogous to the Mace Head LP-DOAS the Mobile LP-DOAS repeatedly acquired measurement packets containing atmospheric measurements, shortcut spectra of the LEDs and the respective atmospheric background and shortcut background spectra. Details on the measurement routine are given in Schmitt [2011].

### 7.2.2. Spectral Evaluation

The spectral evaluation followed the standard LP-DOAS scheme described in sec. 7.1.2. Tab. 7.2 shows a summary of the retrieval settings for the different trace gases and Tab. B.1 gives the references for the used literature cross sections. Major differences to the Mace Head LP-DOAS are:

- No night reference spectrum is fitted in the IO retrieval since for most mobile measurement locations no nighttime measurements are available. Also for the longer time series at MRI there are no stable systematic residual structures that would justify this measure. For the same reason also no day reference spectrum is fitted in the  $I_2$  retrieval.
- For the normal grating position the spectral window of the IO retrieval is shifted about 0.6 nm towards longer wavelengths to avoid a systematic residual structure occurring between 425 nm to 426 nm.
- Different fitting windows were used for the IO retrieval for the period between July 25 and July 27 2012 where the grating was turned to include the  $I_2$  absorption. There reason are once again systematic residual structures occurring below 433 nm for this grating position.
- For the same reason also the  $I_2$  spectral fitting window had to be move about 10 nm towards longer wavelengths compared to the analysis settings used for the Mace Head LP-DOAS.

An example for a DOAS fit with an IO mixing ratio of  $(34.6 \pm 2.0)$  ppt is shown in Fig. 7.4. The analyzed spectrum was recorded at MRI on August 25 2012 at 15:48 UTC.

trace gas	spectral window (nm)	DOAS polynomial	high pass iterations	fitted references
IO, NO <sub>2</sub>	426 – 448	3rd order	2000	IO, NO <sub>2</sub> , H <sub>2</sub> O

**I<sub>2</sub> measurements between July 25 and July 27 2012:**

IO, NO <sub>2</sub>	433 – 448	3rd order	2000	IO, NO <sub>2</sub> , H <sub>2</sub> O
I <sub>2</sub>	524 – 543	3rd order	-	I <sub>2</sub> , OIO, NO <sub>2</sub> , H <sub>2</sub> O, O <sub>4</sub>

**Table 7.2.** | Overview of the analysis settings for the MoLP-DOAS. Additionally, all fits include the atmospheric background spectrum and the shortcut spectrum. References for the used literature cross sections are given in the appendix in Tab. B.1.

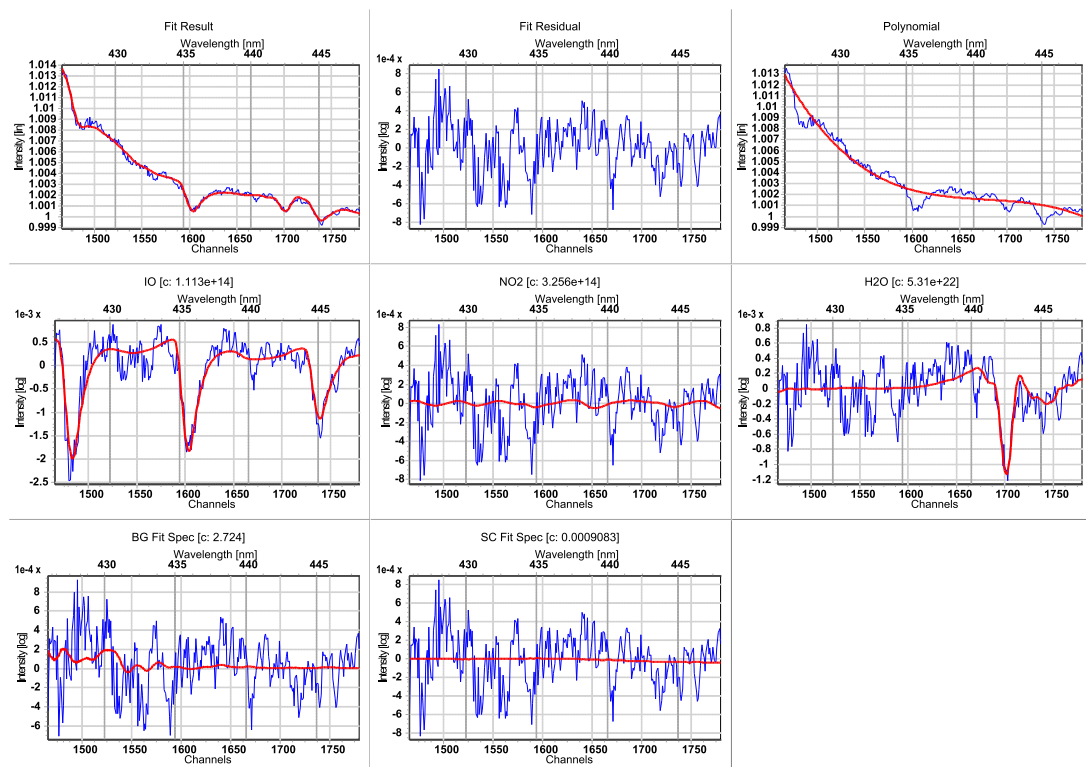


**Figure 7.4.** | Example for the spectral retrieval of IO with the MoLP-DOAS. The spectrum was recorded at the MRI on August 25 2012 at 12:24 UTC. The red lines shows the fitted references and the blue line the sum of fit result and fit residual. The retrieved IO mixing ratios is  $(34.6 \pm 2.0)$  ppt.

### 7.3. Amundsen LP-DOAS

The Amundsen LP-DOAS, shown in Fig. 7.5, is a fully atomized high precision LP-DOAS system. It was already applied successfully in numerous field campaigns and a detailed description of the instrument can be found in [Pöhler et al., 2010]. Therefore only a brief description of the instrument will be given here. The Amundsen LP-DOAS follows the principle mono-static fiber based LP-DOAS design introduced in sec. 4.3.2. As light source a 75W xenon arc lamp (Osram XBO, not ozone-free) was used, which covers a broad spectral range in the UV-VIS region. Spectral analysis was performed with a Acton 300i spectrometer with a spectral resolution of 0.5 nm . The spectra were recorded with a 2048 × 512 pixel back tinned CCD camera from Roper Scientific (Spec-10:2KBUV) in full vertical binning mode. A spectrum covered a spectral range of about 80 nm and the center wavelength could be adjusted by turning the motorized grating of the Acton 300i spectrometer.

#### 7.3.1. Measurement Sequence

Measurements were performed in four spectral ranges specified in Tab. 7.3 with center wavelengths 330 nm, 400 nm, 560 nm, 640 nm. The measurement sequence applied during the New Zealand Campaign was similar to the other LP-DOAS instruments described above. First a set of eight atmospheric spectra and nine Lamp reference spectra (shortcut) was recorded, with each atmospheric spectrum being nested between two shortcuts. The atmospheric measurement



**Figure 7.5.** | Telescope of the Amundsen LP-DOAS setup at Shag Point New Zealand.

name	spectral window	comment
330 nm	291 nm to 375 nm	measured all day and night
400 nm	362 nm to 445 nm	measured all day and night
560 nm	524 nm to 602 nm	measured all day and night
640 nm	604 nm to 681 nm	nighttime measurement from 19h to 6h NZST

**Table 7.3.** | Overview of the spectral windows measured by the Amundsen LP-DOAS

sequence was followed by the a measurement sequence with blocked light source to acquire an atmospheric background spectrum and the corresponding background shortcut (a dark spectrum).

### 7.3.2. Data Analysis

The analysis of the measured spectra is very similar to the procedure previously described in sec. 7.1.2. In the following the DOAS retrieval settings for the evaluation of the measurements of the New Zealand campaign 2013 and deviations form the standard evaluation procedure are given for the different trace gases. Literature literature references to the used absorption cross sections are given in the appendix in Tab. B.1.

**IO** was evaluated in the split spectral range from 416.2 nm to 429.1 nm and from 434.1 nm to 441.3 nm which includes the three strongest and most characteristic IO absorption bands at 420 nm, 427 nm and 436 nm, found in the measured spectral range. The gap in the spectral window was chosen to avoid an unknown systematic spectral structure at 431 nm. Additionally to IO also literature spectra of  $\text{NO}_2$  and  $\text{H}_2\text{O}$  were included in the fit. As for the IO evolution of the Mace Head LP-DOAS an atmospheric nighttime measurement recorded at an SZA between  $110^\circ$  and  $180^\circ$  was included to account for systematic instrumental effects and unknown absorbers. Using a nighttime reference spectrum is justified since  $\text{I}_2$  photolysis is required for the formation of IO. Even though including an atmospheric nighttime measurement didn't change the retried IO values significantly it helped to reduce the detection limit. An additional deviation to the normal retrieval procedure was to include the inverse shortcut spectrum  $1/I_0$  to account for stray light (see sec. 4.2.2.1) which turned out to be a problem for the used Acton spectrometer in this spectral range. For removal of spectrally broad structures a binomial high pass filter with 2000 iterations was applied and a 4th order polynomial was included in the DOAS fit. For the evaluation blocks of 32 spectra were added to reduce the photonic noise yielding an average RMS of  $1.2 \cdot 10^{-4}$  in the residual spectrum and gave a time resolution of about 45 min (depending on the visibility). Figure 7.6 shows example DOAS fit with an IO mixing ratios of  $(0.9 \pm 0.2)$  ppt. This was one of the strongest IO signals measured during the New Zealand 2013 campaign. However, the significance of the fit is debatable since there are still systematic residual structures at the strongest absorption lines of IO (427 nm and 436 nm) this is further discussed in sec. 13.3 for the results of the New Zealand campaign.

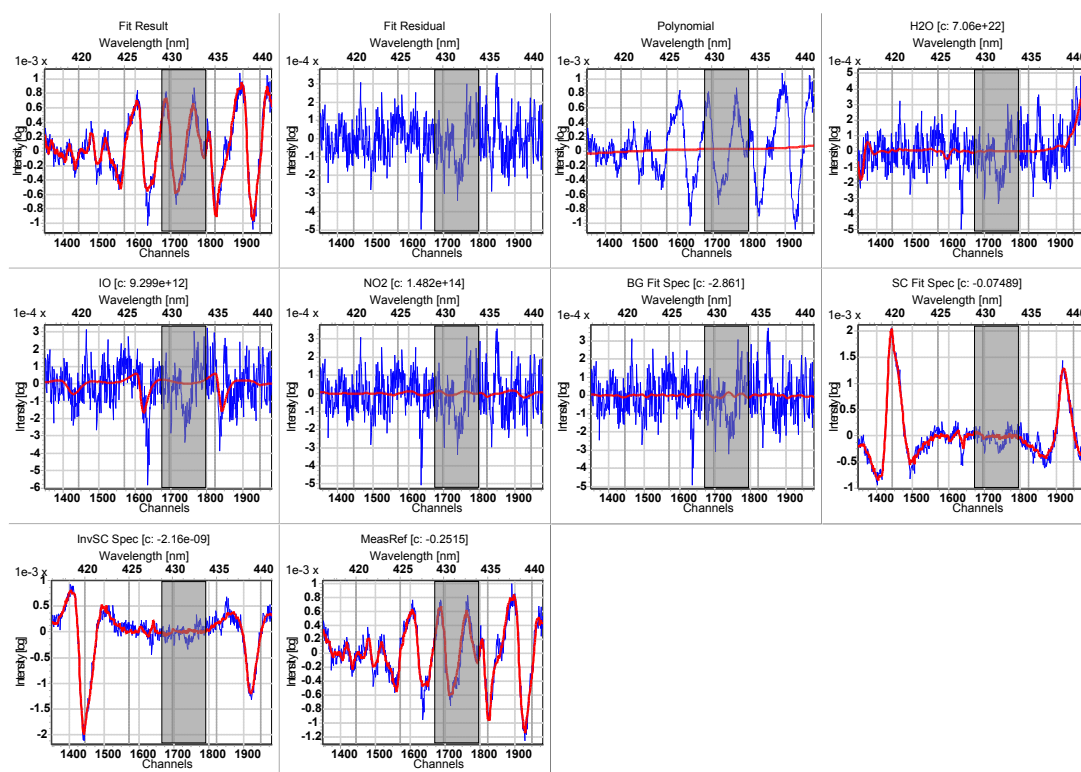


**Figure 7.6.** | Example for the spectral retrieval of IO with the Amundsen LP-DOAS.

The spectrum was recorded on March 27th 2013 at 10:06 NZST. The gray area marks the gap in the split fit range, red lines shows the fitted references and the blue line the sum of fit result and fit residual. The retrieved IO mixing ratios is  $(0.9 \pm 0.2)$  ppt.

**NO<sub>2</sub>** was evaluated with the same retrieval setting as IO with the exception that no nighttime reference could be used since NO<sub>2</sub> is expected to be present day and night. Also due to the strong NO<sub>2</sub> signal the number of added spectra was reduced to 8 for an increased the time resolution of about 10 min.

**I<sub>2</sub> and OIO** were evaluated in the spectral range from 530.5 nm to 565.3 nm where they both have their strongest differential absorption. Additionally the fit contained the reference spectra of NO<sub>2</sub> and H<sub>2</sub>O which also absorb in this spectral region and the optical density of an atmospheric daytime reference. The daytime reference is an atmospheric measurement recorded during the last or next day at an SZA between 75° and 85°. Additionally to the reduction of systematic instrumental effects the main purpose of the daytime reference was to account for strong H<sub>2</sub>O absorption between 540 nm to 548 nm (OD ~ 10<sup>-2</sup> peak to peak), which is relatively constant between day and night. The reason for this is that the H<sub>2</sub>O literature cross section are not accurate enough leaving residual structures in the order of up to 10<sup>-3</sup> that would interfere with the DOAS analysis of I<sub>2</sub> and OIO. However, the H<sub>2</sub>O absorption spectrum

is still included in the fit to account for the small difference in H<sub>2</sub>O absorption between the atmospheric measurement and the daytime reference. For I<sub>2</sub> and OIO a daytime reference is justified since they are both not abundant at detectable mixing ratios in the presence of daylight due to rapid photolysis. For removal of spectrally broad structures a binomial high pass filter with 3000 iterations was applied and a 3rd order polynomial was included in the DOAS fit. For the evaluation blocks of 8 spectra were added yielding an average RMS of  $2.2 \cdot 10^{-4}$  in the residual spectrum and a time resolution of about 10 min. Adding blocks of up to 32 spectra was tried but did not significantly improve the analysis in this spectral range.

**NO<sub>3</sub>** was evaluated in the split spectral range from 614.4 nm to 644.8 nm and from 658.3 nm to 673.8 nm. Each spectral window contains one of the two strong NO<sub>3</sub> absorption bands. The spectral gap was necessary since it contains an extremely strong set of absorption bands (OD  $\sim 10^{-1}$ ) which would interfere with the retrieval NO<sub>3</sub> with a typically two orders of magnitude weaker absorption. Additionally the fit contained the reference spectra of NO<sub>2</sub>, H<sub>2</sub>O and O<sub>4</sub> and O<sub>2</sub> which also absorb in this spectral region and the optical density of an atmospheric reference recorded during twilight. Fitting the very strong O<sub>2</sub> absorption (OD  $\sim 5 \cdot 10^{-2}$ ) only by the literature cross section from HITRAN 2012 [Rothman et al., 2013] is known to be insufficiently accurate, leaving residual structures which are known to cause significant interferences with the NO<sub>3</sub> retrieval (Denis Pöhler 2015, pers. comm.). Therefore a twilight reference, an atmospheric measurement recorded at an SZA  $> 90^\circ$ , is fitted which removes most of the very strong oxygen absorption band (OD  $\sim 5 \cdot 10^{-2}$ ) which is constant over the course of a day. For NO<sub>3</sub> a twilight reference is justified since it is not abundant at detectable mixing ratios in the presence of (dim) daylight due to rapid photolysis (see sec. 2.2.3). For the measurements in New Zealand, unfortunately the time difference between the twilight reference and the evaluated nighttime measurements is several days to weeks for most spectra, since measurements with an SZA  $> 90^\circ$  are only available during the first few days of the campaign due to an error in the set time window for the measurements in the 640 nm grating position. This large time difference between two spectra unfortunately introduced some additional systematic residual structures which are accounted for by conservatively scaling the usual measurement error (fit error  $\times 2$ ) by a factor of 1.5. Only 5th order polynomial was used to remove spectrally broad structures, since the application of a binomial high pass filter did not make sense due to the relatively broad absorption peaks of the NO<sub>3</sub>. For the evaluation blocks of 8 spectra were added yielding an average RMS of  $4.5 \cdot 10^{-4}$  in the residual spectrum. This could not be reduced by adding more spectra since the remaining structures at the  $4 \cdot 10^{-4}$  noise level are of systematic, instrumental nature in this spectral range.

**SO<sub>2</sub> and HCHO** were evaluated in the split spectral range from 297.8 nm to 307.4 nm and from 311.6 nm to 324.3 nm where both gases show strong characteristic absorption. The gap in the spectral window was chosen to avoid systematic spectral structures which appear in this region. Additionally the fit contained the reference spectra of O<sub>3</sub> and NO<sub>2</sub> which also absorb in this spectral region. Like for the IO evaluation the inverse shortcut spectrum  $1/I_0$  was fitted to account for stray light. For removal of spectrally broad structures a binomial high pass filter with 2000 iterations was applied and a 4th order polynomial was included in the DOAS fit.

For the evaluation blocks of 16 spectra were added to reduce the photonic noise yielding an average RMS of  $2.7 \cdot 10^{-4}$  in the residual spectrum and gave a time resolution of about 23 min (depending on the visibility).

**BrO and O<sub>3</sub>** were evaluated in the spectral range from 316.6 nm to 345.8 nm which contains strong absorption bands for both gases. Additionally the fit contained the reference spectra of NO<sub>2</sub> and O<sub>4</sub> which also absorb in this spectral region. To avoid known interferences with BrO (Denis Pöhler 2015 per. com.) HCHO was not included in the fit since it was not found in the the SO<sub>2</sub> evaluation range. Also HONO was removed from the fit since a trial run also did not show any significant absorption. Like for the IO evaluation the inverse shortcut spectrum  $1/I_0$  was fitted to account for stray light. For removal of spectrally broad structures a binomial high pass filter with 2000 iterations was applied and a 4th order polynomial was included in the DOAS fit. For the evaluation blocks of 16 spectra were added to reduce the photonic noise yielding an average RMS of  $2.1 \cdot 10^{-4}$  in the residual spectrum and gave a time resolution of about 23 min (depending on the visibility).

# 8

## Other Instrumentation

### 8.1. Ireland Campaigns 2011/12

#### 8.1.1. Meteorological Data

The Mace Head Research Station operated by the National University of Ireland Galway records a full set of meteorological parameters according to the standards set by the World Meteorological Organisation [WMO, 2010]. Data of wind speed, wind direction, surface temperature, relative humidity and atmospheric pressure and solar irradiance were provided by the National University of Ireland Galway (Darius Ceburnis NUIG, pers. com. 2011/12) and the precipitation data was accessed from reliable prognosis ([http://rp5.md/archive.php?wmo\\_id=3963&lang=en](http://rp5.md/archive.php?wmo_id=3963&lang=en) accessed 1/10/2015). Additionally for basic measurements measurements of the local meteorology a mobile Oregon Scientific WMR200 weather station was used. The set of measured parameters and their accuracies are summarized in Tab. 8.1.

parameter	unit	accuracy
wind speed	$\text{m s}^{-1}$	$\pm 3 \text{ m s}^{-1}$ below $10 \text{ m s}^{-1}$ and $\pm 10 \%$ for higher wind speeds
wind direction	$^{\circ}$	$\pm 23^{\circ}$
air temperature	$^{\circ}\text{C}$	$\pm 1^{\circ}\text{C}$ for $T = 0 - 20^{\circ}\text{C}$
relative humidity	$\%$	$\pm 7 \%$
UV-index	a.u. 0 low, 11 extremely high	N.A.

**Table 8.1.** | Summary of meteorological parameters measured Oregon Scientific WMR200 weather station during the Ireland 2011/12 campaign. Specified accuracies were taken from the user manual.

### 8.1.2. Measurements of Tidal Height in Ireland

Data of tidal height, used for the Irish West coast, were measured at Galway Port by the Marine Institute within the frame of the Irish National Tide Gauge Network (<http://www.marine.ie/Home/site-area/data-services/real-time-observations/tidal-observations-imos>) and were accessed over their official data archive <http://data.marine.ie/Dataset/Details/20932>. The tidal height is given in meters relative to the Malin Head Ordnance Datum, which is the official vertical datum of the Irish Grid Reference System. The tidal height measurements have an accuracy better than 1 cm over the entire tidal range, in accordance with the international GLOSS<sup>1</sup> standard.

### 8.1.3. In-situ Particle Measurements

During the campaign of 2012, measurements of the aerosol particle size distribution at the Mace Head Research station were performed by the National University of Ireland Galway. Particle size distributions were sampled using TSI a nano-Scanning Mobility Particle Sizer (SMPS) between 3 and 20 nm and a SMPS between 20 and 500 nm [Wang and Flagan, 1990]. Additionally measurements of both instruments were combined to calculate the total particle concentration between 3 and 500 nm. Both instruments sampled from a 10 m height at a distance of 10 m to 100 m from the intertidal zone [Flanagan et al., 2005].

---

<sup>1</sup>Global Sea Level Observing System <http://www.gloss-sealevel.org/>

## 8.2. New Zealand Campaign 2013

A Vaisala Weather Transmitter WXT520 and a pyranometer (Kipp&Zonen CM11) were applied for continuous measurements of meteorological parameters summarized in Tab. 8.2. Both Instruments were setup 1.5 m above the roof of the Shag Point Cottage as shown in Fig. 13.2. Additionally for measurements of the local wind speed and direction at the CE-DOAS instrument a Metec USA1 sonic anemometer was used.

For in-situ O<sub>3</sub> measurements NIWA applied a Thermo Environmental Instruments Inc. (TEI) Model 49, time-shared dual UV photometric ambient ozone analyzer. However, these measurements only give very rough Ozone values within a factor 1.5-2 due to problems with the instruments calibration and no recalibration was possible at NIWA (Alan Thomas 2013, pers. com.).

### 8.2.1. Measurements of Tidal Height

Data of tidal height were measured at Port Chalmers (station name OTAT, Lat:  $-45.8143^\circ$ , Lon:  $170.6294^\circ$ ) by Land Information New Zealand (<http://www.linz.govt.nz/sea/tides>) and were accessed over their official data archive [http://apps.linz.govt.nz/ftp/sea\\_level\\_data/OTAT/](http://apps.linz.govt.nz/ftp/sea_level_data/OTAT/). The tidal heights have an accuracy better than 1 cm over the entire tidal range, in accordance with the international GLOSS standard. Tidal heights are given as meters above an arbitrary sensor zero which is unfortunately not specified relative to a vertical standard datum but on the other hand no problem for this work since only relative changes are of interest.

### 8.2.2. $\mu$ Dirac Gas Chromatograph (GC)

The  $\mu$ -Dirac instrument is a GC with electron capture detector (GC-ECD) developed by Gostlow et al. [2010] for autonomous measurements of halo carbon species. During the New Zealand 2013 campaign it was applied by NIWA in cooperation with University of Cambridge for the

parameter	unit	accuracy
wind speed	$\text{m s}^{-1}$	$\pm 3\%$ at $10 \text{ m s}^{-1}$
wind direction	$^\circ$	$\pm 3^\circ$
air temperature	$^\circ\text{C}$	$\pm 0.3\text{ }^\circ\text{C}$ at $20\text{ }^\circ\text{C}$
barometric pressure	mbar	$\pm 0.5$ mbar at $T=0\dots 30\text{ }^\circ\text{C}$
relative humidity	%	$\pm 3\%$ within $0\dots 90\%$
solar irradiance	$\text{W m}^{-2}$	N.A.

**Table 8.2.** | Summary of meteorological parameters measured at the Shag Pont Cottage during the New Zealand 2013 campaign. All parameters were measured by a Vaisala Weather Transmitter WXT520 except for solar irradiance measured by a Kipp&Zonen CM11 pyranometer.

species	detection limit (ppt)
CH <sub>2</sub> BrI	0.23
CH <sub>2</sub> ClI	0.22
CH <sub>3</sub> I	0.47
CH <sub>2</sub> Br <sub>2</sub>	0.18
CHBr <sub>3</sub>	0.22
CH <sub>2</sub> BrCl	0.23
CHBr <sub>2</sub> Cl	0.27

**Table 8.3.** | Detection limits of halocarbons measured by the  $\mu$ Direc GC. Data provided by Andrew David Robinson (pers. com. 2013)

measurement of the halogen species CH<sub>2</sub>BrI, CH<sub>2</sub>ClI, CH<sub>3</sub>I, CH<sub>2</sub>Br<sub>2</sub>, CHBr<sub>3</sub>, CH<sub>2</sub>BrCl and CHBr<sub>2</sub>Cl. The instruments detection limits for the different species are summarized in Tab. 8.3.

**Part III.**

**Improvement of DOAS Data  
Analysis**



# 9

## The iterative CE-DOAS (iCE-DOAS) Algorithm

This section introduces the iterative CE-DOAS (iCE-DOAS) algorithm which makes the CE-DOAS evaluation robust against broadband fluctuations of the measured light intensities. Thus, iCE-DOAS overcomes the limitation of the classical approach described in sec. 4.3.3 which requires an absolute stability of the light source intensity and the optical setup between the measurement of  $I_0$  and  $I$ . Instruments applying iCE-DOAS can therefore use a simplified setup to develop compact and lightweight CE-DOAS instruments with high measurement accuracy. A first approach to iCE-DOAS was made in Horbanski [2010], which has been further developed in the frame of this thesis.

Assuming that we know the number densities  $\bar{\rho}_i$  and the total cross sections  $\sigma_i(\lambda)$  of all trace gases with differential absorption, the extinction  $\Delta\epsilon_{\text{Rayleigh}}(\lambda)$  due to differences in Rayleigh scattering between the absorber filled resonator and the “empty resonator” and additional broadband extinction due to scattering and turbulence, we can calculate the true cavity enhanced optical density after eq. (4.34) as

$$D_{\text{CE}}(\lambda) = \ln \left[ 1 + \bar{L}_0(\lambda) \sum_i \sigma_i(\lambda) \bar{\rho}_i + \Delta\epsilon_{\text{Rayleigh}}(\lambda) + \epsilon_{\text{broadband}}(\lambda) \right] \quad (9.1)$$

and thus compute  $K(\lambda)$  and  $\bar{L}_{\text{eff}}(\lambda)$  according to eq. (4.32). While  $\Delta\epsilon_{\text{Rayleigh}}(\lambda)$  is easily calculated from measured pressure and temperature, the number densities  $\bar{\rho}_i$  are generally a priori not known, as well as the broadband extinction  $\epsilon_{\text{broadband}}(\lambda)$ .

The basic idea of iCE-DOAS is to get a first approximation for the number densities of trace gases with differential absorption from a DOAS fit using the path length of the “empty resonator”  $\bar{L}_0(\lambda)$ . Which can then be used to calculate a first approximation of  $\bar{L}_{\text{eff}}(\lambda)$  and subsequently apply DOAS fitting to get better approximations of the trace gas number densities. However, this still leaves the problem of unknown broadband extinction  $\epsilon_{\text{broadband}}(\lambda)$ . For closed path CE-DOAS instruments this is usually no problem since they remove broadband extinction using a fine pored aerosol filter and turbulence can usually be neglected at typical purge rates of few liters per minute. It should also be noted that the broadband extinction could be treated like

a differential absorber if the wavelength dependency imprinted by the wavelength depended path length is sufficiently strong. For the sake of simplicity in the following the broadband extinction  $\epsilon_{\text{broadband}}(\lambda)$  is assumed to be zero.

The iterative evaluation scheme, shown in fig. 9.1, starts by initializing the trace gas number densities to  $\bar{\rho}_i^{(0)}$ . In the simplest case the initial values are zero. Better initial values, e.g. retrieved values from the previous measurement in a time series, can significantly improve the convergence speed. Furthermore, in this step  $\Delta\epsilon_{\text{Rayleigh}}(\lambda)$  is calculated <sup>1</sup>. With these parameters and the previously measured  $\bar{L}_0(\lambda)$  an initial approximation of the true cavity enhanced optical density is calculated according to eq. (9.1), which is then used to calculate an approximation  $\bar{L}_{\text{eff}}^{(1)}(\lambda)$  of the effective path length according to eq. (4.32). Subsequently, in order to account for the wavelength dependency of  $L_{\text{eff}}^{(1)}(\lambda)$ , effective fit references are computed for each trace gas:

$$\vartheta_i^{(1)}(\lambda) = \left( \bar{L}_{\text{eff}}^{(1)}(\lambda) \cdot \sigma_i(\lambda) \right) \quad (9.2)$$

The highly resolved effective fit references are then adapted to the lower spectral resolution of the measurement by convolution with the instrument function  $H(\lambda)$  of the spectrograph:

$$\Theta_i(\lambda) = H(\lambda) \otimes \vartheta_i(\lambda) := \int_0^\infty H(\lambda') \cdot \vartheta_i(\lambda - \lambda') d\lambda' \quad (9.3)$$

The last step of the (first) iteration is a DOAS fit to the measured optical density which uses the effective fit references  $\Theta_i^{(1)}(\lambda)$  to get first estimates for the trace gas number densities  $\bar{\rho}_i^{(1)}$ . In the subsequent iteration these concentrations are used together with the Rayleigh extinction to compute an improved correction factor  $K^{(n+1)}(\lambda)$  and thus better fit references  $\Theta_i^{(1)}(\lambda)$  which are used in a DOAS fit to get a more accurate set of trace gas concentrations  $\bar{\rho}_i^{(n+1)}$ . This scheme is repeated until the approximated  $\bar{\rho}_i$  converge to their true value. Several termination conditions are possible:

- a predefined number of iterations can be given
- a threshold for the RMS or peak to peak value of the fit residual
- a threshold defined by the change of the retrieved densities between the current and the last iteration

The last criterion has proven to be very robust. Thus, the iterative procedure terminated if for all species the change in the number density between the last two iterations is smaller than their DOAS fit errors.

**Strong absorbers:** For strong absorbers with absorption structures much narrower than the spectral resolution of the measurement there is in general no linear relationship between the measured optical density and the trace gas concentrations. As discussed in sec. 4.3.3.1 for CE-DOAS this effect commonly known as saturation effect, is even stronger since the effective path length is also influenced by the optical density. Starting from the second iteration we

---

<sup>1</sup> $\Delta\epsilon_{\text{Rayleigh}}(\lambda)$  is zero if  $I_0$  was measured in air at the same pressure and temperature as  $I$

can easily correct for this effect since we have estimates for the fitted trace gas densities. The saturation corrected fit references are calculated as

$$\Theta_{i,\text{sat.}}^{(n)}(\lambda) = \frac{-1}{\bar{\rho}_i^{(n-1)}} \ln \left[ H(\lambda) \otimes e^{-L_{\text{eff}}^{(n)} \cdot \sigma_i(\lambda) \cdot \bar{\rho}_i^{(n-1)}} \right] \quad (9.4)$$

where  $\bar{\rho}_i^{(n-1)}$  is the trace gas number density retrieved in the last iteration.

## 9.1. Simulations using the iCE-DOAS Algorithm

In order to test the iCE-DOAS algorithm we evaluated modelled measurements (without noise) with different NO<sub>2</sub> concentrations (1 ppbv, 10 ppbv, 100 ppbv, 1000 ppbv, 3000 ppbv). Furthermore, we compared the iCE-DOAS evaluation to evaluations using the classical equation (eq. (4.33)) and investigated their respective sensitivities to broadband fluctuations in the light intensity.

The instrumental parameters for the simulations were similar to the compact closed path CE-DOAS described in 6 with mirror reflectivity  $R(\lambda) = 99.97\%$ , cavity length  $d = 50$  cm and the spectrograph instrument function  $H(\lambda)$  with a FWHM of 0.5 nm. The spectral range of the simulated data evaluation between 458 nm and 480 nm was also matched to this instrument. The intensity  $I_0(\lambda)$  transmitted by the empty cavity was chosen to be unity over the entire spectral range. The intensity transmitted by the absorber filled cavity was then calculated according to Fiedler [2005] as

$$I(\lambda) = I_0(\lambda) \cdot \frac{T(\lambda)(1 - T_0(\lambda)^2 \cdot R(\lambda)^2)}{T_0(\lambda)(1 - T(\lambda)^2 \cdot R(\lambda)^2)} \quad (9.5)$$

with the the single pass transmittance of zero air

$$T_0(\lambda) = \exp(-d \epsilon_{\text{Rayleigh}})$$

and the single pass transmittance for sample air

$$T(\lambda) = \exp(-d (\sigma_{\text{NO}_2} \bar{\rho}_{\text{NO}_2} + \epsilon_{\text{Rayleigh}}))$$

with a NO<sub>2</sub> number density  $\bar{\rho}_{\text{NO}_2}$ . The NO<sub>2</sub> absorption was calculated using the laboratory cross section  $\sigma_{\text{NO}_2}$  of A. C. Vandaele et al. [2002] and for Rayleigh scattering the cross section  $\sigma_{\text{ray}}(\lambda)$  from Bodhaine et al. [1999] was used. In order to capture high resolution features of the NO<sub>2</sub> spectrum the intensity  $I$  was calculated at a spectral resolution of 0.001 nm. In a final step the the measured intensity  $I_{\text{meas}}(\lambda)$  was obtained from the high resolution spectrum  $I(\lambda)$  by convolution with the with the instrument function  $H(\lambda)$ . The modeled measurements are shown in fig. 9.2a).

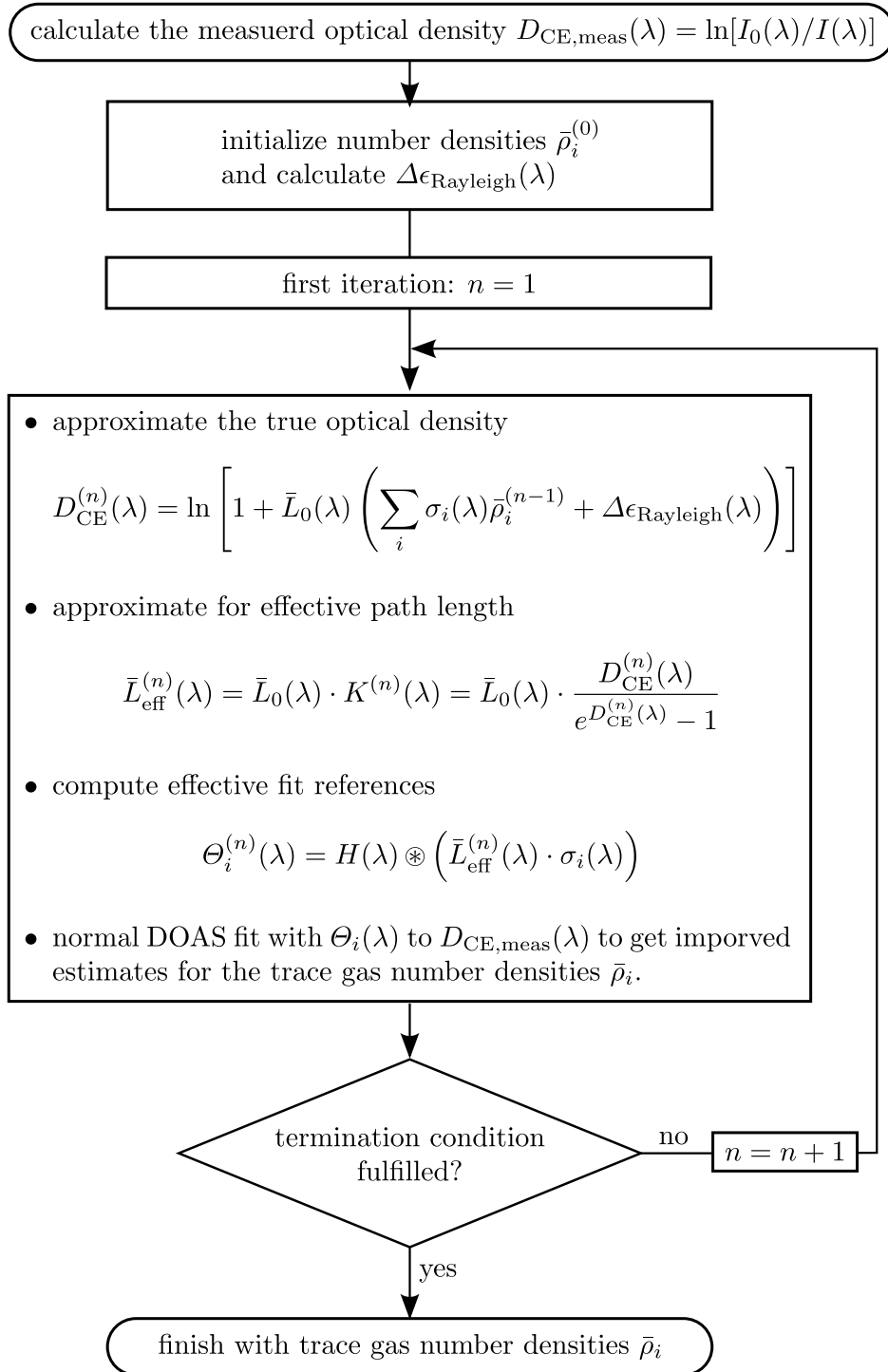


**Figure 9.1.** | Scheme of the iCE-DOAS evaluation

### 9.1.1. Evaluation with the iCE-DOAS Algorithm

The iCE-DOAS algorithm was applied to the spectra modeled in the last section. The performance of the iterative algorithm is illustrated in fig. 9.2. It converges for all tested mixing ratios. Even for a mixing ratio as high as 3000 ppbv the accuracy is better than 99.9% (starting from an initial underestimation of nearly 80%, i.e. without correction only 20% of the true value would be found in this extreme case). As expected the convergence is faster for lower concentrations since they only cause little reduction of the effective light path.

The improvement of the DOAS fit from the first iteration to the final iteration with optimized fit references is illustrated in Fig. 9.2b). In the initial fit (0th iteration) the shape of the NO<sub>2</sub> absorption bands in the simulated optical density and fit reference show significant differences leading to strong residual structures with a peak to peak distance of up to  $8 \cdot 10^{-2}$ . In the subsequent iterations the estimate of the NO<sub>2</sub> concentration are improved and thus the correction factor  $K(\lambda)$ . In the final iteration the simulated NO<sub>2</sub> absorption bands are almost perfectly matched, reducing the fit residual by four orders of magnitude. There are still small residual structures, with increasing magnitude for higher concentrations (fig. 9.2d). The reason for these small differences is that CE-DOAS (and BBCEAS) assumes a weak absorber (see sec. 4.3.3.1), while the calculation of the modeled measurements (eq. (9.5)) does not make this assumption. However, even for mixing ratios as high as 3000 ppbv the residual is still more than one order of magnitude lower than the optimal photonic noise levels ( $1 \cdot 10^{-4}$  peak to peak) which could be achieved with typical spectrographs. Thus, this shows the high accuracy that can be achieved with the iCE-DOAS evaluation.

### 9.1.2. Comparison iCE-DOAS vs. BBCEAS

One of the major motivations for the development of the iCE-DOAS algorithm is the need for an evaluation which is robust against broadband fluctuations of the measured light intensity. In order to test the influence of such intensity fluctuations a drifting light source was simulated by scaling the amplitude of the previously simulated  $I_0$  with values 0.9, 0.7, 0.5 and 0.1. Subsequently cavity enhanced differential optical densities were calculated at the instrument resolution using the scaled  $I_0$  and the previously simulated  $I$  spectra for NO<sub>2</sub> mixing ratios of 1 ppb, 10 ppb, 100 ppb, 1000 ppb, 3000 ppb. Both the iCE-DOAS and the classical/BBCEAS evaluation were applied to the optical densities to retrieve NO<sub>2</sub> mixing ratios. The results shown in fig. 9.3 clearly demonstrate that the iCE-DOAS algorithm is insensitive to broadband intensity fluctuations while in contrast to that the concentrations retrieved by the classical/BBCEAS evaluation show a linear dependency on the broadband light intensity change. This example clearly shows that iCE-DOAS achieves the desired robustness of the data evaluation against broadband fluctuations/drifts of the light intensity.

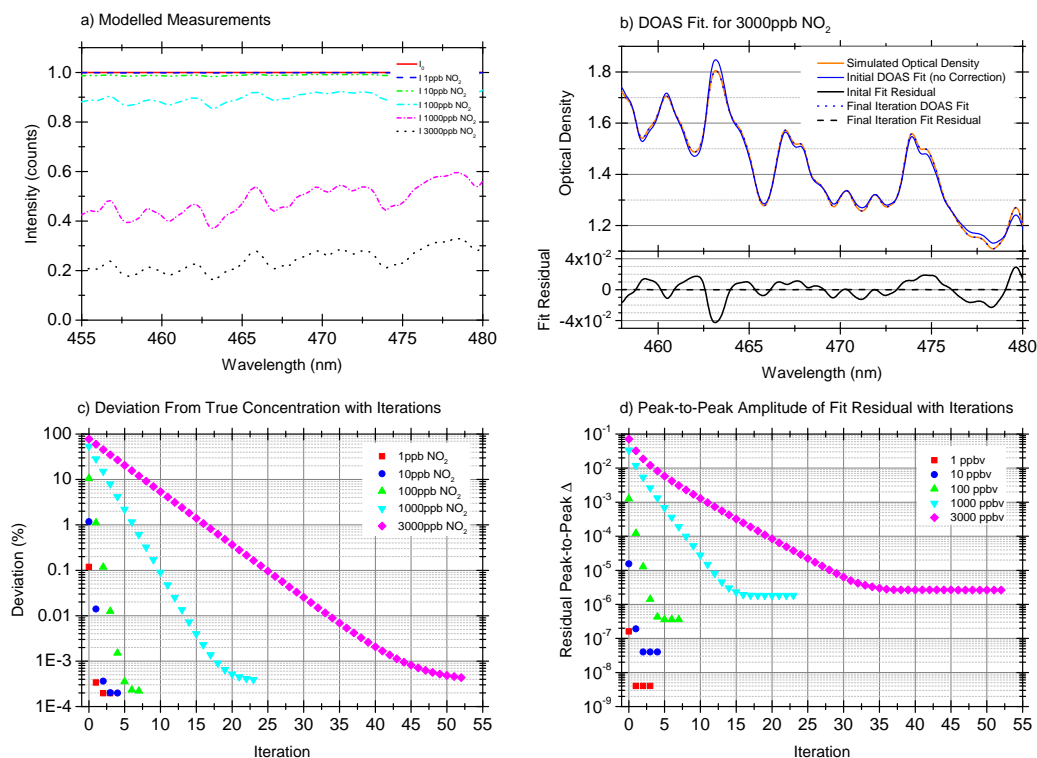


**Figure 9.2. | Simulated iCE-DOAS evaluations.** a) shows the measured spectra, modeled without photon shot noise for different NO<sub>2</sub> mixing ratios. Figure b) shows DOAS fits for a NO<sub>2</sub> mixing ratio of 3000 ppbv. It shows the improvement of the DOAS fit from the initial iteration to the final iteration with optimized fit references. In the final iteration the NO<sub>2</sub> absorption bands in the simulated optical density are almost perfectly matched, reducing the fit residual by four orders of magnitude. The convergence of the retrieved NO<sub>2</sub> towards its true value is shown in c) as a function of the iCE-DOAS iteration number. Plot d) shows the improvement of the fit residual during the iterative evaluation.

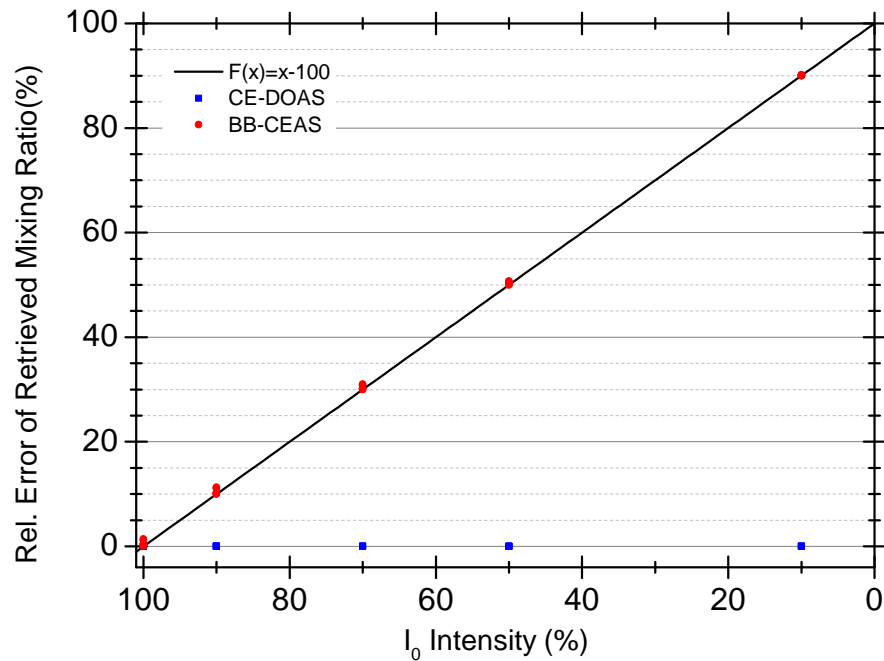


**Figure 9.3.** | Comparison of the underestimation of the true NO<sub>2</sub> concentration as a function of relative light source intensity. Blue dots show the influence on the iCE-DOAS evaluation and red dots the sensitivity of of the classical/BBCEAS evaluation. It can be clearly seen that iCE-DOAS is robust against broadband intensity drifts while the classical/BBCEAS evaluation shows a linear dependence. The modeled spectra did not contain photon shot noise.



# 10

## Correction of Spectrograph Nonlinearity

An important characteristic of the spectrographs applied for DOAS measurements is the linearity of the response to the incident light intensity. In a spectrograph the function of the detector, usually a CCD, is to convert the photons carrying the spectral information into an electronic signal. After digitization, the numerical value  $I^+$ , given in detector counts, should be linear proportional to the incident light intensity  $I$ . Mathematically,  $I$  and  $I^+$  are related by a transfer function  $T$

$$I^+ = T(I) \quad (10.1)$$

As shown in Fig. 10.1 the relative detector linearity  $\beta(I)$  is defined as the ratio of  $T(I)$  and an

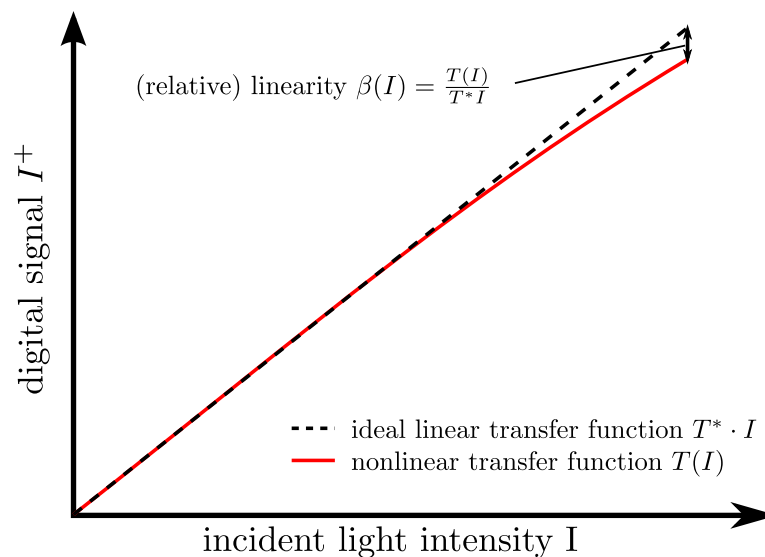


**Figure 10.1.** | Illustration of the nonlinear transfer function for a CCD detector.

ideal linear transfer function  $T^* \cdot I$ .

$$\beta(I) = \frac{T(I)}{T^*I} \quad (10.2)$$

With the definition  $\beta(I_{\text{ref}}) = 1$  at a reference intensity  $I_{\text{ref}}$ . The nonlinearity at an intensity  $I$  is then given as  $\beta(I) - 1$ . For a CCD detector [Boyle and G. E. Smith, 1970] the response function  $T$  is the result of a multi-step process: First the charge generated by a fraction of the incident photons is stored in potential wells, so called pixels, created by electrodes arranged in a regular periodic one or two dimensional array on the surface of the semiconductor. By applying an appropriate waveform to the electrodes the charges are moved to one edge of the semiconductor where they are sent to an amplifier and subsequently converted to their digital numeric representation by an ADC. With a proper device design, for CCD detectors the linearity of the transfer function to the incident light intensity can be better than 99 %<sup>1</sup>. However, recently a growing number of DOAS instruments, especially those designed for mobile applications, apply compact spectrometers like the Avantes spectrometers in the CE-DOAS instruments (chap. 5 and 6), the Ocean optics USB2000 applied in the Mace Head LP-DOAS (sec. 7.1) and the OMT spectrograph used in the MoLP-DOAS (sec. 7.2). Compact spectrometers usually use a simpler design of the readout electronics and often cheaper CCDs, which leads to significantly higher nonlinearity of the transfer function typically in the order of several percent (e.g. Fig. 5.7), which can cause severe problems for the spectral analysis if not corrected properly.

In the following a theoretical examination of the effects of detector nonlinearity is given, followed by a description of two methods to characterize and correct the detector nonlinearity and finally several examples of effects on the data evaluation in this work is given.

## 10.1. Effect of Detector Nonlinearity

According to eq. (10.2) the detector signal is given as

$$I^+ = IT^*\beta(I) \quad \text{and} \quad \frac{dI^+}{dI} = IT^*\frac{d\beta(I)}{dI} + T^*\beta(I) \quad (10.3)$$

If the detector shows a nonlinear intensity response the sensitivity  $\beta(I)$  changes with  $I$  and there exists at least one intensity where  $\frac{d\beta}{dI} \neq 0$ .

The effect of nonlinearity on absorption spectroscopy is demonstrated by the following consideration. The detected optical density  $D_D$  is given by

$$D_D = \ln\left(\frac{I_0^+}{I^+}\right) = \ln\left(\frac{T^*I_0\beta(I_0)}{T^*I\beta(I)}\right) = \underbrace{\ln\left(\frac{I_0}{I}\right)}_D + \ln\left(\frac{\beta(I_0)}{\beta(I)}\right) \quad (10.4)$$

$$\underset{|\beta(I_0)/\beta(I)| \approx 1}{\approx} D + \underbrace{\frac{\beta(I_0) - \beta(I)}{\beta(I)}}_{\text{rel. change in linearity}} \quad (10.5)$$

---

<sup>1</sup>ANDOR Newton CCD data sheet [http://www.andor.com/pdfs/specifications/Andor\\_Newton\\_CCD\\_Specifications.pdf](http://www.andor.com/pdfs/specifications/Andor_Newton_CCD_Specifications.pdf) accessed May 5 2015

The difference between the detected optical density  $D_D$  and the true optical density is therefore given by the second term of the above equation. For a light source with a “constant” spectral intensity distribution the effect would only be caused by the spectral variation due to the differential optical absorption in  $I$  because a constant offset between  $I$  and  $I_0$  would be removed by the high pass filter applied in a DOAS analysis. For example if the detector linearity  $\beta$  varies over the full intensity range of the CCD detector (linearly) by 10 % and the measured signal  $I$  is at about 50 % saturation of the detector, then the error on the optical density would be 5 % of the trace gas optical density, leading to an equivalent error in the retrieved trace gas optical densities. Of course the problem becomes more difficult when measuring several trace gas species with different strength in absorption which is a common problem in many DOAS applications e.g. measurement of HCHO in the presence of high  $O_3$  columns. Then the error in the optical density of the stronger absorber can lead to significant cross correlations due to systematic residual structures as described in sec. 4.2.3.2.

The problems with a nonlinear detector response are even higher if the instrument applies a light source which rapidly varies over a small spectral range like the LEDs applied in this work, which change their light intensity by almost 100 % within 20 nm. Depending on the smoothness of  $\beta(I)$  this can induce significant narrow band spectral structures in  $D_D$  with a peak to peak value of more than  $10^{-3}$  which can cause significant systematic errors, especially for weakly absorbing trace gases as demonstrated in sec. 10.2.1.

For DOAS applications like MAX-DOAS that measure sunlight the spectral variation of the light intensity is even higher due to the highly structured solar spectrum [e.g. Chance and Kurucz, 2010]. For example at a spectral resolution of 0.5 nm the light intensity varies by a factor of three within 2 nm at the well known calcium lines at 393.4 nm and 396.8 nm. Therefore, it is expected that at least for compact spectrometers nonlinearity can also be a significant error source for DOAS applications using sunlight.

### 10.1.1. Characterization of the Detector Nonlinearity

In order to correct for the nonlinearity, we need to determine the inverse of the transfer function  $T$  which can be decomposed into a linear part and a signal dependent correction  $\alpha(I^+)$  which is defined to be unity at a reference signal  $I_{\text{ref}}^+$

$$I = T^{-1}(I^+) = \frac{1}{T^*} I^+ \alpha(I^+) \quad (10.6)$$

In fact it is sufficient to determine  $\alpha(I^+)$  since we are not interested in an absolute intensity calibration. Several methods to characterize the linearity have been described in the literature [e.g. Sanders, 1972; Coslovi and Righini, 1980; Frehlich, 1992]. Ideally one would use an adjustable light source with known spectral power at each intensity level. Then the nonlinearity correction can be determined simply by measuring the detector response  $S$  at known intensity levels  $I$ . However, the estimates in the last section showed that the characterization should be good enough to reduce the nonlinearity to less than one percent and an example in the next section shows that under some circumstances the characterization of nonlinearity need to be better than 0.1 %. Thus for such a light source the accuracy of the set intensities would need to

be better than  $10^{-3}$ , which is very difficult to achieve. In the following three alternative methods will be described.

### 10.1.1.1. Method 1: Varying Exposure Time at Fixed Light Intensity

This is the method used in this work to characterize the nonlinearity of the spectrographs CCD detectors. The basic idea is to record spectra of an intensity stable light source at different exposure times. In our case the light source are high power LEDs (CREE XP-E), which are temperature stabilized with  $\Delta T < 0.1$  K to achieve the required intensity stability (relative intensity variation  $< 10^{-3} \text{ h}^{-1}$ ).

It is assumed that (at a constant number of scans) the number of collected photons is proportional to the exposure time. Thus, in the linear case increasing the exposure  $t_{\text{exp}}$  time by a factor  $x$  should also lead to the same increase of the signal  $I^+$ . In order to determine the deviation from linearity the sensitivity for each saturation level is computed by dividing the signal  $I^+$  by the respective exposure time  $t_{\text{exp}}$ . As we are only interested in the relative change in sensitivity it is normalized by the sensitivity at an arbitrarily chosen reference saturation (usually between 10% and 60% saturation). The normalized (inverse) sensitivity is then given by:

$$S(I^+) = \frac{I^+/t_{\text{exp}}}{I_{\text{ref}}^+/t_{\text{exp,ref}}} \quad (10.7)$$

To reduce the influence of measurement noise this function is usually approximated by a polynomial fit to the measured data. In cases where the non-linearity is more complex a spline interpolation can be a better choice. The non-linearity correction function  $\alpha(S)$  is then simply the reciprocal of  $S(I^+)$ .

$$\alpha(I^+) = \frac{1}{S(I^+)} \quad (10.8)$$

**Precision and accuracy of this method:** From the characterizations performed in this work shown in Fig. 5.4, Fig. 5.7 and Fig. 6.3 it can be seen that this method allows a very precise characterization of the detector nonlinearity. The scatter of the data points for a specific saturation show a Gaussian distribution with a standard deviation of about than 0.1 %, which is also the precision of the nonlinearity correction achieved with this method.

The only drawback of this method is that it relies on the correct timing of the set exposure times. This is especially a problem as for some manufacturers the set exposure time also includes the readout time. Thus the accuracy of this method is manufacturer depended, but at least for the Avantes spectrometers used in this work it does not seem to be a problem.

### 10.1.1.2. Method 2: Differential Intensity Measurements

For some instruments the uncertainties in the exposure time may be too big to derive a good non-linearity correction. For this reason a second method based on the paper from Frehlich, 1992 is presented. It is independent of the absolute light intensities and the the exposure times.

The nonlinearity correction is determined by measuring the superposition of light intensities from two sources as illustrated in Fig. 10.2. The base intensity  $I_0$  is provided by light source one, which is the stronger of the two light sources and variable in intensity. Light source two provides a intensity  $\delta I$ , which is weak compared to  $I_0$  but has a constant intensity throughout the entire measurement.  $\delta I$  can be added and removed form the measured light using a shutter (see Fig. 10.2). The corresponding detector signals are  $I_0^+$  for the base intensity and  $I_{0+\delta}^+$  for the superposition of both light sources. The response of the detector  $\delta I^+(I^+)$  to a small change in intensity  $\delta I$  then be related to the first derivative of the inverse transfer function  $T^{-1}$  using eq. (10.6)

$$\begin{aligned}\delta I &= T^{-1}(I_{0+\delta}^+) - T^{-1}(I_0^+) \\ &= \frac{T^{-1}(I_{0+\delta}^+) - T^{-1}(I_0^+)}{\delta I^+(I^+)} \delta I^+(I^+) \\ &\approx \frac{dT^{-1}(I^+)}{dI^+} \delta I^+(I^+)\end{aligned}\quad (10.9)$$

$$\implies \frac{dT^{-1}(I^+)}{dI^+} = c \delta I^+(I^+) \quad (10.10)$$

where  $c = 1/\delta I$  is a constant. Thus, if  $\delta I^+(I^+)$  is measured at many saturation levels, the inverse transfer function  $T^{-1}(I^+)$  can be obtained up to a constant factor by integration

$$T^{-1}(I^+) = c \int_0^{I^+} \delta I^+(I^{+'}) dI^{+'} \quad (10.11)$$

Since we are not interested in an absolute intensity calibration we can freely choose a reference saturation  $I_{\text{ref}}^+$  where

$$T^{-1}(I_{\text{ref}}^+) = I_{\text{ref}}^+ \quad (10.12)$$

Thus at an arbitrary saturation the inverse transfer function is given by

$$T^{-1}(I^+) = I_{\text{ref}}^+ \frac{\int_0^{I^+} \delta I^+(I^{+'}) dI^{+'}}{\int_0^{I_{\text{ref}}^+} \delta I^+(I^{+'}) dI^{+'}} \quad (10.13)$$

The disadvantage of this method is that by integration the errors of the individual measurements accumulate. This could be improved by increasing the magnitude of the differential signal  $\delta I$ . However, this will reduce the accuracy of the approximation made in eq. (10.10). Therefore, a lab study will be necessary to find an optimal measurement setup and to determine the accuracy of the derived non-linear response function.

### 10.1.1.3. Method 3: Attenuator Method

The attenuator method [Coslovi and Righini, 1980] is also independent of the absolute light intensities and the exposure times. It uses a filter of known optical density as an attenuator. For many intensity levels of a light source, and thus saturation levels of the detector the signal

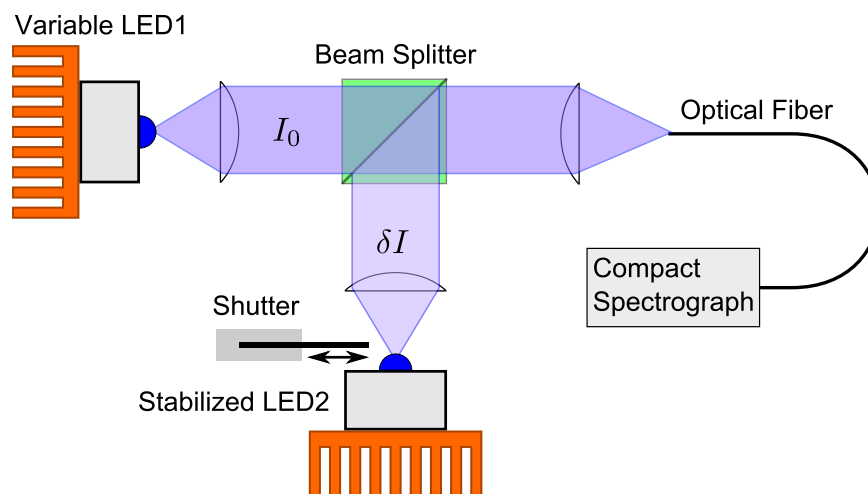


**Figure 10.2.** | Illustration of a setup for the characterization of the detector linearity using differential intensity measurements. LED one provides the base intensity  $I_0$ , which can be variably adjusted. The second LED provides a small but constant “differential” intensity  $\delta I$ , which can be added to  $I_0$  using a shutter.

with and without the filter is measured. Thus for each detector saturation level one gets the apparent optical density of the filter, which should be the same at all saturation if the detector was linear. If the apparent optical density changes with saturation of the detector it can be used to determine the nonlinearity of the detector response [e.g. Coslovi and Righini, 1980].

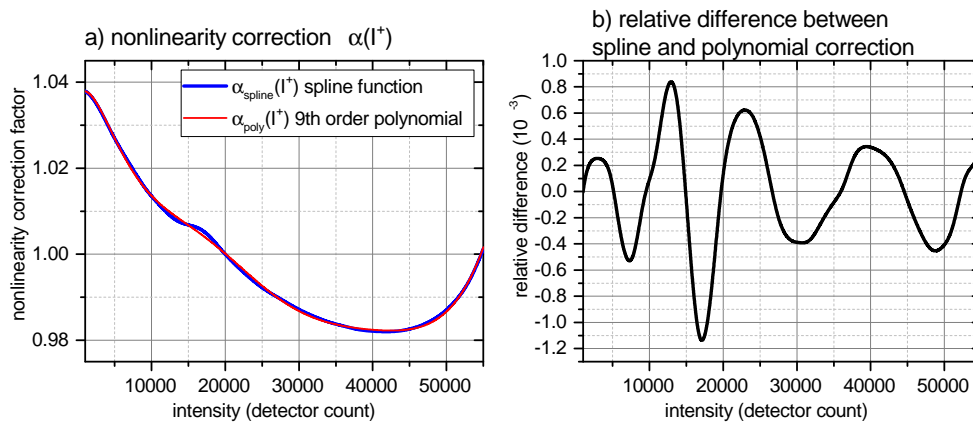
## 10.2. Practical Examples for the Effect of Nonlinearity

The following section discusses effects of nonlinearity encountered in the analysis of spectra measured in the frame of this work, exemplary for the OP-CE-DOAS MK-II system. This system was chosen because the used compact spectrograph (Avantes AvaSpec ULS2048L) has a very pronounced nonlinear detector response, which is illustrated in Fig. 10.3 using the nonlinearity correction function derived in sec. 5.2.1. The magnitude of the correction is about 5 % over the relevant saturation range from 1 % to 80 %. The spline interpolation of the measured correction function also features an odd S-shaped bend in the saturation range between 20 % and 27 % which will show to cause significant spectral problems if nonlinearity is not accounted for.

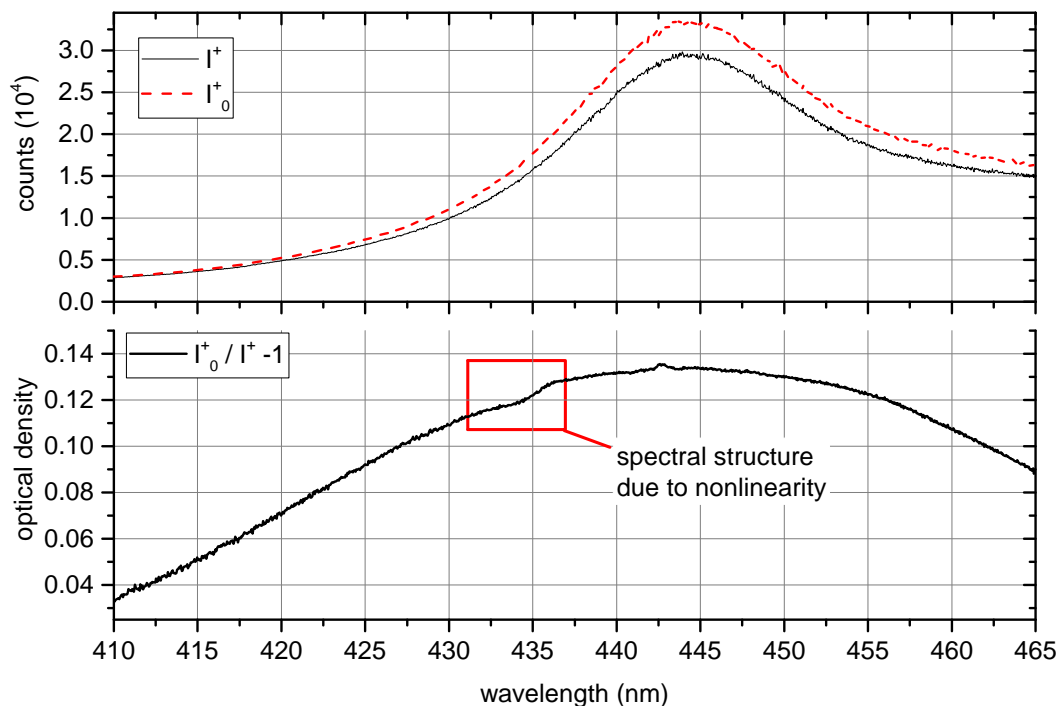
### 10.2.1. CE-DOAS Analysis

Fig. 10.4 shows a typical measurement by the OP-CE-DOAS MK-II with a detector signal  $I_0^+(\lambda)$  from reference measurement in “zero air” and  $I^+(\lambda)$  from an atmospheric measurement. The peak intensity of  $I_0^+(\lambda)$  with  $3.4 \cdot 10^4$  counts corresponds to a detector saturation of 50 %

but towards shorter wavelengths the light intensity decreases by more than a factor four withing 20 nm, due to the strong wavelength dependence of the used LED light source. The peak intensity of  $I^+(\lambda)$  is about 13 % lower compared to  $I_0^+(\lambda)$ , mostly due to broadband mie scattering on atmospheric aerosols and due to atmospheric turbulence. The corresponding effective optical density  $D_{\text{eff}}(\lambda) = \frac{I_0^+(\lambda)}{I^+(\lambda)} - 1$ , shown in Fig. 10.4, has a spectral dip at about 435 nm, which is not caused by trace gas absorption. At this wavelength both detector signals  $I_0^+(\lambda)$  and  $I^+(\lambda)$  correspond to a saturation of 23 % and 26 %, which is in both cases in the saturation range where the nonlinearity correction shows the S-shape bend (see Fig. 10.3). This already hints to a problem with detector nonlinearity. To further investigate this problem, a DOAS analysis was applied to  $D_{\text{eff}}(\lambda)$  as shown in Fig. 10.5 according to the IO retrieval settings for the OP-CE-DOAS MK-II instrument, specified in sec. 5.6. If the detector signals are not corrected for nonlinearity the above mentioned spectral structure at 435 nm is present with a peak to peak value of  $2 \cdot 10^{-3}$ . This has a particularly strong effect on the fit of the IO absorption cross section which finds apparently significant IO with a mixing ratios of  $(5.50 \pm 0.05)$  ppt. However, if the nonlinearity of the detector signals is corrected, using the spline approximation of the correction function, the spectral structure is greatly reduced (peak to peak  $< 6 \cdot 10^{-4}$ ) and the IO mixing ratio reduces to  $(1.2 \pm 0.6)$  ppt which is not significant since it is exactly at the  $2\sigma$  detection limit. It is important to notice that correcting the detector signals by a 9th order polynomial approximation of the correction function is not sufficiently accurate to remove the spectral structures at 435 nm and even seems to amplify spectral structures at 445 nm. Even though the difference of relative difference between the 9th order polynomial and the spline interpolation is only in the in the  $10^{-3}$  range, the polynomial is too stiff to capture the



**Figure 10.3.** | Nonlinearity correction function for the spectrometer used in the OP-CE-DOAS MK-II. a) polynomial approximation (red) and spline interpolation (blue) of the measured nonlinearity correction. b) The relative difference between both curves is in the  $10^{-3}$  range. However, the polynomial is not able to capture the the odd S-shape bend, also present in the measured data in the intensity range between  $1.3 \cdot 10^4$  and  $1.8 \cdot 10^4$  ADC counts, which corresponds to a saturation range between 20 % and 27 %.



**Figure 10.4.** | Example for the effect of detector nonlinearity on the optical density measured by the OP-CE-DOAS MK-II. Top:  $I_0^+(\lambda)$  is the detector signal of a reference measurement in “zero air” and  $I^+(\lambda)$  the detector signal of an atmospheric measurement. Bottom: The effective optical density  $D_{\text{eff}}(\lambda) = \frac{I_0^+(\lambda)}{I^+(\lambda)} - 1$  has a spectral dip at about 435 nm, which is attributed to the nonlinear intensity response of the detector.

S-shape bend in the saturation range between 20 % and 27 % which seems to be the critical difference between both interpolations. Further investigation with higher order polynomial interpolations showed that the error in the nonlinearity correction function needs to be less than  $10^{-4}$  for a sufficiently accurate representation of the S-shape bend required to remove the residual structures at 435 nm.

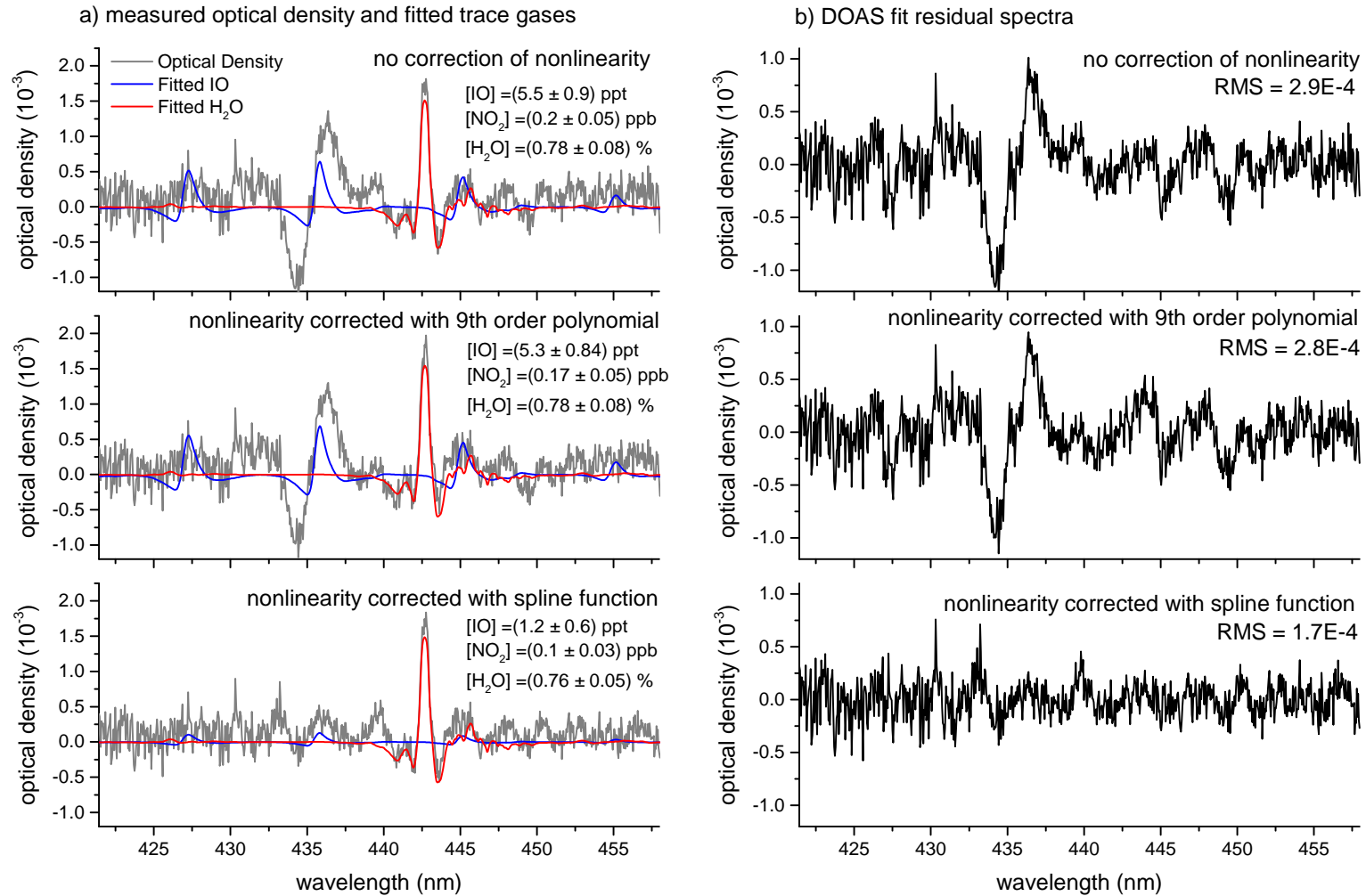


**Figure 10.5.** | Example for the effect of detector nonlinearity on a CE-DOAS evaluation.

a) DOAS analysis applied to optical densities, which were calculated from intensities without nonlinearity correction (top), with nonlinearity correction using the 9th order polynomial  $\alpha_{\text{poly}}$  (middle) and using using the spline function  $\alpha_{\text{spline}}$  (bottom). b) DOAS fit residuals for the evaluations in a)

### 10.2.2. Path Length Calibration by the Helium/air Method.

Calibration of  $\bar{L}_0(\lambda)$  by the Helium/air Method makes use of the broadband intensity change between a resonator filled with air and Helium as described in sec. 4.3.3.2

$$\bar{L}_0(\lambda) = \frac{\frac{I_{\text{air}}(\lambda)}{I_{\text{Helium}}(\lambda)} - 1}{\epsilon_{\text{Helium}}(\lambda) - \epsilon_{\text{air}}(\lambda)} . \quad (4.35)$$

Thus, the difference in detector linearity between the intensity levels  $I_{\text{air}}(\lambda)$  and  $I_{\text{Helium}}(\lambda)$  directly translates in the error of the determined curve for  $\bar{L}_0(\lambda)$ . Figure 10.6 shows as an example the influence on the calibration of the OP-CE-DOAS MK-II system on April 3 2013, which was previously described in sec. 5.3. The error in the order of few percent translates into the effective fit references used in the DOAS evaluation and thus directly causes an error of the retrieved mixing ratios in the same order of magnitude which might be regarded negligible in field applications. However, the error in  $\bar{L}_0(\lambda)$  is also wavelength dependent and even shows differential features which affect the derived effective fit references  $\Theta_i(\lambda)$  of the trace gases  $i$  (see sec. 5.6 and chap. 9) and therefore also introduces systematic residual structures to the fit which become particularly problematic when trying to simultaneously retrieve mixing ratios of strongly and weakly absorbing gases as discussed in sec. 4.2.3.2.

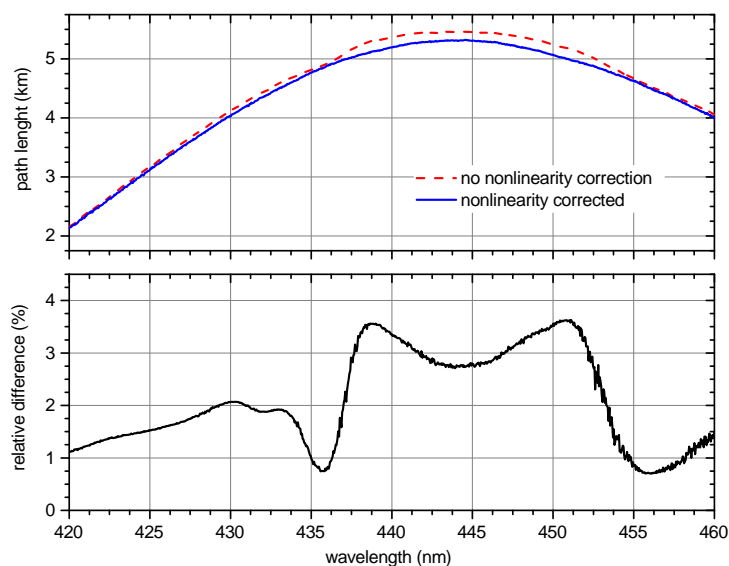


**Figure 10.6.** | Example for the effect of detector nonlinearity on the Helium/air calibration of  $\bar{L}_0(\lambda)$  for the OP-CE-DOAS MK-II system on April 3 2013. Details on the measurements are given in sec. 5.3. If the nonlinearity is not corrected for the measured intensities the retrieved  $\bar{L}_0(\lambda)$  curve deviates by several percent. The error of  $\bar{L}_0(\lambda)$  induced by nonlinearity is wavelength dependent and even shows differential structures affecting the effective fit references used in the DOAS retrieval.

# 11

## A Corrected IO Absorption Cross Section

Open Path CE-DOAS measurements of high IO mixing ratios (several 100 ppt) revealed differences in the relative band strength of the observed IO absorption and the high resolution IO literature cross section of Gómez Martín et al. [2005], commonly used for DOAS retrievals of IO. The observed deviation was particularly strong for the absorption between 443.5 nm and 451.2 nm (IO( $2 \leftarrow 0$ ) band) which was observed to be about 1.5 times stronger than expected. This chapter first discusses the optical absorption spectrum of IO and the uncertainties in the currently used literature cross sections. This is followed by an analysis of the origin of the deviations between the observed IO absorption and the literature cross section. Finally correction factors for the relative strengths of the absorption bands are derived which are used to make a corrected high resolution IO reference spectrum.

### 11.1. The IO absorption cross section

In the UV-VIS wavelength range IO has a prominent system of absorption bands which are strongest between 400 nm to 460 nm. This band system can be attributed to transitions from the IO ( $X^2\Pi_{3/2}$ ) ground state to the IO ( $A^2\Pi_{3/2}$ ) excited state. These are further subdivided into ground state IO( $\nu' \leftarrow 0$ ) transitions originating from the vibrational ground state  $\nu'' = 0$  and vibrationally excited IO( $\nu' \leftarrow \nu''$ ) transitions (mainly from  $\nu'' = 1$ ).

However, due to the high reactivity of IO the experimental determination of its cross section is challenging. Elaborated experimental setups and chemical kinetics calculations are required to determine the IO concentration during a spectroscopic measurement [e.g. Gómez Martín et al., 2005]. Despite these efforts, the literature values for the absorption cross section of the individual transitions still come with relatively high uncertainties of at least 10% to 20% [e.g. Gómez Martín et al., 2005]. There are only few spectrally resolved measurements of the IO absorption cross section [Laszlo et al., 1995; Bloss et al., 2001; Spietz et al., 2005; Gómez Martín et al., 2005], and only the literature spectrum of Gómez Martín et al. [2005] has a sufficiently high resolution (0.07 nm) for DOAS Analysis and is therefore the quasi standard

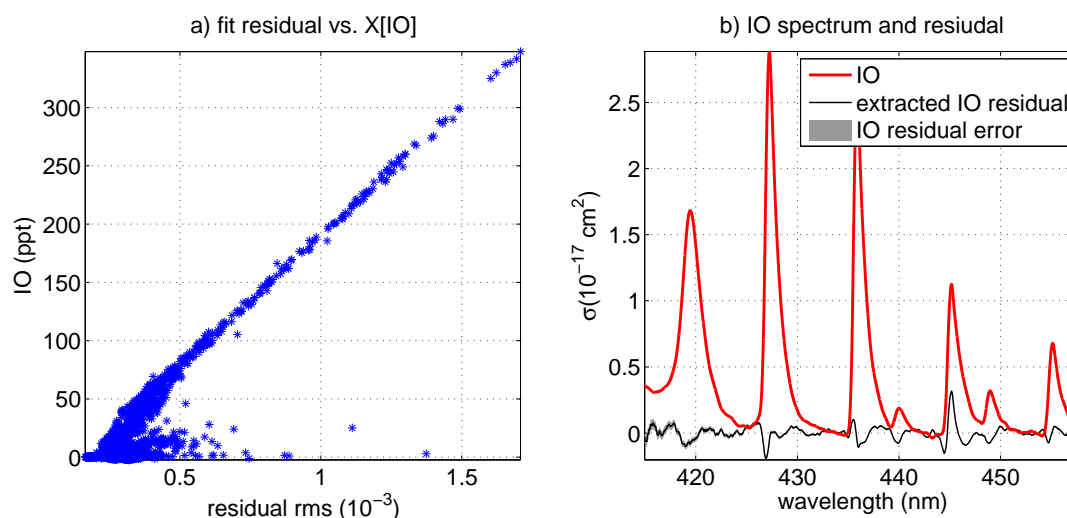


**Figure 11.1.** | Residual analysis for the data set recorded between 03/21 and 04/04/2013 with the OP-CE-DOAS MK-II instrument. The parameters of the DOAS retrieval are summarized in Tab. 11.1. Figure a) shows a pronounced correlation between the RMS of the fit residual and the IO mixing ratio. Figure b) Shows the Gómez Martín et al. [2005] cross section, convoluted to the instrument resolution and the component of the fit residual that correlates with the IO mixing ratio, which was extracted using multiple linear regression (see section 4.2.5.1).

cross section for DOAS analysis.

### 11.1.1. Deviations Between Literature Cross Sections and CE-DOAS measurements

Analysis of the CE-DOAS measurements recorded in the frame of this thesis showed a significant correlation between residual structures and the retrieved IO mixing ratio if the Gómez Martín et al. [2005] IO cross section is used as fitting reference (see Fig. 11.1). Especially the IO(2  $\leftarrow$  0) band (443.5 – 451.2 nm) seems to be underestimated systematically. There are several possible explanations for the deviations:

1. **Wavelength calibration errors** could in principle account for some of the observed residual structures. However, this effect can be ruled out as the error source because:
  - The wavelength to pixel mapping is very well approximated by a 2nd order polynomial. Thus, small errors in the wavelength calibration would be compensated by a global shift and squeeze of the fitted spectra.
  - Very similar residual structures appear in measurements with different DOAS instruments. It is very unlikely that exactly the same calibration error is made several times.

trace gas	lit. cross section	shift
IO	Gómez Martín et al. [2005]	free
NO <sub>2</sub>	A. C. Vandaele et al. [2002]	linked to IO
H <sub>2</sub> O	Rothman et al. [2010]	linked to IO
O <sub>4</sub>	Hermans et al. [1999]	linked to IO

**Table 11.1.** | **DOAS retrieval scenario used for residual analysis.** Before the retrieval a binomial high pass filter with 1000 iterations was applied to the measured data and all fitted cross sections. The DOAS retrieval was performed in the spectral window 417 nm to 461.5 nm. A second order polynomial was fitted simultaneously to the trace gas cross sections.

2. **An Error in the calibration of the path length curve  $L_0(\lambda)$**  could introduce residual structures correlating with the IO concentrations. However, compensation of the residual structures by a correction of  $L_0(\lambda)$  would introduce strong, absorption band like, narrow band features to  $L_0(\lambda)$ , which is not physical. Furthermore, if the residual structures originated from an error in  $L_0(\lambda)$ , the NO<sub>2</sub> retrieval would need to show similar residual structures, which is not the case. Finally, since very similar residual structures appear for measurements with different DOAS instruments, the same calibration error would have been made during different campaigns with different instruments, which is very unlikely.
3. **Spectral resolution of the literature cross section  $\sigma_{\text{IO}}(\lambda)$**  is 0.07 nm, which is only 6 to 7 times better than the spectral resolution of the DOAS instruments used in this thesis. Thus, adaption of the literature spectrum to a DOAS instrument by convolution with the respective instrument function introduces an error leading to systematic residual structures in the DOAS fit. Deconvolution of the literature cross section is desirable, but is generally not possible, since it does not contain the necessary information. However, deconvolution is possible if combined with a subsequent convolution with DOAS instrument  $H_{\text{DOAS}}$  to the lower resolution of the DOAS instrument. This is compared to a normal convolution with the DOAS instrument  $H_{\text{DOAS}}$  in order to assess in order to assess the magnitude of the spectral structures induced by the finite spectral resolution of the literature cross section. Three different deconvolution/convolution methods are used<sup>1</sup>. In all cases the instrument function  $H_{\text{lit}}(\lambda)$  of the literature cross section is assumed to be a Gaussian with 0.07 nm FWHM, and the instrument function of the DOAS instrument  $H_{\text{DOAS}}(\lambda)$  is taken from the characterization of the OP-CE-DOAS MK-II.
  - a) Convolution by a constant instrument function can be turned into a simple multiplication in frequency space, using Fourier-Transformation. Therefore, in frequency space, deconvolution with  $H_{\text{lit}}(\lambda)$  and convolution with  $H_{\text{DOAS}}(\lambda)$  can be calculated as multiplication of  $\hat{\sigma}_{\text{IO}}(\nu)$  with  $\hat{H}_{\text{DOAS}}(\nu)/\hat{H}_{\text{lit}}(\nu)$ , where  $\hat{\sigma}_{\text{IO}}(\nu)$

<sup>1</sup>Deconvolution methods were adapted from a MATLAB script by Johannes Lampel. Also see section 3.1.3 in Lampel [2014]

denotes the Fourier transformed spectra. In order to avoid zero division and noise amplification  $\hat{H}_{\text{lit}}(\nu)$  is set to one if  $|\hat{H}_{\text{lit}}(\nu)|$  is below a threshold  $\gamma$ . This filter is justified as  $|\hat{H}_{\text{DOAS}}(\nu)|$  is also close to zero in these regions. Finally, an inverse Fourier-Transformation is performed to obtain the convoluted cross section in wavelength domain.

- b) Convolution can also be represented as a matrix operation  $C$  on  $\sigma_{\text{IO,lit}}$ . However, simple deconvolution using the inverse is not possible, since  $C$  is degenerate. Truncated singular value decomposition (TSVD) of  $C$  can be used to compute a regularized pseudo inverse  $C_R^{-1}$  [Hansen, 1987]. The regularization parameter  $\gamma$  is chosen appropriately to cut off small, noise dominated singular values.

$$C = U\Sigma V^\dagger \quad (11.1)$$

$$\Sigma_{ii,R}^{-1} = \begin{cases} 0 & \text{if } \Sigma_{ii} < \gamma \\ 1/\Sigma_{ii} & \text{otherwise} \end{cases} \quad (11.2)$$

$$C_R^{-1} = V\Sigma_R^{-1}U^\dagger \quad (11.3)$$

$$\sigma_{\text{IO,deconv}} = C_R^{-1}\sigma_{\text{IO,lit}} \quad (11.4)$$

Finally, convolution with  $H_{\text{DOAS}}(\lambda)$  is used to adapt  $\sigma_{\text{IO,deconv}}(\lambda)$  to the DOAS instrument resolution.

- c) Deconvolution by the Lucy-Richardson method [Richardson, 1972] using  $H_{\text{lit}}(\lambda)$ , as implemented in MATLAB. Adaption of  $\sigma_{\text{IO,deconv}}(\lambda)$  to the DOAS instrument resolution is done by subsequent convolution with  $H_{\text{DOAS}}(\lambda)$ .

As shown in Fig. 11.2 all three deconvolution/convolution methods give almost exactly the same results, and differ to the normal convolution by less than one percent. This difference is one order of magnitude smaller than the residual structures observed in the analysis of CE-DOAS measurements (see Fig. 11.1). Thus, the resolution effect cannot be the main error source.

4. **Errors in the literature cross sections.** Spietz et al. [2005] and Gómez Martín et al. [2005] reported problems for the measurement of the IO(2 ← 0) band. They observed that the strength of the IO(2 ← 0) band relative to the remaining bands changed during their measurements. IO(2 ← 0) appeared smallest in low pressure experiments and recovered systematically when the pressure was increased. A similar but much weaker effect was also observed for the IO(3 ← 0) band. They hypothesize that this effect is caused by a partial population inversion of the excited IO ( $A^2\Pi_{3/2}$ ) state at  $\nu' = 2$  and  $\nu' = 3$ . While IO ( $A^2\Pi_{3/2}$ ) at  $\nu' = 2$  and  $\nu' = 3$  is rapidly quenched to the ground state at atmospheric pressure, it has a sufficiently long life-time (10 ps to 100 ps) at low pressures. Thus, in their low pressure measurements stimulated emission could compete with absorption, lowering the apparent absorption cross section. Other vibrational levels in the IO ( $A^2\Pi_{3/2}$ ) did not show this effect as they have much shorter lifetimes (less than 1 ps [Newman et al., 1998]), being heavily predissociated. This effect could explain the discrepancy at the IO(2 ← 0) band between the CE-DOAS measurement and the

Gómez Martín et al. [2005] cross section, measured at  $p = 30$  mBar, which is low enough for stimulated emission to be effective.

Furthermore, the low pressure conditions in Gómez Martín et al. [2005] can also influence the apparent strength of transitions of electronic ground state vibrationally excited IO ( $X^2\Pi_{3/2}, \nu'' > 0$ ), from now on denoted as IO\*. The reactions used by Gómez Martín et al. [2005] for the formation of IO are known to produce substantial amounts of IO\* [e.g. Durie and Ramsay, 1958; Clyne and Cruse, 1970]. Generally IO\* is rapidly quenched to the ground state. However, at very low pressures (less than 100 mBar) quenching is slow enough to observe a non-equilibrium population of IO\* [Gómez Martín et al., 2005]. If this is not corrected properly, cross sections of IO\* transitions are be overestimated.

Since the first three points can be ruled out as main error source, it is most likely that the observed residual structures in the CE-DOAS analysis originate from errors in the literature cross section.

## 11.2. Correction of the IO Absorption Cross Section

In this section CE-DOAS field measurements with strong IO absorption are used to derive a correction for the high resolution IO spectrum by Gómez Martín et al. [2005] in the wavelength range from 416 nm to 462 nm at atmospheric pressures and room temperature ( $\approx 293$  K).

Spectra with very high IO concentrations were measured in the coastal campaigns, especially during the incubation chamber study in New Zealand (see chapter 13). With IO optical densities up to  $10^{-1}$ , absorption signal to photon noise ratios of more than 100 are reached for many measurements, giving a unique opportunity to retrieve corrections of the strengths, position and shape of individual absorption bands. However, the correction of the band shape is reduced to a spectral squeeze, because the information on the band shape is limited by the relatively low spectral resolution ( $\sim 0.5$  nm) of the spectrographs used for the CE-DOAS measurements in this thesis. The correction for an absorption band IO( $\nu' \leftarrow \nu''$ ), in a wavelength interval centered at  $\lambda_c$ , can then be described by a simple three parameter fit-model with a scaling  $\beta_0$ , a spectral shift  $\beta_1$  and a spectral squeeze  $\beta_2$ :

$$\sigma_{\text{IO}(\nu' \leftarrow \nu''), \text{corr}}(\lambda, \beta_0, \beta_1, \beta_2) = \beta_0 \cdot \sigma_{\text{IO}}(\lambda + \beta_1 + (\lambda - \lambda_c) \cdot \beta_2) \quad (11.5)$$

Positive values of  $\beta_1$  shift the cross section towards shorter wavelengths, positive values of  $\beta_2$  make the absorption band narrower.

The data set used for the retrieval of the correction parameters was recorded in the period between March 25 and April 1 2013 during the seaweed incubation chamber studies in New Zealand. This data set was chosen as it contains the largest number of spectra with a strong IO signal and low NO<sub>2</sub> levels. To ensure a good signal to noise ratio only spectra containing more than 100ppt of IO were used in the analysis. Most spectra with a strong IO signature, acquired during this thesis, also contain absorption from NO<sub>2</sub> and H<sub>2</sub>O, both absorbing in the same spectral region as IO. Spectra containing more than 0.5 ppb NO<sub>2</sub> are discarded (this

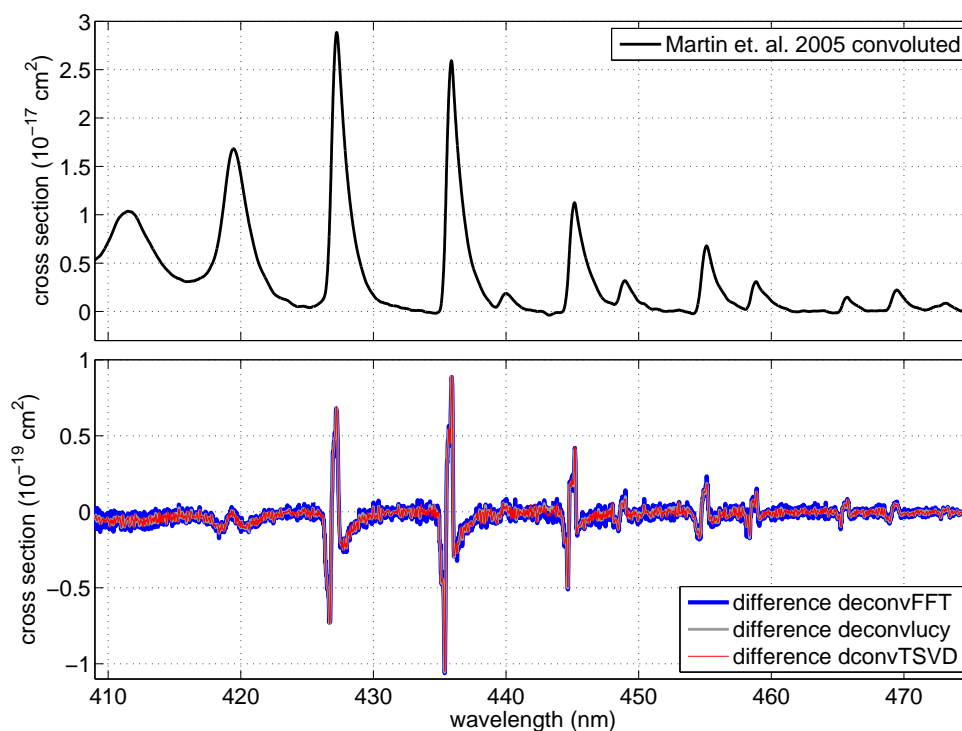


**Figure 11.2.** | Effect of deconvolution on the Gómez Martín et al. [2005] IO cross section.

For the comparison, after deconvolution the high resolution cross sections were adapted to the spectral resolution of the OP-CE-DOAS MK-II. The top plot shows the total absorption cross section at the instrument resolution. The bottom plot shows the difference of the convoluted cross section to the convolution of the deconvolution cross sections, which is, within numerical accuracy, identical for all tested methods. This effect can only account for residual structures on the order of less than 1% of the IO absorption, which is at least one order of magnitude below the residual structures extracted from CE-DOAS measurements (see Fig. 11.1). Thus, this effect cannot be the main error source.

## 11.2. Correction of the IO Absorption Cross Section

IO( $\nu' \leftarrow \nu''$ )	fit-range (nm)	rescaling $\beta_0$ (a.u.)	shift $\beta_1$ (nm)	squeeze $\beta_2$ (a.u.)
5 $\leftarrow$ 0	416.1 – 424.4	0.97 $\pm$ 0.02	-0.03 $\pm$ 0.01	0
4 $\leftarrow$ 0	424.4 – 431.4	1	-0.031 $\pm$ 0.005	0
3 $\leftarrow$ 0	433.5 – 438.5	1.02 $\pm$ 0.01	0.042 $\pm$ 0.004	-0.015 $\pm$ 0.005
4 $\leftarrow$ 1	439.0 – 442.0	0.44 $\pm$ 0.06	-0.05 $\pm$ 0.10	0
2 $\leftarrow$ 0	443.5 – 448.0	1.53 $\pm$ 0.03	0.090 $\pm$ 0.008	0.12 $\pm$ 0.01
3 $\leftarrow$ 1	448.0 – 451.2	0.46 $\pm$ 0.05	-0.01 $\pm$ 0.03	0
1 $\leftarrow$ 0	453.6 – 458.0	1.07 $\pm$ 0.01	-0.055 $\pm$ 0.003	0
2 $\leftarrow$ 1	457.3 – 462.0	0.5 $\pm$ 0.05	-0.064 $\pm$ 0.0019	0

**Table 11.2.** | **Summary of the corrections retrieved for different IO transitions.** The scaling of the band strength was evaluated relative to IO(4  $\leftarrow$  0), since no independent measurement of the true IO concentration was available. IO(4  $\leftarrow$  0) was chosen as scaling reference, as it is assumed to be the best characterized transition in Gómez Martín et al., 2005. Blue entries indicate evaluations with  $\beta_2$  fixed to zero, which was done if the squeeze was not significant or not consistent over the evaluated spectra. Fits with insignificant shift, are indicated by red entries.

corresponds to  $D' \approx 2 \cdot 10^{-3}$  for the OP-CE-DOAS MK-II). This ensures that the absorption signal by of most IO bands in the spectral range from 410 nm to 460 nm is at least 10 times stronger than the NO<sub>2</sub> absorption. After filtering, 65 spectra remain for the analysis, which were corrected for the remaining small NO<sub>2</sub> and H<sub>2</sub>O absorption by the following steps:

1. CE-DOAS retrieval of the NO<sub>2</sub> concentration in the split fit range 414 nm to 432.5 nm, 450.4 nm to 457.5 nm and 460.9 nm to 475.7 nm. The fit range was split to exclude spectral regions where the retrieval of the NO<sub>2</sub> concentration is biased by errors in the simultaneously fitted IO cross section.
2. Subtraction of the NO<sub>2</sub> absorption from the measured spectra using the previously retrieved NO<sub>2</sub> concentrations.
3. CE-DOAS retrieval of the H<sub>2</sub>O concentration in the spectral window 440.8 nm to 445.13 nm.
4. Subtraction of the H<sub>2</sub>O absorption from the measured spectra using the previously retrieved H<sub>2</sub>O concentrations.
5. Binomial high pass filtering with 5000 iterations, of the corrected spectra

For each IO absorption band the correction parameters  $\beta_0, \beta_1, \beta_2$  are determined by a non-linear least squares fit<sup>2</sup> of eq. (11.5) plus a first order polynomial to the measured spectra. Before fitting, the Gómez Martín et al. [2005] literature cross section is convoluted to the instrument resolution and filtered with a binomial high pass filter with 5000 iterations. The

---

<sup>2</sup>MATLAB *lsqcurvefit* implementation of the Levenberg-Marquardt algorithm was used for non-linear least squares fitting

trace gas	lit. cross section	fit range (nm)	shift
IO	Gómez Martín et al. [2005]	425.3 – 447.8	free
IO(2 ← 0)	Gómez Martín et al. [2005]	(442 – 447.8)*	linked to IO
NO <sub>2</sub>	A. C. Vandaele et al. [2002]	425.3 – 447.8	linked to IO
H <sub>2</sub> O	Rothman et al. [2010]	425.3 – 447.8	linked to IO
O <sub>4</sub>	Hermans et al. [1999]	425.3 – 447.8	linked to IO

**Table 11.3.** | **Fit scenario used for the validation of the relative scaling of the IO(2 ← 0) absorption band.** Before the fit a binomial high pass filter with 1000 iterations is applied to the measured spectra and all absorption cross sections. The DOAS fit is performed in the spectral window from 425.3 nm to 447.8 nm. A global shift is allowed to compensate for small errors in the wavelength to pixel mapping. \*The IO(2 ← 0) cross section was extracted from Gómez Martín et al. [2005] in the spectral window 442 nm to 447.8 nm and set zero elsewhere.

spectral windows of the fits, specified in Tab. 11.2, are chosen to contain only individual IO bands. Additionally, each IO band is also fitted with the squeeze parameter fixed to  $\beta_2 = 0$ , to check its influence on the shift  $\beta_1$ .

The fit results are shown in appendix A, Fig. A.1 to Fig. A.8 and summarized in table Tab. 11.2. Scaling of the IO bands was evaluated relative to IO(4 ← 0), since no independent measurement of the true IO concentration was available. IO(4 ← 0) was chosen as scaling reference, as it is assumed to be the best characterized transition in Gómez Martín et al., 2005, being the strongest transition without the anomalous pressure dependence described in section 11.1.1. For all bands where the squeeze  $\beta_2$  was not significant or not stable over the evaluated spectra, the shift was determined using the fit with  $\beta_2$  fixed to zero. Furthermore, for all bands where the shift  $\beta_1$  was not significant it was discarded in the correction.

The most significant correction is found for the IO(2 ← 0) transition, which is up-scaled by 53%, shifted 0.09 nm towards shorter wavelengths and 12% narrower (squeeze), hinting at an insufficient correction of the pressure anomaly in Gómez Martín et al. [2005]. Furthermore the IO( $\nu' \leftarrow 1$ ) transitions of vibrationally excited IO are about 50% weaker after the correction, possibly due to a non-equilibrium population of IO ( $X^2\Pi_{3/2}, \nu'' = 1$ ) in Gómez Martín et al. [2005]. Minor corrections are found for the remaining absorption bands. Comparison with the uncorrected Gómez Martín et al. [2005] cross section is shown in Fig. 11.3.

### 11.2.1. Validation of the Correction for the IO(2 ← 0) Transition

For the IO(2 ← 0) transition a larger data set with IO levels down to 10 ppt could be used to validate the scaling factor  $\beta_0$  determined in the last section. Unfortunately, in the larger data set the signal to noise ratio of the IO absorption is not good enough to validate the shift and squeeze parameter of the IO(2 ← 0), or any parameters of the other bands. IO was fitted over the spectral windows from 425.3 nm to 447.8 nm, simultaneously with NO<sub>2</sub>, O<sub>4</sub>, H<sub>2</sub>O and an additional single band IO(2 ← 0) cross section. The IO(2 ← 0) was extracted

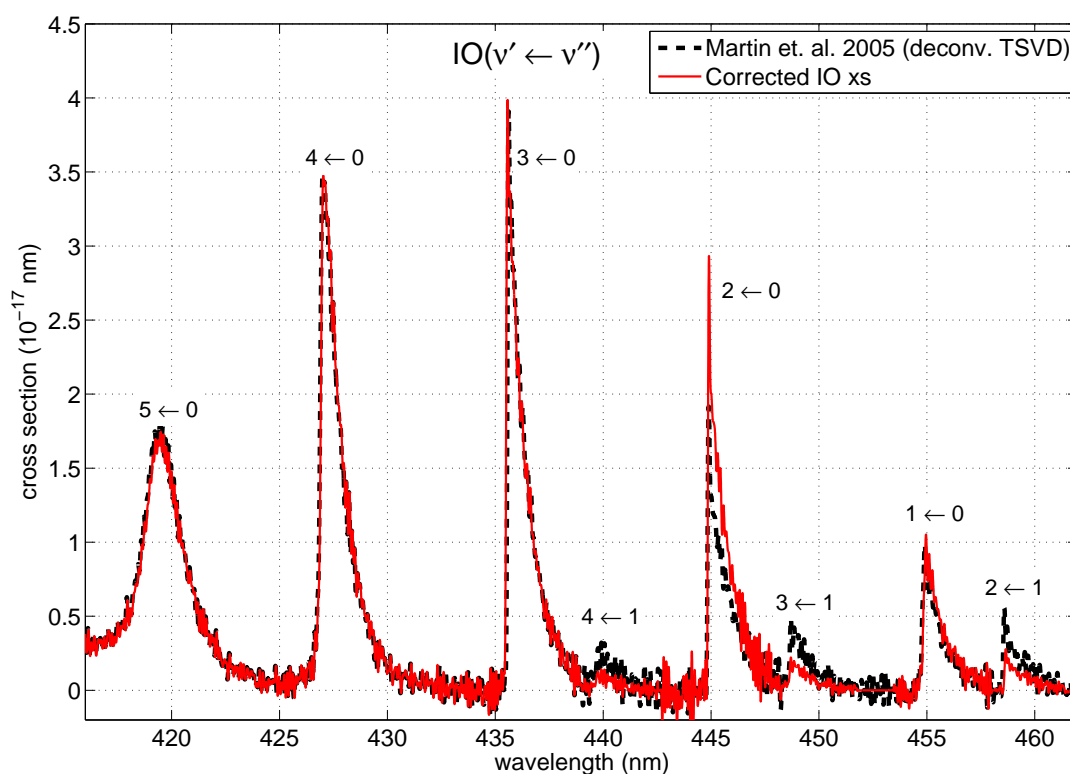


**Figure 11.3.** | Comparison between the IO cross section before and after the correction.

Strongest difference is found for the IO( $2 \leftarrow 0$ ), which becomes 53% stronger, shifted 0.09 nm towards shorter wavelengths and about 12% narrower after correction. Furthermore the transitions of vibrationally excited IO( $\nu' \leftarrow 1$ ) are about 50% weaker after the correction. Minor corrections are found for the remaining absorption bands.

from Gómez Martín et al. [2005] in the spectral range from 442 nm to 447.8 nm, covering the IO( $2 \leftarrow 0$ ) transition, and is zero elsewhere. Thus, the scaling correction for the IO( $2 \leftarrow 0$ ) band can be retrieved from the correlation between the fit of the full IO cross section and the IO( $2 \leftarrow 0$ ) cross section. Detailed information on the fitting scenario is shown in Tab. 11.3.

Five different data sets recorded by three different instruments, during the campaigns in Ireland 2012 and New-Zealand 2013, were used for the retrieval of the scaling factor  $\beta_0$  for the IO( $2 \leftarrow 0$ ) transition. In order to reduce the influence of  $\text{NO}_2$  and systematic errors, the data set was further reduced by the following filters:

- IO mixing ratio more than 10 ppt (from fit of the full IO cross section)
- $\text{NO}_2$  less than 1 ppb
- $\text{NO}_2/\text{IO}$  ratio less than 25, to ensure that IO absorption is stronger than the  $\text{NO}_2$  absorption

correction factor	campaign	instrument	time span	correlation plot
$1.54 \pm 0.01$	IRL 2012	OP-CE-DOAS MK-I	07/19 - 07/25/2012	Fig. A.9
$1.52 \pm 0.01$	IRL 2012	OP-CE-DOAS MK-I	08/05 - 08/06/2012	Fig. A.10
$1.55 \pm 0.03$	IRL 2012	CP-CE-DOAS	07/26 - 08/04/2012	Fig. A.11
$1.52 \pm 0.02$	NZ 2013	OP-CE-DOAS MK-II	03/12 - 03/16/2013	Fig. A.12
$1.526 \pm 0.004$	NZ 2013	OP-CE-DOAS MK-II	03/21 - 04/04/2013	Fig. A.13

**Table 11.4.** | Correction factors for the strength of the  $\text{IO}(2 \leftarrow 0)$  transition, retrieved from different data sets. The derived correction factors, agree with the scaling factor of 1.53 from the last section within 1%

- RMS of the fit residual less than  $10^{-3}$

The corresponding correlation plots between the fit of the full IO cross section and the  $\text{IO}(2 \leftarrow 0)$  cross section are shown in appendix A, Fig. A.13 to Fig. A.11. The derived correction factors, summarized in Tab. 11.4, agree with the scaling factor of 1.53 (section 11.2) within 1%.

### 11.2.2. Effect on the Data Analysis

This section analyzes effects on the DOAS analysis when using the corrected IO cross section determined in this section, instead of the uncorrected Gómez Martín et al. [2005] literature reference. The data set used for this analysis was recorded with the OP-CE-DOAS MK-II instrument from 03/21/2013 to 04/04/2013 in New Zealand, details on the time series for the observed trace gases are given in sec. 13.4. The data was evaluated according to the retrieval scenario in Tab. 11.1 once using the uncorrected Gómez Martín et al. [2005] literature reference and once using the corrected IO cross section. As expected the IO mixing ratios retrieved from both scenarios shows a linear correlation, but IO mixing ratios retrieved using Gómez Martín et al. [2005] are consistently higher by 5% as shown in the Fig. 11.4 a). Fitting over four IO absorption bands ( $5 \leftarrow 0$  to  $1 \leftarrow 0$ ) reduced the effect of the relatively large error in the  $\text{IO}(2 \leftarrow 0)$  band on the retrieved mixing ratios. However, when using smaller spectral ranges the influence of individual absorption bands becomes higher. In CE-DOAS application also the wavelength depended mirror reflectivity and thus  $\bar{L}_0(\lambda)$  changes the weight of the individual bands in the DOAS fit.

Figure 11.4 b) shows the corresponding series of fit residual for the evaluation with the uncorrected Gómez Martín et al. [2005] cross section. Figure 11.4 c), which shows the fit residuals for the corrected IO cross section, clearly shows much smaller systematic residual structures, especially at the  $\text{IO}(2 \leftarrow 0)$  transition. As shown in Fig. 11.4 d) the portion of unaccounted IO in the fit residual is strongly reduced for the retrieval with the corrected IO cross section. However, there is still a linear correlation visible between the fit residuals RMS and the observed IO absorption. Fig. 11.4 e) shows the component of the residual correlating to the IO mixing ratio, which was extracted from the residual series using multiple linear

regression (see sec. 4.2.5.1).

In summary the derived correction of the IO absorption cross section significantly improves the DOAS analysis of IO. The determined correction was derived from field measurements and therefore is only a relative rescaling of the Gómez Martín et al. [2005] literature absorption cross section. Therefore, further laboratory work is necessary to verify this correction and extend it on the absolute scale. Also a higher spectral resolution would be necessary for a broad application with other DOAS instruments.

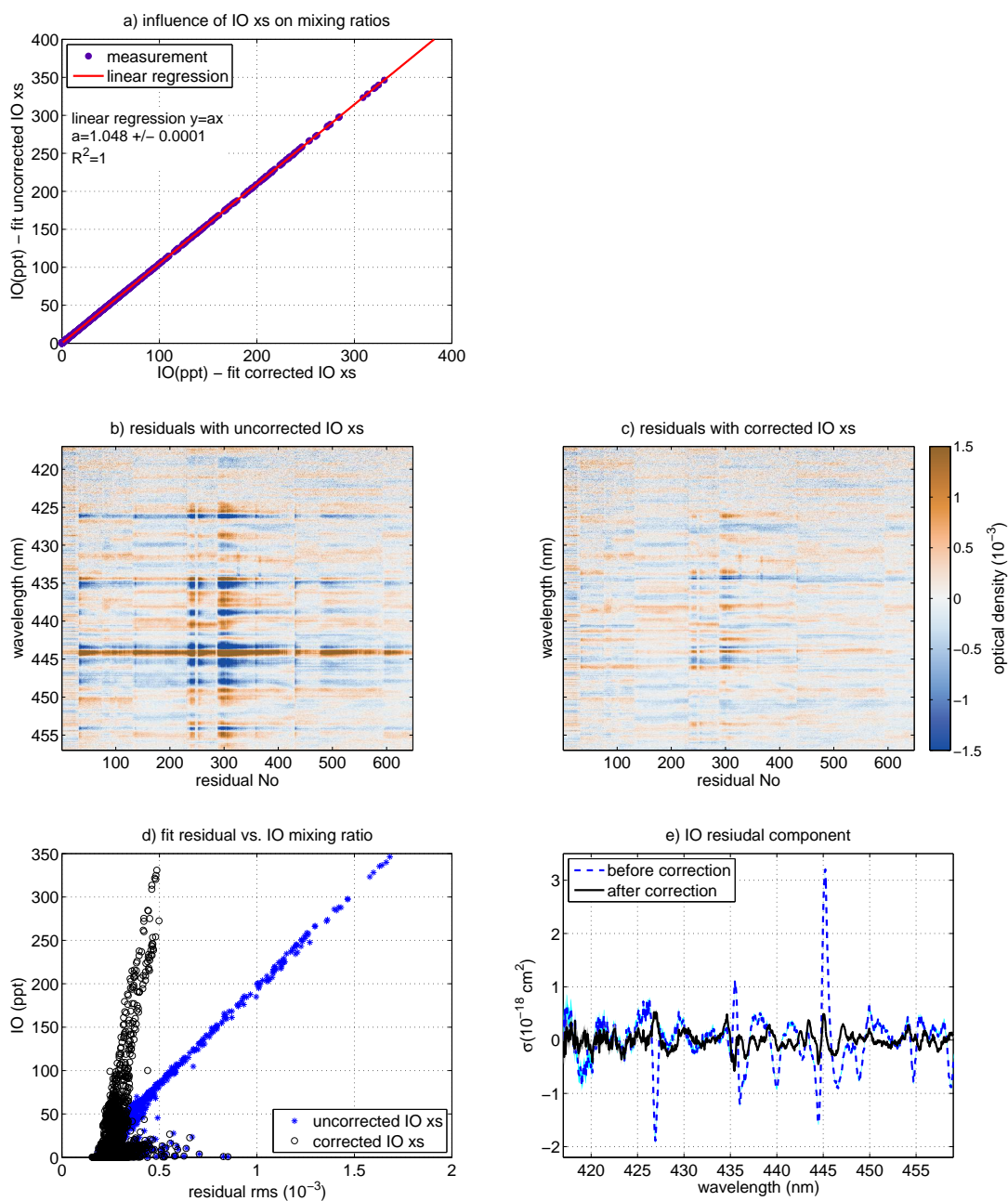


**Figure 11.4.** | Effect of using the corrected IO cross section in the DOAS retrieval. A data set recorded with the OP-CE-DOAS MK-II instrument from 03/21 to 04/04/2013 in New Zealand (see sec. 13.4), was evaluated with the corrected IO cross section derived in this section and the uncorrected literature cross section by Gómez Martín et al. [2005]. a) Using the uncorrected cross section yield 5 % higher IO mixing ratios. b) and c) Time series of residual spectra for the evaluation with the corrected and the uncorrected IO cross section. Horizontal stripes in b) are strong systematic residual structures when using the uncorrected IO cross section. d) Correlation between the RMS of the fit residual and the IO level. e) The residual component correlating with the IO mixing ratios.

## **Part IV.**

# **Investigation of Iodine Emissions from Coastal Seaweed**



# 12

## Ireland 2011/2012

In the frame of this thesis two campaigns were carried out on the west coast of Ireland in late spring 2011 and summer 2012. The objective was to study the atmospheric chemistry of reactive iodine emitted by seaweed using a new generation of mobile LP-DOAS and CE-DOAS instruments. A particular focus was to investigate the spatial distribution of reactive iodine on a local and regional scale, investigate and quantify different emission sources and study emission profiles. It was an aim also to cover two measurement sites that were already investigated before, like Mace Head and the Martin Ryan Institute (MRI), to compare them with our new observations, and very importantly to investigate how representative these previous observations are for the entire coast.

The outline of this chapter is as follows. Section 12.1 gives an overview of the measurement sites and seaweed distribution on the Irish west coast. Section 12.2 presents the measurement concept and the used instruments. Section 12.3 gives an overview on the meteorological conditions during both campaigns. In section 12.4 the measurement results of both campaigns are first summarized, followed by detailed results on a per-site basis, which is combined with detailed descriptions of the measurement sites. The results are analyzed and discussed in the following sections for the chemical interaction between IO and  $\text{NO}_x$  (section 12.6) and the dependence of observed IO on solar irradiance including night time chemistry (section 12.7). The regional distribution of IO in the investigated area is discussed (section 12.8), as well as local IO sources and their spatial distribution in the intertidal zone (section 12.9) and rates for the (secondary) IO emissions are determined (section 12.10). Section 12.11 formulates the conclusions on iodine sources on the Irish West Coast. In section 12.12 these new findings are used for improved estimates of the Irish and global iodine emissions on coastal sites. Summarizing conclusions for the entire chapter are given in section 14.1.

### 12.1. Measurement Sites

Both measurement campaigns took place in the Connemara region on the Irish West Coast, which features a very rugged coastline with many islands, peninsulas and bays. Measurements were performed at eight locations along the coastal strip between Lettermore Island in the south

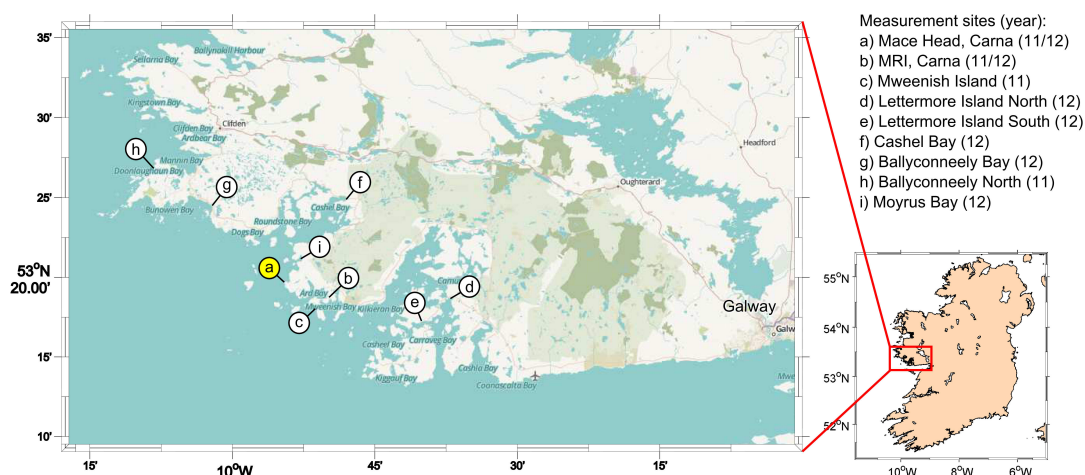


**Figure 12.1. | Overview of the measurement locations for the campaigns in 2011 and 2012.** Measurements took place in the Connemara region on the Irish West coast. Mace Head research station (a) is highlighted yellow as it played a special role, serving as location for reference measurements during the 2012 campaign. Both, Mace Head research station and the Martin Ryan Institute (MRI) are part of the National University of Ireland (NUI), Galway. Map layer [OpenStreetMap HDM](#) ©OpenStreetMap contributors. Shoreline taken from GSHHG [Wessel and W. H. F. Smith, 1996]

and Ballyconneely in the north (see sites labeled a-h in Fig. 12.1). This area is very rural and therefore local sources of anthropogenic emissions are relatively low. However, it is generally not a remote site due to local traffic, small boats and even increased pollution during peat land burning events. The prevailing westerly winds generally transport clean air from the Atlantic Ocean and therefore at the shoreline pollution events are observed mainly when air masses move in from the land or from the European continent.

The shoreline can be divided into the intertidal zone, which is regularly exposed to air due to the tidal movement and the subtidal zone which is always covered by water. The tidal pattern, i.e. the periodic rise and fall of the oceans sea level, at the Irish west coast is semi-diurnal with a period of about 12.5 h between two low waters. Furthermore, the amplitude of the tide is modulated by the relative position of sun and moon leading to a roughly semimonthly pattern [e.g. Morrissey and Sumich, 2011]. The maximum of the tidal amplitude, called spring tide, is found when the moon and sun are in alignment, i.e. at full moon and new moon. Correspondingly, the minimum tidal amplitude, called neap tide, is found when moon and sun are perpendicular relative to the earth, i.e. at half moon. Therefore during each lunar month (~ 27 d) two sets of spring and neap tide are encountered. According to the lunar cycle different low (and high) water marks are defined. The two datums used in this thesis are the average low water over the entire lunar cycle, short Mean Low Water (MLW) and the average low water at spring tide, short Mean Low Water Springs (MLWS).

### 12.1.1. Seaweed

The rocky shores of the Irish West Coast are an ideal habitat for many different seaweed species, about 80 species of green seaweed, 274 species of red seaweed and about about 147 species of brown seaweed [Morrissey et al., 2001]. Over 90 % of the seaweed biomass on the Irish West Coast is made up by brown seaweeds of the families *Laminariaceae* and *Fucaceae* [Irish Seaweed Center, 2001]. With a standing stock of more than 2 Mt fresh weight, the largest contribution comes from *Laminaria digitata* and *Laminaria hyperborea* [Hession et al., 1998; Morrissey et al., 2001], both of the family *Laminariaceae*. The second largest contribution comes from *Ascophyllum nodosum* (family *Fucaceae*), with an estimated standing stock of about 0.3 Mt [Hession et al., 1998], followed by *Fucus vesiculosus* (family *Fucaceae*) which contributes approximately half the biomass of *A. nodosum* [Irish Seaweed Center, 2001].

However, there is a distinct zonation between these dominant seaweed species as shown in Fig. 12.2. *Laminariaceae* species, which are intolerant of air exposure are the dominant species of the subtidal zone where they form large kelp forests. While *Laminaria hyperborea* is found exclusively in the subtidal zone, a small fraction of the *L. digitata* population (5-10 %) grows in the lower part of the intertidal zone around the MLWS. However, the air exposure of these intertidal *L. digitata* is very short ranging from zero during neap tide and a few minutes to an hour during spring tide (personal observation during the 2012 campaign). The dominant seaweed species of the intertidal zone are *Fucaceae* mainly *A. nodosum* and *F. vesiculosus*, growing in the mid-intertidal zone which is exposed to air more than four hours during each tidal period. *Fucus serratus* is another common *Fucaceae* which grows in the mid- to low intertidal zone, closing the gap to the “*Laminaria* zone”. The abundance and distribution of intertidal seaweeds is also dependent on the type of the shore (see Fig. 12.2). Wave sheltered shores and especially bays typically have an extended mid-intertidal zone with dense beds of *A. nodosum* and *F. vesiculosus* that can reach a cover of almost 100 %. With increasing wave exposure the abundance of intertidal seaweed decreases and the more wave resistant *F. vesiculosus* becomes the dominant species. Additional to the standing stock, also drift seaweed, washed up due to storms and tides is present in the intertidal zone and on beaches [Guiry and Blunden, 1991]. Reports by E. Kelly [2005] and Bruton et al. [2009] state that in Connemara every year large quantities of mainly *L. hyperborea* are cast ashore, mostly during the autumn and winter months but these events can occur at any time depending on when storms happen. However, there is little quantitative information on drift seaweed biomass on the Irish West Coast. According to Bruton et al. [2009] in some years up to 20 % of standing stocks of *L. hyperborea* are washed up on the Irish coast.

In the frame of this work, it was tried to get a representative coverage of the area by selecting measurement sites with different types of shores and seaweed population. However, the selection of sites is biased due to the fact that only locations with a close by road and good access could be chosen.

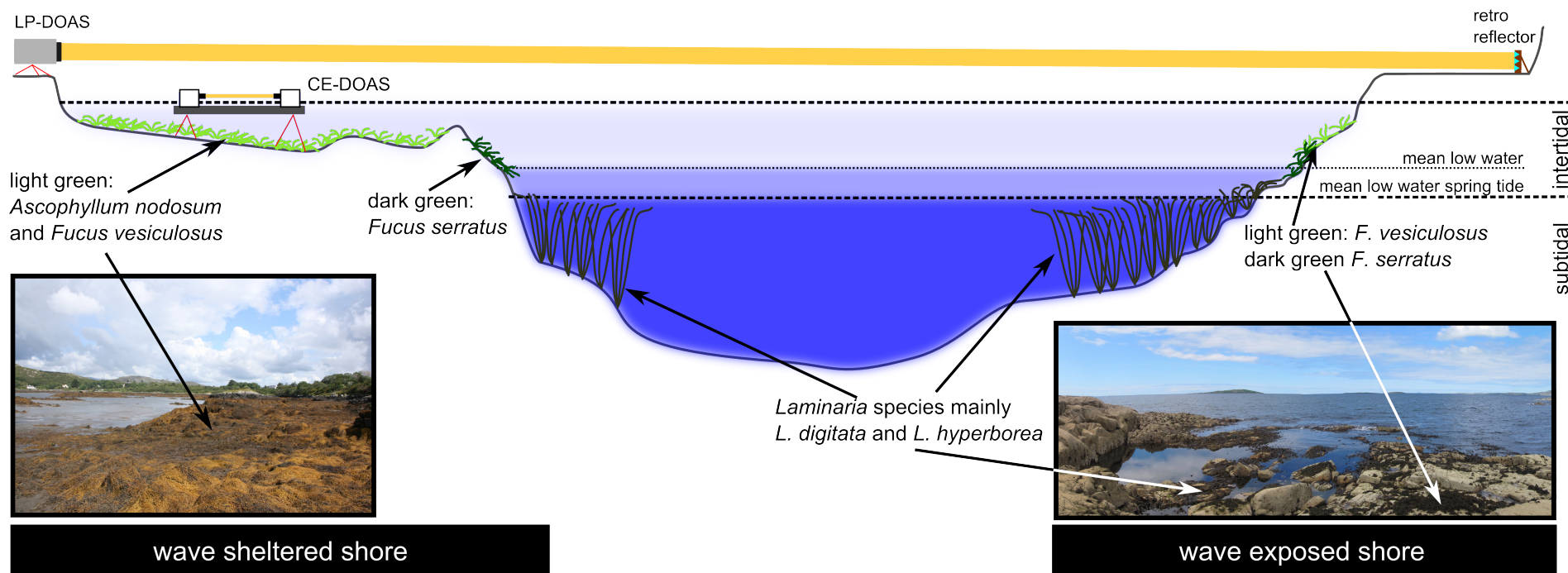


**Figure 12.2.** | Sketch of combined LP-DOAS and CE-DOAS measurements and seaweed distribution on different shore types.

**Measurement principle:** LP-DOAS measures average trace gas concentrations along a several hundred meter to kilometer long light path. The light path crosses intertidal areas with seaweed but also subtidal areas, always covered by water, and land. Complementary point measurements of trace gas concentrations were performed using mobile CE-DOAS instruments. If possible, the CE-DOAS was moved into the intertidal zone during low tide to get in-situ concentrations over seaweeds, the expected major source of reactive iodine. **Shore types:** Wave sheltered shores (left hand side) have an extended intertidal zone with dense seaweed beds, mainly *A. nodosum* and *F. vesiculosus*. On wave exposed shores (right hand side) the intertidal area is generally smaller and the seaweed density is lower.

time period	exposure time (ms/scan)	# scans accumulated
5/19 - 5/21/2011	40	1000
from 5/22/2011	30	1000
7/15 - 7/29/2012	20	1000
from 7/30/2012	10	1000

**Table 12.1.** | Summary for the Open Path CE-DOAS measurement parameters. The exposure times were adapted so that the saturation of the detector did not exceed 60 %. In order to reduce delays due to USB data transfer, 1000 subsequent scans were accumulated in the spectrograph before they were transferred to the PC and saved as a spectrum.

## 12.2. Instrumentation

In order to investigate the reactive iodine chemistry on different spatial scales, a new combination of spatially averaging and in-situ measurement techniques was applied as illustrated in Fig. 12.2. LP-DOAS measures along a several hundred meter to kilometer long light path. It was usually tried to mainly cross seaweed rich intertidal areas, but due to the shape of the shoreline and available locations to setup the telescope and the retro reflector, at least parts of the light path always crossed constantly submerged subtidal areas and even short parts of the land. Thus, LP-DOAS measures average trace gas concentrations over these different areas crossed by the light path. Complementary point measurements of trace gas concentrations were performed using mobile CE-DOAS instruments. If possible, the CE-DOAS was moved into the intertidal zone during low tide to get in-situ concentrations over seaweeds, the expected major source of reactive iodine at the field sites.

In both campaigns the Open Path CE-DOAS Mark I (sec. 5.1) was applied for in-situ measurements of IO and NO<sub>2</sub>. However, some modifications were made between the campaigns. Most importantly, in 2011 broadband CRDS was used for path lengths calibration and in 2012 the wavelength resolved CRDS system was used. Both are described in sec. 5.1. The measurement routine described in sec. 5.1 was followed in both campaigns, but the spectrograph exposure time varied over the campaigns as summarized in Tab. 12.1. During both campaigns the mirrors were contaminated with raindrops or aerosol several times. Mirror cleaning was difficult due to missing clean lab conditions and often was performed in the field. Thus, the optical path lengths obtained after the cleaning process varied strongly. Every time the mirrors had to be cleaned, the measurement series was divided into a new sequence called mirror configuration. An overview of the different mirror configurations with path lengths and light intensities is shown in Fig. C.1 for 2011 and Fig. C.2 for 2012. During the campaign of 2012, the Compact Closed Path CE-DOAS was applied for additional IO and NO<sub>2</sub> in-situ measurements at a higher spatial resolution. A description of the instrument and the measurement routine is given in sec. 6. Since the sampled air passed a particle filter before it entered the closed measurements cell, no contamination of the resonator mirrors did occur during the entire campaign, which made the field operation much easier compared to the Open Path CE-DOAS Mark I instrument.

The MoLP-DOAS was applied in both campaigns for path averaged measurements of IO, NO<sub>2</sub> and I<sub>2</sub>, at different sites. A description of the instrument and the measurement routine

is given in sec. 7.2. Description of the different light paths, which varied between 532 m to 6160 m length, is given in the result section 12.4 for the individual measurement sites. Additionally, in 2012 the stationary “Mace Head LP-DOAS” instrument for IO, I<sub>2</sub>, OIO and NO<sub>2</sub> (sec. 7.1) was applied at Mace Head. The idea was to get reference measurements at Mace Head, reducing the influence of meteorology when comparing the mobile measurements. Additionally it also allowed to set our measurements in relation to previous studies, carried out mainly at Mace Head. It should also be noted that, like in previous studies at Mace Head, the stationary LP-DOAS mostly measured over the constantly submerged intertidal zone (> 90 % of the light path), giving average mixing ratios for the larger coastal area.

The spectroscopic measurements were complemented with basic measurements of the local meteorology at the different measurement sites, using a mobile Oregon Scientific WMR200 weather station. The meteorological station at the Mace Research Station, operated by National University of Ireland Galway, provided a complete set of meteorological parameters, which was the main set of meteorological data used for the data interpretation. During the 2012 campaign, additional nano-SMPS measurements of the particle size distribution at Mace Head were provided by the National University of Ireland Galway. For all measurement locations the tidal height at Galway port is used, which is the closest station of the Irish National Tide Gauge Network. Details on these complementary measurements is provided in sec. (see 8.1).

## 12.3. Meteorology

This section gives a general overview of the meteorological conditions in 2011 and 2012, based on the measurements at Mace Head by NUIG (sec. 8.1.1) and personal observations. Measurements of wind speed and direction at other sites are presented separately in the results section 12.4. At the MRI no local wind measurements are available due to instrumental problems. Fortunately the Mace Head data is relatively representative for MRI since both locations are close by without significant elevations in between.

### 12.3.1. Meteorology 2011

During the 21 days of the campaign the meteorological conditions were relatively cloudy and rainy with only short periods of sunshine. June 2nd was the only cloud free and sunny day. Figure 12.3 shows an overview of the meteorological conditions at Mace Head (for details on the National University of Ireland Galway (NUIG) weather station see sec. 8.1.1). The average air temperature was 11 °C and varied between 7 °C and 18 °C. Relative humidity

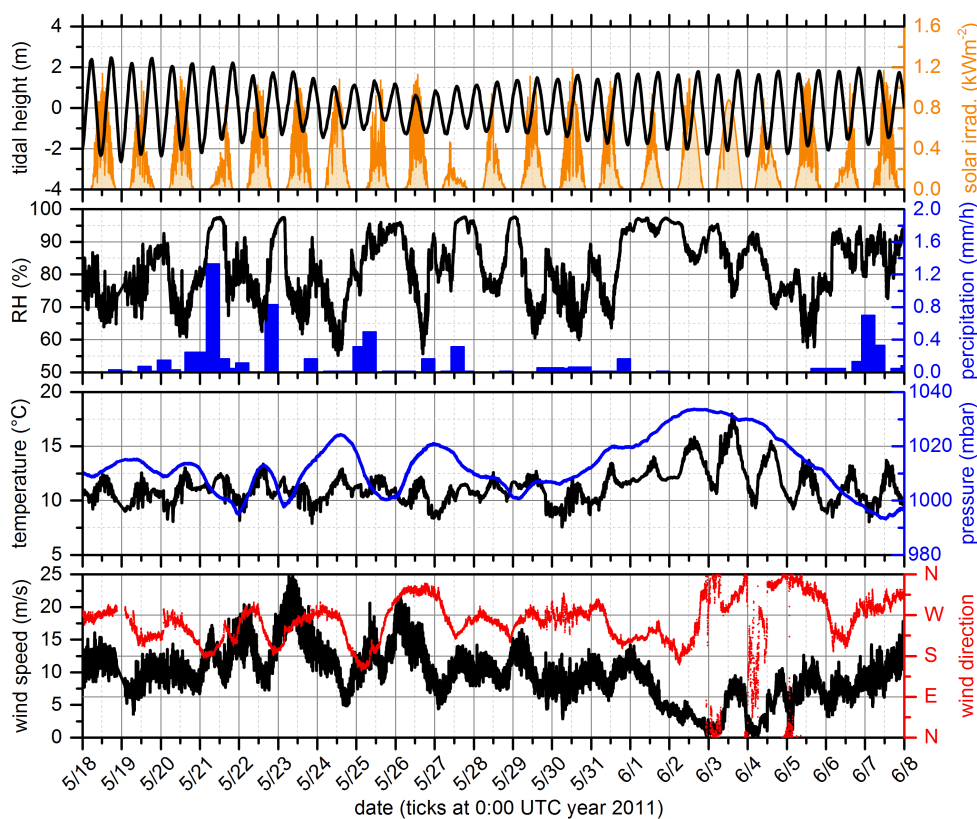


**Figure 12.3.** | Overview of the meteorology at Mace Head during the the 2011 campaign. (Data from Darius Ceburnis NUIG, pers. com.)

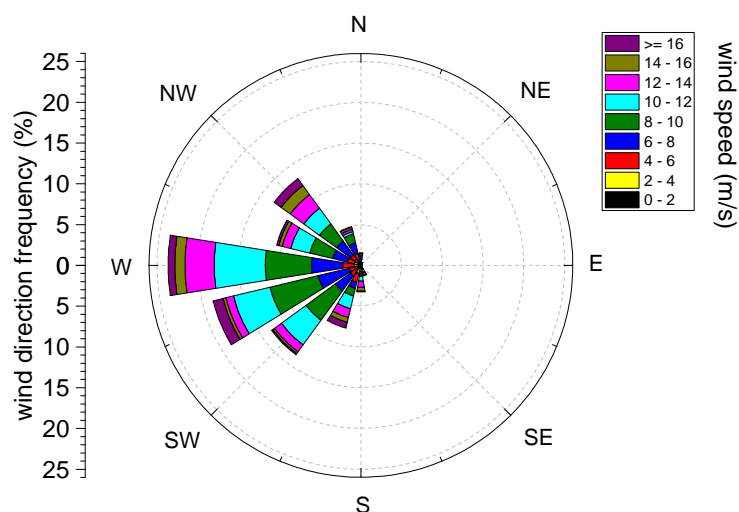


**Figure 12.4.** | Distribution of wind direction and speed at Mace Head during the 2011 campaign. (Data from Darius Ceburnis NUIG, pers. com.)

showed variations between 55 % and 98 %, which is typical for oceanic climate. The wind speed was on average 9.7 m/s which is relatively high but normal for a coastal site. On May 23rd a heavy storm took place with a maximum wind speed of 25.2 m/s and gust up to 31 m/s. The prevalent wind direction was south-west to west (Fig. 12.3) which is in the clean air sector for Mace Head.

### 12.3.2. Meteorology 2012

During the 25 days of the campaign in 2012, the weather was generally warmer and sunnier, as compared to the 2011 campaign, but still only few days were completely free of rain. Most days were cloudy and showed very variable weather conditions with periods of sunshine and quick rain showers. Figure 12.5 shows an overview of the meteorological conditions at Mace Head during this campaign. The average air temperature was 14 °C, varying between 9 °C and 21 °C. Relative humidity varied between 54 % and 99 %. Wind speed was moderate, compared to the previous year, with an average of 6 m/s and a maximum of 16 m/s. At Mace Head the wind direction was mainly west to north-west (Fig. 12.6) leading to relatively clean conditions with NO<sub>2</sub> levels mostly below 0.5 ppb. Between July 30th and August 4th, the wind turned and air masses from the southern and eastern to north-eastern sector were transported to this area, leading to events of elevated NO<sub>2</sub> (see Fig. 12.6).

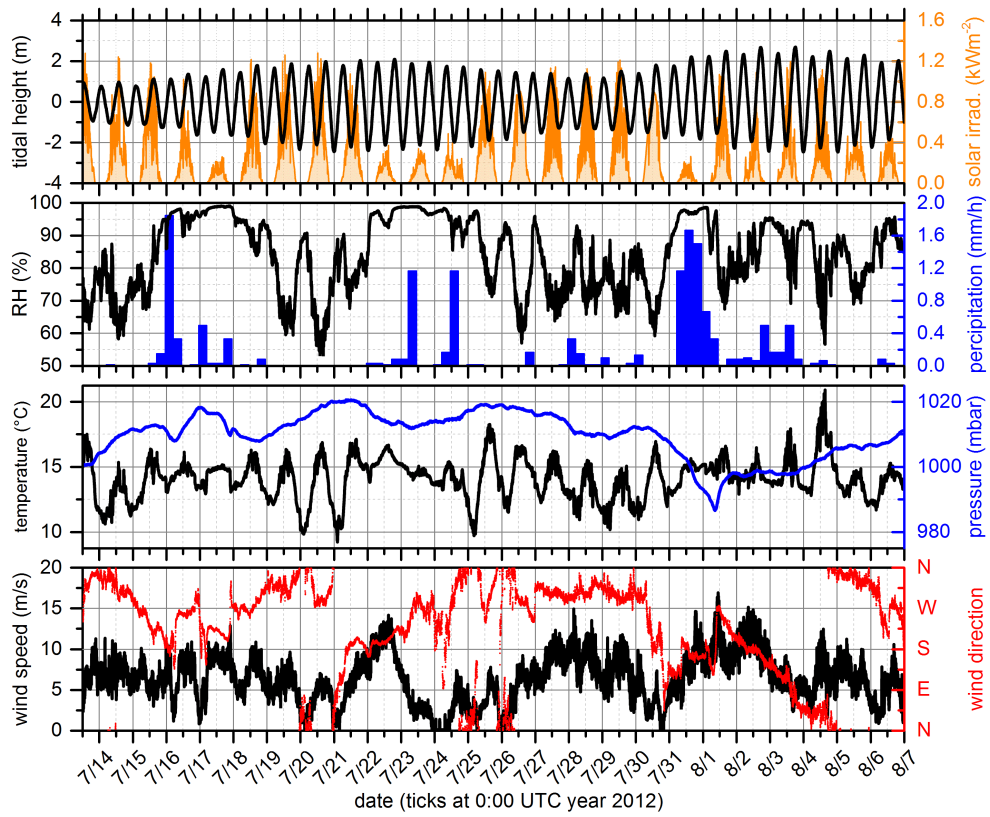


**Figure 12.5.** | Overview of the meteorology at Mace Head during the the 2012 campaign. (Data from Darius Ceburnis NUIG, pers. com.)

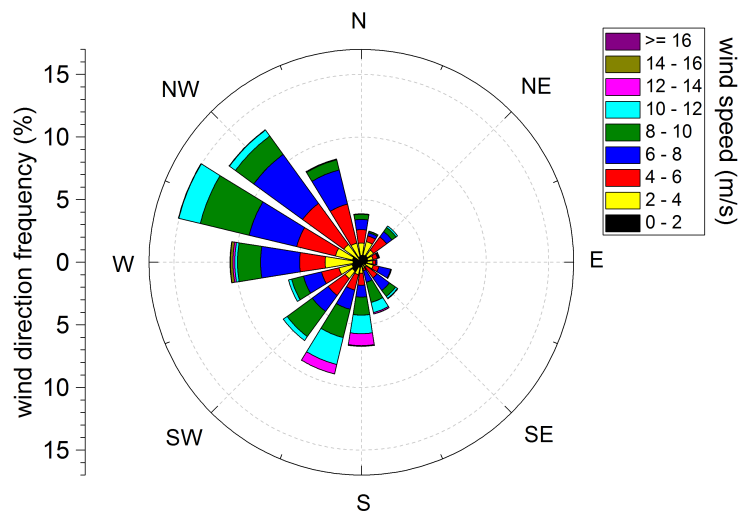


**Figure 12.6.** | Distribution of wind direction and speed at Mace Head during the 2012 campaign. (Data from Darius Ceburnis NUIG, pers. com.)

## 12.4. Results

For the first time, successful direct in-situ measurements of atmospheric IO by Open Path Cavity Enhanced DOAS were performed using the newly developed Open Path CE-DOAS Mark I instrument. These are also the first in-situ observations of IO directly above seaweed in the intertidal zone.

Figure 12.7 and 12.8 show the series of IO and NO<sub>2</sub> mixing ratios observed during the 2011 and 2012 campaign respectively. Tables 12.2, 12.3 and 12.4 give an overview of the resulting mixing ratios and detection limits at every measurement site for the Open Path CE-DOAS, MoLP-DOAS and the Mace Head LP-DOAS respectively. For the MoLP-DOAS, additionally, the lengths of the LP-DOAS light paths are given. Details on the DOAS retrieval are discussed in the instrument sections 5.1 (Open Path CE-DOAS), 6 (Closed Path CE-DOAS), 7.2 (MoLP-DOAS) and 7.1 (Mace Head LP-DOAS). Measurements with the Closed Path CE-DOAS did not give quantitative results due to unknown losses of IO in the sampling system, which is further discussed in sec. 12.5.

IO and NO<sub>2</sub> were regularly observed above their respective detection limits by the Open Path CE-DOAS, MoLP-DOAS and the Mace Head LP-DOAS, while I<sub>2</sub>, OIO and (CHO)<sub>2</sub> could not be detected. In agreement with previous studies, observation of IO always coincided with low tide periods during daytime [e.g. Aliche et al., 1999; Hebestreit, 2001; Seitz et al., 2010; Commane et al., 2011]. Contrary to Saiz-Lopez and Plane [2004] and Mahajan et al. [2009], no IO was identified above the detection limit during nighttime by either the CE-DOAS or the LP-DOAS, which is further discussed in sec. 12.7.1. Open path CE-DOAS in-situ measurements show strong horizontal variations of IO levels on scales between few meters and several ten meters, with the highest IO mixing ratios of several 10 ppt and up to more than 100 ppt when measuring directly above seaweed exposed during low tide. These findings support the “hot-spot” theory described in Burkholder et al. [2004]. Measurements of the vertical IO gradient in the first two meters over seaweed patches show a strong decline of the IO mixing ratio with increasing height (see sec. 12.10). Depending on the measurement site and meteorology also the LP-DOAS could observe several 10 ppt IO on larger scales of several 100 m. A detailed discussion of small scale variations in the IO mixing ratios is given in sec. 12.9. Additionally, strong differences in the IO concentrations were observed between the different sites, with much lower IO levels at Mace Head, as compared to the other sites. This important finding is further discussed in sec. 12.8 as the question arises how representative all previous studies at Mace Head are for the whole coastline.

As expected for a rural area, the observed NO<sub>2</sub> mixing ratios were generally low, with average mixing ratios of less than 300 ppt at most sites. The presence of elevated NO<sub>2</sub> levels > 500 ppt strongly depended on the measurement sites and the wind direction and could be used as an indication for generally polluted air masses.

The shoreline, seaweed abundance and measurement geometry significantly differ between the measurement sites. Therefore, the following sections present more detailed results for each measurement site together with a more detailed description of the respective site and instrumental setup.

Location (year)	IO mixing ratio (ppt)			NO <sub>2</sub> mixing ratio (ppb)		
	average	max.	av. d. l.	average	max.	av. d. l.
Mace Head (11)	3.7 ± 1.1	15.3 ± 1.0	2.3 ± 1.5	0.05 ± 0.07	0.6 ± 0.1	0.13 ± 0.09
Mace Head North (11)	6.3 ± 1.3	25.0 ± 1.6	2.5 ± 0.4	< d. l.	< d. l.	0.13 ± 0.03
MRI (11)*	7.3 ± 0.8	58.0 ± 3.7	1.6 ± 0.8	0.02 ± 0.05	4.2 ± 0.1	0.09 ± 0.05
Mweenish (11)	22.0 ± 0.7	40.0 ± 0.7	1.3 ± 0.2	< d. l.	< d. l.	0.07 ± 0.01
Ballyconneely North (11)	15.4 ± 1.0	30.7 ± 0.8	1.9 ± 0.3	< d. l.	< d. l.	0.11 ± 0.02
Mace Head (12)	1.5 ± 1.0	14.9 ± 0.6	1.9 ± 1.2	0.05 ± 0.05	0.44 ± 0.06	0.11 ± 0.07
MRI (12)**	3.9 ± 1.2	65.8 ± 0.8	2.3 ± 0.8	0.23 ± 0.07	5.2 ± 0.1	0.14 ± 0.05
Lettermore North (12)	20.8 ± 0.7	50.5 ± 0.7	1.4 ± 0.3	0.31 ± 0.04	1.4 ± 0.0	0.08 ± 0.02
Lettermore South (12)	5.3 ± 1.1	24.9 ± 0.7	2.1 ± 0.6	0.70 ± 0.06	2.0 ± 0.0	0.12 ± 0.04
Cashel Bay (12)	27.7 ± 1.1	62.4 ± 1.1	2.3 ± 0.7	0.16 ± 0.05	0.3 ± 0.1	0.10 ± 0.03
Ballyconneely Bay (12)	10.7 ± 0.4	37.4 ± 0.4	0.86 ± 0.03	0.21 ± 0.03	0.6 ± 0.0	0.05 ± 0.00

**Table 12.2.** | Overview of the IO and NO<sub>2</sub> mixing ratios and detection limits measured by the Open Path CE-DOAS. For each species average and maximum mixing ratios and the average detection limit (av. d. l.) is given. Errors for the average mixing ratios are the average measurement errors. For the average detection limit the standard deviation is given as uncertainty. Retrieved (CHO)<sub>2</sub> mixing ratios were always below the detection limit of (0.12 ± 0.03) ppb. \* For the measurements at the MRI in 2011 the period between June 1st and June 2nd was excluded from the calculation of the average detection limit, since the detection limit was about 10 times higher due to instrumental problems. \*\* Profile measurements on July 30th, which went down to 10 cm above the seaweed, were excluded from this overview.

Location (year)	a. p. l. (m)	IO mixing ratio (ppt)			NO <sub>2</sub> mixing ratio (ppb)		
		average	max.	av. d. l.	average	max.	av. d. l.
Mace Head (11)	6160	0.9 ± 0.6	5 ± 1	1.1 ± 0.4	0.07 ± 0.04	0.78 ± 0.03	0.08 ± 0.03
MRI short path (11)	532	2 ± 7	35 ± 7	14 ± 3	0.4 ± 4	2.5 ± 0.5	0.7 ± 0.5
MRI mid path (11)	1112	4 ± 4	27 ± 4	8 ± 3	0.3 ± 0.3	1.3 ± 0.5	0.5 ± 0.2
MRI long path (11)	3780	2 ± 2	19 ± 2	3 ± 1	0.3 ± 0.1	1.8 ± 0.1	0.18 ± 0.07
Mweenish Isl. (11)	1710	5 ± 3	14 ± 3	6.5 ± 0.5	-	< d. l.	0.44 ± 0.03
Ballyconneely North (11)	1002	3 ± 4	11 ± 5	8.7 ± 0.9	-	< d. l.	0.60 ± 0.07
Mace Head South (12)	638	-	< d. l.	11 ± 1	-	< d. l.	0.8 ± 0.1
Moyrus Bay (12)	1978	1 ± 2	14 ± 2	3.5 ± 1.3	0.1 ± 0.2	0.5 ± 0.1	0.3 ± 0.1
MRI (12)	1264	6 ± 2	46 ± 4	3.6 ± 1.6	0.2 ± 0.1	2.3 ± 0.1	0.1 ± 0.1
Lettermore North (12)	1744	4 ± 2	30 ± 2	3.7 ± 0.5	0.1 ± 0.2	0.4 ± 0.2	0.27 ± 0.04
Lettermore South (12)	1616	4 ± 2	14 ± 2	3.6 ± 0.5	0.7 ± 0.2	2.5 ± 0.2	0.27 ± 0.04
Cashel Bay (12)	1396	10 ± 2	19 ± 2	3.8 ± 0.4	0.2 ± 0.1	0.4 ± 0.1	0.28 ± 0.03
Ballyconneely Bay (12)	2070	7 ± 1	18 ± 1	2.1 ± 0.2	0.3 ± 0.1	0.5 ± 0.1	0.15 ± 0.01

**Table 12.3.** | Overview of the IO and NO<sub>2</sub> mixing ratios and detection limits measured by the MoLP-DOAS. For each species average and maximum mixing ratios and the average detection limit (av. d. l.) is given. Errors for the average mixing ratios are the average measurement errors. For the average detection limit the standard deviation is given as uncertainty. Furthermore, the absorption path length (a. p. l.) is provided for each site. Measurements of I<sub>2</sub> at the MRI in 2012 were always below the detection limit of (125 ± 36) ppt.

species	average	maximum	av. d. l.
IO	$(1.0 \pm 0.9)$ ppt	$(13 \pm 1)$ ppt	$(2.2 \pm 0.5)$ ppt
I <sub>2</sub>	-	< det. lim.	$(75 \pm 10)$ ppt
NO <sub>2</sub>	$(0.28 \pm 0.09)$ ppb	$(3.0 \pm 0.1)$ ppb	$(0.18 \pm 0.04)$ ppb
(CHO) <sub>2</sub>	-	< det. lim.	$(0.16 \pm 0.04)$ ppb

**Table 12.4.** | Overview of the mixing ratios and detection limits for the species measured by the Mace Head LP-DOAS during campaign 2012 (light path 6160 m) For each species average and maximum mixing ratios and the average detection limit (av. d. l.) are given. Errors for the average mixing ratios are the average measurement errors. For the average detection limit the standard deviation is given as uncertainty.

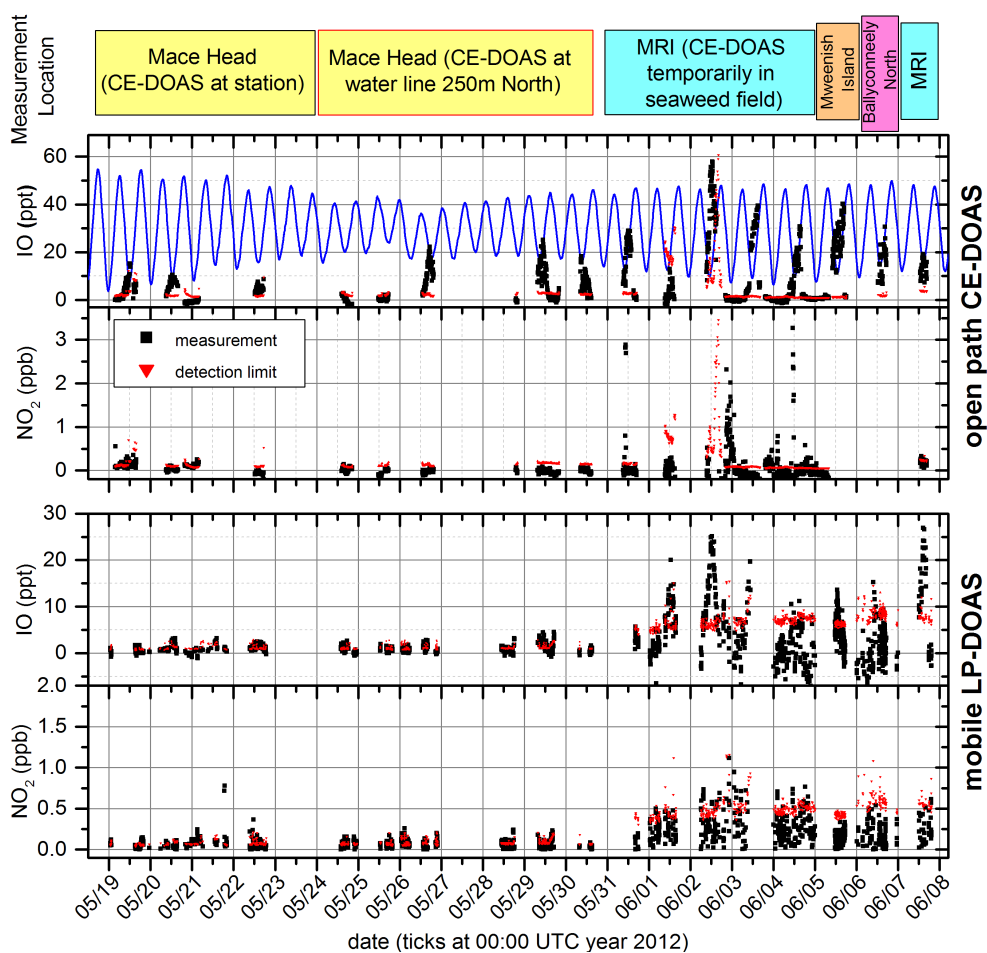


**Figure 12.7.** | Overview of the DOAS measurements during the 2011 campaign. IO and NO<sub>2</sub> mixing ratios observed by the different instruments are shown as black dots, and the respective detection limits in red. The top row indicates the location of the CE-DOAS and the mobile LP-DOAS. For a map of the measurements sites see Fig. 12.1.

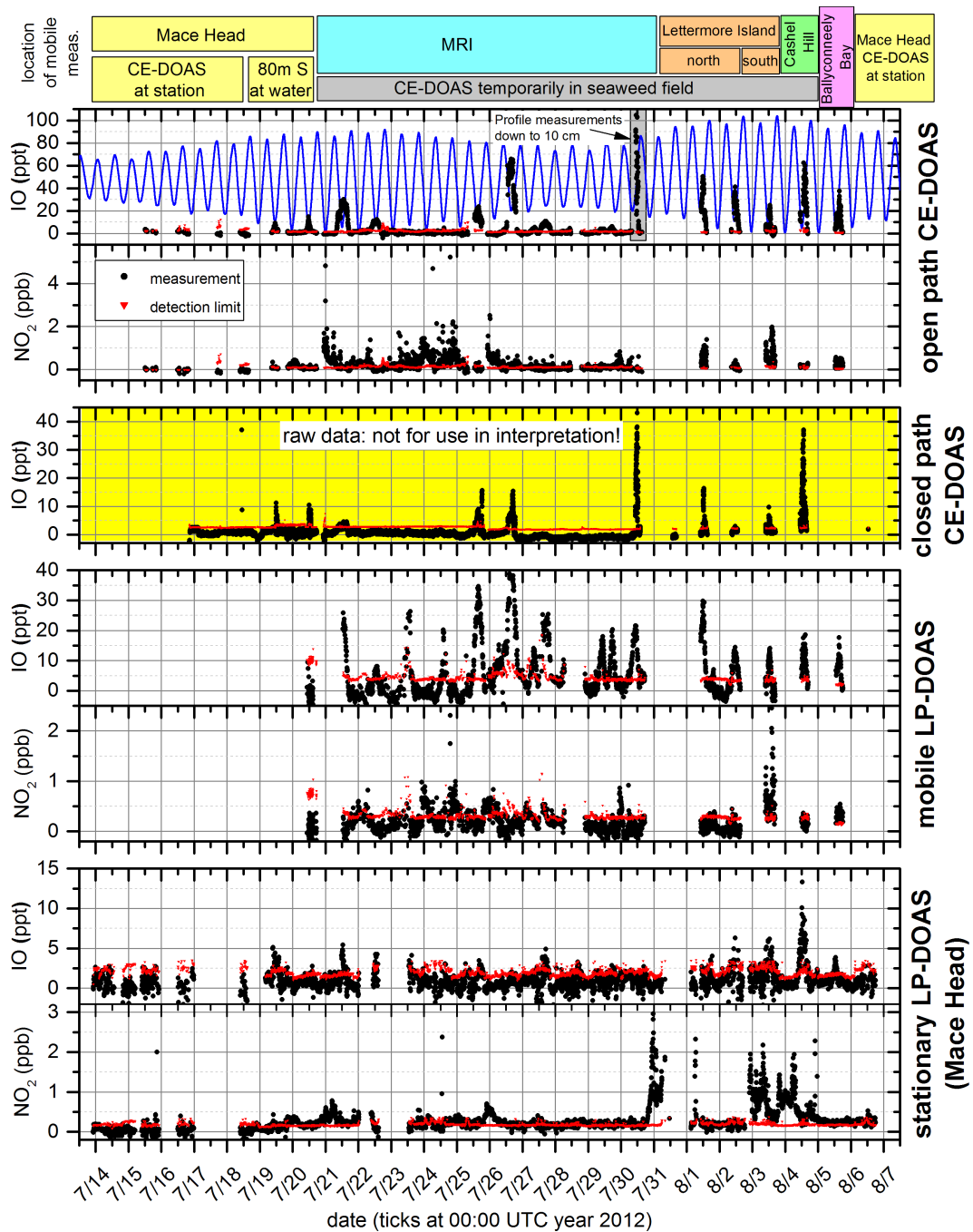


**Figure 12.8.** Overview of the DOAS measurements during the 2012 campaign. IO and NO<sub>2</sub> mixing ratios observed by the different instruments are shown as black dots, and the respective detection limits in red. The top row indicates the location of the CE-DOAS instruments and the mobile LP-DOAS. For a map of the measurements sites see Fig. 12.1. Closed Path CE-DOAS data are not used due to instrumental problems (see sec. 12.5).

### 12.4.1. Mace Head

The Mace Head Atmospheric Research station, operated by NUIG, is located on a remote headland north-west of Carna about 60 km east of Galway. It is a clean air site for wind directions between 180° and 300°, which is the case for 60 % of the air masses arriving at the station. Since local emissions are negligible, the station is ideal for studies under northern hemisphere background conditions. Due to the ideal location and due to the provided infrastructure, necessary for most classic instruments, Mace Head has been the main location for studies of reactive halogen chemistry and iodine emissions by seaweed on the Irish west coast [e.g. Alicke et al., 1999; Hebestreit, 2001; Saiz-Lopez and Plane, 2004; Seitz, 2009; Commane et al., 2011]. LP-DOAS light paths used in previous studies are shown in Fig. 12.9.

The Mace Head research station consists of three laboratory buildings, two lower cottages at about 90 m and the upper cottage at about 300 m from the shore. This is illustrated in the sectional view in Fig. 12.10. Close to the upper cottage is a 10 m meteorological tower where data such as wind speed, wind direction, pressure, temperature, relative humidity and solar radiation are measured continuously.

The shore west to the station, which is strongly wave exposed, is predominantly inhabited by the kelps *L. digitata* and *L. hyperborea* (see Fig. 12.9). Therefore, previous observations of IO at the Mace Head station were attributed to these seaweed species. However, during the 2011 and 2012 campaigns it was observed, that only a small fraction of *L. digitata* is in the intertidal zone and therefore ever exposed to air. This is in agreement with previous measurements, where high IO levels were observed only at spring tide [e.g. Seitz, 2009; Commane et al., 2011]. A much larger abundance of intertidal seaweed was found in the small sheltered bay directly north of the station and the larger Moyrus Bay about 3km north east of the station, both predominantly inhabited by *A. nodosum* and *F. vesiculosus*. Mobile measurements at different locations close to Mace Head, for the first time allowed the estimation of sources relevant for reactive iodine measurements at Mace Head.

Measurements at Mace Head station were made during both campaigns in 2011 and 2012. An overview of instrument locations and the LP-DOAS light path is given in Fig. 12.9.

#### 12.4.1.1. Campaign 2011

Measurements in 2011 were performed between May 19th and May 30th. This period of the campaign was conducted in the frame of the ACTRIS project MaCloud Inc. (Marine Aerosol –Cloud Interactions). MaCloud Inc. was aimed to built on recent advances in marine aerosol formation, both in in terms of secondary and primary formation processes. The project aimed to characterize the growth factor and CCN activity of varying enrichment in sea-spray aerosol by combining different gas phase characterizations with aerosol measurement techniques for chemical and physical characterization. The 2011 summer campaign focused on the primary/secondary and organic/biological impact on cloud microphysics within a high biological activity period. Thus, in addition to the measurements of iodine compounds presented in this thesis, different aerosol mass spectrometry observations were used to quantify marine aerosol organic characteristics with effective cloud nucleating properties.

The MoLP-DOAS measured along the shore between the station and a retro reflector placed

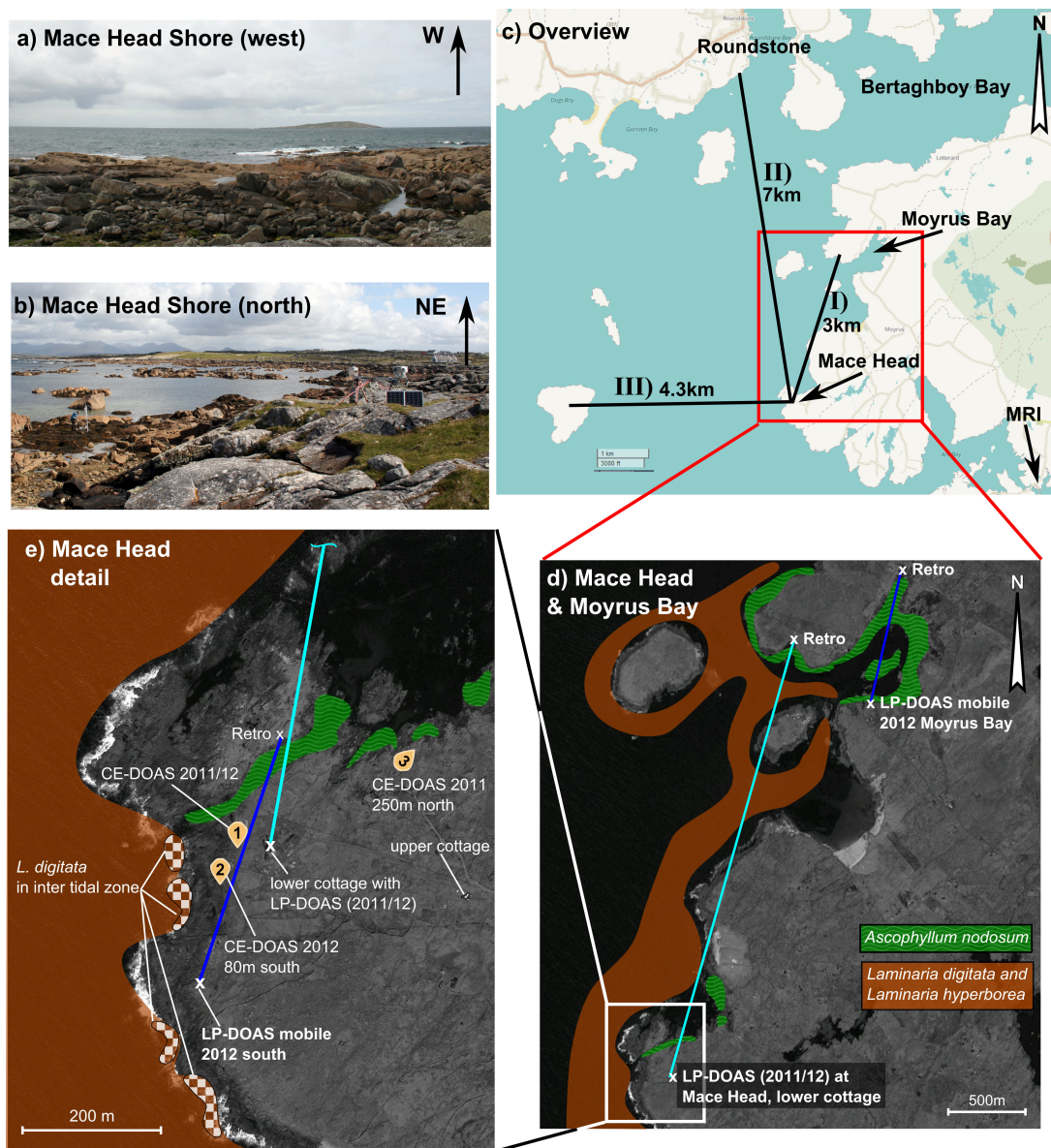


**Figure 12.9.** | **Measurement sites Mace Head and Moyrus Bay.** a),b) Shore at Mace Head in western and northern direction at low tide (water levels  $-1.5$  m and  $-0.6$  m). c) Overview map with LP-DOAS light paths and one way path lengths I) this study, II) Aliche et al. [1999], Seitz [2009] and Hebestreit [2001], III) Saiz-Lopez and Plane [2004]. d) Map of the larger area with the main Mace Head LP-DOAS light path and the MoLP-DOAS light path across Moyrus Bay. e) zoomed map with the different locations of the Open Path CE-DOAS around the Mace Head station, labeled (1) to (3), and the additional MoLP-DOAS light path from the 2012 campaign. The seaweed layer is based on maps from Stefan Schmitt (pers. observ. Ireland 2011/12), Hession et al., 1998 and Irish Seaweed Center [2001]. Satellite images ©Google Earth, ©DigitalGlobe.

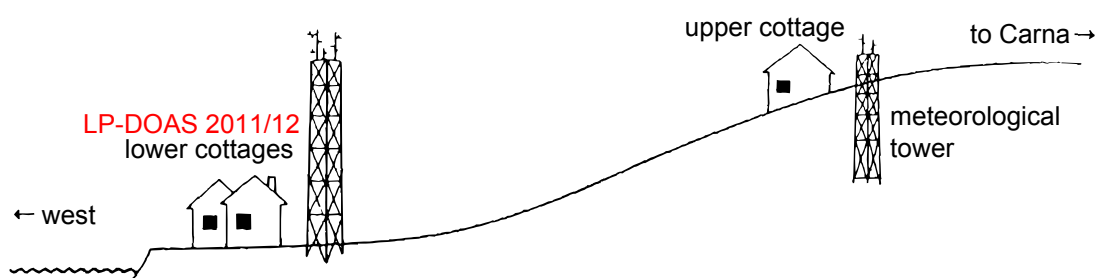


**Figure 12.10.** | East/west sectional view of the Mace Head research station. Adapted from Hebestreit [2001]

3.08 km north, giving an optical light path length of 6.16 km (see Fig. 12.9). Close to the station and close to the reflector the light path crossed dense beds of *A. nodosum* which were exposed during each tidal cycle. The large areas in between, which were always covered with water, were predominantly inhabited by the subtidal species *L. digitata* and *L. hyperborea*. The IO mixing ratios detected by the MoLP-DOAS are shown in Fig. 12.11 and Fig. 12.12. They were relatively low and exceeded the average detection limit of 1.1 ppt only on four days, with a maximum of  $(5 \pm 1)$  ppt on May 29th. Unfortunately, the LP-DOAS time series is relatively fragmented due to mechanical and electronic instabilities of the instrument which was still under development at the time. Also the compact design, particularly the short focal length of the telescope, was not optimal for the long light path at Mace Head.

The Open Path CE-DOAS performed in-situ measurements at two different locations, indicated as (1) and (3) in Fig. 12.9. From May 19th to May 23rd, it measured at location (1) west of the station about 40 m from the shore line where intertidal *L. digitata* is found. On three of the four measurement days, shown in Fig. 12.11, IO could be detected during daytime and low tide, with a maximum IO concentration in a short period around the tidal minimum. The maximum IO mixing ratio of  $(15 \pm 1)$  ppt was observed on May 19th, a day of spring tide. During the subsequent days the IO peak during low tide decreased simultaneously with the tidal amplitude. The only available night measurement on May 21st showed no IO above the detection limit of 2 ppt. Further night measurements were not possible due to frequent rain, when the instrument was not operated to avoid water contamination of the resonator mirrors. Rain is also the reason for the missing measurements on May 21st.

After a one day interruption due to a storm on May 23rd, the Open Path CE-DOAS measured from May 24th to May 30th at location (3), which is about 250 m north of the station and about 10 m from the shore line where *A. nodosum* is predominant. Unfortunately, the bad weather conditions at this site also caused several longer gaps in the IO time series, shown in Fig. 12.12, and did not allow for continuous over night measurements. On May 26th, 29th and 30th IO could be detected during periods of low tide and daytime. The maximum IO mixing ratio of  $(25.0 \pm 1.6)$  ppt was observed on May 29th, which was an almost rain-free day. On this day the anti-correlation between IO and tidal height is seen particularly well, since IO is increased in the morning during low tide, decreases in the early afternoon as the tidal height rises and increases again in the late afternoon during the second low tide of the day just before sunset.

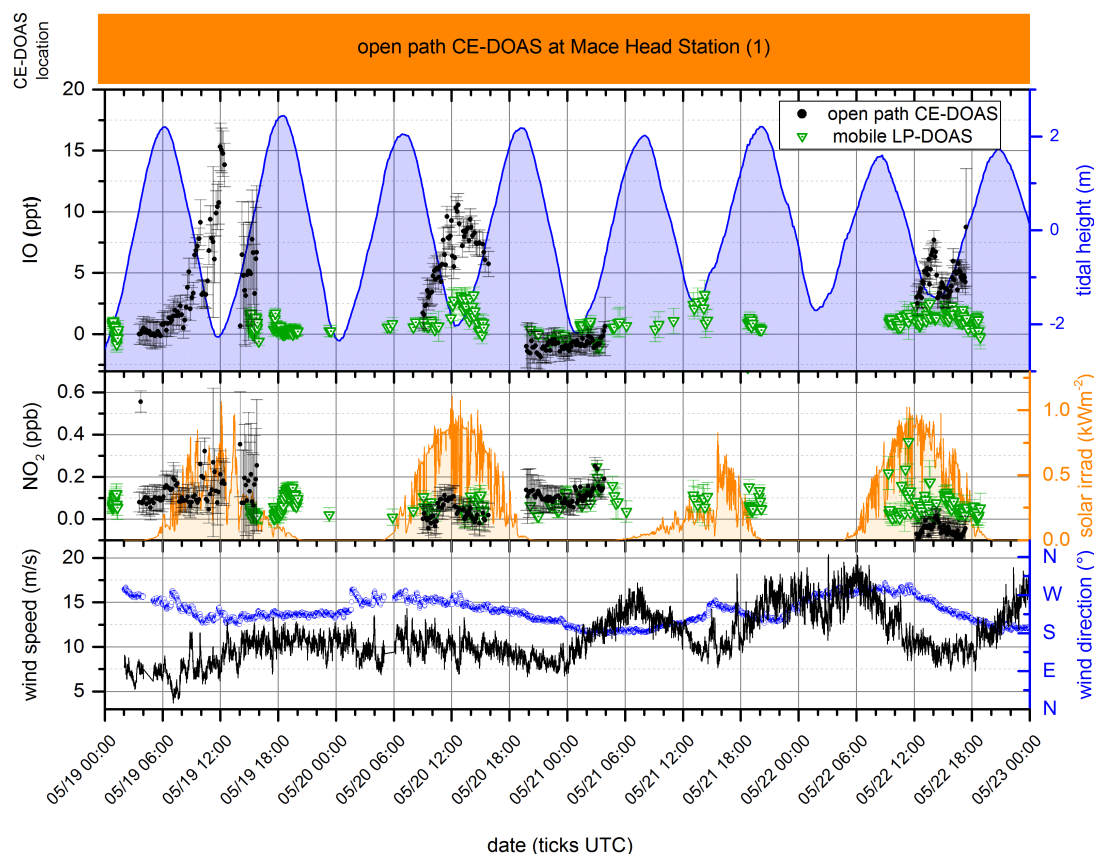


**Figure 12.11.** Detailed results of IO and NO<sub>2</sub> for Mace Head Station from the 2011 campaign. The Open Path CE-DOAS measured at location (1), west of the lower cottage as indicated in Fig. 12.9. IO and NO<sub>2</sub> measurements are shown in the top and middle graph respectively, both for the Open Path CE-DOAS (black), and the MoLP-DOAS (green). Also shown are the tidal height (top), solar irradiance (middle), wind speed and direction (bottom) at the Mace Head Research Station. A description of the tidal and meteorological measurements is given in sec.8.1.1.

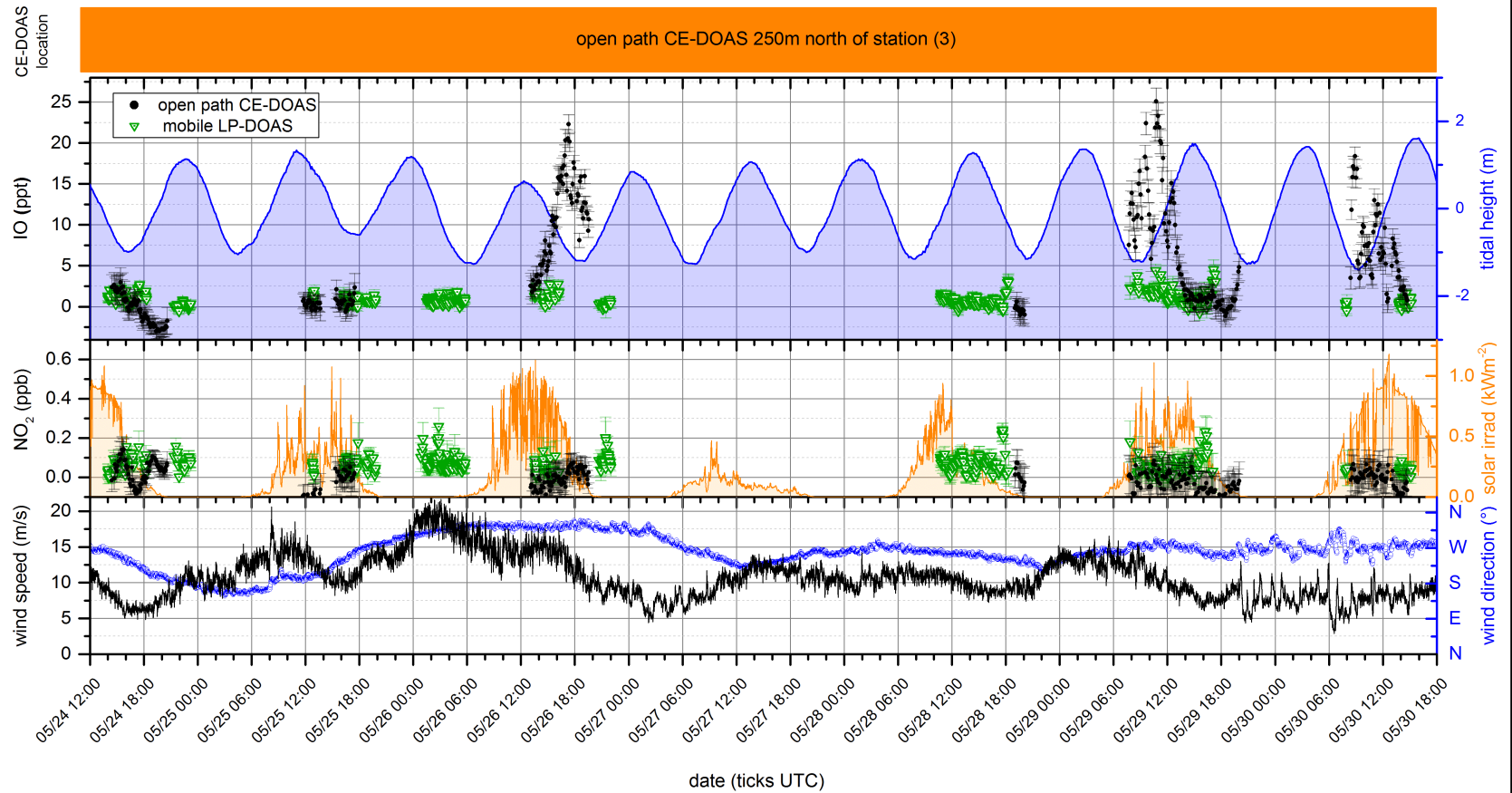


**Figure 12.12.** | Detailed results of IO and  $\text{NO}_2$  for Mace Head North from the 2011 campaign. The Open Path CE-DOAS measured at location (3), about 205 m north of the station as indicated in Fig. 12.9. IO and  $\text{NO}_2$  measurements are shown in the top and middle graph respectively, both for the Open Path CE-DOAS (black), and the MoLP-DOAS (green). Also shown are the tidal height (top), the solar irradiance (middle) and wind speed and direction (bottom) at the Mace Head Research Station. A description of the tidal and meteorological measurements is given in sec. 8.1.1.

### 12.4.1.2. Campaign 2012

**Stationary measurements by the Mace Head LP-DOAS** During the 2012 campaign, a stationary LP-DOAS was used to measure on the same light path as the MoLP-DOAS in the 2011 campaign (see Fig. 12.9). This stationary LP-DOAS measured between July 14th to August 6th, to provide a continuous reference for comparisons with mobile measurements at other locations. Table 12.9 summarizes the detection limits and the observed maximum and average mixing ratios for IO, I<sub>2</sub>, NO<sub>2</sub> and (CHO)<sub>2</sub>. Retrieved I<sub>2</sub> mixing ratios were always below the detection limit of (75 ± 10) ppt. Also additional measurements of (CHO)<sub>2</sub> were always below the detection limit of (0.16 ± 0.04) ppb. IO was detected on 15 of the 22 measurement days above the detection limit of 1.8 ppt and showed a positive correlation to low tide as described in previous studies [Alicke et al., 1999; Hebestreit, 2001; Saiz-Lopez et al., 2006; Seitz, 2009; Commane et al., 2011]. However, on some days the data also show some significant negative IO values which exceed the detection limit due to systematic residual structures. The maximum IO mixing ratio of (13 ± 1) ppt was observed on August 8th which was a day of spring tide. A detailed discussion of the results is given in sec. 12.9.2.1

**Intensive measurement periods at Mace Head** Two sets of intensive measurements were conducted at Mace Head, first at the beginning of the campaign between the July 15th and July 20th and secondly on August 5th and 6th, the last days of the campaign.

From July 15th to July 18th the Open Path CE-DOAS measured in front of the lower cottage at location (1), which was also part of the 2011 campaign. Detailed data for this period is shown in Fig. 12.14. The both the Mace Head LP-DOAS and the CE-DOAS did not detect any significant IO above their respective average detection limits of 2.5 ppt and 3.5 ppt during this period. Interpretation of the data is only possible for July 18th because on the other days frequent rain showers interfered with the measurements. July 18th, was a rain free day and the CE-DOAS was directly downwind of the *L. digitata* patches. The absence of IO on this day can be explained by the insignificant exposure of *L. digitata* during low tide on this day.

Subsequently, on July 19th and 20th the Open Path CE-DOAS measured at location (2) about 80 m further to the south and about 30 m from the shore line where a second patch of *L. digitata* is located in the intertidal zone. Detailed data for this period is shown in Fig. 12.15. On both days an IO peak was observed by the Open Path CE-DOAS during daytime low tide. The increase of the maximum IO mixing ratios by a factor of 1.6 from (9.2 ± 0.8) ppt on July 19th to (14.7 ± 0.8) ppt July 20th correlates with an increase in the tidal amplitude.

On July 20th the MoLP-DOAS was placed at the location indicated in Fig. 12.9 as “LP-DOAS mobile 2012 south” and measured on an additional 0.53 km long light path (two-way), parallel to the shoreline to the west of Mace Head station. However, the IO measurements show no correlation with low tide and no IO could be detected above the rather high detection limit of 10 ppt, caused by the short measurement path.

On August 6th the CE-DOAS measured again at location (1) while the MoLP-DOAS was setup about 3 km north east of the station on a 1.97 km long light path (two-way) across Moyrus Bay (see Fig. 12.9 and Fig. 12.13). A detailed plot of the measurements in this period is shown in Fig. 12.16. The Open Path CE-DOAS observed elevated IO levels during the daytime



**Figure 12.13.** | **Picture across Moyrus Bay.** Taken from the position of the retro reflector towards the LP-DOAS telescope in the south. The speckles on the water are floating blades of *A. nodosum* seaweed. The major part of the seaweeds was already submerged. The picture was taken on August 6th at 17:30 close to high tide at a water level of 1.3 m.

low tide of on average 5 ppt (one peak of  $(14.9 \pm 0.6)$  ppt) and in addition the IO shows a dependency on the wind direction. For the first half of the low tide period with a south westerly wind direction, only a weak increase of the IO mixing ratios with the sinking tide is observed and the maximum IO mixing ratios is  $(3.6 \pm 0.5)$  ppt. At 13:15h the wind direction turned to westerly and the observed IO mixing ratio increases by more than a factor of two and the time series becomes similar to the measurement on July 19th at location (1), which was made at a similar tidal amplitude. This is further discussed in the context of local IO sources in sec. 12.9. Furthermore, the slightly elevated  $\text{NO}_2$  mixing ratios of up to  $(280 \pm 30)$  ppt around 12:50 anti-correlate with the observed IO levels, hinting to chemical reaction between IO and  $\text{NO}_2$  as discussed in sec. 12.6. The IO levels observed by the MoLP-DOAS also correlated with day light and low tide. The average IO mixing ratios detected by the MoLP-DOAS at Moyrus Bay during the low tide period were on average two to three times higher than the simultaneous Open Path CE-DOAS measurements at Mace Head, even though the maximum IO mixing ratio of  $(14 \pm 2)$  ppt (MoLP-DOAS) and  $(14.9 \pm 0.6)$  ppt (Open Path CE-DOAS) are comparable. However, the Mace Head LP-DOAS whose light path was roughly west to south west of the MoLP-DOAS did not detect any significant IO even though both light path were relatively close. These differences between the MoLP-DOAS and the Mace Head LP-DOAS IO levels are further analyzed in section 12.9 in the context of the IO sources and their locations.

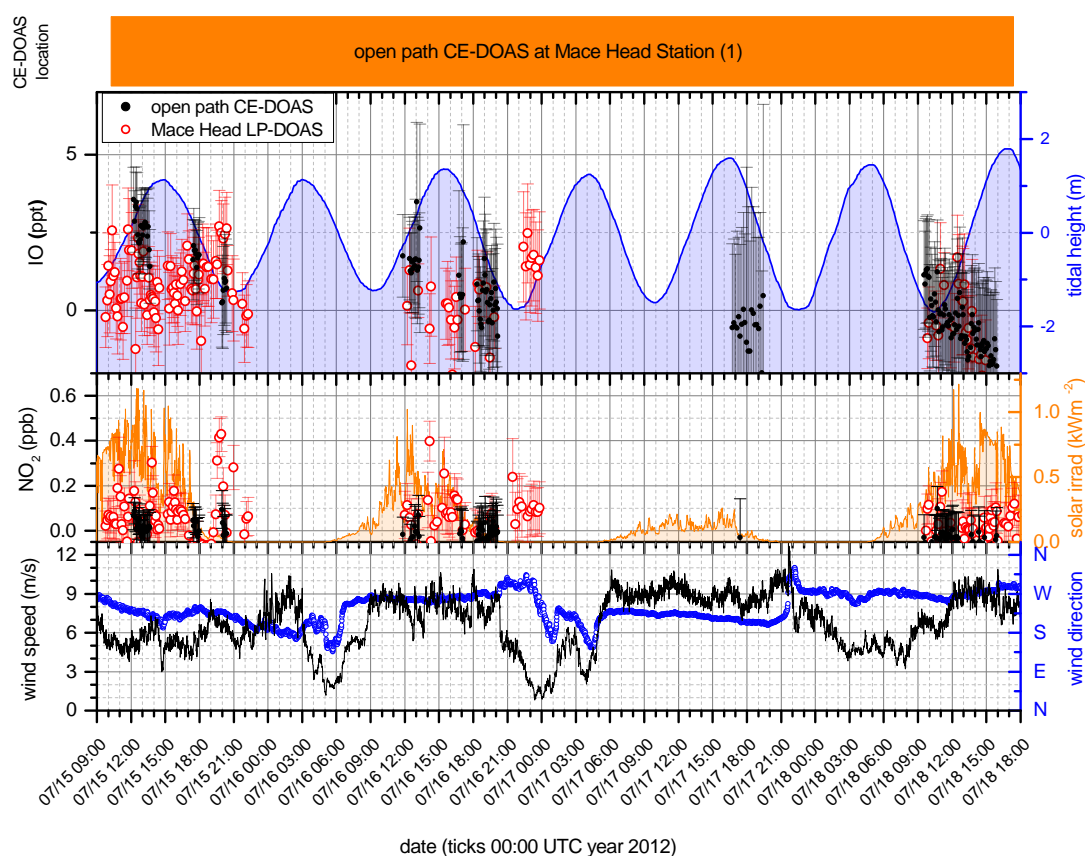


**Figure 12.14.** | Detailed results of IO and  $\text{NO}_2$  for Mace Head Station between July 15th and July 18th 2012. The Open Path CE-DOAS measured at location (1), in front of the lower cottage as indicated in Fig. 12.9. IO and  $\text{NO}_2$  measurements are shown in the top and middle graph respectively, both for the Open Path CE-DOAS (black), and the stationary LP-DOAS (red). Also shown are the tidal height (top), solar irradiance (middle), wind speed and direction (bottom) at the Mace Head Research Station. A description of the tidal and meteorological measurements is given in sec.8.1.1.

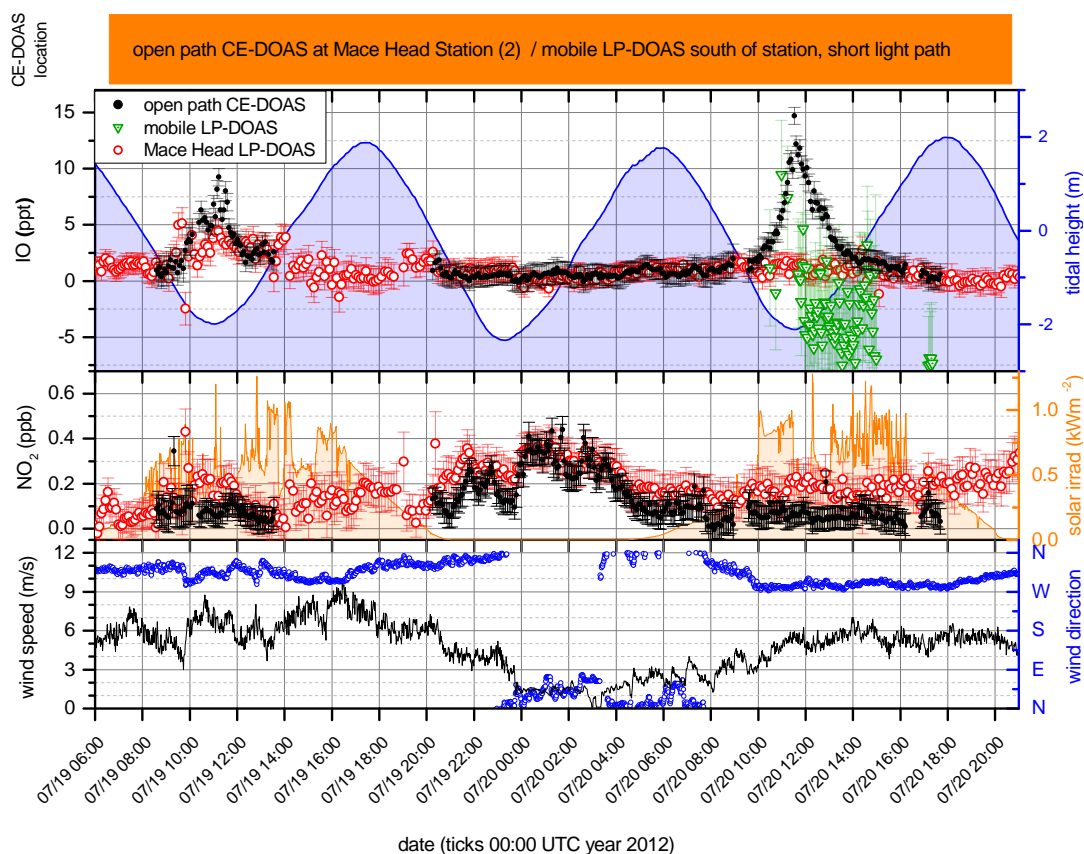


**Figure 12.15.** | Detailed results of IO and NO<sub>2</sub> for Mace Head Station at July 19th and July 20th 2012. Fig. 12.9 shows the measurements the Open Path CE-DOAS measurement location (2) south of Mace Head Station and the MoLP-DOAS light path to the west. IO and NO<sub>2</sub> measurements are shown in the top and middle graph respectively, for the Open Path CE-DOAS (black), and the MoLP-DOAS (green) and the stationary Mace Head LP-DOAS (red). Also shown are the tidal height (top), solar irradiance (middle), wind speed and direction (bottom) at the Mace Head Research Station. A description of the tidal and meteorological measurements is given in sec.8.1.1.

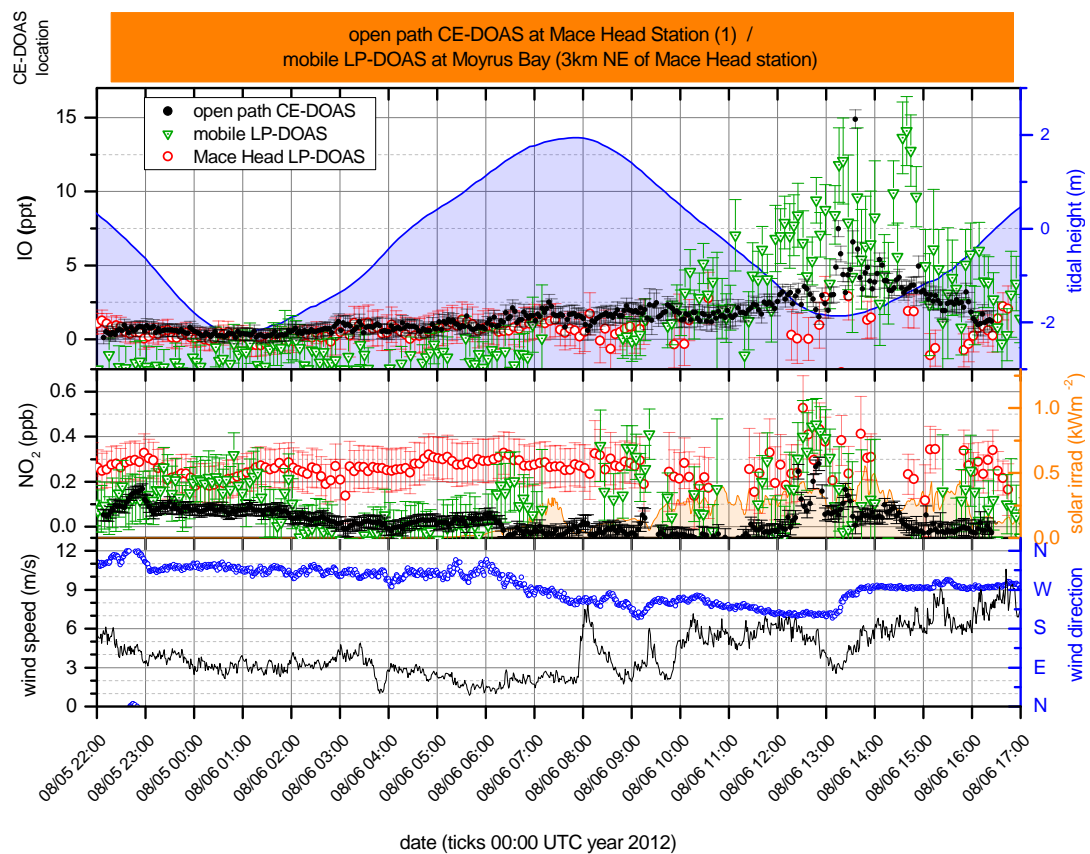


**Figure 12.16.** | Detailed results of IO and NO<sub>2</sub> on at August 6th 2012. The Open Path CE-DOAS measured close to Mace Head station at location (1) while the MoLP-DOAS simultaneously measured at Moyrus Bay (also see Fig. 12.9). ceIO and NO<sub>2</sub> measurements are shown in the top and middle graph respectively, for the Open Path CE-DOAS (black), and the MoLP-DOAS (green) and the stationary Mace Head LP-DOAS (red). Also shown are the tidal height (top), solar irradiance (middle), wind speed and direction (bottom) at the Mace Head Research Station. A description of the tidal and meteorological measurements is given in sec.8.1.1.

### 12.4.2. Martin Ryan Institute

The Martin Ryan Institute (MRI) is located in the south of Carna at the causeway connecting Mweenish Island with the main land, and is about 5 km south-east of Mace Head. The MRI is surrounded by seaweed fields in Mweenish Bay, which covers the north eastern to south western sector, and Ard Bay, which covers the western to north western sector. Thus, it is characterized by iodine source regions for all wind directions except north. An overview of the seaweeds present in the different areas is given in Fig. 12.17. Generally speaking, in the wave sheltered bays *A. nodosum* and *F. vesiculosus* are the co-dominant species of the middle and upper intertidal zone. The latter is also the predominant species in the middle to upper intertidal zone of wave exposed shores. The lower intertidal to subtidal zone of the semi wave exposed outer bays and the wave exposed shore outside of the bays are dominated by *L. digitata*.

In both campaigns CE-DOAS and LP-DOAS measurements were performed in the small bay east of the MRI. Detailed maps with locations of the instruments and the LP-DOAS light paths are provided in Fig. 12.18. Due to the good infrastructure at the MRI this bay was also the location for previous studies of reactive halogen chemistry and iodine emissions from seaweed by Seitz et al. [2010], Huang et al. [2010a], and Huang et al. [2013].

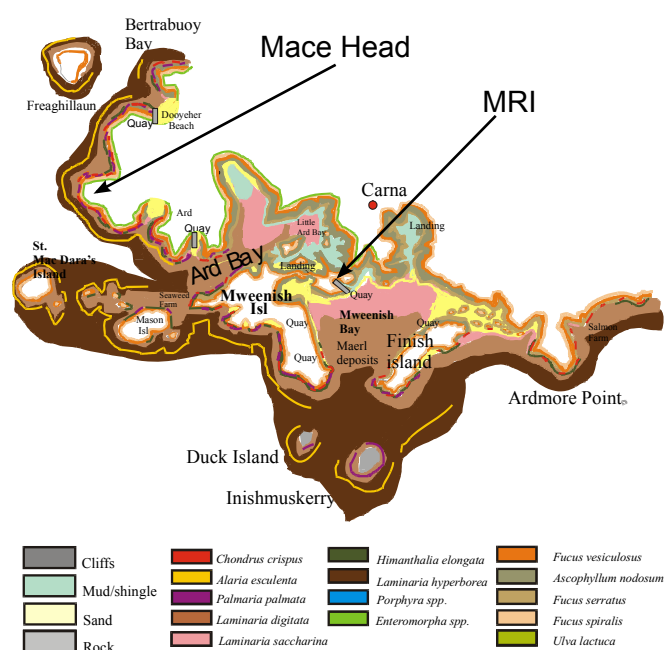


**Figure 12.17.** | Overview on the Seaweed distribution in the vicinity of Mace Head and the Martin Ryan Institute In the wave sheltered bays *A. nodosum* and *F. vesiculosus* are the co-dominant species of the middle and upper intertidal zone. The latter is also the predominant species in the middle to upper intertidal zone of wave exposed shores. The lower intertidal to subtidal zone of the semi wave exposed outer bays and the wave exposed shore outside of the bays are dominated by *L. digitata*. Adapted from Irish Seaweed Center [2001]

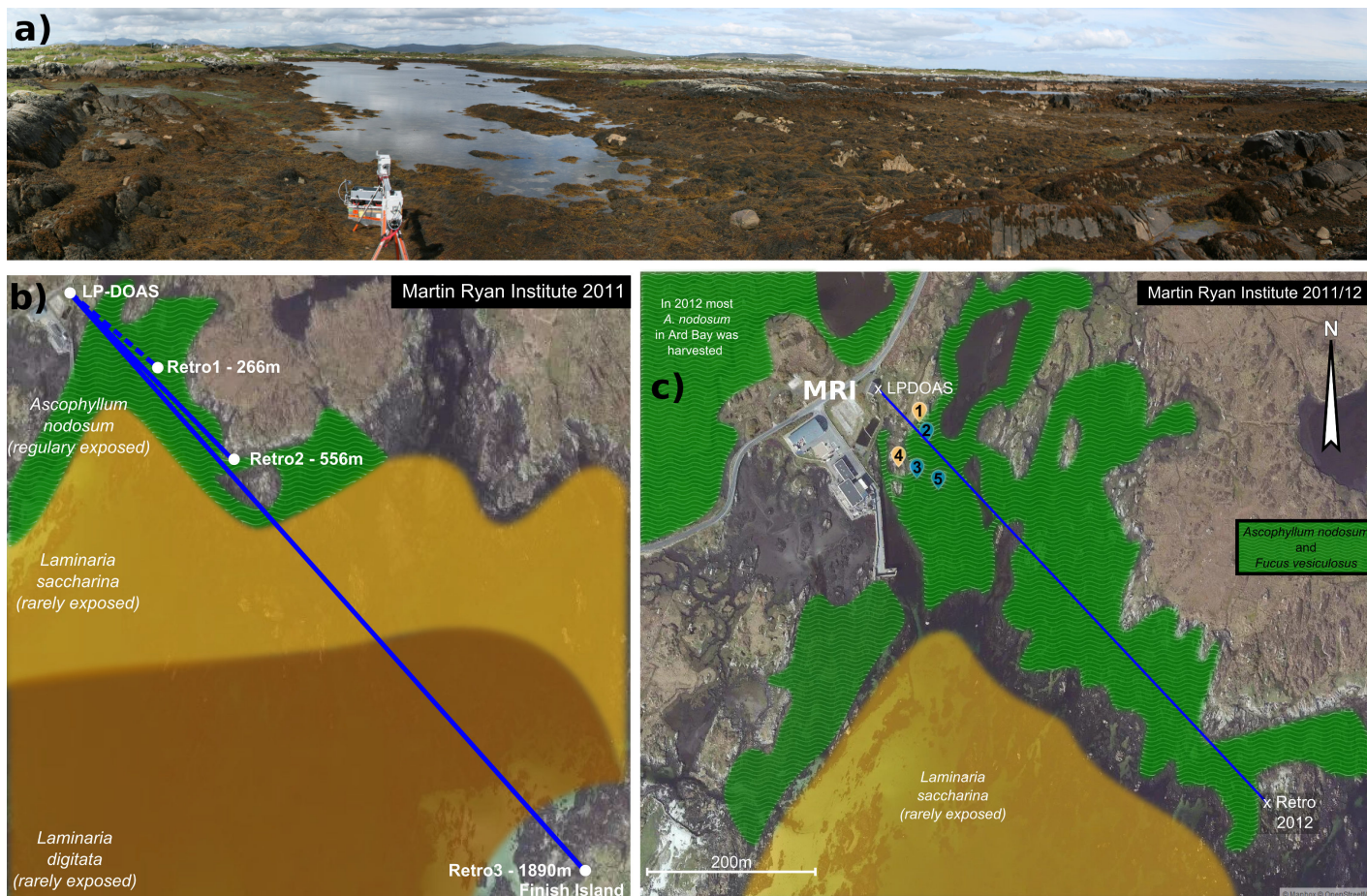


**Figure 12.18.** | Measurement site MRI. a) Intertidal zone at MRI photographed northeastwards from location (3) in c). Picture taken on July 25th at 15:49 close to low tide (water level  $-1.6$  m). b) The three LP-DOAS light paths implemented in the 2011 campaign. a) the 1264 m long (two-way) LP-DOAS light path implemented in the 2012 campaign and the different locations (1-5) of the Open Path CE-DOAS. Land positions (4,1) are marked in orange, and intertidal locations (2,3,5) in blue. The seaweed distribution is based on maps from Stefan Schmitt (pers. observ. Ireland 2011/12), Hession et al., 1998 and Irish Seaweed Center [2001]. Satellite images ©Mapbox, ©OpenStreetMap

### 12.4.2.1. Campaign 2011

In 2011 Open Path CE-DOAS and LP-DOAS measurements at the MRI were performed between May 31st and June 5th and on June 7th. Detailed times series for this period are shown in Fig. 12.19 to Fig. 12.22. Meteorological data from Mace Head was used for the interpretation of the results, since no local meteorological measurements at the MRI were available.

Open path CE-DOAS measurements were performed at three different locations marked as (3), (4) and (5) in Fig. 12.18. Measurements on land were performed at location (4), which also included several nighttime measurements. On each day, several hour-long measurements were performed during low tide in the intertidal bed of *A. nodosum* and *F. vesiculosus* at location (3) and (5). Very high IO mixing ratios were observed during low tide when the CE-DOAS was placed in the intertidal seaweed beds. The highest IO mixing ratio of  $(58.0 \pm 3.7)$  ppt was detected on June 2nd at 12:30h. Measurements on June 3rd and 4th show much higher IO mixing ratios in the seaweed field than on land at similar tidal heights which is further discussed in sec. 12.9. On June 4th an 10 ppt increase in the IO mixing ratio was observed when the Open Path CE-DOAS was lowered down from its normal measurement height of 1.3 m to a height of 0.4 m above the seaweed bed. A repetition of this measurement on July 30th 2012 with a finer height resolution is discussed in sec. 12.10. It yielded up to 131 ppt IO at 25 cm above the seaweed bed. Furthermore, IO levels at fixed locations in seaweed field showed a correlation to the solar radiation (e.g. on June 2nd) and an anti-correlation to  $\text{NO}_2$  (on May 31st and June 4th), which are further discussed in sec. 12.7 and sec. 12.6 respectively. No IO above the average detection limit of 1.6 ppt was detected during the three night time measurements on June 3rd, 4th and 5th, while during low tide at daytime IO up to  $(8.5 \pm 0.7)$  ppt was detected on June 3rd and 4th at the same land positions (see sec. 12.7.1).

In order to determine the spatial distribution of IO, the LP-DOAS measured along three almost parallel light paths with one-way lengths of 266 m, 556 m and 1890 m which crossed the bay in south eastern direction and only one to two meters above the high water spring mark as shown in Fig. 12.18. The middle and long light path are very similar to a previous study in 2007 by Seitz et al. [2010]. On all three light paths the observed IO mixing ratios show a correlation with low tide and daylight. Maximum IO mixing ratios are  $(35 \pm 7)$  ppt on the short light path,  $(27 \pm 4)$  ppt on the middle light path and  $(19 \pm 2)$  ppt on the long light path. This already indicates differences in the horizontal distribution of IO which is discussed in detail in sec. 12.9.1.4.

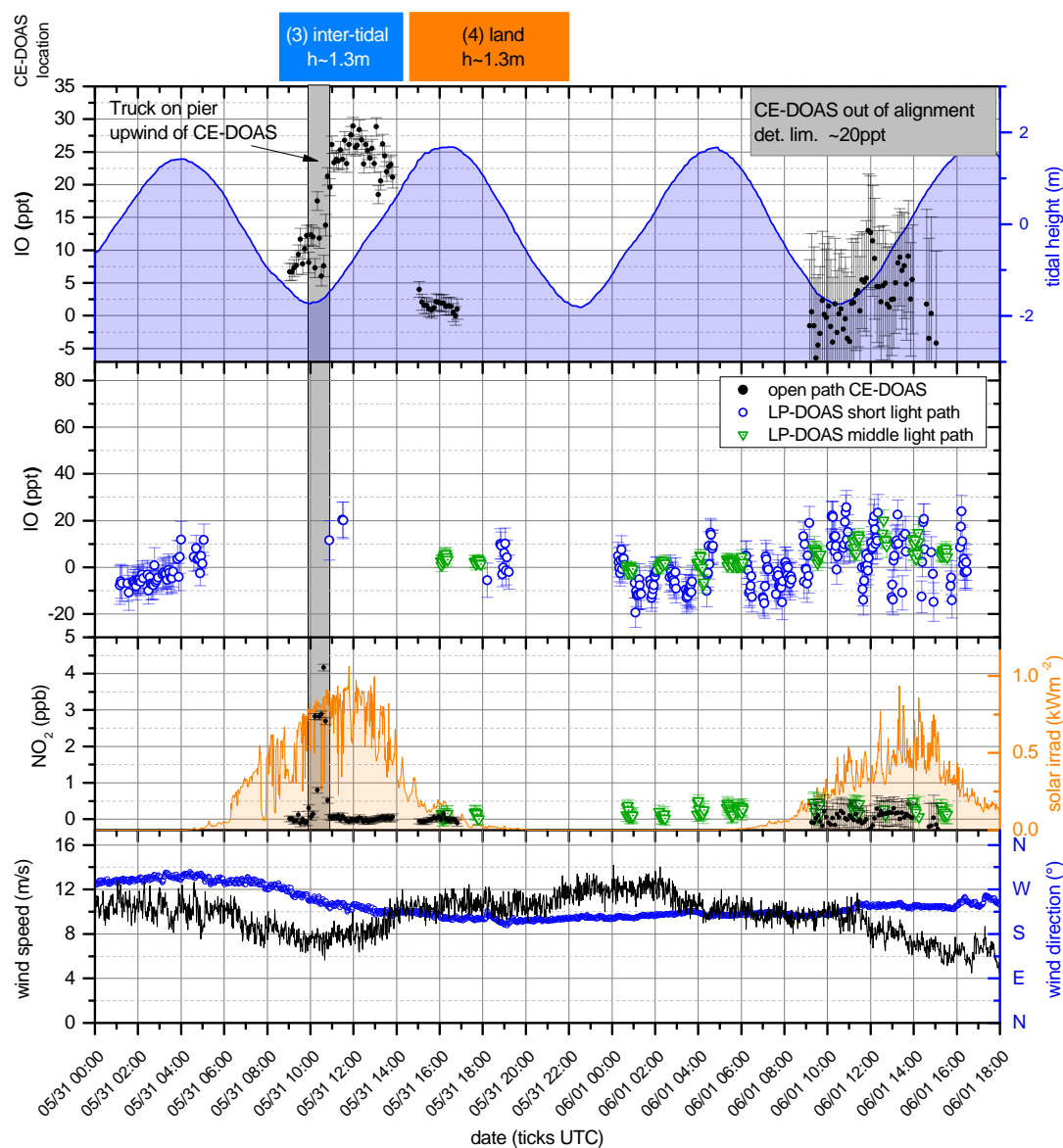


**Figure 12.19.** | Detailed results of IO and  $\text{NO}_2$  for MRI at May 31st and June 1st 2011.

The top row indicates the measurement locations of the Open Path CE-DOAS on land (orange) and in the intertidal zone (blue), and the measured IO mixing ratio. The numbers correspond to the markers in Fig. 12.18. IO measurements along the different LP-DOAS light paths (Fig. 12.18) are shown in the second top graph (no long light path in this period).  $\text{NO}_2$  data is only shown for the Open Path CE-DOAS and the middle LP-DOAS light path. Also shown are the tidal height (top), solar irradiance (2nd from bottom), wind speed and direction (bottom) at the Mace Head Research Station. A description of the tidal and meteorological measurements is given in sec.8.1.1.

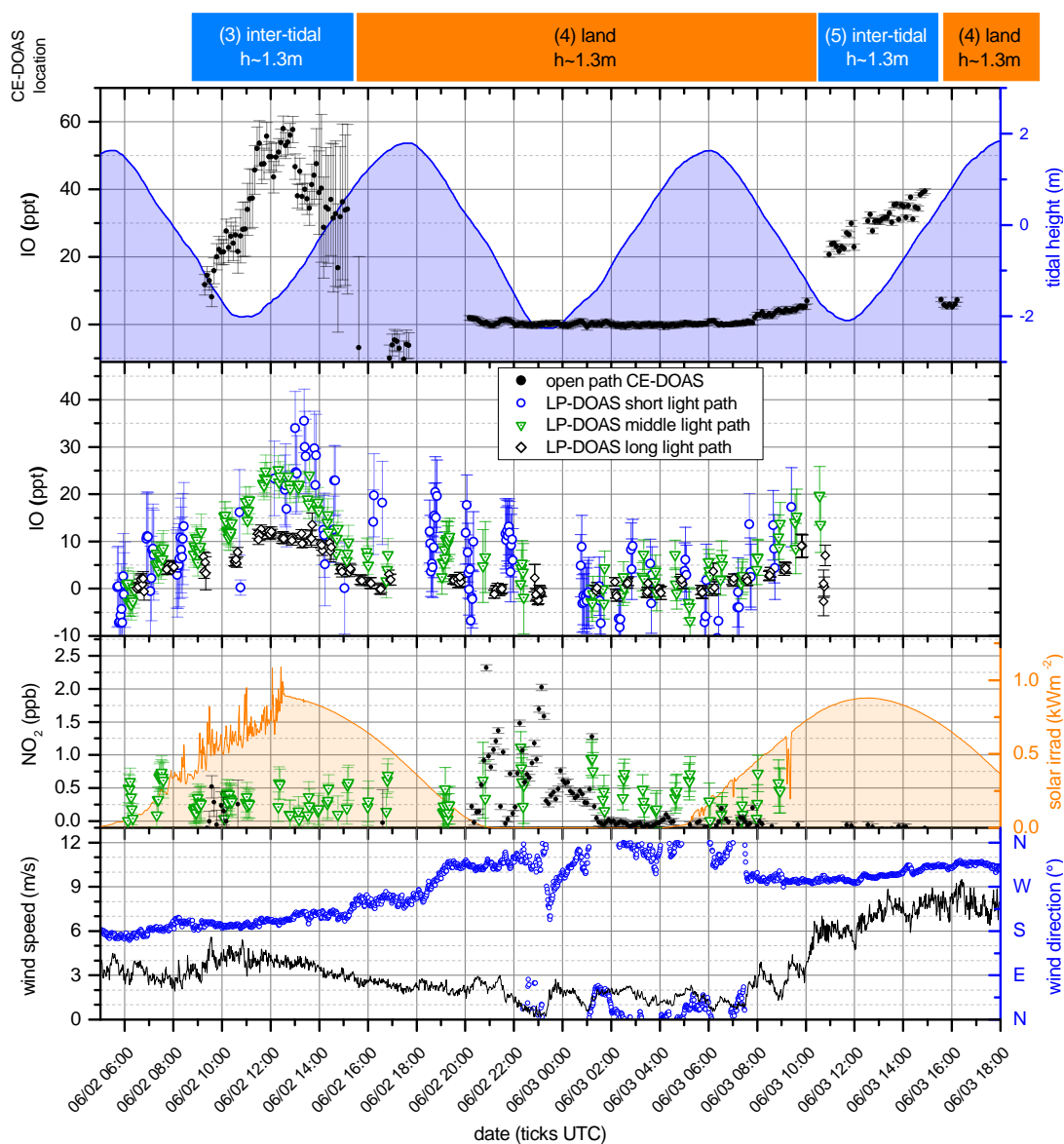


**Figure 12.20.** | Detailed results of IO and  $\text{NO}_2$  for MRI at June 2nd and 3rd 2011. The top row indicates the measurement locations of the Open Path CE-DOAS on land (orange) and in the intertidal zone (blue), and the measured IO mixing ratio. The numbers correspond to the markers in Fig. 12.18. IO measurements along the different LP-DOAS light paths (Fig. 12.18) are shown in the second top graph.  $\text{NO}_2$  data is only shown for the Open Path CE-DOAS and the middle LP-DOAS light path. Also shown are the tidal height (top), solar irradiance (2nd from bottom), wind speed and direction (bottom) at the Mace Head Research Station. A description of the tidal and meteorological measurements is given in sec.8.1.1.

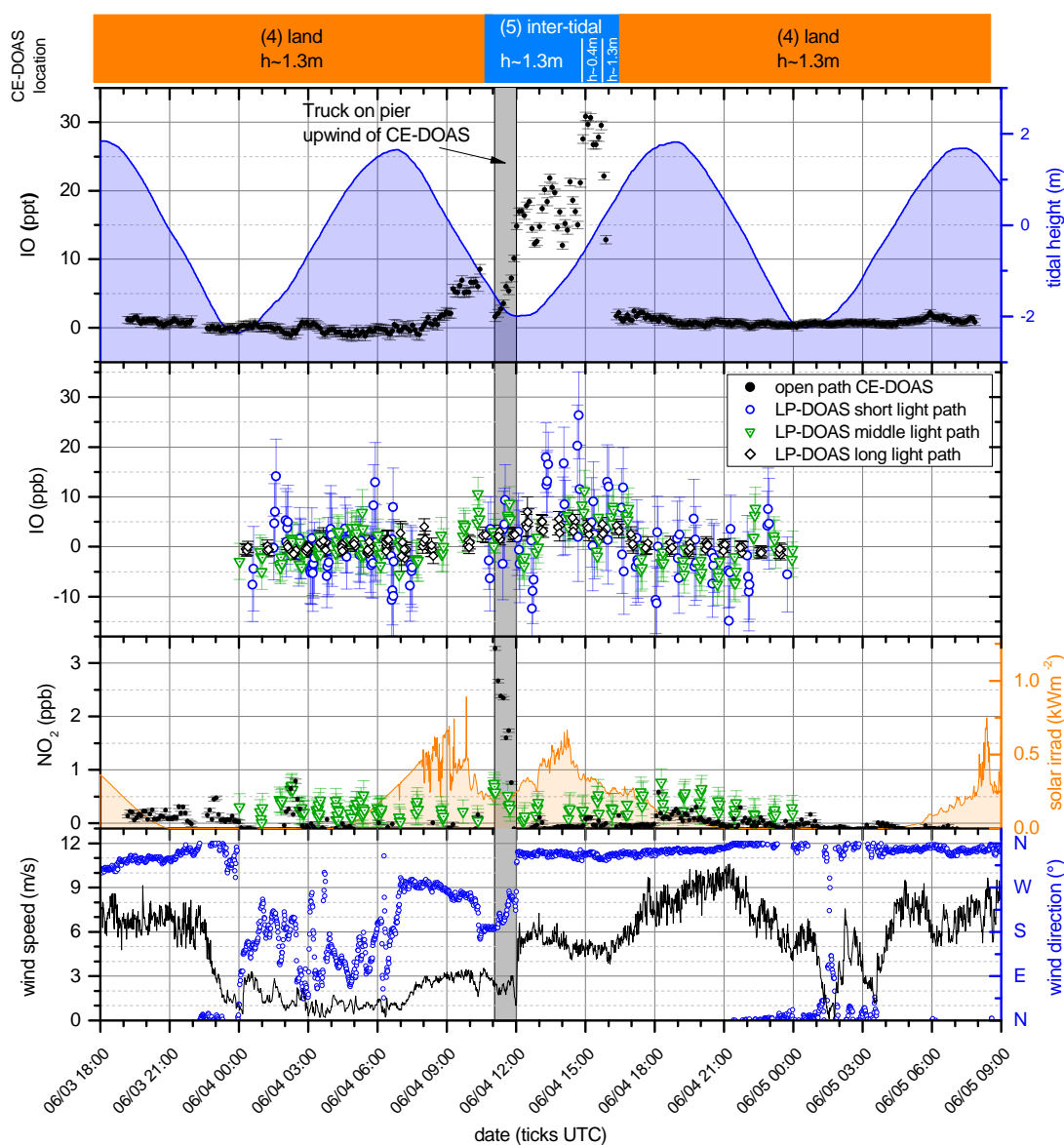


**Figure 12.21.** | Detailed results of IO and NO<sub>2</sub> for MRI at June 4th 2011. The top row indicates the measurement locations of the Open Path CE-DOAS on land (orange) and in the intertidal zone (blue), and the measured IO mixing ratio. The numbers correspond to the markers in Fig. 12.18. IO measurements along the different LP-DOAS light paths (Fig. 12.18) are shown in the second top graph. NO<sub>2</sub> data is only shown for the Open Path CE-DOAS and the middle LP-DOAS light path. Also shown are the tidal height (top), solar irradiance (2nd from bottom), wind speed and direction (bottom) at the Mace Head Research Station. A description of the tidal and meteorological measurements is given in sec.8.1.1.

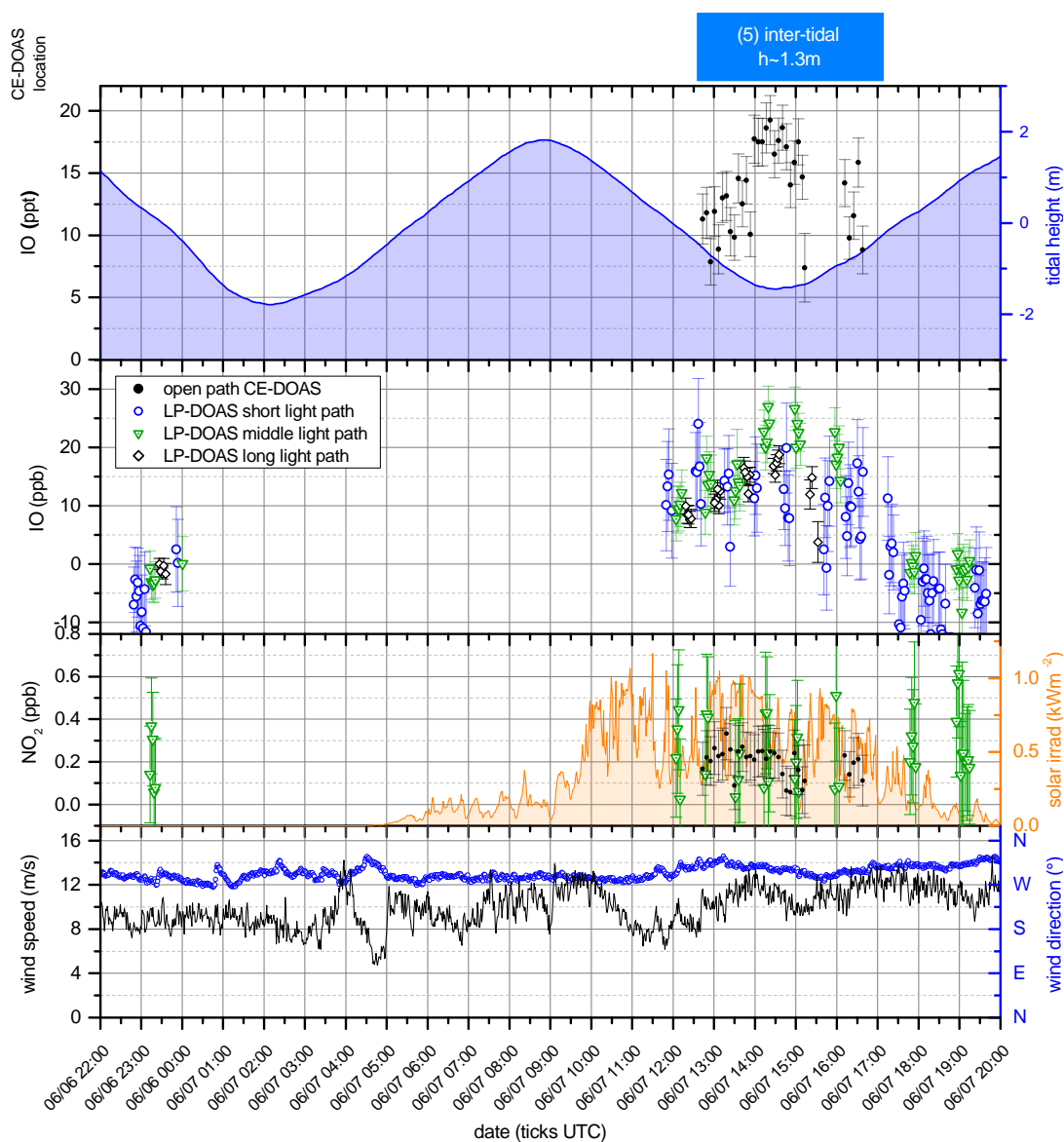


**Figure 12.22.** | Detailed results of IO and NO<sub>2</sub> for MRI at June 6th 2011. The top row indicates the measurement locations of the Open Path CE-DOAS on land (orange) and in the intertidal zone (blue), and the measured IO mixing ratio. The numbers correspond to the markers in Fig. 12.18. IO measurements along the different LP-DOAS light paths (Fig. 12.18) are shown in the second top graph. NO<sub>2</sub> data is only shown for the Open Path CE-DOAS and the middle LP-DOAS light path. Also shown are the tidal height (top), solar irradiance (2nd from bottom), wind speed and direction (bottom) at the Mace Head Research Station. A description of the tidal and meteorological measurements is given in sec.8.1.1.

### 12.4.2.2. Campaign 2012

The MRI was also investigated in the frame of the 2012 campaign. Open path CE-DOAS and MoLP-DOAS measurements were performed for the extended period from July 21st to 30th.

The MoLP-DOAS measured only along one light path corresponding to the middle light path from the previous year, which gives the best sensitivity to IO since it completely covers the relevant intertidal seaweed bed (see sec. 12.9.1.4). For the sake of a higher time resolution and a simpler operation of the instrument the short and long light path were discarded. In combination with further improvements of the MoLP-DOAS it was possible to improve the average IO detection limit to 3.6 ppt, which is more than a factor of two better than in the previous year. Like in 2011 campaign, IO peaks correlated with daytime and low tide. Striking examples for this correlation are the measurements on July 27th and 29th, where IO peaks were observed during the morning and afternoon low tide periods, but vanished during the high tide period around noon. The daily maximum IO levels which were found around the daytime low water varied between  $(8 \pm 2)$  ppt on July 22nd and  $(46 \pm 4)$  ppt on July 26th. Differences between the IO concentrations observed on the individual days can be attributed mainly to the local meteorology, especially solar irradiance (sec. 12.7), wind speed and direction (sec. 12.9) and precipitation.

Simultaneous LP-DOAS measurements at Mace Head also detected elevated IO at daytime low tide on most days. However the levels of IO were about one order of magnitude lower compared to the MoLP-DOAS measurements. MoLP-DOAS measurements and Mace Head LP-DOAS measurements are compared in detail in sec. 12.8.

In 2012 CE-DOAS measurements were performed at two different locations at land (1) and (4) and three different locations ((2), (3) and (5)) in the intertidal zone. Like in the previous year, when placed in the seaweed bed during daytime low tide the Open Path CE-DOAS measures high IO mixing ratios of up to  $(30.1 \pm 0.6)$  ppt at 1.3 m above the seaweed and  $(65.8 \pm 0.8)$  ppt at 45 cm above the seaweed. The good agreement between Open Path CE-DOAS point measurements in the seaweed bed and the LP-DOAS measurements across it suggest a relatively homogeneous IO distribution across the intertidal zone which is further discussed in sec. 12.9.1.2. In order to investigate the vertical distribution of IO, CE-DOAS measurements at 20 different height levels between 0.1 m and 2.2 m were performed on July 30th. The IO mixing ratios showed a strong decrease with height from more than 100 ppt close to the ground down to about 20 ppt at 2 m height. A discussion of the resulting IO height profile is given in sec. 12.10.

The Open Path CE-DOAS was also used to investigate several tidal cycles completely at the land positions (1) and (4) less than 10 m away from the seaweed bed. The observed IO mixing ratios on land show a greater day to day variation compared to the measurements in the intertidal zone. Also a strong variation in the relative IO mixing ratios between the CE-DOAS and the MoLP-DOAS was observed ranging from similar mixing ratios observed by both instruments on July 22nd, to less than 2 ppt observed by the CE-DOAS while the MoLP-DOAS measured up to  $(26.3 \pm 3.9)$  ppt on July 29th. The detailed analysis of the CE-DOAS and MoLP-DOAS results in the context of iodine source locations is given in sec. 12.9.1.2.

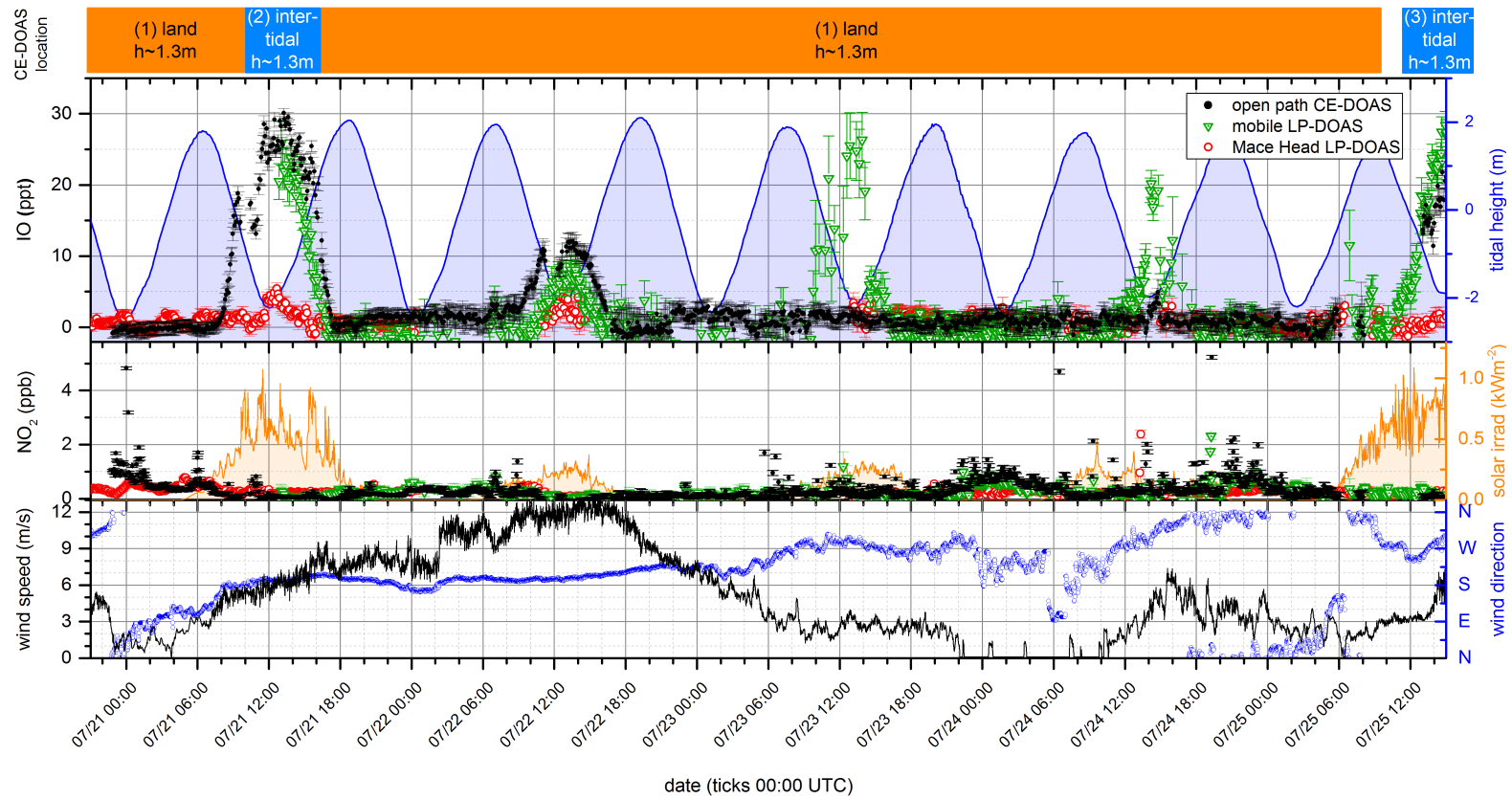


**Figure 12.23.** | Detailed results of IO and  $\text{NO}_2$  for MRI from July 21 to 25 2012. The top row indicates the measurement locations of the Open Path CE-DOAS on land (orange) and in the intertidal zone (blue). The numbers correspond to the markers in Fig. 12.18. IO and  $\text{NO}_2$  measurements are shown in the top and middle graph respectively, for the Open Path CE-DOAS (black), and the MoLP-DOAS (green) and the stationary Mace Head LP-DOAS (red). Also shown are the tidal height (top), solar irradiance (middle), wind speed and direction (bottom) at the Mace Head Research Station. A description of the tidal and meteorological measurements is given in sec.8.1.1.

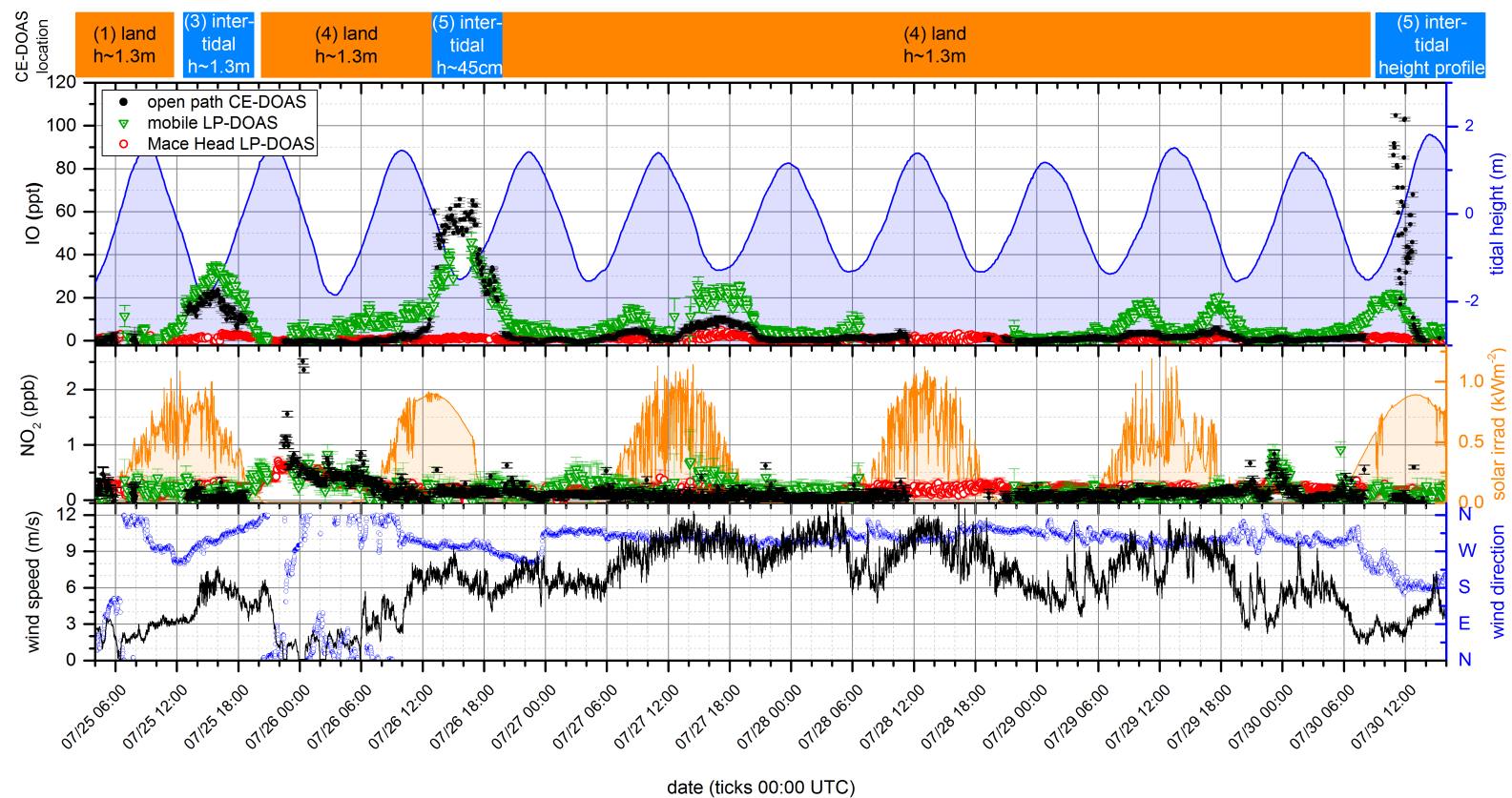


**Figure 12.24.** | Detailed results of IO and NO<sub>2</sub> for MRI from July 25th to 30th 2012. The top row indicates the measurement locations of the Open Path CE-DOAS on land (orange) and in the intertidal zone (blue). The numbers correspond to the markers in Fig. 12.18. IO and NO<sub>2</sub> measurements are shown in the top and middle graph respectively, for the Open Path CE-DOAS (black), and the MoLP-DOAS (green) and the stationary Mace Head LP-DOAS (red). Also shown are the tidal height (top), solar irradiance (middle), wind speed and direction (bottom) at the Mace Head Research Station. A description of the tidal and meteorological measurements is given in sec.8.1.1.

### 12.4.3. Lettermore Island

Lettermore is the east most island of the Ceantar na nOileán island group, about 40 km east of Galway (see Fig. 12.1). These island are about one to two kilometers away from the mainland, forming multiple wave sheltered bays where *A. nodosum* is very abundant in the intertidal zone [Hession et al., 1998]. Measurements were performed at two different locations on Lettermore Island.

#### 12.4.3.1. Lettermore Island north

The Lettermore Island north site is located at the northern shore of Greatman's Bay and south of the road connecting Lettermore Island with the main land (see Fig. 12.25). The shore at the site is wave sheltered and has a large and shallow mid-intertidal zone with a dense seaweed bed dominated by *A. nodosum* and to a smaller extend *F. vesiculosus*. *A. nodosum* extends to the lower intertidal zone where it stays the dominant species. Further very similar seaweed beds are found in the entire Greatman's bay and also in the adjacent Kilkieran Bay and Camus Bay, which are located north west and north of the measurement location respectively [Hession et al., 1998]. Air masses at the site are expected to show some pollution due to the nearby access road and small settlements in almost all wind sectors.

Measurements at Lettermore Island north were performed in 2012 on August 1st and 2nd. The MoLP-DOAS measured parallel to the shore on a 0.87 km long light path (one-way) over the seaweed bed (see Fig. 12.25). Open Path CE-DOAS measurements were performed at three different locations marked in Fig. 12.25. During low tide the Open Path CE-DOAS measured over in the seaweed field at location (1) (on August 1st) and location (2) (on August 2nd). It was moved on both days to location (3) when the water started to cover the intertidal measurement locations. Due to the unstable weather conditions with rain and wind the Open Path CE-DOAS was not operated over night. But during daytime measurements could be performed despite the rainy conditions. Detailed Open Path CE-DOAS and LP-DOAS time series of IO and NO<sub>2</sub> are shown in Fig. 12.26.

The IO was observed by the MoLP-DOAS during all three low tide periods but showed strong variations in the amplitude of the IO peaks. Maximum IO mixing ratios for the three low tide periods of  $(29.7 \pm 2.1)$  ppt at August 1st 11:53h,  $(7.1 \pm 1.8)$  ppt at August 1st 19:39h and  $(14.4 \pm 1.8)$  ppt at August 2nd 11:25h correlate well with the respective solar irradiance of  $\sim 750 \text{ W/m}^2$ ,  $\sim 100 \text{ W/m}^2$  and  $\sim 300 \text{ W/m}^2$ . This is discussed further in sec. 12.7. Another very interesting observation from the MoLP-DOAS data is that the IO levels were not influenced by the two periods of rain showers on August 2nd which is further discussed in sec. 12.9.1.5.

The Open Path CE-DOAS measurements show the same time dependence as the MoLP-DOAS measurements. However, in the periods where the Open Path CE-DOAS measures in the intertidal zone directly above the seaweed the IO levels are about 70 % higher on August 1st and more than 150 % higher on August 2 compared to the MoLP-DOAS. This is further discussed in sec. 12.9.1.2. Furthermore, on August 1st the CE-DOAS observes relatively high NO<sub>2</sub> mixing ratios which are regularly above 0.5 ppb. However, the elevated NO<sub>2</sub> mixing ratios do not seem to influence the simultaneous IO peak, which is further discussed in sec. 12.6.

The stationary Mace Head LP-DOAS observed no significant IO above the 1ppt detection

limit on August 1st, but on August 2nd it observes significantly elevated IO during the daytime low tide with mixing ratios up to  $(6.3 \pm 1.2)$  ppt. The elevated IO on August 2nd is mostly attributed to the southerly wind direction at Mace Head and the relatively high tidal amplitude (see 12.4.1.2). But the peak concentration at Mace Head is still a factor of 4.7 below the MoLP-DOAS measurements and a factor 8 below the Open Path CE-DOAS measurements (see section 12.8).



**Figure 12.25.** | **Measurement site Lettermore Island north.** a) Photograph of the seaweed, from the middle of the causeway in eastern direction. The picture was taken on August 1st at 12:40 close to low tide (water level  $-1.1$  m). b) Map with the MoLP-DOAS light path of 1744 m length (two-way), spanning the intertidal seaweed. The measurement locations (1-3) of the Open Path CE-DOAS are also shown. Location (2) is on land and locations (1) and (3) are in the intertidal zone. The seaweed distribution is based on maps from Stefan Schmitt (pers. observ. Ireland 2012). Satellite images ©Mapbox, ©OpenStreetMap

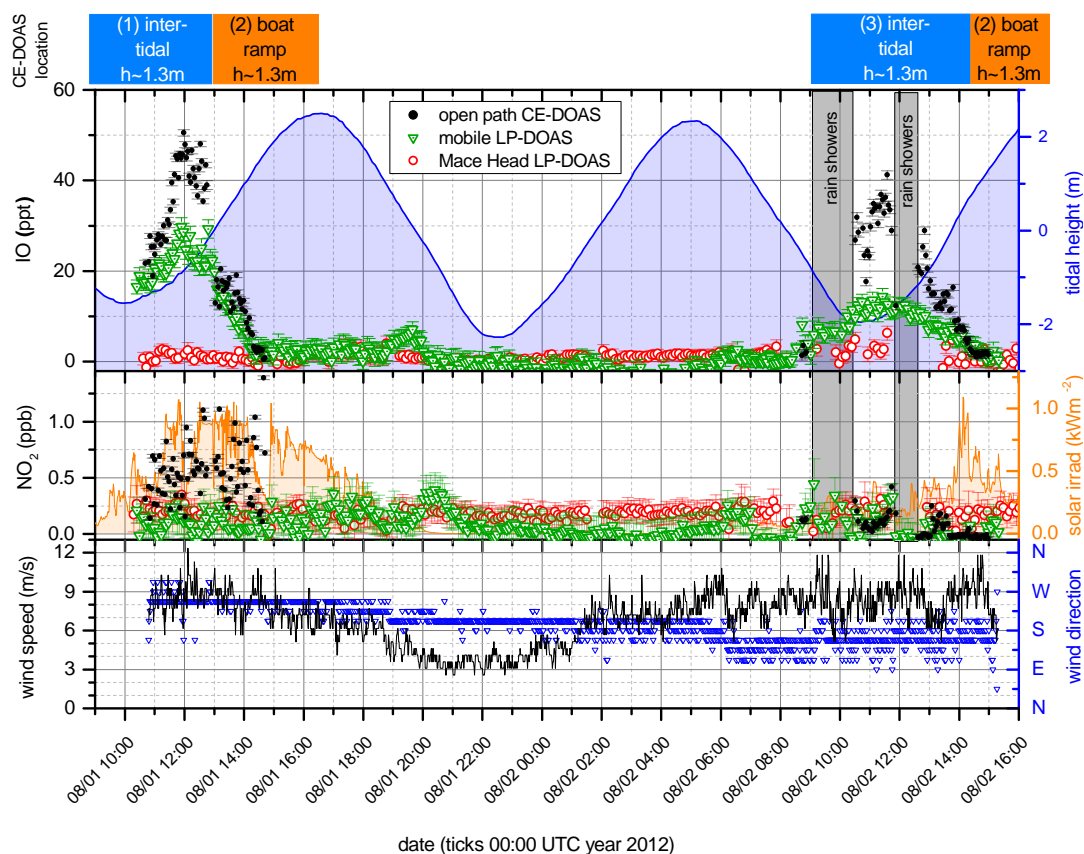


**Figure 12.26.** | Detailed results of IO and NO<sub>2</sub> for Lettermore North. The top row indicates the measurement locations of the Open Path CE-DOAS on land (orange) and in the intertidal zone (blue). The numbers correspond to the markers in Fig. 12.24. IO and NO<sub>2</sub> measurements are shown in the top and middle graph respectively, for the Open Path CE-DOAS (black), and the MoLP-DOAS (green) and the stationary Mace Head LP-DOAS (red). Also shown are the tidal height (top) at Galway port, solar irradiance at Mace Head (middle) and the local wind speed and direction at the Lettermore North site (bottom). A description of the tidal and meteorological measurements is given in sec.8.1.1. Two periods of rain showers are marked on August 2nd, but light drizzle was common during that day.

### 12.4.3.2. Lettermore Island south

The Lettermore Island south site is located on a wave-sheltered bay, formed between the southern shore of Lettermore Island and the neighboring Gorumna Island (see Fig. 12.27). The intertidal zone at the measurement site shows a relatively dense seaweed coverage with roughly equal abundance of *A. nodosum* and *F. vesiculosus*. Other nearby locations with high abundance of *A. nodosum* are Greatman's Bay in the east and Casheen Bay in the west [Hession et al., 1998].

The tidal cycle at the Lettermore Island south site is delayed to the available measurements at Galway Port. The reason for this delay is the relatively narrow connection to Greatman's Bay and to Casheen Bay which limit the water flow in and out of the bay, and thus delaying the tidal cycle and damping the amplitude. Own observations indicate an approximate 60 min delay of the tidal cycle around low tide but since the width of the bays opening narrows with lower tide levels it is assumed that the shift is lower at higher tide levels. Therefore, both the unshifted and a 60 min delayed tidal cycle are shown in Fig. 12.28.

Fig. 12.28 shows the results of the measurements at Lettermore Island performed in 2012 on August 3rd. The MoLP-DOAS measured parallel to the shore on a 0.81 km long light path (one-way) over the seaweed bed (see Fig. 12.27). The Open Path CE-DOAS first measured at position (1. Fig. 12.28) at the beginning of the intertidal zone when most of the seaweed was still submerged. Subsequently with sinking water levels the CE-DOAS was moved further in the intertidal zone to position (2) for measurements directly over the exposed seaweed bed. The CE-DOAS stayed there until the seaweed was again submerged and was subsequently moved back to the land to position (3) before the tripods were too deep in the water.

Like at the previous sites, the IO observed by the MoLP-DOAS shows an anti correlation to the tidal height with a maximum of  $(14 \pm 2)$  ppt at 12:51h, which is close to the tidal minimum. The time dependence of IO point measurements in the seaweed bed (position 2) by CE-DOAS is similar to the MoLP-DOAS but with a higher amplitude of the IO levels which reached  $(24.9 \pm 0.7)$  ppt. The higher maximum IO level observed by the Open Path CE-DOAS compared to the MoLP-DOAS is expected since only about half of the MoLP-DOAS light path crosses intertidal seaweed beds and the rest is over sub tidal areas. For both, LP-DOAS and CE-DOAS measurements the frequent rain showers did not seem to affect the observed IO levels directly, which is further discussed in sec. 12.9.1.5. The  $\text{NO}_2$  mixing ratios observed by the Open Path CE-DOAS and the MoLP-DOAS agree very well which indicates that  $\text{NO}_2$  is well mixed in the observed air masses. However, it is not possible to further investigate the reaction between IO and  $\text{NO}_2$ , since  $\text{NO}_2$  was mainly observed at the beginning and end of the low tide period when IO levels are generally low.

On August 3rd the stationary reference LP-DOAS at Mace Head observed IO mixing ratios of up to  $(7.5 \pm 1.6)$  ppt which are relatively high for this location. However, measurements at Lettermore Island south observed IO much more constantly compared to the reference LP-DOAS at Mace Head.



**Figure 12.27. | Measurement site Lettermore South.** a) Photograph of the measurement site shot from the MoLP-DOAS location in eastern direction. The picture was taken on August 3rd at 13:00 close to low tide (water level  $-1.9$  m). b) Map with the MoLP-DOAS light path of the of 1616 m length (two-way) spanning the intertidal seaweed. The measurement locations (1-3) of the Open Path CE-DOAS are also shown. Location (3) is on land and locations (1) and (2) are in the intertidal zone. The seaweed distribution is based on maps from Stefan Schmitt (pers. observ. 2012) and Hession et al., 1998. Satellite images ©Mapbox, ©OpenStreetMap

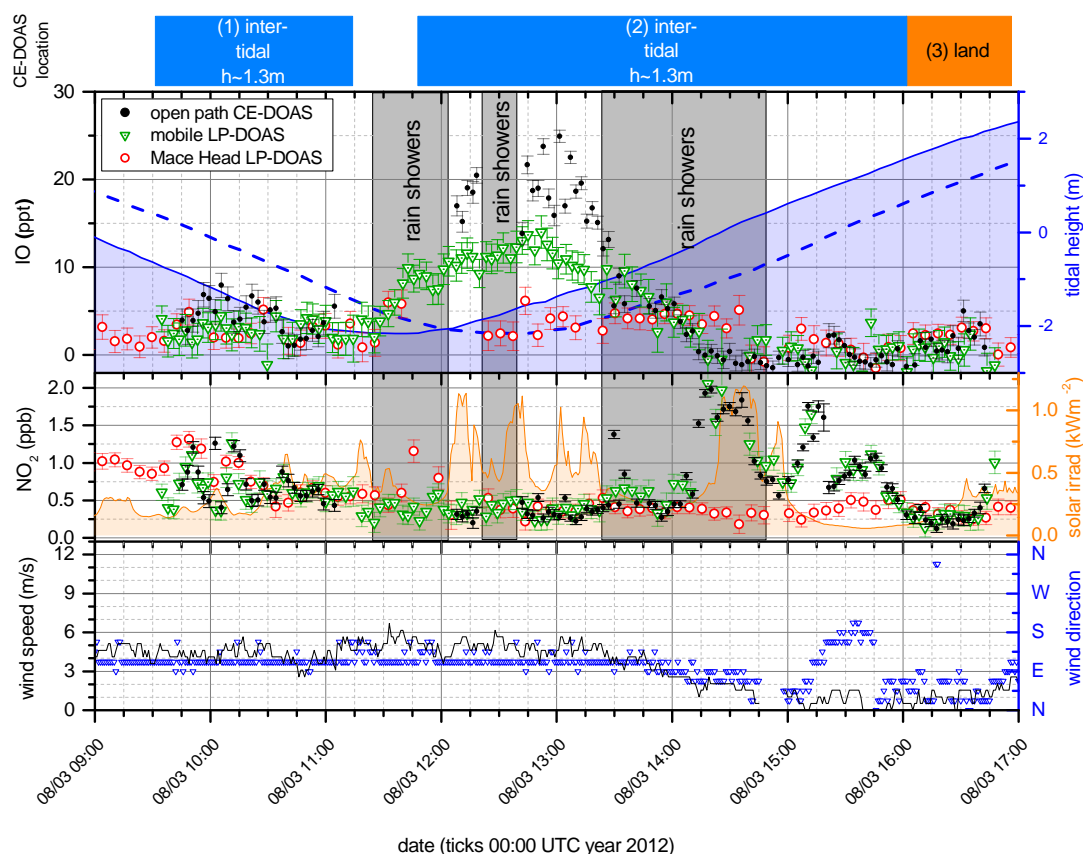


**Figure 12.28.** | Detailed results of IO and NO<sub>2</sub> for Lettermore South. The top row indicates the measurement locations of the Open Path CE-DOAS on land (orange) and in the intertidal zone (blue). The numbers correspond to the markers in Fig. 12.27. IO and NO<sub>2</sub> measurements are shown in the top and middle graph respectively, for the Open Path CE-DOAS (black), and the MoLP-DOAS (green) and the stationary Mace Head LP-DOAS (red). The blue solid line in top graph shows the tidal height at Galway Port, additionally the blue dashed line shows a 60 min shifted tidal cycle, which is a better match to personal observations. Also shown are the solar irradiance at Mace Head (middle) and the local wind speed and direction at the Lettermore South site (bottom). A description of the tidal and meteorological measurements is given in sec.8.1.1. Additionally periods of stronger rain showers are marked, but light drizzle was common during the entire day.

#### 12.4.4. Cashel Bay

Cashel Bay is located about 11 km north north east of Mace Head. In the south west, Cashel Bay opens out into the larger Bertraghboy Bay. In both bays *A. nodosum* and *F. vesiculosus* are the co-dominant species of the intertidal shore forming dense beds [Irish Seaweed Center, 2001]. Local anthropogenic emissions are low since the area is only sparsely populated. A small village, Roundstone, is located about 8 km to the west. The next town is Clifden, which is located about 15 km north-west.

Similar to Lettermore Island south the tidal cycle is delayed compared to the measurements at Galway Port due to the relatively small opening of the bay. Own observations indicate an approximate 45 min delay of the tidal cycle around low tide but since the width of the bays opening narrows with lower tide levels it is assumed that the shift is lower at higher tide levels.

Measurements at the eastern part of Cashel bay were performed on August 4th 2012. The MoLP-DOAS measured across the bay over the intertidal seaweed on a 1.4 km long light path (two-way) (see Fig. 12.29). During low tide, in-situ measurements by Open Path CE-DOAS were performed in the intertidal zone directly over the seaweed bed (position 1). As the water level rose, the CE-DOAS was moved out of the intertidal zone and continued measuring on land (position 2). A detailed time series of the measurements on Cashel bay is shown in Fig. 12.30.

Both the MoLP-DOAS and the Open Path CE-DOAS detected high levels of IO during low tide. They showed the same time dependence for both instruments, but seem to be delayed with respect to the tidal cycle by 1-2 hours. Instead of a clear IO peak the MoLP-DOAS observed relatively constant plateau between 13:15h and 15:00h with an average IO mixing ratio of  $(14 \pm 2)$  ppt and a maximum of  $(19 \pm 2)$  ppt at 14:47h.

The IO mixing ratios observed by the Open Path CE-DOAS at location (1) in the seaweed bed show a much higher temporal variability compared to the MoLP-DOAS measurements. In order to capture these IO variations the data from the Open Path CE-DOAS was evaluated at a time resolution of 10 s for this day (corresponding to 1000 accumulated scans at 10 ms exposure time). In the first measurement period, between 11h and 11:30h, IO varied between 2 ppt and 43 ppt with an average of 15 ppt. In the second period, between 13:20h and 14:50h, IO varied between 5.3 ppt and 81.7 ppt with an average of 38.7 ppt. The gap in between the first two periods is due to instrumental problems. After the second period the CE-DOAS was moved to land position (2) which was about 20 – 30 m downwind of the seaweed. The temporal variability of the IO levels at the land position was lower compared to the measurements in the seaweed bed. In the first 15 – 20 min of the land measurements, when large parts of the intertidal seaweed were still exposed, the IO mixing ratios were on average 44 ppt with a standard deviation of 11 ppt which is comparable to the IO levels observed in the seaweed bed. Later, the IO levels gradually decreased down, with increasing water level until about 16:30h when they went below the detection limit of about 3 ppt. The differences between the MoLP-DOAS and the Open Path CE-DOAS IO measurements and the temporal variability of the latter is caused by different local IO sources and transport processes. This is discussed in sec. 12.9.1.2.

August 4th was also the day where the stationary reference LP-DOAS at Mace Head observed the highest IO mixing ratio during the entire campaign of  $(13 \pm 1)$  ppt. A discussion of the possible source region is given in sec. 12.9.2.1 and the comparison to the mobile measurements is discussed in sec. 12.8.

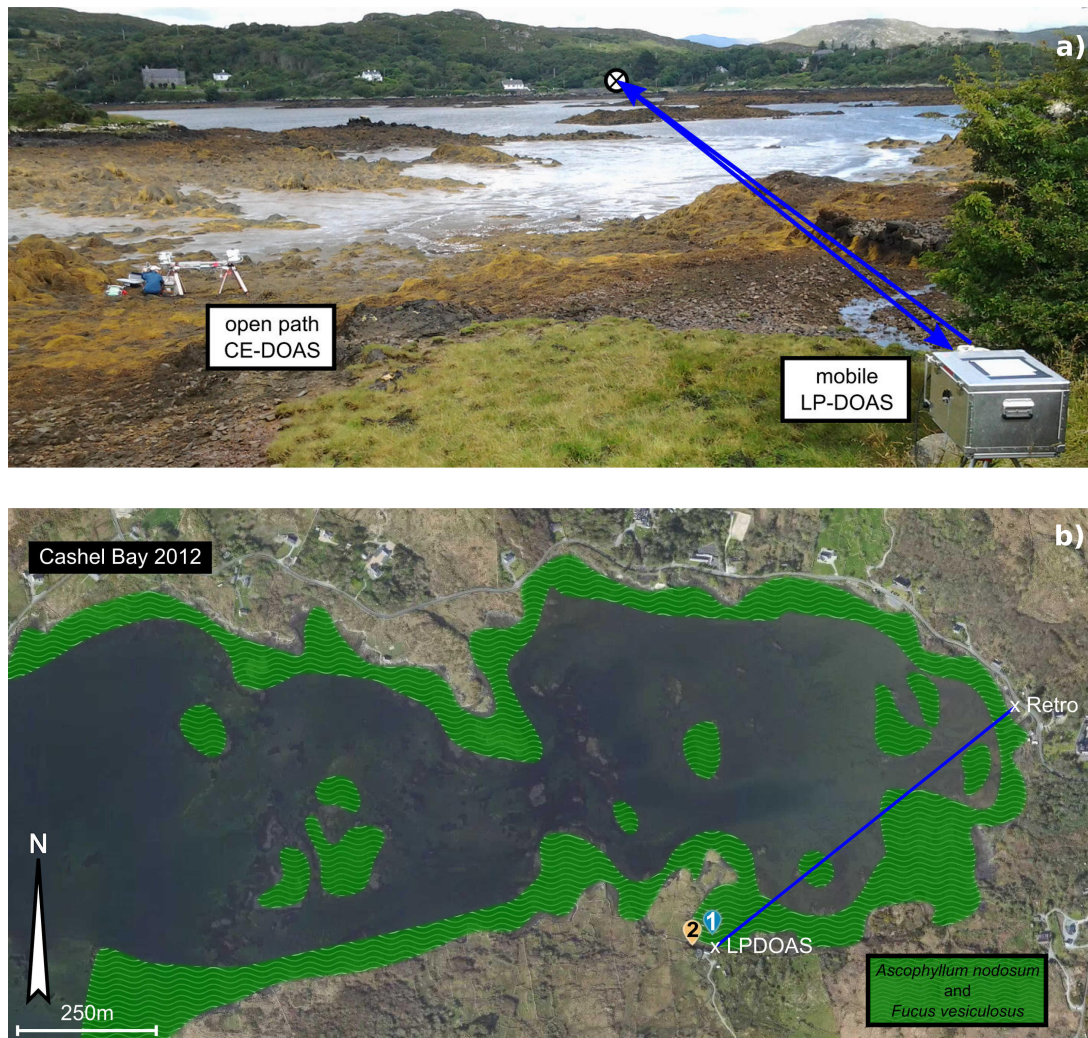


**Figure 12.29.** | Measurement site Cashel Bay. a) Photograph of the measurement site shot from the MoLP-DOAS northeastwards. The picture was taken on August 4th at 11:30 at low tide (tidal height  $-2$  m). b) Map of the measurement site with the MoLP-DOAS light path of 1396 m length (two-way) spanning the intertidal seaweed. Also shown are the measurement locations of the Open Path CE-DOAS in the intertidal zone (1) and on land (2). The seaweed distribution is based on maps from Stefan Schmitt (pers. observ. Ireland 2012), Hession et al., 1998 and Irish Seaweed Center [2001]. Satellite images ©Mapbox, ©OpenStreetMap.

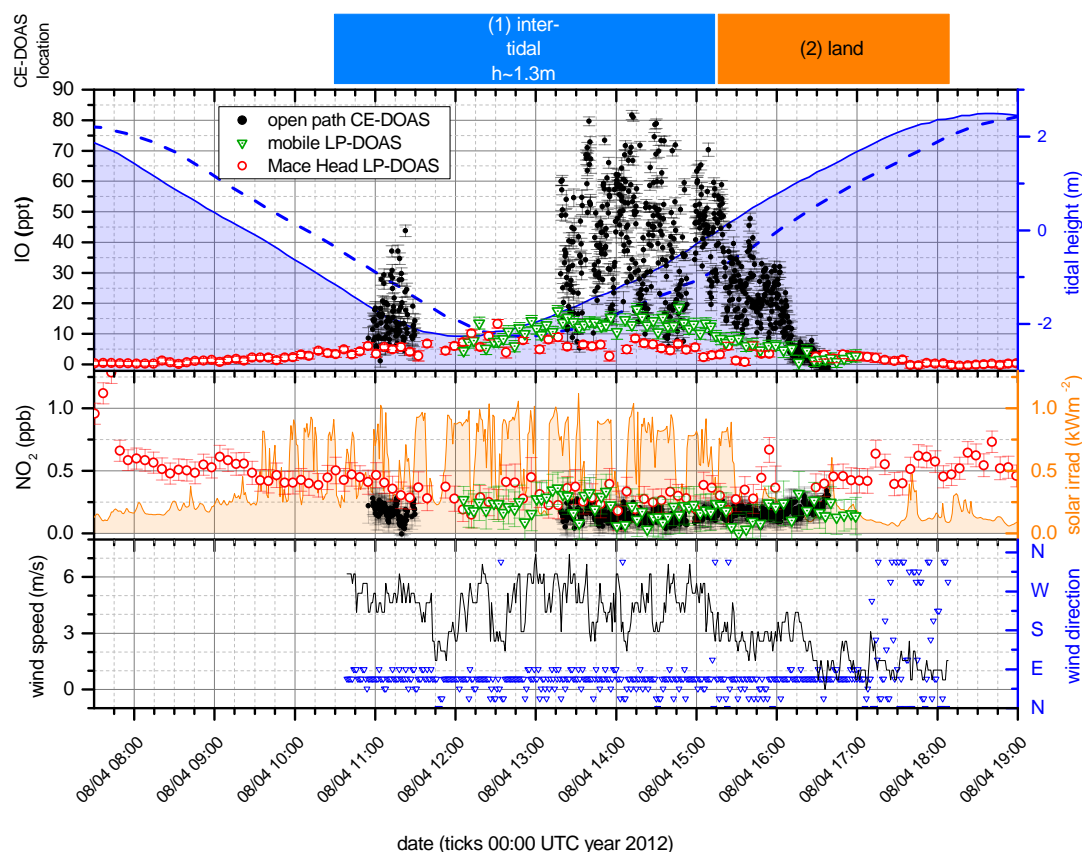


**Figure 12.30.** | Detailed results of IO and NO<sub>2</sub> for Cashel Bay. The top row indicates the measurement locations of the Open Path CE-DOAS on land (orange) and in the intertidal zone (blue). The numbers correspond to the markers in Fig. 12.28. IO and NO<sub>2</sub> measurements are shown in the top and middle graph respectively, for the Open Path CE-DOAS (black), and the MoLP-DOAS (green) and the stationary Mace Head LP-DOAS (red). In order to capture the high temporal variability of IO the shown CE-DOAS data are 10s averages. The blue solid line in top graph shows the tidal height at Galway Port, additionally the blue dashed line shows a 45 min shifted tidal cycle, which is a better match to personal observations. Also shown are the solar irradiance at Mace Head (middle) and the local wind speed and direction at the Cashel Bay site (bottom). A description of the tidal and meteorological measurements is given in sec.8.1.1. Even though the one minute average wind speed was moderate it actually blew in squalls which could not be resolved by the weather station.

### 12.4.5. Ballyconneely

Ballyconneely is a peninsula located about 15 km north east of Mace Head (see Fig. 12.1). Its north-western to south-western shore has a strong exposition to waves and has an abundant kelp resource with *L. hyperborea* being the most prevalent species [Hession et al., 1998]. Considerably calmer conditions are found in the crescent shaped Ballyconneely Bay (see Fig. 12.31) in the south eastern part of the peninsula where *A. nodosum* grows in great abundance in the intertidal zone [Irish Seaweed Center, 2001]. Measurements performed at two locations on Ballyconneely are described in the following.

#### 12.4.5.1. Ballyconneely Bay

Measurements at Ballyconneely Bay were performed in 2012 on August 5th. The MoLP-DOAS measured along the shore over the intertidal seaweed on a 1 km long light path (one-way) (see Fig. 12.31). The Open Path CE-DOAS was operated on a pier for in-situ measurements three to four meters above the adjacent seaweed bed. Like at Cashel Bay the CE-DOAS data was evaluated additionally at 10 s integration time to capture the high temporal variability of IO. The LP-DOAS light path crossed the pier right next to the CE-DOAS both measuring on the same height level.

The detailed time series for Ballyconneely Bay in Fig. 12.32 shows high IO during low tide for both the MoLP-DOAS and the Open Path CE-DOAS, and similar trends in the time dependence of the IO levels. However, the CE-DOAS data show a much higher temporal variability of up to a factor 10 within only two minutes. At 10:30h the maximum IO mixing ratios were observed, which were  $(18 \pm 1)$  ppt for the MoLP-DOAS. For the Open Path CE-DOAS they reached even  $(46.9 \pm 0.8)$  ppt at an averaging time of 10 s and  $(37.4 \pm 0.4)$  for 100 s respectively. The difference between IO levels observed by the Open Path CE-DOAS and MoLP-DOAS and the large variability of the IO mixing ratios observed by the the Open Path CE-DOAS are discussed in sec. 12.9.1.2. Surprisingly, IO was observed by both MoLP-DOAS and the Open Path CE-DOAS for another 45 min after the seaweed was already covered by water at 16:41h. Explanations for this behaviors and implications for the iodine emission by *A. nodosum* are discussed in sec. 12.9.1.5.

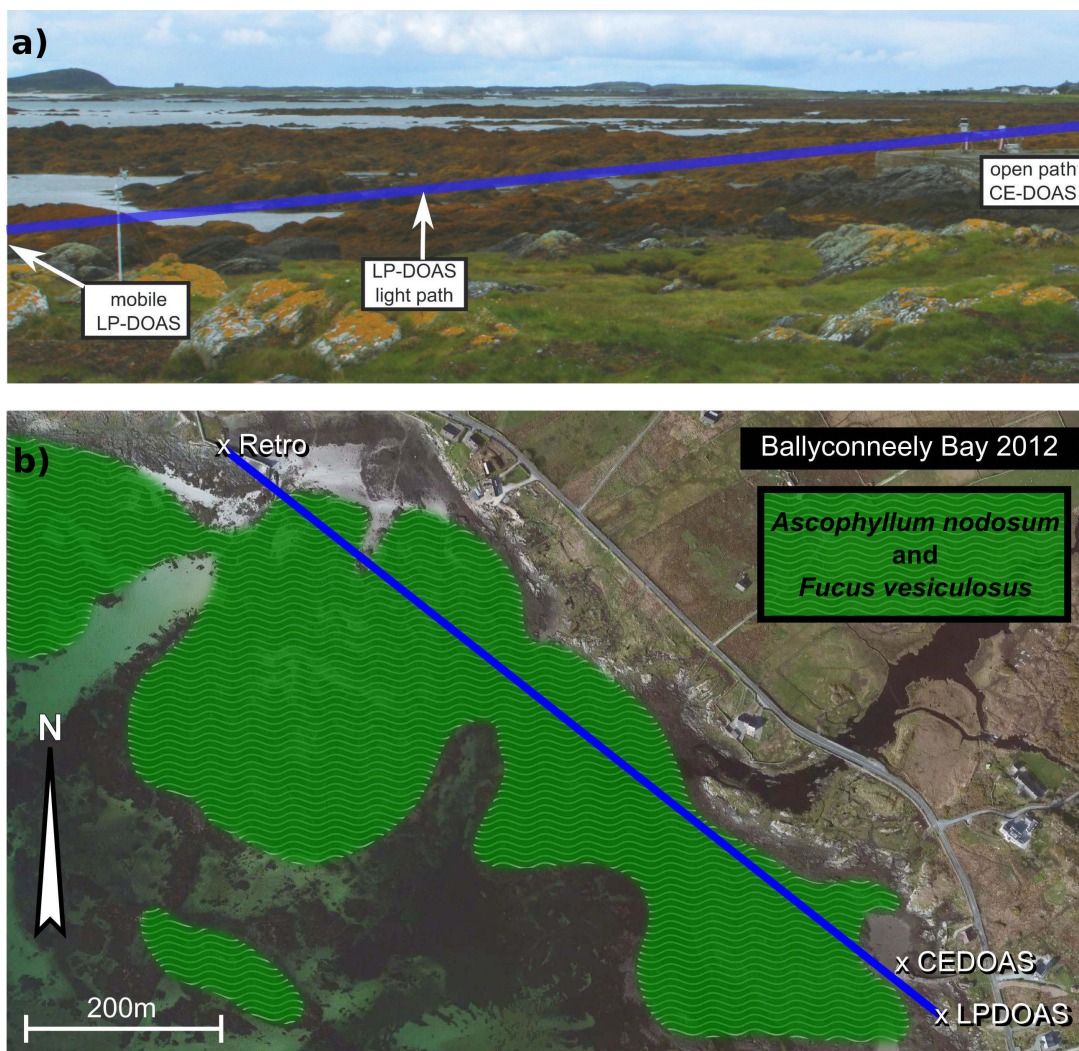


**Figure 12.31.** | **Measurement site Ballyconneely Bay.** a) Photograph of the measurement site short from between the MoLP-DOAS and the CE-DOAS location in northwestern direction. The picture was taken on August 5th at 16:00 in the middle of the tidal cycle (water level 0 m). b) Map of the measurement site with the location of the Open Path CE-DOAS on a pier and the MoLP-DOAS light path of 2070 m length (two-way) spanning over the intertidal seaweed. The seaweed distribution is based on maps from Stefan Schmitt (pers. observ. Ireland 2012), Hession et al., 1998 and Irish Seaweed Center [2001]. Satellite images ©Mapbox, ©OpenStreetMap.

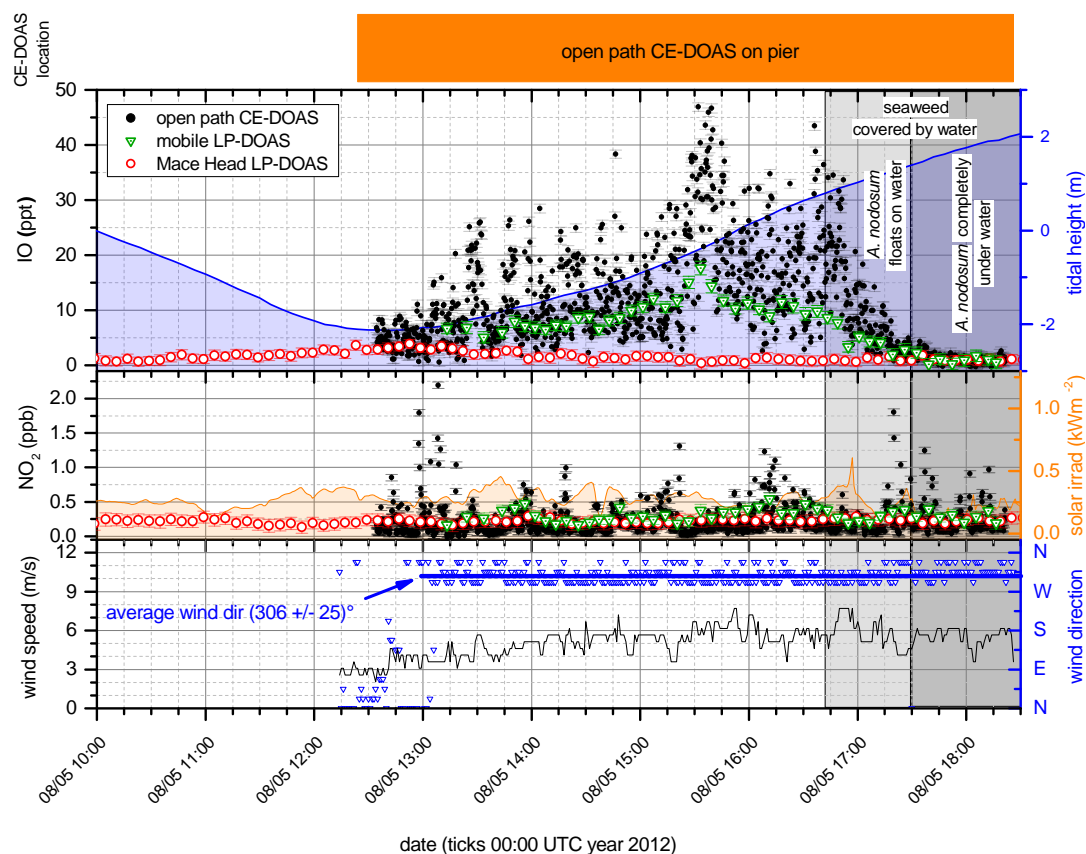


**Figure 12.32.** | Detailed results of IO and  $\text{NO}_2$  for Ballyconneely Bay The Open Path CE-DOAS measured at a fixed location on a pier close to the Seaweed field. IO and  $\text{NO}_2$  measurements are shown in the top and middle graph respectively, for the Open Path CE-DOAS (black), and the MoLP-DOAS (green) and the stationary Mace Head LP-DOAS (red). In order to capture the high temporal variability of IO the shown CE-DOAS data are 10s averages. Also shown are the tidal height (top) at Galway port, solar irradiance at Mace Head (middle) and the local wind speed and direction at Ballyconneely Bay (bottom). Towards the end of low tide two time periods are marked: The light gray are marks the period when *A. Nodosum* float on the water surface. The darker gray area indicates the time when *A. Nodosum* are is completely submerged.

### 12.4.5.2. Northern shore of the Ballyconneely peninsula

The Ballyconneely north site is located at the sandy beaches west of Knock Head, the northernmost point of Ballyconneely. The coastal relief is a mixture of sand beach, flat rock platform, rock islets, reefs and occasional low cliff. A high abundance of mixed *L. digitata* and *L. hyperborea* beds is found in the lower intertidal to subtidal zone [Irish Seaweed Center, 2001]. Due to the high wave exposure, there is no recorded growth of *A. nodosum* or other fucoids [Hession et al., 1998].

Measurements were performed in 2011 on June 7th. On this day, drift seaweed (mainly *L. digitata* and *L. hyperborea*) was very abundant on the beaches in the area, which is common especially after stormy weather. At the measurement site washed up drift seaweed densely covered an area of roughly 30 m × 50 m (see Fig. 12.33). For in-situ measurements the Open Path CE-DOAS was situated in the middle of the drift seaweed patch and the MoLP-DOAS measured along a 1002 m long light path (two-way) which was set up to cross the drift seaweed patch but also went over steeper, more rocky parts of the shore, where *L. digitata* and *L. hyperborea* are found in the lower intertidal to subtidal zone (see Fig. 12.33).

Placed in the patch of drift seaweed, the Open Path CE-DOAS observed significant IO with an average mixing ratio of  $(15 \pm 1)$  ppt and a peak value of 30.7 ppt. In contrast, the LP-DOAS did not detect any significant IO above the detection limit which was on average 8.7 ppt. The differences between the CE-DOAS and LP-DOAS measurements are further discussed in the frame of local sources in sec. 12.9.3.

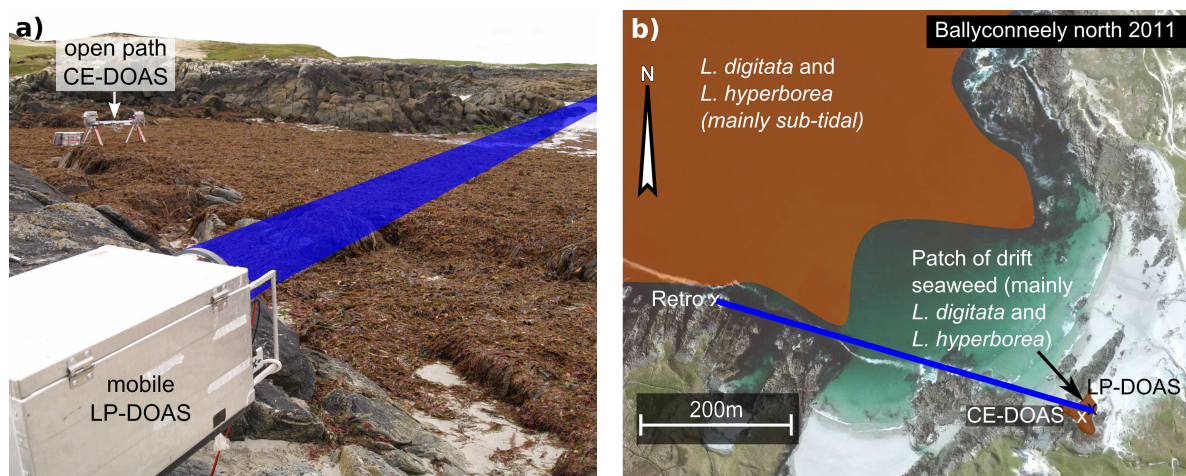


**Figure 12.33.** | Measurement site northern shore of Ballyconneely. a) Picture of the drift seaweed patch with the location of the CE-DOAS and MoLP-DOAS instrument. b) Map with the MoLP-DOAS light path of the MoLP-DOAS of 1002 m length (two-way) and the location of the Open Path CE-DOAS in a patch of drift seaweed. The seaweed distribution is based on maps from Stefan Schmitt (pers. observ. Ireland 2011) and Irish Seaweed Center [2001]. Satellite images ©Mapbox, ©OpenStreetMap.

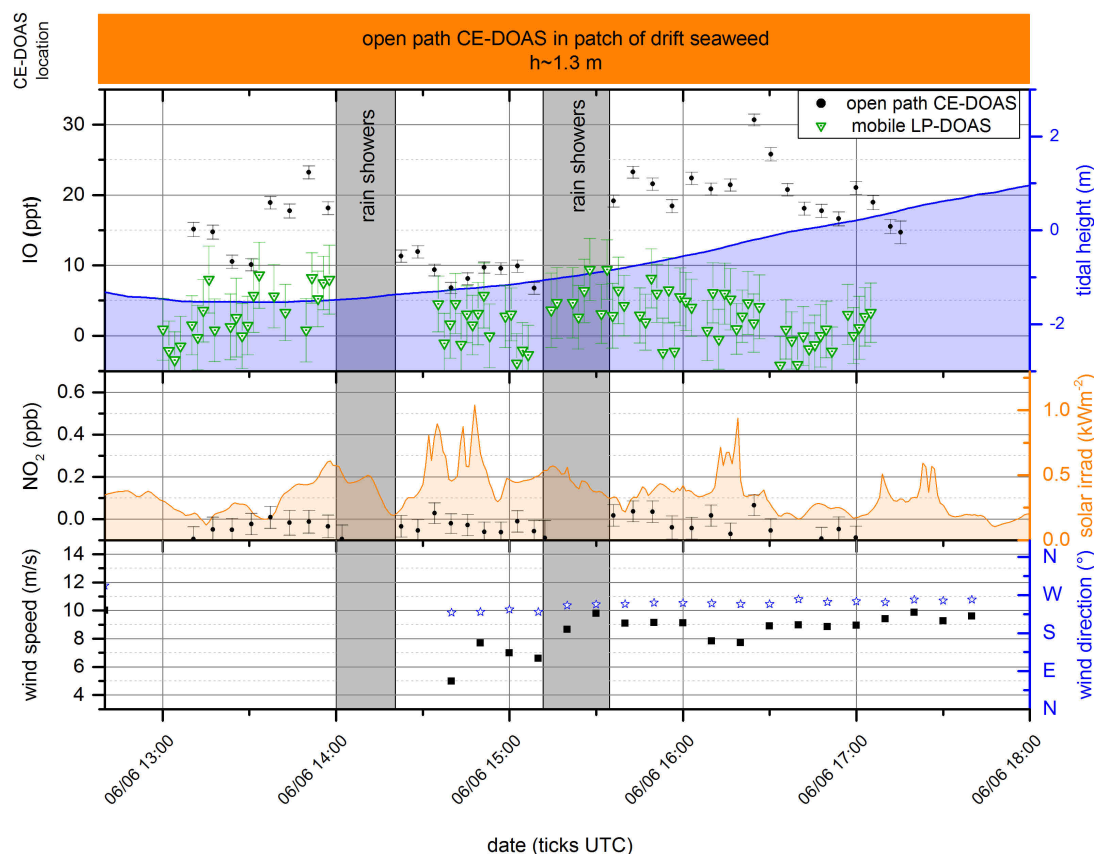


**Figure 12.34.** | Detailed results of IO and  $\text{NO}_2$  for the northern shore of Ballyconneely. The Open Path CE-DOAS and the MoLP-DOAS measured mainly over a patch of drift seaweed and were setup according to Fig. 12.33. The top graph shows IO mixing ratios measured by the Open Path CE-DOAS (black), and the MoLP-DOAS (green).  $\text{NO}_2$  measured by the Open Path CE-DOAS is shown in the middle graph. Also shown are the tidal height (top) at Galway port, solar irradiance at Mace Head (middle) and the local wind speed and direction (bottom) at the Ballyconneely North site. A description of the tidal and meteorological measurements is given in sec.8.1.1. Additionally periods of rain showers are marked in grey, but light drizzle was encountered during the whole day.

### 12.4.6. Mweenish Island

Located directly east of the MRI, Mweenish is a small island that is connected to the land by a road. The southern shore of Mweenish Island has a seaweed population typical for an exposed rocky coast. The upper shore has sparsely populated by fucoids, either *F. spiralis* or *F. vesiculosus*. At some exposed shores *F. serratus* is found in the mid- to lower intertidal zone. High abundance of *L. digitata* and *L. hyperborea* is found in the subtidal zone and to some extent *L. digitata* is also present in the lower intertidal zone. [Irish Seaweed Center, 2001]

Open path CE-DOAS and MoLP-DOAS measurements were performed on June 6th 2011 on the southern shore in a bay with sandy beaches. The measurement setup is shown in Fig. 12.35. Similar to Ballyconneely north, a 20 m × 60 m large patch of drift seaweed mainly composed of *L. hyperborea* and *L. digitata*, was found at the measurement site. The results of the Open Path CE-DOAS and MoLP-DOAS are shown in Fig. 12.36.

From 9:00 to 12:00 and from 14:40 to 16:50 the Open Path CE-DOAS was applied for in-situ measurements in the drift seaweed patch (location (1) in Fig. 12.35) where it observed on average a IO mixing ratio of  $(26.2 \pm 0.7)$  ppt and maximum of  $(40.2 \pm 0.7)$  ppt at a height of 1.3 m above the seaweed. At 12:10 when the tide was close to the low water level the CE-DOAS was moved eastwards to location (2), a small seaweed patch in the mid-intertidal zone, mainly of *F. serratus* and a single *L. digitata* plant. There, it first measured at a height of about 1.3 m above the seaweed and observed an average IO mixing ratio of  $(11.9 \pm 0.6)$  ppt, which is less than half of the IO mixing ratio observed above the drift seaweed. At about 12:40, when the CE-DOAS light path was lowered to a height of 30 cm above the seaweed the average IO mixing ratio increased by more than a factor of two to  $(26.8 \pm 0.6)$  ppt which is consistent with the IO height profile discussed in sect. 12.10. At location (3), the IO mixing ratio dropped below the detection limit of 1 ppt.

The MoLP-DOAS was set up close to the drift weed and measured along a 1710 m long light path (two-way) parallel to the rocky shore. The MoLP-DOAS observed an average IO mixing ratio of  $(5 \pm 3)$  ppt and a maximum value of  $(14 \pm 3)$  ppt. Significant IO above the detection limit of 6.5 ppt was only observed between 12:00h and 14:00h which corresponds to a tidal height of less than -1.5 m. The much lower IO levels observed by the MoLP-DOAS compared to Open Path CE-DOAS measurements at location (1) and (2) in Fig. 12.35 are a further discussed in the frame of local sources in sec. 12.9.3.



**Figure 12.35.** | **Measurement site Mweenish Island.** a) Picture of the measurement site with the CE-DOAS measuring in a patch of washed up drift seaweed. b) Map with the MoLP-DOAS light path of 1710 m length (two-way) and the three locations of the Open Path CE-DOAS. Location (1) is in a patch of drift seaweed on the beach, location (2) a small intertidal seaweed patch, and location (3) is on the grass at the northern end of the beach. The seaweed distribution is based on maps from Stefan Schmitt (pers. observ. Ireland 2011) and Irish Seaweed Center [2001] Satellite images ©Mapbox, ©OpenStreetMap.

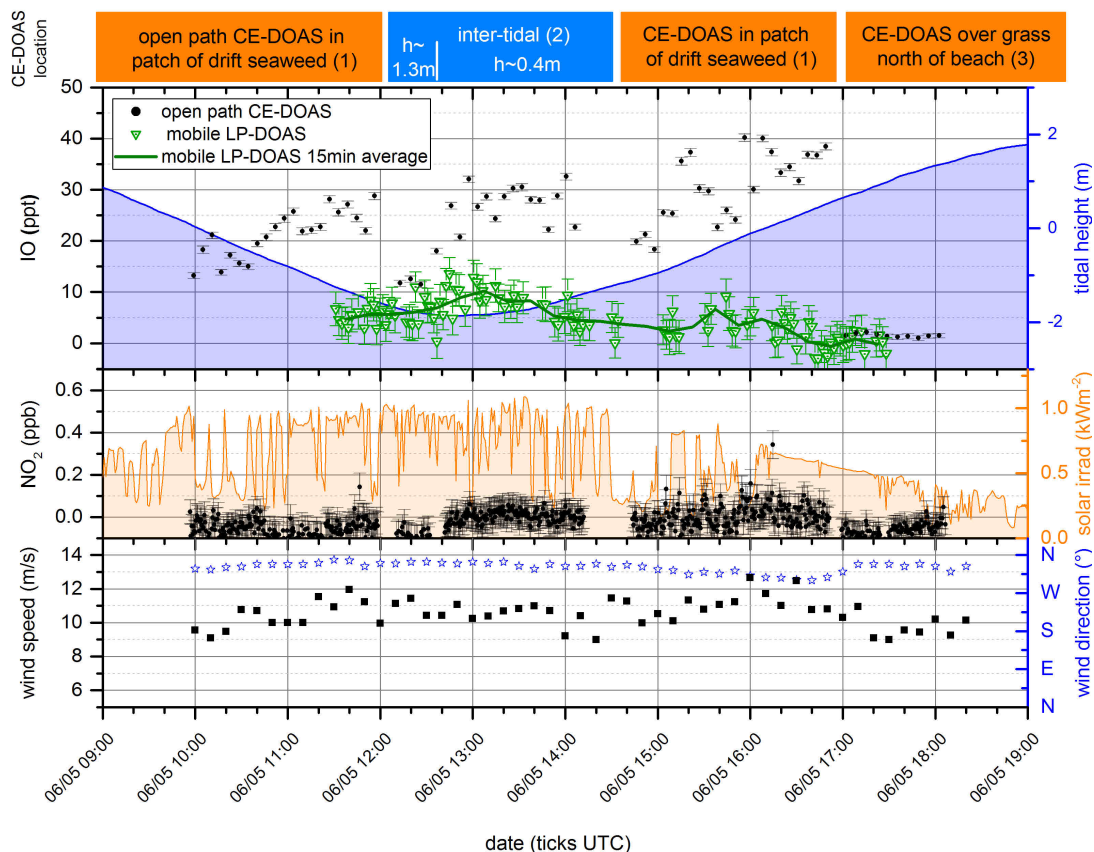


**Figure 12.36.** | Detailed results of IO and NO<sub>2</sub> for Mweenish Island. The top row indicates the measurement locations of the Open Path CE-DOAS on land (orange) and in the intertidal zone (blue). The numbers correspond to the markers in Fig. 12.35. The top graph shows IO mixing ratios measured by the Open Path CE-DOAS (black), and the MoLP-DOAS (green). NO<sub>2</sub> measured by the Open Path CE-DOAS is shown in the middle graph. Also shown are the tidal height (top) at Galway port, solar irradiance at Mace Head (middle) and the local wind speed and direction (bottom) at the Ballyconneely North site. A description of the tidal and meteorological measurements is given in sec.8.1.1.

## 12.5. Discussion of Closed Path CE-DOAS Measurements

Sampling of highly reactive compounds like IO into a closed measurement system is difficult and prone to errors. Major issues are losses on the instruments surfaces/walls and changes in chemical reaction paths due to the absence of sunlight and the respective photochemistry. It was tried to reduce these influences in the Closed Path CE-DOAS by a short sample residence time of less than 3 s in the system and by using inert Teflon parts in the gas flow system. However, even with the applied efforts the Closed Path CE-DOAS measured only about 10% (highly variable) of the IO mixing ratio detected by the Open Path CE-DOAS instrument when both instruments are co-located in a seaweed field where significant IO is present. One approach may be to characterize the losses and correct the measurements. An example time series for July 21st 2012 is shown in Fig. 12.38 and the corresponding correlation plot is shown in Fig. 12.68a). On the other hand, comparisons of NO<sub>2</sub> between open and Closed Path CE-DOAS shows a linear correlation with a slope of approximately 0.9 (see Fig. 12.37). Thus, the NO<sub>2</sub> measurements of both instruments agree within the uncertainty of the optical path length (10%)

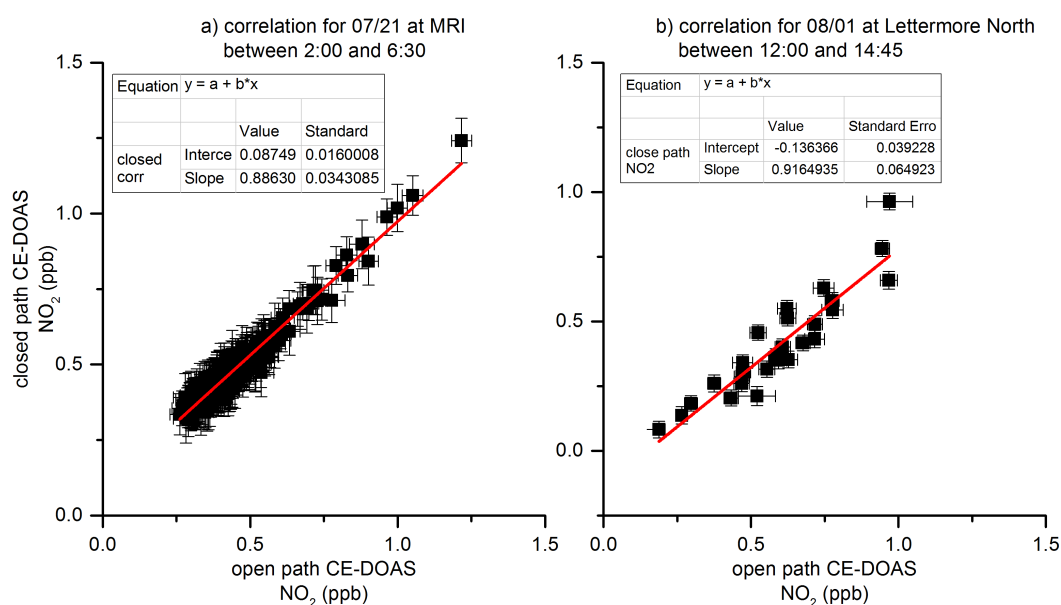


**Figure 12.37.** | Correlation of NO<sub>2</sub> measurements from open and Closed Path CE-DOAS. Measurements for the NO<sub>2</sub> correlation shown in a) were recorded mainly during high tide and night time (no IO was measured by the Open path CE-DOAS). Both instruments were co-located on land and the top cover of the Closed Path CE-DOAS was closed. Measurements for the NO<sub>2</sub> correlation shown in b) were recorded during low tide and day time. Both instruments were co-located in the intertidal zone and the top cover of the Closed Path CE-DOAS was removed.

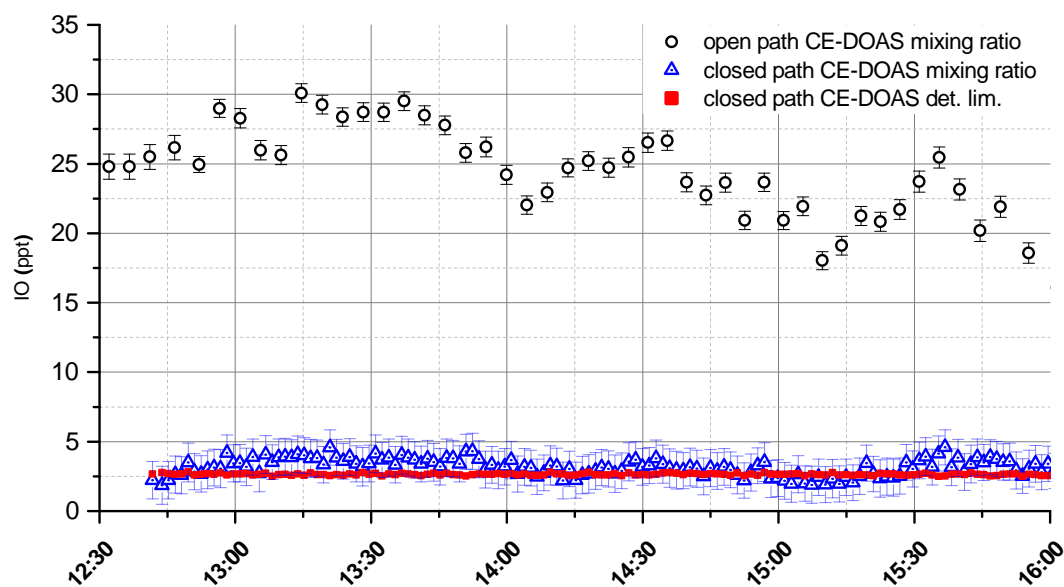


**Figure 12.38.** | Closed Path and Open Path CE-DOAS measurements on July 21st 2012 at the MRI. In this period, both instruments were co-located and measured at the same height level. The top cover of the Closed Path CE-DOAS was always closed.

for both instruments), which allows to rule out a general malfunction or miscalibration of the Closed Path CE-DOAS.

In order to investigate the role of photochemistry, the top cover of the Closed Path CE-DOAS was removed for further side by side comparisons of the two instruments. With the top cover removed, the Teflon tubing, aerosol filter unit and measuring cell are illuminated by direct and scattered sunlight (see Fig. 6.1). This allows the photolysis chemical compounds in the sampled air within the tubing and possibly also the measuring cell. Especially the tubing and the aerosol filter are made of relatively thin PFA (1 – 2mm) so that a substantial amount of the visible sunlight could be transmitted. For the measuring cell, transmission of solar radiation is much weaker because its PTFE walls are already more than 10 mm thick. As shown in Fig. 12.39 and Fig. 12.41 the IO level detected by the closed path CE-DOAS was increased by a factor of 2.4 to 3.0 when the top cover was removed. This increase generally happens almost instantaneously between two subsequently recorded spectra and thus on a time scale of less than 30 s. Additionally, for the removed top cover the IO mixing ratio measured by the closed path CE-DOAS show a stronger variation with changes in the solar irradiance than the Open Path CE-DOAS. This can be seen particularly when the sun disappears behind clouds as shown in the middle of Fig. 12.39 and towards the end of Fig. 12.41. This effect can also be seen in the correlation of IO mixing ratios separated for measurements with closed top cover and open top cover as shown in Fig. 12.42a)-c). In both cases there is a linear correlation but for measurements with open top cover the slope of 0.24 to 0.3 is much higher than the slope of approximately 0.1 for measurements with closed top cover. A particularly striking example

## 12.5. Discussion of Closed Path CE-DOAS Measurements

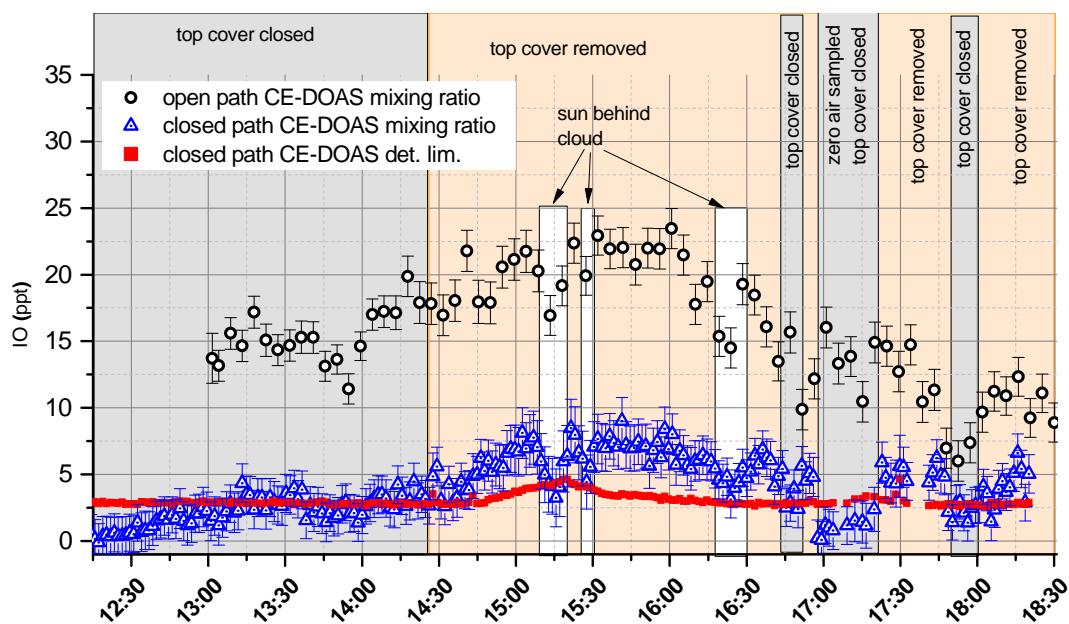


**Figure 12.39.** | Closed Path and Open Path CE-DOAS measurements on July 25th 2012 at the MRI. In this period both instruments are co-located and measure at same height level. The top cover of the Closed Path CE-DOAS was removed in some periods, allowing solar illumination of the gas flow system in the instrument.

are the measurements on June 7th at the MRI with switching between open and closed top cover measurements. The results show distinct linear branches for each configuration in the correlation plot in Fig. 12.42c).

Potential candidates for the loss paths in the Closed Path CE-DOAS are the reaction of IO with  $\text{NO}_2$  and the IO self reaction (see Tab. 2.2) or wall losses. Even though these reactions also occur in ambient air, in the dark Closed Path CE-DOAS the respective back reactions via photolysis of  $\text{IONO}_2$  and OIO are not present. Thus, these loss paths become more efficient compared to ambient air conditions. It was also considered that IO could be lost to aerosol particles on the Teflon membrane filter, which could act as a reservoir of reactive iodine that could be activated by solar radiation. However, this is unlikely because in this case there should be no linear correlation between the Open Path and Closed Path CE-DOAS IO measurements.

In summary the Closed Path CE-DOAS could not be used for reliable IO measurements. The losses for the closed top cover configuration of more than 90 % are too high and the underlying loss mechanisms remain unknown. Also the configuration with opened top cover could not be used because for times scales of several ten minutes required for measurements of the vertical gradient of IO in a seaweed field the solar irradiance at the Open Path CE-DOAS did not stay constant. Thus at least an additional measurement of solar irradiation directly at the Open Path CE-DOAS instrument would have been necessary.

In conclusion, the loss factors are variable and range between 97 % and 70 %. A reliable correction is thus not possible. Additionally, the losses are too high to observe the low IO

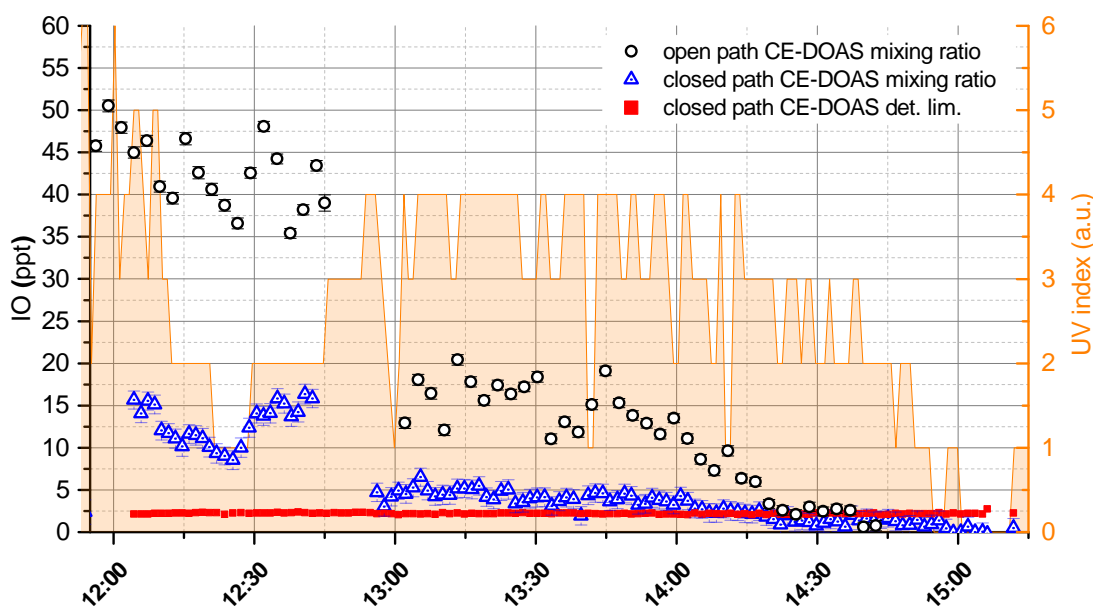


**Figure 12.40.** | Closed Path and Open Path CE-DOAS measurements on August 1st 2012 at Lettermore Island North. In the shown period both instruments are co-located and measure at same height level. The top cover of the Closed Path CE-DOAS was removed for the whole time, allowing solar illumination of the gas flow system in the instrument.

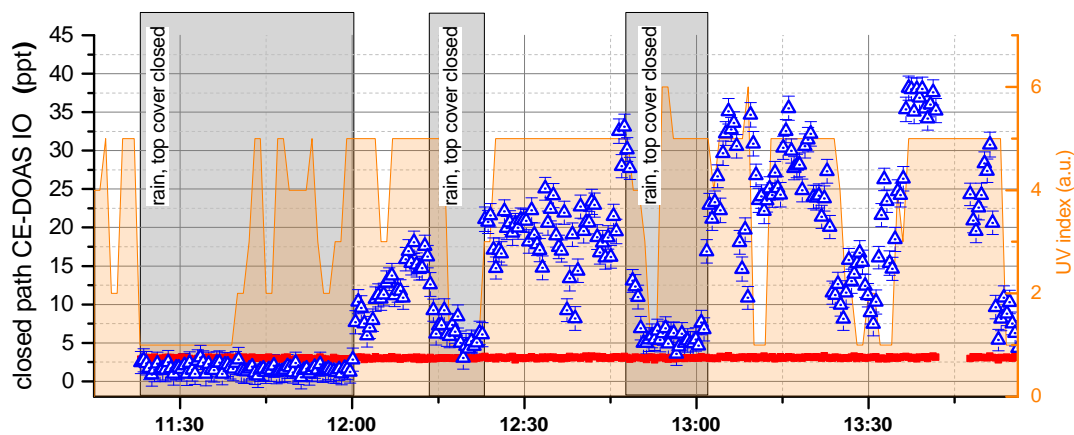


**Figure 12.41.** | Open path CE-DOAS measurements on August 4th 2012 at Cashel Bay. The top cover of the Closed Path CE-DOAS was removed for some periods, allowing solar illumination of the gas flow system in the instrument. No simultaneous Open Path CE-DOAS measurements are available or the shown period.

## 12.5. Discussion of Closed Path CE-DOAS Measurements

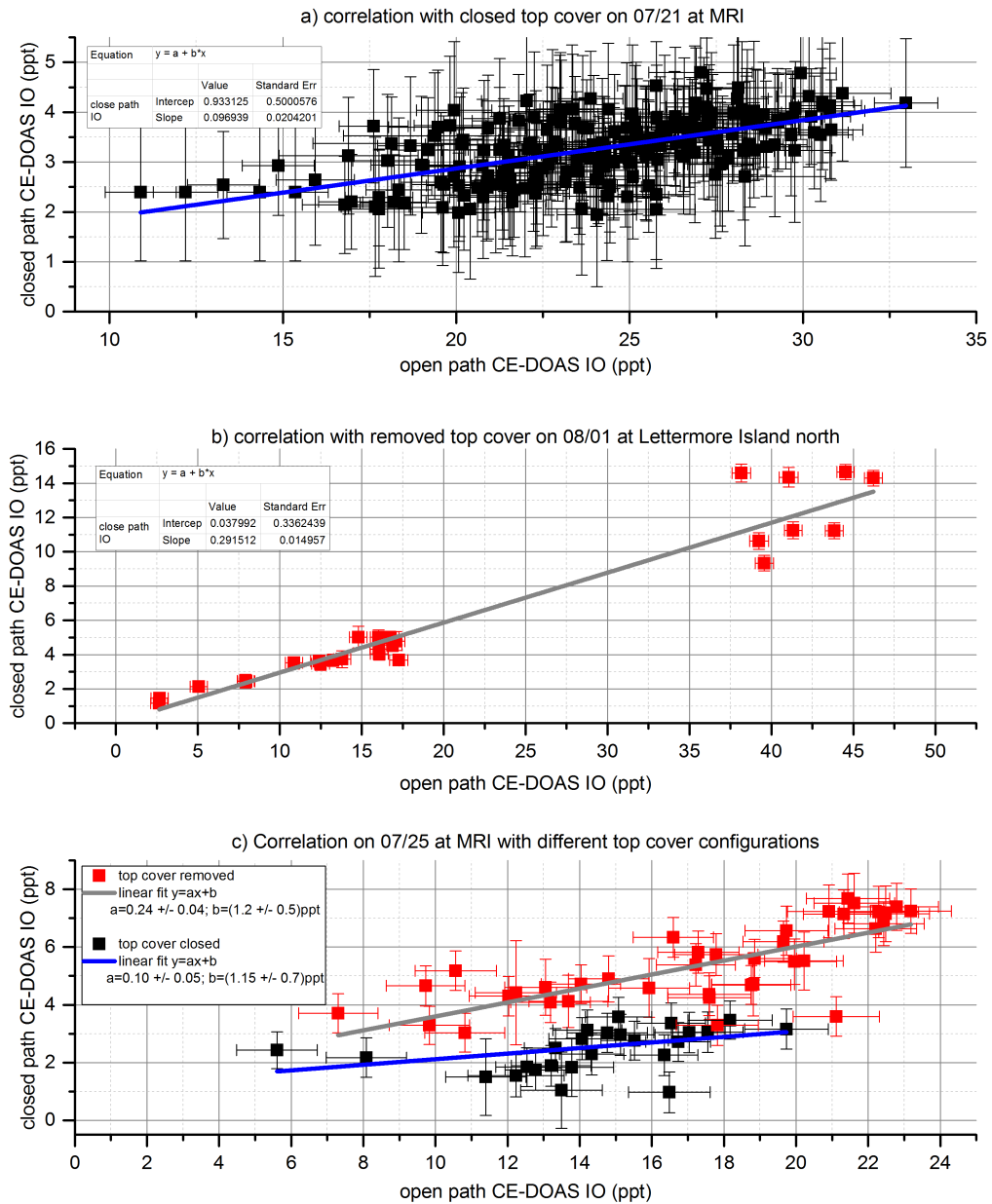


**Figure 12.42.** | Correlation between close path and Open Path CE-DOAS IO measurements. Both instruments measured simultaneously at the same location and the Closed Path CE-DOAS sampled air masses at the height level of the Open Path CE-DOAS light path.

concentrations in many cases.

## 12.6. Discussion of NO<sub>x</sub> - IO Interaction

The Irish west coast is a very rural area and generally considered an clean air location for air masses from the ocean. However, due to local settlements and traffic air masses which passed the land are considered as semi-polluted with NO<sub>2</sub> mixing ratios of several hundred ppt to few ppb. NO<sub>2</sub> acts as sink for IO via reaction R 2.33 and I via reaction R 2.32 forming IONO<sub>2</sub> and INO<sub>2</sub> respectively. Already at 1 ppb NO<sub>2</sub> the formation of IONO<sub>2</sub> through R 2.33 becomes comparably fast to the IO self reaction R 2.24a and the IO photolysis R 2.22. IONO<sub>2</sub> is considered a sink since its photolysis is comparatively slow (0.5 min to 5 min lifetime) and it can be removed by uptake into moist sea-salt aerosol. Therefore, an anti-correlation between IO and high NO<sub>2</sub> levels is expected and has been observed in previous studies Hebestreit [e.g. 2001]. However, two LP-DOAS studies [Stutz et al., 2007; Mahajan et al., 2009] observed high levels of IO in polluted environments. Quantum chemical calculations by Kaltsoyannis and Plane [2008] suggest a possible rapid recycling of IONO<sub>2</sub> back to I<sub>2</sub> by reaction with I atoms R 2.37. However, this is highly speculative since there is no experimental evidence for reaction R 2.37 and there is a two order of magnitude uncertainty in the calculated reaction rate constant. Also the interpretation of [Stutz et al., 2007] and [Mahajan et al., 2009] might be problematic since they assumed that both IO and NO<sub>2</sub> were observed at the same location. However, this must not be true since IO and NO<sub>2</sub> could also be located at different parts of their kilometer long light paths, especially considering the assumed inhomogeneous distribution of IO sources in so called “hot-spots”.

Our measurements with the stationary Mace Head LP-DOAS showed significant NO<sub>2</sub> above

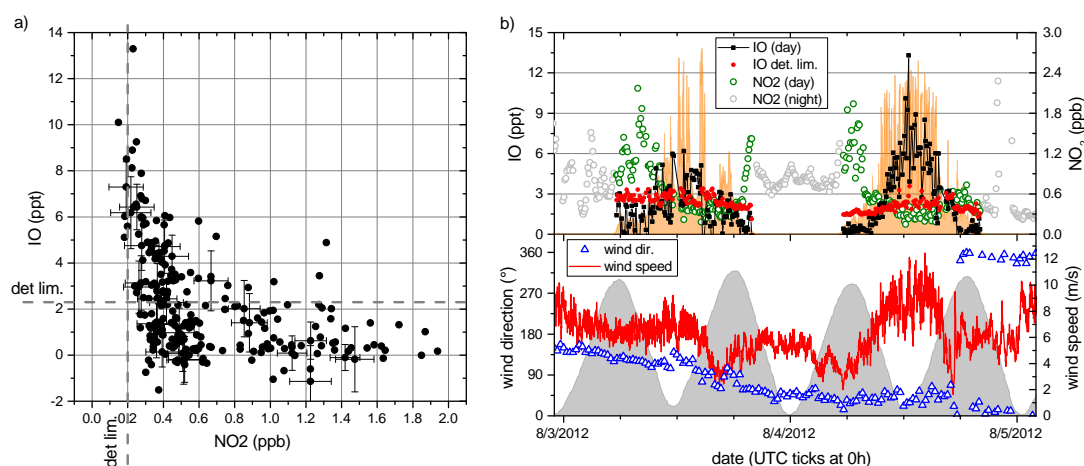


**Figure 12.43.** | IO vs. NO<sub>2</sub>, during daytime, and time series for August 3rd and 4th 2012, observed by the stationary Mace Head LP-DOAS Left: scatter plot IO vs NO<sub>2</sub>, for solar irradiance above 20 W m<sup>-2</sup>, with detection limits (dashed grey lines). Right: time series of IO and NO<sub>2</sub> mixing ratios together with wind speed and direction, tidal height as gray overlay in bottom graph and solar irradiance as orange overlay in the top graph.

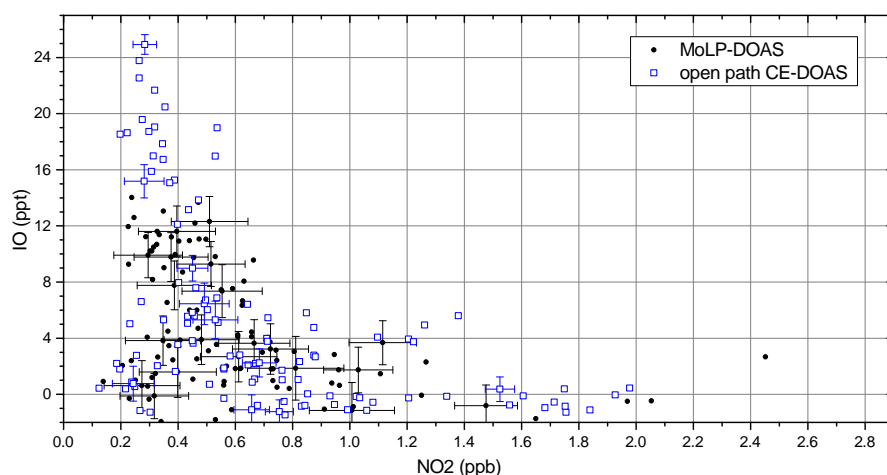


**Figure 12.44.** | IO vs.  $\text{NO}_2$  for measurements at Lettermore Island South on August 3rd 2012, during daytime Black dots show the LP-DOAS data and blue open boxes the Open Path CE-DOAS data. The scatter plot shows an anti correlation between IO and  $\text{NO}_2$ . The corresponding time series is shown in Fig. 12.28

the 0.18 ppb detection limit only on 11 of the 22 measurement days. However, only on two days, August 3rd and 4th 2012, elevated  $\text{NO}_2$  above 300 ppt was observed during daytime where it could possibly interfere with IO. The IO vs.  $\text{NO}_2$  scatter plot for August 3rd and 4th 2012 Figure 12.43 indicates an anti correlation between high IO and high  $\text{NO}_2$  levels. However, the wind direction and speed vary slightly in this period. Therefore, the observed anti correlation between IO vs.  $\text{NO}_2$  could partly be an effect of different air masses observed by the LP-DOAS.

Measurements by the MoLP-DOAS rarely show significant daytime  $\text{NO}_2$ . The few occasions of elevated  $\text{NO}_2$  at MRI (July 22nd, 24th and 30th 2012 see Fig. 12.23 and Fig. 12.24) were all very short peaks of  $\text{NO}_2$ , probably from traffic, and during high tide period where no IO is expected anyways. Lettermore Island south (August 3rd 2012) is the only other site where the MoLP-DOAS observed elevated  $\text{NO}_2$ , as shown in Fig. 12.28. The IO levels were not influenced for  $\text{NO}_2$  mixing ratios up to 0.6 ppb. At 14:14h when  $\text{NO}_2$  increased to about 2 ppb IO went from about 4 ppt below the detection limit of 3 ppt for the MoLP-DOAS and 2.1 ppt for the Open Path CE-DOAS, which observed the very similar IO and  $\text{NO}_2$  levels. Thus, this is another proof for the expected anti-correlation between IO and  $\text{NO}_2$ .

The Open Path CE-DOAS observed elevated  $\text{NO}_2$  levels at some more days, which are discussed in the following. On May 31st 2011 the Open Path CE-DOAS measured in the seaweed bed at MRI. As shown in Fig. 12.19 between 10:31h and 10:42h a truck parking upwind of the CE-DOAS caused an increase of  $\text{NO}_2$  from below 0.16 ppb (det. lim.) to an average of 2.3ppt with a maximum of 4.1 ppt. Immediately when the  $\text{NO}_2$  peak arrived at the CE-DOAS IO levels dropped from 17 ppt to 6 ppt and remained low until the end of the peak after which the IO recovered back to a mixing ratio of 20 ppt. A similar situation was found on June 4th 2011, again during a measurement in the seaweed bed at MRI. The time series shown

in Fig. 12.21 starts with less than 1.3 ppt IO at  $(3.28 \pm 0.04)$  ppb NO<sub>2</sub>, again due to a truck parking upwind of the CE-DOAS. As the NO<sub>2</sub> levels decrease over the subsequent 50 min the IO level simultaneously increases to its final level of  $(16.7 \pm 0.6)$  ppt which is then sustained for the subsequent three hours (without NO<sub>2</sub>). However, it should be noted that at the end of the NO<sub>2</sub> peak also the wind direction changes from SSW to NW and therefore most likely the reduction of NO<sub>2</sub> is due to different air masses.

Furthermore, on August 1st 2012 the CE-DOAS observes relatively high NO<sub>2</sub> mixing ratios of up to more than 1 ppb. However, the elevated NO<sub>2</sub> mixing ratios do not seem to influence the IO levels of up to  $(50.5 \pm 7.0)$  ppt as can be seen from the IO vs. NO<sub>2</sub> scatterplot in Fig. 12.45 and the time series in Fig. 12.26. Especially since there seems to be no anti correlation between the observed IO and the NO<sub>2</sub> peaks. At first sight this is surprising since at 1 ppb NO<sub>2</sub> the reaction  $\text{IO} + \text{NO}_2 \rightarrow \text{IONO}_2$  is expected to be a fast sink for IO with a lifetime of about 10 s. However, as illustrated in Fig. 12.46 NO<sub>2</sub> and IO have a very different spatial distribution. Additionally, a map of the measurement site is shown in Fig. 12.25. The CE-DOAS measured in the seaweed bed about 1.3 m above the seaweed. Thus, the estimated vertical transport time of IO from the seaweed to the CE-DOAS is only 10 s for the typical wind speed of 8 m/s on August 1st, assuming neutral stability conditions and a logarithmic wind profile (see sec. 12.10). On the other hand NO<sub>2</sub> mainly originates from the close by causeway which is at least 5 m above the seaweed bed and for the prevailing westerly wind about 80 m upwind of the CE-DOAS which corresponds to a travel time of 10 s at 8 m/s wind speed. However, the few ppb NO<sub>2</sub> observed by the CE-DOAS is still very low for a vehicle exhaust plume. Also the plume must be relatively narrow since the MoLP-DOAS, whose light path is parallel south to the causeway, measures no elevated NO<sub>2</sub>. This shows that the CE-DOAS is only at the fringe of the plume. Thus, the contact time between IO and NO<sub>2</sub> before the CE-DOAS measurement is expected to be too short ( $\ll 10$  s) to see an anti-correlation between IO and NO<sub>2</sub>.

In summary the results indicate a clear anti-correlation of IO and NO<sub>2</sub> for well mixed air masses. Therefore, no indication for the potential rapid recycling of IONO<sub>2</sub> to I<sub>2</sub> by reaction with I R 2.37 was found.

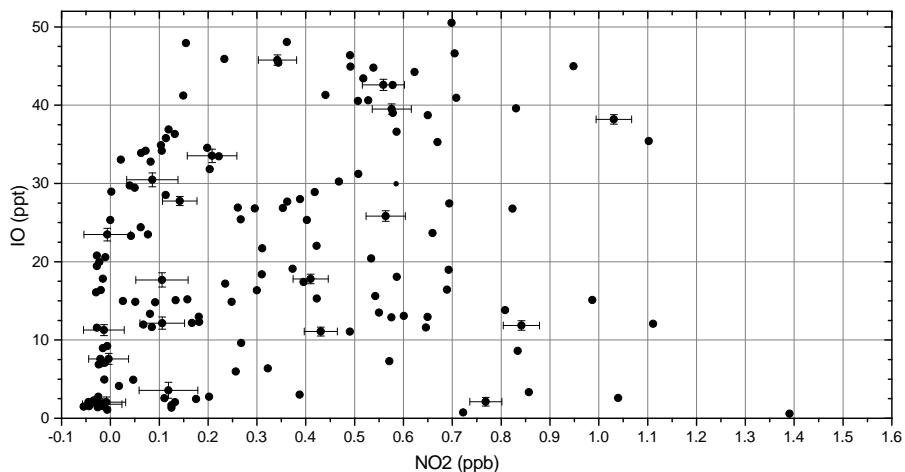


**Figure 12.45.** | IO vs. NO<sub>2</sub> for Open Path CE-DOAS measurements at Lettermore Island North on August 1st and 2nd 2012 No correlation between IO and NO<sub>2</sub> is observed. The corresponding time series is shown in Fig. 12.26

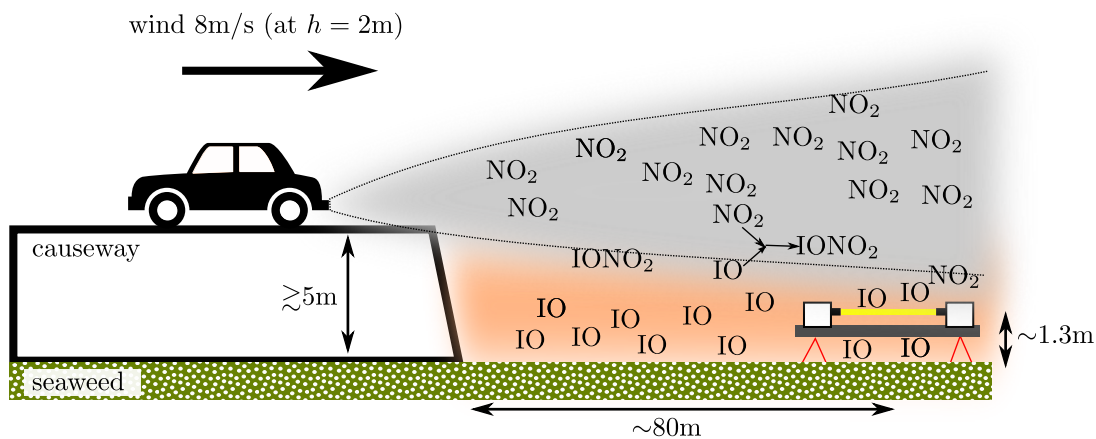


**Figure 12.46.** | Sketch of the IO - NO<sub>2</sub> interaction at Lettermore Island North on August 1st and 2nd 2012 The Open Path CE-DOAS instrument measures IO and NO<sub>2</sub> in the intertidal zone about 1.3 m above the seaweed bed at location (1) in Fig. 12.25. NO<sub>x</sub> (NO+NO<sub>2</sub>) is emitted by traffic on a causeway, which is at least 5 m above the seaweed bed and 80 m up-wind of the CE-DOAS. Reactions between IO and NO<sub>2</sub> can only occur where both air masses air mixed.

## 12.7. Discussion: Correlation of IO and Solar Irradiance

Solar irradiance influences the observed IO mixing ratios in several ways. Firstly through photochemistry (sec. 2.3): the source species emitted by seaweed is  $I_2$ , and to some minor extent iodocarbons. Photolysis of these molecules yields I atoms which rapidly react with  $O_3$  to form IO. Photolysis of OIO and  $IONO_2$  may act as secondary sources of IO but there are still too many open questions on their photochemistry to assess their impact. IO itself is also photoliable, however due to the rapid back reaction of I and  $O_3$  this essentially leads to a null cycle. Details on the photochemistry is given in sec. 2.3.1. Secondly, photolytic stress increases the emission of  $I_2$  by seaweeds which are the dominant  $I_2$  source at coastal sites.

Previous studies at mid-latitude coastal sites observed positive correlations of IO and solar irradiance during low tide periods [e.g. Hebestreit, 2001; Furneaux et al., 2010]. This was also observed during our study in Ireland. As an example the MoLP-DOAS measurements on June 30th 2012 at MRI are shown in Fig. 12.47. The shown time period is limited to tidal height below 0 m because only then most seaweed is exposed to air, a prerequisite for emission of  $I_2$ . Furthermore only the daytime low tide is shown since no significant IO is found during night. A linear increase of IO levels with solar irradiance is observed. However, in the first hour of the time series there is a delay between IO mixing ratios and the solar irradiance. The reason might

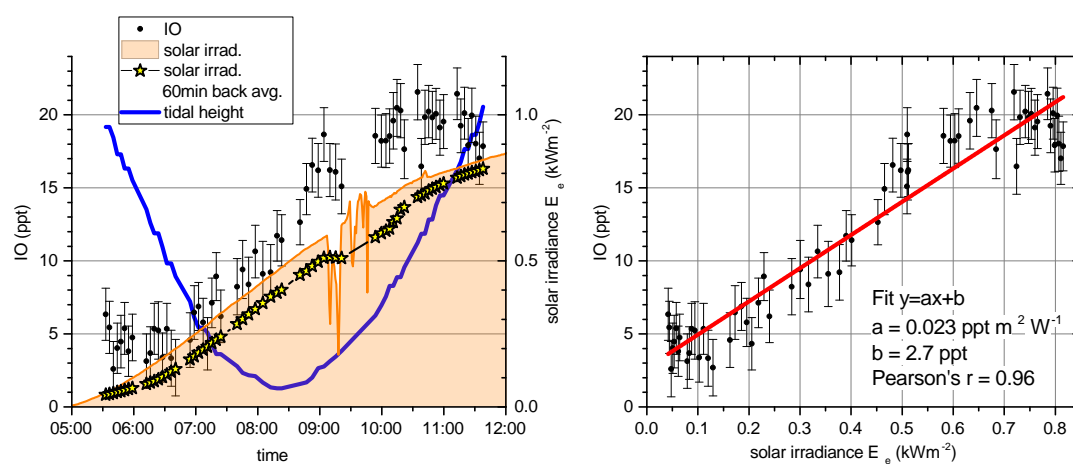


**Figure 12.47.** | Solar radiation and MoLP-DOAS IO measurement at MRI on 07/30/2012 Right: Time series of IO, solar irradiance, and tidal height during low tide with water levels between  $-1.5$  m and 0 m. Additionally shown is the average solar irradiance of the past hour. The averages are constraint to time periods with water levels below 0 m. Left: IO mixing ratios vs. solar irradiance. For the solar irradiance the average solar irradiance of the past hour is used. The scatter shows an excellent positive linear correlation between IO levels and solar irradiance.

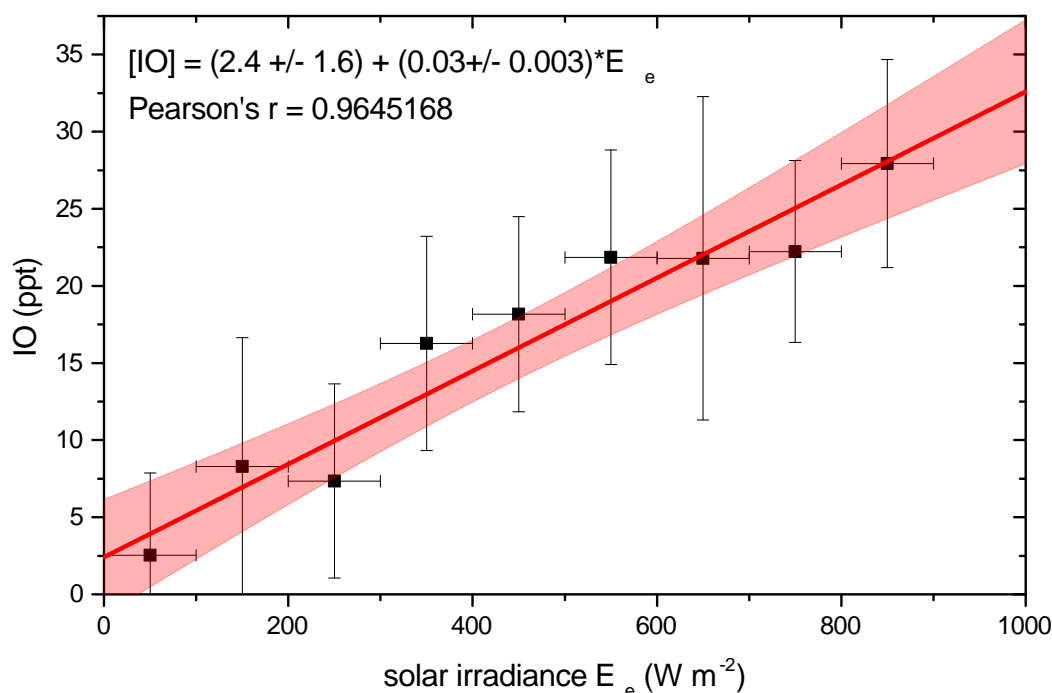


**Figure 12.48.** | Correlation of solar irradiance and IO levels observed by the MoLP-DOAS at MRI IO mixing ratios are given as averages of  $0.1 \text{ kW m}^{-2}$  classes. The averages only consider IO mixing ratios above the detection limit for periods with water levels below 0 m. Additionally a linear fit with 95 % confidence bands is shown.

be that photolytic stress is not only directly caused by the solar irradiance but also by drying out the seaweed which needs some time after exposure to air. A similar effect has been observed in a laboratory study on *A. nodosum* by Kundel et al. [2012], where the full emission potential of the seaweed is only developed after 30 min to 60 min exposure to air. Another reason for using hourly averaged solar irradiance value is that the solar irradiance was measured at Mace Head research station which is several 10 km away from most measurement locations. Thus, variations of the solar irradiance on shorter time scales would probably not be representative for most measurement locations. Therefore, for the analysis of correlations the average solar irradiance of the past hour is used. The solar irradiance is further, constraint to time periods with water levels below 0 m as most seaweeds are not exposed at higher water levels.

Fig. 12.47 shows the scatter plot of IO vs. solar irradiance for all MoLP-DOAS measurements at MRI (IO is averages over solar irradiance classes of  $0.1 \text{ kW m}^{-2}$  during low tide periods with water level below 0 m). It shows an excellent linear correlation between IO and solar irradiance with a Pearson' r of 0.96.

A strong correlation between IO and solar irradiance is also observed at the other measurement locations. A particularly good example are the MoLP-DOAS measurements at Lettermore Island North. The dependence of the IO on the solar irradiance is particularly apparent in

the maximum IO mixing ratios observed in the three low tide periods as shown in Fig. 12.26. The corresponding correlation plot is shown in the appendix Fig. C.3. The MoLP-DOAS observed the highest IO mixing ratios of up to  $(29.7 \pm 2.1)$  ppt in the first low tide period on August 1st between 11:30h and 13:00h when moderate average solar irradiance of about  $750 \text{ W/m}^2$  was present. In the second low tide period, only a small IO peak with a maximum mixing ratio of  $(7.1 \pm 1.8)$  ppt is observed during dusk (solar irradiance  $< 100 \text{ W/m}^2$ ), and after sunset IO immediately drops below the detection limit of 4 ppt. In the third low tide period, during daytime on August 2nd the maximum IO mixing ratio of  $(14.4 \pm 1.8)$  ppt is also much lower compared to the first low tide period which is also consistent with the much lower solar irradiance of about  $250 \text{ W/m}^2$ .

Several further examples for other measurement sites, including measurements by Open Path CE-DOAS, are shown in Fig. C.3 in the appendix.

### 12.7.1. Nighttime IO

Nighttime chemistry of reactive iodine species is still controversially discussed in the scientific community. Saiz-Lopez et al. [2006] proposed the reaction of  $\text{I}_2$  and  $\text{NO}_3$  as a nighttime source of IO to explain their observation of up to 3 ppt by LP-DOAS on a 4.2 km long light path (one way) at Mace Head. However, all other LP-DOAS studies at Mace Head by Aliche et al. [1999], Hebestreit [2001] and Seitz [2009] did not observe any significant nighttime IO above their respective detection limits of 0.5 ppt, 0.3 ppt and 0.6 ppt. Also the only previous IO in-situ measurement at Mace Head by Commane et al. [2011] did not observe IO above their 1.5 ppt detection limit. So far only one other study by Mahajan et al. [2009] at Roscoff, France reported observation of nighttime IO at levels up to  $(3.0 \pm 0.9)$  ppt. However, simultaneous IO point measurements by LIF [Furieux et al., 2010] and also failed to detect any significant IO above their detection limit of about 2 ppt.

In this work, also IO was not observed at night with any instrument. Nighttime IO is analyzed for the Open Path CE-DOAS measurements at the MRI in the 2011 and 2012 campaign (sec. 12.4.2) and the MoLP-DOAS in the 2012 campaign at the MRI (sec. 12.4.2.2) and Lettermore Island North (sec. 12.4.3). MoLP-DOAS at MRI in the 2011 campaign were not used due to instrumental problems. Unfortunately our stationary LP-DOAS measurements at Mace Head could not be used to analyze IO night time chemistry since instrumental problems required the use of a night-time reference in the data evaluation, which probably biased the retrieved nighttime IO values (see sec. 7.1.2).

The histograms for both MoLP-DOAS and Open Path CE-DOAS measurements at MRI are shown in Fig. 12.49 and Fig. 12.50 respectively. No IO was observed during night by both instruments above their detection limits which were on average 2.3 ppt (Open Path CE-DOAS) and 4.0 ppt (MoLP-DOAS) while during daytime both instruments regularly observed high IO mixing ratios of several 10 ppt. The observations at MRI are further supported by the MoLP-DOAS measurements at Lettermore Island North, also did also not observe any night time IO above the detection limit of 4 ppt but measured high daytime IO of up to  $(29.7 \pm 2.1)$  ppt.

In summary measurements in this work did not observe any significant coastal nighttime IO above 2.3 ppt (CE-DOAS) and 4.0 ppt (MoLP-DOAS). We rate this as a contradiction to

the 3 ppt nighttime IO reported by Saiz-Lopez et al. [2006]. They measured on a 4.3 km light path with only a short path in the intertidal zone (see Fig. 12.9) which would indicate much higher in-situ concentrations. However, this was only found during daytime where our observed maximum IO mixing ratios by both CE-DOAS and LP-DOAS were much higher than the maximum daytime IO levels of 7 ppt reported in Saiz-Lopez et al. [2006]. This leads to the conclusion that the observations by Saiz-Lopez et al. [2006] and also Mahajan et al. [2009] are measurement errors.

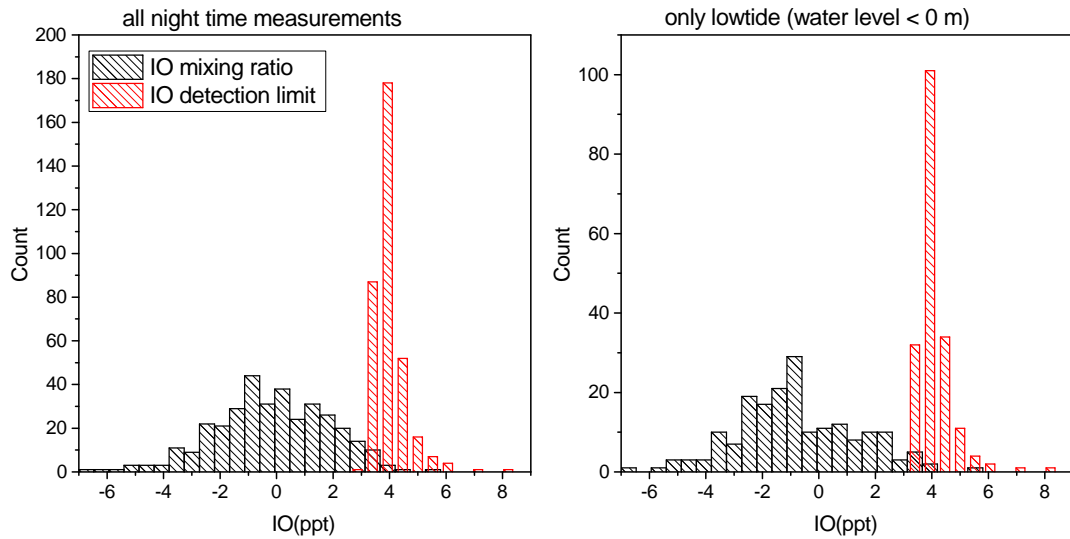


**Figure 12.49.** | Histograms of MoLP-DOAS night time IO measurements at MRI (2012 campaign) Right: all data for solar irradiance below  $1 \text{ W/m}^2$ . Left: only data during low tide periods with tidal height below 0 m. Both histograms do not show significant IO above the detection limit, which was on average 4.0 ppt

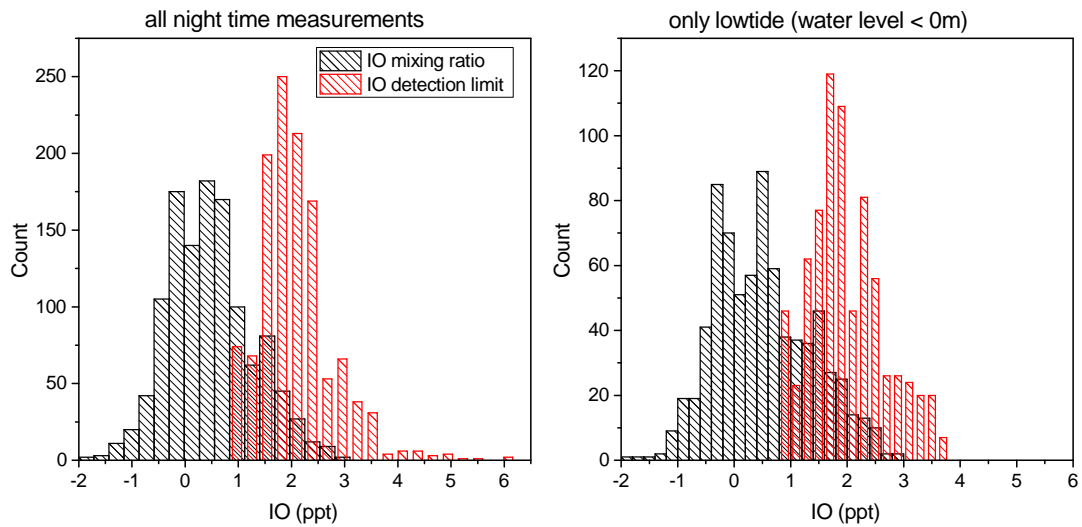


**Figure 12.50.** | Histograms of Open Path CE-DOAS night time IO measurements at MRI (2011 and 2012 campaign) Right: all data for solar irradiance below  $1 \text{ W/m}^2$ . Left: only data during low tide periods with tidal height below 0 m. Both histograms do not show significant IO above the detection limit, which was on average 2.3 ppt.

## 12.8. Discussion of the Regional IO Distribution on the Irish West Coast.

In the literature, assessments of reactive iodine chemistry on the Irish west coast but also extrapolations to its global impact are mostly based on measurements at Mace Head [e.g. Saiz-Lopez et al., 2012]. Firstly most coastal measurement campaigns were performed at this location. Secondly Mace Head was also assumed to be a representative site for a shore dominated by *L. digitata* seaweed, which was considered the dominant emitter of reactive iodine species. However, at Mace Head previous studies observed high IO levels only for extremely low water levels close to spring-tide low water, which are relatively rare events only arising during 6 days of a 27 day tidal cycle (lunar month). During these rare events, path averaging LP-DOAS measurements observed IO up to 7 ppt [Alicke et al., 1999; Hebestreit, 2001; Saiz-Lopez and Plane, 2004; Seitz, 2009] and LIF in-situ measurements at the main station observed IO up to  $(29.3 \pm 8.7)$  ppt [Commane et al., 2011]. First indications for other locations with more regular and potentially also stronger IO emissions were given by Seitz et al. [2010] at the MRI in Mweenish Bay. These are the only IO measurements on the Irish west coast apart from Mace Head. For five days they consecutively observed high IO levels of up to 29 ppt over a seaweed bed during low tide and did not observe a significant dependence on the tidal amplitude. Thus, one of the goals of Ireland campaign was to systematically investigate if Mace Head is a representative location to study reactive iodine chemistry on the Irish west coast.

As indicated in Fig. 12.1 mobile CE-DOAS and LP-DOAS measurements were performed at 10 different locations. Mobile measurements mainly concentrated on wave sheltered bays (7 locations) since they are very common on the Irish west coast and feature the largest areas with inter-tidal seaweed (mainly *A. nodosum* and *F. vesiculosu*) regularly exposed to air during low tide. In order to allow a direct comparison between different measurement sites and Mace Head, a stationary LP-DOAS was installed at the Mace Head research station during the 2012 campaign. This was important, since we found out that meteorology, especially solar irradiance, influences the stress level of seaweed exposed during low tide and thereby its  $I_2$  emission rates (see sec. 12.7). Therefore, most meteorological effects should cancel out when looking at relative IO levels between measurements at Mace Head and other locations, as they are sufficiently close so that meteorological conditions are very similar. Figure 12.51 gives an overview of the mobile Open Path CE-DOAS and the MoLP-DOAS during the 2012 campaign, together with the simultaneous reference measurements at Mace Head. During daytime low tide, on almost all days the mobile measurements observed much higher IO mixing ratios compared to the stationary Mace Head LP-DOAS, which rarely observes IO above its 2.2 ppt detection limit. The only significant exception are the CE-DOAS measurements at Mace Head where IO was only detected during spring tide low water but then also at much higher levels compared to the stationary LP-DOAS. This already shows, that IO observations at Mace Head are much less regular and also much lower in magnitude compared to the other measurement locations in wave sheltered bays.

Fig. 12.52 gives a direct comparison of the maximum and average IO levels observed by the mobile CE-DOAS and MoLP-DOAS to the stationary LP-DOAS reference measurement

Mace Head. Average IO mixing ratios are given for periods of low tide and sufficient solar irradiance ( $>100 \text{ W m}^{-2}$ ). Ratios of IO levels observed by the mobile instruments relative to the stationary LP-DOAS were calculated with modified average values, where all data below the detection limit were set to the detection limit. This made a big difference for the stationary LP-DOAS since most of its measurements were below the detection limit of about 2.2 ppt and dominated by systematic errors which could cause unreasonably low average values and thus too high ratios. For the Open Path CE-DOAS and MoLP-DOAS measurements recalculating the averages for the ratios made no significant difference because for both instruments almost all measurements were above their detection limits. Thus, the ratios for all measurement locations except for Cashel Bay and Lettermore Island south give lower limits, and could be significantly higher.

The ratios for the 2012 campaign show that at all mobile locations, average IO levels observed during daytime low tide by the MoLP-DOAS were two to seven times higher compared to the Mace Head reference measurement. For CE-DOAS measurements in the seaweed bed (or less than 5 m downwind of it) ratios of the average IO levels were even higher with at some sites up to a factor of 13 more IO observed by CE-DOAS compared to the Mace Head reference. Mobile locations in the 2012 campaign were all wave sheltered shores, mainly bays.

The 2011 data is more difficult to compare due to a missing permanent reference measurement at Mace Head. However, also in 2011 the measurements by the CE-DOAS and the MoLP-DOAS at all sites, were much higher compared to the respective measurements at Mace Head. However, the IO levels observed by the MoLP-DOAS at Balleyconnely North and Mweenish Island, where *L. digitata* are the prevailing intertidal seaweed species, are still a factor two lower compared to the MoLP-DOAS measurements at MRI, mainly over *A. nodosum* (middle and short light path). Also a very interesting observation is, that the CE-DOAS measurements at the *A. nodosum* bed 250 m northeast of Mace Head station actually observed on average more than twice the mixing ratio compared to the CE-DOAS measurements directly at the station which is considered to be dominantly influenced by *L. digitata*.

Additionally, for a better comparability amongst the different mobile measurement sites the data was normalized with respect to the solar irradiance. This was done to account for the linear dependence of the observed IO levels on the solar irradiance as shown in sec. 12.7. The resulting averages of the IO mixing ratios per solar irradiance are shown in Fig. 12.53. This does not change the overall picture but emphasizes some mobile sites where the weather was particularly bad, especially Lettermore Island North, and Ballyconneely Bay in 2012, and the CE-DOAS measurements northeast of Mace Head station in 2011.

In conclusion, contrary to the expectation that Mace Head is a hot-spot for iodine emissions, this comparison found that (at the same time) the IO concentrations at other measurement locations, especially those featuring wave sheltered shores, were typically much higher. Two main factors for these much lower concentrations observed at Mace Head were identified: Most importantly, wave sheltered shores are typically much shallower and feature extended beds of seaweed, mainly *A. nodosum* and *F. vesiculosus*, which are regularly exposed. On the opposite at wave exposed shores, like Mace Head, the intertidal zone is much smaller and features a lower inter-tidal seaweed abundance mainly *L. digitata*, which is also less frequently exposed as it is only found in the lower intertidal zone (see sec. 12.1.1). Thus, this comparison identified

intertidal areas of wave sheltered shores as the major source areas for reactive iodine emission on the Irish West Coast, which is further elaborated in the next section 12.9. Additionally, at Mace Head most the LP-DOAS light path (> 90 %) spanned over iodine source free subtidal areas, while for MoLP-DOAS measurements at wave sheltered shores usually at least half of the LP-DOAS light path spanned over the inter tidal area. This factor was certainly even more severe in previous LP-DOAS studies at Mace Head [e.g. Aliche et al., 1999; Hebestreit, 2001; Saiz-Lopez and Plane, 2004; Seitz, 2009] where the light paths were longer and even further away from the coastline 12.9. However, this does not mean that wave-exposed shores would feature higher IO levels with a different light-path, because the lower intertidal zone at these shores is so small that there are no extended areas with high IO levels.

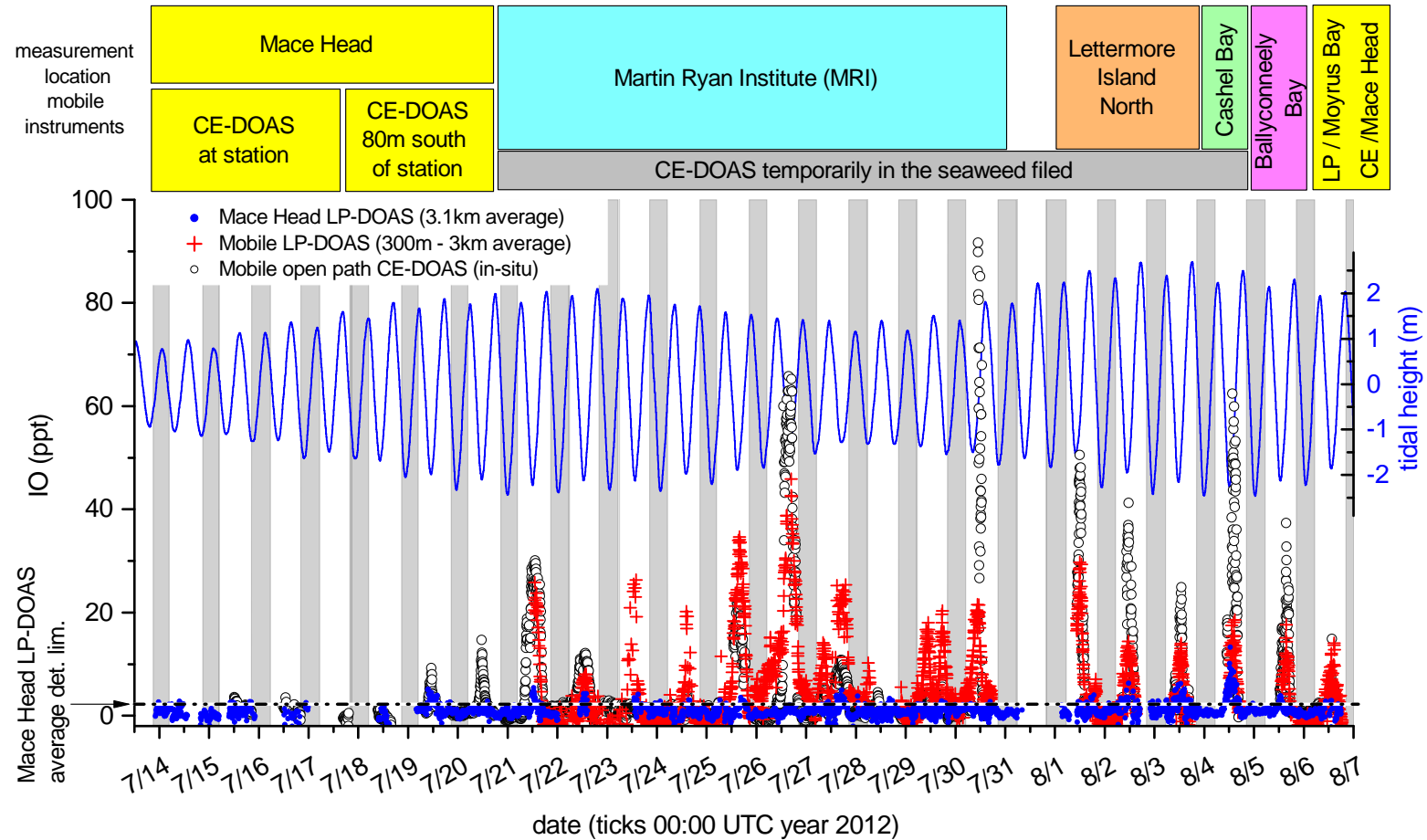


**Figure 12.51. | Overview of IO measurements for the 2012 campaign.** The plot shows simultaneous measurements by the stationary Mace Head LP-DOAS (blue dots) and mobile measurements by the MoLP-DOAS (red crosses) and the Open Path CE-DOAS (open circles). At the top the locations of mobile measurements for the different time periods are indicated. Additionally shown are the tidal height (blue line) and the gray shaded areas indicate night time periods with solar irradiance below  $5 \text{ W m}^{-2}$ .

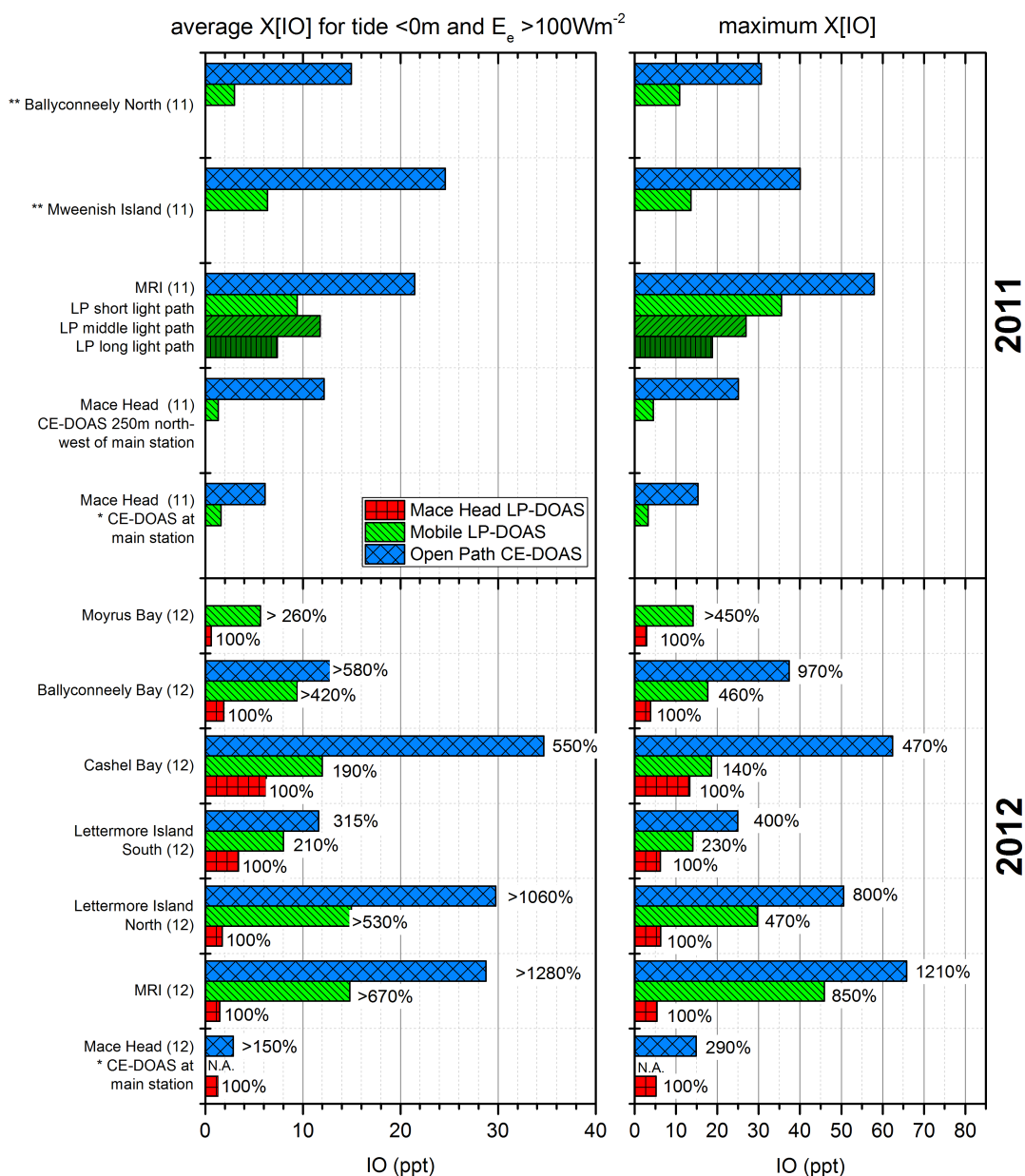


**Figure 12.52.** | Comparison of average and maximum IO mixing ratios for the different sites. Percentage values are relative to the Mace Head LP-DOAS measurements (only for 2012) in the respective time period. CE-DOAS measurements within 5 m (downwind) of exposed intertidal seaweed were used for the average. Exceptions are: \*At Mace Head the distance of the CE-DOAS to the seaweed bed was 30 – 40 m. \*\*CE-DOAS measurements were performed over patches of washed up drift seaweed.

12.8. Discussion of the Regional IO Distribution on the Irish West Coast.

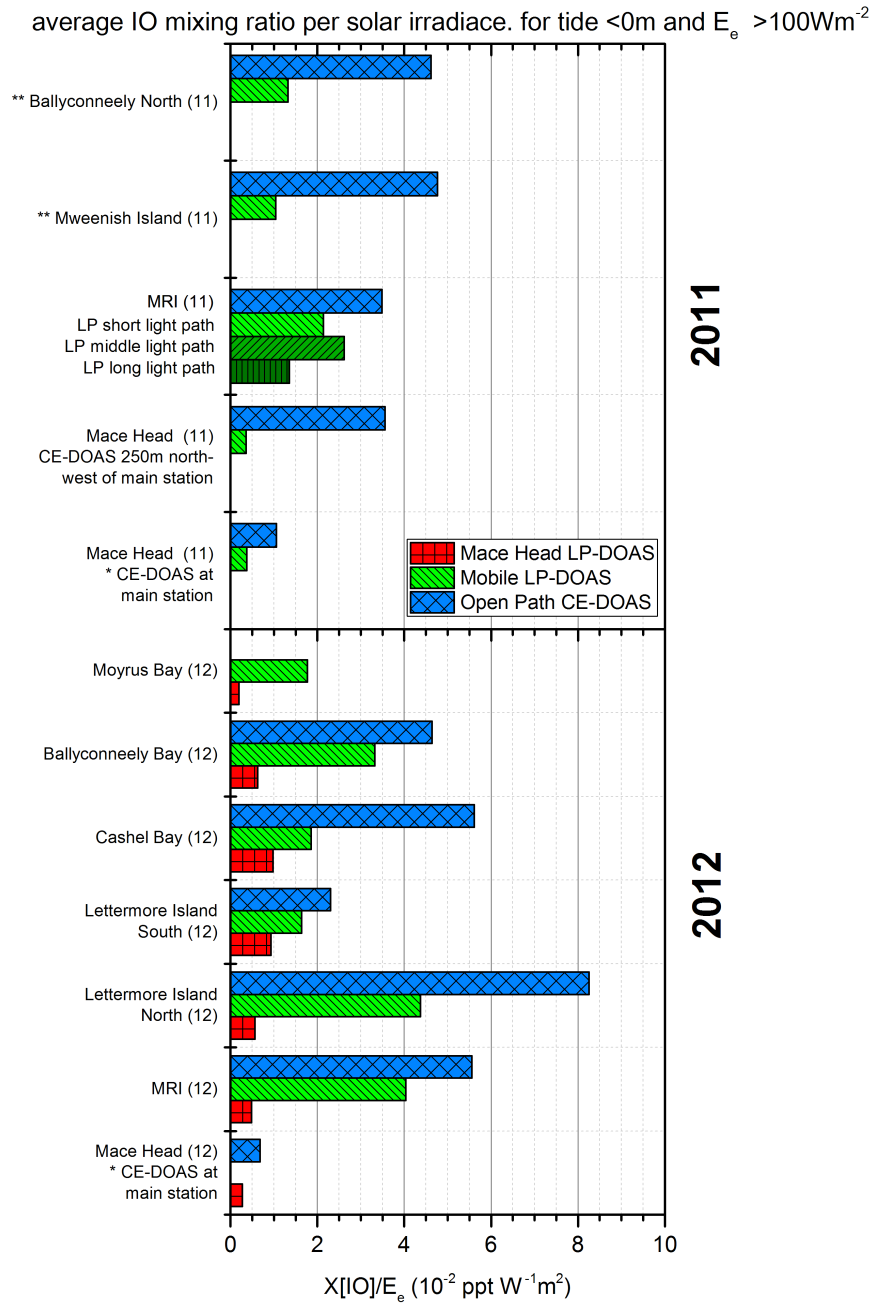


**Figure 12.53.** | Comparison of average IO mixing ratios per solar irradiance for different sites. Ratios to the stationary Mace Head LP-DOAS are not shown since, for this instrument most data was below the detection limit which makes the normalization to solar irradiance problematic. CE-DOAS measurements within 5 m downwind of exposed intertidal seaweed were used for the average. Exceptions are: \*At Mace Head the distance of the CE-DOAS to the seaweed bed was more than 30 – 40 m. \*\*CE-DOAS measurements were performed over patches of washed up drift seaweed.

## 12.9. Discussion of IO Sources and their Spatial Distribution

As described in the introduction (chap. 1) local sources of IO and their distribution are one of the major open questions of the halogen chemistry in the mid-latitude coastal marine boundary layer. The newly developed Open Path CE-DOAS instrument has several advantages to other point measurement techniques of reactive iodine species (see chap. 1 and 5). Particularly, for the first time it allowed to investigate the local IO concentration directly in intertidal seaweed fields, which are believed to be the major sources of reactive iodine species.

Point measurements by Open Path CE-DOAS, which were performed in or very close to the intertidal seaweed beds, generally observed very high IO mixing ratios of more than 20 ppt for extended periods of more than an hour, during daytime low tide. At MRI, Lettermore Island north and Cashel Bay, IO peak levels even exceeded 50 ppt. According to a laboratory and modeling study by Burkholder et al. [2004] these IO levels are sufficient to account for iodine mediated particle bursts observed in the coastal region around Mace Head in this study (see sec. 12.9.2.1) and previous studies [e.g. O'Dowd et al., 2002b; Seitz et al., 2010]. It should be highlighted, that the IO levels close to the seaweed are typically even higher as discussed in sec. 12.10. Thus, IO mixing ratios close to the seaweed are probably very often above 50 ppt. Only point measurements close to the *L. digitata* beds at the Mace Head station seem to fall out of this scheme. At this location in both years maximum IO mixing ratios, measured by CE-DOAS, did not exceed 15 ppt and mixing ratios above 10 ppt were only observed for relatively short time periods of less than 30 min. This is an important difference, which is further discussed in sec. 12.9.2 and also plays an important role for the comparison of the different measurement sites in sec. 12.8.

The high IO mixing ratios measured by Open Path CE-DOAS in the seaweed field during daylight low tide indicates that they are the major source of reactive iodine species as suggested several laboratory studies discussed in sec. 3.1. Different combinations of CE-DOAS point measurements, spatially averaged LP-DOAS measurements and auxiliary data such as meteorology and tidal-height are used to discuss this hypothesis and investigate the spatial distribution of IO. The following discussion is divided into measurements at wave sheltered shores, wave exposed shores and measurements over drift seaweed, because these different environments have a distinct mix of relevant seaweed species.

### 12.9.1. Wave Sheltered Bays

Wave sheltered shores, which are very common at the Irish west coast, usually have flat slopes and therefore an extended upper and mid-intertidal zone with dense beds of *F. vesiculosus* and *A. nodosum*. Measurement sites that fall into this category are the MRI (sec. 12.4.2), Lettermore Island north/south (sec. 12.4.3), Cashel Bay (sec. 12.4.4), Ballyconneely Bay (sec. 12.4.5.1), the small bay north of Mace Head station (sec. 12.4.1) and Moyrus Bay (sec. 12.4.1). In the following, different approaches are used to assess the IO distribution and sources.

### 12.9.1.1. Mobile IO Point Measurements at Different Locations

Differences in IO mixing ratios between subsequent point measurements at different locations can be used in combination with wind direction and wind speed to locate IO sources. Since it was hypothesized that the intertidal seaweeds are the IO sources, we compare IO levels measured directly over the intertidal seaweed beds with preceding and/or succeeding IO measurements on land, outside of the intertidal zone. This comparison works of course best when air masses measured at the land position originate from a background area with no IO sources. Also it is important that all measurements are performed in a time window where the seaweed exposure is similar. At the MRI, measurements suitable for this analysis method were performed on June 3rd and 4th 2011 and on July 26th 2011. The IO levels at the land position were always much lower compared to the measurements over the intertidal seaweed, if the air masses measured at the land position originate from a background area with no or very low seaweed abundance:

- On June 3rd 2011 (Fig. 12.20), when CE-DOAS was moved into the seaweed bed, IO levels increased by a factor of four from  $(5.1 \pm 0.7)$  ppt on land to  $(20.7 \pm 0.8)$  ppt in the seaweed bed. Later, when the CE-DOAS was moved back to the land, IO dropped down more than a factor of five from  $(39.5 \pm 0.7)$  ppt in the seaweed bed to  $(7.3 \pm 0.6)$  ppt on land.
- On June 4th 2011 (Fig. 12.20), when the CE-DOAS was moved from the seaweed bed to the land, an even stronger drop in IO of one order of magnitude from  $(12.8 \pm 0.6)$  ppt in the seaweed field down to  $(1.7 \pm 0.5)$  ppt at land could be observed.
- On July 26th 2012 (Fig. 12.24), when the CE-DOAS was moved into the seaweed bed, IO levels increased by a factor of six from  $(9.8 \pm 1.0)$  ppt on land to  $(60.0 \pm 1.3)$  ppt in the seaweed bed. Later, when the CE-DOAS was move back to the land, IO dropped down more than factor 5 from  $(18.6 \pm 0.8)$  ppt in the seaweed bed to  $(3.5 \pm 1.0)$  ppt on land. When the CE-DOAS was move back to land, the solar radiation of  $50 \text{ W m}^{-2}$  was already relatively low which explains the generally lower IO levels during that time period.

During all described measurements, the seaweed bed in the bay was exposed to air. The significant IO levels on land at June 3rd 2011 and July 26th 2012 are most probably due to a small and relatively sparse seaweed patch west to north west of the instrument location, which was the upwind direction on these two days. On June 4th 2011 the northerly wind direction, which comes almost exclusively form the land, explains the much lower IO levels on land compared to the other days.

Another good examples for the influence of wind direction on the IO levels are the CE-DOAS measurements on July 21st 2012 (Fig. 12.23). On this day the CE-DOAS observed high IO mixing ratios of more than 10 ppt on the land location, which was less than 10 m from the shoreline. The observed IO mixing ratios did not change significantly when the Open Path CE-DOAS was moved 20 m into the seaweed bed. Also when the Open Path CE-DOAS was moved back to the land location towards the end of the low tide period the observed IO mixing ratio of more than 20 ppt at that time did no change significantly. The explanation is prevailing

southerly wind direction on that day, for which the measurement location on land was directly downwind of the seaweed bed. Thus, the mobile Open Path CE-DOAS point measurements give evidence, that the major source of the observed IO is located in the large intertidal seaweed bed.

### 12.9.1.2. Comparison Between CE-DOAS and mobile LP-DOAS Measurements

In this section, IO levels from CE-DOAS point measurements directly in the intertidal seaweed beds are combined with simultaneous path averaged LP-DOAS measurements across seaweed beds to locate IO sources. Simultaneous CE-DOAS point measurements and path averaged LP-DOAS measurements were performed at MRI, Lettermore Island north/south, Cashel Bay and Ballyconneely Bay. At all locations the CE-DOAS point measurements over the intertidal seaweed generally showed higher IO levels compared to path averaged MoLP-DOAS measurements crossing the intertidal seaweed beds. This proves that IO sources are not homogeneously distributed along the MoLP-DOAS light path, but are rather concentrated in strongly emitting hot-spots, the intertidal seaweed patches, as suggested by the previous study of Seitz et al. [2010]. In the following, observations at the individual sites are discussed in more detail:

**MRI:** On most of the days IO levels from CE-DOAS point measurements and path averaging MoLP-DOAS<sup>1</sup> measurements show a good agreement within a factor of 1.5. The detailed time series and the measurement setup are shown in sec. 12.4.2. However, contrary to the expectation the CE-DOAS point measurements over the intertidal seaweed were not always higher than the path averaged LP-DOAS measurements. On June 2nd 2011, July 21st 2012 and July 26th 2012 the CE-DOAS IO measurements relative to the LP-DOAS data were a factor of 2.3, 1.2 and 1.4 higher respectively. But on June 6th 2011 and on July 25th 2012 the IO levels measured by the CE-DOAS were a factor of 1.4 lower compared to the LP-DOAS IO mixing ratios. Thus, in summary the relatively similar IO levels observed by the CE-DOAS and LP-DOAS indicate an extended abundance of reactive iodine sources in the intertidal area along the LP-DOAS light path. The variations in the ratio between the LP-DOAS and CE-DOAS IO levels also indicate significant inhomogeneities in the distribution of the reactive iodine sources in the intertidal area. However, due the large extend of the seaweed bed, wind may mix up IO homogeneously along the LP-DOAS light path, leading to higher IO levels for the MoLP-DOAS if the CE-DOAS is (partly) measuring air masses form the land (with no IO).

**Lettermore Island north:** As shown in Fig. 12.26, both the IO measurements by Open Path CE-DOAS and LP-DOAS show the same time dependence. However, in the periods where the Open Path CE-DOAS measured in the intertidal zone directly above the seaweed, the IO levels were about 70 % higher on August 1st and more than 150 %

---

<sup>1</sup>For the 2011 campaign, at MRI the MoLP-DOAS data from the middle light path (see Fig. 12.18) are used for comparison to the CE-DOAS data, since measurements on this light path give a good coverage of the intertidal bay and are much more accurate compared to the short light path.

higher on August 2nd compared to the MoLP-DOAS. The higher IO levels measured by the CE-DOAS compared to the LP-DOAS are consistent with an inhomogeneous distribution of seaweed along the LP-DOAS light path especially in the middle of the LP-DOAS light path where no seaweed grows. The significantly higher CE-DOAS to LP-DOAS IO ratio on August 2nd compared to August 1st is most likely an effect of changes in the wind direction. As shown in Fig. 12.25, the eastern part of the LP-DOAS light path, which is aligned in east-west direction, is close to the southern edge of the intertidal seaweed bed. Thus, the change of the wind direction from westerly on August 1st to southerly on August 2nd may have transported more IO free air from the bay into the LP-DOAS light path, causing lower IO mixing ratios while the CE-DOAS, which measured on the northern edge of the seaweed bed, would not have been affected.

**Lettermore Island south:** The observations at this site are very similar to Lettermore Island north. Detailed time series and the measurement setup are shown in sec. 12.4.3.2. The detected maximum IO levels, which were reached around noon, were about a factor of 1.7 higher for the CE-DOAS compared to the LP-DOAS. This is consistent with the observation that only less than half of LP-DOAS light path was over the intertidal seaweed beds. Furthermore, the low winds, which blew easterly in direction along the MoLP-DOAS light path, can be assumed to have only little effect on the measurements.

**Cashel Bay:** At this site, which is described in sec. 12.4.4, the Open Path CE-DOAS observed very high IO mixing ratios of up to  $(81.0 \pm 1.4)$  ppt for 10s averages and up to  $(62.4 \pm 1.1)$  ppt for 100 s averages while the IO levels observe by the MoLP-DOAS were on average about three times lower and did not exceed  $(19 \pm 2)$  ppt (see Fig. 12.30). The reason for this is a very inhomogeneous distribution of the iodine emitting seaweed along the LP-DOAS light path. Seaweed is found in a narrow strip along the coastline and several elevated rocks inside the bay which are exposed during low tide. The measurement site with locations of instruments and intertidal seaweed is shown in Fig. 12.29.

Compared to the previously discussed sites, the IO mixing ratios measured by the CE-DOAS show a very high temporal variability of up to more than a factor of three within 20s (see Fig. 12.30). One explanation for this observation lies in the very squally wind during the measurements and the vertical IO gradient over seaweed patches as observed at the MRI (see sec. 12.10). As described in sec. 12.10 the vertical IO gradient decreases with increasing wind-speeds. Neglecting dilution, this leads to higher IO levels at the CE-DOAS instrument height (1.3 m) for higher wind speeds (see sec. 12.10). Thus, squally winds could cause a high temporal variability of the IO levels observed by the CE-DOAS. In addition, for a very patchy distribution of sources, the IO mixing ratios observed by the CE-DOAS become very sensitive to wind speed and direction, since this changes the effective area which is probed and also the amount of dilution. In summary, the high temporal variability of the IO mixing ratios observed by CE-DOAS show the presence of strong IO sources close to the instrument.

**Ballyconneely Bay:** In contrast to the previous sites, the CE-DOAS did not measure in the

seaweed bed but on a pier next to the seaweed bed and at a height of three to four meters above the seaweed bed, as shown in sec. 12.4.5.1. Nevertheless, during low tide, the CE-DOAS point measurements observed on average a factor of two more IO, compared to the MoLP-DOAS. This is again attributed to an inhomogeneous seaweed distribution in the intertidal zone with many elevated rocks, covered by seaweed and small tidal rivers in between which do not vanish at low water (see Fig. 12.31).

Furthermore, IO mixing ratios measured by the Open Path CE-DOAS show a variability of up to a factor of 10 within only two minutes, which is even higher than at Cashel Bay. Since the wind was also very squally on that day the explanation is analogous to Cashel Bay and indicates that there are very strong iodine emitting “hot-spots” in the seaweed bed, where the IO mixing ratio is expected to even exceed the peak mixing ratio observed by the Open Path CE-DOAS of  $(46.9 \pm 0.8)$  ppt.

**Comparison of LP-DOAS to CE-DOAS Measurements Outside the Seaweed Bed:**

Additionally, at the MRI the Open Path CE-DOAS measured continuously at land locations close to the seaweed bed. In combination with the LP-DOAS measurements and local meteorology these measurements can also be used to investigate the IO distribution. Between July 22nd

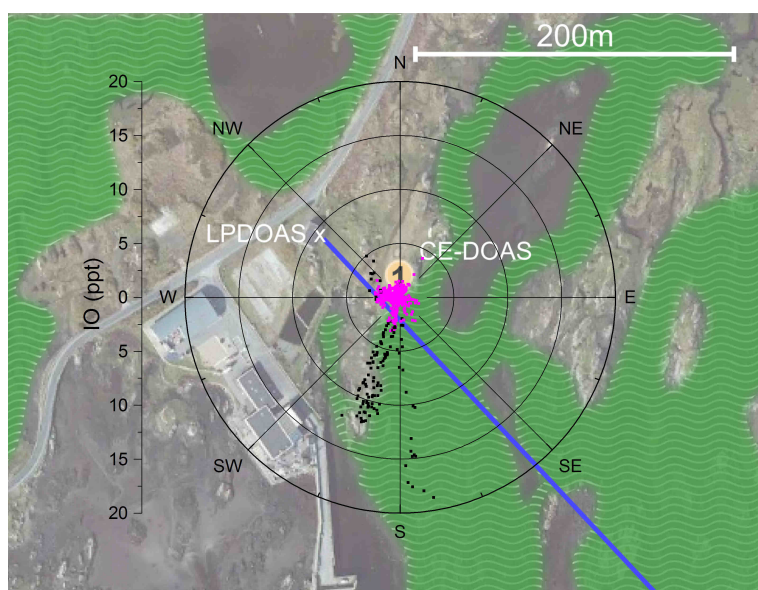


**Figure 12.54.** | IO vs wind direction, for CE-DOAS measurements at MRI land position (1) during daytime. Black points show measurements above the detection limit and magenta points values below the detection limit. Significant IO was mainly detected for southerly wind directions. The seaweed distribution is based on maps from Stefan Schmitt (pers. observ. Ireland 2012) and Hession et al., 1998. Satellite images ©Mapbox, ©OpenStreetMap.

and 24th 2012 the CE-DOAS continuously measured on land at location (1) which was less than 10 m north of the seaweed bed (see Fig. 12.18). On July 22nd for southerly wind the IO time series of CE-DOAS and the LP-DOAS, shown in Fig. 12.23, correlated well with the daytime low tide and showed similar IO levels of up to  $(12 \pm 1)$  ppt and  $(8 \pm 2)$  ppt respectively. However, on July 23rd for westerly winds the CE-DOAS detected no significant IO and on July 24th for westerly to northerly wind only a small peak of  $(5 \pm 2)$  ppt was observed, while the LP-DOAS IO levels correlated well with daylight low tide on both and reached up to  $(26 \pm 4)$  ppt and  $(20 \pm 2)$  ppt on July 23rd and 24th respectively. In order to locate the IO sources the correlation of IO observed by the CE-DOAS and wind direction is visualized as a polar plot shown in Fig. 12.54. The observation of IO by the CE-DOAS correlates mainly with southerly winds which bring air masses from the intertidal bed in the bay. Additionally for north westerly winds, a small peak slightly above the detection limit of 3 – 4 ppt is seen. This corresponds to the small IO peak observed on July 24th which may originate from ArdBay bay located about 100 m to the north west. Thus in summary, the CE-DOAS measurement at land location (1) also show that local seaweed beds are the major IO source at the MRI.

### 12.9.1.3. LP-DOAS Measurements at Moyrus Bay

Moyrus Bay located about 3 km north east of Mace Head station is investigated as a possible source region for the IO observed by the stationary Mace Head LP-DOAS. On August 6th 2012 the MoLP-DOAS measured on a 0.99 km long light path (one-way) across the Moyrus Bay as shown in Fig. 12.55, this figure also shows the stationary Mace Head LP-DOAS light paths which ran almost parallel 500 m to the west but extended about 2.5 km further to the south. From the time series, shown before in Fig. 12.16, it can be clearly seen that the MoLP-DOAS observed significant IO during daytime low tide with a maximum IO mixing ratio of  $(14 \pm 2)$  ppt. A scatter plot of IO vs wind direction, overlaid on a map of the measurement site, is shown in Fig. 12.55. However, simultaneous measurements by the Mace Head LP-DOAS did not show any significant IO above the detection limit of 2.6 ppt. With the prevailing south westerly to westerly winds on the August 6th 2012, this gives evidence that the source of the IO observed by the MoLP-DOAS are most likely the beds of *A. nodosum* in Moyrus Bay and the headland west of it. Thus, on other days with northerly to easterly wind, *A. nodosum* in Moyrus Bay and west of the headland could act as source for IO observed by the Mace Head LP-DOAS.

### 12.9.1.4. LP-DOAS Measurements at MRI

At the MRI the MoLP-DOAS measured for an extended periods of six days in 2011 and nine days in 2012. Thus, compared to other sites there is a relatively large data bases which can be used to investigate IO sources from correlations to wind and tidal height. As described in sec. 12.4.2, during both campaigns a 556 m long light path (one way) was set up crossing the intertidal area in front of the MRI. Furthermore in the 2011 campaign two additional, almost parallel light path were used. The short light path crossed half of the intertidal area and the long light path, which went to Finish Island, extended additionally over subtidal areas, constantly covered by water. Thus, for the 2011 campaign a comparison of the IO mixing ratios along the three light paths, gives additional information on the distribution of IO.

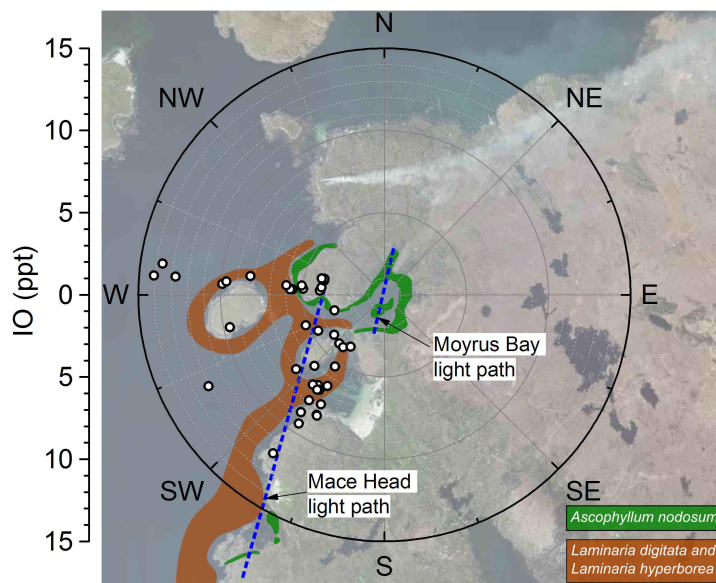


**Figure 12.55.** | **Correlation of wind direction and IO at Moyrus Bay.** IO mixing ratios observed on August 6th 2012 along the Moyrus Bay light path are shown as open dots. Only data above the detection limit is shown. No significant IO was observed along Mace Head light path on August 6th 2012. The seaweed distribution is based on maps from Stefan Schmitt (pers. observ. Ireland 2012/11) and Hession et al., 1998. Satellite images ©Mapbox, ©OpenStreetMap.

**Correlation to Wind and Tides** Correlations to wind and tides are only discussed for the 2012 campaign due to the much better quality of the measurements. The respective correlation plots for the 2011 data, which are compatible to the conclusion drawn in this section, are shown in the appendix C.3.

Figures 12.23 and 12.24 show the IO time series for 2012. The amplitude of the IO peaks, which were found on all days during daytime low tide, does not show a significant difference between spring-tide (July 21st) and neap-tide (July 27th). This is also apparent from the correlation of IO levels with tidal heights shown in Fig. 12.56. Significant IO of up to 10 ppt is observed for a tidal height below 1.5 m and observed IO levels further increase to about 30ppt at tidal height of  $-0.25$  m, below which no significant increase of observed IO is found. In agreement with a previous study by Seitz [2009] the explanation of this lies in the very shallow intertidal zone which is already completely exposed to air for relatively high water levels of  $-0.25$  m, which are reached even during neap tides where the minimum tidal height is at least below  $-1$  m. Thus, this is a further indication that the *A. nodosum* seaweed bed in the intertidal area in front of the MRI is the major source of IO precursors.

Figure 12.57 shows the correlation of IO to wind speed. There is a positive correlation of increased IO mixing ratios and high wind speed up to  $8 \text{ m s}^{-1}$ , but for higher wind speeds the IO levels show a negative correlation to the wind speed. This is similar to the observations

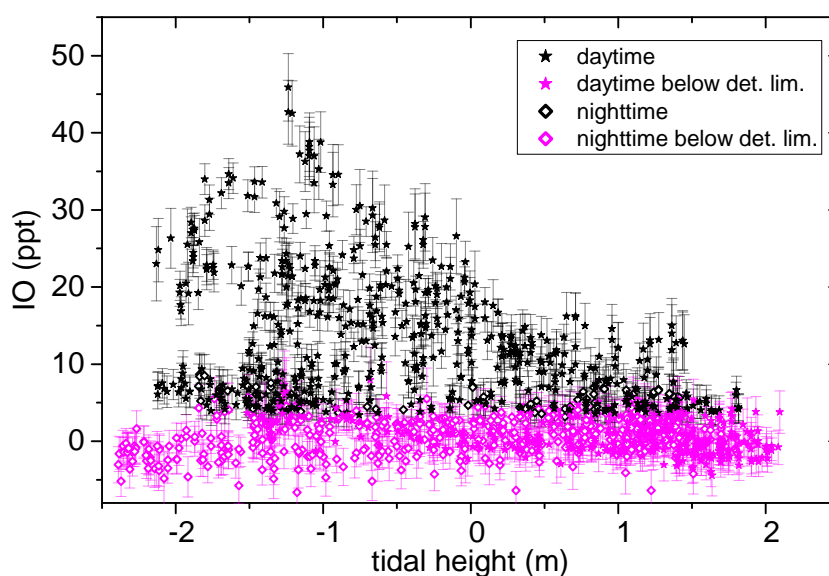


**Figure 12.56.** | Correlation of IO observed by the MoLP-DOAS with tidal height at the MRI during the 2012 campaign. For easier identification data above and below the detection limit are colored differently in black and magenta respectively. An anti-correlation between IO and tidal height is seen for daytime data, while night time data does not show any correlation to tidal height.

of Seitz [2009] where a positive correlation up to wind speeds of  $8 \text{ m s}^{-1}$  are reported. In agreement with Seitz [2009] and the CE-DOAS measurements at Cashel Bay and Ballyconneely Bay the explanation might be increased vertical transport of IO for higher wind speeds into the LP-DOAS light path, which is about two to five meters over seaweed bed. The decrease of IO for wind speeds above  $8 \text{ m s}^{-1}$  might be due to dilution of the measured air masses with IO free air from outside of the seaweed bed. Furthermore, as shown in Fig. 12.58, high IO levels correlate with westerly and southerly winds. However, the dependence of IO to the wind direction is very similar to the frequency distribution of wind directions and thus does not indicate locations of IO sources.

**Spatially Resolved LP-DOAS Measurements:** Long path DOAS measurements only give the average mixing ratio of trace gases along its several 100m to km long light path. Thus, in order to study the horizontal distribution of IO, three almost parallel light paths were established at MRI in 2011 using the MoLP-DOAS as shown in Fig. 12.18. A detailed description of the MRI measurement site is given in sec. 12.4.2. The light paths crossed the bay in south eastern direction and only one to two meters above the high water spring mark. Both the short and the middle light path exclusively traveled the intertidal area, and only crossed beds of *A. nodosum* and *F. vesiculosus*. The short light path (266 m one way length) was established to retro reflector “Retro 1”, placed on a rock in the middle of the intertidal zone. The middle

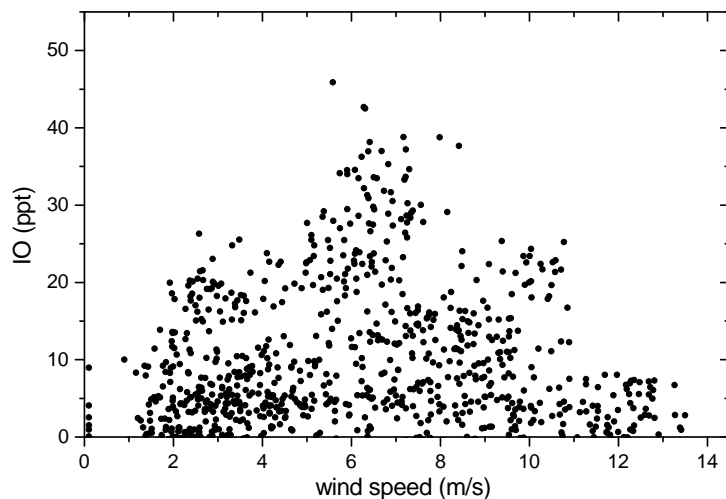


**Figure 12.57.** | Correlation between IO mixing ratios measured by the MoLP-DOAS and wind speed at the MRI during the 2012 campaign. Increased IO mixing ratios show a positive correlation to high wind speeds up to  $8 \text{ m s}^{-1}$ , but for higher wind speeds the IO levels and wind speed seem to anti correlate.

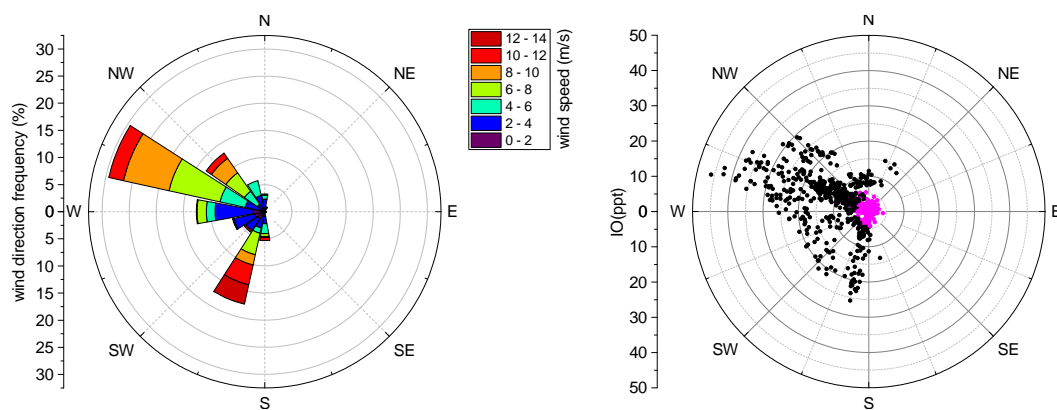


**Figure 12.58.** | Distribution of wind directions and its correlation with IO measured by the MoLP-DOAS at the MRI in 2012. Left: frequency distribution of wind direction and wind speed. Right: correlation of IO with wind direction. High IO levels correlate with westerly and southerly winds. However, this correlation of IO to the wind direction is very similar to the frequency distribution of wind directions and thus does not indicate locations of IO sources.

light path (556 m one way length) was established to “Retro 2” close to the south eastern end of the intertidal area. The long light path (1890 m one way length) was established to “Retro 3” placed on Feenish Island. Thus, except for a small intertidal strip in front of Feenish Island, the additional area crossed by the long light path is over the subtidal zone of Mweenish Bay. The middle light path and the long light path are very similar to the two light paths used in a previous study in 2007 [Seitz et al., 2010], which also investigated the horizontal distribution of IO.

The time series for the measurements at MRI in 2011 are shown in Fig. 12.19 to Fig. 12.22. IO levels observed on all three light paths show a strong correlation to low tide and solar radiation. Maximum IO levels observed on the short light path (of  $35 \pm 7$  ppt) and the middle light path ( $27 \pm 4$  ppt) are relatively similar while the maximum IO mixing ratio of  $19 \pm 2$  ppt on the long light path is significantly lower.

The wind direction plays an important role when comparing the measurements along the three different LP-DOAS light paths. On June 2nd and 3rd, when the prevailing wind direction in the relevant low tide period were south to south west and west respectively, IO mixing ratios along the long light path were significantly lower (factor of two at low water) compared to the middle light path (see Fig. 12.20). There also seems to be a tendency for higher IO mixing ratios along the short light path compared to the middle light path, even though this has to be considered cautiously since their values still agree withing the large uncertainty of the measurements on the short light path. The approximately 50% lower average IO mixing ratio along the long light path compared to the middle light path is a strong indication that the major contribution to the detected IO comes from the *A. nodosum* and *F. vesiculosus* bed which ends shortly after Retro 2. Also, due to the relatively low wind speeds of less than 5 m/s and the prevailing wind from the southern to western sector no IO could be transported from the intertidal zone into the sub-tidal part of the long light path. The tendency of lower IO mixing ratios along the middle light path compared to the short light path could also be explained by the prevailing wind from the southern to western sector. The short light path ends in the middle of the *A. nodosum* and *F. vesiculosus* bed so for both south to south westerly and westerly winds, IO should be distributed homogeneously along the light path. The same applies to large extents for the middle light path, except towards the end close to “Retro 2” where the *A. nodosum* and *F. vesiculosus* bed and also the intertidal zone becomes narrower. Finally, In this last part of the middle light path, air masses from the southern to western sector are likely to carry no IO, since they come either from the land or the large subtidal area, and thus reduce the average IO mixing ratio by dilution.

A different situation was found on July 7th where very similar IO mixing ratios were detected during the low tide period at daytime (see Fig. 12.22). In the measurement period between 12:00h and 19:30h the average wind speed of 11 m/s is relatively high and the prevailing north westerly wind direction is almost perfectly parallel to the LP-DOAS light paths. Thus the IO containing air masses could be quickly transported along the long light path over the intertidal zone (2 min transport time from Retro 2 to Retro 3) and provide similar mixing ratios on the long light path and the shorter light paths.

In conclusion, the measurements along the three LP-DOAS light paths support the theory that the major iodine sources are located in the *A. nodosum* and *F. vesiculosus* beds of the intertidal zone. This is also in agreement with the spatially resolved LP-DOAS measurements

by Seitz et al. [2010], which compared IO levels observed on two light paths very similar to our long and middle light path. They also found that almost all IO (max. 29 ppt) was concentrated on our middle light path, but attributed the iodine emission mainly to *L. saccharina* probably due to the lack of IO in-situ measurements and detailed seaweed maps.

#### 12.9.1.5. IO emission and exposure to air

As discussed above the observed IO correlated to the exposure of seaweed to air during low tide, i.e. generally IO is observed when seaweed is submerged. However in two cases it was also observed that a thin water film covering the seaweed is not sufficient to inhibit the emission of reactive iodine by the seaweed:

**Lettermore North:** On August 2, the elevated IO levels of up to 14 ppt, observed by the MoLP-DOAS during low tide, showed no influence to the two period of rain showers (see Fig. 12.26). Thus, the seaweed did not stop or reduce the emission of iodine into the Atmosphere when their surface is wet, which was expected to reduce their stress level.

**Ballyconneely Bay:** As shown in Fig. 12.32 IO was observed by both, the MoLP-DOAS and the Open Path CE-DOAS, for another 45 min after the seaweed was already covered by water at 16:41h. However, the buoyant fronds of *A. nodosum* were still floating on the water surface, which indicates that also in this case the release of iodine into the atmosphere could proceed through a thin water layer. As the water level rose further, between 16:41h and 17:30h increasing parts of the fronds are dragged under water, as their fronds become too short, until all *A. nodosum* are completely under water at 17:30h. This is consistent with the decrease in the IO level after 16:41h until it is below the detection limit after 17:30h. This effect could stretch the time period of iodine emission at least by an hour for *A. nodosum* seaweed beds and thus significantly increase their effect on air chemistry.

#### 12.9.2. Wave Exposed Shores

Wave exposed shores are generally characterized by much steeper slopes and therefore a much smaller intertidal area compared to wave sheltered shores. The dominant seaweed species are the kelps growing in the lower intertidal zone (*L. digitata*) and the subtidal zone (*L. digitata*, *L. hyperborea*). Thus, due to the steeper slope of the shore and the deeper location of the seaweeds extended exposure is only reached around spring tide where the water level is lowest. However, this makes the seaweed beds inaccessible for Open Path CE-DOAS measurements directly over the seaweed. Therefore, at such locations the Open Path CE-DOAS is setup directly at the shoreline, as close as possible to the seaweed.

CE-DOAS and LP-DOAS measurements at wave exposed shores were performed at Mace Head, Ballyconneely North and Mweenish Island. However, IO from intertidal seaweed was only found at Mace Head while the IO observed at the other two sites is attributed to drift seaweed, which is further discussed in sec. 12.9.3.

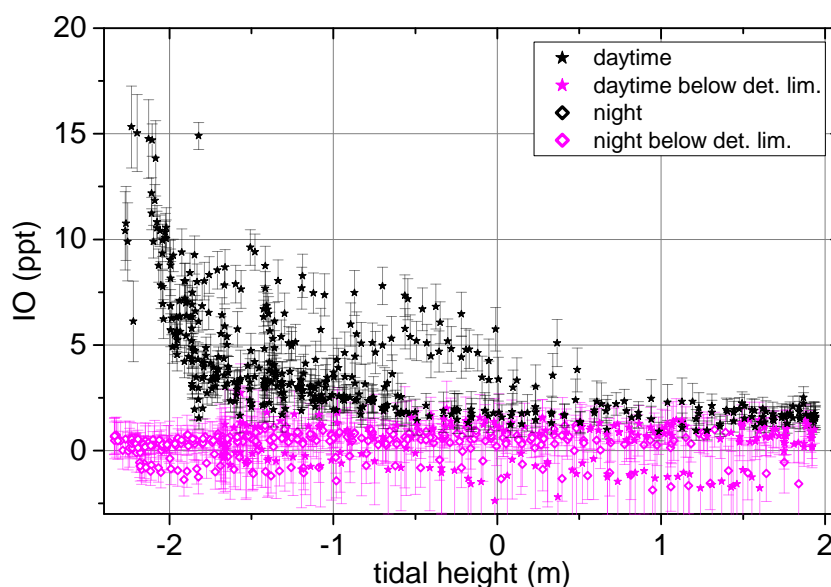


**Figure 12.59.** | Tidal height vs IO observed by CE-DOAS at Mace Head station. A clear anti-correlation of IO mixing ratios with tidal height is observed during day time but there is no correlation to the tide at night. The shown data are CE-DOAS measurements west and south west of the lower cottage from both campaigns 2011 and 2012.

### 12.9.2.1. Mace Head

At Mace Head CE-DOAS measurements were performed at two distinctively different types of shores. As shown in Fig. 12.9 (sec. 12.4.1) the shore west of the lower cottage is very wave exposed and predominantly inhabited by *L. digitata* and *L. hyperborea*. However, northwest to north of the station there is a bay which is much less wave exposed, especially in the strip between the mainland and the close-by Colt Island where *A. nodosum* is abundant. At both shores CE-DOAS measurements were applied on land close to the shoreline since the intertidal area was not accessible.

**Shore West of Station:** The CE-DOAS was setup at two measurement locations 40 m and 30 m from the shoreline (labeled (1) and (2) in Fig. 12.9). The respective IO time series from both campaigns, shown in Figs. 12.11, 12.14, 12.15 and 12.16, show a strong correlation to the tidal amplitude. The highest IO mixing ratio of  $(15 \pm 1)$  ppt was observed on May 19th 2011 and July 20th 2012, both days with spring tide. The scatter plot of IO vs tidal height, shown in Fig. 12.59, confirms that the highest IO levels are observed for a tidal height below  $-2$  m which is only reached around spring tide. Furthermore, a closer analysis shows, that at site (2) (in Fig. 12.9) IO levels above 5 ppt were only reached for a tidal height below  $-1.5$  m. The few observations of more than 5 ppt for a tidal height between 0 m and  $-1.5$  m were all made at location (1). A likely explanation is that the high IO levels of up to 15 ppt originate from *L. digitata* which are exposed to air only at very low water levels below  $-1.5$  m. The lower IO

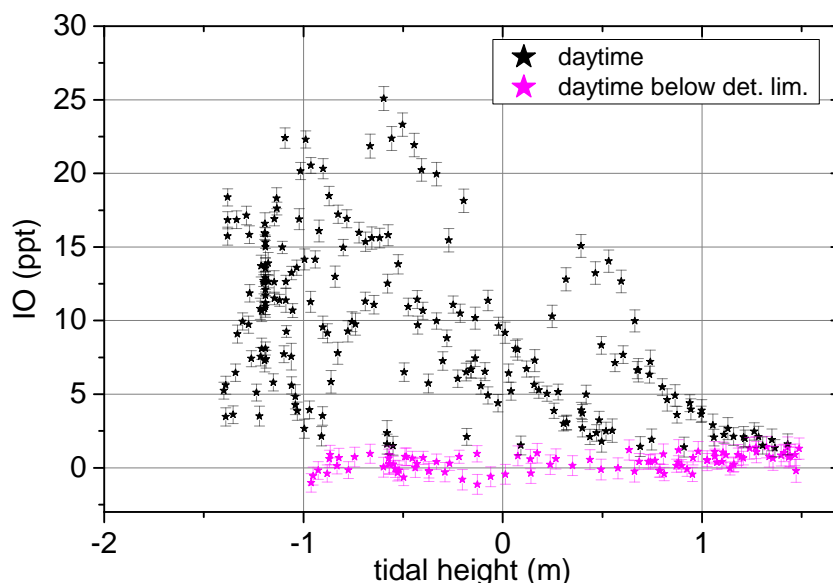


**Figure 12.60.** | Tidal height vs IO observed by CE-DOAS at Mace Head north. The anti-correlation of IO mixing ratios with tidal height is less pronounced compared to the measurements west of Mace Head station. The shown data was recorded during daylight time.

levels observed at site (1), roughly between 0.5 m and  $-1.5$  m tidal height, most likely originate from the close by *A. nodosum* field north-west of the station, since this field is already exposed to air at a water level of 0.5 m. Even though the wind direction was south westerly to westerly on all days this is not necessarily a contradiction to IO from north west, because the wind was measured 300 m from the shore and several 10 m above the water level (see Fig. 12.10). Thus, the local wind direction at the shore could be significantly different due to orographic effects. Our observations are in agreement with the only previous IO point measurements at Mace Head research station by Commane et al. [2011] who measured close to our location (1). They see a strong increase in the observed IO with values up to 29.3 ppt only for spring tide low water at tidal heights around  $-2$  m which they also attribute to exposed *L. digitata*, and also observe some lower IO levels of up to 8.2 ppt for water levels below 0.5 m.

**Shore North-West/North of Station:** In 2011 CE-DOAS measurements were also performed next to the *A. nodosum* bed north-west of the station. The Open Path CE-DOAS was setup about 10 m from the shoreline at the location labeled (3) in Fig. 12.9. Despite relatively rainy conditions, IO was observed on three days with a maximum mixing ratio of  $(25.0 \pm 1.6)$  ppt. The anti correlation between IO and tidal height shown in Fig. 12.60 is less pronounced, compared to the measurements at the shore west of Mace Head station, even though this location is only 250 m away. For tidal heights below 1 m significant IO of more than 5 ppt was observed. Maximum IO levels increase further with falling tide to about 20 ppt

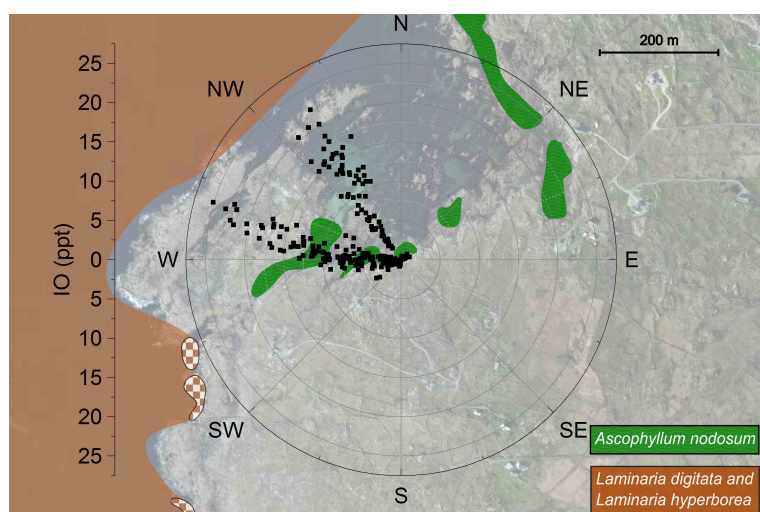


**Figure 12.61.** | Wind direction vs IO observed by CE-DOAS at the shore north-west/north of station. The Instrument was located in the center of the polar plot. Observations of high IO levels correlates with westerly to northwesterly wind directions. The seaweed distribution is based on maps from Stefan Schmitt (pers. observ. Ireland 2011/12) and Hession et al., 1998. Satellite images ©Mapbox, ©OpenStreetMap.

at a tidal height of  $-0.5$  m. No further increase of the maximum IO levels is observed for tidal heights below  $-0.5$  m. It is also important to notice, that already at a tidal height of  $0.5$  m IO levels of  $15$  ppt were observed, while west of Mace Head station such IO mixing ratios were only observed for tidal heights around  $-2$  m. Therefore, there must be a strong IO source close to location (3) which is completely exposed at tidal heights below  $-0.5$  m. The only possible source is the *A. nodosum* bed west to north of the instrument location (3). This is also supported by the correlation to wind directions, depicted in Fig. 12.61. It shows that high IO mixing ratios correlate with westerly to northwesterly wind directions.

**Stationary LP-DOAS Measurements at Mace Head:** The stationary LP-DOAS measurements during the 2012 campaign, which were primarily performed as a reference, also contain information on the distribution of reactive iodine sources in the area. The IO time series, in Fig. 12.8 and more detailed in Fig. 12.66 and Fig. 12.67, shows concentration peaks during daytime low tide. Figure 12.62 shows the correlation of the observed IO with tidal height. As expected from previous observation, it shows an anti-correlation with elevated IO levels below  $0.5$  ppt. There is generally not much increase in the observed IO levels for tidal levels below  $-1$  m, even though the maximum IO mixing ratio of  $(13 \pm 1)$  ppt was observed on August 8th during spring tide.

The correlation of IO with wind speed is shown in Fig. 12.63. Significant IO is observed for wind speed above  $2 \text{ m s}^{-1}$  and maximum IO levels increase for increasing wind speeds. A likely explanation is, that the IO source was below the light path and increasing wind speed results in increased vertical mixing as discussed in sec. 12.9.1.4 for the MRI. Also possible

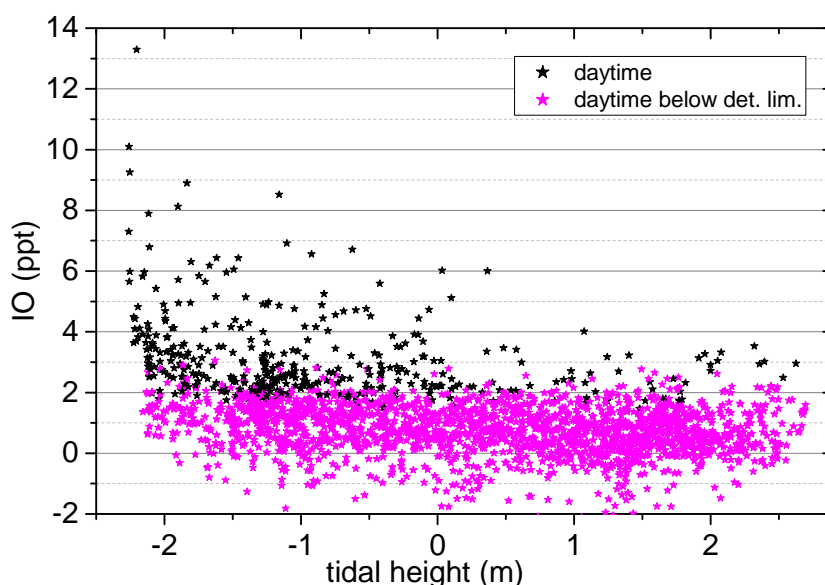


**Figure 12.62.** | Correlation of tidal height and daytime IO observed by the stationary Mace Head LP-DOAS. The data shows an anti-correlation between IO mixing ratios and the tidal height.

is that, due to the short atmospheric life time of IO, only at higher wind speeds IO emissions from distant sources can reach the LP-DOAS light path due to reduced transport time.

In order to locate the sources of IO, Fig. 12.64 shows the distribution of IO with respect to wind direction. Due to the large scatter in the IO measurements, data was averaged over relatively large sectors of  $15^\circ$ . Since IO is only expected for daytime low tide, the average is computed only for periods with solar radiation above  $10 \text{ W m}^{-2}$  and tidal heights below 0 m. Also for averaging all values below the detection limit are set to zero since systematic residual structures in the spectra seemed to cause a 1 ppt to 2 ppt offset on several days (which is generally within the measurement accuracy). In the following the different source regions are discussed in detail based on Fig. 12.64:

**north east** It can be clearly seen that the sector between  $30^\circ$  and  $60^\circ$  is the direction with the highest average values in IO. As discussed in sec. 12.9.1.3 the *A. nodosum* beds in Moyrus Bay in the north east and along the headland directly north of the light path were identified as very likely sources for IO in this sector. Additionally, the more distant Bertraghboy Bay (which includes Cashel Bay) in the north east also features a high abundance of *A. nodosum* and *F. vesiculosus* [e.g. Hession et al., 1998]. However, due to its larger distance to the light path of more than 5 km and the short atmospheric lifetime of IO it is less likely that the seaweed in Bertraghboy Bay is the source of the observed IO.

**east south east** The IO distribution in Fig. 12.64 shows a second strong peak in the ESE sector between  $90^\circ$  and  $135^\circ$ , which is the direction of Ard Bay and Mweenish Bay.

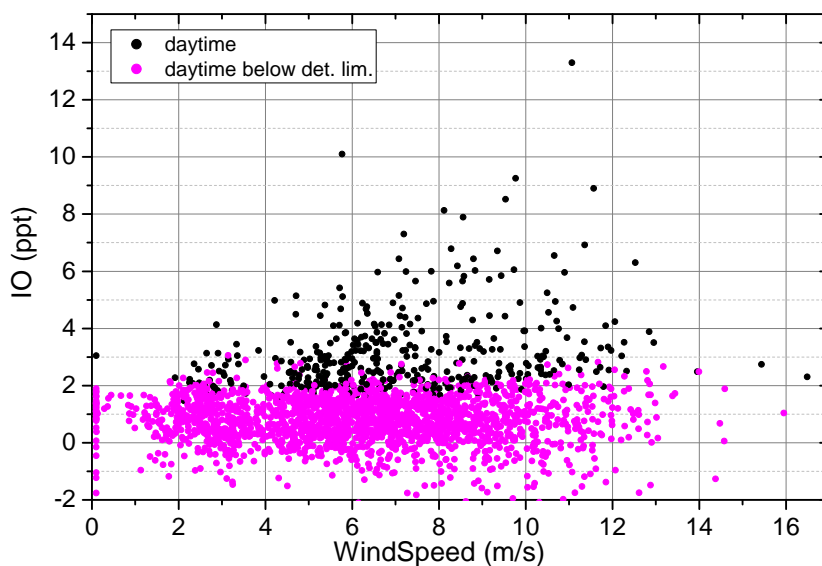


**Figure 12.63.** | Correlation of wind speed and daytime IO observed by the Mace Head LP-DOAS. Significant IO is observed for wind speed above  $2 \text{ m s}^{-1}$  and maximum IO levels increase for increasing wind speeds up to  $11 \text{ m s}^{-1}$ .

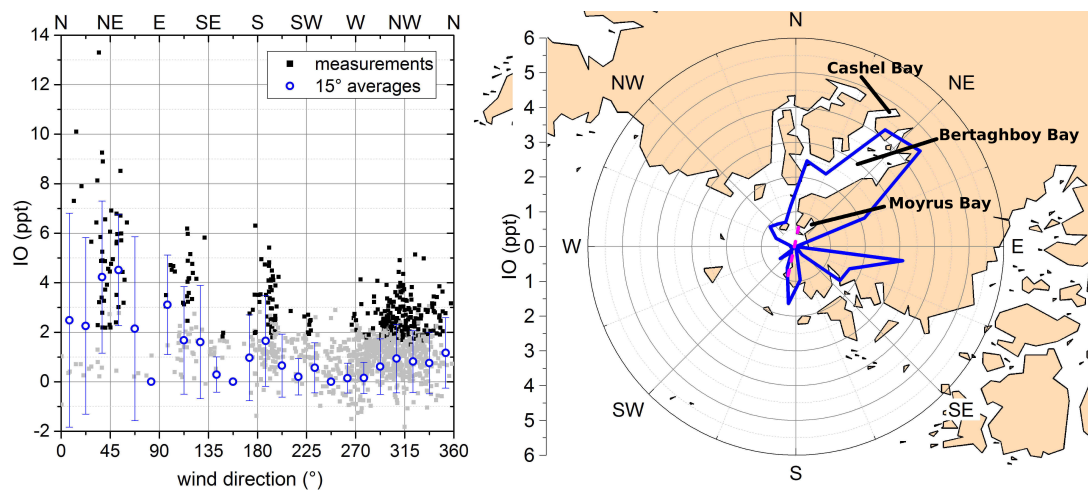


**Figure 12.64.** | Correlation of wind direction and daytime IO observed by the stationary Mace Head LP-DOAS. Left: Daytime data for tidal heights below 0 m (greyed out data is below the det. lim.) with  $15^\circ$  average values in blue. Right: Polar plot of the average IO mixing ratios overlaid on the shoreline taken from GSHHG v2.0 [Wessel and W. H. F. Smith, 1996]. The polar plot is centered on the middle of the Mace Head LP-DOAS light path, shown as pink dashed line.

Both bays feature large beds of *A. nodosum* and *F. vesiculosus* (Fig. 12.17), which were identified as the dominating local IO sources by our measurements at MRI (see sec. 12.4.2 and sec. 12.9.1). There are further bays in east south east direction between Mace Head and Galway Bay (e.g. Greatman Bay and Kilkieran Bay) with high abundance of *A. nodosum* and *F. vesiculosus*. Again, their much further distance (> 10 km) and the short lifetime of IO makes them less likely as the source of the observed IO.

**south** Elevated IO levels were also found for southerly wind. For this direction the most likely source is the *A. nodosum* bed north of Mace Head Station at the southern end of the LP-DOAS light path, where CE-DOAS measurements, discussed earlier in this section, observed high IO levels. Additionally, for southerly winds during spring tide a further contribution could come from the *L. digitata* patches west and south of Mace Head station.

**north west** IO observed for wind from the north western sector could come from the coastline between Roundstone and Ballyconneely Bay where both *A. nodosum* and *L. digitata* is abundant [e.g. Hession et al., 1998].

**west** Almost no significant IO was found for wind directions between south west and north west, even though this was a frequent wind direction. In this direction the only possible source would be the mostly subtidal *L. digitata* which are only exposed to air during low water close to spring tide. Therefore, *L. digitata* could only act as source on about six days per month and only for less than one hour per day. However, during the 2012 campaign spring tide low water did not coincide with westerly winds at Mace Head during daytime.

The results of this work are not in contradiction with a previous campaign in 2007, where up to 4.5 ppt IO was reported for westerly wind [Seitz, 2009] because: Firstly, measurement during the 2007 campaign were performed on days were spring tide coincided with westerly winds. Secondly, Seitz [2009] used a much longer LP-DOAS light path (7 km one way) which extended in north westerly direction to Roundstone (see Fig. 12.9), which makes it sensitive to additional sources in west of round stone, e.g. Ballyconneely Bay. However, the light path in this work was shorter and setup closer to the land, which made it more sensitive to emissions at the coastline close to Mace Head.

**IO Mediated Particle Formation at Mace Head:** As described in sec. 2.3.3 previous studies [e.g. O’Dowd et al., 2002a; McFiggans et al., 2010; Seitz et al., 2010] observed ultra fine particle bursts at coastal sites during daytime low tide with particle concentrations up to  $10^6 \text{ cm}^{-3}$ . These events were linked to the polymerization of iodine oxides [e.g. O’Dowd et al., 2002b; Burkholder et al., 2004; Sellegri et al., 2005].

During our Ireland campaign in 2012 measurements by nano SMPS (data provided by NUIG, see sec. 8.1.3) at Mace Head Atmospheric Research Station also observed bursts of ultra fine particles during daytime low tide on 15 of the 22 measurement day as shown in Fig. 12.66 and Fig. 12.67. The peak level of the concentration of particles between 5 nm and 500 nm of  $2.5 \cdot 10^5 \text{ cm}^{-3}$  is significantly lower to the previously reported maximum concentrations at

## 12.9. Discussion of IO Sources and their Spatial Distribution

Mace Head of  $10^6 \text{ cm}^{-3}$  [O'Dowd et al., 2002a]. Furthermore, only on eight days concentrations of more than  $2 \cdot 10^4 \text{ cm}^{-3}$  were observed. The particle burst in the night of July 31th is excluded from the further discussion because it only contains particles greater than 10 nm and is therefore more likely due to anthropogenic emissions which is also consistent with the northerly wind direction which bring mainly air masses from the land.

In order to analyze the source regions of the particle bursts observed at Mace Head, Fig. 12.65 shows the distribution of the particle concentration with respect to wind direction. The polar plot show average values of  $15^\circ$  sectors, for periods with solar radiation above  $10 \text{ W m}^{-2}$  and tidal heights below 0 m. Days without particle bursts (concentration  $< 1 \cdot 10^3 \text{ cm}^{-3}$ ) were neglected to avoid biasing the averages. The overlay in the polar plot with the average IO mixing ratios observed by the stationary LP-DOAS (see. last paragraph) shows that both have a similar dependence on the wind direction, indicating that both have similar source regions. This is in agreement with the hypothesis that iodine oxide is the precursor or the observed particle bursts. The differences for northerly to north easterly wind direction are not unexpected when comparing path averaged measurements by the LP-DOAS and point measurements by the nano SMPS since they do not measure exactly the same air masses, which is particularly important for close by sources as Moyrus Bay in the north east of Mace Head station.

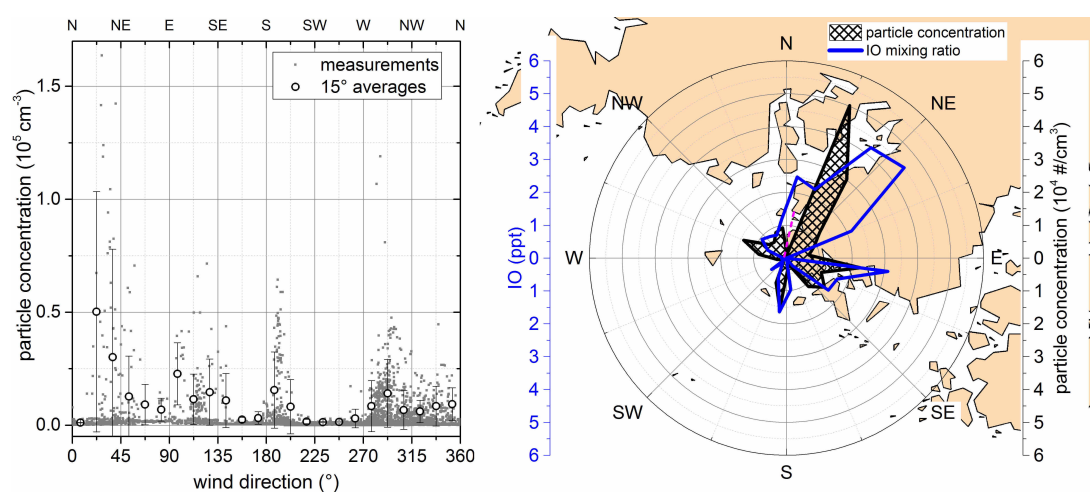


**Figure 12.65.** | **Correlation of wind direction with daytime particle and IO concentrations observed at Mace Head.** Left: Particle concentrations for daytime data and tidal heights below 0 m (geyed out data is below the det. lim.) and  $15^\circ$  average values in blue. Right: Polar plot of the average particle concentrations and IO mixing ratios (Mace Head LP-DOAS data from Fig. 12.64) overlaid on the shoreline taken from GSHHG v2.0 [Wessel and W. H. F. Smith, 1996]. The pink dashed line indicates, the LP-DOAS light path. The polar plot is centered at the Mace Head Research station where the particle concentrations were measured.

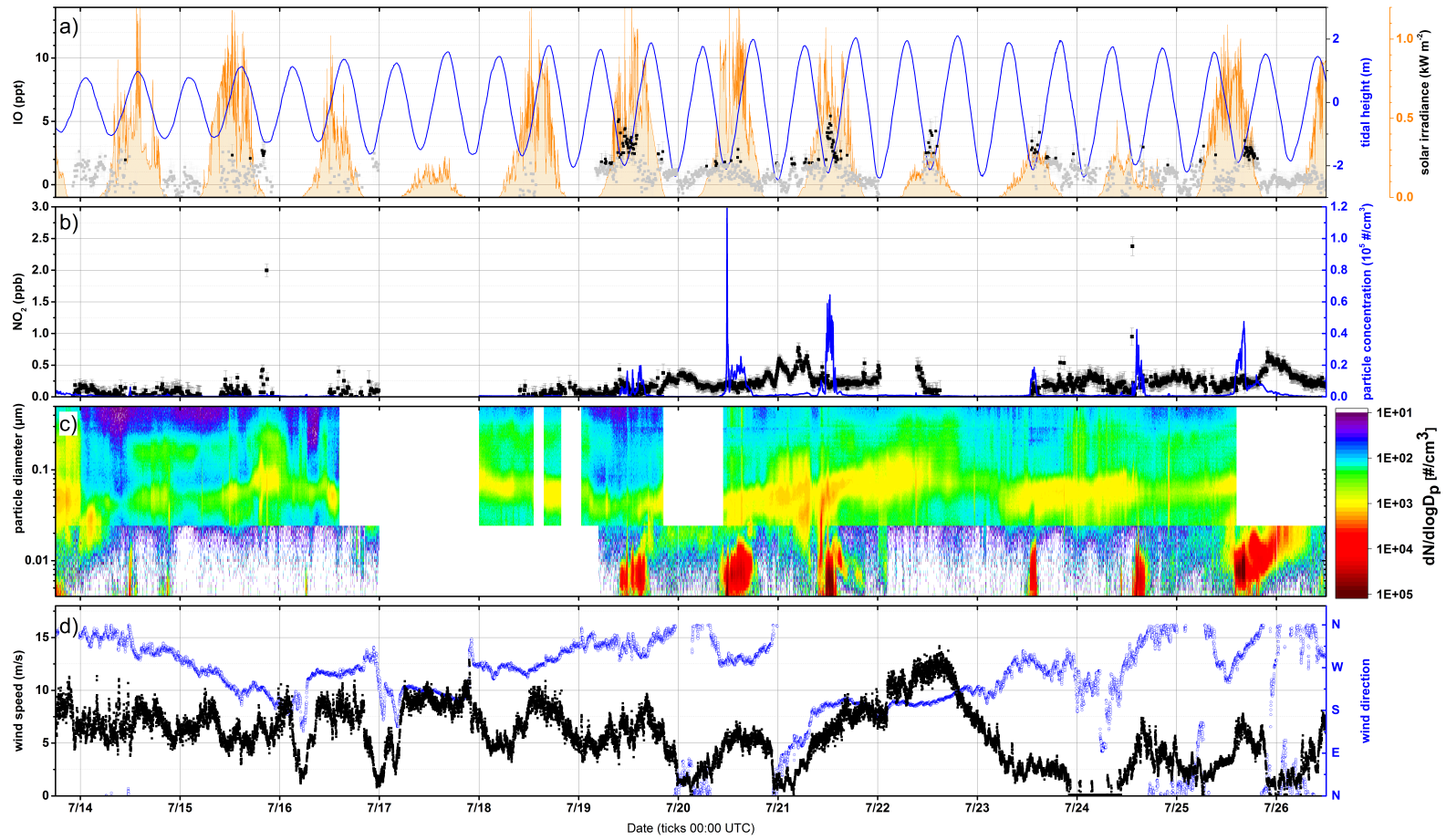


**Figure 12.66.** | Time series of IO and NO<sub>2</sub> (Mace Head LP-DOAS) and aerosol particle concentration (nano-SMPS) at Mace Head. a) IO mixing ratio (black, data below the detection limit is greyed out), tidal height (blue) and solar irradiance (orange). b) LP-NO<sub>2</sub> mixing ratio (black) and total concentration of aerosol particles between 5 and 500 nm (blue). c) Aerosol size size distribution. d) wind speed and (black) and direction (blue).

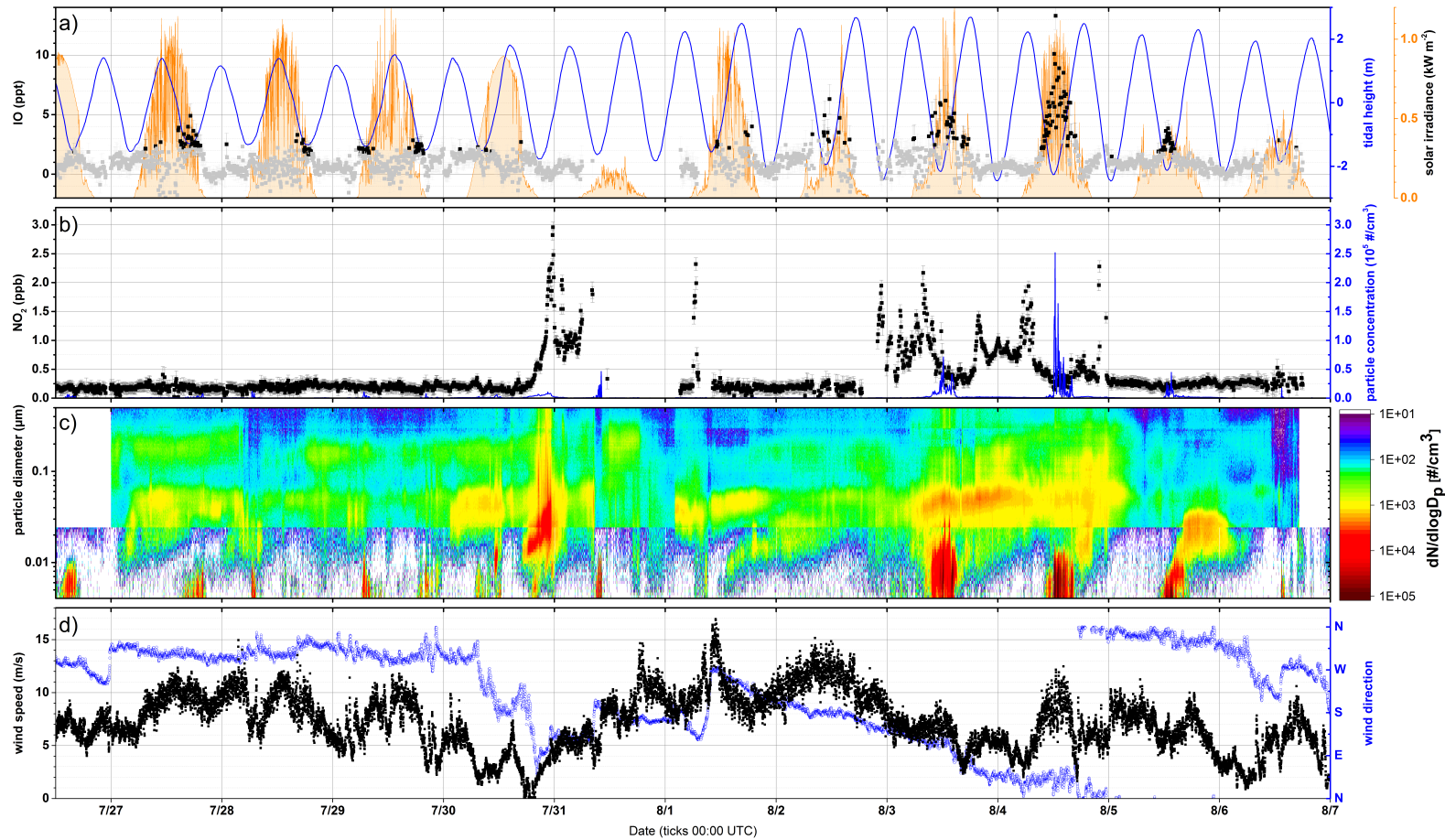


**Figure 12.67.** | Continued, time series of IO and NO<sub>2</sub> (Mace Head LP-DOAS) and aerosol particle concentration (nano-SMPS) at Mace Head. a) IO mixing ratio (black, data below the detection limit is greyed out), tidal height (blue) and solar irradiance (orange). b) LP-NO<sub>2</sub> mixing ratio (black) and total concentration of aerosol particles between 5 and 500 nm (blue). c) Aerosol size size distribution. d) wind speed and (black) and direction (blue).

### 12.9.3. IO over Drift Seaweed Patches

During the 2011 campaign stormy weather caused a large abundance of washed up drift seaweed on wave exposed shores of the Connemara for example on the western shore of Mweenish Island and the northern shore of the Ballyconneely peninsula. As described in sec. 12.1.1 this is not a unique event, but happens regularly after storms. Therefore, the question arose whether the drift seaweed is still capable to emit iodine. In order to investigate this, measurements were performed over patches of washed up drift seaweed, mainly *L. digitata* and *L. hyperborea*, were performed at Mweenish Island and Ballyconneely north during the 2011 campaign. Detailed descriptions of sites and setups are given in sec. 12.4.5.2 for the northern shore of the Ballyconneely and in sec. 12.4.6 for Mweenish Island. At both sites the Open Path CE-DOAS was placed in the middle of the drift seaweed patches which roughly covered an area of 25 m × 55 m. The MoLP-DOAS measured across the patches but also several hundred meters further along the shoreline.

At both sites CE-DOAS measurements in the drift weed patches showed high IO mixing ratios of up to  $(40.2 \pm 0.7)$  ppt at Mweenish Island and up to  $(30.7 \pm 0.8)$  ppt at Ballyconneely. Compared to that the LP-DOAS observed much lower IO mixing ratios of only up to  $(14 \pm 3)$  ppt at Mweenish Island and no significant IO at Ballyconneely (average det. lim. 8.7 ppt). At both sites, this difference in observed IO mixing ratios between the CE-DOAS and the LP-DOAS shows that there is an inhomogeneous distribution of IO with the drift weed patches acting as strongly emitting “hot-spots”. This was also confirmed by moving the CE-DOAS out of the patch. In the following a more detailed analysis is given for the two measurement locations:

**Ballyconneely:** Measurements were performed on June 7th 2011. At the measurement site drift seaweed densely covered an area of roughly 30 m × 50 m (see Fig. 12.33) with a depth of ~ 0.5 m. The Open Path CE-DOAS performed in-situ measurements in the middle of the patch and about 1.3 m above the drift weed. The MoLP-DOAS measured along a 1002 m long light path (two-way) which was setup to cross the drift weed patch but also went over steeper, more rocky parts of the shore where *L. digitata* and *L. hyperborea* are found in the lower intertidal to subtidal zone (see Fig. 12.33). Detailed time series for both the Open Path CE-DOAS and the MoLP-DOAS are shown in Fig. 12.34.

The Open Path CE-DOAS observed an average IO mixing ratio of  $(15 \pm 1)$  ppt and a peak value of 30.7 ppt. This is remarkable since the solar irradiance of  $380 \text{ W m}^{-2}$  was relatively low on that day and the weather was relatively rainy. This interesting finding gives further evidence that IO emissions do not necessarily need sunny weather (see sec. 12.7) and that even wet, water covered seaweed emits iodine (see sec. 12.9.1.5). This also means that on a day of good weather with high solar irradiance even higher IO mixing ratios would be expected. The MoLP-DOAS did not measure significant IO above the 8.7 ppt detection limit. Thus the mixing ratios observed by the CE-DOAS were on average at least a factor 1.7 higher and in the maximum more than a factor of 3.5 ppt higher.

With the local wind direction of SW to SSW (see Fig. 12.33) the air masses measured at the CE-DOAS traveled over land for at least one to two kilometers before arriving at

the drift weed patch. Thus, the washed up drift seaweed is the only source for the high IO levels observed by the CE-DOAS.

**Mweenish Island** Measurements were performed on June 6th 2011 on the southern shore in a bay with sandy beaches as shown in Fig. 12.35. Similar to Ballyconneely north, a 20 m × 60 m large patch of drift seaweed (depth ~ 0.5 m) mainly composed of *L. hyperborea* and *L. digitata*, was found at the measurement site. Detailed time series for both, the Open Path CE-DOAS and the MoLP-DOAS are shown in Fig. 12.36.

Most of the time the Open Path CE-DOAS was applied for in-situ measurements in the drift seaweed patch (location 1) where it observed on average an IO mixing ratio of  $(26.2 \pm 0.7)$  and maximum of  $(40.2 \pm 0.7)$  ppt at a height of 1.3 m above the seaweed. The IO mixing ratio dropped to zero when the CE-DOAS was moved further north out of the path of drift seaweed to location (3). In combination with the prevailing northerly wind direction this gives evidence that the drift seaweed is the source for the IO observed above it.

Furthermore, for a two hour period, when the tide was close to the low water level the CE-DOAS was moved eastwards to location 2, a small seaweed patch in the mid-intertidal zone, mainly of *F. serratus* and a single *L. digitata* plant. First it measured at a height of about 1.3 m above the seaweed where it observed an average IO mixing ratio of  $(11.9 \pm 0.6)$  ppt, which is less than half of the IO mixing ratio observed above the drift seaweed. When the CE-DOAS light path was lowered to a height of 30 cm above the seaweed the average IO mixing ratio increased by more than a factor of two to  $(26.8 \pm 0.6)$  ppt which is consistent with the IO height profile discussed in sect. 12.10. Thus, it could be excluded that the local IO (at location 2) originated from the drift weed patch (location 1). It could however not be distinguished if the main iodine source is the the bed of *F. serratus* or the single *L. digitata*.

The MoLP-DOAS was setup close to the drift weed and measured along a 1710 m long light path (two-way), which crossed the drift weed patch (location 1) and continued parallel to the rocky shore where it also passed close to location 2. The MoLP-DOAS observed an average IO mixing ratio of  $(5 \pm 3)$  ppt and a maximum value of  $(14 \pm 3)$  ppt. Significant IO above the detection limit of 6.5 ppt was only observed between 12:00h and 14:00h which corresponds to a tidal height of less than -1.5 m. The prevailing northern wind direction identifies small seaweed patches along the shoreline, composed of *F. serratus* and a single *L. digitata*, as the major source of the IO observed by the MoLP-DOAS, also since these patches were only exposed for a short period when the water level was below -1.5 m (close to low water). The drift seaweed patch could have also made a contribution to the observed IO, because the IO formed at this location was advected along the MoLP-DOAS light path. However, the drift seaweed patch was already exposed to air a water level at 0 m, and thus its contribution to the IO along the total LP-DOAS light path was only below the detection limit.

## 12.10. Discussion: IO Emission Rates from Vertical IO Profile

The Open Path CE-DOAS allowed for the first time a direct estimate of the (secondary) IO emission rates in a seaweed bed. For this, a vertical IO profile was measured in the seaweed bed at MRI on July 30th which was a relatively sunny day with calm and constant wind conditions (see sec. 12.4.2.2). The seaweed was dominantly composed of *A. nodosum* and some *F. vesiculosus*.

The IO mixing ratio was measured at several height levels between 10 cm and 221 cm as shown in Fig. 12.68. In order to eliminate the influence of meteorology and varying IO emission by the seaweed, a reference height was chosen (26 cm), where measurements were performed more frequently. These, reference measurements were used to normalize the measurements at the other height levels, which were finally scaled to the first reference measurement. The resulting height profile in Fig. 12.69 shows the expected logarithmic decrease of the IO mixing ratio with increasing height, for heights above 20 cm.

Assuming neutral layering, the IO emission rate  $F_{A,IO}$  per unit area, i.e. flux, can be inferred from the trace gas vertical profile [e.g. Roedel, 2000]

$$F_{A,IO} = (c(z_1) - c(z_2)) \frac{u_* \kappa}{\ln \frac{z_2}{z_1}} \quad (12.1)$$

with concentrations  $c(z_i)$  at the height levels  $z_i$ , the friction velocity  $u_*$  and the dimensionless von-Kármán constant  $\kappa \approx 0.4$  [Högström, 1996]. For a given surface roughness length  $z_0$ , the friction velocity  $u_*$  can be calculated from the logarithmic wind profile

$$u(z) = \frac{u_*}{\kappa} \ln \frac{z}{z_0} \quad (12.2)$$

the surface roughness length for the intertidal zone is assumed to be between 0.03 m and 0.1 m according to [WMO, 2010, p. I5-13]. For the wind speed of 2 m/s (Fig. 12.53), measured 2 m above the ground this gives a friction velocity in the range of  $u_* = 0.19 - 0.27$  m/s. From Fig. 12.69 we read IO mixing ratios of  $c(z_1) = 85$  ppt at  $z_1 = 0.21$  m and  $c(z_2) = 8.5$  ppt at  $z_2 = 2.02$  m. Inserting into eq. (12.1) we get

$$F_{A,IO} = 2.6 - 3.6 \frac{\text{ppt m}}{\text{s}} = 2.3 - 3.3 \cdot 10^{17} \frac{\text{molec}}{\text{m}^2 \text{h}} = 390 - 550 \frac{\text{nmol}}{\text{m}^2 \text{h}} = 50 - 70 \frac{\mu\text{gI}}{\text{m}^2 \text{h}} \quad (12.3)$$

During the measurement period the measuring period the solar irradiance was relatively constant with  $(841 \pm 16) \text{ W m}^{-2}$ . This needs to be considered for applying the determined emission rates to other locations or larger scale estimates, due to the linear dependence of the IO emission/formation on solar irradiance (see sec. 12.7). It should also be noted that for unstable atmospheric layering this method would underestimate the flux, due to increased vertical exchange. On the other hand, photo-chemical losses and dilution would lead to an overestimation of the flux.

The emission per gram fresh weight can be estimated using the areal density of seaweed. A study by study by **Selegri2005** specified  $1 - 5 \text{ kgFw m}^{-2}$  for Mweenish Bay. Using the

12.10. Discussion: IO Emission Rates from Vertical IO Profile

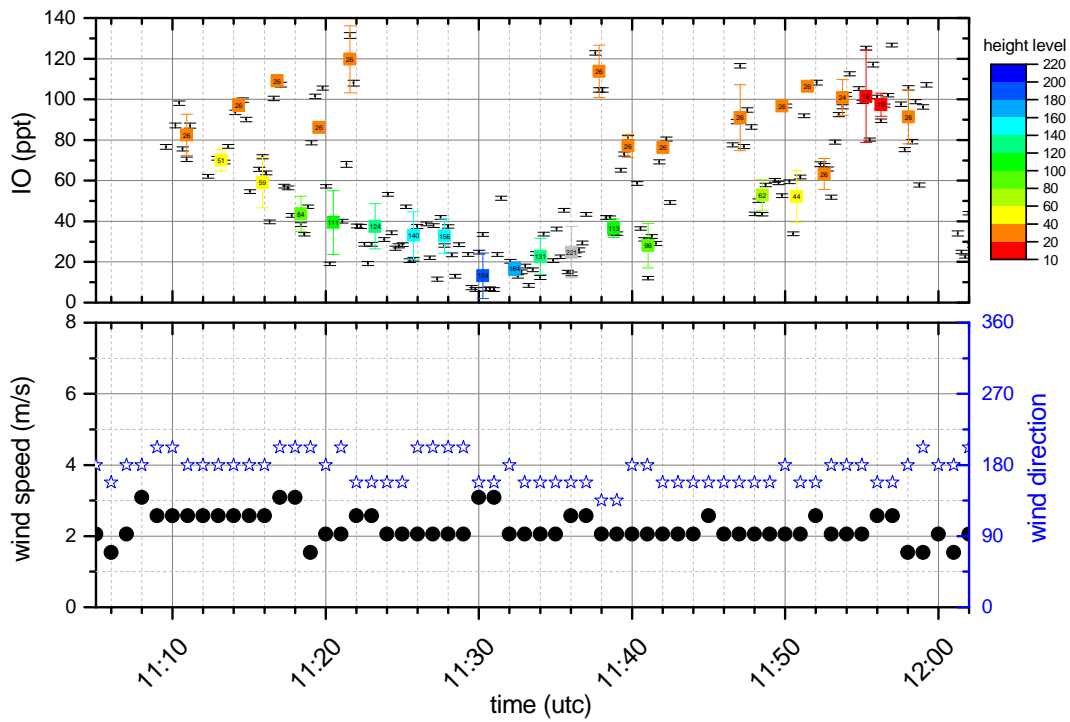


**Figure 12.68.** | Time series for the vertical IO profile measured in the seaweed bed at MRI on July 30th 2012. Average of data measured at the same height level are given as colored boxes, with the color indicating the height level.

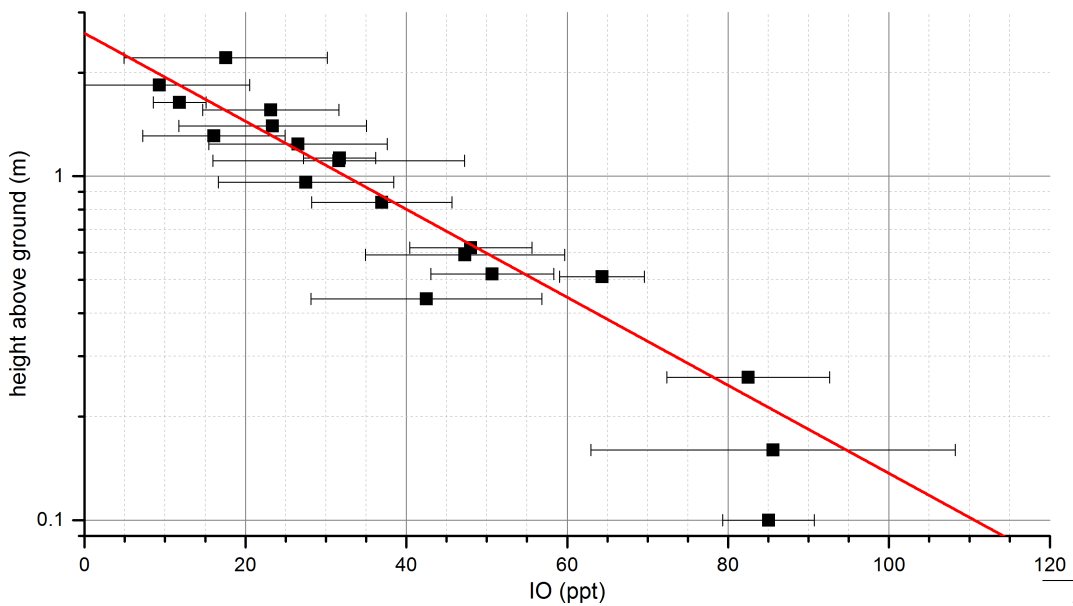


**Figure 12.69.** | IO vertical profile, for the measurement in the seaweed bed at MRI on July 30th 2012.

average areal density of  $2.5 \text{ kgFw m}^{-2}$  yields an iodine emission per fresh weight of about  $3 \text{ pmol (I)/gFw/ min}$ . This value is two orders of magnitude higher than the emission rate of the S. M. Ball et al. [2010] study and in good agreement to the laboratory study by Kundel et al. [2012] where an average of  $2 \text{ pmol (I)/gFw/ min}$  was determined for the first hour of exposure to air. Even though Kundel et al. [2012] found emission rates above  $5 \text{ pmol}_I \text{ gFw}^{-1}$  after 30 min of exposure, this is still in good agreement with our data, considering the uncertainties in the areal density of the seaweed.

## 12.11. Conclusion on Iodine Sources

In this study measurement of the reactive iodine species IO were performed at 10 locations along the Irish west coast using combined path averaging LP-DOAS measurements across inter-tidal areas and CE-DOAS point measurements directly over, or next to, the intertidal seaweed.

Of particular interest was the direct comparison of IO measurements at Mace Head Research station, which was the major location of previous studies [Alicke et al., 1999; Hebestreit, 2001; Saiz-Lopez and Plane, 2004; Seitz, 2009; Commane et al., 2011], with measurements at 7 wave sheltered shores, which were mostly not investigated before. Contrary to the expectation that Mace Head is a “hot-spot” for iodine emissions, this study found that (at the same time) IO at the wave sheltered shores was observed more regularly and at much higher concentrations (see sec. 12.8). During daytime low tide, the MoLP-DOAS observed at wave sheltered shores with extended spatial scales (several hundred meters to kilometers) usually more than three times but up to more than ten times higher IO mixing ratios compared to the shore at Mace Head. These measurements show that this is due to distinctive differences in the dominant sources for reactive iodine one wave exposed shores and on wave sheltered shores.

Wave sheltered shores have a shallow intertidal zone with extended beds of brown seaweeds, mainly *A. nodosum* and also *F. vesiculosus*, which are completely exposed to air during every low tide for an extended period of more than four hours. The unique combination of path averaging LP-DOAS and CE-DOAS point measurements directly above seaweed could identify these seaweeds as a strong source of reactive iodine (see sec. 12.8). Directly (1.3 m) above seaweed CE-DOAS, observed very high IO mixing ratios, exceeding at each site 20 ppt for extended periods of more than an hour and at several sites peak levels even exceeded 50 ppt. Very close (several 10 cm) to the seaweed mixing ratios exceeded even 100 ppt. Therefore our measurements gives the first direct evidence of the “hot-spot” theory by Burkholder et al. [2004] which suggested that local patches with mixing ratios of 50 ppt to 100 ppt are required to explain particle concentrations observed during nucleation events like also observed in this study (see sec. 12.9.2.1) and previous studies [e.g. O’Dowd et al., 2002b; Seitz et al., 2010]. Vertical CE-DOAS profile measurements, showed very high (secondary) IO emission rates of about  $60 \mu\text{g}_I \text{ m}^{-2} \text{ h}^{-1}$  at a solar irradiance of  $840 \text{ W m}^{-2}$  (see sec. 12.10). This is also the first determination of iodine emission rates from seaweed under real field conditions, as opposed to previous studies. Our measurements also showed no significant reduction of iodine emission when these seaweeds are covered by a thin water film (see sec. 12.9.1.5). This has two important implications: Opposed to previous assumptions, strong emissions of reactive iodine were observed even during rainy weather conditions, which is an important finding since this is a typical weather condition on the Irish Coast. Additionally, *A. nodosum* was observed to continues emission of iodine for half an hour to an hour when its already floating on the water towards the end of the low tide period. The observation of high levels of the reactive iodine species of IO above *A. nodosum* and *F. vesiculosus* are also in agreement with a recent study by [Huang et al., 2013]. They reported high  $\text{I}_2$  mixing ratios of more than 100 ppt for measurements few cm above intertidal *A. nodosum* and *F. vesiculosus* at several location around Mace Head. However, their measurements are difficult to compare since they use a passive

chemical sampling technique (diffusion denuder sampling, with GC-MS quantification in a laboratory) which has several drawbacks. To get a sufficiently high signal they need long sampling times (typically hours) giving them typically only one data point per low tide period. Also this method is very prone to interferences with other trace gas species, often leading to unpublishable data, which always leaves doubts on the validity of these measurements.

On the other side, at wave exposed shores like Mace Head, the inter tidal zone is much smaller and features a lower inter-tidal seaweed abundance mostly in the lower intertidal zone where some *L. digitata* grows. CE-DOAS measurements at Mace Head station, in this work, observed significant local IO emissions from *L. digitata* only for extremely low water levels close to spring-tide low water, which are relatively rare events only occurring on about 6 days of a 27 day tidal cycle and only for short time periods of less than an hour. This result is also in agreement with a recent in-situ study by Commane et al. [2011], which found the same dependence of IO concentrations on the tidal amplitude. Further, in this work it was found that local IO emissions from *L. digitata* played only a minor role for IO levels observed on the 3 km long Mace Head LP-DOAS light path (see sec. 12.9.2.1). The few events of high IO levels observed by the LP-DOAS could all be linked to IO emission at close by wave sheltered bays. Additionally, this work found, that washed up drift seaweed can also be a strong local source with observed local IO mixing ratios of up to 40 ppt. It is known that large quantities of drifting seaweed are cast ashore after storm events. However, there is currently no quantitative information on the covered areas, the biomass of washed up drift and their residence time on the beach. Thus, it is currently not possible to estimate the precise contribution to the coastal iodine emissions.

In conclusion, this work found that the major sources at the Irish West Coast are wave sheltered shores and not as previously believed wave exposed shores. Wave sheltered shores are very common on the Irish West Coast and represent much larger intertidal areas which a much higher seaweed density, mainly *A. nodosum* and also *F. vesiculosus*, compared to wave exposed shores with a low density of *L. digitata* in the lower inertial zone. Also the seaweed in the intertidal zone of wave sheltered bays is much more regularly and much longer exposed to air compared to inter tidal seaweed. The total emissions from wave sheltered shores are much larger, even if the emission per kg seaweed might be lower. Therefore, this work shows that Irish and Global emissions of reactive iodine, from coastal areas, should be much higher compared to estimates based on studies at Mace Head.

## 12.12. Estimating the Irish and Global Iodine Emission from IO Observations

There are only few studies which tried to estimate the regional or global emission rates of iodine into the atmosphere. Studies by Laturus et al. [2000] and Giese et al. [1999] estimated the global contribution of subtidal macro algae releasing iodocarbons, mostly  $\text{CH}_2\text{I}_2$ , into the ocean and subsequent emission into the atmosphere to be  $10^7 - 1 \cdot 10^8 \text{ g}_I \text{ a}^{-1}$ . Similarly, [Manley and Dastoor, 1987] estimates a global emission of  $\text{CH}_3\text{I}$  from subtidal *Laminariales* (kelp) to be  $2 \cdot 10^8 \text{ g}_I \text{ a}^{-1}$ . Saiz-Lopez et al. [2012] stated emission rates of  $1 \cdot 10^{10} \text{ g}_I \text{ a}^{-1}$  of dihalomethanes ( $\text{CH}_2\text{ICl}$ ,  $\text{CH}_2\text{IBr}$ , and  $\text{CH}_2\text{I}_2$ ) based on the production from mid latitude seaweed species, presumably at Mace Head, but details of this assessment remain unclear.

However, these values are not expected to be in any way representative for coastal sites, where the major source of reactive iodine is the emission of molecular iodine by inter-tidal seaweed during low tide. Also these values are based on only view observations, thus large errors in these estimates could be realistic.

An estimate of the iodine emission on the Irish coast is made based on the findings of this work, that wave sheltered coastlines are the major source region. At wave sheltered shore the intertidal *A. nodosum* and *F. vesiculosus* beds are roughly cover a 50 – 100 m wide stipe (pers. observ.). Assuming that about 20 % of the 7400 m long Irish coastline (assuming a scale length of 25 m<sup>2</sup>) feature sheltered coastlines and is covered by seaweed gives an emitting area of  $0.7 - 1.5 \cdot 10^8 \text{ m}^2$ . Scaling the emission rates determined in 12.10 to a typical daylight solar irradiance at the Irish coast of  $400 \text{ W m}^{-2}$  and using the observed daily exposure of 6 h (this includes that one some days two low tide cycles occur during daylight) yields a yearly emission of  $(0.4 - 1) \cdot 10^7 \text{ g}_I \text{ a}^{-1}$  on the Irish coast.

Estimating the global emission rate of seaweed is difficult, because there is no quantitative global assessment of the intertidal seaweed resource. Therefore, the following calculation was only done to get an idea of the order of magnitude of the global contribution from coastal iodine emissions. Assuming the mission rate for the Irish Coast is representative for the global seaweed population, a simple extrapolation to the global  $2 \cdot 10^6 \text{ km shoreline}^3$  gives a global emission rate between  $(1 - 3) \cdot 10^9 \text{ g}_I \text{ a}^{-1}$  for a seaweed coverage of 20 % of the world shoreline. However, this number might overestimate the global iodine emissions from coastal areas since Ireland has a very large intertidal seaweed abundance compared to other areas of the world (e.g. New Zealand see chap. 13). Compared to the intertidal seaweed, the distribution of the mainly subtidal *Laminariales* (kelp) is much better known. De Vooy [1979] states 60 000 km for the length of all coastlines where kelp beds are expected. At least for the northern atlantic it is known, that subtidal kelp has the same geographical distribution as the intertidal seaweed *A. nodosum* and *F. vesiculosus* [Mann, 1972; Naylor, 1976, e.g.]. Therefore, in first order

<sup>2</sup>Due to the rugged nature of the coastline its reported length strongly depends on the scale length  $\Delta$  of the measurement [Mandelbrot, 1967]. [McCartney et al., 2010] determined for the length of the Irish coast:  $L = 15\,550 \text{ m} \cdot \Delta^{-0.23}$

<sup>3</sup>The  $2 \cdot 10^6 \text{ km}$  length of the global shoreline is extrapolated using the relation  $L = 1.2 \cdot 10^6 \text{ km} \cdot \Delta^{-0.23}$  for a scale length of 100 m. The relation was determined form Crossland et al. [2005]

approximation this is also assumed to be correct globally (even though with other intertidal seaweed species). Using the 60 000 km also as shoreline for our global estimate gives a yearly iodine emission from coastal seaweed of  $(2 - 4) \cdot 10^8 \text{ g}_I \text{ a}^{-1}$ .

Compared to the global ocean emission of  $10^{11} - 10^{12} \text{ g}_I \text{ a}^{-1}$  [Saiz-Lopez et al., 2012], the contribution of coastal emissions seems minor on a global scale. However, these numbers are still under investigation and might be much lower. On the local scale these strong emissions of reactive iodine by seaweed however have a significant impact due to their ability to form particles and change the chemical properties of the atmosphere. The iodine particle formation events reported by O'Dowd et al. [2002b] and also in this study (see sec. 12.9.2.1) arise only at the high iodine levels at these coastal sites and not for locally low IO concentrations due to open ocean emissions (0.5 – 2 ppt). Thus, coastal iodine emissions could locally influence cloud micro physical properties and therefore also have an impact on the climate. Beyond atmospheric implications, there are also indications that high iodine emissions from seaweeds may cause a significant increase in human iodine intake through the respiration of gaseous iodine compounds [Smyth et al., 2011].

Furthermore, for a better estimate of the emissions from the Irish coastline, better information on the intertidal areas covered by seaweed, especially on sheltered bays, is needed e.g., from satellite or aerial observations. For better global estimations not only the intertidal areas covered by seaweed are relevant but also the locally different seaweed species. The observations in New Zealand (chap. 13) show very different emissions. Therefore, better global estimates require a better global picture of the involved seaweed species and their emissions.

# 13

## New Zealand 2013

Explorative measurements at the east coast of the New Zealand South Island were carried out as part of a BMBF (01DR12100) and DFG (PO 1801/1-1) funded pilot study in collaboration with the National Institute of Water and Atmospheric Research, a research institute based in New Zealand. The goal of this study was to investigate whether seaweeds endemic to southern hemisphere and the pacific ocean, where no previous measurements were available, can act as a source of reactive iodine species. Furthermore it was a goal to compare their emissions to previously investigated seaweeds of the mid-latitude North Atlantic Ocean to get a better picture of the global emission potential from coastal seaweeds. In this chapter the measurement sites and instrumentation will be described first followed by an overview of the meteorological conditions. Sections 13.3 and 13.4 gives an overview of the results, which are discussed in sections 13.5 and 13.6.

### 13.1. Measurement Sites and Instrumentation

Measurements at the east coast of the South Island were performed from March 2nd to April 6th 2013, which is in late summer to early fall season of the southern hemisphere, on the 10 km long coastal strip between Shag Point and Moraki shown in Fig. 13.1. The measurement location was mainly chosen to allow LP-DOAS measurements to cross a seaweed rich coastal area in order to capture possible halogen emissions from there (Fig. 13.1, left panel). The shoreline between Shag Point and Moraki is wave exposed and features steep cliffs and sandy beaches, which is typical for the shoreline of the South Island. The major inter-tidal seaweed species is *Durvillaea antarctica*, which is attached to rocks found below the cliff or just off the beach. However, as typical for exposed shores most of the seaweed grows subtidal. Additionally, drift seaweed, mainly composed of subtidal seaweed species, is abundant on the sandy beaches especially after storms.

Generally, the area is very rural with small settlements at Shag Point and Moeraki and therefore the density of anthropogenic sources in the area is low. The closest major cities are Dunedin 55 km to the south west and Oamaru 42 km to the north east. Since some pollution was expected in the investigated area since most homes are heated by simple wood and coal heating

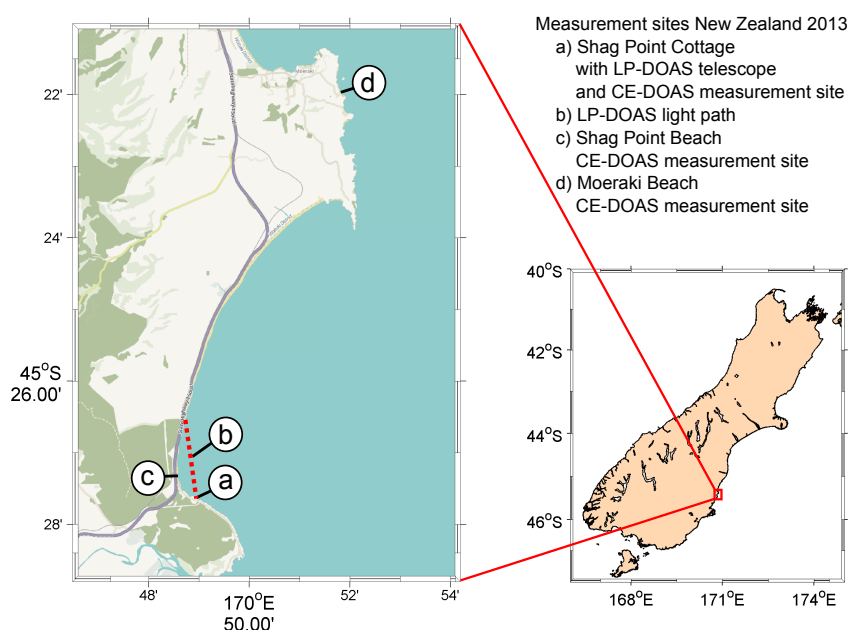


**Figure 13.1.** | Overview of the measurement locations for the New Zealand Campaign 2013. Measurements took place on the coastal strip between Shag Point and Moeraki. Map layer [OpenStreetMap HDM](#) ©OpenStreetMap contributors. Shoreline taken from GSHHG [Wessel and W. H. F. Smith, 1996]

and also since one of the major north-south transit roads (Highway 1) and train tracks run next right next to the shoreline.

The Amundsen LP-DOAS was applied for path averaged measurements of a multitude of trace gas species, mainly  $O_3$ ,  $NO_2$  and the reactive iodine species IO,  $I_2$  and OIO. Fig. 13.1 shows the light path which extended from the LP-DOAS instrument at the Shag Point Cottage (shown in Fig. 13.2) to a retro reflector in a distance of 2080 m (absorption path length 4160 m) and crossed the water at a height of about 8 m to 15 m. The instrumental setup and measurement routine are described in sec. 7.3.

Similar to the Ireland campaign the OP-CE-DOAS MK-II was applied for in-situ measurements of IO and  $NO_2$ , since the spatial distribution of seaweeds, the investigated sources of reactive iodine, was expected to be very inhomogeneous. The mobile CE-DOAS was deployed several times at the cottage, and at beaches close to Shag Point and Moeraki, as indicated in Fig. 13.1. The most abundant seaweed resource exposed to air were patches of washed up drift seaweed, which are a mixture of different seaweed species. Therefore, in order to investigate individual seaweed species, a closed chamber was setup around the resonator (e.g. see Fig. 13.25) and seaweed samples were placed in the chamber to measure the IO mixing ratios. The OP-CE-DOAS MK-II measurement routine and instrumental setup are described in sec. 5.

Spectroscopic measurements were complemented with in-situ ozone measurements, a weather station, and additional mobile measurements at the CE-DOAS location of wind speed



**Figure 13.2. | Shag Point Cottage with Instruments.** Top: Shown are the LP-DOAS, measuring along the light path indicated in Fig. 13.1, the CE-DOAS in (open) atmospheric measurement configuration (as on 03/07/2013) and on the roof of the cottage, the weather station Vaisala WXT520 and Kipp&Zonen CM11 is mounted. Bottom: The Cottage is located on a cliff about 15 m above the shoreline.

and direction. Details on these instrumentation is provided in sec. 8.2. Additionally, after March 21st, NIWA in cooperation with University of Cambridge applied a  $\mu$ -Dirac GC (see sec. 8.2.2) for measurements of halocarbons (such as  $\text{CH}_2\text{IBr}$ ,  $\text{CH}_2\text{ICl}$ ,  $\text{CH}_3\text{I}$  and  $\text{CHBr}_3$ ) which could act as sources of reactive halogen oxides. The  $\mu$ -Dirac GC was mostly applied to the CE-DOAS chamber measurements. An overview of the results is given in the appendix D.1.

### 13.1.1. Seaweed

Compared to the Irish coast, the shore at the east coast of the New Zealand south island is generally much steeper, and the tidal amplitude is at least a factor two lower. Also, in this area there are much less wave sheltered bays compared to Ireland. Therefore, the intertidal zone is generally much narrower and more wave exposed compared to Ireland. However, the coastline also features some areas with extensive sheltered waterways, particularly at Fiordland and the Malborough Sounds Adams [1997]. New Zealand has a very rich seaweed flora with about 1000 species but a quantitative assessment of their abundance and distribution is still missing, most likely because there is no seaweed industry in New Zealand which was one of the main initiators for these kinds of studies in Ireland. Therefore in the following only a qualitative description of the seaweeds encountered during this study is given which is only representative for the coast of the New Zealand south island and mainly based on Adams [1997].

***Macrocystis pyrifera*** is a brown seaweed of the order *Laminariales* (kelp), which grows exclusively in the subtidal zone in dense forests in the subtidal area. *M. pyrifera* is the dominant kelp of the southern hemisphere and one of the fastest growing organisms in the world which can reach up to 45m length in some regions. As for the rest of the southern hemisphere, also in New Zealand this species is expected to make the largest biomass (see sec. 3). During this study *Macrocystis Pyrifera* made up the largest biomass of the washed drift on the Shag Point Beach. Figure 13.22 shows a picture of washed up drift.

***Durvillaea antarctica*** is a large and brown seaweed (up to 10 m length) and the only abundant intertidal seaweed on the shores of the east coast of the New Zealand South Island. It grows in the mid and lower intertidal zone and is therefore regularly exposed to air during low tide. A distinctive feature is the honeycomb structure within the blade which provides high buoyancy. Therefore, as the low tide comes blades float on top of the water and are exposed to air long before the hold fast. Its very large holdfast attaches it firmly to intertidal rocks, which allows it to grow in the intertidal zone of the wave exposed shores. Other than its common name “bull kelp” suggests it belongs to the order *Fucales* (like e.g., *A. nodosum*). A picture of intertidal *D. antarctica* is shown in Fig. D.1.

***Hormosira banksii***, commonly known as Neptune’s necklace, is a small palm sized brown seaweed species found in mid-intertidal rock pools on the shore of Australia and New Zealand. It while it belongs to the order *Fucales*, it does not have blades but is instead characterized by chains of brown hollow beads. A picture of a specimen is shown in Fig. 13.27.

***Marginariella urvilliana*** is a brown seaweed only found on the shore of New Zealand. It usually grows on rocks below the low water mark and only during the lowest spring tide of the year some of the plants growing higher on the shore will be exposed to air. [Parsons, 1978]

During this work *M urvilliana* was found as one of the major constituents of the drift seaweed patches.

*Rhodophyllis membranacea* is the only red seaweed investigated in this study. The plants are palm sized with red, thin and flat-branched, blades. *R. membranacea* grows on rock in deep subtidal water on the shores of New Zealand and southern Australia. During this work *R. membranacea* was found as a common species of washed up drift seaweed patches.

## 13.2. Meteorology

A meteorological station (Vaisala WXT520) and a pyranometer (Kipp&Zonen CM11) setup 1.5 m above the roof of the Shag Point Cottage. They provided measurements of air temperature, air pressure, relative humidity, wind direction, wind speed and solar irradiance. Additionally, a sonic anemometer (Metek USA-1) was always setup next to the open path CE-DOAS instrument for local measurements of the wind speed and direction. More details on the meteorological instrumentation are provided in sec. 8.2.

Figure 13.3 shows an overview of the meteorological conditions at the Shag Point Cottage during the 35 day long measurement period. Most of the days were sunny and partly cloudy, except for four rainy days. The average wind speed of  $2.1 \text{ m s}^{-1}$  was very low for a coastal site. Fig. 13.4 shows the distinct day/night pattern of wind direction and wind speed. During daytime (9h to 19h NZST) mostly onshore wind from north eastern direction was observed, while during nighttime (22h to 7h NZST) the wind direction was mainly offshore from southern to south western direction. Figure 13.4 b) shows that high wind speeds above  $4 \text{ m s}^{-1}$  were almost exclusively observed during daytime, while during nighttime the wind speed was mostly below  $2 \text{ m s}^{-1}$ . The average air temperature was  $13.7^\circ\text{C}$  with a maximum of  $22.7^\circ\text{C}$  and a minimum of  $5.3^\circ\text{C}$ . The tidal height, measured at Port Chalmers by Land Information New Zealand, varied between 3.5 m and 5.75 m. The tidal variation had its maximum daily amplitude of 2 m on March 3rd a day of spring tide and the minimum daily amplitude of 1 m was observed during neap tide on March 19th. This tidal range is relatively small compared to the Irish west coast, where a daily variation of more than 5 m was observed during spring tide.

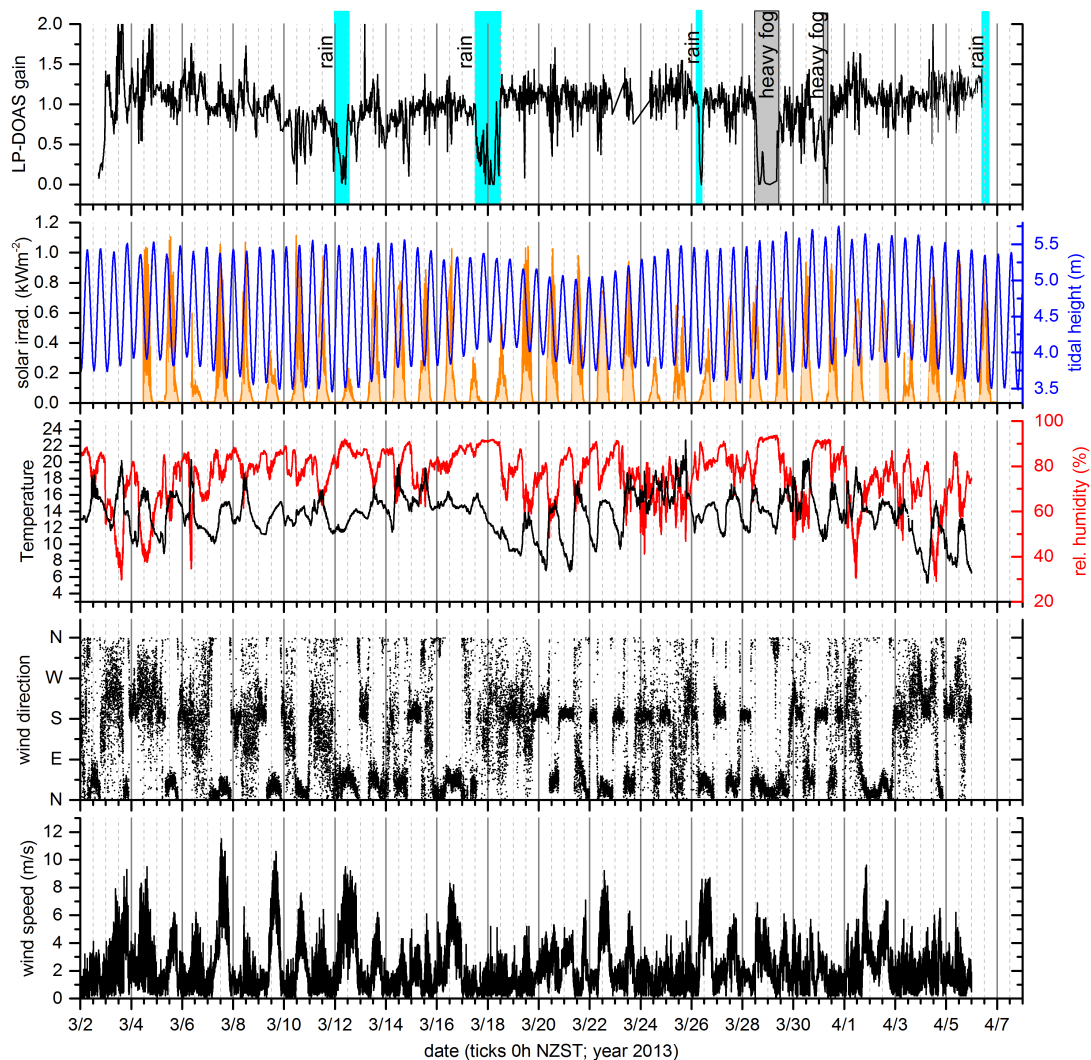


**Figure 13.3.** | Overview of the meteorology at Shag Point during the New Zealand campaign. Wind speed, wind direction, solar irradiance, air temperature and relative humidity were measured at the Shag Point Cottage. The LP-DOAS gain is the ratio between the intensity of atmospheric and lamp (short cut) measurements, and thus an indicator for the visibility. Rain periods were determined from personal observations and a continuous picture series from a webcam pointing along LP-DOAS light path. The shown tidal data measured at Port Chalmers, was provided by Land Information New Zealand. Details on the meteorological instrumentation and tidal observations are provided in sec. 8.2.

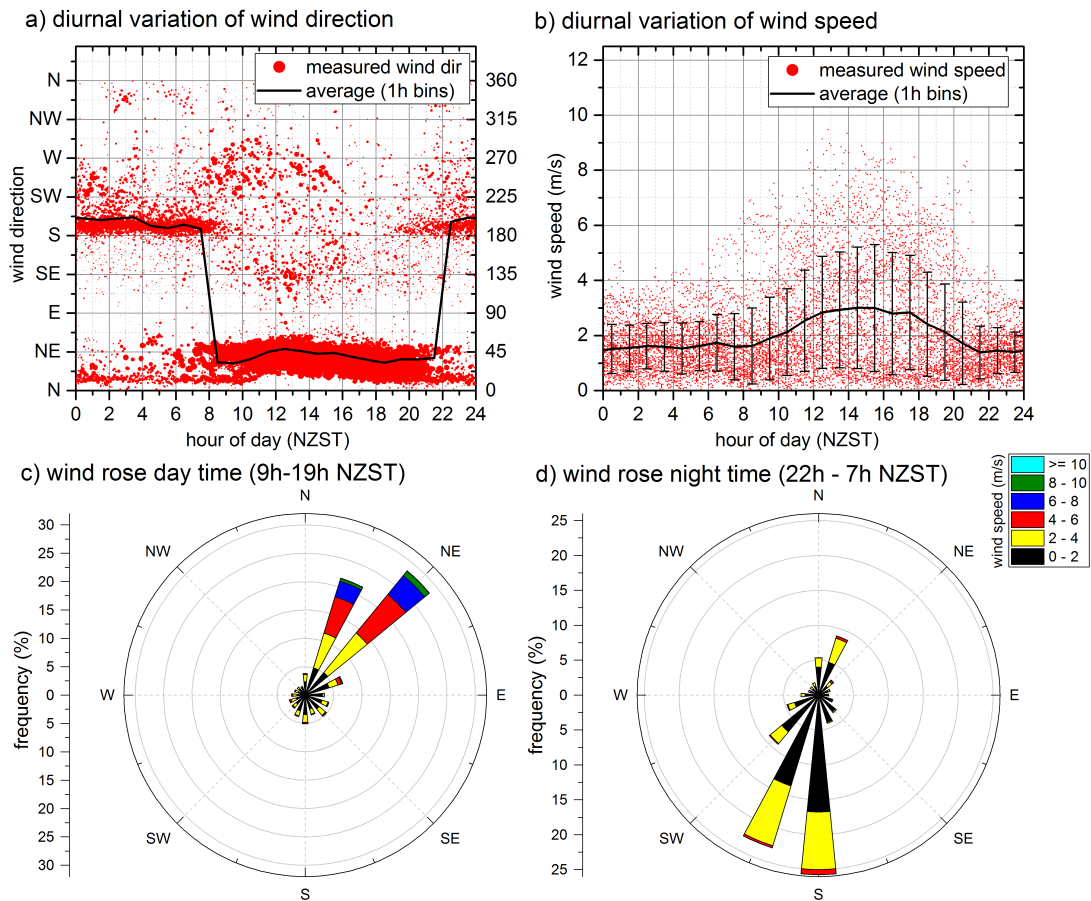


**Figure 13.4.** | Distribution of the wind direction at the Shag Point Cottage. a) Diurnal variations of the wind direction: Measured wind directions in red are averaged (using (u,v) wind vectors) in one hour bins shown in as black line. To guide the eye, the size of the red dots, showing the measured wind direction, is scaled by the wind speed, since the wind direction for very low wind speeds is ill defined. The wind direction shows a clear day/night pattern with prevailing north easterly direction during daytime and southerly direction during nighttime. b) Diurnal variation of wind: The measured wind speed shown in red is averaged in one hour bin shown as black line with error bars indicating the standard deviation of the average. High wind speeds above  $4 \text{ m s}^{-1}$  were almost exclusively observed during daytime, while the wind speed at night was typically calm with wind speeds below  $2 \text{ m s}^{-1}$ . c) and d) Wind roses show the distribution of wind speed and direction during daytime and nighttime.

### 13.3. LP-DOAS Results

Measurements at four different wavelength regions were evaluated to retrieve mixing ratios of: BrO, HCHO, O<sub>3</sub> and SO<sub>2</sub> (330 nm); IO and NO<sub>2</sub> (400 nm); I<sub>2</sub> and OIO (560 nm); NO<sub>3</sub> (640 nm). The analysis procedure and retrieval settings are described in sec. 7.3.2. Table 13.1 lists observed average and maximum mixing ratios and the average detection limit for the measured trace gases. Figure 13.5 show time series of IO and species observed above the detection limit and Fig. 13.6 shows histograms of mixing ratios and detection limits of IO and species which were not observed significantly above their detection limit.

#### 13.3.1. Non-Halogen Species

The non-halogen species NO<sub>2</sub> and SO<sub>2</sub> and O<sub>3</sub> are an indicator for the quality of air masses reaching the measurement site. The NO<sub>2</sub> time series shows daily observation of high mixing ratios more than 2 ppb almost every day with a peak mixing ratio of  $(9.51 \pm 0.05)$  ppb observed on March 8th at 3:27. Thus, the observed air masses show relatively high level of pollution for a rural area. Fig. 13.7 shows the diurnal cycle of NO<sub>2</sub> with relatively low mixing ratios, typically below 0.5 ppt during daytime and much higher levels during night time, on average above 2 ppt. The diurnal cycle of NO<sub>2</sub> is expected due the photolysis of NO<sub>2</sub> during daytime which changes the photo stationary state of NO and NO<sub>2</sub> (see sec. 2.2.2.1). Additionally, the NO<sub>2</sub> levels may be influenced by the diurnal cycle of the wind direction described in sec. 13.2: during daytime due to the onshore winds the LP-DOAS observes mainly cleaner marine air masses while during night air masses observed by the LP-DOAS are expected to show more pollution due to the dominant offshore wind direction, which brings air masses from the land where close by settlements and the highway 1 act as pollution sources.

The observed O<sub>3</sub> mixing ratios was on average  $(18 \pm 1)$  ppb, which is a typical value for

species	average	maximum	average det. lim.
IO	$(0.20 \pm 0.25)$ ppt	$(1.2 \pm 0.3)$ ppt	$(0.5 \pm 0.1)$ ppt
I <sub>2</sub>	$(-2 \pm 7)$ ppt	$(22 \pm 6)$ ppt	$(13 \pm 2)$ ppt
OIO	$(-0.1 \pm 1.1)$ ppt	$(4.7 \pm 0.9)$ ppt	$(2.1 \pm 0.3)$ ppt
BrO	$(-0.3 \pm 0.5)$ ppt	$(2.7 \pm 0.6)$ ppt	$(1.1 \pm 0.1)$ ppt
O <sub>3</sub>	$(18 \pm 1)$ ppb	$(30 \pm 1)$ ppb	$(2.2 \pm 0.2)$ ppb
NO <sub>2</sub>	$(1.59 \pm 0.04)$ ppb	$(9.51 \pm 0.05)$ ppb	$(0.07 \pm 0.01)$ ppb
SO <sub>2</sub>	$(0.12 \pm 0.03)$ ppb	$(3.48 \pm 0.03)$ ppb	$(0.05 \pm 0.01)$ ppb
NO <sub>3</sub>	$(3.3 \pm 1.1)$ ppt	$(7.4 \pm 1.2)$ ppt	$(2.3 \pm 0.2)$ ppt
HCHO	$(-47 \pm 215)$ ppt	$(1150 \pm 230)$ ppt	$(430 \pm 50)$ ppt

**Table 13.1.** | Overview of the mixing ratios and detection limits for the species measured by the Amundsen LP-DOAS For each species average and maximum mixing ratios and the average detection limit (det. lim.) are given. Errors for the average mixing ratios are the average measurement errors. For the average detection limit the standard deviation is given as uncertainty.

a rural area in the southern hemisphere and also the southern hemisphere open ocean (see sec. 2.2.2 and [Hartmann et al., 2013]). The diurnal cycle of  $O_3$  shown in Fig. 13.7 shows a variation in the order of 50 % and anti correlates to  $NO_2$ , with maximum  $O_3$  mixing ratios in the afternoon (average  $\sim 22$  ppb) and a minimum in the early morning (average  $\sim 13$  ppb), which is expected since during daytime  $O_3$  is produced from the photolysis of  $NO_2$  and during nighttime lost in the oxidation of  $NO$  to  $NO_2$  (see sec. 2.2.2.1).

$SO_2$  was regularly observed above the detection limit of  $(0.05 \pm 0.01)$  ppb with a maximum mixing ratios of  $(3.48 \pm 0.03)$  ppb which is a further indication for the degree of pollution in the observed air masses. Compared to  $NO_2$  the observation of elevated  $SO_2$  levels was less regular and as expected did not show a diurnal cycle. The most likely sources are local heating with coal and shipping routes off the coast.

Furthermore,  $NO_3$  was observed regular during night with an average mixing ratio of 3.3 ppt

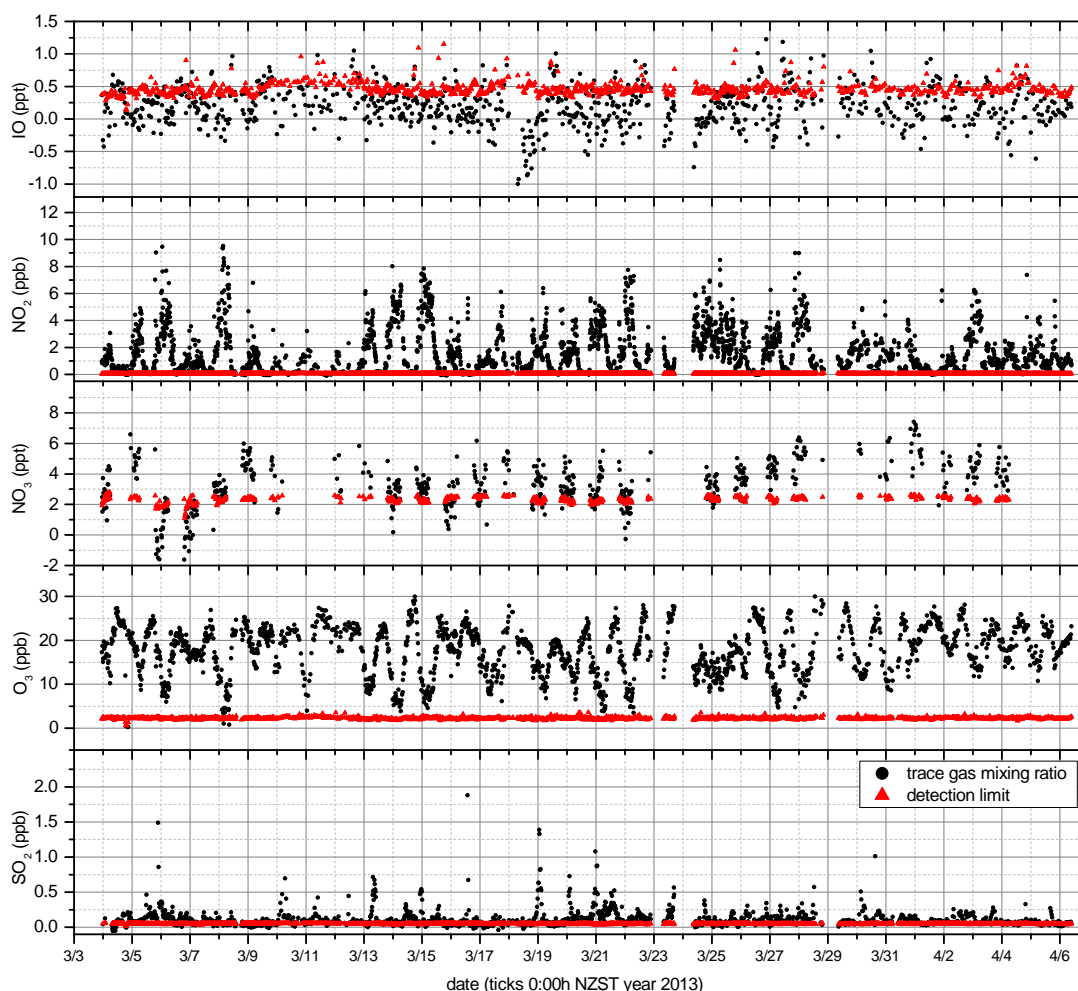


Figure 13.5. | Time series of trace gases observed by the Amundsen LP-DOAS

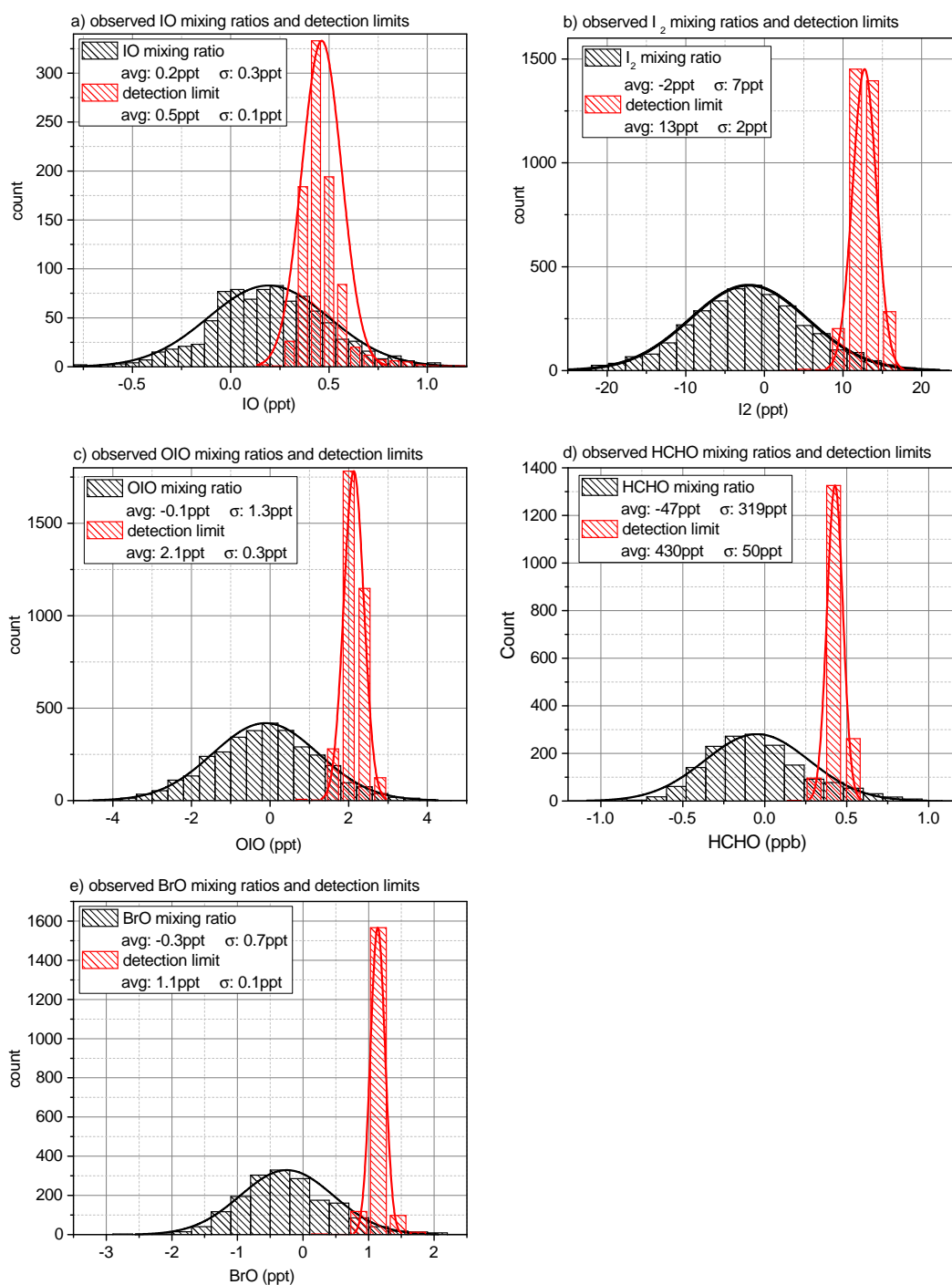
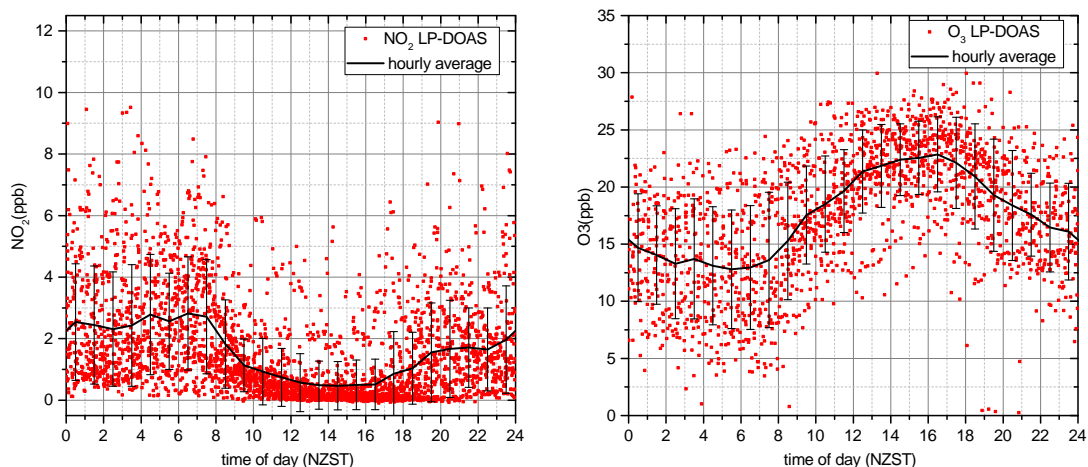


Figure 13.6. | Histograms of mixing ratios observed by the Amundsen LP-DOAS for trace gases close to or below the detection limit.



**Figure 13.7.** | Diurnal variation of  $\text{NO}_2$  and  $\text{O}_3$  during the New Zealand campaign 2013.  $\text{NO}_2$  (left) and  $\text{O}_3$  (right) mixing ratios observed by the LP-DOAS were averaged in one hour bins to get their average diurnal variation. The error bars show the standard deviation of the respective averages.

and a maximum of  $(7.4 \pm 1.2)$  ppt which is plausible considering the nighttime  $\text{NO}_2$  and  $\text{O}_3$  levels. No significant HCHO absorption was found in the recorded spectra, even though the maximum values of  $(1.1 \pm 0.2)$  ppb and few other data points seem above their detection limits of. The histogram of mixing ratios and detection limits in Fig. 13.6d) shows that the observation of HCHO was not statistically significant above its detections limit which was on average 0.43 ppb.

### 13.3.2. Halogen Species

During the New Zealand campaign it was attempted to measure  $\text{I}_2$  and the halogen oxides IO, OIO and BrO. Even though the maximum values presented in Table 13.1 and few other data points seem above their detection limits of, no significant absorption features of  $\text{I}_2$ , OIO and BrO was found in the recorded spectra. Histograms of mixing ratios and detection limits in Fig. 13.6 also shows that the observation of  $\text{I}_2$ , OIO and BrO was not statistically significant above their detections limits which were on average 13 ppt for  $\text{I}_2$ , 2.1 ppt for OIO and 1.1 ppt for BrO.

IO was also mostly below the detection limit which was on average 0.5 ppt but the time series in Fig. 13.5 shows several observations of about 1 ppt which would be two times above the detection limits. It is however debatable if these observations are significant since the data has a lot of scatter and often only one or two data points are above the detection limit. The DOAS fit, exemplarily shown in Fig. 7.6, also leaves some doubts since there are often systematic residual structures around the fitted IO absorption bands. The histogram of the observed IO mixing ratios also shows that if IO was present it would be mostly close to or below the detection limit.

## 13.4. CE-DOAS Results

The results of the CE-DOAS measurements are illustrated in Fig. 12.51. Time series of IO and  $\text{NO}_2$  are shown together with the corresponding solar irradiance and tidal height. Also annotated are measurement locations as shown in the overview map in Fig. 13.1 and the measurement configuration which changed between open atmospheric measurements and measurements of seaweed samples in a closed teflon chamber. The data evaluation proceeded as described in sec. 5.6. In the standard evaluation 10 measured spectra were added (50000 scans) to reduce the photonic noise yielding a time resolution of about 2 min. For time periods with a strong IO signal individual spectra (with 5000 scans) were evaluated for a better time resolution of about 12 s.

$\text{NO}_2$  was almost always observed above its detection limit of 0.08 ppb with a maximum mixing ratio of  $(11.60 \pm 0.05)$  on March 27th 19:06 NZST.  $(\text{CHO})_2$  was always below its detection limit which was on average 103 ppt.

The open atmospheric measurements for the first time observed coastal IO in southern hemisphere with a maximum mixing ratio of  $(68.4 \pm 1.2)$  ppt (10 s time resolution) on April 4th. However, observed mixing ratios showed a strong dependence on the location of the CE-DOAS, seaweed abundance and meteorology as discussed in sec. 13.5. Measurements where the CE-DOAS was applied to chamber incubation experiments of different seaweed species showed even higher IO mixing ratios of up to  $(616 \pm 4)$  ppt (10 s time resolution) on March 28th for a sample of *Marginariella urvilliana* showing that southern hemisphere seaweed species can also act as strong source of IO. Detailed results for the individual seaweed species are given together with the discussion in sec. 13.6.

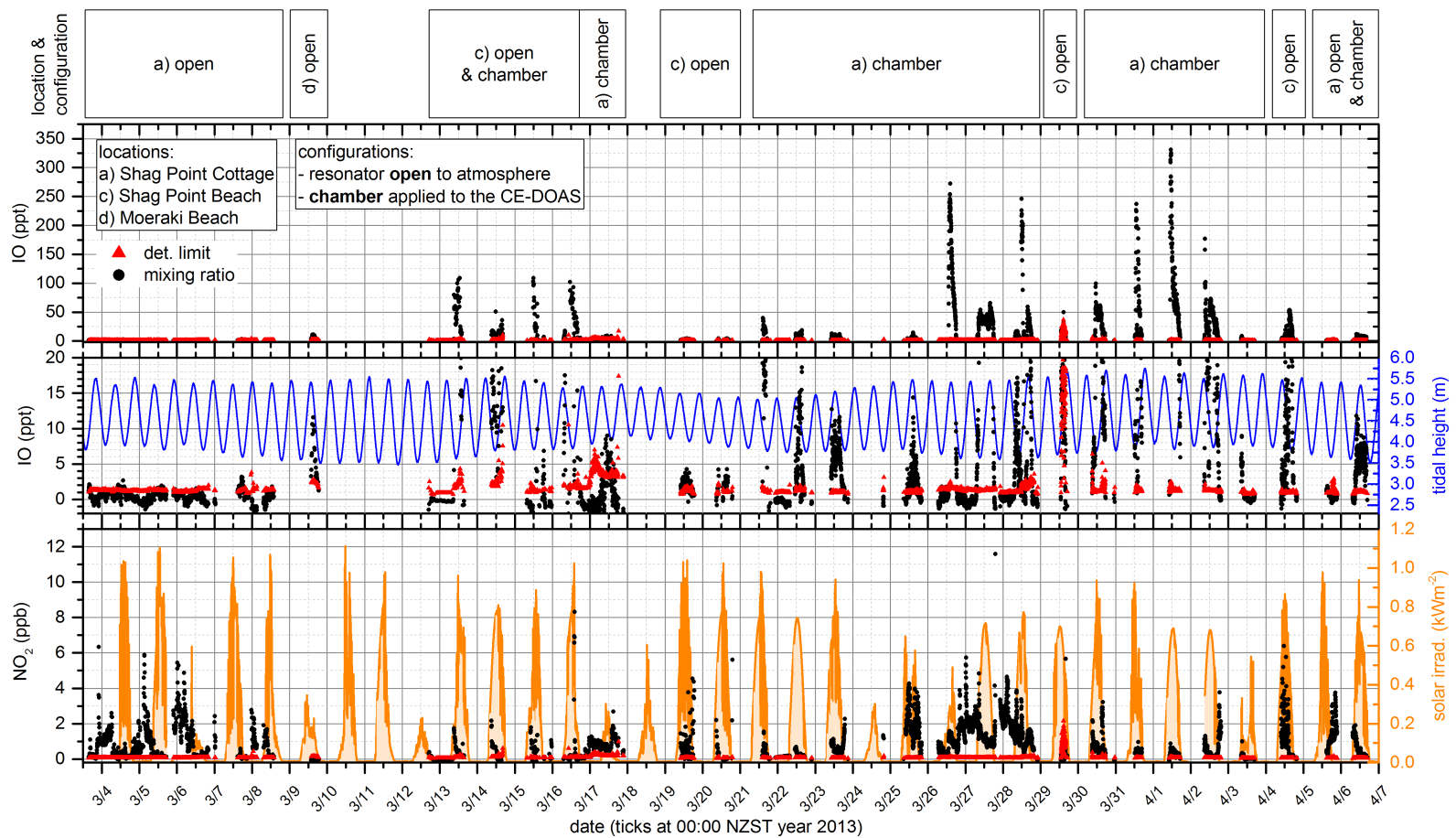


**Figure 13.8.** | Time series for IO and NO<sub>2</sub> measured by the CE-DOAS during the New Zealand campaign 2013. On top the different measurement locations and configurations are indicated. The measurement locations follow the labeling of the overview map in Fig. 13.1. The CE-DOAS was applied in **open** configuration with an open resonator towards the atmosphere and in **chamber** configuration where seaweed samples were placed in a closed chamber setup around the resonator (see Fig. 13.17). The top and middle plot show the IO time series at different y-scales to cover the large range of observed mixing. Additionally the time series of NO<sub>2</sub> mixing ratios, solar irradiance and tidal height are shown.

## 13.5. Discussion of Atmospheric Measurements

The following sections discuss the results of the open path CE-DOAS in “open” measurement configuration and the results of the LP-DOAS measurements.

As shown in the Fig. 13.12, Fig. 13.14 and Fig. 13.15 on three days, March 9th and 14th and April 4th, open path CE-DOAS measurements observed high IO mixing ratios above 10 ppt at Shag Point Beach and Moeraki Beach. On the other hand, as shown in Fig. 13.13, an order of magnitude less IO was observed by the open path CE-DOAS on March 19th and 20th. Also CE-DOAS measurements in the garden of Shag Point Cottage observed only one significant IO peak on March 7th with a maximum mixing ratio of  $(3.2 \pm 0.6)$  ppt as shown in Fig. 13.16. Furthermore, as shown in the section 13.3.2 the LP-DOAS observed only occasional and sporadic IO above the 0.5 ppt detection limit with a maximum mixing ratio of 1.2 ppt, and the time series showed no correlation to the tidal height.

These measurement results reveal strong local IO sources at Shag Point Beach and Moeraki Beach with a very inhomogeneous distribution. The distribution of seaweed at Shag Point, the CE-DOAS measurement location and the LP-DOAS light path are illustrated in Fig. 13.9. The only inter-tidal seaweed species abundant in the investigated area is *Durvillaea antarctica* which grows on rocks mainly several 10 m to 100 m meter off the shore. However, the LP-DOAS light crossed several of these patches at a height of 8 m to 15 m and did generally not observe IO above 0.5 ppt, and very importantly also no tidal pattern. Therefore, the *D. antarctica* cannot be the major source of the high IO levels above 10 ppt observed by the CE-DOAS. However, the observation IO by the CE-DOAS correlated with the abundance of washed up drift seaweed around the instruments location. As shown in Fig. 13.12, Fig. 13.14 and Fig. 13.15 on the three days (3/9, 3/14, 4/4) where the CE-DOAS observed high IO mixing ratios it measured downwind of large patches of drift seaweed. On the other hand on 3/19 and 3/20, shown in Fig. 13.13, when the CE-DOAS observed one order of magnitude less IO the drift weed abundance in the area around the instrument was very low. The low IO mixing ratios observed during CE-DOAS measurements in the garden of Shag Point Cottage also fit in this picture since this location is about 500 meter south east of Shag Point Beach and 15 m above a rocky shore with low drift weed abundance (see Fig. 13.2).

The patches of washed up drift seaweed, identified as the major source of the observed IO, are a mix of several mostly subtidal seaweed species as shown in Fig. D.1. In terms of mass and volume the most abundant drift species was *Macrocystis pyrifera* a brown seaweed. The other brown drift seaweeds that could be identified were *D. antarctica*, *Marginariella urvilliana* and *Hormosira banksii*. There were also several red seaweed species in the mix but only *Rhodophyllis membranacea* could be identified. *Rhodophyllis membranacea* was one of the most abundant red seaweed species in the mix, and stands out by its pungent smell. Variation of seaweed abundance at Shag Point Beach was recorded on three days of the campaign using a GPS tracks. The resulting maps in Fig. 13.11 show the high variability in the spatial distribution and abundance of drift seaweed. Most drift seaweed was observed after stormy weathers, which then declines again over subsequent days of calmer weather.

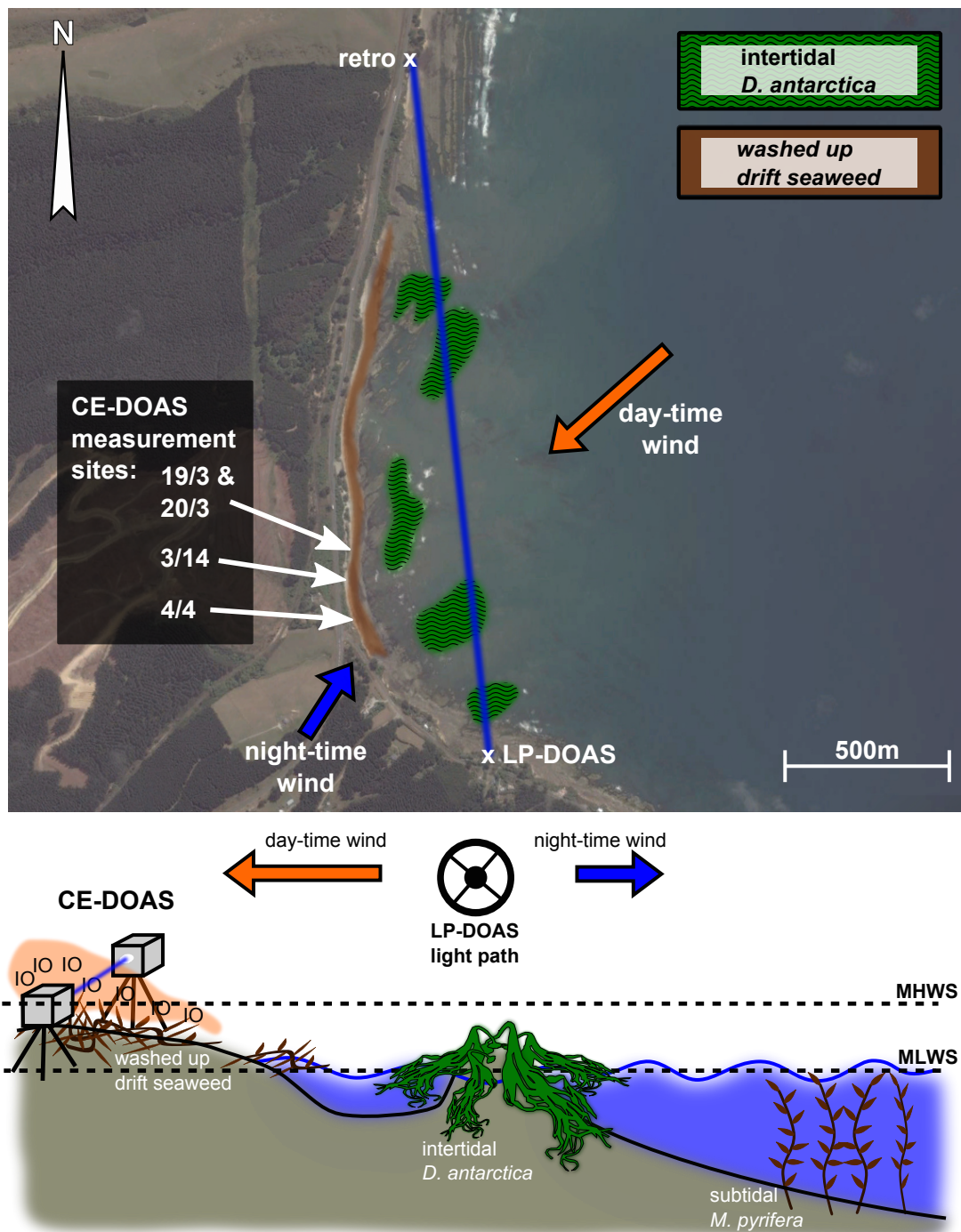


**Figure 13.9.** | Illustration of the IO measurements at Shag Point Beach. Top: The map shows the LP-DOAS light path, CE-DOAS measurement sites, the general distribution of intertidal seaweed and washed up drift seaweed and the prevalent daytime and nighttime wind directions. Bottom: Sectional view of Shag Point Beach with the LP-DOAS and CE-DOAS measurement locations. The dashed lines mark the intertidal zone which is defined by the mean spring tide range from MLWS to MHWS.

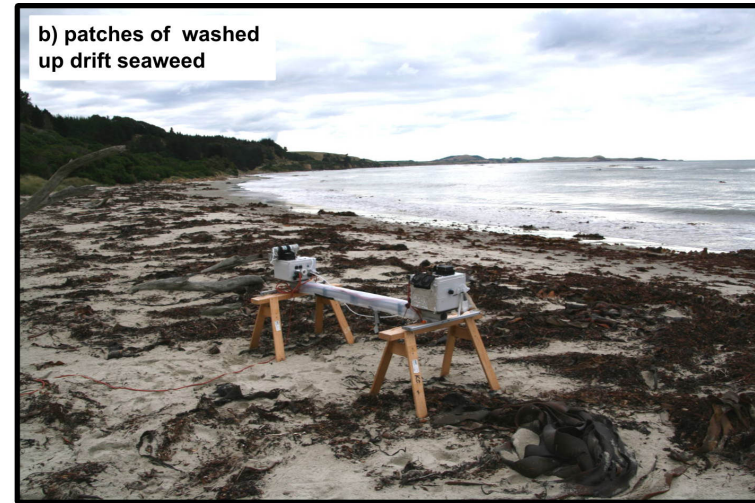


**Figure 13.10.** | Pictures of Seaweed Found at Shag Point Beach. a) Exposed intertidal *D. antarctica* during low tide, growing on rocks several 10 m off the shore. b) Patches of drift seaweed at Shag Point Beach (photographed on April 4th). c) Freshly washed up drift seaweed patch, mainly *M. pyrifera*, in the intertidal area of Shag Point Beach (photographed on April 12th). d) Mix of washed up brown and red seaweed (photographed on April 4th).



**Figure 13.11.** | Variation of distribution of the drift seaweed washed up at Shag Point Beach. The distribution of drift seaweed, shown for three days during the 2013 campaign, was determined from GPS tracks.

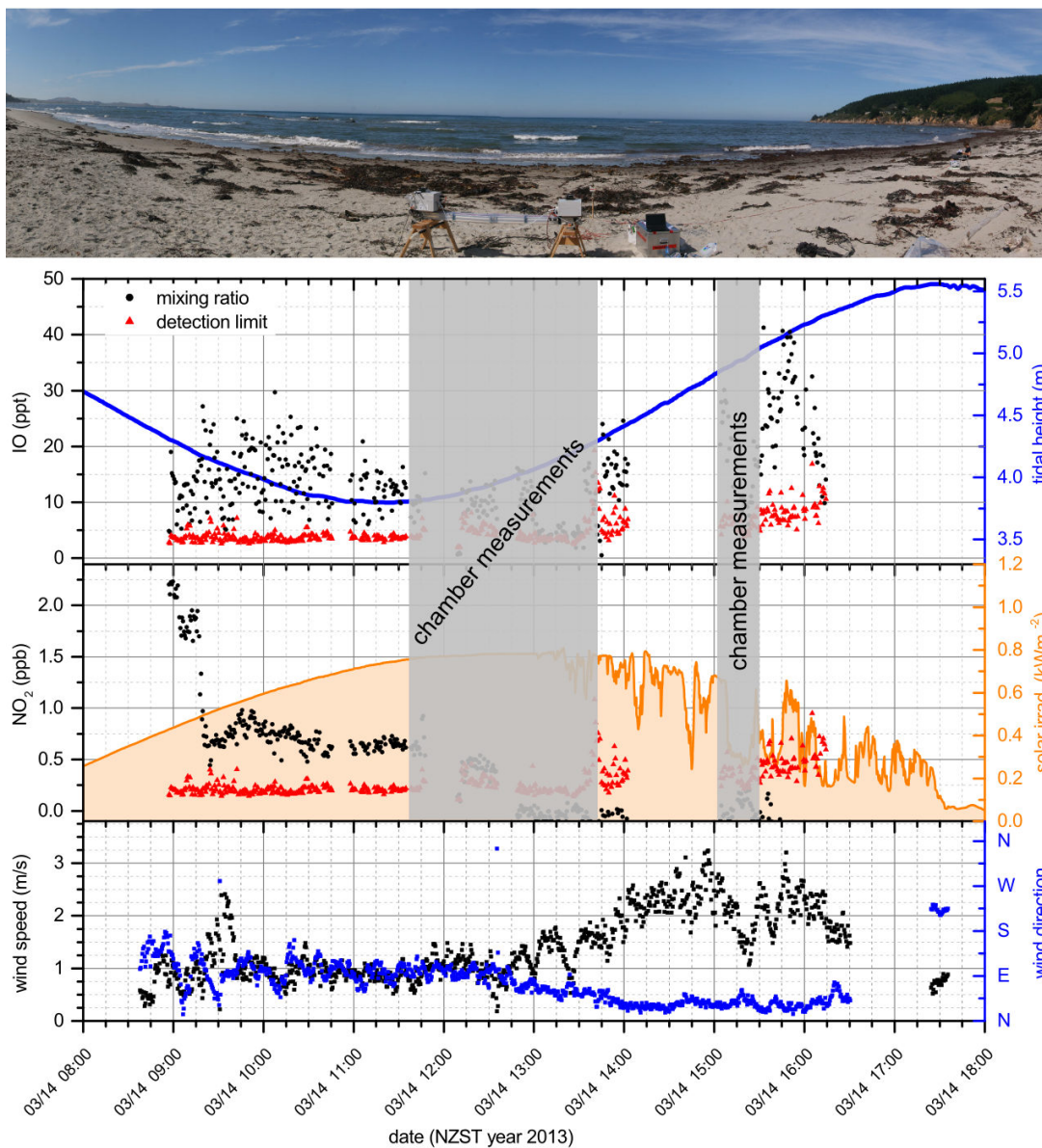


**Figure 13.12.** | CE-DOAS ambient air measurements Shag Point Beach on March 14th.

Shown are the atmospheric IO (top) and NO<sub>2</sub> (middle) mixing ratios measured by the CE-DOAS. The greyed out areas indicate periods where the incubation chamber was applied. Further shown are the tidal height at Port Chalmers (top), the solar radiation at Shag Point Cottage (middle) and the local wind speed and direction at the CE-DOAS (bottom). Details on the auxiliary measurements are given in sec. 8.2.

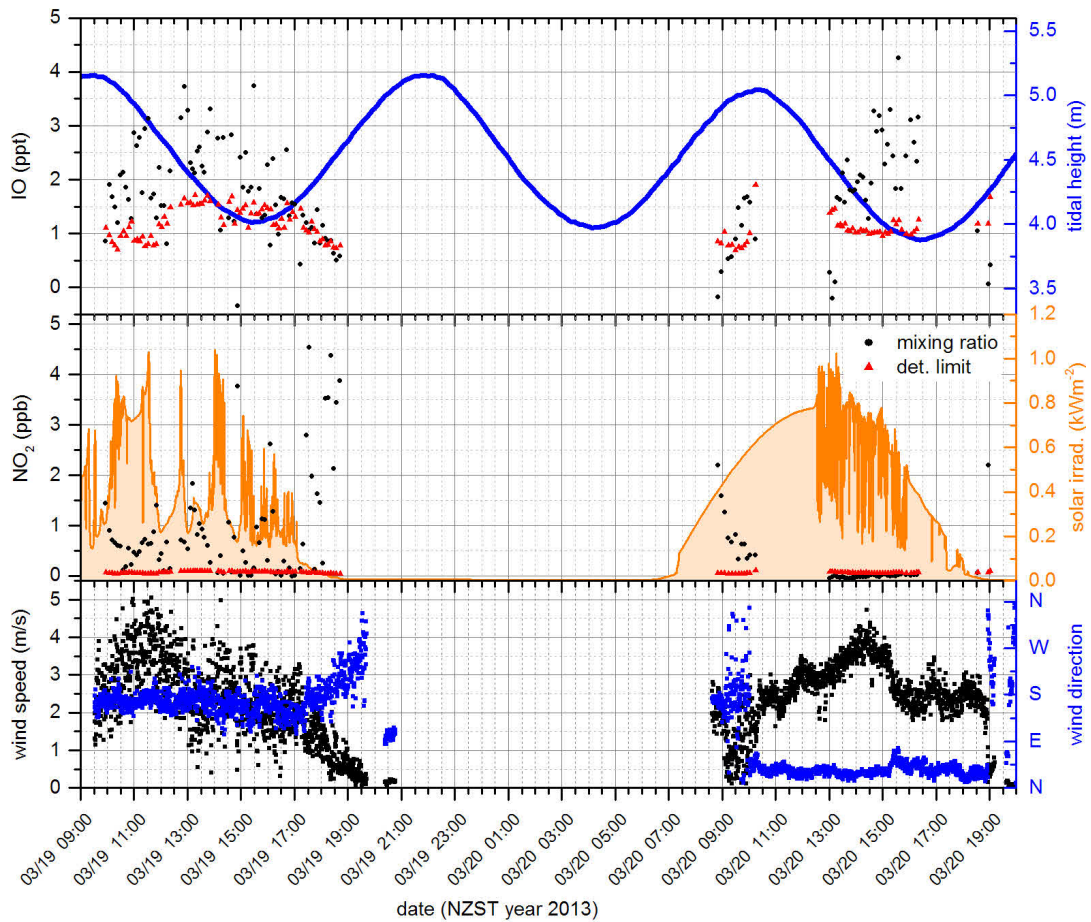


**Figure 13.13.** | CE-DOAS ambient air measurements at Shag Point Beach on March 19th and 20th. Shown are the atmospheric IO (top) and  $\text{NO}_2$  (middle) mixing ratios measured by the CE-DOAS. Further shown are the tidal height at Port Chalmers (top), the solar radiation at Shag Point Cottage (middle) and the local wind speed and direction at the CE-DOAS (bottom). Details on the auxiliary measurements are given in sec. 8.2.

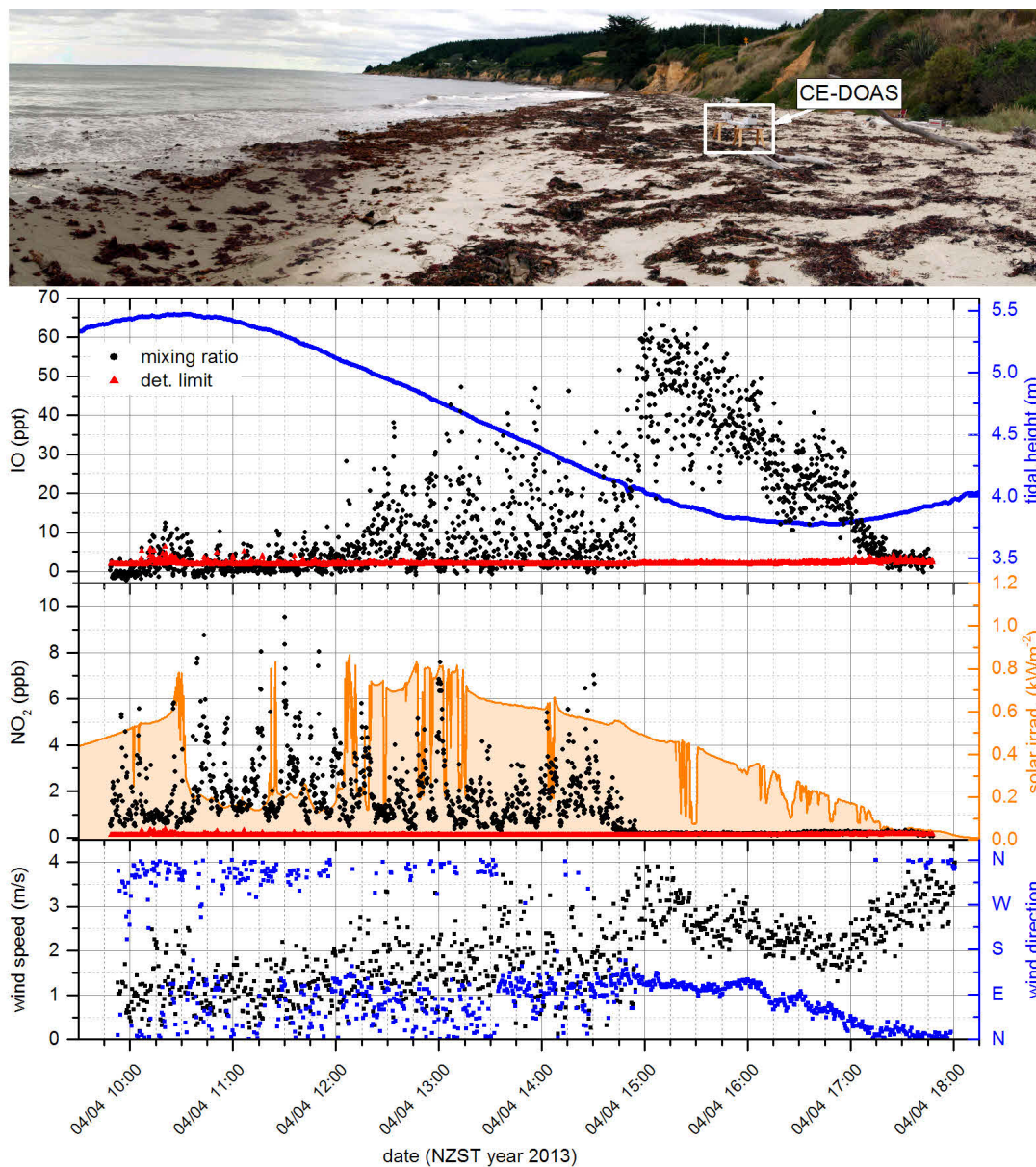


**Figure 13.14.** | CE-DOAS ambient air measurements at Shag Point Beach on April 4th. Shown are the atmospheric IO (top) and NO<sub>2</sub> (middle) mixing ratios measured by the CE-DOAS. Further shown are the tidal height at Port Chalmers (top), the solar radiation at Shag Point Cottage (middle) and the local wind speed and direction at the CE-DOAS (bottom). Details on the auxiliary measurements are given in sec. 8.2

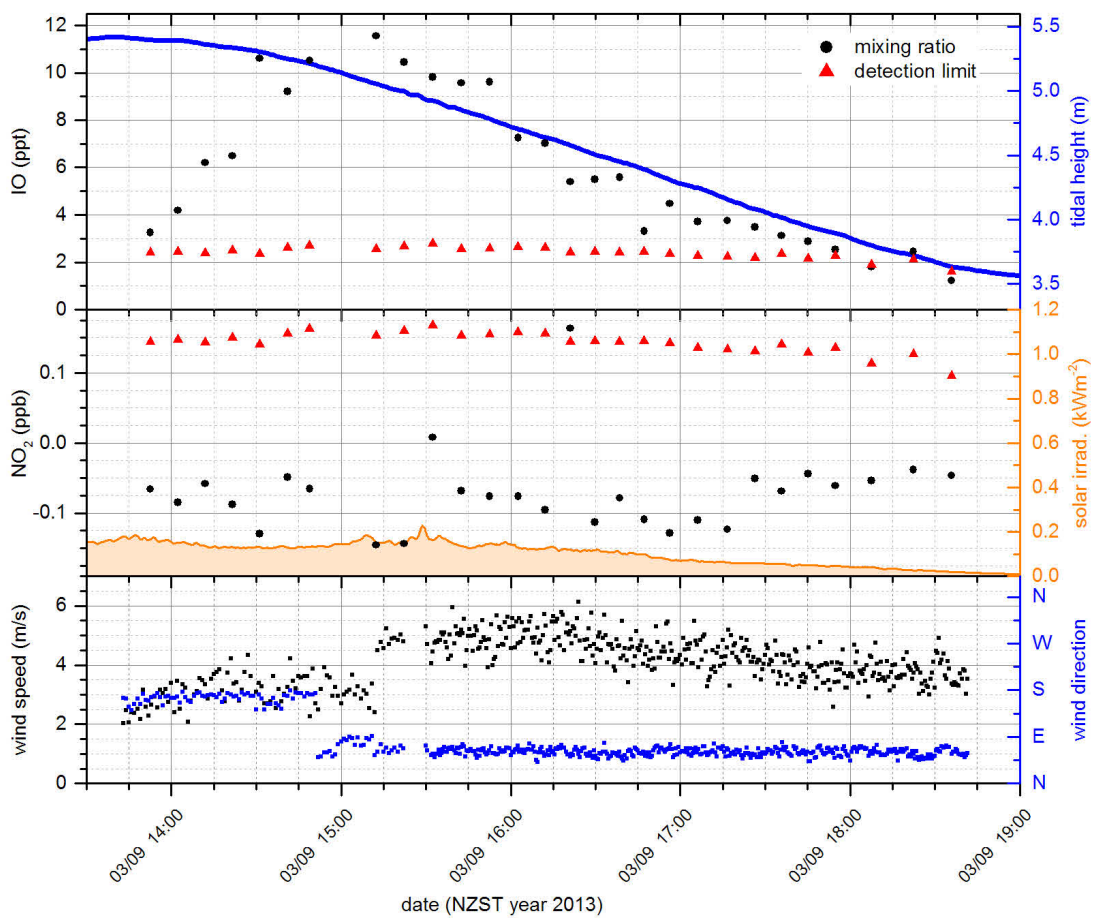


**Figure 13.15.** | CE-DOAS ambient air measurements at the Moeraki Beach on March 9th. Shown are the atmospheric IO (top) and  $\text{NO}_2$  (middle) mixing ratios measured by the CE-DOAS. Further shown are the tidal height at Port Chalmers (top), the solar radiation at Shag Point Cottage (middle) and the local wind speed and direction at the CE-DOAS (bottom). Details on the auxiliary measurements are given in sec. 8.2

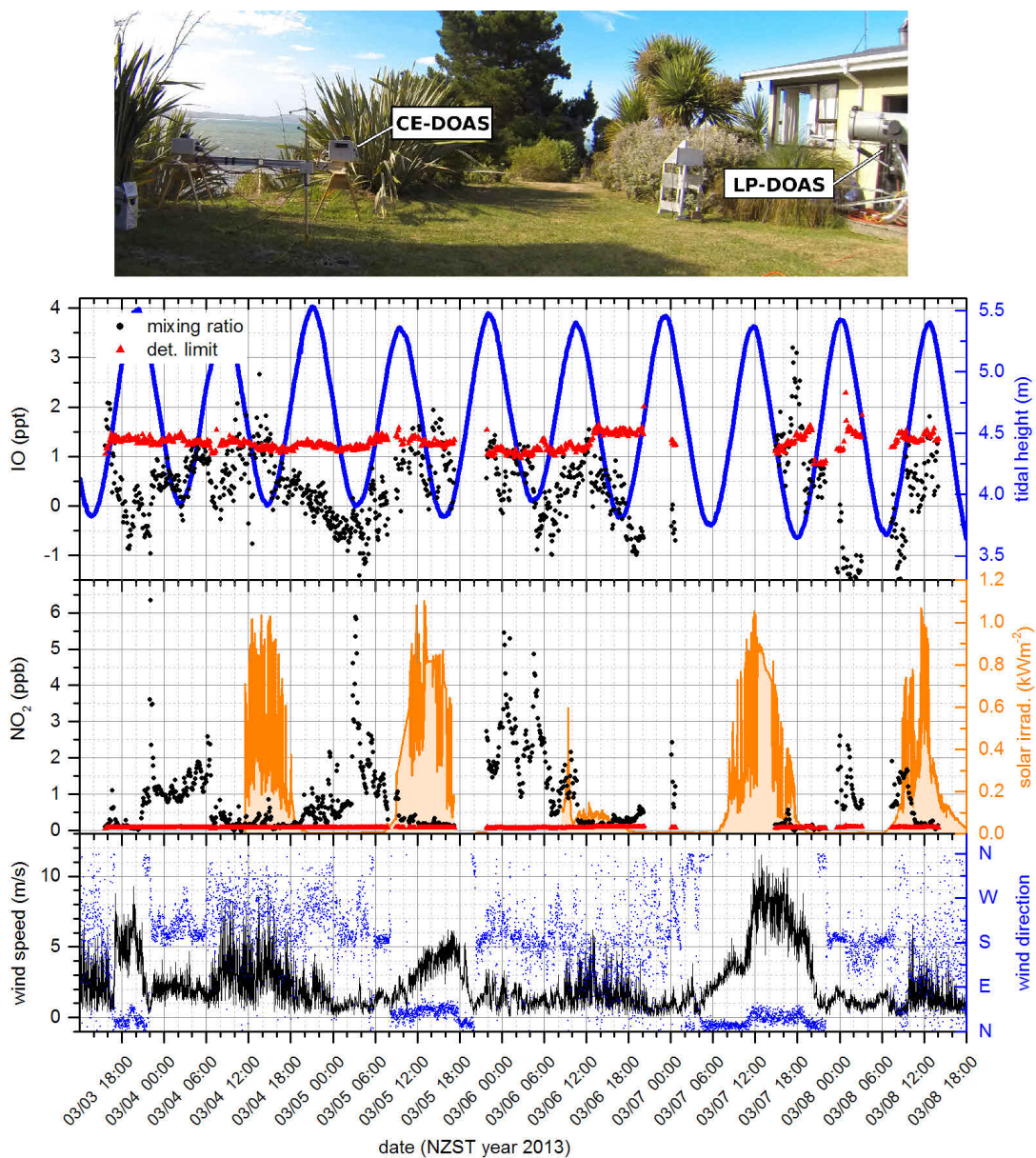


**Figure 13.16.** | CE-DOAS ambient air measurements at the Shag Point Cottage from March 3rd to 8th. Shown are the atmospheric IO (top) and NO<sub>2</sub> (middle) mixing ratios measured by the CE-DOAS. Further shown are the tidal height at Port Chalmers (top), the solar radiation at Shag Point Cottage (middle) and the local wind speed and direction at the CE-DOAS (bottom). Details on the auxiliary measurements are given in sec. 8.2



**Figure 13.17.** | **CE-DOAS with closed chamber.** In order to measure halocarbons and and ozone additional sample lines are connected to the chamber.

## 13.6. Discussion of Chamber Measurements

As discussed in the last section, atmospheric measurements identified washed up drift seaweed patches as the most likely source of the observed IO. In order to test this hypothesis it was desired to individually specifically measure the emission of the seaweed patches and their constituents. For this a closed chamber was was setup around the resonator to separate the probed air volume from the atmosphere. As shown in Fig. 13.17 the chamber with an air volume of 130 L ( $\sim 2 \text{ m}^2$  surface area) was realized by sealing the space between the sender and receiver box with a Teflon film (FEP 200A, DuPont, thickness 0.05 mm). Teflon film was chosen due to its inert surface, reducing wall losses of the highly reactive IO but also due to its good transmittance of solar radiation, necessary for the formation of IO from photolysis of  $\text{I}_2$  and potentially some very short-lived halo carbons. Additionally, since the chamber reduces the air exchange, trace gases emitted/formed in the chamber are accumulated, which further enhances the sensitivity of the CE-DOAS measurement. However, some exchange of air in the chamber was provided by the zero air flow from the mirror purge of  $Q_{\text{mirror purge}} = 4 \text{ L min}^{-1}$ . Additionally, this improvised chamber had several leaks which caused wind driven exchange with ambient air. Measurements of an  $\text{NO}_2$  peak from a passing container ship on March 16th (Fig. 13.22) allowed to estimate the wind driven air exchange time to be less than 2 min giving an air flow of  $64.5 \text{ L min}^{-1}$  at a wind speed of  $6 \text{ m s}^{-1}$ . As first order approximation the wind driven air flow at other times was linearly extrapolated using the wind speed  $v_{\text{wind}}$  as

$$Q_{\text{wind}}(v_{\text{wind}}) = 11 \frac{\text{L/min}}{\text{m/s}} \cdot v_{\text{wind}}. \quad (13.1)$$

However, this is a very rough approximation which is expected to be correct only within a factor three since it neglects the wind direction relative to the direction of the chamber and also the leaks were different each time after the chamber was removed and reapplied.

### 13.6.1. IO Mixing Ratios for Different Seaweeds

First chamber measurements were performed on March 13th directly on top of a patch of washed up drift seaweed as shown in 13.20. Very high IO mixing ratios were observed with a maximum of 192.1 ppt and an average of 65 ppt (over the first two hours). This gives further evidence to our finding, that patches of washed up drift seaweed are the major source of the high IO levels observed by open path CE-DOAS at Shag Point Beach and Moeraki Beach (see sec. 13.5).

Furthermore, major constituents of the drift seaweed patches were investigated individually in the closed chamber. These were the subtidal seaweed species *Macrocystis pyrifera*, *Rhodophyllis membranacea* and the intertidal species *Durvillaea antarctica*, *Marginariella urvilliana* and *Hormosira banksii*. Table 13.2 gives an overview of the samples, their weight and observed maximum and average mixing ratios. Time series of the incubation experiments and pictures of the seaweed samples are shown in Fig. 13.21 to Fig. 13.28. During all incubation experiments, for all species except *Durvillaea antarctica* very high IO mixing ratios with average values of several 10 ppt and peaks above 100 ppt were observed. In the following details on the incubation experiments are given for the different seaweed species:

***Macrocystis pyrifera*:** For a 4 kg (fresh weight) sample, freshly washed up on March 16th (Fig. 13.22), IO peaks with a mixing ratio of  $(168 \pm 2)$  ppt immediately after inserting the sample into the chamber. Within 20 min IO declines to about 70 ppt and sustains for about 2 hours until IO is completely depleted by a high  $\text{NO}_2$  plume (max  $(10.0 \pm 0.1)$  ppb) from a passing container ship entering the chamber through leaks. After 30 min the plume passed and IO rose again to about 40 ppt and in the subsequent 1.5 h slowly declined to 20 ppt until the measurement ended.

Subsequent incubation of several days old, partly decayed samples (March 22nd, 23rd, 25th) showed much lower mixing ratios and no consistent time dependence for observed IO mixing ratios as shown exemplarily in Fig. 13.24 for the measurements on March 23.

***Durvillaea antarctica*** specimen with several meters long blades attached to a stipe, were too large for the chamber. Therefore, for the investigated specimen were cut only a single blade and the stipe, which still had a fresh weight of 5 kg, were put into the chamber (see Fig. 13.23). However, despite their high bio mass no significant IO was observed on March 15th and also the few ppt of IO observed for the sample on 3/22 (Fig. 13.23), which was still very low compared to all other (fresh) seaweeds especially considering their fresh weight, were most likely only a chamber contamination from a previous measurement.

***Hormosira banksii*:** A sample of three specimens with a 300 g total fresh weight was investigated on March 30th. A picture of one of the three specimens and the IO time series are shown in Figure 13.27. After insertion into the chamber IO levels rose within 15 min from below the 2.2 ppt detection limit to the peak value of  $(125 \pm 1)$  ppt and after further 7 minutes stabilized at a mixing ratio of about 48 ppt which was sustained for more than three hours until the experiment ended.

***Marginariella urvilliana***: One complete specimen of 400 g fresh weight was investigated on March 28th. A picture of the sample and the IO time series are shown in Figure 13.26. Immediately after inserting the sample IO peaked at  $(616 \pm 4)$  ppt for about 20 s and after that was observed relatively constantly with an average mixing ratio of 190 ppt (stdev 40 ppt) for almost three hours until the sample was removed from the chamber. After removing the sample IO was still observed constantly at an average mixing ratio of 110 ppt for another 5 min until the Teflon film covering the bottom part of the chamber was removed. After that the side walls and top cover still sealed the chamber towards the bottom and significant IO was still observed at an average average mixing ratio of 32 ppt and only dropped to below the detection limit (4 ppt) when the rest of the chamber was removed. After removing the sample the only plausible source for the observed IO, or its precursors, was a liquid layer that accumulated during the experiment on the Teflon film, particularly on the bottom part of the chamber. This is supported by the fact that no IO was observed in the empty chamber after the Teflon film was cleaned and dried.

In a subsequently experiment on March 31st a specimen was divided into blades and stipe with receptacles, each about 300 g in fresh weight, and both parts were investigated in the chamber separately. Pictures of the two parts and the corresponding time series are shown in Fig. 13.28. For both part of the plant high IO mixing ratios with similar peak values of  $(286 \pm 2)$  ppt for the blades and  $(223 \pm 2)$  ppt for the stipe with receptacles. A comparison of the of the temporal mission profile is not sensible since both parts were measured subsequently and thus the stipe with receptacles was exposed more than one hour long to air before it was put in the chamber while the blades were relatively fresh at the beginning of the measurement.

***Rhodophyllis membranacea***: A single specimen of only 50 g fresh weight was investigated on March 15th. A picture of the sample and the IO time series are shown in Fig. 13.21. After the sample was insert in the chamber IO levels rose within 8 min from blow 2 ppt to more than 100ppt and sustained around that level for 30 min with peaks up to  $(120 \pm 1)$  ppt. Over the following 20 min IO levels declined to about 50ppt. In summary for at least 50 min this specimen showed remarkably high IO mixing ratios of up 120 ppt to considering its very low fresh weight of 50 g. After that the IO the measurement was disturbed by a stronger and more variable wind speed which, caused stronger but also more variable introduction of fresh ambient air into the chamber.

A second sample of 8 specimen with a total fresh weight of 400 g was incubated for two days from March 26th to 27th. The sample and the IO time series are shown in Fig. 13.25. After inserting the sample into the chamber, IO levels rose for about 30min from below 3 ppt to an average level of 230 ppt which was sustained for about one hour with peaks up to  $(307 \pm 2)$  ppt. After that IO levels constantly declined down to about 30 ppt after 3.5h and with the sun set about 18:00h NZST IO completely vanished. The sample stayed in the chamber over night and on the next day IO reappeared after sunrise but the major increase from below 10 ppt to about 45 ppt happened about one hour later. Over the rest of the day IO levels remained relatively constant with an average value of 39 ppt (std. dev. 8 ppt). Again, after 18:00h NZST with the setting sun IO vanished

within 20 min.

### 13.6.2. Estimated IO Emission Rates

Using the air flow  $Q = Q_{\text{mirror purge}} + Q_{\text{wind}}$  into the chamber and the fresh weight  $m_{\text{fresh}}$  of the samples IO emission rates were estimated from the observed IO mixing ratios.

$$F_{m,IO} = \frac{X(IO) \cdot Q}{V_{\text{molar}} \cdot m_{\text{fresh}}} \quad (13.2)$$

where  $V_{\text{molar}} = \frac{RT}{p} = 24.0 \text{ mol L}^{-1}$  is the molar volume of air (ideal gas) for  $p = 1013 \text{ mBar}$  and  $T = 20 \text{ }^\circ\text{C}$ . The uncertainty of this estimate is however relatively high because of the uncertainty introduced by the estimate of air flow and seaweed weight is already a factor six. Furthermore, the estimated emission rates assume no or negligible chemical losses of IO on the time scale of the residence time of the air in the chamber, which was estimated from  $Q$  to be 30min to 2min for wind speeds between  $0 \text{ m s}^{-1}$  and  $6 \text{ m s}^{-1}$ . The results should therefore be understood as semi-quantitative.

The incubation experiments are summarized in Tab. 13.2 by seaweed species, which are listed in approximate order of descending emission rates: *R. membranacea* > *M. urvilliana* > *H. banksii* > *M. pyrifera* >> *D. antarctica*. The incubation studies show that the various seaweed

seaweed species	comment	day	fresh weight (g)	IO mixing ratio (ppt)		IO emission rate pmol/min/gFw		relative emission strength
				average	peak	average	peak	
<i>R. membranacea</i>		3/15	50	57	120 ± 1	<b>0.6</b>	<b>1.6</b>	strong ↓ weak
<i>R. membranacea</i>	(8 algae)	3/26	400	194	307 ± 2	<b>0.43</b>	<b>0.74</b>	
<i>R. membranacea</i>	2nd day in chamber	3/27	400	39	70 ± 1	0.06	0.13	
<i>M. urvilliana</i>		3/28	400	183.9	616 ± 4	<b>0.26</b>	<b>0.6</b>	
<i>M. urvilliana</i>	(only blades)	3/31	300	177	286 ± 2	0.23	0.45	
<i>M. urvilliana</i>	(stipe & receptacles)	3/31	300	83	223 ± 1	0.1	0.36	
<i>H. banksii</i>	(3 algae)	3/30	300	52	125 ± 1	<b>0.1</b>	<b>0.24</b>	
<i>M. pyrifera</i>		3/16	4000	72	169 ± 2	<b>0.04</b>	<b>0.08</b>	
<i>M. pyrifera</i>	(partly decayed)	3/22	2000	8	51 ± 1	$2 \cdot 10^{-3}$	0.015	
<i>M. pyrifera</i>	(partly decayed)	3/23	2000	4	17 ± 2	$1.2 \cdot 10^{-3}$	$4.5 \cdot 10^{-3}$	
<i>M. pyrifera</i>	(partly decayed) high NO <sub>2</sub> > 2 ppb	3/25	2000	5	20 ± 1	$9 \cdot 10^{-4}$	$6.5 \cdot 10^{-3}$	
<i>D. antarctica</i>	(stipe & one blade)	3/15	5000		< 2.7	<b>&lt; 3 · 10<sup>-4</sup></b>		
<i>D. antarctica</i>	(one blade)	3/22	5000	(2.6)*	(6 ± 1)*	(3 · 10 <sup>-4</sup> )*	(7 · 10 <sup>-4</sup> )*	

**Table 13.2.** | IO mixing ratios measured during chamber incubation experiments of different seaweed species. The entries are grouped by seaweed species and are listed in approximate order of descending emission rates. Since no scale was available, sample weights were estimated, and are supposed to be correct only within a factor 2. For longer incubation experiments average mixing ratios are given for the first two hours. The given IO emission rates have a factor 6 uncertainty and should only be used in a qualitative manner rather than quantitatively. \* *D. antarctica* measurements on March 22nd are most likely corrupted by a chamber contamination.

species have significantly different emission rates, covering three orders of magnitude. The red seaweed *R. membranacea* emitted strongest with an average (secondary) IO emission of about 0.5 pmol (I)/ min /gFw. The weakest emitter was *D. antarctica* with no significant emission above  $3 \cdot 10^{-4}$  pmol (I)/ min /gFw.

Compared to northern hemisphere species, the observed IO emission rates for *R. membranacea* are of the same order as the I<sub>2</sub> emission rates for *F. vesiculosus* of 0.62 pmol (I)/ min /gFw but much lower compared to the strongly emitting *L. digitata* with average emission rates of more than 5.2 pmol (I)/ min /gFw (see [Kundel et al., 2012] and sec. 3.1.2). Since *R. membranacea* was the strongest emitter in our experiments, this seems to indicate a relatively low emission potential of southern hemispheric seaweed species. However, in a recent laboratory incubation study by Ashu-Ayem et al. [2012] the observed primary I<sub>2</sub> emission from *L. digitata* were two orders of magnitude higher than to the observed (secondary) IO levels. In their study *L. digitata* were incubated in a Teflon bag chamber enclosing a two channel CE-DOAS instrument for measurements of IO and I<sub>2</sub>. They simultaneously observed peak IO levels of about 150 ppt and I<sub>2</sub> levels of more than 20 000 ppt, in the presence of sufficient O<sub>3</sub> levels of 50 ppb and simulated solar irradiance. This indicates, that also for our chamber measurements, the primary emission of I<sub>2</sub> is likely to be much higher than our emission rates inferred from the observed IO mixing ratios.

### 13.6.2.1. Limitations and losses of IO in the Chamber

In the following several possible IO loss mechanisms and chemical limitations of IO level in our chamber are discussed:

1. Ashu-Ayem et al. [2012] attributed the huge difference between I<sub>2</sub> and IO levels to the loss of IO by its second order self reaction, which is very fast at IO levels of more than 100 ppt, and subsequent particle formation (see sec. 2.3.3).
2. Since IO is formed from the reaction of an iodine atom with Ozone, a low O<sub>3</sub> levels or its absence would limit the observed IO levels. Low O<sub>3</sub> levels were observed during experiments with *R. membranacea* (March 26th) and *M. urvilliana* (March 28th and 31st). During these experiments at times with high IO levels above 200 ppt, O<sub>3</sub> levels observed by the TEI O<sub>3</sub> monitor dropped below 2 ppb, which was most probably already below the detection limit (due to the instrumental limitation described in sec. 8.2). Therefore, during some experiments the observed IO levels may be limited by the lack of O<sub>3</sub>.
3. Due to local pollution, NO<sub>2</sub> levels were in the ppb range during several incubation experiments. At these NO<sub>2</sub> levels the loss of I atoms to IONO<sub>2</sub> by the reaction with NO<sub>2</sub> becomes competitive to the IO formation by the reaction with O<sub>3</sub> even at ambient O<sub>3</sub> levels above 10 ppb. The reason is the five times higher reaction rate constant for the reaction of I with NO<sub>2</sub> compared to the reaction with O<sub>3</sub>. Additionally, NO<sub>2</sub> levels in the order of 1 ppb cause a short IO lifetime against loss to IONO<sub>2</sub> of about 10 s. However, the effectiveness of this loss strongly depends on the poorly understood fate of IONO<sub>2</sub> as described in sec. 2.3.2.

4. Even though a Teflon is considered an inert material, our closed path CE-DOAS measurements in the Ireland campaign of this study (see sec. sec:discussClosedPathCEDOAS) showed that IO measurements in a closed Teflon cell can be critically influenced by wall and photochemical losses.

Indications for limitations of IO, by a lack of Ozone were given additionally by three chamber experiments on April 1st and 2nd where the top cover was removed. As shown in Fig. 13.29 and Fig. 13.30, during these experiments, the chamber was turned upside down so that the top was open and only the bottom part and the side walls remained. For *M. urvilliana* the IO per gram fresh weight, observed over the first 30 min of the experiment, was about the same compared to the closed chamber measurements on March 28th. And for a sample of *M. pyrifera* the IO per gram fresh weight, observed over the first 30 min of the experiment, was even a factor two higher. This was surprising since much lower IO levels were expected for the case of a removed top-cover due to much higher dilution with ambient air. Therefore this indicates, that for these two experiments with the removed top cover the IO formation was less limited or the losses were lower, compared to the closed chamber. On the other hand for the open top cover on April 2nd with a sample of *H. banksii* the IO per gram fresh weight was four times lower compared to the closed chamber experiment on March 30th. Thus this indicates that for the weaker emitting *H. banksii*, IO in the closed chamber was less limited, which is consistent the observation that the O<sub>3</sub> levels stayed constant in the closed chamber experiment on March 30th.

In summary, it is expected that the IO levels observed in the closed chamber were generally limited by the high NO<sub>2</sub> levels in the ppb range. Additionally for high IO of several 10 ppt IO depletion due to the IO self reaction and subsequent particle formation was most probably the case. For very high IO levels of more than 100 ppt the IO mixing ratios it is also likely that the IO levels were limited to the (almost) complete depletion of Ozone in the chamber. In consequence, this could cause a significant underestimation of the derived IO emission rates. For the determination of IO emission rates the high uncertainty of the air flow into the chamber was problematic as well as the uncertainty in the fresh weight of the seaweed samples. Therefore, for future campaigns an improved chamber setup with controlled air flow as shown in Fig. 13.18 is recommended. Also additionally to IO the CE-DOAS should be extended to measure I<sub>2</sub> since this is the primary emission of seaweeds and additionally less reactive compared to IO thus would avoid the uncertainties in the determined emission rates due to chemical reactions.

### 13.6.3. Iodocarbons as Possible IO Sources

During the incubation experiments the  $\mu$ -Dirac GC was applied to the chamber for measurements of several halocarbons (see sec. 8.2.2). Average and maximum mixing ratios for the different incubation experiments are summarized Fig. 13.19 and the corresponding time series can be found in the appendix in Fig. D.1. However, due to their long atmospheric lifetime of several days to weeks (see Tab. 3.4) most species are irrelevant as sources of reactive halogen species (RHS) in the incubation experiments even though most of them, including CH<sub>3</sub>I, were observed at high mixing ratios of several 100 ppt. Also in the atmosphere these species can only contribute to the RHS background level but cannot to explain the observed highly elevated

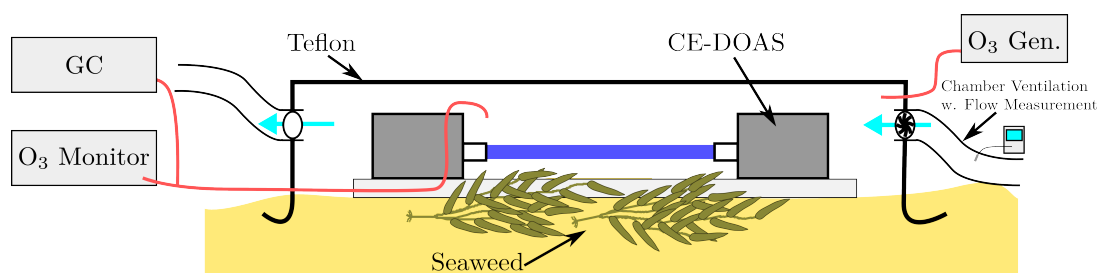


**Figure 13.18.** | Sketch of an improved chamber setup recommended for future chamber experiments. The most important improvements would be a controlled ventilation of the chamber and the possibility to enrich the air with Ozone by a  $O_3$  generator. Furthermore the CE-DOAS should be extended to allow measurements of  $I_2$  which is most likely the species directly emitted by the seaweeds.

levels of IO at coastal sites.  $CH_2IBr$  and  $CH_2ICl$  with photolytic lifetimes of 1 h and several hours respectively are the only observed halocarbons which are short lived enough to act as potential IO sources in the incubation experiments. However,  $CH_2CII$  was not observed at mixing ratios above 8 ppt and is therefore irrelevant as source of IO.  $CH_2IBr$  was observed at mixing ratios of several 10 ppt during three incubation experiments which are discussed in the following:

***Rhodophyllis membranacea* on March 26th:** The average  $CH_2IBr$  mixing ratios over the entire incubation period was 26.46 ppt. However in the first two hours when the average IO mixing ratios was 194 ppt the observed  $CH_2CII$  mixing ratios was only 5 ppt, which rules it out as a significant IO source.

***Rhodophyllis membranacea* on March 27th** was the second day of incubation for the sample from March 26th which was already partly decayed. On this day the daily average  $CH_2IBr$  of 53 ppt was higher compared to the average IO level of 39 ppt which were both relatively constant over the entire day. The typical air exchange time in the chamber was about 8 min on that day. Thus, neglecting other IO losses  $CH_2IBr$  could account for about 20 % of the observed IO.

***M. urvilliana* on March 28th:** Only one data point was of  $(130 \pm 70)$  ppt  $CH_2IBr$  was measured for the first 30 min of the incubation. In this period the average IO mixing ratio of 200 ppt was however significantly higher. Therefore with the air exchange time of 12 s on that day,  $CH_2IBr$  could only account for about 10 % of the observed IO, neglecting other IO losses. Also, the IO peak level of  $(616 \pm 4)$  ppt was reached immediately ( $\sim 30$  s) after placing the sample in the chamber, which could not be explained with a slowly photolyzing precursor like  $CH_2IBr$ . Thus  $CH_2IBr$  played at most a minor role as source of IO also on that day.

In summary, none of the observed iodocarbons could act as a major source of the IO levels observed in the chamber experiments. The only possible contribution from halocarbons remains

$\text{CH}_2\text{I}_2$ , which has a typical photolytic lifetime of 4 min. Unfortunately this species cannot be measured by the  $\mu$ -Dirac GC. However, the most likely source of the observed IO is molecular  $\text{I}_2$  with a typical photolytic lifetime of about 10 s, especially since the rapid appearance of IO after inserting the samples into the chamber (peak concentrations often within 30 s) requires a quick photolysis of the precursor.

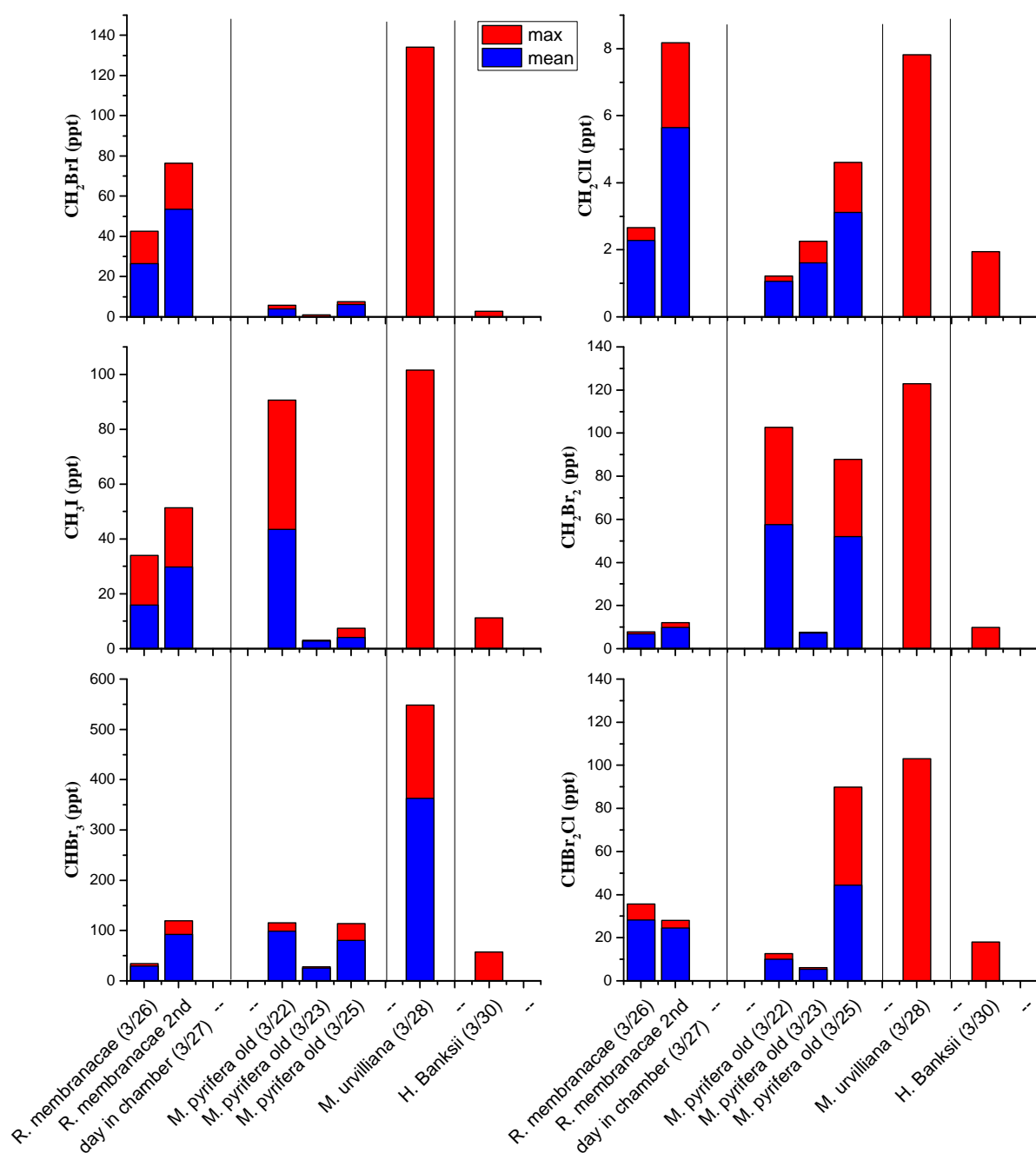


**Figure 13.19.** | Halocarbon mixing ratios observed for (closed) chamber incubation experiments with of different seaweed species. Average values are given for the entire incubation period, due to the low time resolution of the  $\mu$ -Dirac GC. The corresponding time series can be found in the appendix in Fig. D.1



CE-DOAS & chamber over drift seaweed patch with *M. pyrifera*, *D. antarctica* and red seaweed

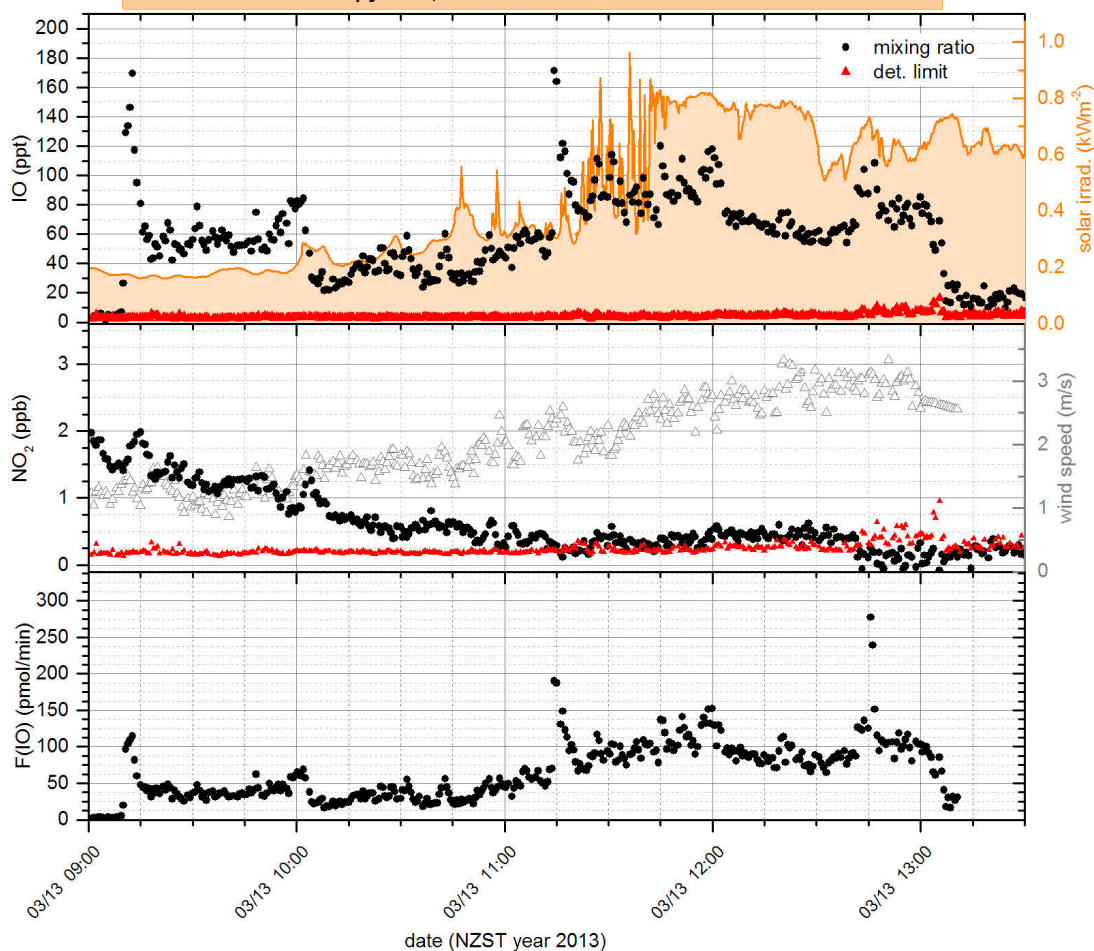


**Figure 13.20.** | Incubation experiment over a patch of mixed drift seaweed at Shag Point Beach on March 13th. Shown are the IO and NO<sub>2</sub> mixing ratios in the chamber measured by the CE-DOAS. The orange bar on top indicates the duration of the experiment. The bottom graph shows the derived IO emission rates which have at least a factor 6 uncertainty. Further shown are the the local wind speed next to the chamber measured by the mobile Metek USA 1 sonic anemometer and the solar irradiance at Shag Point Cottage (see sec. 8.2).

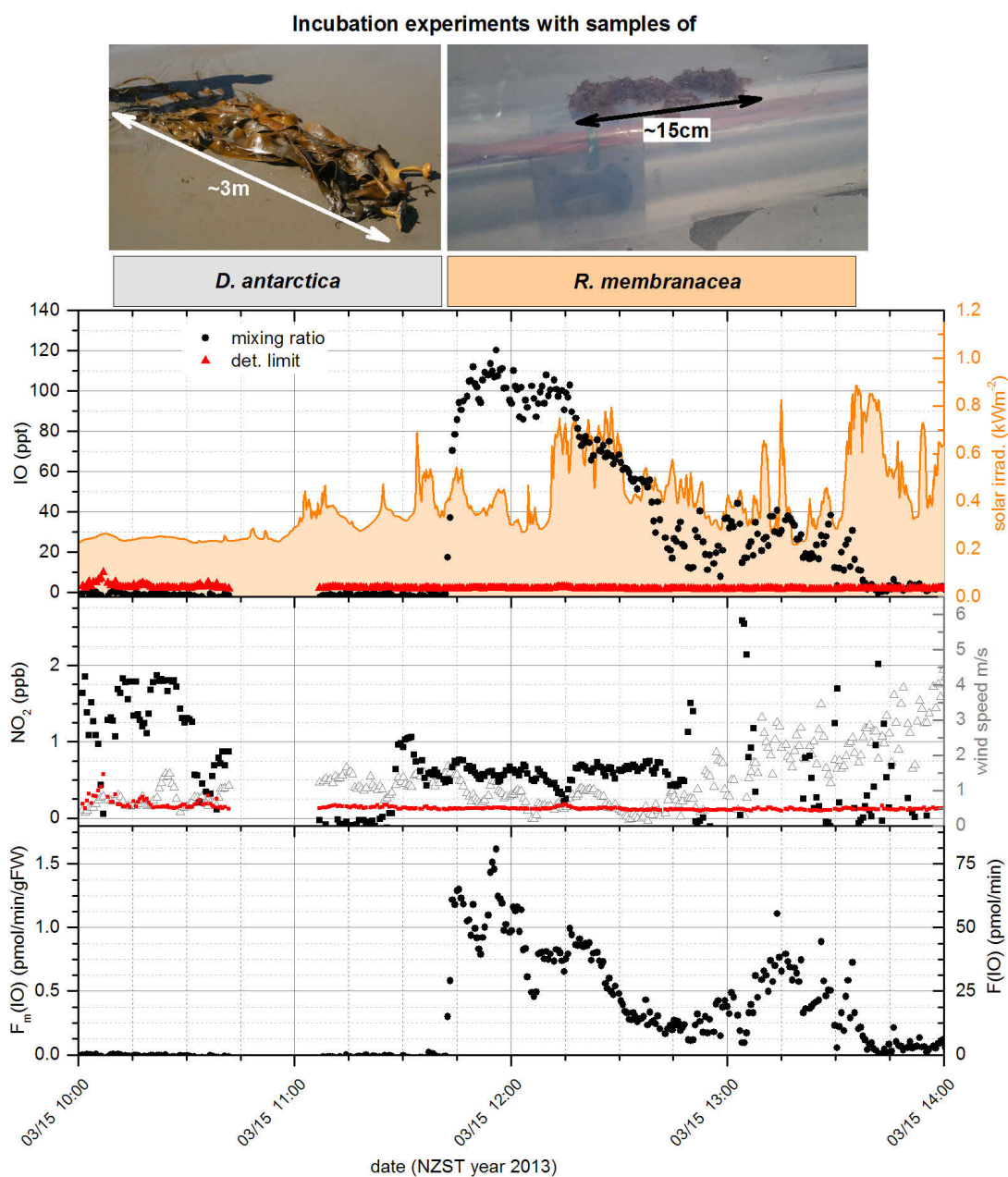


**Figure 13.21.** | Incubation experiment with samples of *D. antarctica* and *R. membranacea* on March 15th. Shown are the IO and  $\text{NO}_2$  mixing ratios in the chamber. Samples of *D. antarctica* (stipe and one blade, 5 kgFw) and *R. membranacea* (50 gFw) were measured successively as indicated by the gray and orange bar on top. The bottom graph shows the derived IO emission rates which have at least a factor 6 uncertainty. Solar irradiance and wind speed given as in Fig. 13.20.

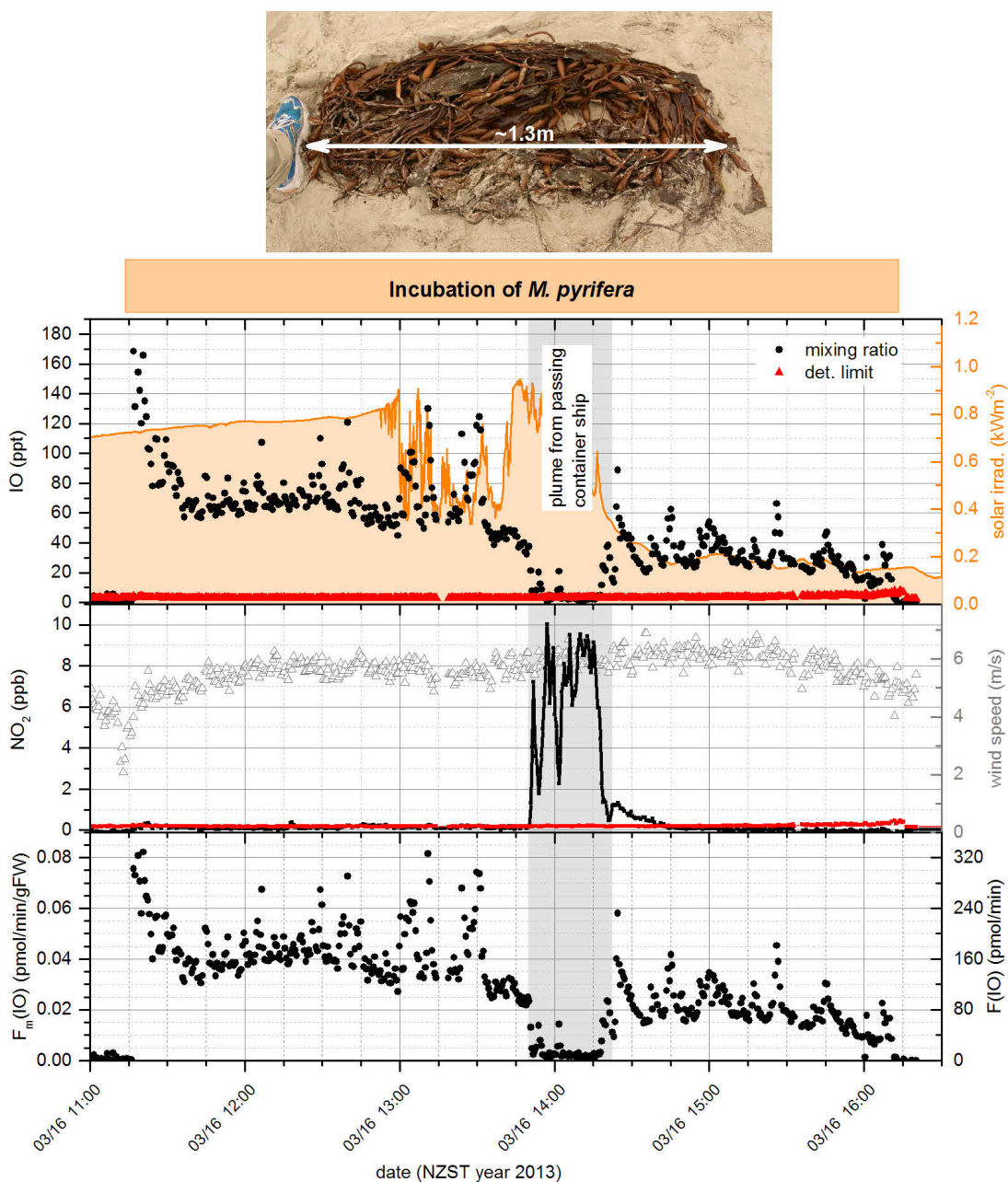


**Figure 13.22.** | Incubation experiment with a sample of *M. pyrifera* on March 16th. Shown are the IO and NO<sub>2</sub> mixing ratios in the chamber. The orange bar on top indicates the period when the *M. pyrifera* sample (4 kgFw) was incubated. The gray area makes the time when a ship plume with high NO<sub>2</sub> passed through the chamber. The bottom graph shows the derived IO emission rates which have at least a factor 6 uncertainty. Solar irradiance and wind speed given as in Fig. 13.20.

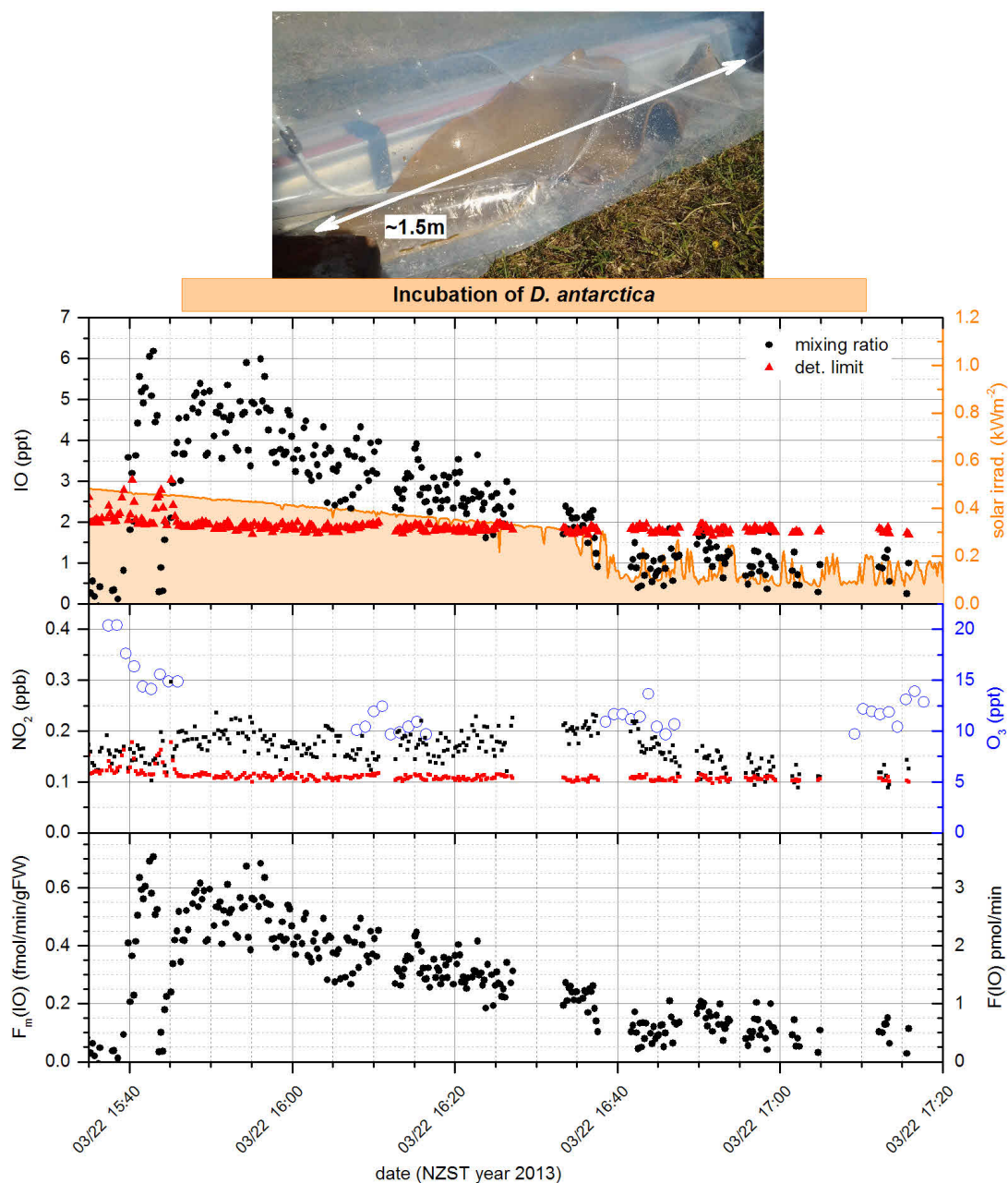


**Figure 13.23.** | Incubation experiment with a sample of *D. antarctica* on March 22nd.

The orange bar on top indicates the period when the *D. antarctica* sample (5 kgFw) was incubated. The top and middle graph show the IO and NO<sub>2</sub> mixing ratios in the chamber (black) measured by the CE-DOAS and their respective detection limits (red). The blue circles in the middle graph show the O<sub>3</sub> mixing ratios in the chamber measured by the TSI monitor (see sec. 8.2). Solar irradiance given as in Fig. 13.20. The bottom graph shows the derived IO emission rates which have at least a factor 6 uncertainty.

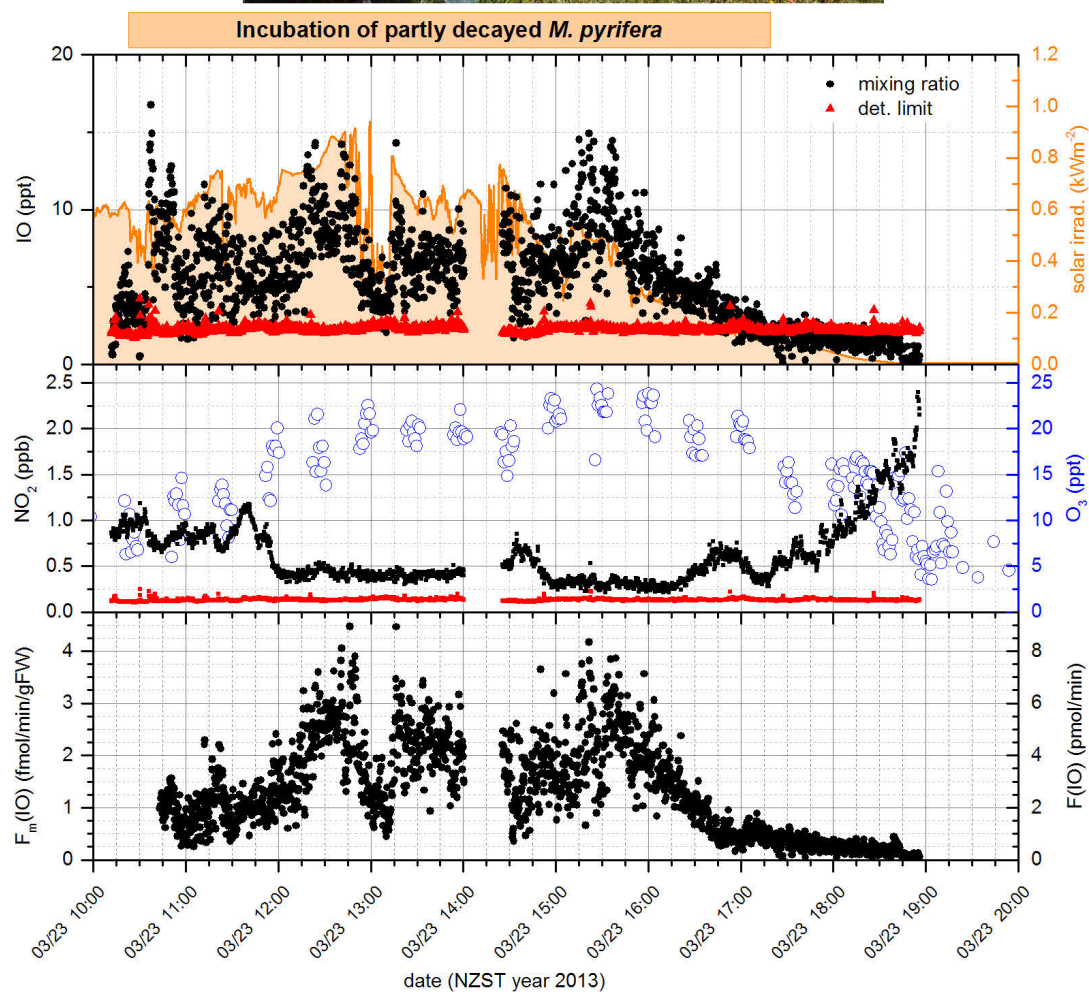


**Figure 13.24.** | Incubation experiment with a sample of a partly decayed *M. pyrifer* on **March 23rd**. The orange bar on top indicates the period when the *M. pyrifer* sample (2 kgFw) was incubated. IO, NO<sub>2</sub> and O<sub>3</sub> mixing ratios in the chamber and the solar irradiance are given as in Fig. 13.23. The bottom graph shows the derived IO emission rates which have at least a factor 6 uncertainty.

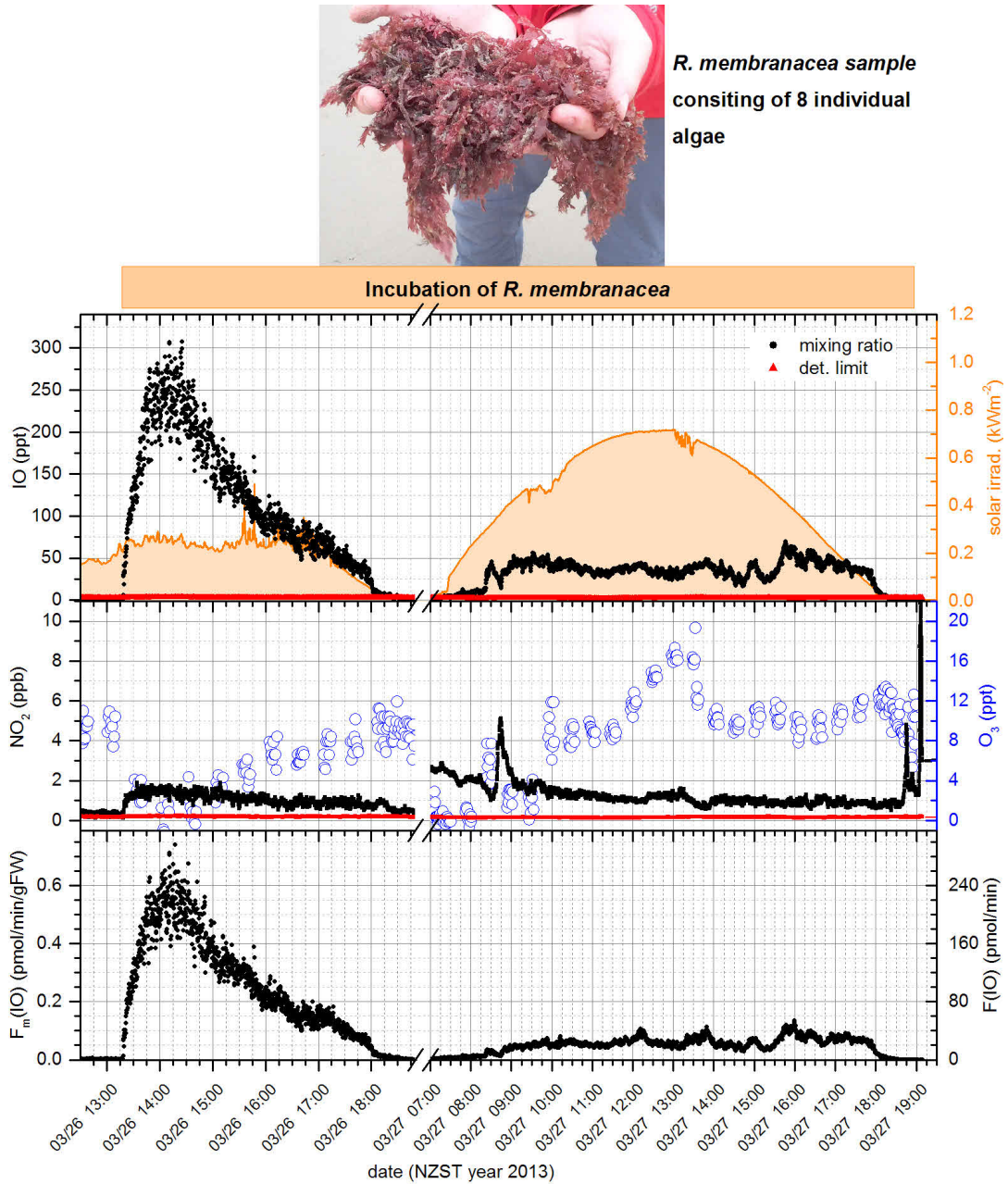


**Figure 13.25.** | Incubation experiment with a sample of a *R. membranacea* on March 26th & 27th. The orange bar on top indicates the period when the *R. membranacea* sample (8 specimen, 400 gFw) was incubated. The bottom graph shows the derived IO emission rates which have at least a factor 6 uncertainty. IO, NO<sub>2</sub> and O<sub>3</sub> mixing ratios in the chamber and the solar irradiance are given as in Fig. 13.23.

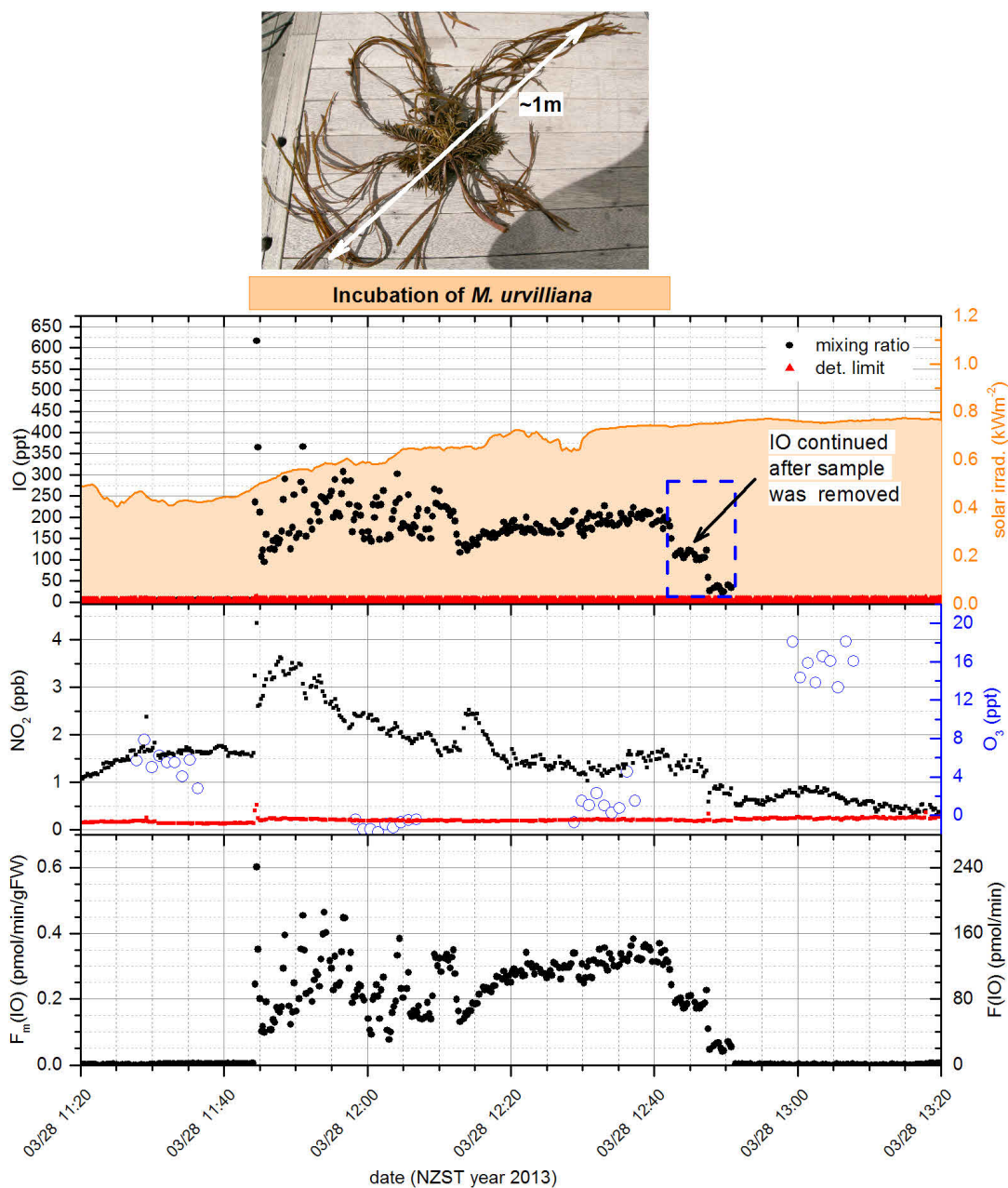


**Figure 13.26.** | Incubation experiment with a sample of a *M. urvilliana* on March 28th. The orange bar on top indicates the period when the *M. urvilliana* sample (400 gFw) was incubated. IO, NO<sub>2</sub> and O<sub>3</sub> mixing ratios in the chamber and the solar irradiance are given as in Fig. 13.23. The bottom graph shows the derived IO emission rates which have at least a factor 6 uncertainty.

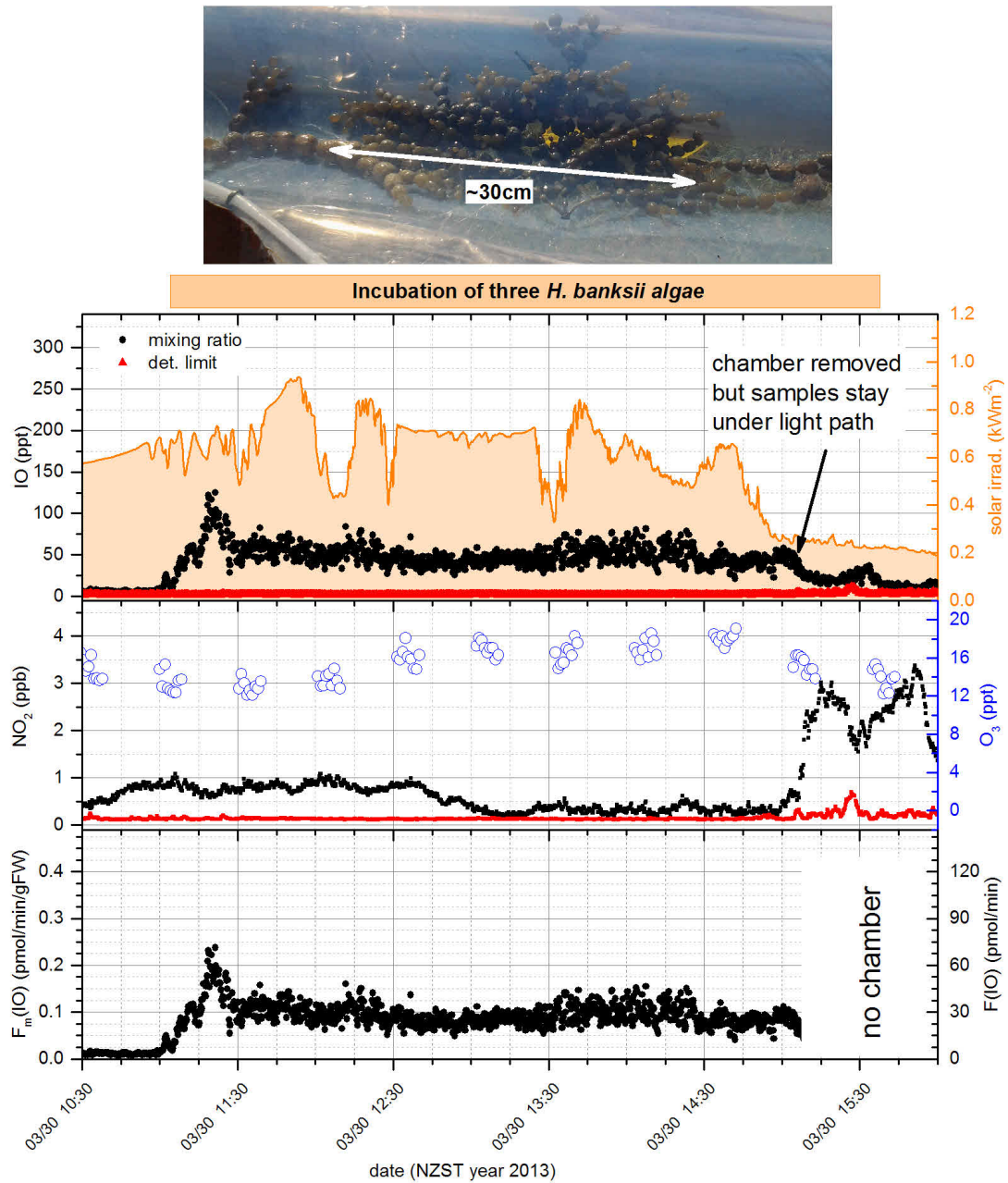


**Figure 13.27.** | Incubation experiment with a sample of a *H. banksii* on March 30th. The orange bar on top indicates the period when the *M. urvilliana* sample (400 gFW) was incubated. IO, NO<sub>2</sub> and O<sub>3</sub> mixing ratios in the chamber and the solar irradiance are given as in Fig. 13.23. The bottom graph shows the derived IO emission rates which have at least a factor 6 uncertainty.

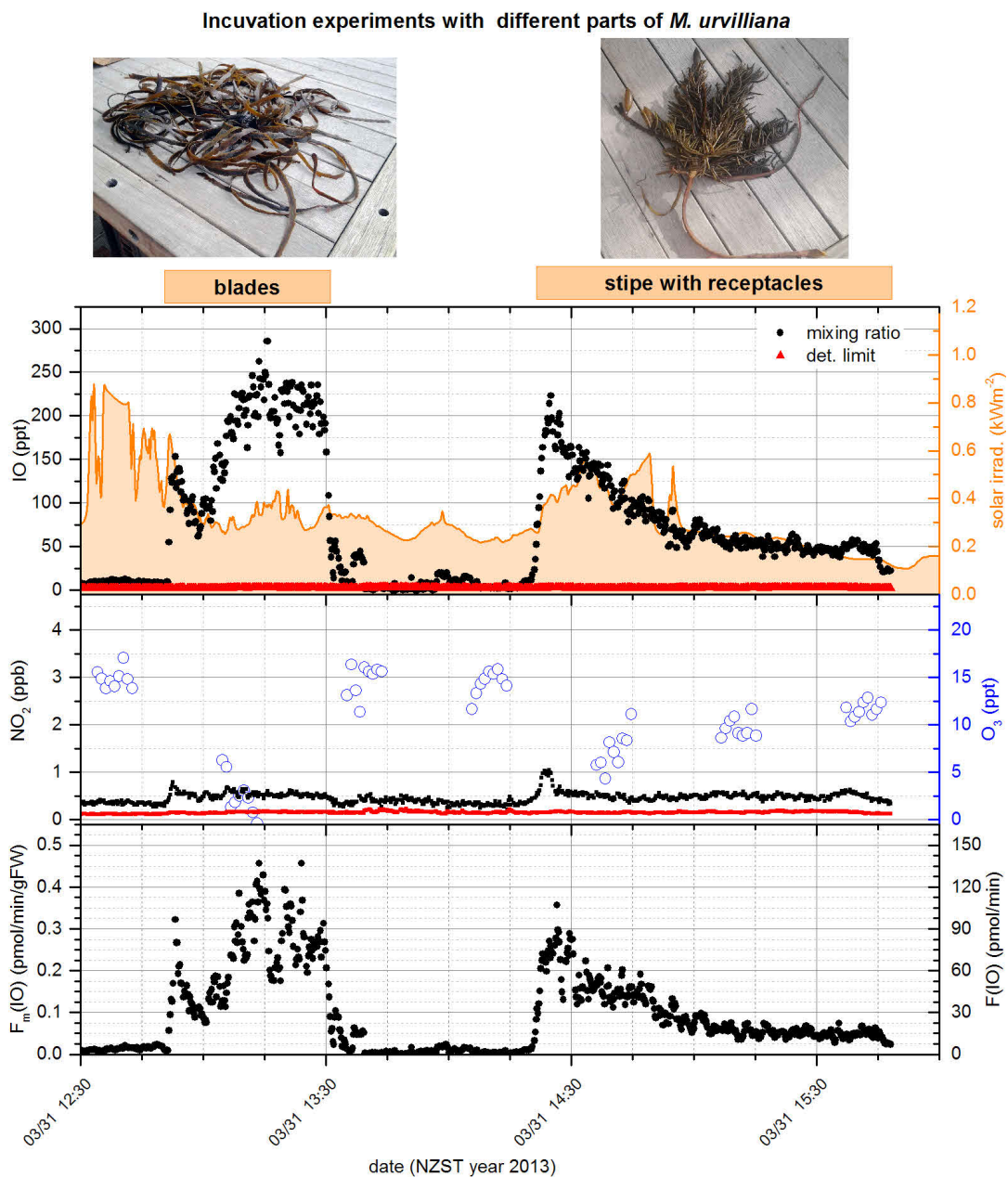


**Figure 13.28.** | Incubation experiment with a samples of a *M. urvilliana* on March 31st.

As indicated in the top pictures a specimen was subdivided into blades and stipe with receptacles. Both parts (each 300 gFw) were incubated separately as indicated by the orange bar. IO, NO<sub>2</sub> and O<sub>3</sub> mixing ratios in the chamber and the solar irradiance are given as in Fig. 13.23. The bottom graph shows the derived IO emission rates which have at least a factor 6 uncertainty.

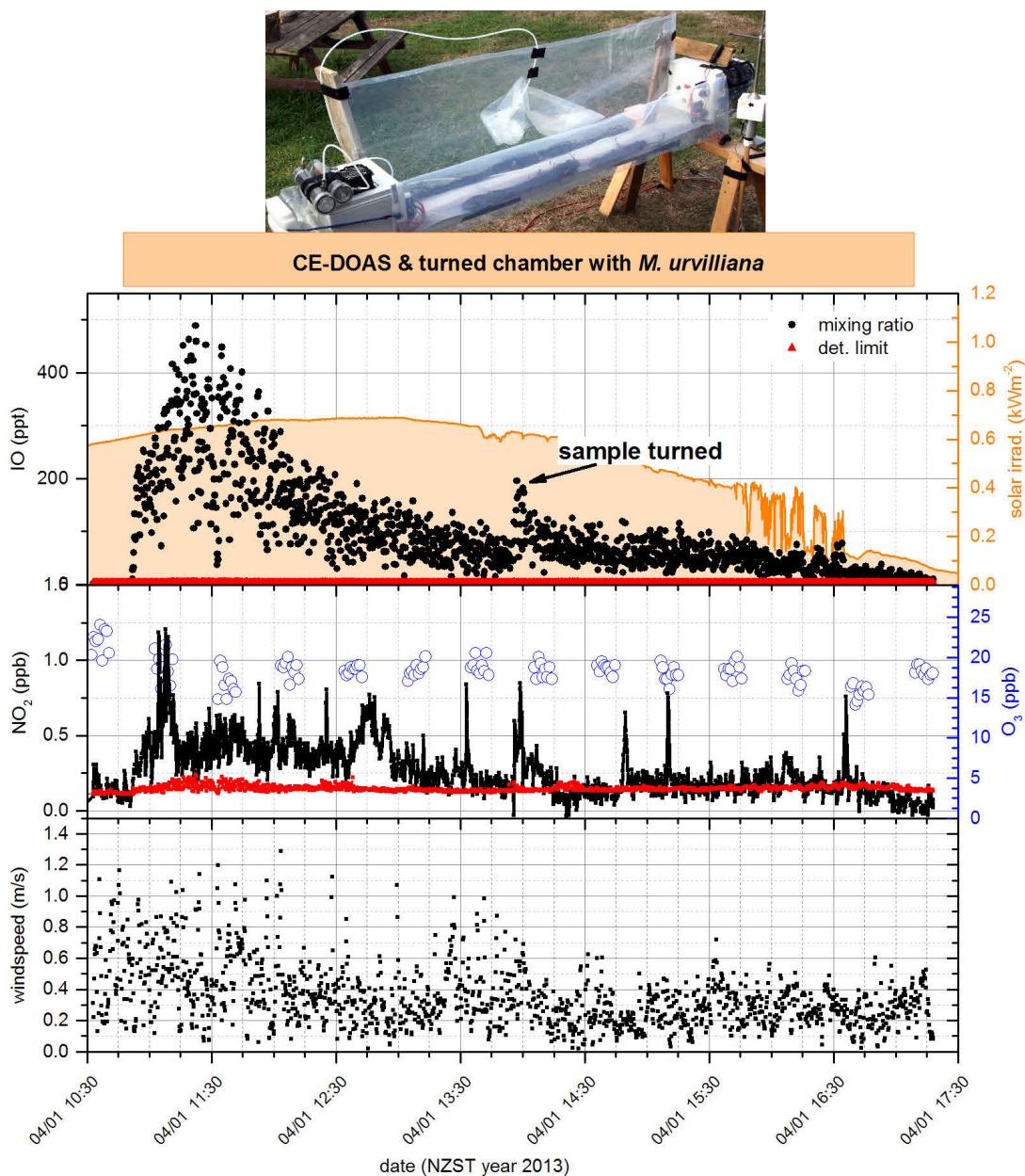


**Figure 13.29.** | CE-DOAS with turned chamber and sample of *M. urvilliana* on April 1st. As shown on the top picture the top of the chamber was open to enhance air exchange. The orange bar on top indicates the period when the *M. urvilliana* sample (two specimens, 1 kgFw) was measured. IO, NO<sub>2</sub> and O<sub>3</sub> mixing ratios in the chamber and the solar irradiance are given as in Fig. 13.23. The bottom graph gives the local wind speed measured directly above the chamber by the Metek sonic anemometer.

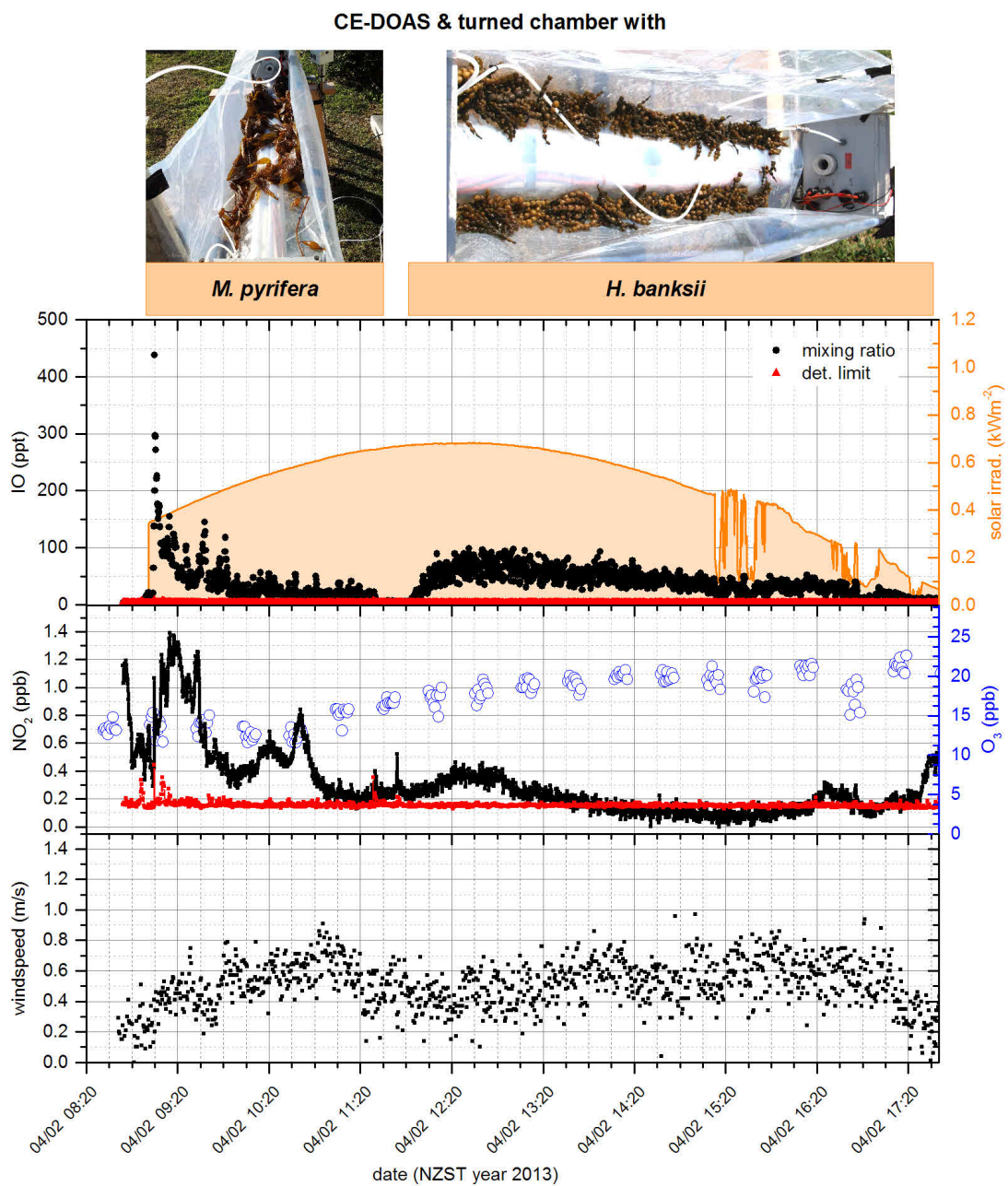


**Figure 13.30.** | CE-DOAS with turned chamber and samples of *M. pyrifera* and *H. banksii* on April 2ndst. As shown on the top picture the top of the chamber was open to enhance air exchange. The sample of *M. pyrifera* (2 kgFw) and *H. banksii* (12 specimen, 1.2 kgFw) were measured individually as indicated by the orange bars on top. IO, NO<sub>2</sub> and O<sub>3</sub> mixing ratios in the chamber and the solar irradiance are given as in Fig. 13.23. The bottom graph gives the local wind speed measured directly above the chamber by the Metek sonic anemometer.

# **Part V.**

## **Conclusions & Outlook**



# 14

## Conclusions and Outlook

### 14.1. Conclusions

In the frame of this work extensive studies were conducted to improve the knowledge on the coastal emissions of reactive iodine species from seaweeds and their distribution. In order to achieve this goal, the DOAS methodology was further developed, particularly Cavity Enhanced (CE-) DOAS, and successfully applied in two extensive field studies on the Irish West Coast and one exploitative in New Zealand.

### DOAS Instrumentation and Data Analysis

The most important improvements in terms of DOAS Instrumentation and Data Analysis were:

- The first mobile Open Path CE-DOAS Instrument was developed, and optimized for measurements of IO in the field with a typical detection limit of 1 – 2 ppt (chap. 5). All components were integrated in a waterproof, light weight ( $\sim 30$  kg) and transportable ( $\sim 2.3 \times 0.2 \times 0.4$  m<sup>3</sup>) setup, which allows easy handling by two persons even in difficult terrain. Furthermore, due to its low power consumption ( $\sim 40$  W) and 12 V supply voltage this new instrument can be battery operated, which allows its application in remote areas where no power supply is available. This instrument for the first time allowed to measure IO directly at the sources in the inter tidal area. Furthermore, the direct optical measurement of IO, using an open measurement cell towards the atmosphere, avoids problems with chemical interferences and losses, e.g. on walls and sampling lines, inherent to other measurement techniques.

A further major technical advancement was the integration of a novel system for a simpler and more accurate wavelength depended calibration of the absorption light path during field measurements (sec. 5.4). This new system co-developed in this work and Zielcke [2015], uses a tiltable interference filter to measure wavelength resolved Cavity Ringdown curves and thus the length of the absorption light path at different wavelengths. A comparison with the established calibration using different Rayleigh scatterers (air vs

helium) shows an excellent agreement within the errors. This novel method has several advantages: Firstly, it can be applied reliably in the field while the calibration with Rayleigh scatterers is limited to laboratory application. Thus enabling more accurate determination of the absorption light path during field campaigns. Secondly, this method does not require consumable gases which are classified as dangerous goods and therefore problematic during field campaigns in remote areas.

- Additionally to the Open Path CE-DOAS, an even lighter (5 kg) and more compact ( $\sim 0.72 \times 0.18 \times 0.28$  m<sup>3</sup>) Closed Path CE-DOAS instrument for measurements of IO, NO<sub>2</sub> and (CHO)<sub>2</sub> was developed. The use of an closed sampling cell, and filtering of aerosols from the sampled air allowed to achieve an IO detection limit of 2 ppt with an four times shorter resonator compared to the open path instrument, and furthermore has the advantage that the resonator mirrors are protected from contamination. The use of a new iterative CE-DOAS evaluation scheme, developed in this thesis (chap.9), allowed to further simplify the setup (no temperature stabilized light source) and made it more robust for field applications.

However, a comparison of Open Path CE-DOAS and Closed Path CE-DOAS IO measurements showed that more than 90 % of the ambient IO is lost in the sampling system and the closed measuring cell and the loss is highly variable (sec. 12.5). Thus, the Closed Path CE-DOAS is not applicable for IO measurement. This further shows that the use of a Teflon based sampling system and measurement cell, which is considered as an inert material, does not allow the measurement of a highly reactive gas like IO. Therefore, also other IO measurements with instruments using a similar IO sampling, particularly Grilli et al. [2012b], are considered to give wrong data which strongly underestimates the true atmospheric IO concentration.

The Closed Path CE-DOAS has however, proven as a very sensitive and reliable instrument for NO<sub>2</sub> measurements and has been successfully applied for measurements under clean background conditions [e.g. Herlyn, 2015] and for mobile measurements in polluted urban environments [e.g. Kanatschnig, 2014].

- Open path CE-DOAS measurements of high IO mixing ratios (several 100 ppt) revealed differences in the relative band strength of the observed IO absorption in comparison to the literature cross section of Gómez Martín et al. [2005], commonly used for DOAS retrievals of IO (chap 11). The observed deviation was particularly strong for the absorption between 443.5 nm and 451.2 nm (IO(2 ← 0) band) which was observed to be about 1.5 times stronger than expected. Field measurements were subsequently used to derive correction factors for the relative strengths of the absorption bands and to build a corrected high resolution IO reference spectrum. Using the corrected IO in DOAS evaluations reduced the retrieved IO mixing ratios by 5 %, but more important it reduced the systematic residual structures of the IO fit by a factor of 5 and therefore significantly improved the simultaneous measurement of NO<sub>2</sub> in the presence of high IO mixing ratios.

## Irish West Coast

In this study measurement of the reactive iodine species IO were performed at 10 locations along the Irish west coast using combined path averaging LP-DOAS measurements across inter-tidal areas and CE-DOAS point measurements directly over, or next to, the intertidal seaweed (chap 12).

Particularly high IO mixing ratios were observed by the open path CE-DOAS when measuring in the inter-tidal zone of wave sheltered bays during low-tide directly exposed brown seaweeds, mainly *A. nodosum* and also *F. vesiculosus*. The unique combination with path averaging LP-DOAS measurements across the seaweed bed and beyond could identify these seaweeds as a strong source of reactive iodine (see sec. 12.8). 1.3 m above the seaweed, CE-DOAS observed very high IO mixing ratios, exceeding at each site 20 ppt for extended periods of more than an hour and at several sites peak levels even exceeded 50 ppt. Very close (several 10 cm) to the seaweed mixing ratios exceeded even 100 ppt. Therefore this study gives the first direct evidence of the “hot-spot” theory by Burkholder et al. [2004] which suggested that local patches with mixing ratios of 50 ppt to 100 ppt are required to explain particle concentrations observed during nucleation events like also observed in this study (see sec. 12.9.2.1) and previous studies [e.g. O’Dowd et al., 2002b; Seitz et al., 2010]. Vertical CE-DOAS profile measurements *A. nodosum* and also *F. vesiculosus*, showed very high (secondary) IO emission rates of about  $60 \mu\text{gI m}^{-2} \text{h}^{-1}$  at a solar irradiance of  $840 \text{ W m}^{-2}$  (see sec. 12.10). This is the first determination of iodine emission rates from seaweed under real field conditions. This study also shows that wave sheltered shores at the Irish West Coast, which feature a shallow intertidal zone with extended beds of brown seaweeds, mainly *A. nodosum* and also *F. vesiculosus*, are the strongest source of reactive iodine.

On the other side, at wave exposed shores like Mace Head, the inter tidal zone is much smaller and features a lower inter-tidal seaweed abundance mostly in the lower intertidal zone where some *L. digitata* grows. CE-DOAS measurements at Mace Head station, in this work, observed significant local IO emissions from *L. digitata* only for extremely low water levels close to spring-tide low water, which are relatively rare events only occurring on about 6 days of a 27 day tidal cycle and only for short time periods of less than an hour. Further, in this work it was found that local IO emissions from *L. digitata* played only a minor role for IO levels observed on the 3 km long Mace Head LP-DOAS light path (see sec. 12.9.2.1). The few events of high IO levels observed by the LP-DOAS could all be linked to IO emission at close by wave sheltered bays.

Additionally, this work found, that washed up drift seaweed can also be a strong local source with observed local IO mixing ratios of up to 40 ppt. It is known that large quantities of drifting seaweed are cast ashore after storm events. However, there is currently no quantitative information on the covered areas, the biomass of washed up drift and their residence time on the beach. Thus, it is currently not possible to estimate the precise contribution to the coastal iodine emissions.

Furthermore, at all sites a clear linear correlation between the observed the solar irradiance was observed which indicated increasing stress levels of seaweed under higher solar irradiance. Measurements in this study also showed no significant reduction of iodine emission when these seaweeds are covered by a thin water film (see sec. 12.9.1.5). This has two important

implications: Opposed to previous assumptions, strong emissions of reactive iodine were observed even during rainy weather conditions, which is an important finding since this is a typical weather condition on the Irish Coast. Additionally, *A. nodosum* was observed to continue emission of iodine for half an hour to an hour when its already floating on the water towards the end of the low tide period.

Measurements in this work did not observe any significant coastal nighttime IO above 2.3 ppt (CE-DOAS) and 4.0 ppt (MoLP-DOAS), even at sites where several 10 ppt of IO were present during daytime low tide (see sec. 12.7.1). However, previous nighttime observations of Saiz-Lopez et al. [2006] and Mahajan et al. [2009] would have suggested much higher nighttime IO for our measurements. This leads to the conclusion that the previous observations of nighttime IO were most likely measurement errors.

As expected during pollution events, a clear anti-correlation between  $\text{NO}_2$  and IO was observed for well mixed air masses (see sec. 12.6). No indication for the previously suggested rapid recycling of  $\text{IONO}_2$  to  $\text{I}_2$  by reaction with I R 2.37 was found.

Of particular interest was the direct comparison of IO measurements at Mace Head Research station, which was the major location of previous studies [Alicke et al., 1999; Hebestreit, 2001; Saiz-Lopez and Plane, 2004; Seitz, 2009; Commane et al., 2011], with measurements at 7 wave sheltered shores, which were mostly not investigated before. Contrary to the expectation that Mace Head is a hot-spot for iodine emissions, this study found that (at the same time) IO at the wave sheltered shores was observed more regularly and at much higher concentrations (see sec. 12.8). During daytime low tide, the MoLP-DOAS observed at these locations usually more than three times but up to more than ten times higher IO mixing ratios compared to the shore at Mace Head. These measurements show that this is due to distinctive differences in the dominant sources for reactive iodine on wave exposed shores and on wave sheltered shores.

In conclusion, this work found that the major sources at the Irish West Coast are wave sheltered shores and not as previously believed wave exposed shores. Wave sheltered shores are very common on the Irish West Coast and represent much larger intertidal areas with a much higher seaweed density, mainly *A. nodosum* and also *F. vesiculosus*, compared to wave exposed shores with a low density of *L. digitata* in the lower inertial zone. Also the seaweed in the intertidal zone of wave sheltered bays is much more regularly and much longer exposed to air compared to intertidal seaweed. The total emissions from wave sheltered shores are much larger, even if the emission per kg seaweed might be lower. Therefore, this work shows that Irish and global emissions of reactive iodine, from coastal areas, should be much higher compared to estimates based on studies at Mace Head (only using emissions of wave exposed shores).

Based on these findings and the estimated rates for seaweed beds at wave sheltered shores, determined in this work, the yearly iodine emission on the Irish coast was estimated to be  $(0.4 - 1) \cdot 10^7 \text{ g}_I \text{ a}^{-1}$  (see sec. 12.12). An attempt to extend these estimates to the world shorelines yields global emissions between  $2 \cdot 10^8 \text{ g}_I \text{ a}^{-1}$  and  $3 \cdot 10^9 \text{ g}_I \text{ a}^{-1}$ . This estimate comes however with large uncertainties, since there is too little knowledge on the global abundance, distribution and emission of intertidal seaweed. While this is relatively low compared to estimated global iodine emissions ( $10^{11} - 10^{12} \text{ g}_I \text{ a}^{-1}$ ), on the local scale these strong emissions of reactive iodine by seaweed have a significant impact due to their ability to form particles and change

the chemical properties of the atmosphere. The iodine particle formation events reported by O'Dowd et al. [2002b] and also in this study (see sec. 12.9.2.1) arise only at the high iodine levels at these coastal sites and not for locally low IO concentrations due to open ocean emissions (0.5 – 2 ppt). Thus, coastal iodine emissions could locally influence cloud micro physical properties and therefore also have an impact on the climate. Beyond atmospheric implications, there are also indications that high iodine emissions from seaweeds may cause a significant increase in human iodine intake through the respiration of gaseous iodine compounds [Smyth et al., 2011].

## New Zealand

An exploitative study was conducted on the East Coast of the New Zealand South Island using a combination of path averaging LP-DOAS measurements across a bay and Open Path CE-DOAS point measurements in the intertidal zone of two beaches (chap. 13). High IO mixing ratios above 10 ppt with peak levels up to 68 ppt were observed by the Open Path CE-DOAS on three days during daytime low tide. These are the first observations of IO emitted at a southern hemispheric coastal site, showing that also seaweeds found beyond the Northern Atlantic can act as strong sources of reactive iodine species. A comparison between the Open Path CE-DOAS point measurements and path averaging LP-DOAS measurements across the inter-tidal zone identified patches of washed up drift seaweed as the major source of the observed IO. The five major seaweed species of the drift seaweed patches, *Macrocystis pyrifera*, *Durvillaea antarctica*, *Marginariella urvilliana*, *Rhodophyllis membranacea* and *Hormosira banksii*, were identified. These seaweeds are different from the species found in the Northern Atlantic and specific for New Zealand and Australia (*M. urvilliana*, *R. membranacea* and *H. banksii*), the southern hemisphere (*D. antarctica*) the southern hemisphere plus west coast of North American (*M. pyrifera*). Since the iodine emission potential of these seaweed species was unknown, their emission was individually investigated by the CE-DOAS using an improvised incubation chamber.

The incubation experiments showed high IO levels above 100 ppt for four species, but no significant IO for *Durvillaea antarctica*. Furthermore, emission rates per gram fresh weight were estimated. The emission rates are in approximate descending order: *R. membranacea* > *M. urvilliana* > *H. banksii* > *M. pyrifera* > *D. antarctica*. The strongest IO emission rate of about 0.5 pmol (I)/ min /gFw was found for the red seaweed species *R. membranacea*. While this seems low, low compared to northern hemispheric seaweed, it has to be noticed that seaweeds actually emit molecular iodine which might be two orders of magnitude higher compared to the (secondary) IO emission rates (see sec. 13.6.2).

On a global perspective this observation showed that the distribution of seaweed at the shore of the east coast of the New Zealand south island is very different compared to Irish West Coast. It has a very steep and wave exposed shoreline with only a narrow inter-tidal area. The only abundant intertidal seaweed species is *Durvillaea antarctica* which showed not significant reactive iodine emission in the incubation chamber experiments. The iodine emitting seaweed species are either subtidal (*R. membranacea* and *M. pyrifera*), grow in the lowest part of the intertidal zone where they are rarely exposed to air (*M. urvilliana*) or occur only at small

patches in the intertidal zone (*H. banksii*). Therefore, the emission from intertidal seaweed at the east coast of the New Zealand south island is considered negligible, and the only significant emission is expected to come from patches of washed up drift seaweed. However, significant amounts of washed up drift seaweed is only expected for short periods after storm events. Therefore the east coast of the New Zealand south island is considered an area with much lower emission of reactive iodine compared to the Irish West Coast.

### 14.2. Outlook

This work showed strong variation of the reactive iodine emission between different types of shores even on the regional scale of the Irish West Coast. Therefore for better regional and global estimates, better information on the intertidal areas covered by seaweed and also the occurrence of drift seaweeds (extent and frequency) is needed e.g., from satellite or aerial observations. For better global estimations not only the intertidal areas covered by seaweed are relevant but also the locally different seaweed species. The observations in New Zealand (chap. 13) showed very different emissions. Therefore, better global estimates require a better global picture of the involved seaweed species and their emissions.

The combination of the Open Path CE-DOAS with an incubation chamber proved as a valuable tool to investigate the emissions of reactive iodine from individual seaweed species during field studies. However for future campaigns several modifications are suggested (see sec. 13.6.2.1). Particularly, a second channel for the measurement of the primary  $I_2$  emission from seaweed is expected to give more reliable emission rates, also since  $I_2$  is much less reactive compared to IO and thus would avoid the uncertainties in the determined emission rates due to chemical losses. A second  $I_2$  channel would also be very valuable for future field measurements in the intertidal zone to better qualify the total iodine emission as well as gas phase reaction mechanisms.

# **Part VI.**

## **Appendix**



# A

## A Corrected IO Absorption Cross Section

### A.1. Correction Factors for IO Bands

A.1 to A.8 give the fit results for corrections of the Gómez Martín et al. [2005] IO cross section, using 65 IO absorption spectra measured with CE-DOAS as described in 11.2. For the correction a simple three parameter fit-model with a scaling  $\beta_0$ , a spectral shift  $\beta_1$  and a spectral squeeze  $\beta_2$  was used:

$$\sigma_{\text{IO}(\nu' \leftarrow \nu''), \text{corr}}(\lambda, \beta_0, \beta_1, \beta_2) = \beta_0 \cdot \sigma_{\text{IO}}(\lambda + \beta_1 + (\lambda - \lambda_c) \cdot \beta_2) \quad ((11.5))$$

where  $\sigma_{\text{IO}}$  is the Gómez Martín et al. [2005] cross section of a specific absorption band. The scaling factor  $\beta_0$  is relative to the IO(4  $\leftarrow$  0) band, which was assumed to be the best characterized transition in the Gómez Martín et al., 2005 cross section. In order to assess the significance of the fit parameters  $\beta_1$  and  $\beta_2$ , the model function was fitted three times: first with fixed  $\beta_1 = \beta_2 = 0$ , then with a free shift  $\beta_1$  but fixed squeeze  $\beta_2 = 0$  and finally with free shift and squeeze. Each of A.1 to A.8 shows the same sub figures which are described in the following. Subfigures a), b) and c) show the effect of allowing a free shift and squeeze on the fit residual for each of the 65 measured spectra. Subfigure d) shows the determined scaling parameter  $\beta_0$  for each spectrum, for a fixed squeeze (black stars with error bands, solid black line is the average) and for a free squeeze (blue dots with error bands, the dashed blue line is the average). The only exception is the IO(4  $\leftarrow$  0) transition (Fig. A.2) where subfigure d) gives the IO mixing ratio. Subfigure e) gives the fitted shift for each spectrum, for a fixed squeeze (black stars, solid black line is the average) and for a free squeeze (blue dots, dashed blue line is the average). Subfigure f) gives the fitted shift for each spectrum (blue stars) error confidence bands, the dashed blue line is the average squeeze. A summary of the retrieved corrections is given in Tab. 11.2.

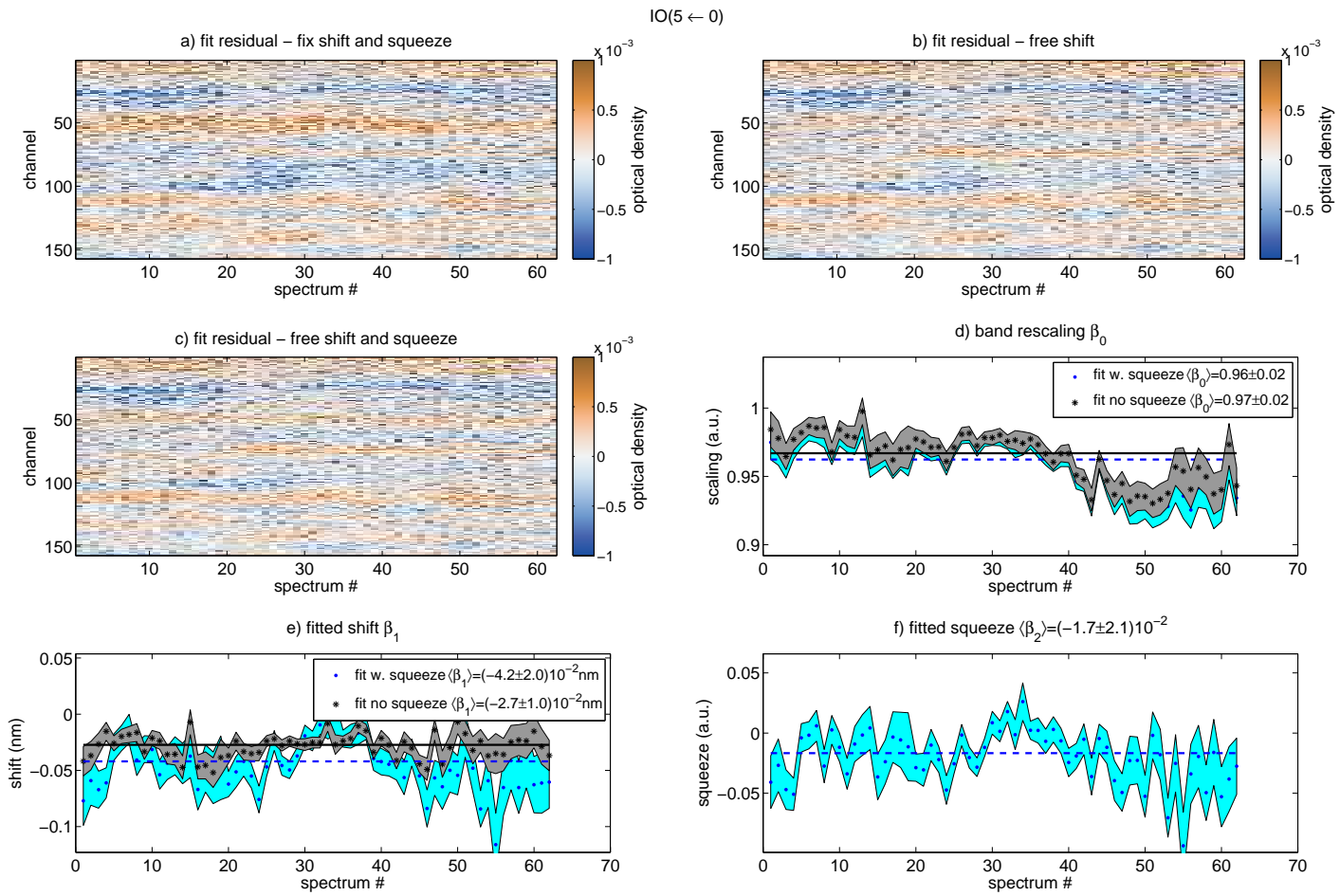
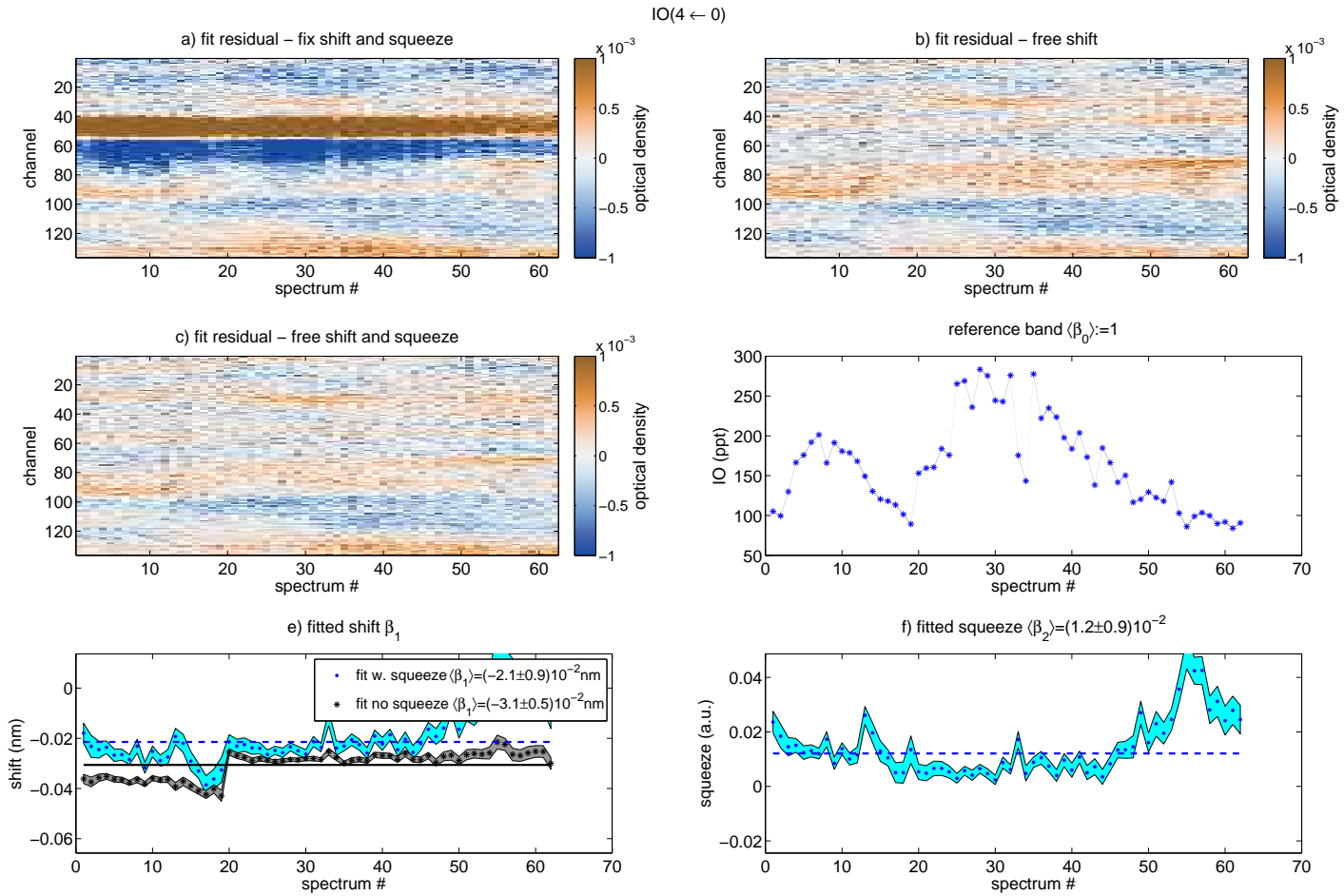


Figure A.1. | Corrections of IO(5 ← 0) fitted in the range 416.1 nm to 424.40 nm



**Figure A.2.** | Corrections of IO(4 ← 0) fitted in the range 424.4 nm to 431.4 nm

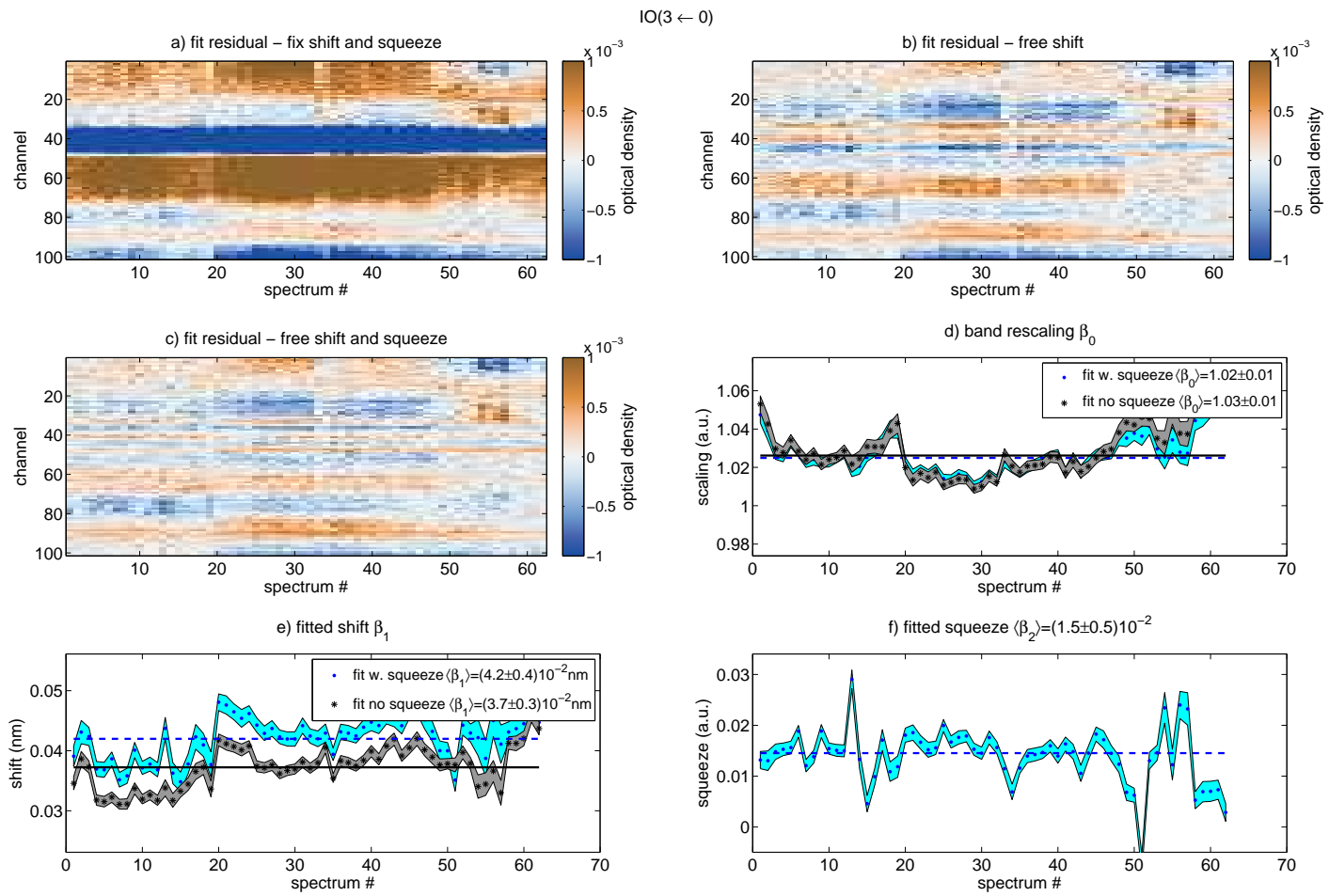
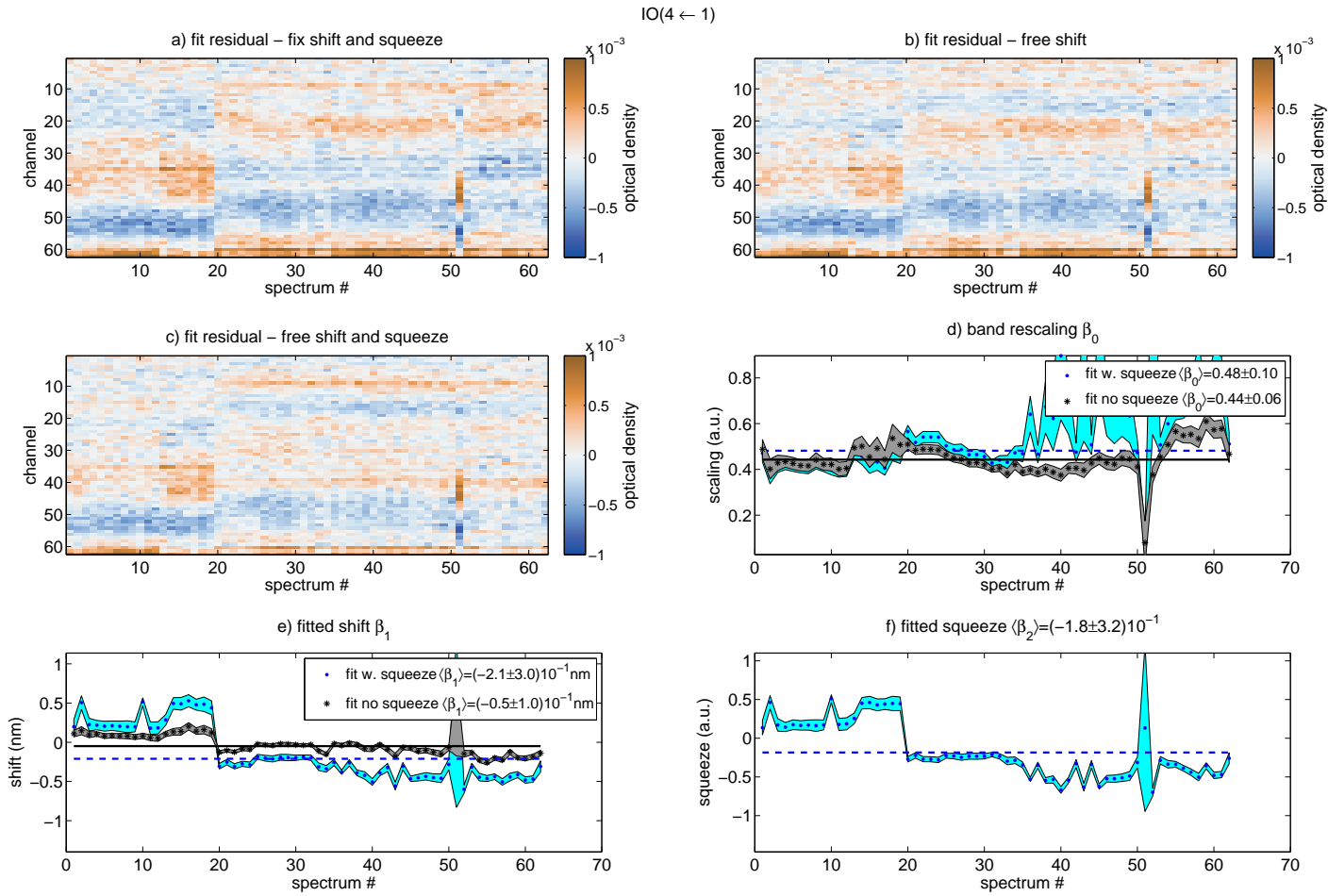
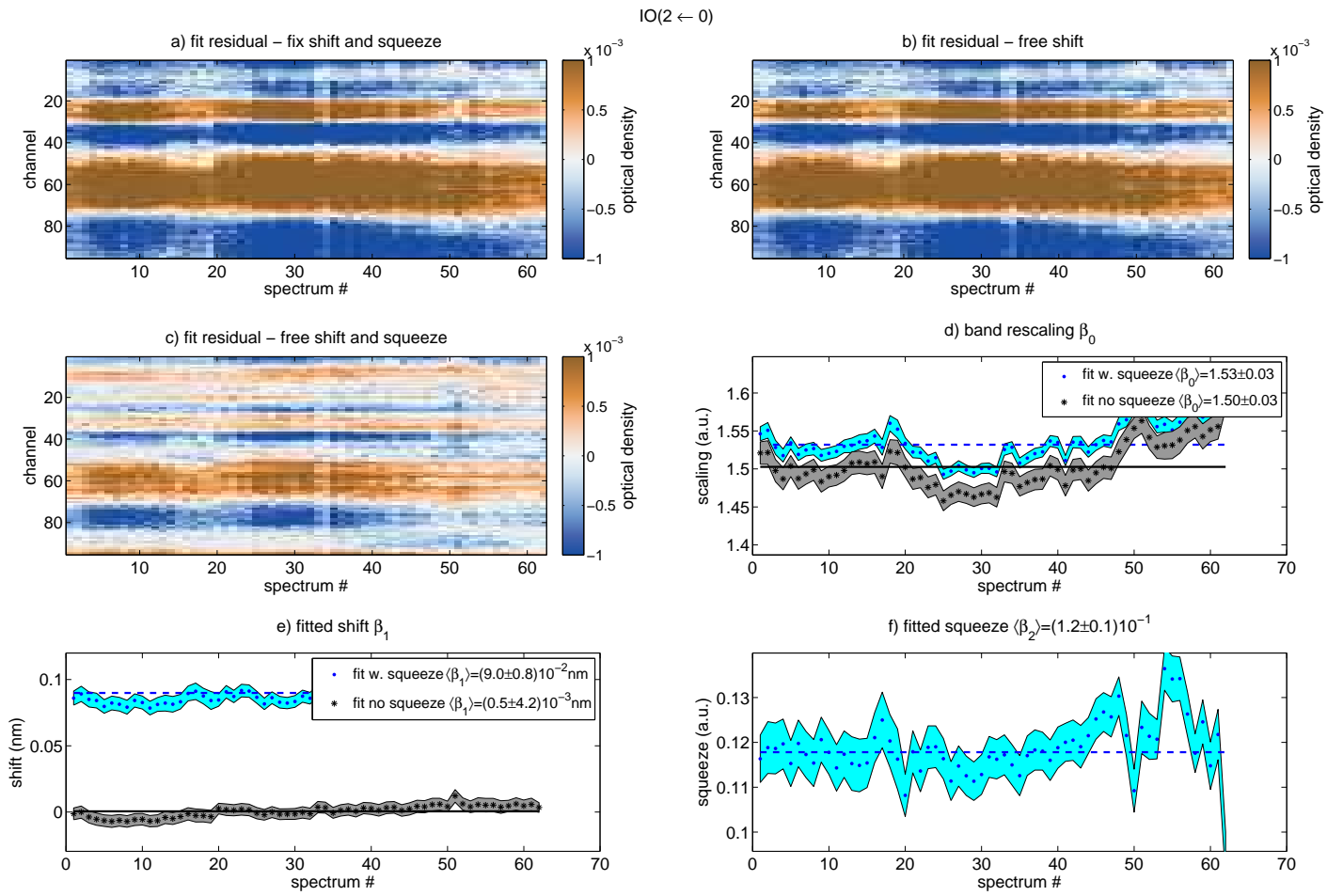


Figure A.3. | Corrections of IO(3 ← 0) fitted in the range 433.5 nm to 438.5 nm



**Figure A.4.** | Corrections of IO( $4 \leftarrow 1$ ) fitted in the range 439 nm to 442 nm



**Figure A.5.** | Corrections of IO( $2 \leftarrow 0$ ) fitted in the range 443.5 nm to 448 nm

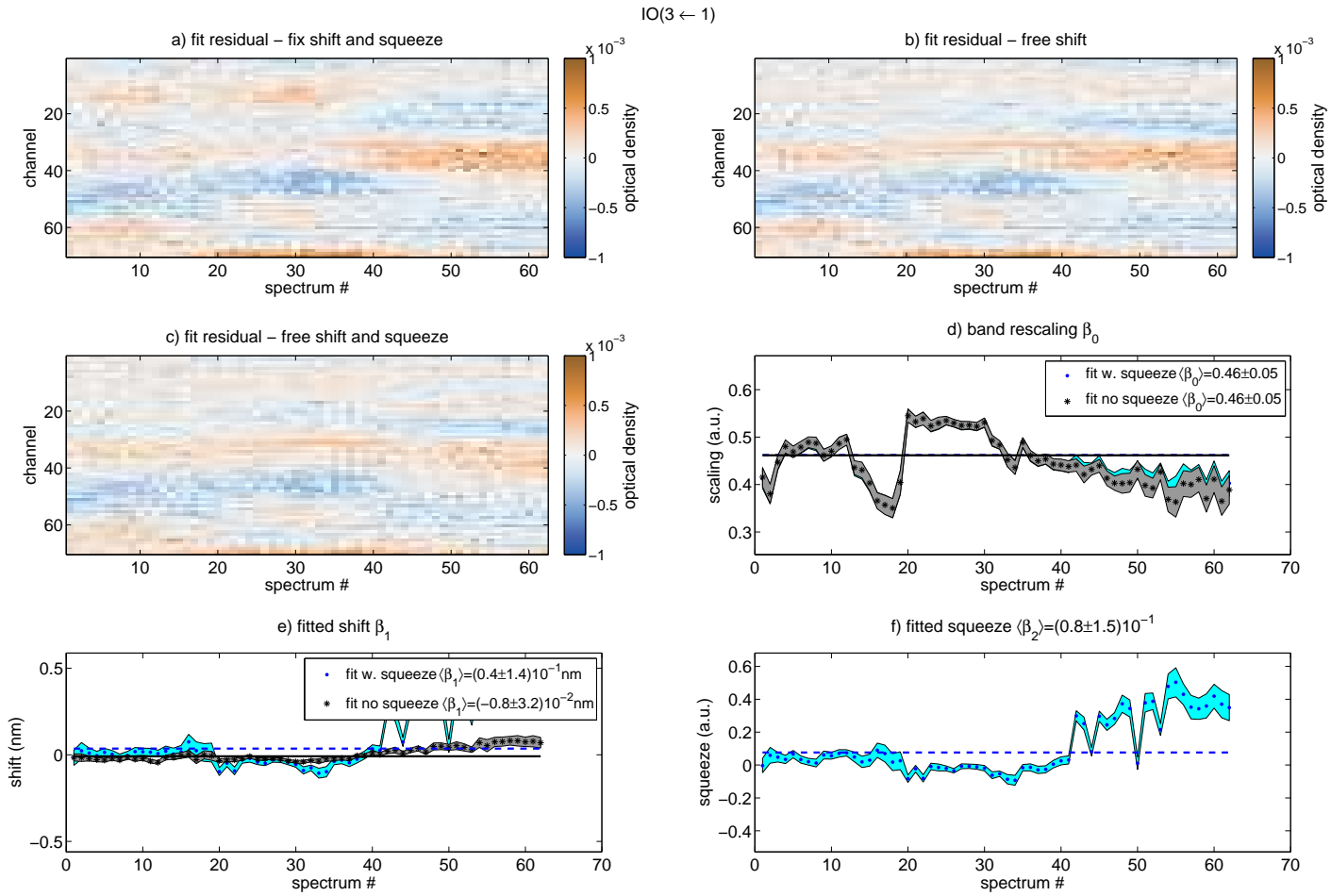


Figure A.6. | Corrections of IO(3 ← 1) fitted in the range 448 nm to 451.2 nm

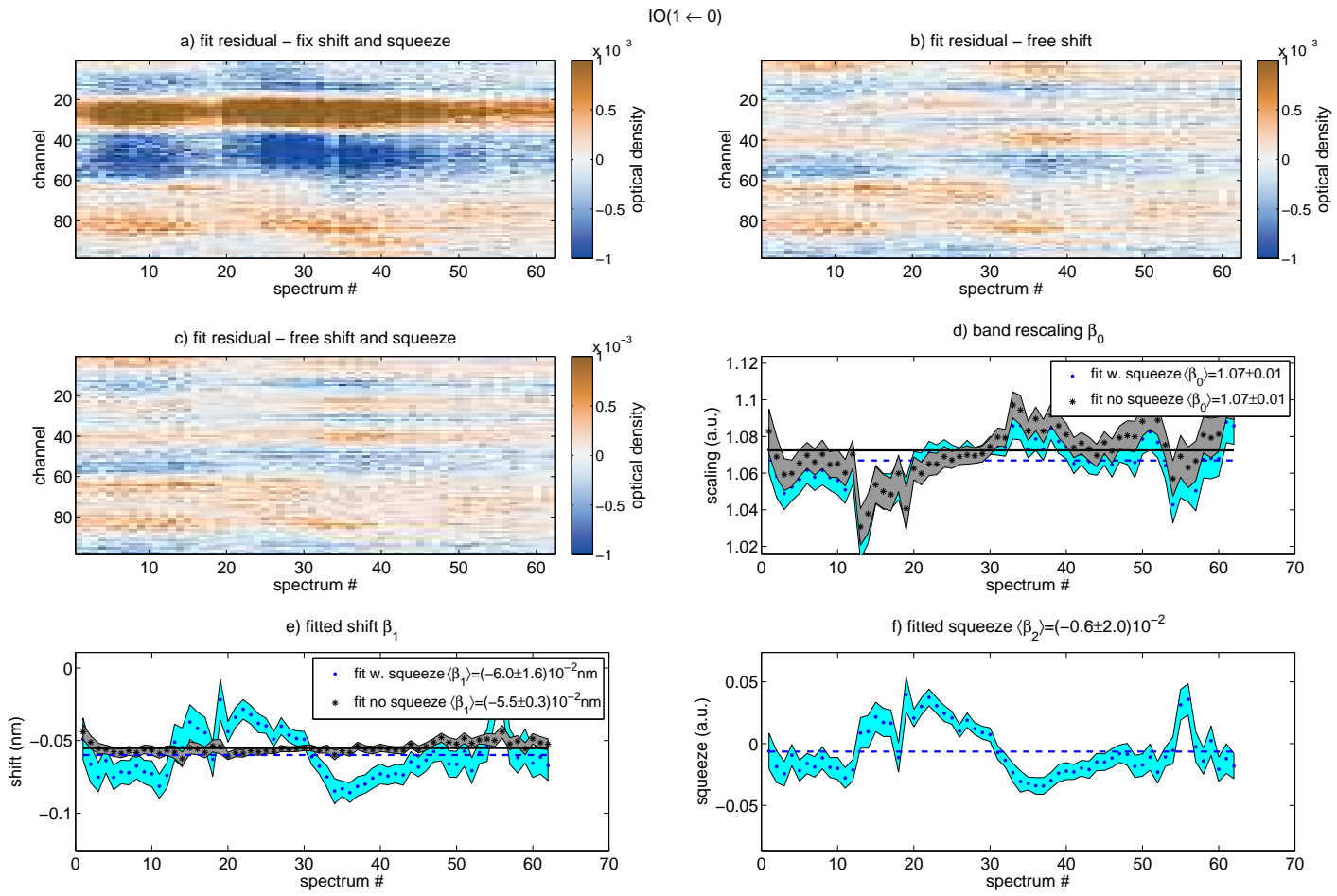
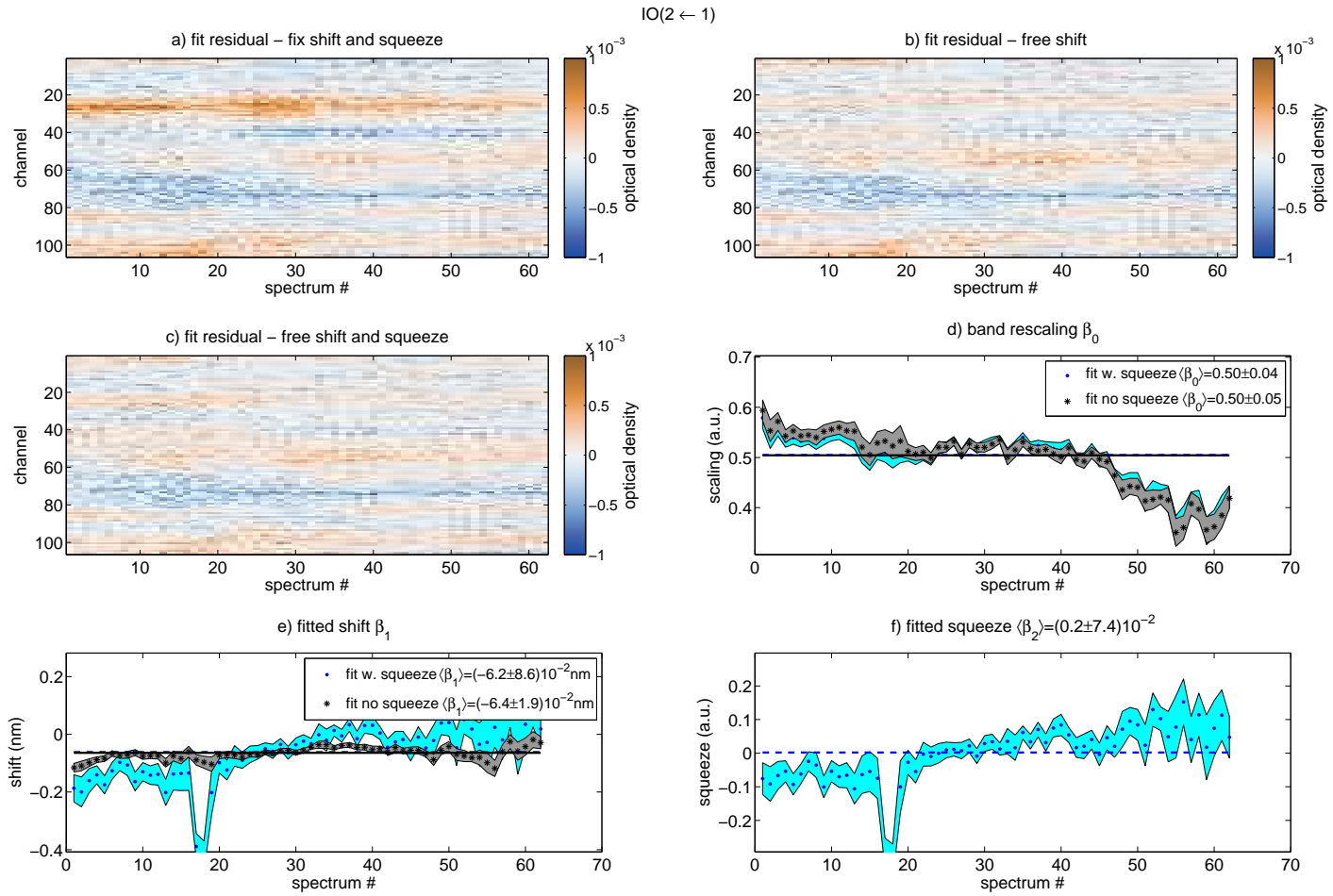


Figure A.7. | Corrections of IO( $1 \leftarrow 0$ ) fitted in the range 453.6 nm to 458 nm



**Figure A.8.** | Corrections of IO(2 ← 1) fitted in the range 457.3 nm to 462 nm

## A.2. Validation of the Correction for the IO( $2 \leftarrow 0$ ) Transition

This section provides the correlation plots for the validation of the IO( $2 \leftarrow 0$ ) transition using further field measurements. IO was fitted over the spectral windows from 425.3 nm to 447.8 nm, simultaneously with NO<sub>2</sub>, O<sub>4</sub>, H<sub>2</sub>O and an additional single band IO( $2 \leftarrow 0$ ) cross section. The IO( $2 \leftarrow 0$ ) was extracted from Gómez Martín et al. [2005] in the spectral range from 442 nm to 447.8 nm, covering the IO( $2 \leftarrow 0$ ) transition, and is zero elsewhere. Thus, the scaling correction for the IO( $2 \leftarrow 0$ ) band can be retrieved from the correlation between the fit of the full IO cross section and the IO( $2 \leftarrow 0$ ) cross section.

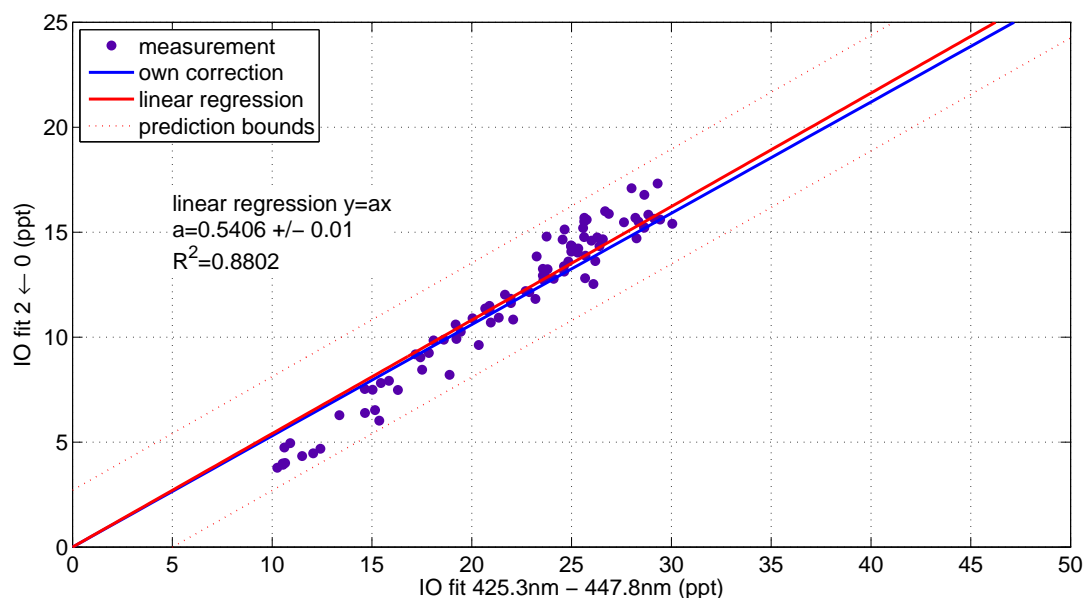


**Figure A.9.** | Correlation between the fit of the full IO cross section (425.3 – 447.8 nm) and the IO( $2 \leftarrow 0$ ) band for Open Path CE-DOAS measurements between July 19th and 25th 2012 during the Ireland Campaign campaign.

## A.2. Validation of the Correction for the IO(2 ← 0) Transition

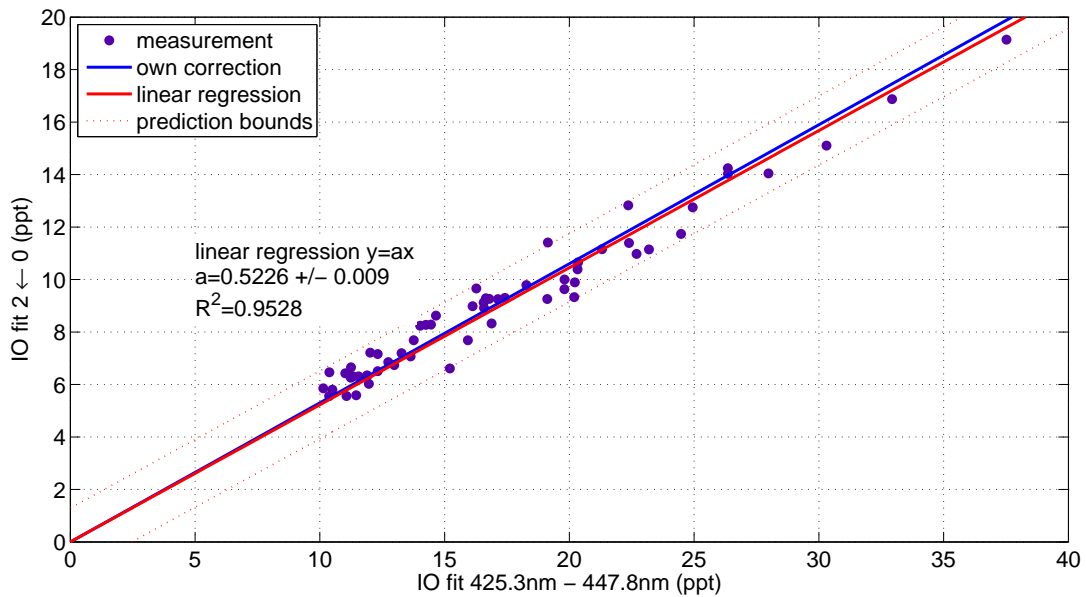


**Figure A.10.** | Correlation between the fit of the full IO cross section (425.3 – 447.8 nm) and the IO(2 ← 0) band for Open Path CE-DOAS measurements between August 5th and 6th 2012 during the Ireland Campaign campaign.

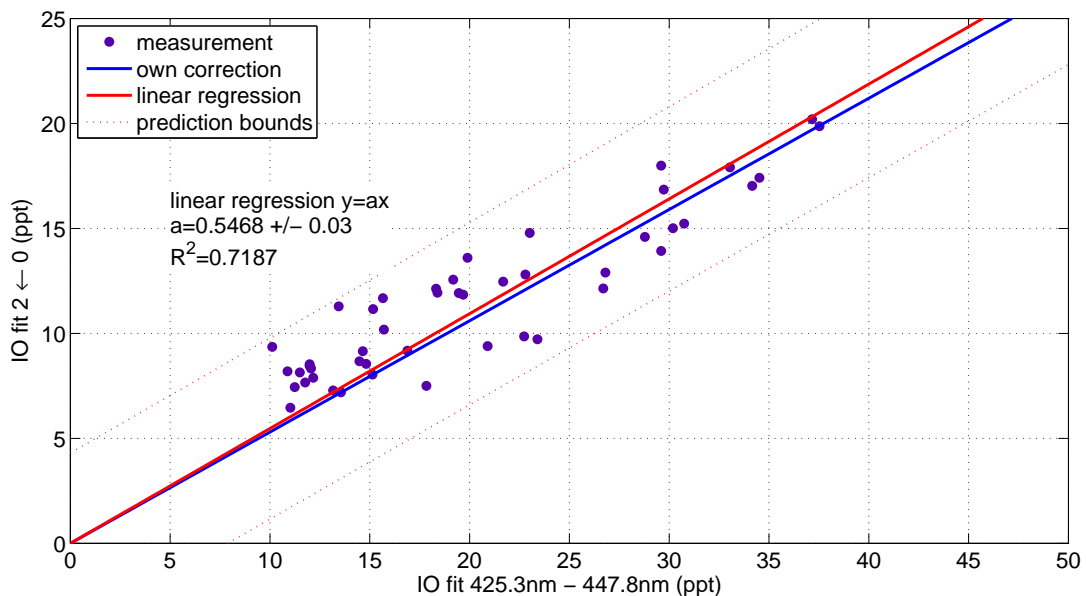


**Figure A.11.** | Correlation between the fit of the full IO cross section (425.3 – 447.8 nm) and the IO(2 ← 0) band for Closed Path CE-DOAS measurements between July 26th and August 4th 2012 during the Ireland Campaign campaign.

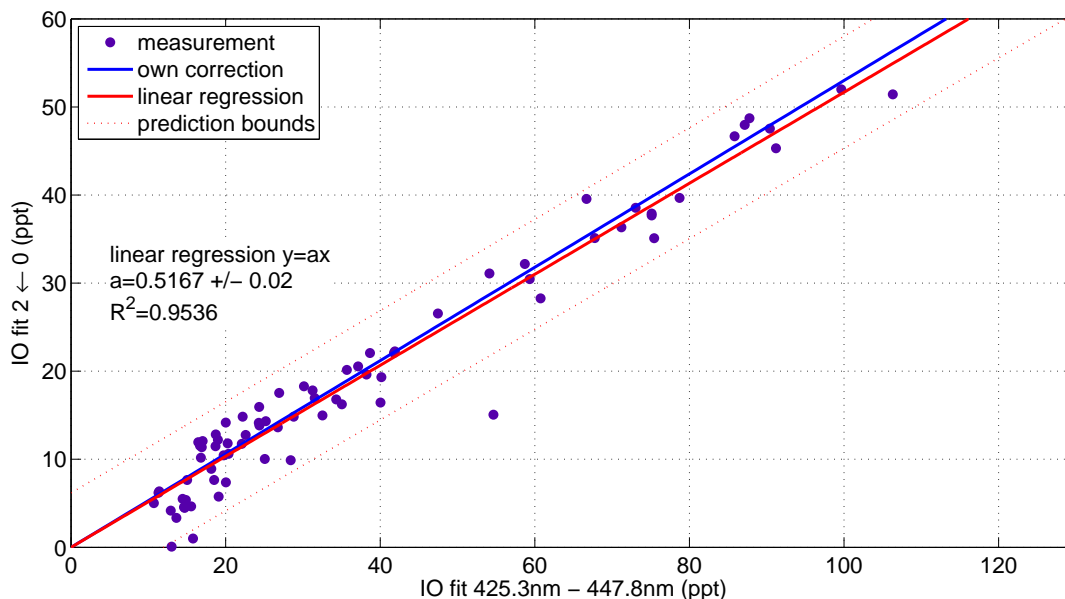


**Figure A.12.** | Correlation between the fit of the full IO cross section (425.3 – 447.8 nm) and the IO(2 ← 0) band for Open Path CE-DOAS measurements between March 12th and 16th 2013 during the New Zealand campaign.

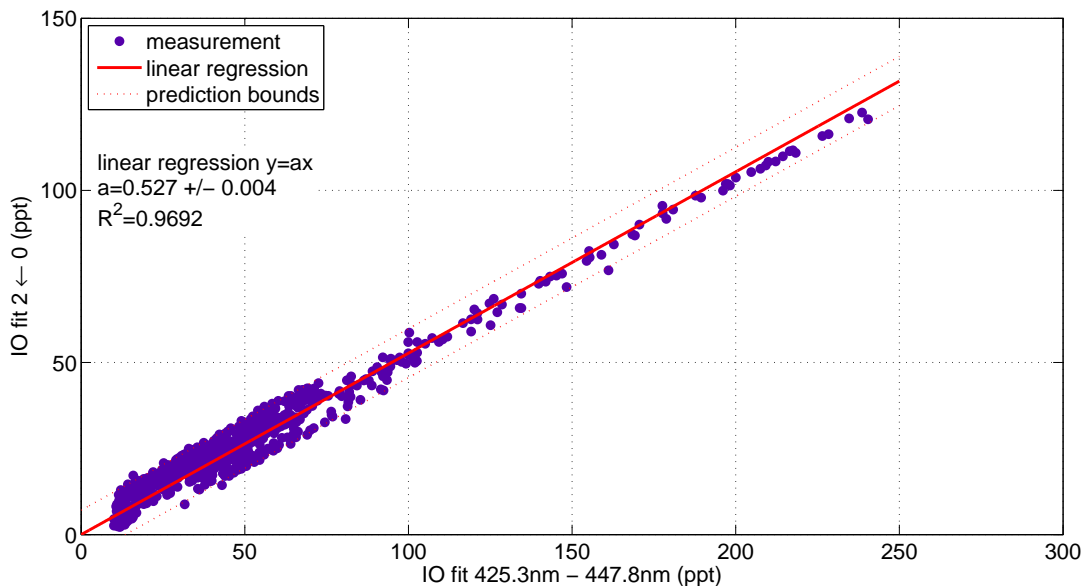


**Figure A.13.** | Correlation between the fit of the full IO cross section (425.3 – 447.8 nm) and the IO(2 ← 0) band for Open Path CE-DOAS measurements between March 21st and April 4th 2013 during the New Zealand campaign.

# B

## Spectral Retrieval

### B.1. Used Literature Absorption Cross Sections

species	reference	comment
BrO	Fleischmann et al. [2004]	$T = 298$ K
(CHO) <sub>2</sub>	Volkamer et al. [2005]	$T = 296$ K
H <sub>2</sub> O	HITEMP, Rothman et al. [2010] w. corr. by Lampel et al. [2015]	$T = 293$ K, $p = 1013$ mbar
HONO	Stutz et al. [2000]	
HCHO	Meller and Moortgat [2000]	$T = 298$ K
I <sub>2</sub>	Spietz et al. [2006]	$T = 298$ K
IO	own correction of Spietz et al. [2005]	see chapter 11
OIO	Spietz [2005]	$T = 298$ K
NO <sub>2</sub>	for BrO: A. Vandaele et al. [1998] otherwise: A. C. Vandaele et al. [2002]	$T = 294$ K, $p = 1013$ mbar $T = 294$ K, $p = 1013$ mbar
O <sub>4</sub>	for BrO: Thalman and Volkamer [2013] otherwise: Hermans et al. [1999]	$T = 293$ K $T = 293$ K
O <sub>2</sub>	HITRAN 2012 Rothman et al. [2013]	$T = 293$ K, $p = 1013$ mbar
O <sub>3</sub>	Bogumil et al. [2003]	$T = 293$ K
NO <sub>3</sub>	Yokelson et al. [1994]	$T = 298$ K
SO <sub>2</sub>	Bogumil et al. [2003]	$T = 298$ K

**Table B.1.** | Literature references for the absorption cross sections used in the DOAS retrievals.



# C

## Ireland Campaign 2011/2012 Supplementary

### C.1. Open path CE-DOAS intensities and path lengths

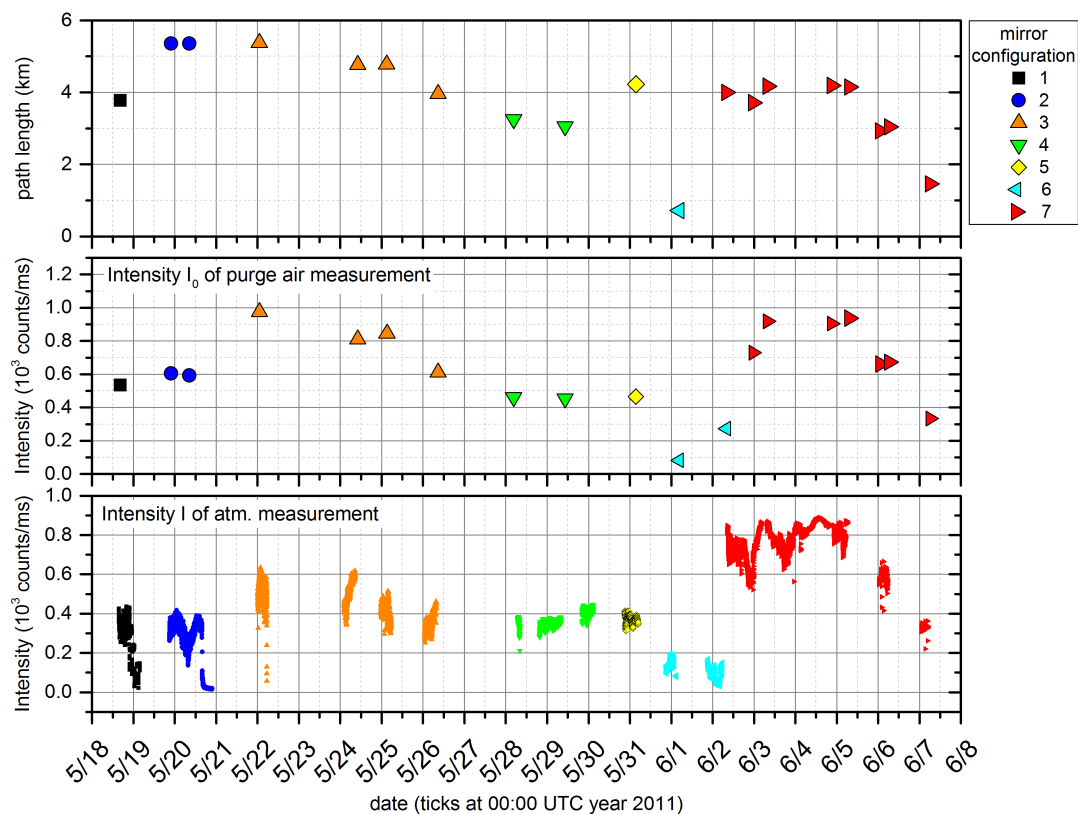


**Figure C.1.** | Open path CE-DOAS optical path length and light intensities during the Ireland 2011 campaign. The top plot shows the BCCRDS path length. In the middle plot the intensity of purge air measurements is shown. The bottom plot show the intensities of the actual atmospheric measurements. All intensity values are averages over the fit window.

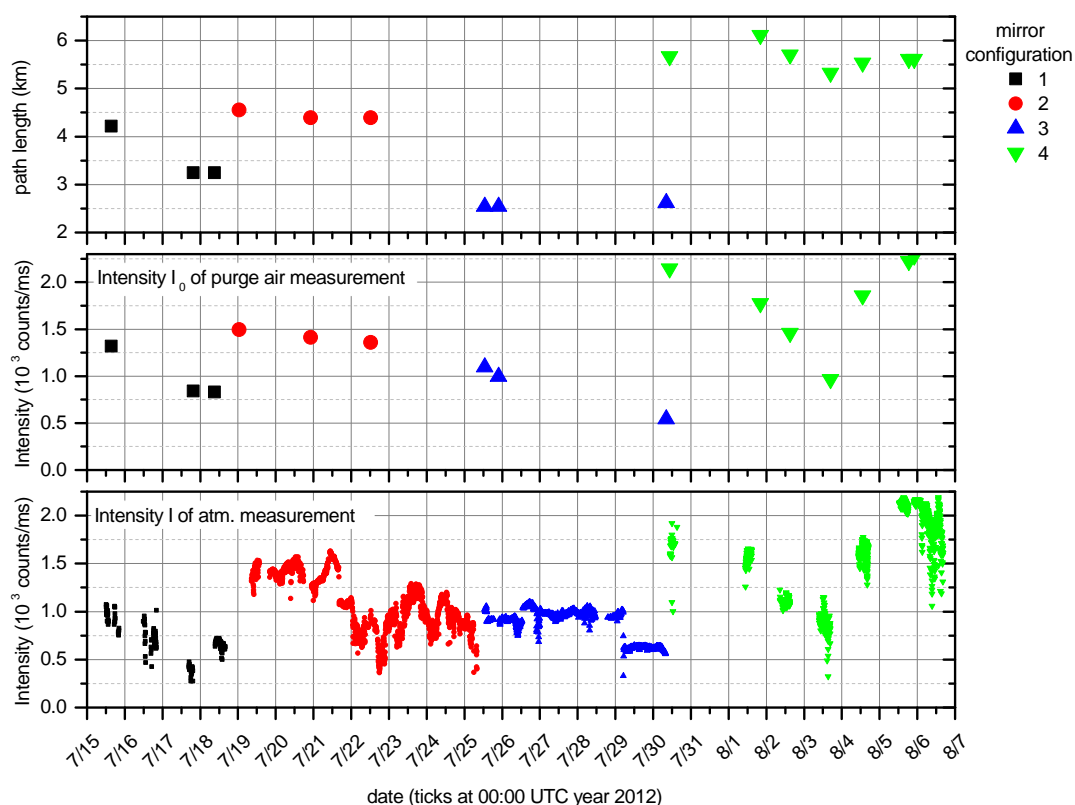


**Figure C.2.** | Open path CE-DOAS optical path length and light intensities during the Ireland 2012 campaign. The top plot shows the optical path length at  $\lambda = 441.6$  nm. In the middle plot the intensity of purge air measurements is shown. The bottom plot show the intensities of the actual atmospheric measurements. All intensity values are averages over the fit window.

## C.2. Correlation Between IO Mixing Ratios and Solar Irradiation.

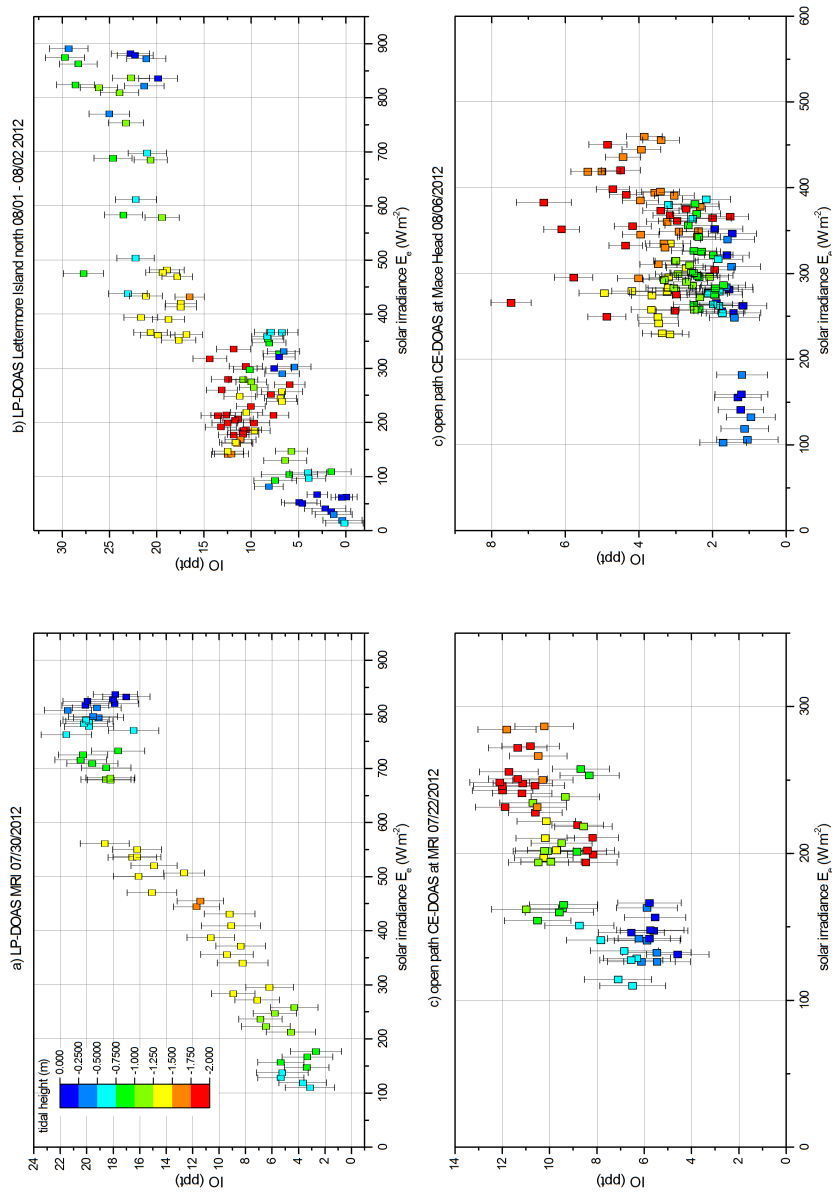
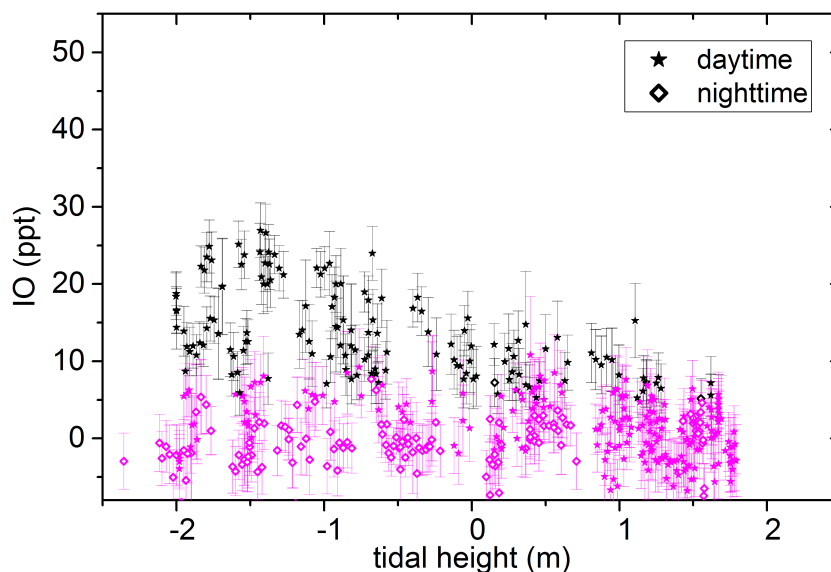
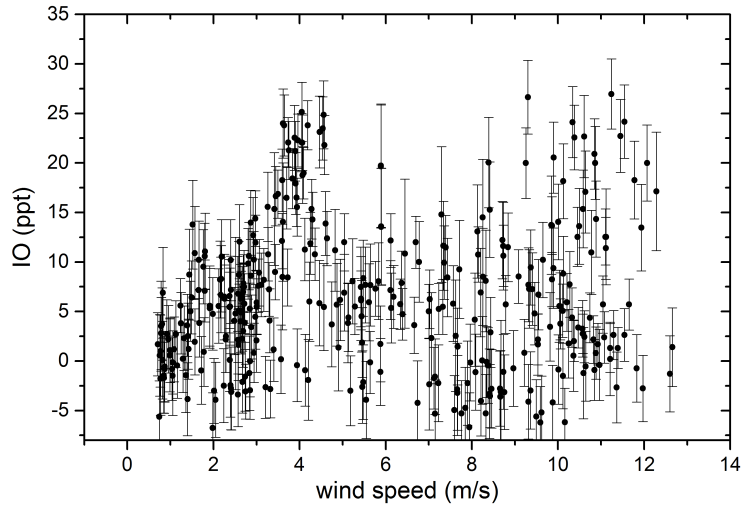


Figure C.3. | Further examples for the correlation between IO mixing ratios and solar irradiation.

### C.3. Correlation Plots for LP-DOAS Measurements at MRI 2011



**Figure C.4.** | Correlation of tidal height and IO observed by the MoLP-DOAS at the MRI in 2011. The data shows night time and daytime IO observed on the middle light path. For easier identification data above and below the detention limit are colored differently in black and magenta respectively. An anti correlation between tidal height and IO can be seen for daytime while the night time observations do not show any dependence on tidal height. However, due to the noisiness of the data the analysis is less clear compared to the measurements in 2012 discussed in sec. 12.9.1.4



**Figure C.5. | Correlation between IO mixing ratios and wind speed at MRI in 2011.**  
Increased IO mixing ratios show a positive correlation to high wind speeds

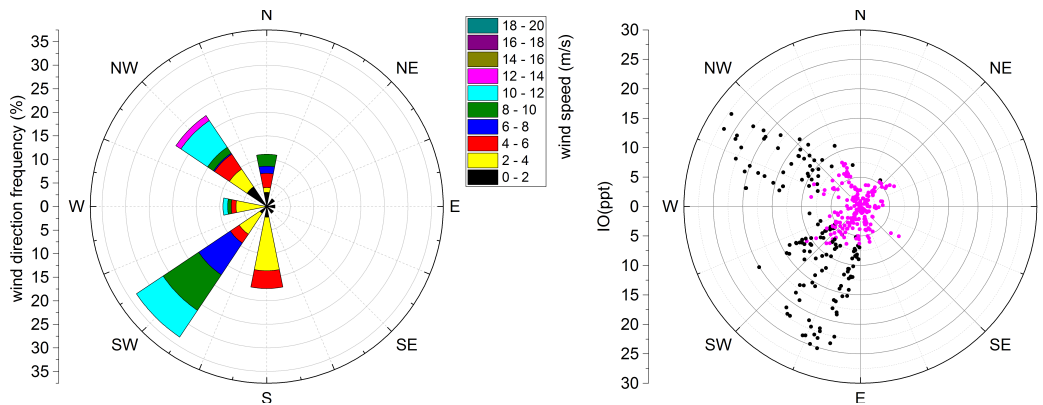


**Figure C.6. | Distribution of wind directions and correlation to IO at the MRI in 2011.**  
Left: frequency distribution of wind direction and wind speed. Right: correlation of IO with wind direction. High IO levels correlate with westerly and southerly winds. However, this correlation of IO to the wind direction is very similar to the frequency distribution of wind directions and thus does not indicate locations of IO sources.

# D

## New Zealand Campaign 2013 Supplementary

### D.1. GC Measurements of Halocarbons

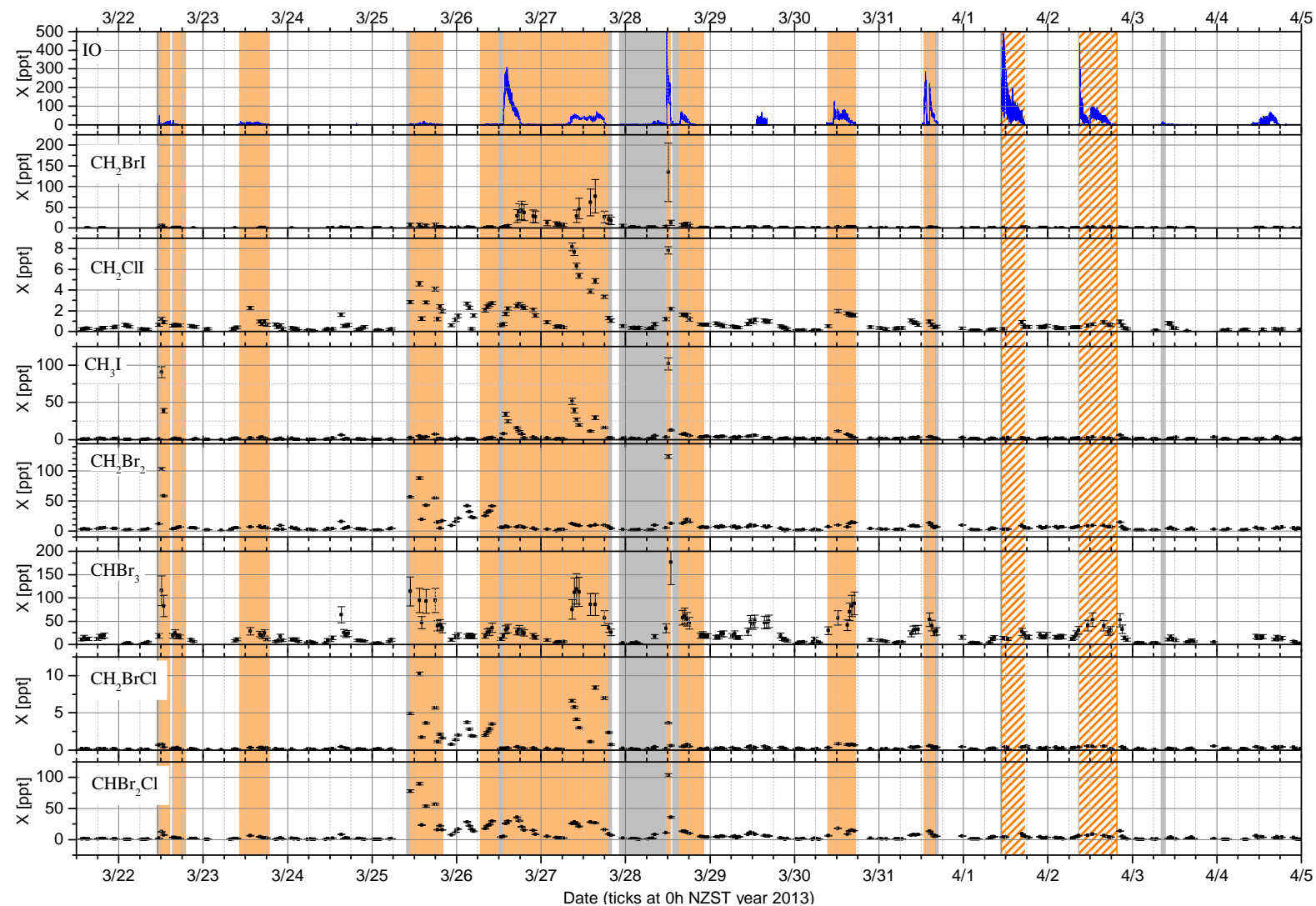


**Figure D.1.** | Time Series of Halocarbons measured by the  $\mu$ Dirac GC. Coloured areas indicated times periods when the GC was applied to the CE-DOAS chamber. Grey - empty closed chamber; orange - closed chamber with seaweed sample; orange with white stripes - chamber with removed top cover and seaweed sample. Details on the chamber and the seaweed samples are given in sec. 13.6. GC data provided by Andrew David Robinson, University of Cambridge (pers. com. 2013)

# Nomenclature

## Constants

---

$c_0$	speed of light in vacuum, $c_0 = 299792458$ m/s NIST, 2010
$k_B$	Boltzman's constant $k_B = 1.3806488 \cdot 10^{-23}$ J/K NIST, 2010
$N_A$	Avogadro's number $N_A = 6.02214129 \cdot 10^{23}$ mol <sup>-1</sup> NIST, 2010
$c_{\text{air}}$	speed of light in air, $c_{\text{air}} = \frac{c_0}{n_{\text{air}}} \approx 0.9997c_0$
$h, \hbar = h/(2\pi)$	Planck constant , $h = 6.62606957 \cdot 10^{-34}$ Js NIST, 2010
$n_{\text{air}}$	refractive index of dry air $n_{\text{air}} = 1.0002805$ at 450 nm, $T = 15$ °C, $p = 1013$ mBar and 450 ppm CO <sub>2</sub> Ciddor, 1996
$R$	molar gas constant $R = 8.3144621$ J K <sup>-1</sup> mol <sup>-1</sup> NIST, 2010

## Mathematical Notation

---

$(f \otimes h)(\cdot)$	convolution of functions $f(\cdot)$ and $h(\cdot)$ .....see sec. 4.2.1
$ x $	absolute value of $x$
$\approx 123.456$	approximately 123.456
$\bar{x}$	arithmetic mean of a sample $x_1, x_2, \dots, x_n$ , or average value of a continuous function $x(\cdot)$
$\delta(\cdot)$	Dirac's $\delta$ -distribution
$\hat{f}(\nu) = \mathcal{F}[f(\lambda)](\nu)$	Fourier transform of function $f(\lambda)$
$O(g)$	Landau notation of the error term in an approximation. The error is smaller than $c \cdot  g(x) $ when $x$ is close enough to 0
$\text{Var}(X)$	variance of random variable $X$
$X^\dagger$	Hermitian transpose of matrix $X$
$X^T$	transpose of matrix $X$

## Variables

---

$\bar{L}_0(\lambda)$	average length of the light path in a zero air purged resonator cell
$\bar{L}_{\text{eff}}(\lambda)$	effective length of the light path in a CE-DOAS measurement
$F_{A,i}$	emission rate for gas species $i$ per unit area, i.e. flux
$F_{m,i}$	emission rate species $i$ per mass
$F_i$	emission rate for gas species $i$
$\lambda$	wavelength
$\mathcal{R}(\lambda)$	residual spectrum of a DOAS fit
$\rho_i$	number density of species $i$
$\sigma'_i$	differential absorption cross section of species $i$
$\sigma_i$	absorption cross section of species $i$
$\tau$	cavity ring down decay constant
$\tau_0$	cavity ring down decay constant for a zero air purged resonator cell
$\Theta_i$	cavity enhanced effective absorption cross section of species $i$ , at the (low) instrument resolution
$\theta_i$	cavity enhanced effective absorption cross section of species $i$
$D'(\lambda)$	differential optical density
$D(\lambda)$	optical density
$d_0$	displacement of the mirrors in a resonator cell
$D_{\text{CE}}(\lambda)$	cavity enhanced optical density
$D_{\text{eff}}(\lambda)$	cavity enhanced effective optical density $I_0/I - 1$
$E_e$	solar irradiance ( $W/m^2$ )
$H(\lambda)$	line spread function of a spectrograph, also called instrument function
$I$	light intensity
$I_0$	initial light intensity or intensity of reference measurement
$I_{\text{stray}}$	intensity of the stray light component
$j$	photolysis frequency
$L$	length of the optical light path

$Q$	volumetric flow rate
$S_i$	absorption cross section of species $i$ , at the (low) instrument resolution



## Glossary

- ADC** analog digital converter.
- BB-CRDS** broadband CRDS.
- CCD** charge coupled device.
- CCN** could condensation nuclei.
- CE-DOAS** Cavity Enhanced DOAS.
- CP-CE-DOAS** Compact Closed Path CE-DOAS.
- CRDS** Cavity Ring Down Spectroscopy.
- DMS** dimethyl sulfide.
- DOAS** Differential Optical Absorption Spectroscopy.
- FWHM** full width at half maximum.
- GC** gas chromatograph.
- GC-MS** gas chromatography - mass spectrometry.
- iCE-DOAS** iterative CE-DOAS.
- LED** light emitting diode.
- LIF** Laser Induced Fluorescence.
- LP-DOAS** Long Path DOAS.
- MAX-DOAS** Multi Axis DOAS.
- MBL** marine boundary layer.
- MHWS** Mean High Water Springs, the mean level of the two successive low waters during spring tide.
- MLWS** Mean Low Water Springs, the mean level of the two successive high waters during spring tide.
- MoLP-DOAS** Mobile Compact LP-DOAS.
- MRI** Martin Ryan Institute.
- NIWA** National Institute of Water and Atmospheric Research.
- NUIG** National University of Ireland Galway.
- NZST** New Zealand Standard Time (UTC + 12h).
- OP-CE-DOAS MK-I** Open Path CE-DOAS Mark I.
- OP-CE-DOAS MK-II** Open Path CE-DOAS Mark II.
- PMT** photomultiplier tube.
- RHS** reactive halogen species.
- RMS** root mean squared.
- SMPS** Scanning Mobility Particle Sizer.
- SZA** solar zenith angle.
- UV-Vis** ultraviolet-visible.
- VOC** volatile organic compound.
- WLR-CRDS** wavelength resolved CRDS.



# Bibliography

- Adams, N. (1997). *Common Seaweeds of New Zealand*. Canterbury University Press.
- Albritton, D., A. Schmeltekopf, and R. Zare (1976). „Molecular Spectroscopy: Modern Research“. In: Orlando, Florida: Academic Press. Chap. An introduction to the least-squares fitting of spectroscopic data, pp. 1–67.
- Alicke, B., K. Hebestreit, J. Stutz, and U. Platt (1999). „Iodine oxide in the marine boundary layer“. In: *Nature* 397.6720, pp. 572–573. ISSN: 0028-0836. DOI: [10.1038/17508](https://doi.org/10.1038/17508).
- Allan, B. J., G. McFiggans, J. M. C. Plane, and H. Coe (2000). „Observations of iodine monoxide in the remote marine boundary layer“. In: *Journal of Geophysical Research: Atmospheres* 105.D11, pp. 14363–14369. ISSN: 2156-2202. DOI: [10.1029/1999JD901188](https://doi.org/10.1029/1999JD901188).
- Allan, B., N. Carslaw, H. Coe, R. Burgess, and J. Plane (1999). „Observations of the Nitrate Radical in the Marine Boundary Layer“. English. In: *Journal of Atmospheric Chemistry* 33.2, pp. 129–154. DOI: [10.1023/A:1005917203307](https://doi.org/10.1023/A:1005917203307).
- Anthofer, M. S. (2013). „Cavity Enhanced DOAS Measurements of Iodine Oxide“. Diplomarbeit. Universität Heidelberg.
- Ashu-Ayem, E. R., U. Nitschke, C. Monahan, J. Chen, S. B. Darby, P. D. Smith, C. D. O’Dowd, D. B. Stengel, and D. S. Venables (2012). „Coastal Iodine Emissions. 1. Release of I<sub>2</sub> by *Laminaria digitata* in Chamber Experiments“. In: *Environmental Science & Technology* 46.19, pp. 10413–10421. DOI: [10.1021/es204534v](https://doi.org/10.1021/es204534v).
- Atkinson, R., D. L. Baulch, R. A. Cox, J. N. Crowley, R. F. Hampson, R. G. Hynes, M. E. Jenkin, M. J. Rossi, and J. Troe (2004). „Evaluated kinetic and photochemical data for atmospheric chemistry: Volume I - gas phase reactions of O<sub>x</sub>, HO<sub>x</sub>, NO<sub>x</sub> and SO<sub>x</sub> species“. In: *Atmos. Chem. Phys.* 4.6, pp. 1461–1738. DOI: [10.5194/acp-4-1461-2004](https://doi.org/10.5194/acp-4-1461-2004).
- Atkinson, R., D. L. Baulch, R. A. Cox, J. N. Crowley, R. F. Hampson, R. G. Hynes, M. E. Jenkin, M. J. Rossi, and J. Troe (2007). „Evaluated kinetic and photochemical data for atmospheric chemistry: Volume III – gas phase reactions of inorganic halogens“. In: *Atmospheric Chemistry and Physics* 7.4, pp. 981–1191. DOI: [10.5194/acp-7-981-2007](https://doi.org/10.5194/acp-7-981-2007).
- Atkinson, R. (2000). „Atmospheric chemistry of VOCs and NO<sub>x</sub>“. In: *Atmospheric Environment* 34.12–14, pp. 2063–2101. DOI: [10.1016/S1352-2310\(99\)00460-4](https://doi.org/10.1016/S1352-2310(99)00460-4).

- Baily, N. A. and S. Kelly (1955). „Iodine Exchange in *Ascophyllum*“. In: *Biological Bulletin* 109.1, pp. 13–21. ISSN: 00063185. DOI: [10.2307/1538655](https://doi.org/10.2307/1538655).
- Ball, S. M., A. M. Hollingsworth, J. Humbles, C. Leblanc, P. Potin, and G. McFiggans (2010). „Spectroscopic studies of molecular iodine emitted into the gas phase by seaweed“. In: *Atmospheric Chemistry and Physics* 10.13, pp. 6237–6254. DOI: [10.5194/acp-10-6237-2010](https://doi.org/10.5194/acp-10-6237-2010).
- Ball, S., J. M. Langridge, and R. L. Jones (2004). „Broadband cavity enhanced absorption spectroscopy using light emitting diodes“. In: *Chem. Phys. Lett.* 398, p. 68.
- Barrie, L. A. and U. Platt (1997). „Arctic tropospheric chemistry: an overview“. In: *Tellus B* 49.5. DOI: [10.1034/j.1600-0889.49.issue5.2.x](https://doi.org/10.1034/j.1600-0889.49.issue5.2.x).
- Bell, T. W., K. C. Cavanaugh, and D. A. Siegel (2015). „Remote monitoring of giant kelp biomass and physiological condition: An evaluation of the potential for the Hyperspectral Infrared Imager (HyspIRI) mission“. In: *Remote Sensing of Environment* 167. Special Issue on the Hyperspectral Infrared Imager (HyspIRI), pp. 218–228. ISSN: 0034-4257. DOI: [10.1016/j.rse.2015.05.003](https://doi.org/10.1016/j.rse.2015.05.003).
- Bevington, P. (1969). *Data reduction and error analysis for the physical sciences*. New York: McGraw-Hill.
- Bilde, M., T. J. Wallington, C. Ferronato, J. J. Orlando, G. S. Tyndall, E. Estupinan, and S. Haberkorn (1998). „Atmospheric Chemistry of CH<sub>2</sub>BrCl, CHBrCl<sub>2</sub>, CHBr<sub>2</sub>Cl, CF<sub>3</sub>CHBrCl, and CBr<sub>2</sub>Cl<sub>2</sub>“. In: *The Journal of Physical Chemistry A* 102.11, pp. 1976–1986. DOI: [10.1021/jp9733375](https://doi.org/10.1021/jp9733375).
- Bloss, W. J., D. M. Rowley, R. A. Cox, and R. L. Jones (2001). „Kinetics and Products of the IO Self-Reaction“. In: *The Journal of Physical Chemistry A* 105.33, pp. 7840–7854. DOI: [10.1021/jp0044936](https://doi.org/10.1021/jp0044936).
- Bobrowski, N., G. Honninger, B. Galle, and U. Platt (2003). „Detection of bromine monoxide in a volcanic plume“. In: *Nature* 423.6937, pp. 273–276. DOI: [10.1038/nature01625](https://doi.org/10.1038/nature01625).
- Bodhaine, B., N. Wood, E. Dutton, and S. J.R. (1999). „On Rayleigh Optical Depth Calculations“. In: *J. Atmos. Oceanic Technol.* 16, pp. 1854–1861. DOI: [10.1175/1520-0426\(1999\)016<1854:ORODC>2.0.CO;2](https://doi.org/10.1175/1520-0426(1999)016<1854:ORODC>2.0.CO;2).
- Bogumil, K., J. Orphal, T. Homann, S. Voigt, P. Spietz, O. Fleischmann, A. Vogel, M. Hartmann, H. Kromminga, H. Bovensmann, J. Frerick, and J. Burrows (2003). „Measurements of molecular absorption spectra with the {SCIAMACHY} pre-flight model: instrument characterization and reference data for atmospheric remote-sensing in the 230–2380 nm region“. In: *Journal of Photochemistry and Photobiology A: Chemistry* 157.2–3. Atmospheric Photochemistry, pp. 167–184. DOI: [10.1016/S1010-6030\(03\)00062-5](https://doi.org/10.1016/S1010-6030(03)00062-5).

- Boucher, O., C. Moulin, S. Belviso, O. Aumont, L. Bopp, E. Cosme, R. von Kuhlmann, M. G. Lawrence, M. Pham, M. S. Reddy, J. Sciare, and C. Venkataraman (2003). „DMS atmospheric concentrations and sulphate aerosol indirect radiative forcing: a sensitivity study to the DMS source representation and oxidation“. In: *Atmospheric Chemistry and Physics* 3.1, pp. 49–65. DOI: 10.5194/acp-3-49-2003.
- Boyle, W. S. and G. E. Smith (1970). „Charge Coupled Semiconductor Devices“. In: *Bell System Technical Journal* 49.4, pp. 587–593. DOI: 10.1002/j.1538-7305.1970.tb01790.x.
- Brown, S. S. and J. Stutz (2012). „Nighttime radical observations and chemistry“. In: *Chem. Soc. Rev.* 41 (19), pp. 6405–6447. DOI: 10.1039/C2CS35181A.
- Bruton, T., H. Lyons, Y. Lerat, M. Stanley, and M. B. Rasmussen (2009). *A Review of the Potential of Marine Algae as a Source of Biofuel in Ireland*. Sustainable Energy Authority of Ireland, report pp. 92. URL: [http://www.seai.ie/Publications/Renewables\\_Publications\\_/Bioenergy/Algaereport.pdf](http://www.seai.ie/Publications/Renewables_Publications_/Bioenergy/Algaereport.pdf).
- Burkholder, J. B., J. Curtius, A. R. Ravishankara, and E. R. Lovejoy (2004). „Laboratory studies of the homogeneous nucleation of iodine oxides“. In: *Atmospheric Chemistry and Physics* 4.1, pp. 19–34. DOI: 10.5194/acp-4-19-2004.
- Butler, J. H., D. B. King, J. M. Lobert, S. A. Montzka, S. A. Yvon-Lewis, B. D. Hall, N. J. Warwick, D. J. Mondeel, M. Aydin, and J. W. Elkins (2007). „Oceanic distributions and emissions of short-lived halocarbons“. In: *Global Biogeochemical Cycles* 21.1. GB1023, n/a–n/a. ISSN: 1944-9224. DOI: 10.1029/2006GB002732.
- Carpenter, L. J., S. M. MacDonald, M. D. Shaw, R. Kumar, R. W. Saunders, R. Parthipan, J. Wilson, and J. Plane (2013). „Atmospheric iodine levels influenced by sea surface emissions of inorganic iodine“. In: *Nature Geosci* 6.2, pp. 108–111. DOI: 10.1038/ngeo1687.
- Carpenter, L. J., G. Malin, P. S. Liss, and F. C. Küpper (2000). „Novel biogenic iodine-containing trihalomethanes and other short-lived halocarbons in the coastal east Atlantic“. In: *Global Biogeochemical Cycles* 14.4, pp. 1191–1204. ISSN: 1944-9224. DOI: 10.1029/2000GB001257.
- Carpenter, L. J., S. Reimann, J. Burkholder, C. Clerbaux, B. Hall, R. Hossaini, J. Laube, and S. Yvon (2014). „Ozone-Depleting Substances (ODSs) and Other Gases of Interest to the Montreal Protocol, Chapter 1“. In: *Scientific Assessment of Ozone Depletion: 2014*. Global Ozone Research and Monitoring Project – Report No. 55, World Meteorological Organization, Geneva, Switzerland. Chap. 1. URL: [http://www.esrl.noaa.gov/csd/assessments/ozone/2014/chapters/chapter1\\_2014OzoneAssessment.pdf](http://www.esrl.noaa.gov/csd/assessments/ozone/2014/chapters/chapter1_2014OzoneAssessment.pdf).
- Carpenter, L. J., W. T. Sturges, S. A. Penkett, P. S. Liss, B. Alicke, K. Hebestreit, and U. Platt (1999). „Short-lived alkyl iodides and bromides at Mace Head, Ireland: Links to biogenic sources and halogen oxide production“. In: *Journal of Geophysical Research: Atmospheres* 104.D1, pp. 1679–1689. ISSN: 2156-2202. DOI: 10.1029/98JD02746.

- Casal, G., N. Sánchez-Carnero, J. Domínguez-Gómez, T. Kutser, and J. Freire (2012). „Assessment of AHS (Airborne Hyperspectral Scanner) sensor to map macroalgal communities on the Ría de Vigo and Ría de Alán coast (NW Spain)“. English. In: *Marine Biology* 159.9, pp. 1997–2013. ISSN: 0025-3162. DOI: [10.1007/s00227-012-1987-5](https://doi.org/10.1007/s00227-012-1987-5).
- Chambers, R. M., A. C. Heard, and R. P. Wayne (1992). „Inorganic gas-phase reactions of the nitrate radical: iodine + nitrate radical and iodine atom + nitrate radical“. In: *The Journal of Physical Chemistry* 96.8, pp. 3321–3331. DOI: [10.1021/j100187a028](https://doi.org/10.1021/j100187a028).
- Chameides, W. and J. C. G. Walker (1973). „A photochemical theory of tropospheric ozone“. In: *Journal of Geophysical Research* 78.36, pp. 8751–8760. DOI: [10.1029/JC078i036p08751](https://doi.org/10.1029/JC078i036p08751).
- Chance, K. and R. Kurucz (2010). „An improved high-resolution solar reference spectrum for earth’s atmosphere measurements in the ultraviolet, visible, and near infrared“. In: *Journal of Quantitative Spectroscopy and Radiative Transfer* 111.9. Special Issue Dedicated to Laurence S. Rothman on the Occasion of his 70th Birthday., pp. 1289–1295. DOI: [10.1016/j.jqsrt.2010.01.036](https://doi.org/10.1016/j.jqsrt.2010.01.036).
- Charlson, R. J., J. E. Lovelock, M. O. Andreae, and S. G. Warren (1987). „Oceanic phytoplankton, atmospheric sulphur, cloud albedo and climate“. In: *Nature* 326.6114, pp. 655–661. DOI: [10.1038/326655a0](https://doi.org/10.1038/326655a0).
- Cicerone, R. J. (1981). „Halogens in the atmosphere“. In: *Reviews of Geophysics* 19.1, pp. 123–139. ISSN: 1944-9208. DOI: [10.1029/RG019i001p00123](https://doi.org/10.1029/RG019i001p00123).
- Ciddor, P. E. (1996). „Refractive index of air: new equations for the visible and near infrared“. In: *Appl. Opt.* 35.9, pp. 1566–1573. DOI: [10.1364/AO.35.001566](https://doi.org/10.1364/AO.35.001566).
- Clyne, M. A. A. and H. W. Cruse (1970). „Rates of elementary reactions involving the BrO( $X^2\Pi$ ) and IO( $X^2\Pi$ ) radicals. Part 2.-Reactions of the BrO and IO radicals“. In: *Trans. Faraday Soc.* 66, pp. 2227–2236. DOI: [10.1039/TF9706602227](https://doi.org/10.1039/TF9706602227).
- Commane, R., K. Seitz, C. S. E. Bale, W. J. Bloss, J. Buxmann, T. Ingham, U. Platt, D. Pöhler, and D. E. Heard (2011). „Iodine monoxide at a clean marine coastal site: observations of high frequency variations and inhomogeneous distributions“. In: *Atmospheric Chemistry and Physics* 11.13, pp. 6721–6733. DOI: [10.5194/acp-11-6721-2011](https://doi.org/10.5194/acp-11-6721-2011).
- Coslovi, L. and F. Righini (1980). „Fast determination of the nonlinearity of photodetectors“. In: *Appl. Opt.* 19.18, pp. 3200–3203. DOI: [10.1364/AO.19.003200](https://doi.org/10.1364/AO.19.003200).
- Courtois, B. (1813). „Sur un nouvel acide formé avec la substance découverte par M. Courtois“. In: *Annales de Chimie* 88, pp. 311–318.
- Crossland, C. J., D. Baird, J.-P. Ducrottoy, H. Lindeboom, R. W. Buddemeier, W. C. Dennison, B. A. Maxwell, S. V. Smith, and D. P. Swaney (2005). „The Coastal Zone – a Domain of Global Interactions“. In: *Coastal Fluxes in the Anthropocene*. Ed. by C. J. Crossland,

- H. H. Kremer, H. J. Lindeboom, J. I. Marshall Crossland, and M. D. A. Le Tissier. Global Change – The IGBP Series. Springer Berlin Heidelberg, pp. 1–37. ISBN: 978-3-540-25450-8. DOI: [10.1007/3-540-27851-6\\_1](https://doi.org/10.1007/3-540-27851-6_1).
- Crutzen, P., M. G. Lawrence, and U. Pöschl (1999). „On the background photochemistry of tropospheric ozone“. In: *Tellus A* 51.1, pp. 123–146. DOI: [10.1034/j.1600-0870.1999.t01-1-00010.x](https://doi.org/10.1034/j.1600-0870.1999.t01-1-00010.x).
- Crutzen, P. and P. Zimmermann (1991). „The changing photochemistry of the troposphere“. In: *Tellus B* 43.4, pp. 136–151. DOI: [10.1034/j.1600-0889.1991.t01-1-00012.x](https://doi.org/10.1034/j.1600-0889.1991.t01-1-00012.x).
- Crutzen, P. and M. Lawrence (2000). „The Impact of Precipitation Scavenging on the Transport of Trace Gases: A 3-Dimensional Model Sensitivity Study“. English. In: *Journal of Atmospheric Chemistry* 37.1, pp. 81–112. DOI: [10.1023/A:1006322926426](https://doi.org/10.1023/A:1006322926426).
- De Vooy, C. G. N. (1979). „The Global Carbon Cycle“. In: ed. by B. Bolin, E. T. Degens, S. Kempe, and P. Ketner. John Wiley, Chichester. Chap. Primary Production in Aquatic Environments.
- Dillon, T. J., M. E. Tucceri, R. Sander, and J. N. Crowley (2008). „LIF studies of iodine oxide chemistry Part 3. Reactions  $\text{IO} + \text{NO}_3 \rightarrow \text{OIO} + \text{NO}_2$ ,  $\text{I} + \text{NO}_3 \rightarrow \text{IO} + \text{NO}_2$  and  $\text{CH}_2\text{I} + \text{O}_2 \rightarrow$  (products): implications for the chemistry of the marine atmosphere at night“. In: *Phys. Chem. Chem. Phys.* 10 (11), pp. 1540–1554. DOI: [10.1039/B717386E](https://doi.org/10.1039/B717386E).
- Dixneuf, S., A. A. Ruth, S. Vaughan, R. M. Varma, and J. Orphal (2009). „The time dependence of molecular iodine emission from *Laminaria digitata*“. In: *Atmospheric Chemistry and Physics* 9.3, pp. 823–829. DOI: [10.5194/acp-9-823-2009](https://doi.org/10.5194/acp-9-823-2009).
- Durie, R. A. and D. A. Ramsay (1958). „ABSORPTION SPECTRA OF THE HALOGEN MONOXIDES“. In: *Canadian Journal of Physics* 36.1, pp. 35–53. DOI: [10.1139/p58-005](https://doi.org/10.1139/p58-005).
- Eger, P. (2014). „Improving Long-Path DOAS measurements with a Laser Driven Light Source and a new fibre configuration“. MA thesis. Heidelberg University.
- Farman, J. C., B. G. Gardiner, and J. D. Shanklin (1985). „Large losses of total ozone in Antarctica reveal seasonal ClO<sub>x</sub>/NO<sub>x</sub> interaction“. In: *Nature* 315.6016, pp. 207–210. URL: [10.1038/315207a0](https://doi.org/10.1038/315207a0).
- Fiedler, S. E. (2005). „Incoherent Broad-Band Cavity-Enhanced Absorption Spectroscopy“. PhD thesis. Technische Universität Berlin.
- Finlayson-Pitts, B. J., M. J. Ezell, and J. N. Pitts (1989). „Formation of chemically active chlorine compounds by reactions of atmospheric NaCl particles with gaseous N<sub>2</sub>O<sub>5</sub> and ClONO<sub>2</sub>“. In: *Nature* 337.6204, pp. 241–244. DOI: [10.1038/337241a0](https://doi.org/10.1038/337241a0).

- Finlayson-Pitts, B. J. and J. N. Pitts (2000). *Chemistry of the Upper and Lower Atmosphere*. First Edition. San Diego, California: Academic Press. ISBN: 0-12-257060-x.
- Finlayson-Pitts, B. and S. Johnson (1988). „The reaction of {NO<sub>2</sub>} with NaBr: Possible source of BrNO in polluted marine atmospheres“. In: *Atmospheric Environment (1967)* 22.6, pp. 1107–1112. ISSN: 0004-6981. DOI: [10.1016/0004-6981\(88\)90340-X](https://doi.org/10.1016/0004-6981(88)90340-X).
- Flanagan, R. J., M. Geever, and C. D. O’Dowd (2005). „Direct Measurements of New-Particle Fluxes in the Coastal Environment“. In: *Environ. Chem.* 2.4, pp. 256–259. DOI: [10.1071/EN05069](https://doi.org/10.1071/EN05069).
- Fleischmann, O. C., M. Hartmann, J. P. Burrows, and J. Orphal (2004). „New ultraviolet absorption cross-sections of BrO at atmospheric temperatures measured by time-windowing Fourier transform spectroscopy“. In: *Journal of Photochemistry and Photobiology A: Chemistry* 168.1–2, pp. 117–132. DOI: [10.1016/j.jphotochem.2004.03.026](https://doi.org/10.1016/j.jphotochem.2004.03.026).
- Frehlich, R. G. (1992). „Estimation of the nonlinearity of a photodetector“. In: *Appl. Opt.* 31, pp. 5926–5929. DOI: [10.1364/AO.31.005926](https://doi.org/10.1364/AO.31.005926).
- Frieß, U., T. Deutschmann, B. S. Gilfedder, R. Weller, and U. Platt (2010). „Iodine monoxide in the Antarctic snowpack“. In: *Atmospheric Chemistry and Physics* 10.5, pp. 2439–2456. DOI: [10.5194/acp-10-2439-2010](https://doi.org/10.5194/acp-10-2439-2010).
- Frieß, U., J. Hollwedel, G. König-Langlo, T. Wagner, and U. Platt (2004). „Dynamics and chemistry of tropospheric bromine explosion events in the Antarctic coastal region“. In: *Journal of Geophysical Research: Atmospheres* 109.D6. DOI: [10.1029/2003JD004133](https://doi.org/10.1029/2003JD004133).
- Frieß, U., T. Wagner, I. Pundt, K. Pfeilsticker, and U. Platt (2001). „Spectroscopic measurements of tropospheric iodine oxide at Neumayer Station, Antarctica“. In: *Geophysical Research Letters* 28.10, pp. 1941–1944. DOI: [10.1029/2000GL012784](https://doi.org/10.1029/2000GL012784).
- Frieß, U., J. Zielcke, D. Pöhler, T. Hay, K. Kreher, and U. Platt. (2013). „Iodine monoxide in the antarctic marine boundary layer: Recent discoveries“. In: *EGU General Assembly Conference Abstracts*. Vol. 15, p. 8643.
- Furneaux, K. L., L. K. Whalley, D. E. Heard, H. M. Atkinson, W. J. Bloss, M. J. Flynn, M. W. Gallagher, T. Ingham, L. Kramer, J. D. Lee, R. Leigh, G. B. McFiggans, A. S. Mahajan, P. S. Monks, H. Oetjen, J. M. C. Plane, and J. D. Whitehead (2010). „Measurements of iodine monoxide at a semi polluted coastal location“. In: *Atmospheric Chemistry and Physics* 10.8, pp. 3645–3663. DOI: [10.5194/acp-10-3645-2010](https://doi.org/10.5194/acp-10-3645-2010).
- Gazha, P., T. Yunusov, T. Shadrina, and A. Andrianov (1983). „Iodine-containing complexes of the Black Sea alga *Phyllophora nervosa*“. English. In: *Chemistry of Natural Compounds* 19.6, pp. 733–737. ISSN: 0009-3130. DOI: [10.1007/BF00575182](https://doi.org/10.1007/BF00575182).

- Geyer, A. (2000). „THE ROLE OF THE NITRATE RADICAL IN THE BOUNDARY LAYER - OBSERVATIONS AND MODELING STUDIES“. PhD thesis. Heidelberg University.
- Giese, B., F. Laturus, F. C. Adams, and C. Wiencke (1999). „Release of Volatile Iodinated C<sub>1</sub>–C<sub>4</sub> Hydrocarbons by Marine Macroalgae from Various Climate Zones“. In: *Environmental Science & Technology* 33.14, pp. 2432–2439. DOI: [10.1021/es980731n](https://doi.org/10.1021/es980731n).
- Glasow, R. von and P. J. Crutzen (2004). „Model study of multiphase DMS oxidation with a focus on halogens“. In: *Atmospheric Chemistry and Physics* 4.3, pp. 589–608. DOI: [10.5194/acp-4-589-2004](https://doi.org/10.5194/acp-4-589-2004).
- Glasow, R. von and P. Crutzen (2003). „4.02 - Tropospheric Halogen Chemistry“. In: *Treatise on Geochemistry*. Ed. by H. D. H. K. Turekian. Oxford: Pergamon, pp. 1–67. ISBN: 978-0-08-043751-4. DOI: [10.1016/B0-08-043751-6/04141-4](https://doi.org/10.1016/B0-08-043751-6/04141-4).
- Glasow, R. von, R. von Kuhlmann, M. G. Lawrence, U. Platt, and P. J. Crutzen (2004). „Impact of reactive bromine chemistry in the troposphere“. In: *Atmospheric Chemistry and Physics* 4.11/12, pp. 2481–2497. DOI: [10.5194/acp-4-2481-2004](https://doi.org/10.5194/acp-4-2481-2004).
- Gómez Martín, J. C., S. H. Ashworth, A. S. Mahajan, and J. M. C. Plane (2009). „Photochemistry of OIO: Laboratory study and atmospheric implications“. In: *Geophysical Research Letters* 36.9, p. L09802. DOI: [10.1029/2009GL037642](https://doi.org/10.1029/2009GL037642).
- Gómez Martín, J. C., P. Spietz, and J. P. Burrows (2005). „Spectroscopic studies of the I<sub>2</sub>/O<sub>3</sub> photochemistry: Part 1: Determination of the absolute absorption cross sections of iodine oxides of atmospheric relevance“. In: *Journal of Photochemistry and Photobiology A: Chemistry* 176.1–3. In Honour of Professor Richard P. Wayne, pp. 15–38. DOI: [10.1016/j.jphotochem.2005.09.024](https://doi.org/10.1016/j.jphotochem.2005.09.024).
- Gómez Martín, J. C., P. Spietz, and J. P. Burrows (2007). „Kinetic and Mechanistic Studies of the I<sub>2</sub>/O<sub>3</sub> Photochemistry“. In: *The Journal of Physical Chemistry A* 111.2. PMID: 17214469, pp. 306–320. DOI: [10.1021/jp061186c](https://doi.org/10.1021/jp061186c).
- Gostlow, B., A. D. Robinson, N. R. P. Harris, L. M. O’Brien, D. E. Oram, G. P. Mills, H. M. Newton, S. E. Yong, and J. A. Pyle (2010). „μDirac: an autonomous instrument for halocarbon measurements“. In: *Atmospheric Measurement Techniques* 3.2, pp. 507–521. DOI: [10.5194/amt-3-507-2010](https://doi.org/10.5194/amt-3-507-2010).
- Gower, J. F. R. and S. A. King (2011). „Distribution of floating Sargassum in the Gulf of Mexico and the Atlantic Ocean mapped using MERIS“. In: *International Journal of Remote Sensing* 32.7, pp. 1917–1929. DOI: [10.1080/01431161003639660](https://doi.org/10.1080/01431161003639660).
- Graham, M. H., B. P. Kinlan, L. D. Druehl, L. E. Garske, and S. Banks (2007). „Deep-water kelp refugia as potential hotspots of tropical marine diversity and productivity“. In: *Proceedings of the National Academy of Sciences* 104.42, pp. 16576–16580. DOI: [10.1073/pnas.0704778104](https://doi.org/10.1073/pnas.0704778104).

- Grilli, R., G. Méjean, S. Kassi, I. Ventrillard, C. Abd-Alrahman, E. Fasci, and D. Romanini (2012a). „Trace measurement of BrO at the ppt level by a transportable mode-locked frequency-doubled cavity-enhanced spectrometer“. English. In: *Applied Physics B* 107.1, pp. 205–212. ISSN: 0946-2171. DOI: [10.1007/s00340-011-4812-9](https://doi.org/10.1007/s00340-011-4812-9).
- Grilli, R., G. Méjean, S. Kassi, I. Ventrillard, C. Abd-Alrahman, and D. Romanini (2012b). „Frequency Comb Based Spectrometer for in Situ and Real Time Measurements of IO, BrO, NO<sub>2</sub>, and H<sub>2</sub>CO at pptv and ppqv Levels“. In: *Environ. Sci. Technol.* 46.19, pp. 10704–10710. DOI: [10.1021/es301785h](https://doi.org/10.1021/es301785h).
- Großmann, K., U. Frieß, E. Peters, F. Wittrock, J. Lampel, S. Yilmaz, J. Tschirner, R. Sommariva, R. von Glasow, B. Quack, K. Krüger, K. Pfeilsticker, and U. Platt (2013). „Iodine monoxide in the Western Pacific marine boundary layer“. In: *Atmospheric Chemistry and Physics* 13.6, pp. 3363–3378. DOI: [10.5194/acp-13-3363-2013](https://doi.org/10.5194/acp-13-3363-2013). URL: <http://www.atmos-chem-phys.net/13/3363/2013/>.
- Gschwend, P. M., J. K. MacFralane, and K. A. Newman (1985). „Volatile Halogenated Organic Compounds Released to Seawater from Temperate Marine Macroalgae“. In: *Science* 227.4690, pp. 1033–1035. DOI: [10.1126/science.227.4690.1033](https://doi.org/10.1126/science.227.4690.1033).
- Guiry, M. and G. Blunden (1991). *Seaweed resources in Europe: Uses and potential*. John Wiley & Sons Ltd., Chichester.
- Haagen-Smit, A. J. (1952). „Chemistry and Physiology of Los Angeles Smog“. In: *Industrial & Engineering Chemistry* 44.6, pp. 1342–1346. ISSN: 0019-7866. DOI: [10.1021/ie50510a045](https://doi.org/10.1021/ie50510a045).
- Hansen, P. (1987). „The truncated SVD as a method for regularization“. English. In: *BIT Numerical Mathematics* 27.4, pp. 534–553. ISSN: 0006-3835. DOI: [10.1007/BF01937276](https://doi.org/10.1007/BF01937276).
- Harnisch, J. (1999). „Reactive Fluorine Compounds“. English. In: *Reactive Halogen Compounds in the Atmosphere*. Ed. by P. Fabian and O. Singh. Vol. 4E. The Handbook of Environmental Chemistry. Springer Berlin Heidelberg, pp. 81–111. ISBN: 978-3-540-64090-5. DOI: [10.1007/10628761\\_3](https://doi.org/10.1007/10628761_3).
- Hartmann, D., A. Klein Tank, M. Rusticucci, L. Alexander, S. Brönnimann, Y. Charabi, F. Dentener, E. Dlugokencky, D. Easterling, A. Kaplan, B. Soden, P. Thorne, M. Wild, and P. Zhai (2013). „Observations: Atmosphere and Surface“. In: *Climate Change 2013: The Physical Science Basis. Contribution of Working Group I to the Fifth Assessment Report of the Intergovernmental Panel on Climate Change*. Ed. by T. Stocker, D. Qin, G.-K. Plattner, M. Tignor, S. Allen, J. Boschung, A. Nauels, Y. Xia, V. Bex, and P. Midgley. Cambridge, United Kingdom and New York, NY, USA: Cambridge University Press. Chap. 2, pp. 159–254. ISBN: 978-1-107-66182-0. DOI: [10.1017/CBO9781107415324.008](https://doi.org/10.1017/CBO9781107415324.008).

- Hausmann, M. and U. Platt (1994). „Spectroscopic measurement of bromine oxide and ozone in the high Arctic during Polar Sunrise Experiment 1992“. In: *Journal of Geophysical Research: Atmospheres* 99.D12, pp. 25399–25413. DOI: [10.1029/94JD01314](https://doi.org/10.1029/94JD01314).
- Hay, C. H. (1977). „A biological study of *Durvillaea antarctica* (Chamisso) Hariot and *D. Willana Lindauer* in New Zealand“. PhD thesis. University of Canterbury. URL: <http://hdl.handle.net/10092/5690>.
- Hebestreit, K. (2001). „Halogen Oxides in the Mid-Latitudinal Planetary Boundary Layer“. PhD thesis. Heidelberg University.
- Hebestreit, K., J. Stutz, D. Rosen, V. Matveiv, M. Peleg, M. Luria, and U. Platt (1999). „DOAS Measurements of Tropospheric Bromine Oxide in Mid-Latitudes“. In: *Science* 283.5398, pp. 55–57. DOI: [10.1126/science.283.5398.55](https://doi.org/10.1126/science.283.5398.55).
- Herlyn, L. (2015). „Development of a Heatable  $NO_2$ -CE-DOAS Instrument for the Detection of Halogen Nitrates through Thermolysis“. Diplomarbeit. Heidelberg Universität.
- Hermans, C., A. Vandaele, M. Carleer, S. Fally, R. Colin, A. Jenouvrier, B. Coquart, and M.-F. Mérienne (1999). „Absorption cross-sections of atmospheric constituents:  $NO_2$ ,  $O_2$ , and  $H_2O$ “. In: *Environ. Sci. and Pollut. Res.* 6.3. <http://spectrolab.aeronomie.be/o2.htm> Accessed 08/01/2009, pp. 151–158. DOI: [10.1007/BF02987620](https://doi.org/10.1007/BF02987620).
- Hession, C., M. Guiry, S. Mc Garvey, and D. Joyce (1998). *Mapping and Assessment of the Seaweed Resources (*Ascophyllum nodosum*, *Laminaria* spp.) off the West Coast of Ireland*. Tech. rep. Marine Resource Series No.5. Accessed 02/11/2015. Marine Institute. URL: <http://hdl.handle.net/10793/202>.
- Hoffmann, T., C. D. O’Dowd, and J. H. Seinfeld (2001). „Iodine oxide homogeneous nucleation: An explanation for coastal new particle production“. In: *Geophysical Research Letters* 28.10, pp. 1949–1952. ISSN: 1944-8007. DOI: [10.1029/2000GL012399](https://doi.org/10.1029/2000GL012399).
- Högström, U. (1996). „Review of some basic characteristics of the atmospheric surface layer“. In: *Boundary-Layer Meteorology* 78.3-4, pp. 215–246. DOI: [10.1007/BF00120937](https://doi.org/10.1007/BF00120937).
- Holla, R., S. Schmitt, U. Frieß, D. Pöhler, J. Zingler, U. Corsmeier, and U. Platt (2015). „Vertical distribution of BrO in the boundary layer at the Dead Sea“. In: *Environ. Chem.* 12.4, pp. 438–460. DOI: [10.1071/EN14224](https://doi.org/10.1071/EN14224).
- Holland, F., A. Hofzumahaus, J. Schäfer, A. Kraus, and H.-W. Pätz (2003). „Measurements of OH and  $HO_2$  radical concentrations and photolysis frequencies during BERLIOZ“. In: *J. of Geophys. Res.* 108, p. 8246. DOI: [10.1029/2001JD001393](https://doi.org/10.1029/2001JD001393).
- Hollwedel, J., M. Wenig, S. Beirle, S. Kraus, S. Käßahl, W. Wilms-Grabe, U. Platt, and T. Wagner (2004). „Year-to-year variations of spring time polar tropospheric BrO as seen by

- {GOME}“. In: *Advances in Space Research* 34.4. Trace Constituents in the Troposphere and Lower Stratosphere, pp. 804–808. ISSN: 0273-1177. DOI: 10.1016/j.asr.2003.08.060.
- Hönninger, G., N. Bobrowski, E. R. Palenque, R. Torrez, and U. Platt (2004). „Reactive bromine and sulfur emissions at Salar de Uyuni, Bolivia“. In: *Geophysical Research Letters* 31.4. L04101, n/a–n/a. ISSN: 1944-8007. DOI: 10.1029/2003GL018818.
- Hönninger, G. (2002). „Halogen Oxide Studies in the Boundary Layer by Multi Axis Differential Optical Absorption Spectroscopy and Active Longpath-DOAS“. PhD thesis. Heidelberg University. URL: <http://www.ub.uni-heidelberg.de/archiv/1940>.
- Horbanski, M. (2010). „A Compact Resonator Based Instrument for DOAS Measurements of Ambient Nitrogen Dioxide“. Diploma Thesis. Heidelberg University.
- Hou, X., C. Chai, Q. Qian, X. Yan, and X. Fan (1997). „Determination of chemical species of iodine in some seaweeds (I)“. In: *Science of The Total Environment* 204.3, pp. 215–221. ISSN: 0048-9697. DOI: 10.1016/S0048-9697(97)00182-4.
- Huang, R.-J., K. Seitz, J. Buxmann, D. Pöhler, K. E. Hornsby, L. J. Carpenter, U. Platt, and T. Hoffmann (2010a). „In situ measurements of molecular iodine in the marine boundary layer: the link to macroalgae and the implications for O<sub>3</sub>, IO, OIO and NO<sub>x</sub>“. In: *Atmospheric Chemistry and Physics* 10.10, pp. 4823–4833. DOI: 10.5194/acp-10-4823-2010.
- Huang, R.-J., K. Seitz, T. Neary, C. D. O’Dowd, U. Platt, and T. Hoffmann (2010b). „Observations of high concentrations of I<sub>2</sub> and IO in coastal air supporting iodine-oxide driven coastal new particle formation“. In: *Geophysical Research Letters* 37.3, n/a–n/a. ISSN: 1944-8007. DOI: 10.1029/2009GL041467.
- Huang, R.-J., U. R. Thorenz, M. Kundel, D. S. Venables, D. Ceburnis, K. F. Ho, J. Chen, A. L. Vogel, F. C. Küpper, P. P. A. Smyth, U. Nitschke, D. B. Stengel, H. Berresheim, C. D. O’Dowd, and T. Hoffmann (2013). „The seaweeds *Fucus vesiculosus* and *Ascophyllum nodosum* are significant contributors to coastal iodine emissions“. In: *Atmospheric Chemistry and Physics* 13.10, pp. 5255–5264. DOI: 10.5194/acp-13-5255-2013.
- Hulst, H. C. v. d. (1981). *Light scattering by small particles*. Reprint. Dover Publications Inc.
- Ingham, T., M. Cameron, and J. N. Crowley (2000). „Photodissociation of IO (355 nm) and OIO (532 nm): Quantum Yields for O(<sup>3</sup>P) and I(<sup>2</sup>P<sub>J</sub>) Production“. In: *The Journal of Physical Chemistry A* 104.34, pp. 8001–8010. DOI: 10.1021/jp001166p.
- Irish Seaweed Center (2001). *Connemara Seaweed Survey*. National University of Ireland, Galway, Internal report, pp. 1–44.
- Jimenez, J. L., R. Bahreini, D. R. Cocker, H. Zhuang, V. Varutbangkul, R. C. Flagan, J. H. Seinfeld, C. D. O’Dowd, and T. Hoffmann (2003). „New particle formation from photooxidation

- of diiodomethane (CH<sub>2</sub>I<sub>2</sub>)“. In: *Journal of Geophysical Research: Atmospheres* 108.D10. ISSN: 2156-2202. DOI: [10.1029/2002JD002452](https://doi.org/10.1029/2002JD002452).
- Jones, C. E., K. E. Hornsby, R. Sommariva, R. M. Dunk, R. von Glasow, G. McFiggans, and L. J. Carpenter (2010). „Quantifying the contribution of marine organic gases to atmospheric iodine“. In: *Geophysical Research Letters* 37.18. L18804, n/a–n/a. ISSN: 1944-8007. DOI: [10.1029/2010GL043990](https://doi.org/10.1029/2010GL043990).
- Joseph, D. M., S. H. Ashworth, and J. M. C. Plane (2007). „On the photochemistry of IONO<sub>2</sub> : absorption cross section (240-370 nm) and photolysis product yields at 248 nm“. In: *Phys. Chem. Chem. Phys.* 9 (41), pp. 5599–5607. DOI: [10.1039/B709465E](https://doi.org/10.1039/B709465E).
- Junkermann, W., U. Platt, and A. Volz-Thomas (1989). „A photoelectric detector for the measurement of photolysis frequencies of ozone and other atmospheric molecules“. English. In: *Journal of Atmospheric Chemistry* 8.3, pp. 203–227. DOI: [10.1007/BF00051494](https://doi.org/10.1007/BF00051494).
- Kaltsoyannis, N. and J. M. C. Plane (2008). „Quantum chemical calculations on a selection of iodine-containing species (IO, OIO, IONO<sub>2</sub>, (IO)<sub>2</sub>, I<sub>2</sub>O<sub>3</sub>, I<sub>2</sub>O<sub>4</sub> and I<sub>2</sub>O<sub>5</sub>) of importance in the atmosphere“. In: *Phys. Chem. Chem. Phys.* 10 (13), pp. 1723–1733. DOI: [10.1039/B715687C](https://doi.org/10.1039/B715687C).
- Kanatschnig, F. (2014). „Optimierung eines NO<sub>2</sub> -CE-DOAS Messinstruments und mobile in situ Messung in einem städtischen Gebiet“. Bachelorarbeit. Heidelberg University.
- Kelly, E. (2005). *The role of kelp in the marine environment*. Irish Wildlife Manuals 17. National Parks, Wildlife Service, Department of Environment, Heritage, and Local Government, Dublin, Ireland. URL: <http://www.npws.ie/sites/default/files/publications/pdf/IWM17.pdf>.
- Kiehl, J. T., T. L. Schneider, P. J. Rasch, M. C. Barth, and J. Wong (2000). „Radiative forcing due to sulfate aerosols from simulations with the National Center for Atmospheric Research Community Climate Model, Version 3“. In: *Journal of Geophysical Research: Atmospheres* 105.D1, pp. 1441–1457. DOI: [10.1029/1999JD900495](https://doi.org/10.1029/1999JD900495).
- Kraus, S. (2006). „DOASIS - A Framework Design for DOAS“. URL <https://doasis.iup.uni-heidelberg.de/bugtracker/projects/doasis/index.php>. PhD thesis. Heidelberg University.
- Kreher, K., P. V. Johnston, S. W. Wood, B. Nardi, and U. Platt (1997). „Ground-based measurements of tropospheric and stratospheric BrO at Arrival Heights, Antarctica“. In: *Geophysical Research Letters* 24.23, pp. 3021–3024. DOI: [10.1029/97GL02997](https://doi.org/10.1029/97GL02997).
- Kundel, M., U. Thorenz, J. Petersen, R.-J. Huang, N. Bings, and T. Hoffmann (2012). „Application of mass spectrometric techniques for the trace analysis of short-lived iodine-containing volatiles emitted by seaweed“. English. In: *Analytical and Bioanalytical Chemistry* 402.10, pp. 3345–3357. DOI: [10.1007/s00216-011-5658-z](https://doi.org/10.1007/s00216-011-5658-z).
- Küpper F. Cpper, F. C., N. Schweigert, E. Ar Gall, J.-M. Legendre, H. Vilter, and B. Kloareg (1998). „Iodine uptake in Laminariales involves extracellular, haloperoxidase-

- mediated oxidation of iodide“. English. In: *Planta* 207.2, pp. 163–171. ISSN: 0032-0935. DOI: 10.1007/s004250050469.
- Küpper, F. C., L. J. Carpenter, G. B. McFiggans, C. J. Palmer, T. J. Waite, E.-M. Boneberg, S. Woitsch, M. Weiller, R. Abela, D. Grolimund, P. Potin, A. Butler, G. W. Luther, P. M. H. Kroneck, W. Meyer-Klaucke, and M. C. Feiters (2008). „Iodide accumulation provides kelp with an inorganic antioxidant impacting atmospheric chemistry“. In: *Proceedings of the National Academy of Sciences* 105.19, pp. 6954–6958. DOI: 10.1073/pnas.0709959105.
- Lampel, J., D. Pöhler, J. Tschritter, U. Frieß, and U. Platt (2015). „On the relative absorption strengths of water vapour in the blue wavelength range“. In: *Atmospheric Measurement Techniques* 8.10, pp. 4329–4346. DOI: 10.5194/amt-8-4329-2015.
- Lampel, J. (2010). „Ship-borne MAX-DOAS measurements of tropospheric halogen oxides on Atlantic transects“. Diplomarbeit. Heidelberg University.
- Lampel, J. (2014). „Measurements of reactive trace gases in the marine boundary layer using novel DOAS methods.“ PhD thesis. Heidelberg University. URL: <http://www.ub.uni-heidelberg.de/archiv/17394>.
- Landwehr, S. (2010). „Design of a compact Long Path DOAS instrument based on fiber-optics.“ Diploma Thesis. Heidelberg University.
- Laszlo, B., M. J. Kurylo, and R. E. Huie (1995). „Absorption cross sections, kinetics of formation, and self-reaction of the IO radical produced via the laser photolysis of N<sub>2</sub>O/I<sub>2</sub>/N<sub>2</sub> mixtures“. In: *The Journal of Physical Chemistry* 99.30, pp. 11701–11707. DOI: 10.1021/j100030a013.
- Laternus, F., B. Giese, C. Wiencke, and F. C. Adams (2000). „Low-molecular-weight organoiodine and organobromine compounds released by polar macroalgae“ The influence of abiotic factors“. English. In: *Fresenius' Journal of Analytical Chemistry* 368.2-3, pp. 297–302. ISSN: 0937-0633. DOI: 10.1007/s002160000491.
- Lawrence, M. G., P. Jöckel, and R. von Kuhlmann (2001). „What does the global mean OH concentration tell us?“ In: *Atmospheric Chemistry and Physics* 1.1, pp. 37–49. DOI: 10.5194/acp-1-37-2001.
- Lee, R. E. (2008). *Phycology*. 4th ed. Cambridge, New York, Melbourne, Madrid, Cape Town, Singapore, São Paulo: Cambridge University Press. ISBN: 978-0-521-86408-4.
- Leighton, P. (1961). *Photochemistry of air pollution*. New York: Academic Press. ISBN: 9780124333345.
- Lelieveld, J., F. J. Dentener, W. Peters, and M. C. Krol (2004). „On the role of hydroxyl radicals in the self-cleansing capacity of the troposphere“. In: *Atmospheric Chemistry and Physics* 4.9/10, pp. 2337–2344. DOI: 10.5194/acp-4-2337-2004.

- Lelieveld, J., W. Peters, F. J. Dentener, and M. C. Krol (2002). „Stability of tropospheric hydroxyl chemistry“. In: *Journal of Geophysical Research: Atmospheres* 107.D23. 4715, doi: 10.1029/2002JD002272.
- Leser, H., G. Hönninger, and U. Platt (2003). „MAX-DOAS measurements of BrO and NO<sub>2</sub> in the marine boundary layer“. In: *Geophysical Research Letters* 30.10, n/a–n/a. doi: 10.1029/2002GL015811.
- Levenberg, K. (1944). „A method for the solution of certain non-linear problems in least squares.“ In: *Quart. Appl. Math.* 2, pp. 164–168.
- Levy, H. (1971). „Normal Atmosphere: Large Radical and Formaldehyde Concentrations Predicted“. In: *Science* 173.3992, pp. 141–143. doi: 10.1126/science.173.3992.141.
- Little, C. and J. A. Kitching (1996). *The Biology of Rocky Shores*. Oxford University Press.
- Mahajan, A. S., J. C. Gómez Martín, T. D. Hay, S.-J. Royer, S. Yvon-Lewis, Y. Liu, L. Hu, C. Prados-Roman, C. Ordóñez, J. M. C. Plane, and A. Saiz-Lopez (2012). „Latitudinal distribution of reactive iodine in the Eastern Pacific and its link to open ocean sources“. In: *Atmospheric Chemistry and Physics* 12.23, pp. 11609–11617. doi: 10.5194/acp-12-11609-2012.
- Mahajan, A. S., J. M. C. Plane, H. Oetjen, L. Mendes, R. W. Saunders, A. Saiz-Lopez, C. E. Jones, L. J. Carpenter, and G. B. McFiggans (2010a). „Measurement and modelling of tropospheric reactive halogen species over the tropical Atlantic Ocean“. In: *Atmospheric Chemistry and Physics* 10.10, pp. 4611–4624. doi: 10.5194/acp-10-4611-2010.
- Mahajan, A. S., H. Oetjen, A. Saiz-Lopez, J. D. Lee, G. B. McFiggans, and J. M. C. Plane (2009). „Reactive iodine species in a semi-polluted environment“. In: *Geophysical Research Letters* 36.16, p. L16803. doi: 10.1029/2009GL038018.
- Mahajan, A. S., M. Shaw, H. Oetjen, K. E. Hornsby, L. J. Carpenter, L. Kaleschke, X. Tian-Kunze, J. D. Lee, S. J. Moller, P. Edwards, R. Commane, T. Ingham, D. E. Heard, and J. M. C. Plane (2010b). „Evidence of reactive iodine chemistry in the Arctic boundary layer“. In: *Journal of Geophysical Research: Atmospheres* 115.D20. D20303, n/a–n/a. ISSN: 2156-2202. doi: 10.1029/2009JD013665.
- Mäkelä J. M., J. M., T. Hoffmann, C. Holzke, M. Väkevä, T. Suni, T. Mattila, P. P. Aalto, U. Tapper, E. I. Kauppinen, and C. D. O’Dowd (2002). „Biogenic iodine emissions and identification of end-products in coastal ultrafine particles during nucleation bursts“. In: *Journal of Geophysical Research: Atmospheres* 107.D19. 8110, ISSN: 2156-2202. doi: 10.1029/2001JD000580.
- Mandelbrot, B. (1967). „How Long Is the Coast of Britain? Statistical Self-Similarity and Fractional Dimension“. In: *Science* 156.3775, pp. 636–638. doi: 10.1126/science.156.3775.636.

- Manley, S. L. and M. N. Dastoor (1987). „Methyl halide (CH<sub>3</sub>X) production from the giant kelp, *Macrocystis*, and estimates of global CH<sub>3</sub>X production by kelp1“. In: *Limnology and Oceanography* 32.3, pp. 709–715. ISSN: 1939-5590. DOI: [10.4319/lo.1987.32.3.0709](https://doi.org/10.4319/lo.1987.32.3.0709).
- Mann, K. (1972). „Ecological energetics of the seaweed zone in a marine bay on the Atlantic coast of Canada. I. Zonation and biomass of seaweeds“. English. In: *Marine Biology* 12.1, pp. 1–10. ISSN: 0025-3162.
- Martin, M., D. Pöhler, K. Seitz, R. Sinreich, and U. Platt (2009). „BrO measurements over the Eastern North-Atlantic“. In: *Atmospheric Chemistry and Physics* 9.24, pp. 9545–9554. DOI: [10.5194/acp-9-9545-2009](https://doi.org/10.5194/acp-9-9545-2009).
- McCartney, M., G. Abernethy, and L. Gault (2010). „The Divider Dimensions of the Irish Coast“. In: *Irish Geography* 43.3, pp. 277–284. DOI: [10.1080/00750778.2011.582632](https://doi.org/10.1080/00750778.2011.582632).
- McElroy, M. B., R. J. Salawitch, S. C. Wofsy, and J. A. Logan (1986). „Reductions of Antarctic ozone due to synergistic interactions of chlorine and bromine“. In: *Nature* 321.6072, pp. 759–762. DOI: [10.1038/321759a0](https://doi.org/10.1038/321759a0).
- McFiggans, G., C. S. E. Bale, S. M. Ball, J. M. Beames, W. J. Bloss, L. J. Carpenter, J. Dorsey, R. Dunk, M. J. Flynn, K. L. Furneaux, M. W. Gallagher, D. E. Heard, A. M. Hollingsworth, K. Hornsby, T. Ingham, C. E. Jones, R. L. Jones, L. J. Kramer, J. M. Langridge, C. Leblanc, J.-P. LeCrane, J. D. Lee, R. J. Leigh, I. Longley, A. S. Mahajan, P. S. Monks, H. Oetjen, A. J. Orr-Ewing, J. M. C. Plane, P. Potin, A. J. L. Shillings, F. Thomas, R. von Glasow, R. Wada, L. K. Whalley, and J. D. Whitehead (2010). „Iodine-mediated coastal particle formation: an overview of the Reactive Halogens in the Marine Boundary Layer (RHAMBLe) Roscoff coastal study“. In: *Atmospheric Chemistry and Physics* 10.6, pp. 2975–2999. DOI: [10.5194/acp-10-2975-2010](https://doi.org/10.5194/acp-10-2975-2010).
- McFiggans, G., H. Coe, R. Burgess, J. Allan, M. Cubison, M. R. Alfarra, R. Saunders, A. Saiz-Lopez, J. M. C. Plane, D. Wevill, L. Carpenter, A. R. Rickard, and P. S. Monks (2004). „Direct evidence for coastal iodine particles from *Laminaria* macroalgae – linkage to emissions of molecular iodine“. In: *Atmospheric Chemistry and Physics* 4.3, pp. 701–713. DOI: [10.5194/acp-4-701-2004](https://doi.org/10.5194/acp-4-701-2004).
- McFiggans, G., J. M. C. Plane, B. J. Allan, L. J. Carpenter, H. Coe, and C. O’Dowd (2000). „A modeling study of iodine chemistry in the marine boundary layer“. In: *Journal of Geophysical Research: Atmospheres* 105.D11, pp. 14371–14385. ISSN: 2156-2202. DOI: [10.1029/1999JD901187](https://doi.org/10.1029/1999JD901187).
- Meinen, J. (2007). „Design and Assembling of a Broadband Cavity Ringdown and Cavity Enhanced Absorption Spectrometer using Light Emitting Diodes“. Diplomarbeit. Heidelberg University.

- Meller, R. and G. K. Moortgat (2000). „Temperature dependence of the absorption cross sections of formaldehyde between 223 and 323 K in the wavelength range 225–375 nm“. In: *Journal of Geophysical Research: Atmospheres* 105.D6, pp. 7089–7101. DOI: [10.1029/1999JD901074](https://doi.org/10.1029/1999JD901074).
- Merten, A. (2008). „Neues Design von Langpfad-DOAS-Instrumenten basierend auf Faseroptiken und Anwendung der Untersuchung der urbanen Atmosphäre“. PhD thesis. Universität Heidelberg. URL: <http://www.ub.uni-heidelberg.de/archiv/8499>.
- Michanek, G. (1975). *Seaweed resources of the ocean*. Tech. Pap. 130. 127 pp. FAO Fish.Circ.
- Molina, M. J. and F. S. Rowland (1974). „Stratospheric sink for chlorofluoromethanes: chlorine atom-catalysed destruction of ozone“. In: *Nature* 249.5460, pp. 810–812. DOI: [10.1038/249810a0](https://doi.org/10.1038/249810a0).
- Monks, P. S. (2005). „Gas-phase radical chemistry in the troposphere“. In: *Chem. Soc. Rev.* 34 (5), pp. 376–395. DOI: [10.1039/B307982C](https://doi.org/10.1039/B307982C).
- Morrissey, J., S. Kraan, and M. Guiry (2001). *A Guide to Commercially Important Seaweeds on the Irish Coast*. Tech. rep. Accessed 02/11/2015. Bord Iascaigh Mhara/Irish Sea Fisheries Board, Dun Laoghaire, Co Dublin, Ireland. URL: [http://www.nuigalway.ie/research/seaweed\\_centre/documents/a\\_guide\\_to\\_commercially\\_important\\_seaweeds\\_isc.zip](http://www.nuigalway.ie/research/seaweed_centre/documents/a_guide_to_commercially_important_seaweeds_isc.zip).
- Morrissey, J. and J. L. Sumich (2011). *Introduction to the Biology of Marine Life*. Jones and Bartlett Learning, Sudbury, Mississauga, London.
- Mössinger, J. C., D. M. Rowley, and R. A. Cox (2002). „The UV-visible absorption cross-sections of IONO<sub>2</sub>“. In: *Atmospheric Chemistry and Physics* 2.3, pp. 227–234. DOI: [10.5194/acp-2-227-2002](https://doi.org/10.5194/acp-2-227-2002).
- Mössinger, J. C., D. E. Shallcross, and R. A. Cox (1998). „UV-VIS absorption cross-sections and atmospheric lifetimes of CH<sub>2</sub>Br<sub>2</sub>, CH<sub>2</sub>I<sub>2</sub> and CH<sub>2</sub>BrI“. In: *J. Chem. Soc., Faraday Trans.* 94 (10), pp. 1391–1396. DOI: [10.1039/A709160E](https://doi.org/10.1039/A709160E).
- Naylor, J. (1976). *PRODUCTION, TRADE AND UTILIZATION OF SEaweEDS AND SEAWEED PRODUCTS*. Tech. Pap. 159. FAO Fisheries.
- Netten, C. van, S. H. Cann, D. Morley, and J. van Netten (2000). „Elemental and radioactive analysis of commercially available seaweed“. In: *Science of The Total Environment* 255.1â€“3, pp. 169–175. ISSN: 0048-9697. DOI: [10.1016/S0048-9697\(00\)00467-8](https://doi.org/10.1016/S0048-9697(00)00467-8).
- Newman, S. M., W. H. Howie, I. C. Lane, M. R. Upson, and A. J. Orr-Ewing (1998). „Predissociation of the A<sup>2</sup>Pi<sub>3/2</sub> state of IO studied by cavity ring-down spectroscopy“. In: *J. Chem. Soc., Faraday Trans.* 94 (18), pp. 2681–2688. DOI: [10.1039/A805103H](https://doi.org/10.1039/A805103H).

- Nightingale, P. D., G. Malin, and P. S. Liss (1995). „Production of chloroform and other low molecular-weight halocarbons by some species of macroalgae“. In: *Limnology and Oceanography* 40.4, pp. 680–689. DOI: [10.4319/lo.1995.40.4.0680](https://doi.org/10.4319/lo.1995.40.4.0680).
- NIST (2010). *CODATA Internationally recommended values of the Fundamental Physical Constants*. accessed 2014-03-25. URL: <http://physics.nist.gov/cuu/Constants/>.
- Nitschke, U., A. Ruth, S. Dixneuf, and D. Stengel (2011). „Molecular iodine emission rates and photosynthetic performance of different thallus parts of *Laminaria digitata* (Phaeophyceae) during emersion“. In: *Planta* 233.4, pp. 737–748. DOI: [10.1007/s00425-010-1334-3](https://doi.org/10.1007/s00425-010-1334-3).
- Noxon, J. F. (1975). „Nitrogen Dioxide in the Stratosphere and Troposphere Measured by Ground-Based Absorption Spectroscopy“. In: *Science* 189.4202, pp. 547–549. DOI: [10.1126/science.189.4202.547](https://doi.org/10.1126/science.189.4202.547).
- O’Dowd, C. D., K. Hämeri, J. M. Mäkelä, L. Pirjola, M. Kulmala, S. G. Jennings, H. Berresheim, H.-C. Hansson, G. de Leeuw, G. J. Kunz, A. G. Allen, C. N. Hewitt, A. Jackson, Y. Viisanen, and T. Hoffmann (2002a). „A dedicated study of New Particle Formation and Fate in the Coastal Environment (PARFORCE): Overview of objectives and achievements“. In: *Journal of Geophysical Research: Atmospheres* 107.D19. 8108, DOI: [10.1029/2001JD000555](https://doi.org/10.1029/2001JD000555).
- O’Dowd, C. D., J. L. Jimenez, R. Bahreini, R. C. Flagan, J. H. Seinfeld, K. Hämeri, L. Pirjola, M. Kulmala, S. G. Jennings, and T. Hoffmann (2002b). „Marine aerosol formation from biogenic iodine emissions“. In: *Nature* 417.6889, pp. 632–636. DOI: [10.1038/nature00775](https://doi.org/10.1038/nature00775).
- O’Keefe, A. and D. A. G. Deacon (1988). „Cavity ring-down optical spectrometer for absorption measurements using pulsed laser sources“. In: *Rev. Sci. Instrum.* 59, p. 2544. DOI: [10.1063/1.1139895](https://doi.org/10.1063/1.1139895).
- Oswald, R., T. Behrendt, M. Ermel, D. Wu, H. Su, Y. Cheng, C. Breuninger, A. Moravek, E. Mougin, C. Delon, B. Loubet, A. Pommerening-Röser, M. Sörgel, U. Pöschl, T. Hoffmann, M. Andreae, F. Meixner, and I. Trebs (2013). „HONO Emissions from Soil Bacteria as a Major Source of Atmospheric Reactive Nitrogen“. In: *Science* 341.6151, pp. 1233–1235. DOI: [10.1126/science.1242266](https://doi.org/10.1126/science.1242266).
- Palmer, C. J., T. L. Anders, L. J. Carpenter, F. C. Küpper, and G. B. McFiggans (2005). „Iodine and Halocarbon Response of *Laminaria digitata* to Oxidative Stress and Links to Atmospheric New Particle Production“. In: *Environ. Chem.* 2.4, pp. 282–290. DOI: [10.1071/EN05078](https://doi.org/10.1071/EN05078).
- Parsons, M. J. (1978). „Marginariella, a genus of brown seaweeds found only in New Zealand“. In: *Canterbury Botanical Society*.
- Pechtl, S., E. R. Lovejoy, J. B. Burkholder, and R. von Glasow (2006). „Modeling the possible role of iodine oxides in atmospheric new particle formation“. In: *Atmospheric Chemistry and Physics* 6.2, pp. 505–523. DOI: [10.5194/acp-6-505-2006](https://doi.org/10.5194/acp-6-505-2006).

- Perner, D., D. H. Ehhalt, H. W. Pätz, U. Platt, E. P. Röth, and A. Volz (1976). „OH - Radicals in the lower troposphere“. In: *Geophysical Research Letters* 3.8, pp. 466–468. doi: [10.1029/GL003i008p00466](https://doi.org/10.1029/GL003i008p00466).
- Peters, C., S. Pechtl, J. Stutz, K. Hebestreit, G. Hönninger, K. G. Heumann, A. Schwarz, J. Winterlik, and U. Platt (2005). „Reactive and organic halogen species in three different European coastal environments“. In: *Atmospheric Chemistry and Physics* 5.12, pp. 3357–3375. doi: [10.5194/acp-5-3357-2005](https://doi.org/10.5194/acp-5-3357-2005).
- Peters, C. (2005). „Studies of Reactive Halogen Species (RHS) in the Marine and mid-Latitudinal Boundary Layer by Active Longpath Differential Optical Absorption Spectroscopy“. PhD thesis. Heidelberg University.
- Platt, U. and G. Hönninger (2003). „The role of halogen species in the troposphere“. In: *Chemosphere* 52.2. Naturally Produced Organohalogens, pp. 325–338. issn: 0045-6535. doi: [10.1016/S0045-6535\(03\)00216-9](https://doi.org/10.1016/S0045-6535(03)00216-9).
- Platt, U. and E. Lehrer (1997). *Arctic Tropospheric Ozone Chemistry, ARCTOC, Final Report of the EU-Project No. EV5V-CT93-0318, Heidelberg*.
- Platt, U. and T. Wagner (1998). „Satellite mapping of enhanced BrO concentrations in the troposphere“. In: *Nature* 395.6701, pp. 486–490. issn: 0028-0836. doi: [10.1038/26723](https://doi.org/10.1038/26723).
- Platt, U. and C. Janssen (1995). „Observation and role of the free radicals NO<sub>3</sub>, ClO, BrO and IO in the troposphere“. In: *Faraday Discuss.* 100, pp. 175–198. doi: [10.1039/FD9950000175](https://doi.org/10.1039/FD9950000175).
- Platt, U., J. Meinen, D. Pöhler, and T. Leisner (2009). „Broadband Cavity Enhanced Differential Optical Absorption Spectroscopy (CE-DOAS) - applicability and corrections“. In: *Atmos. Meas. Tech.* 2, pp. 713–723.
- Platt, U., D. Perner, and H. Pätz (1979). „Simultaneous measurements of atmospheric CH<sub>2</sub>O, O<sub>3</sub> and NO<sub>2</sub> by differential optical absorption“. In: *J. Geophys. Res.* 84, pp. 6329–6335. doi: [10.1029/JC084iC10p06329](https://doi.org/10.1029/JC084iC10p06329).
- Platt, U. and J. Stutz (2008). *Differential Optical Absorption Spectroscopy - Principles and Application*. 1. Heidelberg, Germany: Springer. doi: [10.1007/978-3-540-75776-4](https://doi.org/10.1007/978-3-540-75776-4).
- Pöhler, D., L. Vogel, U. Frieß, and U. Platt (2010). „Observation of halogen species in the Amundsen Gulf, Arctic, by active long-path differential optical absorption spectroscopy“. In: *Proceedings of the National Academy of Sciences* 107.15, pp. 6582–6587. doi: [10.1073/pnas.0912231107](https://doi.org/10.1073/pnas.0912231107).
- Pollack, S. A. (1966). „Angular Dependence of Transmission Characteristics of Interference Filters and Application to a Tunable Fluorometer“. In: *Appl. Opt.* 5.11, pp. 1749–1756. doi: [10.1364/AO.5.001749](https://doi.org/10.1364/AO.5.001749).

- Press, W., B. Flannery, S. Teukolsky, and W. Vetterling (1992). *Numerical Recipes in FORTRAN*. Cambridge University Press.
- Puenteadura, O., M. Gil, A. Saiz-Lopez, T. Hay, M. Navarro-Comas, A. Gómez-Pelaez, E. Cuevas, J. Iglesias, and L. Gomez (2012). „Iodine monoxide in the north subtropical free troposphere“. In: *Atmospheric Chemistry and Physics* 12.11, pp. 4909–4921. DOI: [10.5194/acp-12-4909-2012](https://doi.org/10.5194/acp-12-4909-2012).
- Rattigan, O. V., D. E. Shallcross, and R. A. Cox (1997). „UV absorption cross-sections and atmospheric photolysis rates of CF<sub>3</sub>I, CH<sub>3</sub>I, C<sub>2</sub>H<sub>5</sub>I and CH<sub>2</sub>ICl“. In: *J. Chem. Soc. Faraday Trans.* 93 (16), pp. 2839–2846. DOI: [10.1039/A701529A](https://doi.org/10.1039/A701529A).
- Rayleigh, L. (1899). „On the transmission of light through an atmosphere containing many small particles in suspension, and on the origin of the blue of the sky“. In: *Phil. Mag.* 47.287, pp. 375–384. DOI: [10.1080/14786449908621276](https://doi.org/10.1080/14786449908621276).
- Read, K. A., A. S. Mahajan, L. J. Carpenter, M. J. Evans, B. V. E. Faria, D. E. Heard, J. R. Hopkins, J. D. Lee, S. J. Moller, A. C. Lewis, L. Mendes, J. B. McQuaid, H. Oetjen, A. Saiz-Lopez, M. J. Pilling, and J. M. C. Plane (2008). „Extensive halogen-mediated ozone destruction over the tropical Atlantic Ocean“. In: *Nature* 453.7199, pp. 1232–1235. DOI: [10.1038/nature07035](https://doi.org/10.1038/nature07035).
- Reed, D. C. and M. A. Brzezinski (2009). „Kelp Forests“. In: *The management of natural coastal carbon sinks*. Ed. by G. Laffoley D.d'A. & Grimsditch. IUCN, Gland, Switzerland, pp. 31–37. ISBN: 978-2-8317-1205-5. URL: <https://portals.iucn.org/library/sites/library/files/documents/2009-038.pdf>.
- Richardson, W. H. (1972). „Bayesian-Based Iterative Method of Image Restoration“. In: *J. Opt. Soc. Am.* 62.1, pp. 55–59. DOI: [10.1364/JOSA.62.000055](https://doi.org/10.1364/JOSA.62.000055).
- Richter, A., F. Wittrock, M. Eisinger, and J. P. Burrows (1998). „GOME observations of tropospheric BrO in northern hemispheric spring and summer 1997“. In: *Geophysical Research Letters* 25.14, pp. 2683–2686. ISSN: 1944-8007. DOI: [10.1029/98GL52016](https://doi.org/10.1029/98GL52016).
- Richter, U. and D. W. R. Wallace (2004). „Production of methyl iodide in the tropical Atlantic Ocean“. In: *Geophysical Research Letters* 31.23. L23S03, n/a–n/a. ISSN: 1944-8007. DOI: [10.1029/2004GL020779](https://doi.org/10.1029/2004GL020779).
- Roedel, W. (2000). *Physik unserer Umwelt - Die Atmosphäre*. 3. Heidelberg, Germany: Springer.
- Rosenfeld, D., U. Lohmann, G. B. Raga, C. D. O'Dowd, M. Kulmala, S. Fuzzi, A. Reissell, and M. O. Andreae (2008). „Flood or Drought: How Do Aerosols Affect Precipitation?“ In: *Science* 321.5894, pp. 1309–1313. DOI: [10.1126/science.1160606](https://doi.org/10.1126/science.1160606).
- Rothman, L., I. Gordon, Y. Babikov, A. Barbe, D. C. Benner, P. Bernath, M. Birk, L. Bizzocchi, V. Boudon, L. Brown, A. Campargue, K. Chance, E. Cohen, L. Coudert, V. Devi, B. Drouin,

- A. Fayt, J.-M. Flaud, R. Gamache, J. Harrison, J.-M. Hartmann, C. Hill, J. Hodges, D. Jacquemart, A. Jolly, J. Lamouroux, R. L. Roy, G. Li, D. Long, O. Lyulin, C. Mackie, S. Massie, S. Mikhailenko, H. Müller, O. Naumenko, A. Nikitin, J. Orphal, V. Perevalov, A. Perrin, E. Polovtseva, C. Richard, M. Smith, E. Starikova, K. Sung, S. Tashkun, J. Tennyson, G. Toon, V. Tyuterev, and G. Wagner (2013). „The {HITRAN2012} molecular spectroscopic database“. In: *Journal of Quantitative Spectroscopy and Radiative Transfer* 130. {HITRAN2012} special issue, pp. 4–50. DOI: [10.1016/j.jqsrt.2013.07.002](https://doi.org/10.1016/j.jqsrt.2013.07.002).
- Rothman, L., I. Gordon, R. Barber, H. Dothe, R. Gamache, A. Goldman, V. Perevalov, S. Tashkun, and J. Tennyson (2010). „HITEMP, the high-temperature molecular spectroscopic database“. In: *Journal of Quantitative Spectroscopy and Radiative Transfer* 111.15, pp. 2139–2150. DOI: [10.1016/j.jqsrt.2010.05.001](https://doi.org/10.1016/j.jqsrt.2010.05.001).
- Saenko, G., Y. Kravtsova, V. Ivanenko, and S. Sheludko (1978). „Concentration of Iodine and bromine by plants in the seas of Japan and Okhotsk“. English. In: *Marine Biology* 47.3, pp. 243–250. ISSN: 0025-3162. DOI: [10.1007/BF00541002](https://doi.org/10.1007/BF00541002).
- Saiz-Lopez, A., R. W. Saunders, D. M. Joseph, S. H. Ashworth, and J. M. C. Plane (2004). „Absolute absorption cross-section and photolysis rate of I<sub>2</sub>“. In: *Atmospheric Chemistry and Physics* 4.5, pp. 1443–1450. DOI: [10.5194/acp-4-1443-2004](https://doi.org/10.5194/acp-4-1443-2004).
- Saiz-Lopez, A., J. A. Shillito, H. Coe, and J. M. C. Plane (2006). „Measurements and modelling of I<sub>2</sub>, IO, OIO, BrO and NO<sub>3</sub> in the mid-latitude marine boundary layer“. In: *Atmospheric Chemistry and Physics* 6.6, pp. 1513–1528. DOI: [10.5194/acp-6-1513-2006](https://doi.org/10.5194/acp-6-1513-2006).
- Saiz-Lopez, A., A. S. Mahajan, R. A. Salmon, S. J.-B. Bauguitte, A. E. Jones, H. K. Roscoe, and J. M. C. Plane (2007). „Boundary Layer Halogens in Coastal Antarctica“. In: *Science* 317.5836, pp. 348–351. DOI: [10.1126/science.1141408](https://doi.org/10.1126/science.1141408).
- Saiz-Lopez, A. and J. M. C. Plane (2004). „Novel iodine chemistry in the marine boundary layer“. In: *Geophysical Research Letters* 31.4, p. L04112. DOI: [10.1029/2003GL019215](https://doi.org/10.1029/2003GL019215).
- Saiz-Lopez, A., J. M. C. Plane, A. R. Baker, L. J. Carpenter, R. von Glasow, J. C. Gómez Martín, and R. W. Saunders (2012). „Atmospheric Chemistry of Iodine“. In: *Chemical Reviews* 112.3, pp. 1773–1804. DOI: [10.1021/cr200029u](https://doi.org/10.1021/cr200029u).
- Saleh, B. E. A. and M. C. Teich (1991). *Fundamentals of Photonics*. New York: John Wiley & Sons, Inc. DOI: [10.1021/j100083a015](https://doi.org/10.1021/j100083a015).
- Sander, R., Y. Rudich, R. von Glasow, and P. J. Crutzen (1999). „The role of BrNO<sub>3</sub> in marine tropospheric chemistry: A model study“. In: *Geophysical Research Letters* 26.18, pp. 2857–2860. ISSN: 1944-8007. DOI: [10.1029/1999GL900478](https://doi.org/10.1029/1999GL900478).
- Sander, S. P., J. Abbatt, J. R. Barker, J. B. Burkholder, R. R. Friedl, D. M. Golden, R. E. Huie, C. E. Kolb, M. J. Kurylo, G., K. Moortgat, V. L. Orkin, and P. H. Wine (2011). „Chemical

- Kinetics and Photochemical Data for Use in Atmospheric Studies, Evaluation No. 17“. In: *JPL Publication 10-6, Jet Propulsion Laboratory, Pasadena*. URL: <http://jpldataeval.jpl.nasa.gov>.
- Sanders, C. L. (1972). „Accurate Measurements of and Corrections for Nonlinearities in Radiometers“. In: *J. Res. Nat. Bur. Stand.* 76A, pp. 437–453.
- Santelices, B. (2007). „The discovery of kelp forests in deep-water habitats of tropical regions“. In: *Proceedings of the National Academy of Sciences* 104.49, pp. 19163–19164. DOI: [10.1073/pnas.0708963104](https://doi.org/10.1073/pnas.0708963104).
- Saunders, R. W., R. Kumar, J. C. G. Martín, A. S. Mahajan, B. J. Murray, and J. M. C. Plane (2010). „Studies of the Formation and Growth of Aerosol from Molecular Iodine Precursor“. In: *Z. Phys. Chem. (Munich)* 224.7-8, pp. 1095–1117. DOI: [10.1524/zpch.2010.6143](https://doi.org/10.1524/zpch.2010.6143).
- Saunders, R. W. and J. M. C. Plane (2005). „Formation Pathways and Composition of Iodine Oxide Ultra-Fine Particles“. In: *Environ. Chem.* 2.4, pp. 299–303. DOI: [10.1071/EN05079](https://doi.org/10.1071/EN05079).
- Schiel, D. R. and M. F. Foster (1986). „The structure of subtidal algal stands in temperate waters“. In: *Oceanography And Marine Biology*.
- Schmitt, S. (2011). „A compact long path DOAS instrument based on fibre-optics and LEDs“. Diploma Thesis. Heidelberg University.
- Schönhardt, A., A. Richter, F. Wittrock, H. Kirk, H. Oetjen, H. K. Roscoe, and J. P. Burrows (2008). „Observations of iodine monoxide columns from satellite“. In: *Atmospheric Chemistry and Physics* 8.3, pp. 637–653. DOI: [10.5194/acp-8-637-2008](https://doi.org/10.5194/acp-8-637-2008).
- Schroeder, W. H., K. G. Anlauf, L. A. Barrie, J. Y. Lu, A. Steffen, D. R. Schneeberger, and T. Berg (1998). „Arctic springtime depletion of mercury“. In: *Nature* 394.6691, pp. 331–332. ISSN: 0028-0836. DOI: [10.1038/28530](https://doi.org/10.1038/28530).
- Seinfeld, H. and N. Pandis (2006). *Atmospheric Chemistry and Physics: From Air Pollution to Climate Change*. Vol. 2. Hoboken, New Jersey: John Wiley & Sons, Inc.
- Seitz, K., J. Buxmann, D. Pöhler, T. Sommer, J. Tschritter, T. Neary, C. O’Dowd, and U. Platt (2010). „The spatial distribution of the reactive iodine species IO from simultaneous active and passive DOAS observations“. In: *Atmospheric Chemistry and Physics* 10.5, pp. 2117–2128. DOI: [10.5194/acp-10-2117-2010](https://doi.org/10.5194/acp-10-2117-2010).
- Seitz, K. (2009). „The Spatial Distribution of Reactive Halogen Species at the Irish West Coast“. PhD thesis. Heidelberg University. URL: <http://www.ub.uni-heidelberg.de/archiv/9442>.
- Sellegrì, K., Y. J. Yoon, S. G. Jennings, C. D. O’Dowd, L. Pirjola, S. Cautenet, H. Chen, and T. Hoffmann (2005). „Quantification of Coastal New Ultra-Fine Particles Formation from In situ and Chamber Measurements during the BIOFLUX Campaign“. In: *Environ. Chem.* 2.4, pp. 260–270. DOI: [10.1071/EN05074](https://doi.org/10.1071/EN05074).

- Shah, M., R. G. Wuilloud, S. S. Kannamkumarath, and J. A. Caruso (2005). „Iodine speciation studies in commercially available seaweed by coupling different chromatographic techniques with UV and ICP-MS detection“. In: *J. Anal. At. Spectrom.* 20 (3), pp. 176–182. DOI: 10.1039/B415756G.
- Sihler, H. (2012). „Halogen Activation in the Polar Troposphere“. PhD thesis. Heidelberg University. URL: <http://www.ub.uni-heidelberg.de/archiv/13663>.
- Sihler, H., C. Kern, D. Pöhler, and U. Platt (2009). „Applying light-emitting diodes with narrowband emission features in differential spectroscopy“. In: *Opt. Lett.* 34.23, pp. 3716–3718. DOI: 10.1364/OL.34.003716.
- Simpson, W. R., R. von Glasow, K. Riedel, P. Anderson, P. Ariya, J. Bottenheim, J. Burrows, L. J. Carpenter, U. Frieß, M. E. Goodsite, D. Heard, M. Hutterli, H.-W. Jacobi, L. Kaleschke, B. Neff, J. Plane, U. Platt, A. Richter, H. Roscoe, R. Sander, P. Shepson, J. Sodeau, A. Steffen, T. Wagner, and E. Wolff (2007). „Halogens and their role in polar boundary-layer ozone depletion“. In: *Atmospheric Chemistry and Physics* 7.16, pp. 4375–4418. DOI: 10.5194/acp-7-4375-2007.
- Simpson, W. R., S. S. Brown, A. Saiz-Lopez, J. A. Thornton, and R. v. Glasow (2015). „Tropospheric Halogen Chemistry: Sources, Cycling, and Impacts“. In: *Chemical Reviews*. DOI: 10.1021/cr5006638.
- Smyth, P., R. Burns, R. Huang, T. Hoffman, K. Mullan, U. Graham, K. Seitz, U. Platt, and C. O’Dowd (2011). „Does iodine gas released from seaweed contribute to dietary iodine intake?“ English. In: *Environmental Geochemistry and Health* 33.4, pp. 389–397. ISSN: 0269-4042. DOI: 10.1007/s10653-011-9384-4.
- Solomon, S. (1999). „Stratospheric ozone depletion: A review of concepts and history“. In: *Reviews of Geophysics* 37.3, pp. 275–316. DOI: 10.1029/1999RG900008.
- Spietz, P., J. Gómez Martín, and J. P. Burrows (2006). „Effects of column density on I<sub>2</sub> spectroscopy and a determination of I<sub>2</sub> absorption cross section at 500 nm“. In: *Atmospheric Chemistry and Physics* 6.8, pp. 2177–2191. DOI: 10.5194/acp-6-2177-2006.
- Spietz, P. (2005). „Absorption cross sections for iodine species of relevance to the photolysis of mixtures of I<sub>2</sub> and O<sub>3</sub> and for the atmosphere“. PhD thesis. Univ. of Bremen, Germany.
- Spietz, P., J. C. G. Martín, and J. P. Burrows (2005). „Spectroscopic studies of the I<sub>2</sub>/O<sub>3</sub> photochemistry: Part 2. Improved spectra of iodine oxides and analysis of the IO absorption spectrum“. In: *Journal of Photochemistry and Photobiology A: Chemistry* 176.1–3. In Honour of Professor Richard P. Wayne, pp. 50–67. DOI: 10.1016/j.jphotochem.2005.08.023.
- Steffen, A., T. Douglas, M. Amyot, P. Ariya, K. Aspö, T. Berg, J. Bottenheim, S. Brooks, F. Cobbett, A. Dastoor, A. Dommergue, R. Ebinghaus, C. Ferrari, K. Gardfeldt, M. E. Goodsite, D. Lean, A. J. Poulain, C. Scherz, H. Skov, J. Sommar, and C. Temme (2008). „A

- synthesis of atmospheric mercury depletion event chemistry in the atmosphere and snow“. In: *Atmospheric Chemistry and Physics* 8.6, pp. 1445–1482. DOI: [10.5194/acp-8-1445-2008](https://doi.org/10.5194/acp-8-1445-2008).
- Stocker, T., D. Qin, G. K. Plattner, M. Tignor, S. Allen, J. Boschung, A. Nauels, V. B. Y. Xia, and P. Midgley, eds. (2013). *Climate Change 2013: The Physical Science Basis. Contribution of Working Group I to the Fifth Assessment Report of the Intergovernmental Panel on Climate Change*. Cambridge, United Kingdom and New York, NY, USA: Cambridge University Press. ISBN: 9781107415324. DOI: [10.1017/CBO9781107415324](https://doi.org/10.1017/CBO9781107415324).
- Stutz, J., E. S. Kim, U. Platt, P. Bruno, C. Perrino, and A. Febo (2000). „UV-visible absorption cross sections of nitrous acid“. In: *Journal of Geophysical Research: Atmospheres* 105.D11, pp. 14585–14592. DOI: [10.1029/2000JD900003](https://doi.org/10.1029/2000JD900003).
- Stutz, J., O. Pikel'naya, S. C. Hurlock, S. Trick, S. Pechtl, and R. von Glasow (2007). „Daytime OIO in the Gulf of Maine“. In: *Geophysical Research Letters* 34.22, n/a–n/a. DOI: [10.1029/2007GL031332](https://doi.org/10.1029/2007GL031332).
- Stutz, J. (1996). „Messung der Konzentration troposphärischer Spurenstoffe mittels Differentieller-Optischer-Absorptionsspektroskopie: Eine neue Generation von Geräten und Algorithmen“. PhD thesis. Universität Heidelberg.
- Stutz, J., R. Ackermann, J. D. Fast, and L. Barrie (2002). „Atmospheric reactive chlorine and bromine at the Great Salt Lake, Utah“. In: *Geophysical Research Letters* 29.10, ISSN: 1542-9576. DOI: [10.1029/2002GL014812](https://doi.org/10.1029/2002GL014812).
- Stutz, J. and U. Platt (1996). „Numerical analysis and error estimation of differential optical absorption spectroscopy measurements with least squares methods“. In: *Appl. Opt.* 35, pp. 6041–6053. DOI: [10.1364/AO.35.006041](https://doi.org/10.1364/AO.35.006041).
- Stutz, J. and U. Platt (1997). „Improving long-path differential optical absorption spectroscopy with a quartz-fiber mode mixer“. In: *Appl. Opt.* 36.6, pp. 1105–1115. DOI: [10.1364/AO.36.001105](https://doi.org/10.1364/AO.36.001105).
- Su, H., Y. Cheng, R. Oswald, T. Behrendt, I. Trebs, F. X. Meixner, M. O. Andreae, P. Cheng, Y. Zhang, and U. Pöschl (2011). „Soil Nitrite as a Source of Atmospheric HONO and OH Radicals“. In: *Science* 333.6049, pp. 1616–1618. DOI: [10.1126/science.1207687](https://doi.org/10.1126/science.1207687).
- Thalman, R. and R. Volkamer (2013). „Temperature dependent absorption cross-sections of O<sub>2</sub>-O<sub>2</sub> collision pairs between 340 and 630 nm and at atmospherically relevant pressure“. In: *Phys. Chem. Chem. Phys.* 15 (37), pp. 15371–15381. DOI: [10.1039/C3CP50968K](https://doi.org/10.1039/C3CP50968K).
- Thieser, J. (2008). „Cavity Enhanced DOAS: Geräteentwicklung und in-situ Feldmessungen von NO<sub>3</sub>“. Diplomarbeit. Universität Heidelberg.
- Toumi, R. (1994). „BrO as a sink for dimethylsulphide in the marine atmosphere“. In: *Geophysical Research Letters* 21.2, pp. 117–120. DOI: [10.1029/93GL03536](https://doi.org/10.1029/93GL03536).

- Truesdale, V. W., A. J. Bale, and E. M. S. Woodward (2000). „The meridional distribution of dissolved iodine in near-surface waters of the Atlantic Ocean“. In: *Progress in Oceanography* 45.3â€“4, pp. 387–400. ISSN: 0079-6611. DOI: [10.1016/S0079-6611\(00\)00009-4](https://doi.org/10.1016/S0079-6611(00)00009-4).
- Truesdale, V. W., C. Canosa-Mas, and G. W. Luther III (1994). „Kinetics of disproportionation of hypiodous acid“. In: *J. Chem. Soc., Faraday Trans. 90* (24), pp. 3639–3643. DOI: [10.1039/FT9949003639](https://doi.org/10.1039/FT9949003639).
- Tschritter, J. (2013). „Untersuchung mariner Halogenemissionen im tropischen Atlantik“. PhD thesis. Heidelberg. URL: <http://www.ub.uni-heidelberg.de/archiv/15312>.
- Tucceri, M. E., D. Holscher, A. Rodriguez, T. J. Dillon, and J. N. Crowley (2006). „Absorption cross section and photolysis of OIO“. In: *Phys. Chem. Chem. Phys.* 8 (7), pp. 834–846. DOI: [10.1039/B512702E](https://doi.org/10.1039/B512702E).
- Vandaele, A. C., C. Hermans, S. Fally, M. Carleer, R. Colin, M.-F. Mérienne, A. Jenouvrier, and B. Coquart (2002). „High-resolution Fourier transform measurement of the NO<sub>2</sub> visible and near-infrared absorption cross-section: Temperature and Pressure effects“. In: *J. Geophys. Res.* 107.D18, DOI: [10.1029/2001JD000971](https://doi.org/10.1029/2001JD000971).
- Vandaele, A., C. Hermans, P. Simon, M. Carleer, R. Colin, S. Fally, M. Mérienne, A. Jenouvrier, and B. Coquart (1998). „Measurements of the {NO<sub>2</sub>} absorption cross-section from 42 000 cm<sup>-1</sup> to 10 000 cm<sup>-1</sup> (238–1000 nm) at 220 K and 294 K“. In: *Journal of Quantitative Spectroscopy and Radiative Transfer* 59.3–5. Atmospheric Spectroscopy Applications 96, pp. 171–184. DOI: [10.1016/S0022-4073\(97\)00168-4](https://doi.org/10.1016/S0022-4073(97)00168-4).
- Verhaeghe, E. F., A. Fraysse, J.-L. Guerquin-Kern, T.-D. Wu, G. Deves, C. Mioskowski, C. Leblanc, R. Ortega, Y. Ambroise, and P. Potin (2008). „Microchemical imaging of iodine distribution in the brown alga *Laminaria digitata* suggests a new mechanism for its accumulation“. In: *JBIC Journal of Biological Inorganic Chemistry* 13.2, pp. 257–269. DOI: [10.1007/s00775-007-0319-6](https://doi.org/10.1007/s00775-007-0319-6).
- Vilter, H. (1984). „Peroxidases from phaeophyceae: A vanadium(V)-dependent peroxidase from *Ascophyllum nodosum*“. In: *Phytochemistry* 23.7, pp. 1387–1390. ISSN: 0031-9422. DOI: [10.1016/S0031-9422\(00\)80471-9](https://doi.org/10.1016/S0031-9422(00)80471-9).
- Vogel, L., H. Sihler, J. Lampel, T. Wagner, and U. Platt (2013). „Retrieval interval mapping: a tool to visualize the impact of the spectral retrieval range on differential optical absorption spectroscopy evaluations“. In: *Atmos. Meas. Tech.* 6.2, pp. 275–299. DOI: [10.5194/amt-6-275-2013](https://doi.org/10.5194/amt-6-275-2013).
- Volkamer, R., S. Baidar, T. L. Campos, S. Coburn, J. P. DiGangi, B. Dix, E. W. Eloranta, T. K. Koenig, B. Morley, I. Ortega, B. R. Pierce, M. Reeves, R. Sinreich, S. Wang, M. A. Zondlo, and P. A. Romashkin (2015). „Aircraft measurements of BrO, IO, glyoxal, NO<sub>2</sub>, H<sub>2</sub>O, O<sub>2</sub>–<sub>2</sub> and aerosol extinction profiles in the tropics: comparison with aircraft-/ship-based in situ and

- lidar measurements“. In: *Atmospheric Measurement Techniques* 8.5, pp. 2121–2148. DOI: 10.5194/amt-8-2121-2015.
- Volkamer, R., P. Spietz, J. Burrows, and U. Platt (2005). „High-resolution absorption cross-section of glyoxal in the UV-vis and IR spectral ranges“. In: *J. Photochem. Photobiol. A: Chem.* 172.1, 35–46. DOI: 10.1016/j.jphotochem.2004.11.011.
- Wada, R., J. M. Beames, and A. J. Orr-Ewing (2007). „Measurement of IO radical concentrations in the marine boundary layer using a cavity ring-down spectrometer“. In: *Journal of Atmospheric Chemistry* 58.1, pp. 69–87. DOI: 10.1007/s10874-007-9080-z.
- Wang, S. C. and R. C. Flagan (1990). „Scanning Electrical Mobility Spectrometer“. In: *Aerosol Science and Technology* 13.2, pp. 230–240. DOI: 10.1080/02786829008959441. eprint: <http://dx.doi.org/10.1080/02786829008959441>.
- Washenfelder, R. A., A. O. Langford, H. Fuchs, and S. S. Brown (2008). „Measurement of glyoxal using an incoherent broadband cavity enhanced absorption spectrometer“. In: *Atmos. Chem. Phys.* 8, pp. 7779–7793. DOI: 10.5194/acp-8-7779-2008.
- Wayne, R., G. Poulet, P. Biggs, J. Burrows, R. Cox, P. Crutzen, G. Hayman, M. Jenkin, G. L. Bras, G. Moortgat, U. Platt, and R. Schindler (1995). „Halogen oxides: Radicals, sources and reservoirs in the laboratory and in the atmosphere“. In: *Atmospheric Environment* 29.20. Halogen oxides: Radicals, sources and reservoirs in the laboratory and in the atmosphere, pp. 2677–2881. DOI: 10.1016/1352-2310(95)98124-Q.
- Wenig, M., B. Jähne, and U. Platt (2005). „Operator representation as a new differential optical absorption spectroscopy formalism“. In: *Appl. Opt.* 44.16, pp. 3246–3253. DOI: 10.1364/AO.44.003246.
- Wessel, P. and W. H. F. Smith (1996). „A global, self-consistent, hierarchical, high-resolution shoreline database“. In: *Journal of Geophysical Research: Solid Earth* 101.B4, pp. 8741–8743. DOI: 10.1029/96JB00104. URL: <https://www.ngdc.noaa.gov/mgg/shorelines/gshhs.html>.
- Wever, R., M. G. M. Tromp, B. E. Krenn, A. Marjani, and M. V. Tol (1991). „Brominating activity of the seaweed *Ascophyllum nodosum*: impact on the biosphere“. In: *Environmental Science & Technology* 25.3, pp. 446–449. DOI: 10.1021/es00015a010.
- Whalley, L. K., K. L. Furneaux, T. Gravestock, H. M. Atkinson, C. S. E. Bale, T. Ingham, W. J. Bloss, and D. E. Heard (2007). „Detection of iodine monoxide radicals in the marine boundary layer using laser induced fluorescence spectroscopy“. In: *Journal of Atmospheric Chemistry* 58.1, pp. 19–39. DOI: 10.1007/s10874-007-9075-9.
- Winter, J. M. and B. S. Moore (2009). „Exploring the chemistry and biology of vanadium-dependent haloperoxidase“. In: *Journal of Biological Chemistry* 284.28, pp. 18577–18581. DOI: 10.1074/jbc.R109.001602.

- WMO (2010). *WMO Guide to Meteorological Instruments and Methods of Observation*. 2008 edition. WMO No 8. ISBN: 978-92-63-10008-5. URL: [http://library.wmo.int/pmb\\_ged/wmo\\_8\\_en-2012.pdf](http://library.wmo.int/pmb_ged/wmo_8_en-2012.pdf).
- Yilmaz, S. (2012). „Retrieval of Atmospheric Aerosol and Trace Gas Vertical Profiles using Multi-Axis Differential Optical Absorption Spectroscopy“. PhD thesis. Heidelberg University. URL: <http://www.ub.uni-heidelberg.de/archiv/13128>.
- Yin, F., D. Grosjean, and J. Seinfeld (1990). „Photooxidation of dimethyl sulfide and dimethyl disulfide. I: Mechanism development“. English. In: *Journal of Atmospheric Chemistry* 11.4, pp. 309–364. DOI: 10.1007/BF00053780.
- Yokelson, R. J., J. B. Burkholder, R. W. Fox, R. K. Talukdar, and A. R. Ravishankara (1994). „Temperature Dependence of the NO<sub>3</sub> Absorption Spectrum“. In: *The Journal of Physical Chemistry* 98.50, pp. 13144–13150. DOI: 10.1021/j100101a009.
- Young, E. G. and W. M. Langille (1958). „THE OCCURRENCE OF INORGANIC ELEMENTS IN MARINE ALGAE OF THE ATLANTIC PROVINCES OF CANADA“. In: *Canadian Journal of Botany* 36.3, pp. 301–310. DOI: 10.1139/b58-026.
- Yung, Y. L., J. P. Pinto, R. T. Watson, and S. P. Sander (1980). „Atmospheric Bromine and Ozone Perturbations in the Lower Stratosphere“. In: *J. Atmos. Sci.* 37.2, pp. 339–353. DOI: 10.1175/1520-0469(1980)037<0339:ABAOPI>2.0.CO;2.
- Zeng, T., Y. Wang, K. Chance, E. V. Browell, B. A. Ridley, and E. L. Atlas (2003). „Widespread persistent near-surface ozone depletion at northern high latitudes in spring“. In: *Geophysical Research Letters* 30.24. 2298, n/a–n/a. ISSN: 1944-8007. DOI: 10.1029/2003GL018587.
- Zielcke, J. (2015). „Observations of reactive bromine, iodine and chlorine species in the Arctic and Antarctic with Differential Optical Absorption Spectroscopy“. PhD thesis. Heidelberg University. URL: <http://archiv.ub.uni-heidelberg.de/volltextserver/18932/>.



# Aknowledgements

## *Vielen Dank/ Thank you:*

- Ganz speziell und auch an erster Stelle möchte ich mich bei meinem Doktorvater Prof. Dr. Ulrich Platt bedanken, der mir die Möglichkeit gegeben hat diese spannende Arbeit durchzuführen. Die zahlreichen Anregungen und Diskussionen waren von unschätzbarem Wert für diese Arbeit.
- Vielen Dank an PD Dr. Christoph Garbe für die unkomplizierte Übernahme des Zweitgutachtens.
- Mein allergrößter Dank gilt Dr. Denis Pöhler der mir während der gesamten Arbeit mit Rat und Tat zur Seite stand. Besonders großer Dank gebührt Ihm für seinen unermüdlichen Einsatz während, der Messkampagnen in Irland und den Fernsupport in Neuseeland, für die guten Ratschläge und Ideen zum Instrumentenbau und für die Hilfe bei der LP-DOAS Datenauswertung.
- Einen genauso herzlichen Dank an Stefan Schmitt für die super Zusammenarbeit während der Messkampagnen in Irland und Neuseeland und die vielen Diskussionen und Anregungen zur Datenauswertung und -interpretation.
- Dr. John Crowley und Prof. Dr. Jos Lelieveld möchte ich ebenfalls herzlich Danken als weitere Mitglieder meines PAC-Komitees.
- I would like to thank Prof. Dr. Collin O'Dowd and Dr. Darius Ceburnis from NUIG for the great support during both Ireland Capaigns, paticularly for the possibility to use the infrastructure at the Mace Head Reasrch station and for providing met data and nano-SMPS measurements.
- Many thanks to Dr. Richard Fitzgerald and the Staff at MRI for the possibility to use their laboratories during both Ireland Campaigns and for the great support.
- Special thanks goes to the Heron family for the warm welcome in Carna and for being fantastic hosts.
- I would like to thank Dr. Karin Kreher, Dr. Paul Johnston and Allan Thomas for great collaboration and support during the New Zealand Campaign, particularly for organizing the infrastructure. I would also like to thank Colleen our neighbor in Shag Point for the nice dinner evenings and great stories.
- Der gesamten Arbeitsgruppe Luftchemie für die gute Arbeitsatmosphäre.

## Appendix D. Acknowledgements

---

- Vielen dank an alle Koellegen und Freunde die diese Arbeit Korrektur gelesen und Anregungen beigesteuert haben: Denis Pöhler, Jan Krieger, Johannes Lampel, Lara Penth, Peter Lübcke und Zoë Davis.
- Vielen Dank Johannes Zielcke für die gute Zusammenarbeit der Konstruktion der Cavites, und den gemeinsamen Sommer im Cavity Labor. Mit viel Club Mate, Red Bull und der einen oder anderen Fluchtirade konnten die meisten Probleme erfolgreich gelöst werden.
- Vielen Dank an meine wunderbaren Bürokollegen Lara Penth, Stefan Schmitt und Jan-Marcus Nasse für die schöne Zeit, die vielen wissenschaftlichen und Diskussionen, und den ganzen Wahnsinn.
- I would like to thank my friends for their support in the last years. Besonders bedanken möchte ich mich bei Jan und Taba für die schönen Kino und Kochabende und die aufmunternden Worte während der finalen Phase meiner Doktorarbeit. Vielen Dank an Katharina und die “Häll-Clique” für die vielen schönen und verrückten Abende. Many tanks to Little Monster for being an awesome friend and for the many serious and even more cheerfully silly conversations.
- Meinen Mitbewohnern Clarissa, Matthias und Samantha danke ich für die schöne Zeit und dass ihr mich in den letzten Wochen vor der Abgabe ausgehalten habt.
- Zu guter Letzt möchte ich mich ganz Herzlich bei meinen Eltern und meiner Schwester bedanken für die großartige Unterstützung, dass ihr immer an mich geglaubt habt und dafür dass es euch gibt.